UNIVERSITAT DE BARCELONA

Nanostructured Metal Sulfides for Electrochemical Energy Conversion

Yong Zuo

Aquesta tesi doctoral està subjecta a la llicència ***Reconeixement- NoComercial – SenseObraDerivada 4.0. Espanya de Creative Commons***.

Esta tesis doctoral está sujeta a la licencia ***Reconocimiento - NoComercial – SinObraDerivada 4.0. España de Creative* Commons**.

This doctoral thesis is licensed under the ***Creative Commons Attribution-NonCommercial-NoDerivs 4.0. Spain License***.

Tesi doctoral

Nanostructured Metal Sulfides for Electrochemical Energy Conversion

Autor:

Yong Zuo

Director:

Prof. Andreu Cabot

UNIVERSITAT DE BARCELONA

Nanostructured Metal Sulfides for Electrochemical Energy Conversion

Memòria presentada per optar al grau de doctor per la Universitat de Barcelona

Programa de doctorat en Nanociències

Autor:

Yong Zuo

Director:

Prof. Andreu Cabot

Tutor:

Prof. Joan Ramón Morante

Lloc on s'ha dut a terme la tesi

Institut de Recerca en Energia de Catalunya (IREC)

UNIVERSITAT DE BARCELONA

Contents

Acknowledgements

Four years ago, when I got the chance to pursue my PhD degree outside China, I was a little bit nervous but also excited about the amazing journey I would step on. Time flies, almost four years later, I am sitting in front of my desk in a quiet room, in this hard time due to COVID-19 issue, taking a longtime to look back of my past four years. I can't believe it is time to say goodbye to all of you, since I can still clear remember the first day when I stepped in this amazing Mediterranean city of Barcelona. Sincerely, I have a lot of thanks to all the people who have helped me, taught me, and supported me. I don't think it can be possible to fulfill my PhD without your generous assistance!

First and foremost, I would like to convey my deepest gratefulness to my supervisor Prof. Andreu Cabot. I want to thank you so much for the valuable chance you gave me, not only accepting me as your student, but also supporting me a special visit at EPFL in Switzerland. Thank you for opening me a beautiful world of nanoscience and advising me a lot in it. You encouraged me and gave me freedom to roam in the wonderful research world, and when I got stuck or confused, you were always there to share me your smart ideas and suggestions. I want to say that your critical way of thinking, rigorous logic and inspiring insights have impressed me significantly, and I have learnt a lot from you, which are really important treasures for a young researcher like me to become a future scholar like you. Thank you!

Secondly, I want to thank our friendly Functional Nanomaterials group members, Michaela, Taisiia, Pablo, Ievgenii, Alberto, Marcos, Mike, Sergi, Swapneel, Parizi, and especially the Chinese community including Prof. Kai Pan, Dr. Zhishan, Yu Liu, Junfeng, Xiaoting, Junshan, Yu Zhang, Mengyao, Congcong, Chaoqi, Ruifeng, Xiang, Dawei, Ke and Zhifu. I wish you have a wonderful future! And also I would like to thank other fantastic people from other groups in IREC, Pengyi, Haibing, Qin. Many thanks to the nice IREC people who did good job to guarantee us a wonderful conditions, in terms of both research work and daily life. Thanks for your hard work!

Also, I am grateful to the nice characterization work from Prof. Jordi Arbiol group at ICN2 in UAB, including Ting Zhang, Xu Han. Your fantastic TEM images and professional analysis gave me useful instructions on research work, and also made my research results much easier to be published in decent journals with high impact factor.

I want to give my appreciation to Prof. Jordi Llorca group in UPC for their excellent XPS measurements and analysis. Special thanks go to Dr. N.J. Divins for your patient characterization work and data analysis in Cu_2S work.

I would like to thank Prof. Jun Liu and Dr. Xijun Xu from South China University of Technology for the electrochemical measurements of the Li-ion batteries.

Specially, I want to sincerely thank Prof. Kevin Sivula group at EPFL in Switzerland, including Yongpeng Liu, Nestor Guijarro, Liang Yao. Thank you for your nice characterization work and analysis in photoelectrochemical part in SnS_2-Pt work and *in-situ* Raman part in Cu_2S work. Special thanks go to Yongpeng for the suggestive talk.

Besides, I want to express my big appreciation to Prof. Raffaella Buonsanti at EPFL in Switzerland. Thank you for hosting me as a visiting student in your nice group, and I indeed have learnt a lot. I also want to thank all the nice people in your group for the generous help and interesting talk. Special thanks go to Pranit Iyengar for sharing your tidy fume hood with me, and showing me how to do the electrocatalytic CO_2 reduction and data analysis.

I also want to thank all the friends who helped me and cared about me. Special thanks go to Jennifer Ho for all your heartful assistance from the day I came here.

The financial support for my PhD research work is from China Scholarship Council (No. 201606500001). Many thanks for giving me this precious opportunity!

Last but not least, my appreciation beyond words should be given to my beloved family members: my parents, brother, sister-in-law, parents-in-law, and my wife. Thank you for your true love and persistent support! No matter where I will be, you are always my harbor of soul. Specially, to my future Dr. wife, XUENI DI, it is really my biggest fortune to have you. You have made my life colorful and wonderful. Thank you for all your company, support, and encouragement. I will always remember our life in this romantic city. Let's step together to the beautiful future, and I promise you will have it! Te quiero!

¡Muchas gracias a todos!

Barcelona, Spain

April, 2020

List of Publications

The research work during my PhD period can be included in four peer-reviewed publications. The full copy of each of the publication can be found in the Annex part in the end of the thesis. The list of the publication is shown as follows:

1. **Y. Zuo**, Y. Liu, J. Li, R. Du, X. Han, T. Zhang, J. Arbiol, N.J. Divins, J. Llorca, N. Guijarro, K. Sivula, A. Cabot. In-situ Electrochemical Oxidation of Cu_2S into CuO Nanowires as a Durable and Efficient Electrocatalyst for Oxygen Evolution Reaction. *Chemistry of Materials*. **2019**, 31, 7732-7743.

2. **Y. Zuo**, Y. Liu, J. Li, R. Du, X. Yu, C Xing, T. Zhang, L. Yao, J. Arbiol, J. Llorca, K. Sivula, N. Guijarro, A. Cabot. Solution-Processed Ultrathin SnS_2-Pt Nanoplates for Photoelectrochemical Water Oxidation. *ACS Applied Materials & Interfaces*, **2019**, 11, 6918-6926.

3. **Y. Zuo**, J. Li, R. Du, X. Yu, T. Zhang, X. Wang, J. Arbiol, J. Llorca, A. Cabot. A SnS_2 Molecular Precursor for Conformal Nanostructured Coatings. *Chemistry of Materials*. **2020**, 32, 2097-2106.

4. **Y. Zuo**, X. Xu, C. Zhang, J. Li, R. Du, X. Wang, X. Han, J. Arbiol, J. Llorca, J. Liu, A. Cabot. SnS_2/g-C_3N_4/Graphite Nanocomposites as Durable Lithium-Ion Battery Anode with High Pseudocapacitance Contribution. *Electrochimica Acta*, **2020**, 349, 136369.

Apart from the publication listed above, I also contributed to some other projects during my PhD period, which are not shown in this thesis. Some of these publications are listed below:

5. J. Li, **Y. Zuo**, J. Liu, X. Wang, X. Yu, R. Du, T. Zhang, P. Tang, M. Infante-Carrió, J. Arbiol, J. Llorca, Z. Luo, A. Cabot. Superior methanol electrooxidation performance of (110)-faceted nickel polyhedral nanocrystals. *Journal of Materials Chemistry A*, **2019**, 7, 22036-22043.

6. M. Li, Y. Liu, Y. Zhang, **Y. Zuo**, J. Li, K. Lim, D. Cadavid, K. Ng, A. Cabot*. Crystallographically textured SnSe nanomaterials produced from the liquid phase sintering of nanocrystals. *Dalton Transactions*. **2019**, 48, 3641-3647.

7. P. Shaw, M. Meyns, **Y. Zuo**, A. Grau-Carbonell, P. Lagoudakis, M. Charlton, S. Martí-Sánchez, J. Arbiol, A. Cabot, A. Kanaras. Colloidal Synthesis of CsX Nanocrystals (X= Cl, Br, I). *Nanomaterials*, **2018**, 8, 506.

8. J. Li, Z. Luo, **Y. Zuo**, J. Liu, T. Zhang, P. Tang, J. Arbiol, J. Llorca, A. Cabot. NiSn bimetallic nanoparticles as stable electrocatalysts for methanol oxidation reaction. *Applied Catalysis B: Environmental*, **2018**, 234, 10-18.

9. J. Li, Z. Luo, F. He, **Y. Zuo**, C. Zhang, J. Liu, X. Yu, R. Du, T. Zhang, M. Infante-Carrió, P. Tang, J. Arbiol, J. Llorca, A. Cabot. Colloidal Ni–Co–Sn nanoparticles as efficient electrocatalysts for the methanol oxidation reaction. *Journal of Materials Chemistry A*, **2018**, 6, 22915-22924.

Authors' Contributions

The work presented in this thesis was carried out in the Functional Nanomaterials group of Catalonia Institute for Energy Research. In all the publications presented in this thesis, Yong Zuo, contributed to the mainly part of the work, including experiment design, material synthesis, electrochemical measurements, data analysis and original paper writing. Prof. Andreu Cabot conceived and guided the project, significantly participated in the results discussion and manuscript corrections. The contribution of co-author for each paper has been indicated below this paragraph. The impact factor in 2018/2019 of the journal where the manuscript was published is also provided. According to the Journal Citation Reports, all the publications belong to the 1st quartile. None of the publications in this thesis was presented in any other PhD theses.

Chapter 2:

Y. Zuo, Y. Liu, J. Li, R. Du, X. Han, T. Zhang, J. Arbiol, N.J. Divins, J. Llorca, N. Guijarro, K. Sivula, A. Cabot. In-situ Electrochemical Oxidation of Cu_2S into CuO Nanowires as a Durable and Efficient Electrocatalyst for Oxygen Evolution Reaction. *Chemistry of Materials*. **2019**, 31, 7732-7743.

Impact Factor 2018/19: 10.159

In this work, Y. Zuo designed the experiments, produced the nanoparticles, conducted XRD, TEM, SEM-EDX characterization, oxygen evolution reaction measurements, and wrote the first draft of the manuscript. J. Li and R. Du significantly contributed to the results discussion. X. Han, T. Zhang and J. Arbiol performed structural and compositional characterization by means of HRTEM and EELS, and discussed the results. N.J. Divins and J. Llorca measured and discussed XPS data. Y. Liu, N. Guijarro and K. Sivula carried out the *in-situ* Raman measurements and discussed the results. A. Cabot conceived and guided the project, and supervised the work. The manuscript was corrected and improved by all authors.

Chapter 3:

Y. Zuo, Y. Liu, J. Li, R. Du, X. Yu, C Xing, T. Zhang, L. Yao, J. Arbiol, J. Llorca, K. Sivula, N. Guijarro, A. Cabot. Solution-Processed Ultrathin SnS_2-Pt Nanoplates for

Photoelectrochemical Water Oxidation. *ACS Applied Materials & Interfaces*, **2019**, 11, 6918-6926.

Impact Factor 2018/19: 8.456

In this work, Y. Zuo designed the experiments, produced the nanoparticles, conducted XRD, TEM, SEM-EDX and FT-IR characterization, photoelectrochemical measurements, and wrote the first draft of the manuscript. J. Li, R. Du and X. Yu significantly contributed to the results discussion. T. Zhang and J. Arbiol performed structural and compositional NPLs characterization by means of HRTEM and EELS, and discussed the results. J. Llorca measured and discussed XPS data. Y. Liu, K. Sivula and N. Guijarro carried out the PEIS measurements and discussed the results. A. Cabot conceived and guided the project, and supervised the work. The manuscript was corrected and improved by all authors.

Chapter 4:

Y. Zuo, J. Li, R. Du, X. Yu, T. Zhang, X. Wang, J. Arbiol, J. Llorca, A. Cabot. A SnS_2 Molecular Precursor for Conformal Nanostructured Coatings. *Chemistry of Materials*. **2020**, 32, 2097-2106.

Impact Factor 2018/19: 10.159

In this work, Y. Zuo designed the experiments, produced the molecular ink, conducted XRD, TEM, SEM-EDX, UV-Vis spectra, FT-IR characterization, photoelectrochemical measurements, and wrote the first draft of the manuscript. J. Li, R. Du, X. Yu and X. Wang contributed to the results discussion and improvement. T. Zhang and J. Arbiol performed structural and compositional characterization by means of HRTEM and EELS, and discussed the results. J. Llorca measured and discussed XPS data. A. Cabot conceived and guided the project, and supervised the work. The manuscript was corrected and improved by all authors.

Chapter 5:

Y. Zuo, X. Xu, C. Zhang, J. Li, R. Du, X. Wang, X. Han, J. Arbiol, J. Llorca, J. Liu, A. Cabot. SnS_2/g-C_3N_4/Graphite Nanocomposites as Durable Lithium-Ion Battery Anode

with High Pseudocapacitance Contribution. *Electrochimica Acta*, **2020**, 349, 136369.

Impact Factor 2018/19: 5.383

In this work, Y. Zuo designed the experiments, produced the electrode materials, conducted XRD, SEM-EDX, FT-IR, TG characterizations and wrote the first draft of the manuscript. X. Xu conducted the performance test on LIB. C. Zhang, J. Li, R. Du and X. Wang significantly contributed to the results discussion. X. Wang contributed to the design of TOC figure. X. Han and J. Arbiol performed structural and compositional characterization by means of HRTEM and EELS, and discussed the results. J. Llorca measured and discussed XPS data. A. Cabot and J. Liu conceived and guided the project, and supervised the work. The manuscript was corrected and improved by all authors.

Prof. Andreu Cabot

certifies that the information provided above is true.

Barcelona, April, 2020

Preface

The research work in this thesis was developed by the PhD candidate of Yong Zuo at Catalonia Institute for Energy Research (IREC) located in Sant Adrià de Besòs, Barcelona, in the period 2016-2020, supported by the China Scholarship Council (No. 201606500001). This thesis is focused on synthesis of nanostructured metal sulfides for electrochemical energy conversion.

This thesis is divided into 9 chapters, including an introductory chapter and 4 chapters of experimental work, and 4 chapters of results, discussion, conclusions and outlook are presented at the end. Within the 4 chapters of experimental work, four kinds of nanomaterials based on metal sulfides, namely Cu_2S (chapter 2) and SnS_2 (chapter 3-5), have been produced and their applications in energy conversion, namely electrochemical oxygen evolution (first block: chapter 2), photoelectrochemical water splitting (second block: chapter 3 and 4), and lithium ion battery (third block: chapter 5) have been investigated.

In the first block included as chapter 2, the *in-situ* transformation on electrocatalyst has been taken advantage of to produce CuO nanowire array from its "pre-catalyst" of Cu_2S through oxygen evolution reaction (OER) process. The *in-situ* chemical, structural and morphological transformation during the OER has been elucidated, and the Cu_2S-derived CuO electrocatalyst shows extraordinary performance towards OER.

In the second block, chapter 3, a hot-injection solution-based process was detailed to produce ultrathin SnS_2 nanoplates (NPLs). To improve its performance towards photoelectrochemical (PEC) water splitting, a series amount of Pt nanodomain was grown on their surface via *in-situ* reduction of a Pt salt, and working electrodes based on SnS_2-Pt heterostructured nanocomposite were drop-casted on the surface of fluorine doped tin oxide (FTO) glass slides for posterior PEC test. The optimized loading amount of Pt on SnS_2-NPLs showed a six-fold improvement on PEC performance. However, the drop-casted samples suffer from moderate charge transfer and feeble mechanical stability, which prevents the improvement of PEC performance. To solve this issue, a simple, versatile and scalable amine/thiol-based molecular ink to produce SnS_2 nanostructured layers on the conductive substrates directly has been investigated, and a significant

enhancement on PEC performance has been seen, as shown in chapter 4 included in this same block.

The third block of chapter 5 is based on an interesting phenomenon happened during the synthetic process of SnS_2 in chapter 3 in the second block, where a significant difference of morphology on SnS_2 has been observed by using surfactant oleylamine (OAm) or not. With the addition of OAm and oleic acid (OAc) mixture, pure SnS_2 NPLs could be formed, while SnS_2 microflowers (MFLs) will be produced with no OAm addition. Since SnS_2 can be a promising lithium-ion battery (LIB) anode candidate, and thus a comparison on LIB performance based on these two different structured SnS_2 is meaningful to undertake, and finally a combination of SnS_2-NPL/g-C_3N_4/Graphite nanocomposite has been demonstrated to be the best sample for LIB application among the counterparts.

After the experimental chapters, four chapters of results, discussion of results, conclusions and outlook has been indicated, and the CV of the author is also attached at the end of the thesis.

Summary of Results

Energy crisis is one of the biggest challenges humankind are facing. The current drastic exploitation of fossil fuels could finish all the known fossil sources within the earth crust by the end of this century. To solve the current situation, abundant and environmental-benign renewable sources like sunlight, wind and hydroelectric have drawn people's attention, and are expected to be the dominant energy sources of the future. However, the intrinsic fluctuation of these renewable energy sources requires to simultaneously develop strategies to store the surplus energy during overproduction to make it available when needed. Therefore to store this fluctuating energy into synthetic fuels or in batteries becomes meaningful. In this thesis, four nanostructured catalysts based on two kinds of metal sulfides, namely Cu_2S and SnS_2, were produced and optimized to improve their performance towards three key electrochemical energy conversion processes, namely electrochemical oxygen evolution, photoelectrochemical water splitting and lithium-ion batteries.

In the first chapter, a general introduction is presented to explain the motivation of the thesis topic. In chapter 2, a metallic copper substrate was used as current collector and chemical template to produce Cu_2S nanorod arrays for electrochemical oxygen evolution reaction (OER). Suitable characterization tools were applied to investigate the chemical, structural and morphological transformation in OER operation, during which the initial Cu_2S nanorod arrays would perform as a "pre-catalyst" that in-situ changed to CuO nanowires. Notably, the Cu_2S-derived CuO showed significant improved OER performance compared with that of CuO prepared by directly annealing a $Cu(OH)_2$ precursor, in terms of both activity and stability. Thus obtained electrocatalyst ranked among the best Cu-based OER catalysts reported so far, with an overpotential of 286 mV to deliver a geometric current density of 10 mA/cm^2 (Cu_2S-derived CuO/copper foam). The results were published in *Chemistry of Materials* in 2019.

To take advantage of the unlimited solar energy, an ultrathin SnS_2 NPL with a suitable band gap around 2.2 eV was produced via a hot-injection solution-based process in chapter 3, and the roles of surfactant OAm and OAc were investigated. The synthesized SnS_2 NPLs were drop-casted on FTO after proper treatment and its PEC performance towards water oxidation under simulated sun light was evaluated. The unsatisfied

performance of bare SnS_2 motivated me to deposit Pt NPs on its surface as cocatalyst via *in-situ* reduction of a Pt salt. The resulting SnS_2-Pt heterostructures with optimal Pt amount showed significant improvement (six fold) towards PEC water oxidation. Mott-Schottky analysis and PEC impedance spectroscopy (PEIS) were used to analyze in more detail the effect of Pt on the PEC performance, and the enhanced activity of the SnS_2-Pt photoanode could be ascribed to the intimate contact between Pt NPs and SnS_2 NPLs, where a useful semiconductor-noble metal synergetic effect through an efficient charge transfer of the photogenerated carriers from the semiconductor to the metal domain happens. This work was published in *ACS Applied Materials & Interfaces* in 2019.

The optimal SnS_2-Pt heterostructure developed in the previous work presented acceptable performance towards PEC water splitting. However, it still suffered from a moderate stability due to the peel-off of the catalyst layer from the FTO surface. To solve this problem, in chapter 4 we detail a simple, versatile and scalable amine/thiol-based molecular ink to grow SnS_2 nanostructured layers directly on conductive substrates such as FTO, stainless steel and carbon cloth. Such nanostructured layers on FTO were characterized by excellent photocurrent densities. The same strategy was used to produce SnS_2-graphene composites, $SnS_{2-x}Se_x$ ternary coatings and even phase pure $SnSe_2$ layers. Finally, the potential of this precursor ink to produce gram scale amounts of unsupported SnS_2 was also investigated. The results were published in *Chemistry of Materials* in 2020.

Tin disulfide is not only an excellent photocatalyst, but also a promising anode material for Li-ion batteries (LIB). In chapter 5, nanostructured SnS_2 with different morphologies produced in chapter 3 were tested as LIB anodes. We found out that thin SnS_2 NPLs provided the highest performance. Thereafter, a colloidal synthesis strategy to grow the same SnS_2 NPLs within a matrix of porous g-C_3N_4 (CN) and graphite plates (GPs) was developed and the obtained materials were tested for LIB application. Such hierarchical SnS_2/CN/GP composites using SnS_2-NPL as active materials, porous CN to provide avenues for electrolyte diffusion and ease the volumetric expansion of SnS_2, and GP as "highways" for charge transport displayed excellent rate capabilities (536.5 mAh g^{-1} at 2.0 A g^{-1}) and an outstanding stability (~99.7 % retention after 400 cycles), which were partially associated with a high pseudocapacitance contribution (88.8 % at 1.0 mV s^{-1}). The excellent electrochemical properties of these nanocomposites were ascribed to the synergy created between the three nanocomposite components. This work has been accepted by *Electrochimica Acta* in 2020.

Resumen de Resultados

La crisis energética es uno de los mayores desafíos que enfrenta la humanidad. La drástica explotación actual de los combustibles fósiles podría terminar con todas las fuentes fósiles conocidas en la corteza terrestre para fines de este siglo. Para resolver la situación actual, las fuentes renovables abundantes y benignas para el medio ambiente, como la luz solar, el viento y la hidroeléctrica, han llamado la atención de la gente y se espera que sean las fuentes de energía dominantes del futuro. Sin embargo, la fluctuación intrínseca de estas fuentes de energía renovables requiere desarrollar simultáneamente estrategias para almacenar el excedente de energía durante la sobreproducción para que esté disponible cuando sea necesario. Por lo tanto, almacenar esta energía sobrante en combustibles sintéticos o en baterías se vuelve significativo. En esta tesis, cuatro catalizadores nanoestructurados basados en dos tipos de sulfuros metálicos, a saber, Cu_2S y SnS_2, se producen y se optimizan para mejorar su rendimiento hacia tres procesos clave de conversión de energía electroquímica, a saber, la evolución electroquímica de oxígeno, la descomposición fotoelectroquímica del agua y las baterías de iones de litio.

En el primer capítulo, se presenta una introducción general para explicar la motivación del tema de tesis. En el capítulo 2, se usó un sustrato de cobre metálico como colector de corriente y plantilla química para producir matrices de las nanovarillas de Cu_2S para la reacción electroquímica de evolución de oxígeno (OER). Se aplicaron herramientas de caracterización adecuadas para investigar la transformación química, estructural y morfológica en la operación OER, durante la cual las matrices iniciales de las nanovarillas de Cu_2S funcionarían como un "pre-catalizador" que in situ cambió a nanohilos de CuO. En particular, el CuO derivado de Cu_2S mostró un rendimiento de OER significativamente mejor cuando comparado al de CuO preparado mediante el recocido directo de un precursor de $Cu(OH)_2$, tanto en términos de actividad como de estabilidad. El electrocatalizador obtenido de este modo figura entre los mejores catalizadores OER basados en Cu reportados hasta ahora, con un sobrepotencial de 286 mV para entregar una densidad de corriente geométrica de 10 mA/cm^2 (CuO derivado de Cu_2S / espuma de cobre). Los resultados se publicaron en *Chemistry of Materials* en 2019.

Para aprovechar la energía solar ilimitada, en el capítulo 3 se produjo un SnS_2 NPL ultrafino con una banda prohibida alrededor de 2.2 eV a través de un proceso basado en una solución de inyección en caliente, y se investigaron los roles del surfactante OAm y

OAc. Los NPL de SnS_2 sintetizados se fundieron en FTO después del tratamiento adecuado y se evaluó su rendimiento de PEC hacia la oxidación del agua bajo luz solar simulada. El bajo rendimiento del SnS_2 puro me motivó a depositar nanopartículas de Pt en su superficie como cocatalizador a través de la reducción in situ de una sal de Pt. Las heteroestructuras de SnS_2-Pt con una cantidad óptima de Pt mostraron una mejora significativa (seis veces) hacia la oxidación de agua mediante PEC. El análisis de Mott-Schottky y la espectroscopía de impedancia PEC (PEIS) se utilizaron para analizar con más detalle el efecto de Pt sobre el rendimiento de PEC, y la actividad mejorada del fotoanodo SnS_2-Pt podría atribuirse al contacto íntimo entre Pt NPs y SnS_2 NPLs , donde ocurre un útil efecto sinergético de semiconductores de metales nobles a través de una transferencia de carga eficiente de los portadores fotogenerados del dominio de semiconductores al metal. Este trabajo fue publicado en *ACS Applied Materials & Interfaces* en 2019.

La estructura mejorada de SnS_2-Pt desarrollada en el trabajo anterior presentaba un rendimiento aceptable hacia la descomposición del agua mediante PEC. Sin embargo, todavía sufría una estabilidad moderada debido al desprendimiento de la capa de catalizador de la superficie de FTO. Para resolver este problema, en el capítulo 4 detallamos una tinta molecular simple, versátil y escalable a base de amina/tiol para cultivar capas nanoestructuradas de SnS_2 directamente sobre sustratos conductores como FTO, acero inoxidable y tela de carbón. Tales capas nanoestructuradas en FTO se caracterizaron por excelentes densidades de fotocorriente. Se utilizó la misma estrategia para producir compuestos de grafeno-SnS_2, recubrimientos ternarios $SnS_{2-x}Se_x$ e incluso capas de $SnSe_2$ puro en fase. Finalmente, también se investigó el potencial de esta tinta precursora para producir cantidades en escala de gramo de SnS_2 sin soporte. Los resultados fueron publicados en *Chemistry of Materials* en 2020.

El disulfuro de estaño no solo es un excelente fotocatalizador, sino también un prometedor material anódico para las baterías de iones de litio (LIB). En el capítulo 5, el SnS_2 nanoestructurado con diferentes morfologías producidas en el capítulo 3 fueron estudiados como ánodos LIB. Descubrimos que los NPL delgados SnS_2 proporcionaban el mayor rendimiento. Posteriormente, se desarrolló una estrategia de síntesis coloidal para cultivar los mismos NPL de SnS_2 dentro de una matriz de g-C_3N_4 (CN) poroso y placas de grafito (GP) y los materiales obtenidos fueron investigados para la aplicación en LIB. Tales compuestos jerárquicos SnS_2/CN/GP que usan SnS_2-NPL como materiales

activos, CN poroso para proporcionar vías para la difusión de electrolitos y facilitar la expansión volumétrica de SnS_2, y GP como "autopistas" para el transporte de carga mostraron excelentes capacidades de velocidad (536.5 mAh g^{-1} a 2.0 A g^{-1}) y una estabilidad excepcional (~ 99.7 % de retención después de 400 ciclos), que se asociaron parcialmente con una alta contribución de pseudocapacidad (88.8 % a 1.0 mV s^{-1}). Las excelentes propiedades electroquímicas de estos nanocompuestos se atribuyeron a la sinergia creada entre los tres componentes del nanocompuesto. Este trabajo fue publicado en *Electrochimica Acta* en 2020.

List of Abbreviations

CV	cyclic voltammetry
CC	carbon cloth
CN	graphitic carbon nitride (g-C_3N_4)
CM	copper mesh
CF	copper foam
Edt	ethanedithiol
En	ethylenediamine
EDX	energy-dispersive X-ray spectroscopy
EELS	electron energy loss spectroscopy
EIS	electrochemical Impedance Spectroscopy
FTO	fluorine doped tin oxide
FTIR	fourier transform infrared spectroscopy
GP	graphite plate
GO	graphene oxide
HER	hydrogen evolution reaction
HRTEM	high-resolution transmission electron microscopy
HAADF	high angle annular dark-field imaging
LIB	lithium-ion battery
MFL	microflowers
NC	nanocrystal
NP	nanoparticle
NW	nanowire
NPL	nanoplate
NMP	N-methy1-2-pyrrolidone
OER	oxygen evolution reaction

OAm	oleylamine
OAc	oleic acid
PEC	photoelectrochemical
PEIS	photoelectrochemical impedance spectroscopy
PVDF	polyvinylidene fluoride
RHE	reversible hydrogen electrode
SEM	scanning electron microscope
SEI	solid-electrolyte interface
SS	stainless steel
TG	thermogravimetry
XRD	X-ray diffraction
XPS	X-ray photoelectron spectroscopy

Chapter 1

General Introduction

1.1 The Renewable Energy

The history of civilization has been driven by the development and control of new forms of energy. However, with the rapid development of the society and explosion of population, to secure the future energy supply has becomes one of the humanity's top issues.[1,2] As can been seen in Figure 1.1a, the Energy Information Administration (EIA) foresees that world energy consumption will grow by nearly 50 % between 2018 and 2050. Most of this growth comes from countries that are not in the Organization for Economic Cooperation and Development (OECD), where strong economic growth is driving demand. Currently, fossil fuels, including petroleum, natural gas and coal, currently provide the main part of energy consumption, e.g. 81 % in U.S. in 2018 (Figure 1.1b). According to the current consumption rate and known fossil resource reserves, we will run out of all the fossil fuels at around the end of this century.[3] Apart from the energy crisis, the drastic consumption of fossil fuels is leading to another one of the top issues, greenhouse effect due to huge emission of CO_2, a very common byproduct from fossil fuel consumption.[1] Therefore, to decrease the share of fossil fuel from the total energy consumption in the very near future is extremely urgent.

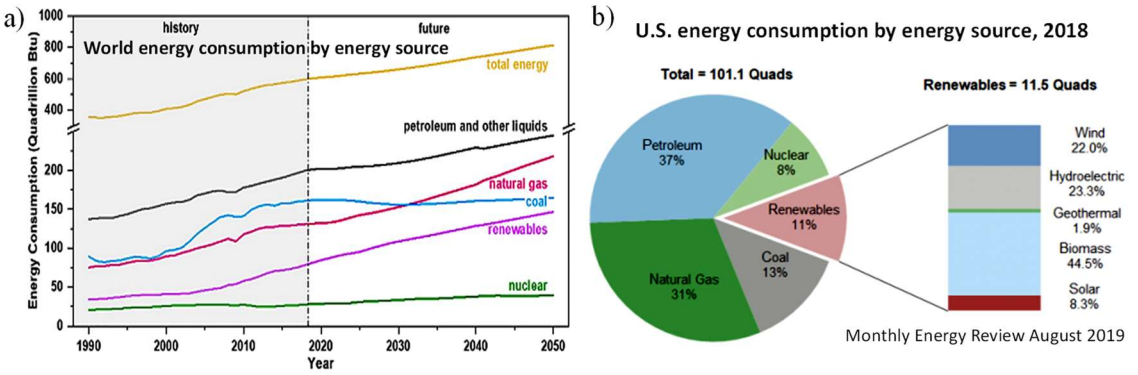

Figure 1.1. (a) World energy consumption by energy source. (b) U.S. energy consumption by energy source in 2018. Quadrillion Btu = 293 billion kWh. Data obtained from EIA: U.S. Energy Information Administration, 2019.[4]

To relieve the energy crisis and environmental issue, the renewable energy can be a good alternative. Still taking the U.S. as an example, the renewable energy contributed

11 % of its total energy consumption in 2018, among which the biomass, hydroelectric, wind, solar and geothermal source shared 44.5 %, 23.3 %, 22 %, 8.3 % and 1.9 % of the 11.5 quadrillion Btu (3.22 trillion kWh) of renewable energy consumed, respectively (Figure 1.1b). According to EIA's project, the renewable energy will become an important energy source of primary energy consumption by 2050, playing a role as important as coal does, and can be even more dominant in further future.[4]

1.2 Energy Conversion Technology

To meet the requirements of renewable and clean energy, the source should be endless and environmental benign.[5] In this direction, the energy, mostly in form of electricity, produced from sunlight, hydropower and wind becomes promising, and has already contributed the main part (53.6 %) of renewable energy, as aforementioned. However, unlike the conventional fossil fuels, solar energy and wind are intermittent and heavily depend on either the time of daylight (*eg.* solar energy) or weather (*eg.* wind), which presents serious disadvantages in energy generation, usage and load balance to ensure the stability and reliability in power network. To solve this issue, we need to develop systems able to compensate for the fluctuating character of these energy supplies. Hence, to store this energy into chemical products, such as chemical fuels or H_2 (Figure 1.2a), or batteries and then convert it back when needed in future (Figure 1.2b) is the best solution.

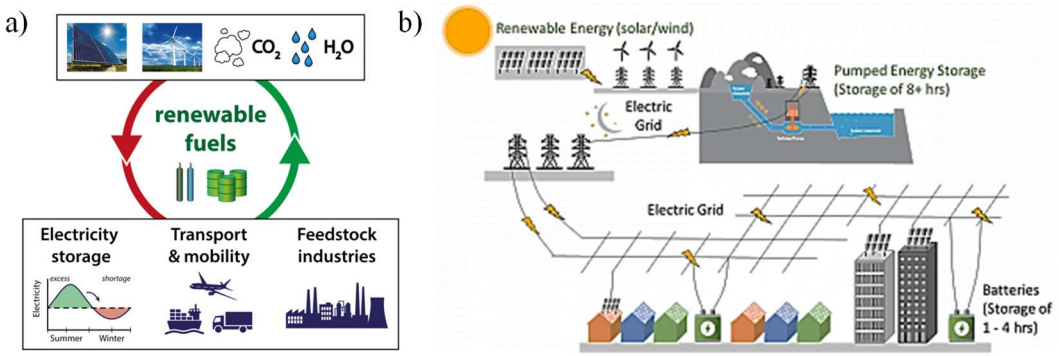

Figure 1.2. (a) An overview of the current technological developments and challenges of fuels and chemicals produced from renewable energy.[6] (b) Renewable energy storage process.[7]

To meet the cost-effectiveness requirements of energy conversion and storage, the optimization of functional materials in the system/module, such as: a) oxygen evolution electrocatalysts; b) water splitting photoelectrocatalyts; and c) lithium-ion battery

electrodes is becoming critical. Several key factors should be optimized, namely, efficiency (related to the current density), lifetime, durability, cost, environmental impact and portability (related to powder density).

1.2.1 Electrochemical Oxygen Evolution

The low efficiency of the oxygen evolution reaction (OER) is considered as one of the major bottlenecks in water splitting for the storage of renewable energy in form of molecular fuels like H_2.[8] To accelerate the water splitting reaction, hydrogen and oxygen evolution catalysts are applied as cathodes and anodes, respectively (Figure 1.3a). The reaction pathway of OER depends on the pH of electrolyte. In acidic medium, OER takes place by converting two water molecules into oxygen molecule and protons, while in alkaline and neutral media, four hydroxide ions are oxidized to dioxygen and water (Figure 1.3b). Herein we can see that OER is a four electron-proton coupled reaction, while only two electron-transfer happens in its counterpart reaction, hydrogen evolution reaction (HER). Thus a higher energy (higher overpotential) is generally required to overcome the kinetic barrier to occur in half reaction of OER.[9]

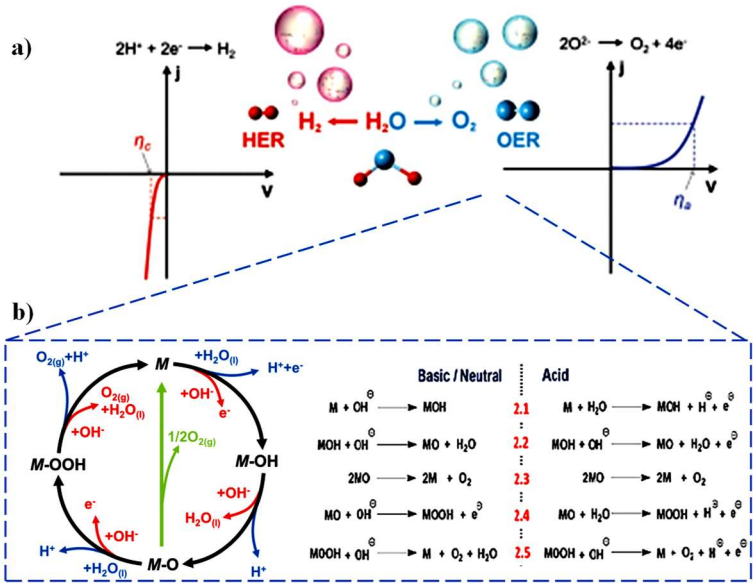

Figure 1.3. (a) Polarization curves for HER (left) and OER (right). The η_c and η_a are the overpotentials for cathode and anode at the same current (j), respectively.[9] (b) The OER mechanism for acid (blue line) and alkaline (red line) conditions. The black line indicates that the oxygen evolution involves the formation of a peroxide (M-OOH) intermediate (black line) while another route for direct reaction of two adjacent oxo (M–O) intermediates (green) to produce oxygen is possible as well.[9,10]

In the past several decades, various catalysts have been engineered to improve the electrocatalytic activity of OER under different electrolyte environments. For instance, the rutile RuO_2 presents excellent OER performance in both acidic and alkaline media.[11–13] However, the RuO_2 becomes highly unstable under high anodic potential by being oxidized to RuO_4 compound and dissolved in the electrolyte solution.[14] As a substitution, IrO_2 exhibits good OER catalytic activity as well. Nevertheless, IrO_2 also suffers from a similar issue to be dissolved (IrO_3 form) in solution under anodic potential,[15,16] even though it can sustain a higher anodic potential than RuO_2 does.[17] More importantly, the involvement of noble metals of Ru and Ir makes them less promising among OER catalysts. Thus the development of highly efficient and robust OER catalysts based on earth-abundant elements is becoming a topic of capital significance.[18–21] To evaluate the performance of electrocatalyst, three key parameters related to the electrocatalytic kinetic, overpotential (η), current density (j) and Tafel slope (b), are concerned.[9]

1.2.2 Photoelectrochemical Water Splitting

The photoelectrochemical (PEC) water splitting can be regarded as the electrochemical water splitting under light irradiation.[22] This system can be dated back to 1972, when Fujishima and Honda first introduced the PEC water splitting system with high efficiency and low cost using a semiconductor of TiO_2.[23] The principle behind PEC water splitting is to convert solar energy to hydrogen by applying an external bias on the photovoltaic materials immersed in a water electrolyte.[24]

In PEC system, at least one of the working electrode materials is a semiconductor with a suitable band gap to absorb light. The additional voltage required to carry out the reactions (*eg.* water splitting) is provided by an external bias. That's to say, the overpotential for HER/OER is partially compensated by the photogenerated voltage of light absorbers, and thus the hydrogen evolution or oxygen evolution could occur at a potential lower than 0 V versus reversible hydrogen electrode (RHE) or lower than 1.23 V versus RHE. Hence, instead of parameters of overpotential and Tafel slope in system of electrochemical water splitting, the onset potential and photocurrent density at 1.23 V versus RHE for OER and 0 V versus RHE for HER become the elementary parameters to evaluate the performance in PEC system.[22]

To improve the efficiency towards PEC water splitting, the electronic properties of the photoelectrodes should be concerned. Figure 1.4a and b represent the n-type and p-

type semiconductors involved in the PEC water splitting system, respectively. In Figure 1.4c, a system containing both the p-type semiconductor (for HER) and n-type semiconductor (for OER) is shown. To increase the PEC efficiency, the key point is to reduce the recombination of photogenerated carriers. On the other hand, nanostructuring the semiconductor can be beneficial for the generation of charge carries on the surface due to its increased surface to volume ratio, thus facilitating the water splitting process with a 50 %-90 % increase in efficiency of PEC water splitting.[24,25] Additionally, the construction of heterostructured photocatalysts (n-n, n-p and p-p junctions or co-catalyst such as metal domains) can also help the separation and migration of charge carriers, and the recombination of the photogenerated carriers can be hence reduced (Figure 1.5).[26–28]

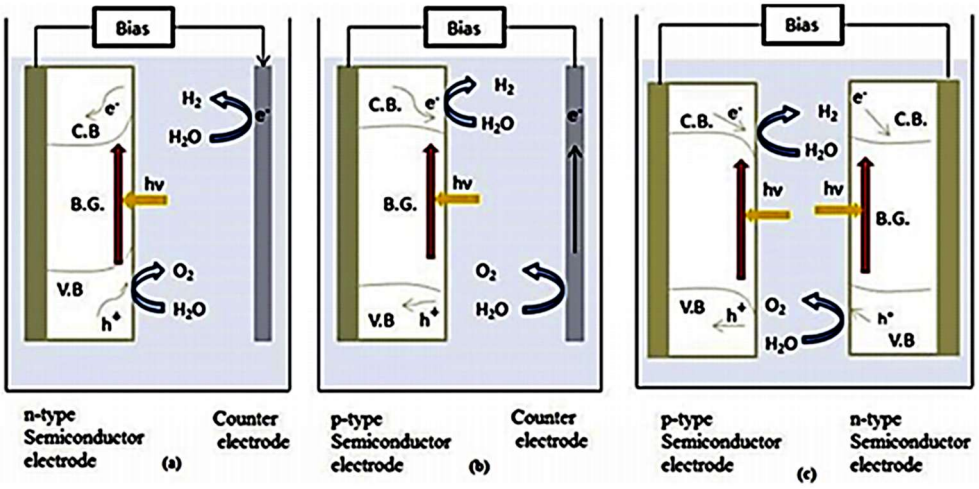

Figure 1.4. Scheme of PEC water splitting using n-type and p-type semiconductors.

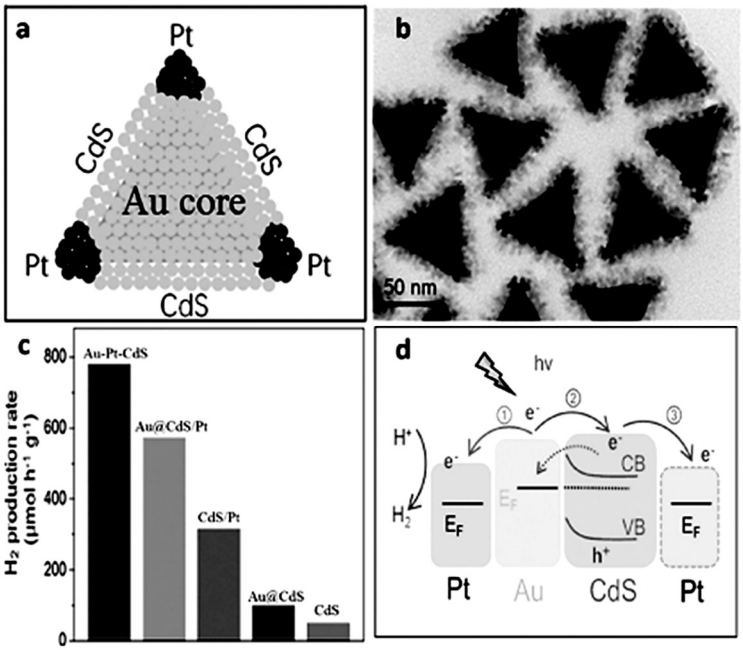

Figure 1.5. (a) Schematic illustrating the Au-Pt-CdS hetero-nanostructures. (b) TEM image of Au-Pt-CdS hetero-nanostructures. (c) Photocatalytic H_2 production of CdS, Au@CdS, CdS/Pt, Au@CdS/Pt, and Au-Pt-CdS under visible light ($\lambda > 420$ nm) irradiation. (d) Schematic illustration of the multipathway electron transfer in Au-Pt-CdS hetero-nanostructures.[29]

1.2.3 Lithium-ion Battery

As a type of rechargeable battery, lithium-ion batteries (LIBs) have become dominant power sources for portable electronics and electric vehicles and are growing in popularity for aerospace and military applications.[30] The technology of LIB was largely developed by John Goodenough, Stanley Whittingham, Akira Yoshino and Rachid Yazami in the 1970s-1980s,[31,32] and then commercialized by Sony and Asahi Kasei team led by Yoshio Nishi in 1991. A lithium-ion battery is composed by four essential components: anode, electrolyte, membrane separator and cathode. In the most commercially popular LIB, the graphite is applied as anode, while layered $LiCoO_2$ or $LiFePO_4$ or $LiMn_2O_4$ is used as cathode, and 1 M $LiPF_6$ in ethylene carbonate/diethylcarbonate (EC/DEC, 1/1 volume) as electrolyte.[30] In working conditions, lithium-ions are removed from the negative electrode (anode) through an electrolyte to the positive electrode (cathode) during discharge, and back when charging. Electrode materials are usually intercalated compounds with minimum structural variations after intercalation/de-intercalation of Li-ions. The membrane separator plays a role of barrier between anode and cathode to avoid a short circuit and to allow only Li-ions to pass. The schematic of working principle of LIB and a fabricated coin cell is shown in Figure 1.6. The reactions take place at the electrodes are as follows:

$$LiCoO_2 \leftrightarrow Li_{1-x}CoO_2 + x\,Li + x\,e^- \text{ (cathode) } (0 < x \leq 1) \qquad \text{eq. 1.1}$$

$$6C + x\,Li + x\,e^- \leftrightarrow Li_xC_6 \text{ (anode)} \qquad \text{eq. 1.2}$$

The whole reaction is: $LiCoO_2 + 6C \leftrightarrow Li_{1-x}CoO_2 + Li_xC_6$ $(0 < x \leq 1)$ eq. 1.3

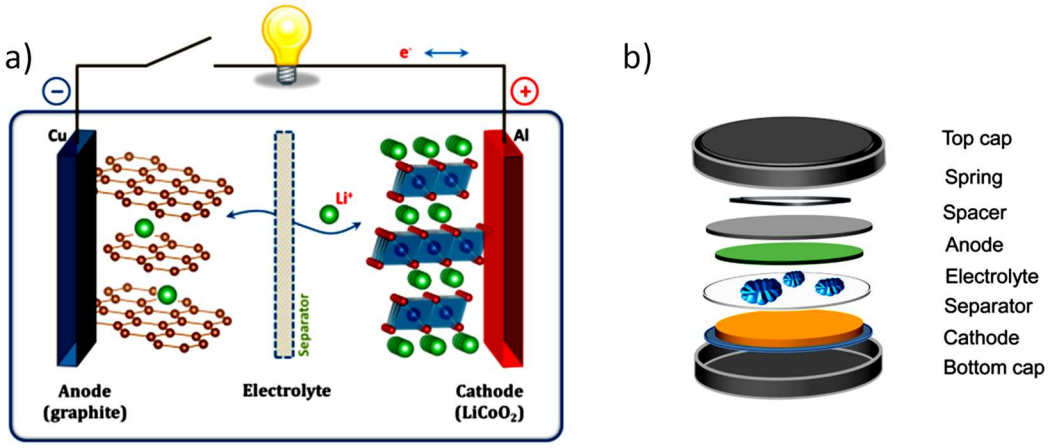

Figure 1.6. Schematic illustration of (a) working principle of the Li-ion battery ($LiCoO_2/Li^+$/electrolyte/graphite).[33] (b) the fabricated coin cell.[34]

The commercial graphite anodes provide a modest theoretical capacity of 372 mAh g^{-1},[35,36] which is far away from the requirements of the next generation of LIBs with high-energy and power density.[37] Therefore, alternative anode materials based on Si,[38,39] Ge [40,41] or Sn [42,43] are being actively developed.

To improve the capacity of anode materials, several strategies can be adopted: a) Nano-engineering of electrode material. When moving from the bulk to nanostructures, the electrode material/electrolyte contact area can be enlarged significantly and thus permitting higher Li-ion transfer rate across the interface for LIBs and a large number of ion absorption sites. Besides, the shorter path length for ionic/electronic transport ensures faster diffusion rates; b) Combining the active materials with porous high surface area materials with excellent electric conductivity, eg. carbon-based networks like graphene, thus i) buffering the strain from volume changes, preventing the aggregation and detachment of active materials during charging-discharging cycling; ii) providing additional necessary paths for ionic/electronic transport; iii) further improving the electric conductivity to facilitate fast charge transport.[44–46]

1.3 Nanostructured Metal Sulfide

Nanomaterials are those materials that have at least one dimension in the range of 1-100 nm.[47] The nanoscaled size can lead to unique optical, electronic, or mechanical properties unlike its corresponding bulk materials, and thus has gained increased scientific and commercial attention.[48]

Nanostructured metal sulfides have received huge attention over the past several decades due to their low cost and toxicity, suitable electronic band gap, exposed active sites and their promising catalytic activity in electrocatalysis and photocatalysis.[49] Metal sulfides generally have a shallow valence band [50–52] and exhibit a robust quantum size effect due to the small effective mass,[53–55] compared to the corresponding metal oxides. In addition, the ability of control on sizes, shapes, compositions, crystal forms and hybridization towards metal sulfides gives them the potential to optimize the band gap, electrical conductivity, surface morphology, durability, *etc.,* which are beneficial for energy conversion such as photocatalysis, battery and electrocatalysis of water splitting, as illustrated in Figure 1.7.[56–60]

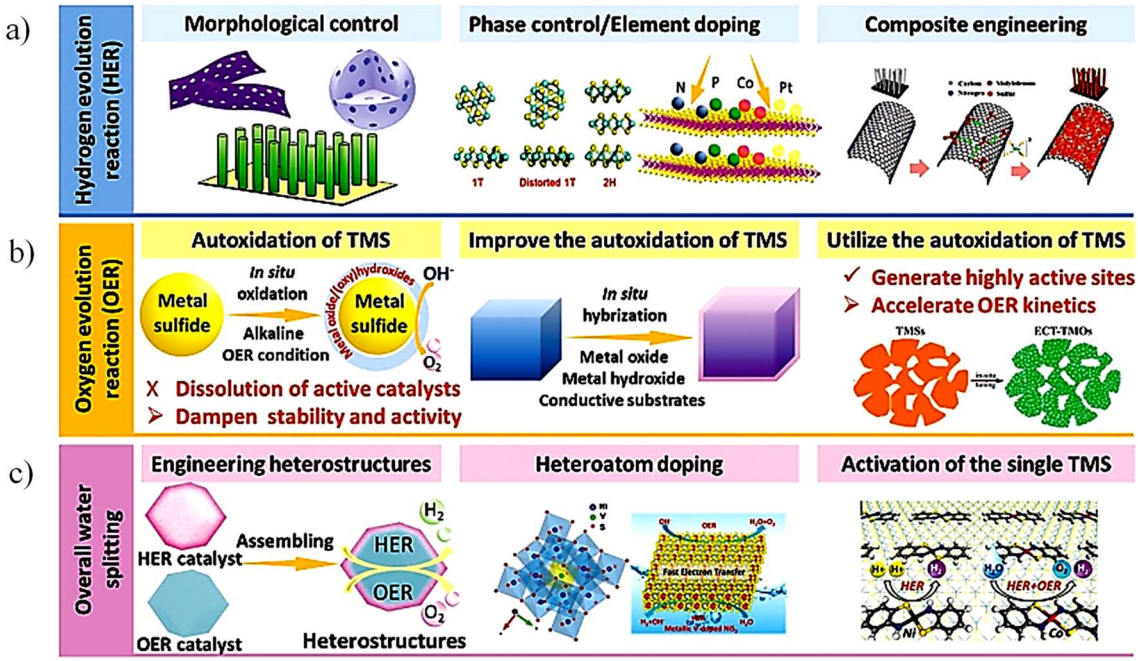

Figure 1.7. Illustration of metal sulfides for electrochemical water splitting. (a) Strategies for optimizing the catalytic performance of TMS for HER. Left part: Reproduced from Ref.[61] Middle part: Reproduced from Ref.[62] Right part: Reproduced from Ref.[63] (b) The current challenge and corresponding solutions of TMS for OER. Left and middle parts: Reproduced from Ref.[61] Right part: Reproduced from Ref.[64] (c) Pathways to create bifunctional catalysts for overall water splitting. Left part: Reproduced from Ref.[61] Middle part: Reproduced from Ref.[65] Right part: Reproduced from Ref.[66]

1.4 Synthesis of Nanostructured Metal Sulfide

To date, a variety of methods have been developed to prepare high-quality metal sulfides with nanostructured morphology, including the hydrothermal,[67–69] electrochemical deposition,[70–73] gas sulfidation,[74–76] colloidal synthesis,[77–79] *in-situ* synthesis,[80–85] *etc*.

Among which the colloidal synthesis and *in-situ* synthesis will be mainly applied to produce nanostructured metal sulfides involved in this thesis, and thus will be detailed in the following text.

1.4.1 Colloidal Synthesis

Colloidal synthesis routes produce materials in the form of colloids. A common strategy to produce colloidal chalcogenide nanocrystals is using an organic solvent and oxygen-free conditions to thermally react or decompose a precursor, typically inorganic salts or organometallic compounds, in the presence of surfactants that control the nanocrystal growth and provide them with colloidal stability.[86–89] Two strategies are generally used to produce colloidal nanocrystals, namely "heat up" and "hot injection", both of which target homogenous nucleation to produce NPs.[86] In the case of heat up process, all precursors, ligands and solvents are added and mixed in a flask at low temperature initially, followed by heating up to a desired reaction temperature for nanocrystal (NC) nucleation and growth, as shown in Figure 1.8a. As for the case of hot injection, a technique pioneered by the Bawendi group in 1993 to synthesize monodisperse Cd chalcogenide NC,[90] the high supersaturation degree is induced upon rapid injection of a precursor or reactant at high temperature, and an instantaneous burst of nucleation happens by relieving the excess free energy of the supersatuation (Figure 1.8b).[87,91]

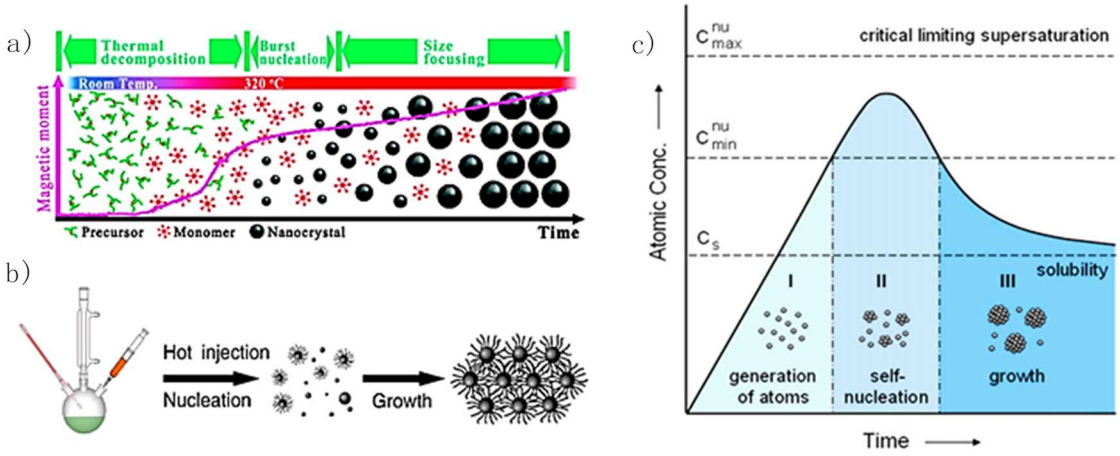

Figure 1.8. Schematic illustration of the colloidal heat-up and hot injection techniques. (a) Heat-up technique. All the precursors are mixed together in the initial stages and are steadily heated up to the desired reaction temperature.[92] (b) Hot-injection technique, where a rapid injection of a precursor solution into a hot solvent leads to a temporal separation of the nucleation and growth stages.[87] (c) LaMer model describing the three different steps of the nucleation and growth process for monodisperse NCs, as a function of the reaction time and monomer concentration. The saturation concentration (C_s) and minimum nucleation concentration ($C_{nu,min}$) are marked in the plot.[93,94]

Although both the heat up and hot injection techniques involve an initial nucleation burst followed by growth on the existing nuclei, frequently better size-uniformity is achieved in the hot injection approach because the injection results in a uniform NC growth due to a single nucleation event.[86,95–97]

Regarding to the formation mechanism of monodisperse NPs in colloidal synthesis process, the "burst nucleation" initially proposed by LaMer and Dinegar in 1950 was accepted as an important concept.[94] The LaMer growth process can be divided into three steps, as shown in Figure 1.8c.[93,98] In step one, the atomic concentration (or free monomers) in solution increases rapidly with time, along with the decomposition of the precursor by heating.[93] Since the energy barrier to initiate a nucleation event is pretty high, the monomers cannot grow into nuclei spontaneously at the saturation concentration (C_s). Hence, the monomer concentration should increase until reaching to its minimum nucleation concentration ($C_{nu,\,min}$). In step two, the monomer concentration reaches to the $C_{nu,\,min}$ and the system is supersaturated at this point, thus containing enough energy to overcome the barrier energy to initiate the nucleation event (burst nucleation),[99] where the monomers start to aggregate into small clusters/nuclei via self-nucleation. These small nuclei grow at an accelerate rate to relieve the supersaturation condition and thus resulting in a significant reduction of monomer concentration in solution. Once the monomer concentration decreases to below the level of the minimum nucleation concentration, the nucleation events would stop and the process goes to the next step. In step three, the nuclei grow into larger sized nanoparticles (NPs), controlled by the monomers diffusion via ongoing precursor decomposition, and this growth process can only occur slightly over the saturation point (C_s), since it is less energy consuming.[86] Figure 1.9 illustrates one of the most explored nanocrystal of copper sulfide with different morphology by using colloidal synthesis approach.

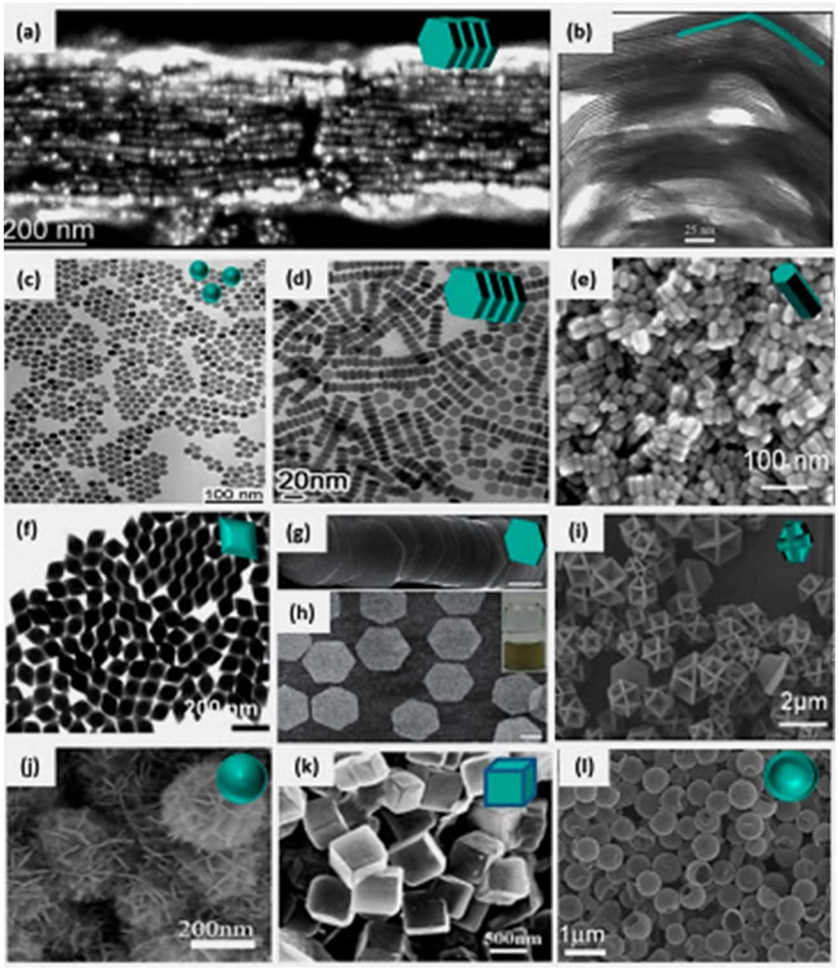

Figure 1.9. Colloidal synthesized copper sulfide with different morphology: (a) Cu_2S nanoplates deposited onto a substrate, forming 3D colloidal crystals.[100] (b) Ultrathin Cu_2S nanowires.[101] (c) Cu_2S spherical particles.[102] (d) Cu_2S nanoplates with face-to-face stacks of nanoplates evident, which could be misinterpreted as nanorods.[103] (e) $Cu_{1.94}S$ nanorods.[104] (f) $Cu_{1.96}S$ dodecahedrons formed at high precursor concentrations.[105] (g) Ultrathin CuS nanosheets (scale bar = 200 nm) forming domino-like superstructures. (h) A monolayer of CuS nanosheets on a Si substrate (scale bar = 200 nm), with the inset showing a photograph of the CuS nanosheets in solution. Panels g–h were reproduced from Ref.[106] (i) CuS cuboctahedrons.[107] (j) Hierarchical flower-like CuS nanospheres.[108] (k) Cu_xS nanocubes prepared from Cu_2O crystal templates.[109] (l) Hollow CuS spheres with a thin-shell.[110]

1.4.2 In-situ Synthesis

Nanoparticles obtained from routes such as colloidal synthesis suffer from several issues when applied in electrocatalysis. On the one hand, the NPs need to be deposited on the current collector with the assistance of polymeric binder (*eg.* nafion), which inevitably results in poor charge transfer (high resistance), and buried active sites,[111–113] as shown in Figure 1.10a. The low electrical conductivity of electrocatalysts basically requires the use of conductive additives such as carbon materials.[114] However, the carbon additive is

possible to be oxidized/etched under high anodic potential, which deteriorates its catalytic performance such as OER.[115] On the other hand, the lower mechanic adhesive stability of electrocatalyst powder on the substrate means the loading mass cannot be too much, generally lower than 1 mg/cm^2, which means limited catalytic active sites. Besides, the loaded electrocatalyst could be feasible to peel off from the surface of substrate during longterm working, especially under an industrial-level current density of $>$ 500 mA/cm^2.[116–118]

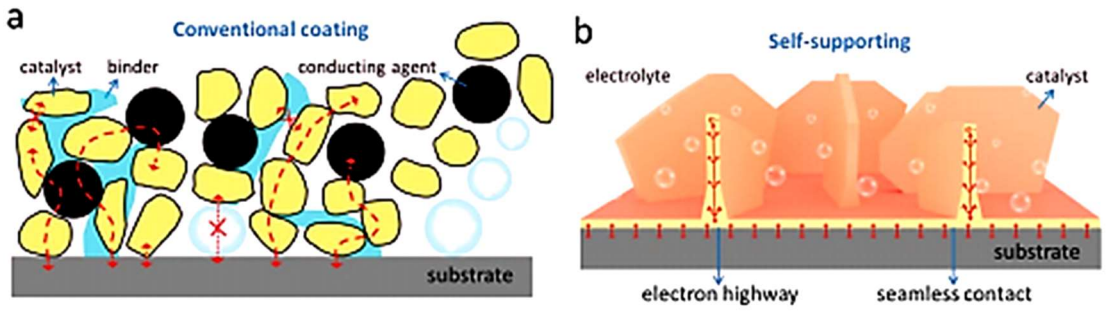

Figure 1.10. Schematic of the structural and electrochemical features of: (a) conventional powdery catalysts casted on current collectors with polymer binder and carbon additives; b) self-supported electrode with in situ fabricated catalysts on the substrates.[119]

Compared with the conventional NPs-casted electrodes, *in-situ* fabricated self-supported electrodes with active materials *in-situ* grown on the surface of conductive substrates are more desirable due to the following several merits: a) the *in-situ* fabrication process avoids the posterior deposition process and the application of binder and conductor additives, which simplifies the production process and decreases the cost of electrodes;[120] b) the substrate can rivet and distribute well the catalyst arrays, resulting in a high mass loading of catalyst sites;[121] c) the contact between catalyst materials/sites and substrate is more intimate due to absence of binders, thus facilitating the charge transfer and strengthening the adhesion of catalysts. All the advantages mentioned above favor the catalytic process and durability of self-supported electrocatalyst electrodes for large-current-density applications (Figure 1.10b).[122]

To produce self-supported electrocatalysts, typical synthesis routes such as hydrothermal, electrodeposition, vapor deposition, vacuum filtration and freeze drying have been applied, as shown in Figure 1.11a-d. Regarding to the substrate, the common ones are metal plate/mesh/foam, carbon fiber/paper/cloth and FTO/ITO glass slides. For instance, Jin group produced different shaped CoS_2 of film, microwire arrays and

nanowire arrays on the graphite disk substrate (Figure 1.11e). Nanostructured CoS_2 presented both superior catalytic performance and durability due to facilitated gas release evolved from electrode surface, compared with that of planar film and microwire electrodes (Figure 1.11 f).[123]

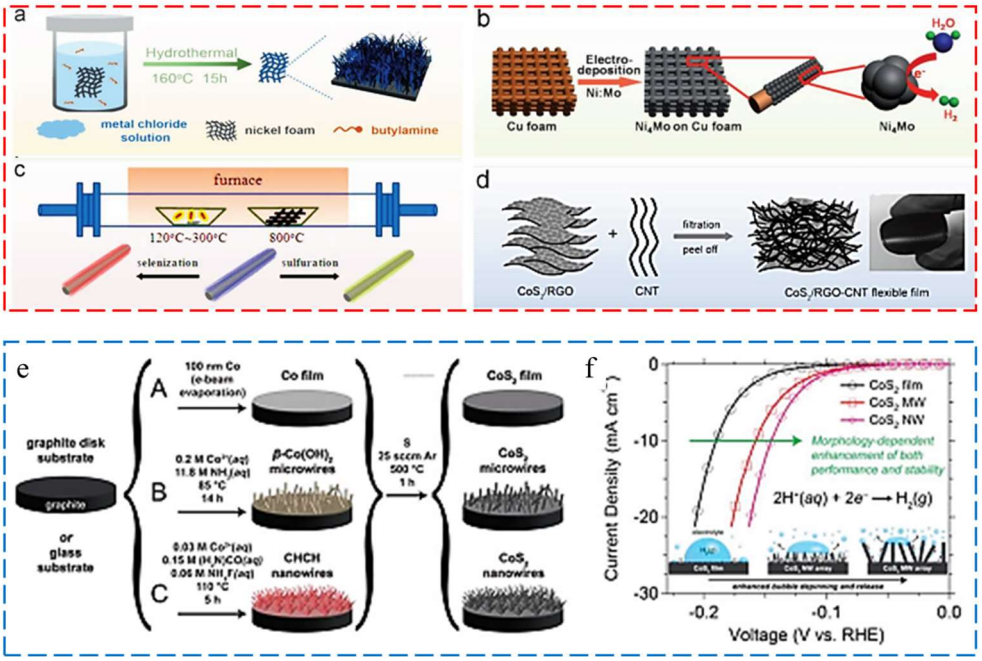

Figure 1.11. In-situ fabrication synthetic strategies for self-supported electrodes: (a) Hydrothermal growth of oxyhydroxides on nickel foam.[124] (b) Electrodeposition of Ni-Mo electrocatalysts on Cu foam.[125] (c) Chemical vapor deposition of WS_2, WSe_2, and $WS_{2(1-x)}Se_{2x}$ on carbon fiber.[126] (d) Filtration and peeling off process to obtain freestanding nanocomposite of CoS_2 and reduced graphene oxide–carbon nanotubes (RGO-CNT).[127] Self-supported Co chalcogenides for the HER. (e) Synthesis of CoS_2 in forms of film, microwire array and nanowire array on graphite disk substrates and (f) the corresponding polarization curves. The inset in (f) schematically depicts bubble release behaviors on different electrode surfaces.[123]

1.5 Challenges

Metal sulfides have been widely investigated by researches due to their abundant element composition, low toxic and mature synthesis techniques. However, there are still some challenges in different energy conversion systems, as detailed separately below:

For the electrocatalysis of OER, it should be noted that the metal sulfide is thermodynamic less stable under oxidizing potentials, and therefore can be oxidized to its corresponding metal oxide/hydroxides, especially in the aqueous media under strong oxidative condition, as illustrated in Figure 1.12.[128] In this direction, it is crucial to carry out characterization analysis towards the surface structural and composition during/after

the OER reactions, to understand what are the true catalytically active sites of such claimed OER catalysts of metal sulfides. Besides, to clear elucidate the transformation process using an easy-accessed characterization tools, and even *in-situ* techniques is appealed. Finally, the potential of this transformation on electrocatalysts has been underestimated or even disregarded in many cases.

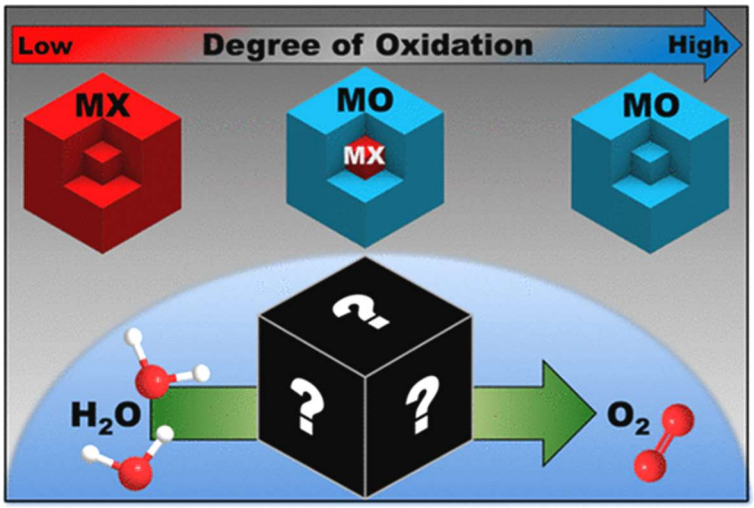

Figure 1.12. Possible reaction pathways for a hypothetical metal X-ide catalyst during water oxidation. Depending on the degree of oxidation, the oxidation can occur from the outer surface to the inner core. In many cases, the oxidized portions will be more porous than the initial X-ide.[129] X-ide herein can be sulfide, carbide or pnictide.

For the photocatalysis of water splitting, how to improve the utilization efficiency of solar energy is the point we concerned a lot. In this direction, the introduction of cocatalyst into suitable metal sulfides could be a good approach as we aforementioned. However, the cocatalyst always goes to the precious metal domains like Ag,[130] Au,[131] Pt.[132] In this direction, to decrease the cost of catalyst as much as we can, we need to determine the optimal amount of precious metallic co-catalyst, and in the meantime to liberate its maximal catalytic activity. Besides, the stability of metal sulfide-cocatalyst in PEC water splitting should be noted as well.

For the battery field, the current commercialized graphite anode suffers from the relatively low theoretical energy density (372 mAh g^{-1}).[35,36] Alternatively, SnS_2-based anode materials stand out on account of its potentially higher lithium storage capacities (1231 mAh g^{-1} for SnS_2).[133] However, the big volume changes and low electrical conductivity in SnS_2 during charge-discharge cycling limit its potential application in LIB.[134,135] Hence, how to increase the electric conductivity and accommodate the volume

changes to prevent the aggregation of active SnS_2 during cycling becomes really meaningful.

1.6 Objectives

Taking all the aspects mentioned above, the goal of this thesis is to develop nanostructured non-toxic metal sulfide-based catalysts for electrochemical energy conversion technologies. The selected metal sulfides will be low-cost and non-toxic, and efficient in energy conversion after using proper optimization approaches. Keeping these aims in mind, the specific objects are defined as following:

1) To demonstrate the possibility to obtain excellent-performed electrocatalysts from the *in-situ* oxidation of metal sulfides in OER conditions. For this objective, taking *in-situ* synthesized Cu_2S nanorod arrays on the surface of copper substrate as a representative object, I will elucidate the transformation process of Cu_2S during catalytic OER condition, and the compound *in-situ* formed will be compared with the directly produced counterpart towards OER performance.

2) To develop solution-based synthesis methods to produce metal sulfides with suitable band gap, and further taking proper optimization approach aforementioned to improve its application performance towards PEC water splitting. For this objective, ultrathin SnS_2 nanoplates will be produced. An optimal Pt nanodomains will be then deposited on its ultrathin surface to serve as cocatalyst, and improved PEC performance will be expected.

3) To develop a suitable protocol to produce conformal coated metal sulfide layers. These conformal coated layers would show higher adhesive stability and better electric conductivity than that of post-deposited NPs on substrates. For this objective, conformal coated SnS_2 layer will be prepared on different conductive substrate, and its improved performance towards PEC water splitting will be demonstrated.

4) To gain understanding on the shape-dependent LIB performance in metal sulfides. The outperformed shaped candidate could be further hybridized with suitable additive materials having high surface area and electric conductivity. For this objective, two kinds of SnS_2 NPs with different morphology will be prepared, and subsequently combined with proper additives to provide an excellent electrochemical performance for LIB application.

1.7 References

(1) Adams, W. W.; Baughman, R. H. Retrospective: Richard E. Smalley (1943-2005). *Science.* **2005**, *310* (5756), 1916.

(2) Shen, Y. B.; Zhang, Y. T.; Han, S. J.; Wang, J. W.;Peng, Z. Q.; Chen, L. W. Unlocking the Energy Capabilities of Lithium Metal Electrode with Solid-State Electrolytes. *Joule*, **2018**, *2* (9), 1674-1689.

(3) Grant, L. *THE CASE FOR FEWER PEOPLE: The NPG Forum Papers*; 2006.

(4) EIA. U.S. Energy Information Administration (EIA) http://www.eia.gov/ (accessed Mar 26, 2020).

(5) Lai, C. H.; Lu, M. Y.; Chen, L. J. Metal Sulfide Nanostructures: Synthesis, Properties and Applications in Energy Conversion and Storage. *J. Mater. Chem.* **2012**, *22* (1), 19–30.

(6) DIFFER - TMC - TU/e: Renewable Fuels | Science & the Energy Challenge https://www.scienceandtheenergychallenge.nl/node/11 (accessed Mar 26, 2020).

(7) San Vicente Energy Storage Facility Study https://www.sdcwa.org/san-vicente-energy-storage-facility (accessed Mar 26, 2020).

(8) Zhao, D.; Pi, Y.; Shao, Q.; Feng, Y.; Zhang, Y.; Huang, X. Enhancing Oxygen Evolution Electrocatalysis via the Intimate Hydroxide-Oxide Interface. *ACS Nano* **2018**, *12* (6), 6245–6251.

(9) Suen, N. T.; Hung, S. F.; Quan, Q.; Zhang, N.; Xu, Y. J.; Chen, H. M. Electrocatalysis for the Oxygen Evolution Reaction: Recent Development and Future Perspectives. *Chem. Soc. Rev*. **2017**, *46*(2), 337–365.

(10) Bandal, H.; Reddy, K. K.; Chaugule, A.; Kim, H. Iron-Based Heterogeneous Catalysts for Oxygen Evolution Reaction; Change in Perspective from Activity Promoter to Active Catalyst. *J. Power Sources*. **2018**, *395*, 106–127.

(11) Reier, T.; Oezaslan, M.; Strasser, P. Electrocatalytic Oxygen Evolution Reaction (OER) on Ru, Ir, and Pt Catalysts: A Comparative Study of Nanoparticles and Bulk Materials. *ACS Catal.* **2012**, *2* (8), 1765–1772.

(12) Lee, Y.; Suntivich, J.; May, K. J.; Perry, E. E.; Shao-Horn, Y. Synthesis and Activities of Rutile IrO_2 and RuO_2 Nanoparticles for Oxygen Evolution in Acid and Alkaline Solutions. *J. Phys. Chem. Lett*. **2012**, *3*(3), 399–404.

(13) Frydendal, R.; Paoli, E. A.; Knudsen, B. P.; Wickman, B.; Malacrida, P.; Stephens, I. E. L.; Chorkendorff, I. Benchmarking the Stability of Oxygen Evolution Reaction Catalysts: The Importance of Monitoring Mass Losses. *ChemElectroChem* **2014**, *1* (12), 2075–2081.

(14) Kötz, R. XPS Studies of Oxygen Evolution on Ru and RuO_2 Anodes. *J. Electrochem. Soc.* **1983**, *130* (4), 825.

(15) Antolini, E. Iridium as Catalyst and Cocatalyst for Oxygen Evolution/Reduction in Acidic Polymer Electrolyte Membrane Electrolyzers and Fuel Cells. *ACS Catal*. **2014**, *4*(5),1426–1440.

(16) Kötz, R. Anodic Iridium Oxide Films. *J. Electrochem. Soc.* **1984**, *131* (1), 72.

(17) Cherevko, S.; Geiger, S.; Kasian, O.; Kulyk, N.; Grote, J. P.; Savan, A.; Shrestha, B. R.; Merzlikin, S.; Breitbach, B.; Ludwig, A.; Mayrhofer, K. Oxygen and Hydrogen Evolution Reactions on Ru, RuO_2, Ir, and IrO_2 Thin Film Electrodes in Acidic and Alkaline Electrolytes: A Comparative Study on Activity and Stability. *Catal. Today* **2016**, *262*, 170–180.

(18) Zhang, J.; Wang, T.; Pohl, D.; Rellinghaus, B.; Dong, R.; Liu, S.; Zhuang, X.; Feng, X. Interface Engineering of MoS_2/Ni_3S_2 Heterostructures for Highly Enhanced Electrochemical Overall-Water-Splitting Activity. *Angew. Chem. Int. Ed.* **2016**, *55* (23), 6702–6707.

(19) Song, F.; Schenk, K.; Hu, X. A Nanoporous Oxygen Evolution Catalyst Synthesized by Selective Electrochemical Etching of Perovskite Hydroxide $CoSn(OH)_6$ Nanocubes. *Energy Environ. Sci.* **2016**, *9* (2), 473–477.

(20) Jin, Y.; Wang, H.; Li, J.; Yue, X.; Han, Y.; Shen, P. K.; Cui, Y. Porous MoO_2 Nanosheets as Non-Noble Bifunctional Electrocatalysts for Overall Water Splitting. *Adv. Mater.* **2016**, *28* (19), 3785–3790.

(21) Liu, Y.; Liang, X.; Gu, L.; Zhang, Y.; Li, G. D.; Zou, X.; Chen, J. S. Corrosion Engineering towards Efficient Oxygen Evolution Electrodes with Stable Catalytic Activity for over 6000 Hours. *Nat. Commun.* **2018**, *9* (1), 1–10.

(22) Li, D.; Shi, J.; Li, C. Transition-Metal-Based Electrocatalysts as Cocatalysts for Photoelectrochemical Water Splitting: A Mini Review. *Small* **2018**, *14* (23), 1704179.

(23) Fujishima, A.; Honda, K. Electrochemical Photolysis of Water at a Semiconductor Electrode. *Nature* **1972**, *238* (5358), 37–38.

(24) Joy, J.; Mathew, J.; George, S. C. Nanomaterials for Photoelectrochemical Water Splitting -Review. *Int. J. Hydrogen Energy* **2018**, *43*(10), 4804–4817.

(25) Szymanski, P.; El-Sayed, M. A. Some Recent Developments in Photoelectrochemical Water Splitting Using Nanostructured TiO_2: A Short Review. *Theor Chem Acc* **2012**, *131*, 1202.

(26) Dong, G.; Du, B.; Liu, L.; Zhang, W.; Liang, Y.; Shi, H.; Wang, W. Synthesis and Their Enhanced Photoelectrochemical Performance of ZnO Nanoparticle-Loaded CuO Dandelion Heterostructures under Solar Light. *Appl. Surf. Sci.* **2017**, *399*, 86–94.

(27) Li, J.; Zhou, J.; Hao, H.; Li, W. Controlled Synthesis of Fe_2O_3 Modified Ag- 010 $BiVO_4$ Heterostructures with Enhanced Photoelectrochemical Activity toward the Dye Degradation. *Appl. Surf. Sci.* **2017**, *399*, 1–9.

(28) Li, L.; Liu, C.; Qiu, Y.; Mitsuzak, N.; Chen, Z. Convex-Nanorods of A-Fe_2O_3/CQDs Heterojunction Photoanode Synthesized by a Facile Hydrothermal Method for Highly Efficient Water Oxidation. *Int. J. Hydrogen Energy* **2017**, *42* (31), 19654–19663.

(29) Ma, L.; Chen, K.; Nan, F.; Wang, J. H.; Yang, D. J.; Zhou, L.; Wang, Q. Q. Improved Hydrogen Production of Au–Pt–CdS Hetero-Nanostructures by Efficient Plasmon-Induced Multipathway Electron Transfer. *Adv. Funct. Mater.* **2016**, *26* (33), 6076–6083.

(30) Kulkarni, P.; Nataraj, S. K.; Balakrishna, R. G.; Nagaraju, D. H.; Reddy, M. V. Nanostructured Binary and Ternary Metal Sulfides: Synthesis Methods and Their Application in Energy Conversion and Storage Devices. *J. Mater. Chem. A*. **2017**, *5* (42), 22040–22094.

(31) NobelPrize.org. The Nobel Prize in Chemistry 2019 https://www.nobelprize.org/prizes/chemistry/2019/summary/ (accessed Mar 26, 2020).

(32) 2013 IEEE Medal for Environmental and Safety Technologies https://www.ieee.org/about/awards/bios/environmental-safety-recipients.html (accessed Mar 26, 2020).

(33) Goodenough, J. B.; Park, K. S. The Li-Ion Rechargeable Battery: A Perspective. *J. Am. Chem. Soc.* **2013**, *135*(4), 1167–1176.

(34) Talaie, E.; Bonnick, P.; Sun, X.; Pang, Q.; Liang, X.; Nazar, L. F. Methods and Protocols for Electrochemical Energy Storage Materials Research. *Chem. Mater*. **2017**, *29* (1), 90–105.

(35) Kaskhedikar, N. A.; Maier, J. Lithium Storage in Carbon Nanostructures. *Adv. Mater.* **2009**, *21* (25–26), 2664–2680.

(36) Ding, L. X.; Li, G. R.; Wang, Z. L.; Liu, Z. Q.; Liu, H.; Tong, Y. X. Porous Ni@Pt Core-Shell Nanotube Array Electrocatalyst with High Activity and Stability for Methanol Oxidation. *Chem. - A Eur. J.* **2012**, *18* (27), 8386–8391.

(37) Li, X.; Feng, Y.; Li, M.; Li, W.; Wei, H.; Song, D. Smart Hybrids of Zn_2GeO_4 Nanoparticles and Ultrathin G-C_3N_4 Layers: Synergistic Lithium Storage and Excellent Electrochemical Performance. *Adv. Funct. Mater.* **2015**, *25* (44), 6858–6866.

(38) Chan, C. K.; Peng, H.; Liu, G.; McIlwrath, K.; Zhang, X. F.; Huggins, R. A.; Cui, Y. High-Performance Lithium Battery Anodes Using Silicon Nanowires. *Nat. Nanotec.* **2008**, *3* (1), 31–35.

(39) Hu, Y. S.; Demir-Cakan, R.; Titirici, M. M.; Müller, J. O.; Schlögl, R.; Antonietti, M.; Maier, J. Superior Storage Performance of a Si@SiO_x/C Nanocomposite as Anode Material for Lithium-Ion Batteries. *Angew. Chem. Int. Ed.* **2008**, *47* (9), 1645–1649.

(40) Wang, X. L.; Han, W. Q.; Chen, H.; Bai, J.; Tyson, T. A.; Yu, X. Q.; Wang, X. J.; Yang, X. Q. Amorphous Hierarchical Porous GeO_x as High-Capacity Anodes for Li Ion Batteries with Very Long Cycling Life. *J. Am. Chem. Soc.* **2011**, *133* (51), 20692–20695.

(41) Kim, H.; Son, Y.; Park, C.; Cho, J.; Choi, H. C. Catalyst-Free Direct Growth of a Single to a Few Layers of Graphene on a Germanium Nanowire for the Anode Material of a Lithium Battery. *Angew. Chem. Int. Ed.* **2013**, *52* (23), 5997–6001.

(42) Liu, Y.; Yu, X. Y.; Fang, Y.; Zhu, X.; Bao, J.; Zhou, X.; Lou, X. W. (David). Confining SnS_2 Ultrathin Nanosheets in Hollow Carbon Nanostructures for Efficient Capacitive Sodium Storage. *Joule* **2018**, *2* (4), 725–735.

(43) Guo, W.; Wang, Y.; Li, Q.; Wang, D.; Zhang, F.; Yang, Y.; Yu, Y. SnO_2@C@VO_2 Composite Hollow Nanospheres as an Anode Material for Lithium-Ion Batteries. *ACS Appl. Mater. Interfaces* **2018**, *10* (17), 14993–15000.

(44) Tang, J.; Zhong, X.; Li, H.; Li, Y.; Pan, F.; Xu, B. In-Situ and Selectively Laser Reduced Graphene Oxide Sheets as Excellent Conductive Additive for High Rate Capability $LiFePO_4$ Lithium Ion Batteries. *J. Power Sources* **2019**, *412*, 677–682.

(45) Guo, A.; Chen, E.; Wygant, B. R.; Heller, A.; Mullins, C. B. Lead Oxide Microparticles Coated by Ethylenediamine-Cross-Linked Graphene Oxide for Lithium Ion Battery Anodes. *ACS Appl. Energy Mater.* **2019**, *2* (5), 3017–3020.

(46) Yao, W.; Wu, S.; Zhan, L.; Wang, Y. Two-Dimensional Porous Carbon-Coated Sandwich-like Mesoporous SnO_2/Graphene/Mesoporous SnO_2 Nanosheets towards High-Rate and Long Cycle Life Lithium-Ion Batteries. *Chem. Eng. J.* **2019**, *361*, 329–341.

(47) Mansoori, G. A. An Introduction to Nanoscience and Nanotechnology; Springer, Cham, 2017; pp 3–20.

(48) Portela, C. M.; Vidyasagar, A.; Krödel, S.; Weissenbach, T.; Yee, D. W.; Greer, J. R.; Kochmann, D. M. Extreme Mechanical Resilience of Self-Assembled Nanolabyrinthine Materials. *Proc. Natl. Acad. Sci.* **2020**, *117* (11), 201916817.

(49) Chandrasekaran, S.; Yao, L.; Deng, L.; Bowen, C.; Zhang, Y.; Chen, S.; Lin, Z.; Peng, F.; Zhang, P. Recent Advances in Metal Sulfides: From Controlled Fabrication to Electrocatalytic, Photocatalytic and Photoelectrochemical Water Splitting and Beyond. *Chem. Soc. Rev*. **2019**, *48* (15), 4178–4280.

(50) Shiga, Y.; Umezawa, N.; Srinivasan, N.; Koyasu, S.; Sakai, E.; Miyauchi, M. A Metal Sulfide Photocatalyst Composed of Ubiquitous Elements for Solar Hydrogen Production. *Chem. Commun.* **2016**, *52* (47), 7470–7473.

(51) Chhowalla, M.; Shin, H. S.; Eda, G.; Li, L. J.; Loh, K. P.; Zhang, H. The Chemistry of Two-Dimensional Layered Transition Metal Dichalcogenide Nanosheets. *Nat. Chem.* **2013**, *5* (4), 263–275.

(52) Wang, Q. H.; Kalantar-Zadeh, K.; Kis, A.; Coleman, J. N.; Strano, M. S. Electronics and Optoelectronics of Two-Dimensional Transition Metal Dichalcogenides. *Nat. Nanotech.* **2012**, *7* (11), 699–712.

(53) Wang, Y.; Herron, N. Nanometer-Sized Semiconductor Clusters: Materials Synthesis, Quantum Size Effects, and Photophysical Properties. *J. Phys. Chem*. **1991**, *95* (2), 525–532.

(54) Hoffman, A. J.; Mills, G.; Yee, H.; Hoffmann, M. R. Q-Sized CdS: Synthesis, Characterization, and Efficiency of Photoinitiation of Polymerization of Several Vinylic Monomers. *J. Phys. Chem.* **1992**, *96* (13), 5546–5552.

(55) Voiry, D.; Fullon, R.; Yang, J.; De Carvalho Castro E Silva, C.; Kappera, R.; Bozkurt, I.; Kaplan, D.; Lagos, M. J.; Batson, P. E.; Gupta, G.; et al. The Role of Electronic Coupling between Substrate and 2D MoS_2 Nanosheets in Electrocatalytic Production of Hydrogen. *Nat. Mater.* **2016**, *15* (9), 1003–1009.

(56) Li, Y.; Wang, H.; Xie, L.; Liang, Y.; Hong, G.; Dai, H. MoS_2 Nanoparticles Grown on Graphene: An Advanced Catalyst for the Hydrogen Evolution Reaction. *J. Am. Chem. Soc.* **2011**, *133* (19), 7296–7299.

(57) Yu, X. Y.; (David) Lou, X. W. Mixed Metal Sulfides for Electrochemical Energy Storage and Conversion. *Adv. Energy Mater.* **2018**, *8* (3), 1701592.

(58) Chopra, N. G.; Luyken, R. J.; Cherrey, K.; Crespi, V. H.; Cohen, M. L.; Louie, S. G.; Zettl, A. Boron Nitride Nanotubes. *Science.* **1995**, *269* (5226), 966–967.

(59) Zhao, Y.; Wang, L. P.; Sougrati, M. T.; Feng, Z.; Leconte, Y.; Fisher, A.; Srinivasan, M.; Xu, Z. A Review on Design Strategies for Carbon Based Metal Oxides and Sulfides Nanocomposites for High Performance Li and Na Ion Battery Anodes. *Adv. Energy Mater.* **2017**, *7* (9), 1601424.

(60) Iwashina, K.; Iwase, A.; Ng, Y. H.; Amal, R.; Kudo, A. Z-Schematic Water Splitting into H_2 and O_2 Using Metal Sulfide as a Hydrogen-Evolving Photocatalyst and Reduced Graphene Oxide as a Solid-State Electron Mediator. *J. Am. Chem. Soc.* **2015**, *137* (2), 604–607.

(61) Guo, Y.; Park, T.; Yi, J. W.; Henzie, J.; Kim, J.; Wang, Z.; Jiang, B.; Bando, Y.; Sugahara, Y.; Tang, J.; Yamauchi, Y. Nanoarchitectonics for Transition-Metal-Sulfide-Based Electrocatalysts for Water Splitting. *Adv. Mater.* **2019**, *31* (17), 1807134.

(62) Voiry, D.; Mohite, A.; Chhowalla, M. Phase Engineering of Transition Metal Dichalcogenides. *Chem. Soc. Rev.* **2015**, *44*(9), 2702–2712.

(63) Li, D. J.; Maiti, U. N.; Lim, J.; Choi, D. S.; Lee, W. J.; Oh, Y.; Lee, G. Y.; Kim, S. O. Molybdenum Sulfide/N-Doped CNT Forest Hybrid Catalysts for High-Performance Hydrogen Evolution Reaction. *Nano Lett.* **2014**, *14* (3), 1228–1233.

(64) Chen, W.; Wang, H.; Li, Y.; Liu, Y.; Sun, J.; Lee, S.; Lee, J. S.; Cui, Y. In Situ Electrochemical Oxidation Tuning of Transition Metal Disulfides to Oxides for Enhanced Water Oxidation. *ACS Cent. Sci.* **2015**, *1* (5), 244–251.

(65) Liu, H.; He, Q.; Jiang, H.; Lin, Y.; Zhang, Y.; Habib, M.; Chen, S.; Song, L. Electronic Structure Reconfiguration toward Pyrite NiS_2 via Engineered Heteroatom Defect Boosting Overall Water Splitting. *ACS Nano* **2017**, *11* (11), 11574–11583.

(66) Zhao, Y.; Li, Q.; Shi, L.; Wang, J. Exploitation of the Large-Area Basal Plane of MoS_2 and Preparation of Bifunctional Catalysts through On-Surface Self-Assembly. *Adv. Sci.* **2017**, *4* (12), 1700356.

(67) Ding, J.; Zhou, Y.; Li, Y.; Guo, S.; Huang, X. MoS_2 Nanosheet Assembling Superstructure with a Three-Dimensional Ion Accessible Site: A New Class of Bifunctional Materials for Batteries and Electrocatalysis. *Chem. Mater.* **2016**, *28* (7), 2074–2080.

(68) Liu, J.; Xue, D. Rapid and Scalable Route to CuS Biosensors: A Microwave-Assisted Cu-Complex Transformation into CuS Nanotubes for Ultrasensitive Nonenzymatic Glucose Sensor. *J. Mater. Chem.* **2011**, *21* (1), 223–228.

(69) Bao, S. J.; Li, C. M.; Guo, C. X.; Qiao, Y. Biomolecule-Assisted Synthesis of Cobalt Sulfide Nanowires for Application in Supercapacitors. *J. Power Sources* **2008**, *180* (1), 676–681.

(70) Zhang, C.; Cai, X.; Qian, Y.; Jiang, H.; Zhou, L.; Li, B.; Lai, L.; Shen, Z.; Huang, W. Electrochemically Synthesis of Nickel Cobalt Sulfide for High-Performance Flexible Asymmetric Supercapacitors. *Adv. Sci.* **2018**, *5* (2), 1700375.

(71) Sun, Y.; Liu, C.; Grauer, D. C.; Yano, J.; Long, J. R.; Yang, P.; Chang, C. J. Electrodeposited Cobalt-Sulfide Catalyst for Electrochemical and Photoelectrochemical Hydrogen Generation from Water. *J. Am. Chem. Soc.* **2013**, *135* (47), 17699–17702.

(72) Liu, J.; Wang, J.; Ku, Z.; Wang, H.; Chen, S.; Zhang, L.; Lin, J.; Shen, Z. X. Aqueous Rechargeable Alkaline $Co_xNi_{2-x}S_2/TiO_2$ Battery. *ACS Nano* **2016**, *10* (1), 1007–1016.

(73) Khani, H.; Wipf, D. O. Iron Oxide Nanosheets and Pulse-Electrodeposited Ni-Co-S Nanoflake Arrays for High-Performance Charge Storage. *ACS Appl. Mater. Interfaces* **2017**, *9* (8), 6967–6978.

(74) Jurca, T.; Moody, M. J.; Henning, A.; Emery, J. D.; Wang, B.; Tan, J. M.; Lohr, T. L.; Lauhon, L. J.; Marks, T. J. Low-Temperature Atomic Layer Deposition of MoS_2 Films. *Angew. Chem. Int. Ed.* **2017**, *56* (18), 4991–4995.

(75) Shi, J.; Ma, D.; Han, G. F.; Zhang, Y.; Ji, Q.; Gao, T.; Sun, J.; Song, X.; Li, C.; Zhang, Y.; Liu, Z. Controllable Growth and Transfer of Monolayer MoS_2 on Au Foils and Its Potential Application in Hydrogen Evolution Reaction. *ACS Nano* **2014**, *8* (10), 10196–10204.

(76) Yonemoto, B. T.; Hutchings, G. S.; Jiao, F. A General Synthetic Approach for Ordered Mesoporous Metal Sulfides. *J. Am. Chem. Soc.* **2014**, *136* (25), 8895–8898.

(77) Zuo, Y.; Liu, Y.; Li, J.; Du, R.; Yu, X.; Xing, C.; Zhang, T.; Yao, L.; Arbiol, J.; Llorca, J.; Sivula, K.; Guijarro, N.; Cabot, A. Solution-Processed Ultrathin SnS_2-Pt Nanoplates for Photoelectrochemical Water Oxidation. *ACS Appl. Mater. Interfaces* **2019**, *11* (7), 6918–6926.

(78) Huang, S.; Zai, J.; Ma, D.; He, Q.; Liu, Y.; Qiao, Q.; Qian, X. Colloidal Synthesis of Wurtz-Stannite Cu_2CdGeS_4 Nanocrystals with High Catalytic Activity toward Iodine Redox Couples in Dye-Sensitized Solar Cells. *Chem. Commun.* **2016**, *52*(72), 10866–10869.

(79) Rhodes, J. M.; Jones, C. A.; Thal, L. B.; MacDonald, J. E. Phase-Controlled Colloidal Syntheses of Iron Sulfide Nanocrystals via Sulfur Precursor Reactivity and Direct Pyrite Precipitation. *Chem. Mater.* **2017**, *29* (19), 8521–8530.

(80) He, G.; Qiao, M.; Li, W.; Lu, Y.; Zhao, T.; Zou, R.; Li, B.; Darr, J. A.; Hu, J.; Titirici, M. M.; Parkin, I. P. S, N-Co-Doped Graphene-Nickel Cobalt Sulfide Aerogel: Improved Energy Storage and Electrocatalytic Performance. *Adv. Sci.* **2017**, *4* (1), 1600214.

(81) Lei, Y.; Pakhira, S.; Fujisawa, K.; Wang, X.; Iyiola, O. O.; Perea López, N.; Laura Elías, A.; Pulickal Rajukumar, L.; Zhou, C.; Kabius, B.; Alem, N.; Endo, M.; Lv. R.; Mendoza-Cortes, J.; Terrones, M. Low-Temperature Synthesis of Heterostructures of Transition Metal Dichalcogenide Alloys ($W_xMo_{1-x}S_2$) and Graphene with Superior Catalytic Performance for Hydrogen Evolution. *ACS Nano* **2017**, *11* (5), 5103–5112.

(82) Xiao, J.; Wan, L.; Yang, S.; Xiao, F.; Wang, S. Design Hierarchical Electrodes with Highly Conductive $NiCo_2S_4$ Nanotube Arrays Grown on Carbon Fiber Paper for High-Performance Pseudocapacitors. *Nano Lett.* **2014**, *14* (2), 831–838.

(83) Wang, D. Y.; Gong, M.; Chou, H. L.; Pan, C. J.; Chen, H. A.; Wu, Y.; Lin, M. C.; Guan, M.; Yang, J.; Chen, C. W.; Wang, Y. L.; Hwang, B. J.; Chen, C. C.; Dai, H. J. Highly Active and Stable Hybrid Catalyst of Cobalt-Doped FeS_2 Nanosheets-Carbon Nanotubes for Hydrogen Evolution Reaction. *J. Am. Chem. Soc.* **2015**, *137* (4), 1587–1592.

(84) Liu, W.; Niu, H.; Yang, J.; Cheng, K.; Ye, K.; Zhu, K.; Wang, G.; Cao, D.; Yan, J. Ternary Transition Metal Sulfides Embedded in Graphene Nanosheets as Both the Anode and

Cathode for High-Performance Asymmetric Supercapacitors. *Chem. Mater.* **2018**, *30* (3), 1055–1068.

(85) Chen, P.; Zhou, T.; Zhang, M.; Tong, Y.; Zhong, C.; Zhang, N.; Zhang, L.; Wu, C.; Xie, Y. 3D Nitrogen-Anion-Decorated Nickel Sulfides for Highly Efficient Overall Water Splitting. *Adv. Mater.* **2017**, *29* (30), 1701584.

(86) Coughlan, C.; Ibáñez, M.; Dobrozhan, O.; Singh, A.; Cabot, A.; Ryan, K. M. Compound Copper Chalcogenide Nanocrystals. *Chem. Rev*. **2017**, *117* (9), 5865-6109.

(87) Park, J.; Joo, J.; Soon, G. K.; Jang, Y.; Hyeon, T. Synthesis of Monodisperse Spherical Nanocrystals. *Angew. Chem. Int. Ed.* **2007**, *46* (25), 4630–4660.

(88) Talapin, D. V.; Lee, J. S.; Kovalenko, M. V.; Shevchenko, E. V. Prospects of Colloidal Nanocrystals for Electronic and Optoelectronic Applications. *Chem. Rev.* **2010**, *110* (1), 389–458.

(89) Carey, G. H.; Abdelhady, A. L.; Ning, Z.; Thon, S. M.; Bakr, O. M.; Sargent, E. H. Colloidal Quantum Dot Solar Cells. *Chem. Rev.* **2015**, *115* (23), 12732-12763.

(90) Murray, C. B.; Norris, D. J.; Bawendi, M. G. Synthesis and Characterization of Nearly Monodisperse CdE (E = S, Se, Te) Semiconductor Nanocrystallites. *J. Am. Chem. Soc.* **1993**, *115* (19), 8706–8715.

(91) De Mello Donegá, C.; Liljeroth, P.; Vanmaekelbergh, D. Physicochemical Evaluation of the Hot-Injection Method, a Synthesis Route for Monodisperse Nanocrystals. *Small* **2005**, *1* (12), 1152–1162.

(92) Soon, G. K.; Piao, Y.; Park, J.; Angappane, S.; Jo, Y.; Hwang, N. M.; Park, J. G.; Hyeon, T. Kinetics of Monodisperse Iron Oxide Nanocrystal Formation by "Heating-up" Process. *J. Am. Chem. Soc.* **2007**, *129* (41), 12571–12584.

(93) Xia, Y.; Xiong, Y.; Lim, B.; Skrabalak, S. E. Shape-Controlled Synthesis of Metal Nanocrystals: Simple Chemistry Meets Complex Physics? *Angew. Chem. Int. Ed.* **2009**, *48* (1), 60–103.

(94) Lamer, V. K.; Dinegar, R. H. Theory, Production and Mechanism of Formation of Monodispersed Hydrosols. *J. Am. Chem. Soc.* **1950**, *72* (11), 4847–4854.

(95) Hayward, R. C.; Saville, D. A.; Aksay, I. A. Electrophoretic Assembly of Colloidal Crystals with Optically Tunable Micropatterns. *Nature* **2000**, *404* (6773), 56–59.

(96) Peng, X.; Wickham, J.; Alivisatos, A. P. Kinetics of II-VI and III-V Colloidal Semiconductor Nanocrystal Growth: "Focusing" of Size Distributions. *J. Am. Chem. Soc.* **1998**, *120* (21), 5343-5344.

(97) Yin, Y.; Alivisatos, A. P. Colloidal Nanocrystal Synthesis and the Organic-Inorganic Interface. *Nature*. **2005**, *437*, 664–670.

(98) Thanh, N. T. K.; Maclean, N.; Mahiddine, S. Mechanisms of Nucleation and Growth of Nanoparticles in Solution. *Chem. Rev.* **2014**, *114* (15), 7610-7630

(99) Schladt, T. D.; Schneider, K.; Schild, H.; Tremel, W. Synthesis and Bio-Functionalization of Magnetic Nanoparticles for Medical Diagnosis and Treatment. *Dalton Trans*. **2011**, *40*, 6315-6343.

(100) Sigman, M. B.; Ghezelbash, A.; Hanrath, T.; Saunders, A. E.; Lee, F.; Korgel, B. A. Solventless Synthesis of Monodisperse Cu_2S Nanorods, Nanodisks, and Nanoplatelets. *J. Am. Chem. Soc.* **2003**, *125* (51), 16050–16057.

(101) Liu, Z.; Xu, D.; Liang, J.; Shen, J.; Zhang, S.; Qian, Y. Growth of Cu_2S Ultrathin Nanowires in a Binary Surfactant Solvent. *J. Phys. Chem. B* **2005**, *109* (21), 10699–10704.

(102) Han, W.; Yi, L.; Zhao, N.; Tang, A.; Gao, M.; Tang, Z. Synthesis and Shape-Tailoring of Copper Sulfide/Indium Sulfide-Based Nanocrystals. *J. Am. Chem. Soc.* **2008**, *130* (39), 13152–13161.

(103) Wang, Y.; Hu, Y.; Zhang, Q.; Ge, J.; Lu, Z.; Hou, Y.; Yin, Y. One-Pot Synthesis and Optical Property of Copper(I) Sulfide Nanodisks. *Inorg. Chem.* **2010**, *49* (14), 6601–6608.

(104) Kruszynska, M.; Borchert, H.; Bachmatiuk, A.; Rümmeli, M. H.; Büchner, B.; Parisi, J.; Kolny-Olesiak, J. Size and Shape Control of Colloidal Copper(I) Sulfide Nanorods. *ACS Nano* **2012**, *6* (7), 5889–5896.

(105) Li, W.; Shavel, A.; Guzman, R.; Rubio-Garcia, J.; Flox, C.; Fan, J.; Cadavid, D.; Ibáñez, M.; Arbiol, J.; Morante, J. R.; Cabot, A. Morphology Evolution of $Cu_{2-x}S$ Nanoparticles: From Spheres to Dodecahedrons. *Chem. Commun.* **2011**, *47* (37), 10332–10334.

(106) Du, Y.; Yin, Z.; Zhu, J.; Huang, X.; Wu, X. J.; Zeng, Z.; Yan, Q.; Zhang, H. A General Method for the Large-Scale Synthesis of Uniform Ultrathin Metal Sulphide Nanocrystals. *Nat. Commun.* **2012**, *3* (1), 1–7.

(107) Wu, C.; Yu, S. H.; Antonietti, M. Complex Concaved Cuboctahedrons of Copper Sulfide Crystals with Highly Geometrical Symmetry Created by a Solution Process. *Chem. Mater.* **2006**, *18* (16), 3599–3601.

(108) Meng, X.; Tian, G.; Chen, Y.; Zhai, R.; Zhou, J.; Shi, Y.; Cao, X.; Zhou, W.; Fu, H. Hierarchical CuS Hollow Nanospheres and Their Structure-Enhanced Visible Light Photocatalytic Properties. *CrystEngComm* **2013**, *15* (25), 5144–5149.

(109) Jiao, S.; Xu, L.; Jiang, K.; Xu, D. Well-Defined Non-Spherical Copper Sulfide Mesocages with Single-Crystalline Shells by Shape-Controlled Cu_2O Crystal Templating. *Adv. Mater.* **2006**, *18* (9), 1174–1177.

(110) Gao, J.; Li, Q.; Zhao, H.; Li, A.; Liu, C.; Gong, Q.; Qi, L. One-Pot Synthesis of Uniform Cu_2O and CuS Hollow Spheres and Their Optical Limiting Properties. *Chem. Mater.* **2008**, *20* (19), 6263–6269.

(111) Zuo, Y.; Li, J.; Yu, X.; Du, R.; Zhang, T.; Wang, X.; Arbiol, J.; Llorca, J.; Cabot, A. A SnS_2 Molecular Precursor for Conformal Nanostructured Coatings. *Chem. Mater.* **2020**, *32*, 2097–2106.

(112) Li, J.; Zuo, Y.; Liu, J.; Wang, X.; Yu, X.; Du, R.; Zhang, T.; Infante-Carrió, M. F.; Tang, P.; Arbiol, J.; Llorca, J.; Luo, Z.; Cabot, A. Superior Methanol Electrooxidation Performance of (110)-Faceted Nickel Polyhedral Nanocrystals. *J. Mater. Chem. A* **2019**, *7* (38), 22036–22043.

(113) Xia, C.; Jiang, Q.; Zhao, C.; Hedhili, M. N.; Alshareef, H. N. Selenide-Based Electrocatalysts and Scaffolds for Water Oxidation Applications. *Adv. Mater.* **2016**, *28* (1), 77–85.

(114) Ye, R.; Del Angel-Vicente, P.; Liu, Y.; Arellano-Jimenez, M. J.; Peng, Z.; Wang, T.; Li, Y.; Yakobson, B. I.; Wei, S. H.; Yacaman, M. J.; et al. High-Performance Hydrogen Evolution from $MoS_{2(1-x)}P_x$ Solid Solution. *Adv. Mater.* **2016**, *28* (7), 1427–1432.

(115) Katsounaros, I.; Cherevko, S.; Zeradjanin, A. R.; Mayrhofer, K. J. J. Oxygen Electrochemistry as a Cornerstone for Sustainable Energy Conversion. *Angew. Chem. Int. Ed.* **2014**, *53* (1), 102–121.

(116) Morales-Guio, C. G.; Stern, L. A.; Hu, X. Nanostructured Hydrotreating Catalysts for Electrochemical Hydrogen Evolution. *Chem. Soc. Rev*. **2014**, *43*, 6555-6569.

(117) Chen, Y.; Yu, G.; Chen, W.; Liu, Y.; Li, G. D.; Zhu, P.; Tao, Q.; Li, Q.; Liu, J.; Shen, X.; Li, H.; Huang, X.; Wang, D.; Asefa, T.; Zou, X. Highly Active, Nonprecious Electrocatalyst Comprising Borophene Subunits for the Hydrogen Evolution Reaction. *J. Am. Chem. Soc.* **2017**, *139* (36), 12370–12373.

(118) Sun, H.; Xu, X.; Yan, Z.; Chen, X.; Jiao, L.; Cheng, F.; Chen, J. Superhydrophilic Amorphous Co-B-P Nanosheet Electrocatalysts with Pt-like Activity and Durability for the Hydrogen Evolution Reaction. *J. Mater. Chem. A* **2018**, *6* (44), 22062–22069.

(119) Sun, H.; Yan, Z.; Liu, F.; Xu, W.; Cheng, F.; Chen, J. Self-Supported Transition-Metal-Based Electrocatalysts for Hydrogen and Oxygen Evolution. *Adv. Mater.* **2020**, *32* (3), 1806326.

(120) Chen, G. F.; Ma, T. Y.; Liu, Z. Q.; Li, N.; Su, Y. Z.; Davey, K.; Qiao, S. Z. Efficient and Stable Bifunctional Electrocatalysts Ni/NixMy (M = P, S) for Overall Water Splitting. *Adv. Funct. Mater.* **2016**, *26* (19), 3314–3323.

(121) Yan, Z.; Sun, H.; Chen, X.; Liu, H.; Zhao, Y.; Li, H.; Xie, W.; Cheng, F.; Chen, J. Anion Insertion Enhanced Electrodeposition of Robust Metal Hydroxide/Oxide Electrodes for Oxygen Evolution. *Nat. Commun.* **2018**, *9* (1), 1–9.

(122) Zou, X.; Wu, Y.; Liu, Y.; Liu, D.; Li, W.; Gu, L.; Liu, H.; Wang, P.; Sun, L.; Zhang, Y. In Situ Generation of Bifunctional, Efficient Fe-Based Catalysts from Mackinawite Iron Sulfide for Water Splitting. *Chem* **2018**, *4* (5), 1139–1152.

(123) Faber, M. S.; Dziedzic, R.; Lukowski, M. A.; Kaiser, N. S.; Ding, Q.; Jin, S. High-Performance Electrocatalysis Using Metallic Cobalt Pyrite (CoS_2) Micro- and Nanostructures. *J. Am. Chem. Soc.* **2014**, *136* (28), 10053–10061.

(124) Pi, Y.; Shao, Q.; Wang, P.; Lv, F.; Guo, S.; Guo, J.; Huang, X. Trimetallic Oxyhydroxide Coralloids for Efficient Oxygen Evolution Electrocatalysis. *Angew. Chem. Int. Ed.* **2017**, *56* (16), 4502–4506.

(125) Wang, Y.; Zhang, G.; Xu, W.; Wan, P.; Lu, Z.; Li, Y.; Sun, X. A 3D Nanoporous Ni-Mo Electrocatalyst with Negligible Overpotential for Alkaline Hydrogen Evolution. *ChemElectroChem* **2014**, *1* (7), 1138–1144.

(126) Xu, K.; Wang, F.; Wang, Z.; Zhan, X.; Wang, Q.; Cheng, Z.; Safdar, M.; He, J. Component-Controllable $WS_{2(1-x)}Se_{2x}$ Nanotubes for Efficient Hydrogen Evolution Reaction. *ACS Nano* **2014**, *8* (8), 8468–8476.

(127) Peng, S.; Li, N.; Han, X.; Sun, W.; Srinivasan, M.; Mhaisalkar, S. G.; Cheng, F.; Yan, Q.; Chen, J.; Ramakrishna, S. Cobalt Sulfide Nanosheet/Graphene/Carbon Nanotube Nanocomposites as Flexible Electrodes for Hydrogen Evolution. *Angew. Chem. Int. Ed.* **2014**, *53* (46), 12594–12599.

(128) Jin, S. Are Metal Chalcogenides, Nitrides, and Phosphides Oxygen Evolution Catalysts or Bifunctional Catalysts? *ACS Energy Lett*. **2017**, *2* (8), 1937-1938.

(129) Wygant, B. R.; Kawashima, K.; Mullins, C. B. Catalyst or Precatalyst? The Effect of Oxidation on Transition Metal Carbide, Pnictide, and Chalcogenide Oxygen Evolution Catalysts. *ACS Energy Lett.* **2018**, *3* (12), 2956–2966.

(130) Yang, W.; Zhang, L.; Hu, Y.; Zhong, Y.; Wu, H. Bin; Lou, X. W. Microwave-Assisted Synthesis of Porous Ag_2S-Ag Hybrid Nanotubes with High Visible-Light Photocatalytic Activity. *Angew. Chem. Int. Ed.* **2012**, *51* (46), 11501–11504.

(131) Kuang, P. Y.; Zheng, P. X.; Liu, Z. Q.; Lei, J. L.; Wu, H.; Li, N.; Ma, T. Y. Embedding Au Quantum Dots in Rimous Cadmium Sulfide Nanospheres for Enhanced Photocatalytic Hydrogen Evolution. *Small* **2016**, *12* (48), 6735–6744.

(132) Ng, B. J.; Putri, L. K.; Kong, X. Y.; Shak, K. P. Y.; Pasbakhsh, P.; Chai, S. P.; Mohamed, A. R. Sub-2 nm Pt-Decorated $Zn_{0.5}Cd_{0.5}S$ Nanocrystals with Twin-Induced Homojunctions for Efficient Visible-Light-Driven Photocatalytic H_2 Evolution. *Appl. Catal. B Environ.* **2018**, *224*, 360–367.

(133) Yin, L.; Cheng, R.; Song, Q.; Yang, J.; Kong, X.; Huang, J.; Lin, Y.; Ouyang, H. Construction of Nanoflower SnS_2 Anchored on G-C_3N_4 Nanosheets Composite as Highly Efficient Anode for Lithium Ion Batteries. *Electrochim. Acta* **2019**, *293*, 408–418.

(134) Shang, H.; Zuo, Z.; Li, L.; Wang, F.; Liu, H.; Li, Y.; Li, Y. Ultrathin Graphdiyne Nanosheets Grown In Situ on Copper Nanowires and Their Performance as Lithium-Ion Battery Anodes. *Angew. Chem. Int. Ed.* **2018**, *57* (3), 774–778.

(135) Wu, L.; Zheng, J.; Wang, L.; Xiong, X.; Shao, Y.; Wang, G.; Wang, J. H.; Zhong, S.; Wu, M. PPy-Encapsulated SnS_2 Nanosheets Stabilized by Defects on a TiO_2 Support as a Durable Anode Material for Lithium-Ion Batteries. *Angew. Chem. Int. Ed.* **2019**, *58* (3), 811–815.

Chapter 2

In-situ Electrochemical Oxidation of Cu_2S into CuO Nanowires as a Durable and Efficient Electrocatalyst for Oxygen Evolution Reaction

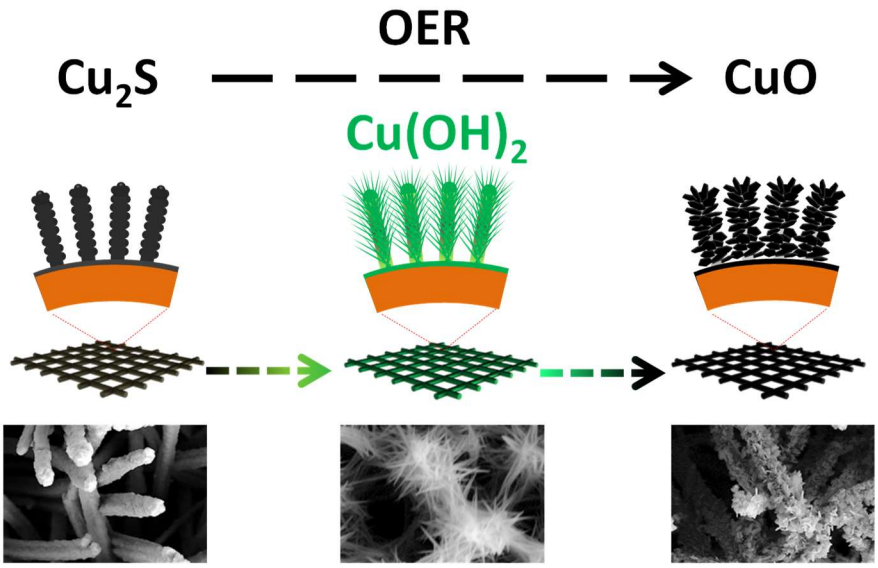

2.1 Abstract

The development of cost-effective oxygen evolution catalysts is of capital importance for the deployment of large scale energy storage systems based on metal-air batteries and reversible fuel cells. In this direction, a wide range of materials have been explored, especially in more favorable alkaline conditions, and several metal chalcogenides have particularly demonstrated excellent performances. However, chalcogenides are thermodynamically less stable than the corresponding oxides and hydroxides under oxidizing potentials in alkaline media. While this instability in some cases has prevented the application of chalcogenides as oxygen evolution catalysts, and it has been disregarded in some other, we propose to use it in our favor to produce high performance oxygen evolution catalysts. We characterize here the *in-situ* chemical, structural and

morphological transformation during the oxygen evolution reaction (OER) in alkaline media of Cu_2S into CuO nanowires (NWs), mediating the intermediate formation of $Cu(OH)_2$. We also test their OER activity and stability under OER operation in alkaline media, and compare them with the OER performance of $Cu(OH)_2$ and CuO nanostructures directly grown on the surface of a copper mesh. We demonstrate here that CuO produced from *in-situ* electrochemical oxidation of Cu_2S displays an extraordinary electrocatalytic performance toward OER, well above that of CuO and $Cu(OH)_2$ synthesized without this transformation.

2.2 Introduction

Driven by energy and environmental crises resulting from the fast consumption of fossil fuels, the share of renewable energies such as wind and photovoltaics is steadily growing. To sustain this growth, besides increasing cost-efficiency of the generation technologies, we need to develop large scale and cost-effective power storage systems able to compensate for the fluctuating character of these energy supplies. In this direction, metal-air batteries, reversible fuel cells and electrolyzers are the most promising technologies for large scale and distributed energy storage, but all of them are limited by the same essential and sluggish reaction step: oxygen evolution.[1–3] The oxygen evolution reaction (OER) involves breaking O-H bonds to form O=O bonds, what comprises four sequential proton-coupled electron transfer steps.[4–7] Currently noble metals are used to catalyze this reaction, but activities and stabilities are still not satisfactory and the high cost of these catalysts compromises the system cost-effectiveness. Thus the development of highly efficient and robust OER catalysts based on earth-abundant elements is a topic of capital importance.[8–13]

Transition metal oxides and (oxy)hydroxides are the main alternative to noble metals as OER catalysts, reaching performances close to those of IrO_2/RuO_2 in alkaline media.[14,15] Additionally, several reports have claimed metal phosphides,[16–18] nitrides,[19–22] selenides[23,24] and sulfides[25–28] to be excellent OER catalysts. However, some of these compounds are thermodynamically unstable under harsh OER conditions and may suffer chemical transformation during operation.[2,6,29–31] While this instability has been ignored in most studies, when analyzed in detail, the excellent performances obtained for chalcogenides and pnictides have in some cases been related not to the chalcogenide or pnictide cations, but to the *in-situ* formed oxide or (oxy)hydroxide.[32–39] For example, the

OER activity of CoS_x,[40] NiS,[27] NiSe,[6] and $Ni_xFe_{1-x}Se_2$[41] catalysts was demonstrated to be related to the partial or complete oxidization of the chalcogenide to the corresponding oxide/(oxy)hydroxide.

The performances of oxides and hydroxides grown during OER operation may be even higher than that of oxides and hydroxides grown by other routes because of the following hypothesis: i) During the *in-situ* growth of the oxide/hydroxide nanostructured material, avenues for effective electrolyte diffusion may be created; ii) During the rapid chemical transformation at ambient temperature, an increase of the surface area through the material recrystallization in the form of smaller crystallites may be obtained. iii) A high density of defects, including ion vacancies, grain boundaries and metastable phases, may be obtained in these growth conditions; iv) New catalytic sites with higher activity may be *in-situ* created due to the intimate relation between the structure growth and the electrocatalytic OER process; v) Residual chalcogen and phosphorous cations facilitating OER process by modifying the adsorption energy of reaction intermediates. [42–45]

Herein, take copper as illustrating electrocatalyst, we demonstrate the possibility to obtain OER electrocatalysts with enhanced performance from the *in-situ* oxidation of a chalcogenide in OER conditions. With this purpose, we first report on the chemical, structural and morphological transformation during OER operation of Cu_2S nanowires (NWs) grown on the surface of a copper mesh (CM). We subsequently investigate the effect that these transformations have on the OER activity of Cu_2S and Cu_2S-derived nanostructures and demonstrate the OER performance of the compound *in-situ* formed during operation to outperform that of the same compound obtained by other processes, both in terms of activity and stability.

2.3 Experimental section

2.3.1 Chemicals

Ammonium persulfate (APS, $(NH_4)_2S_2O_8$, ≥98.0 %) and sodium sulfide nonahydrate ($Na_2S·9H_2O$, ≥98.0 %) were purchased from Aldrich. Sodium hydroxide (NaOH, 98.5 %) was purchased from Acros. All chemicals were used as received without further purification. Cu mesh (CM) with a wire diameter of about 200 μm and a pore size of 400 μm, and Cu foam (CF) with a thickness of 1 mm and a pore size of 120 PPI were purchased from Kunshan GuangJiaYuan new materials Co. Ltd. Deionized water (DW,

18.6 MΩ · cm) obtained using a purification system (Mini-Q Water) was used for all experiments.

2.3.2 Synthesis of $Cu(OH)_2$/CM

$Cu(OH)_2$ NWs on CM [$Cu(OH)_2$/CM] were prepared following an earlier report with some modifications.[46,47] Briefly, a piece of CM (2.5 cm×1 cm) was thoroughly cleaned using ethanol/acetone and HCl (5 mol/L) for 30 minutes, and then rinsed with plenty of DW. The cleaned CM was then immersed in a solution of NaOH (40 mmol), APS (2 mmol) and DW (20 mL) at room temperature for 30 min. The obtained $Cu(OH)_2$/CM was then washed carefully using DW and then dried using nitrogen flow.

2.3.3 Synthesis of Cu_2S/CM

Cu_2S NWs on CM (Cu_2S/CM) were prepared by an anion exchange route. $Cu(OH)_2$/CM were immersed in a Na_2S solution (20 mL DW, 0.1 mol/L) for 1 h at 60 °C. The obtained black Cu_2S/CM was carefully washed using DW and ethanol and then dried naturally.

2.3.4 Synthesis of CuO/CM-AN

CuO NWs on Cu mesh (CuO/CM-AN) were prepared by annealing $Cu(OH)_2$/CM under Ar atmosphere for 2 h at 200 °C, reached using a temperature ramp of 5 °C/min. The obtained CuO/CM-AN was collected without any further treatment.

2.3.5 Synthesis of Cu_2S/CF

Cu_2S NWs on CF (Cu_2S/CF) were prepared using a similar procedure as the one used to produce Cu_2S/CM, but using a CF instead of a CM and increasing the sulfurization time to 2 h to complete the ion exchange.

2.3.6 Materials Characterization

X-ray diffraction (XRD) patterns were obtained on a Bruker AXS D8 Advance X-ray diffractometer (Bruker, Karlsruhe, Germany) operating at 40 kV and 40 mA with Ni-filtered (2 μm thickness) Cu Kα1 radiation (λ = 1.5406 Å). Scanning electron microscope (SEM) analysis was carried out in a Zeiss Auriga microscope (Carl Zeiss, Jena, Germany) with an energy dispersive X-ray spectroscopy (EDX) detector at 20 kV to study composition. Transmission electron microscopy (TEM) characterization was carried out on a Zeiss Libra 120 (Carl Zeiss, Jena, Germany), operating at 120 kV. High-resolution

TEM (HRTEM) images were obtained using a field emission gun FEI Tecnai F20 microscope at 200 kV with a point-to-point resolution of 0.19 nm. High angle annular dark-field (HAADF) scanning TEM (STEM) was combined with electron energy loss spectroscopy (EELS) in the Tecnai microscope by using a Gatan Quantum filter. For TEM characterization, tiny powder samples were carefully collected by folding the Cu substrate to peel the surface materials. The collected powder was dispersed in ethanol by 30 s sonication and then drop casted on a 200 mesh copper grid. X-ray photoelectron spectroscopy (XPS) was carried out on a Specs system (Specs GmbH, Berlin, Germany) equipped with a Mg anode XR50 source operating at 250 W and a Phoibos 150 MCD-9 detector (Specs GmbH, Berlin, Germany). The pressure in the analysis chamber was kept below 10^{-7} Pa. Data processing was performed with the CasaXPS program (Casa Software Ltd., UK). Binding energy (BE) values were centered by using the Cu 2p peak at 932.7 eV.

2.3.7 Electrochemical Measurements

Electrochemical measurements were conducted in a three-electrode system using an electrochemical workstation (Metrohm Autolab). Characterized samples were used as working electrode (partially cut to leave the working area as 1×1 cm); while a graphite rod with a diameter of 6 mm was used as the counter electrode and a Hg/HgO (1 M KOH, 0.098 V *vs.* RHE) was applied as the reference electrode. 1 M KOH was used as electrolyte. The electrolyte was purged with O_2 for 30 min prior to each measurement. The following formula was used to convert the potentials to the reversible hydrogen electrode (RHE) standard scale:

$$E \textit{ vs. } RHE = E_{Hg/HgO} + E^{o}_{Hg/HgO} + 0.059 \times pH = E_{Hg/HgO} + 0.924 \text{ (V)}$$

While the following formula was applied to calculate the overpotentials:

$$\eta = E - 1.23 \text{ (V)} = E_{Hg/HgO} - 0.306 \text{ (V)}$$

Polarization curves were obtained using cyclic voltammetry (CV) at 100 mV/s when analyzing chemical transformations and at 5 mV/s when analyzing OER performance. Structural, chemical and morphological characterization of the electrodes after operation/activation was carried out by cutting a small piece of working electrode (*ca.* 3×3mm triangle). All tests were done under static circumstance without a magnet bar stirring on bottom. All the experiments were performed at room temperature of *ca.* 15 ^{o}C.

2.3.8 Electrochemical Surface Area (ECSA)

To estimate the effective ECSA, CV measurements were conducted to check the electrochemical double layer capacitance of samples at the non-faradic potential region to. Typically, a series of CV were performed at various scan rates (10 mV/s, 20 mV/s, 40 mV/s, etc.) in 1.22-1.32 V *vs.* RHE. The double layer capacitance (C_{dl}) was determined using the equation $\Delta J/2 = \nu \times C_{dl}$, in which ΔJ corresponds to the current density between the anodic and cathodic sweeps at 1.27 V *vs.* RHE against the scan rate. The slope of the fitting line is equal to twice of the C_{dl} value, which is proportional to the electrochemical surface area of the materials. ECSA was then calculated by dividing C_{dl} by C_s ($ECSA=C_{dl}/C_s$), where C_s is the specific electrochemical double-layer capacitance of an atomically smooth surface, which can be considered as 0.04 mF/cm^2 based on typical values reported previously.[48,49] This comparison makes sense only when the measurements of materials are carried out under the same condition.

2.3.9 Electrochemical Impedance Spectroscopy (EIS)

EIS was conducted on the working electrodes under the OER operating conditions at the anodic bias that delivered a geometric current density of *ca.* 10 mA/cm^2 (0.68 V *vs.* Hg/HgO). A sinusoidal voltage with amplitude of 10 mV and a scanning frequency ranging from 100 mHz to 1 MHz was applied to carry out the measurements.

2.3.10 iR Correction

The OER curves in this work are shown without iR correction. However, to display the accurate performance on OER operation, we did iR correction towards the overpotential that delivers a geometric current density of 10 mA/cm^2 according to the following formula:

$$\eta_{corrected} = \eta - iR_s \times 90\ \%$$

R_s indicates the solution resistance and can be measured using EIS. In our work, the R_s was measured as 4.7 Ω at 10 mA/cm^2 for Cu_2S-derived CuO/CM.

2.3.11 In-situ Raman Spectroscopy

In-situ Raman measurements were performed with a Raman microscope (Horiba Jobin Yvon XploRA PLUS) coupled to an optical microscope (Olympus BX41). The objective lens (Olympus MPlan N, 50×, NA=0.75) was covered with optically transparent Teflon

film (American Durafilm 50A, 0.013 mm) to prevent potential damage from electrolytes. Raman excitation was provided by a 532 nm laser (Horiba DPSS). A 3-electrode configuration was set up in a 3D printed Raman electrochemical cell that was fit onto the manual Olympus XY stage. The 3-electrode configuration was connected to a Bio-Logic SP-50 potentiostat. The *in-situ* Raman characterization was performed by stopping the cycling voltammetry after 10, 20, 50, 100 and 200 cycles completion, respectively, on an as-prepared working electrode.

2.4 Results and Discussion

$Cu(OH)_2$ NWs were grown at the surface of a CM by immersing it in an aqueous solution of NaOH/APS for 30 min. During this process, the initial reddish brown CM turned greenish-blue (Figure 2.1a). XRD patterns of the produced layers fitted well with the standard JCPDF card #13-0420 corresponding to $Cu(OH)_2$ (Figure 2.2a). SEM micrographs of $Cu(OH)_2$/CM displayed a homogeneous distribution of faceted NWs with an average thickness of *ca.* 200 nm (Figure 2.2b) and an average length of *ca.* 15 μm (Figure 2.1c). The growth mechanism of $Cu(OH)_2$ NWs from Cu surfaces was previously described and it is illustrated in Figure 2.1d.[50] Briefly, surface Cu is oxidized by $S_2O_8^{2-}$ ions to Cu^{2+}, which immediately reacts with OH^- in solution to subsequently recrystallize $Cu(OH)_2$ nanostructures on the CM surface.[50]

$Cu(OH)_2$/CM was sulfurized by immersion in a Na_2S solution (Figure 2.2c). During this transformation, the layer color changed from greenish-blue to black (Figure 2.1a). XRD analysis showed the produced layers to have a hexagonal Cu_2S crystal phase (JCPDS #23-0961), with no evidence of crystalline Cu_xO impurities. EDX analyses confirmed the atomic ratio between Cu and S to be close to that of stoichiometric Cu_2S (Figure 2.3). Cu_2S nanostructures maintained the original $Cu(OH)_2$ NW geometry, but displayed much rougher surfaces that contained flake-like crystallites with an average size of *ca.* 50 nm in diameter and *ca.* 10 nm in thickness (Figures 2.2c, 2.2d, 2.1c). HRTEM analysis confirmed the crystallographic phase of the crystallites to match that of hexagonal Cu_2S (space group = P63/mmc) with a=b=3.8900 Å and c=6.6800 Å (Figure 2.2d, right side). EELS chemical composition maps displayed a homogeneous distribution of both Cu and S throughout the NWs (Figure 2.2e).

XPS analysis of Cu_2S/CM (Figure 2.2f) displayed a main Cu 2p doublet at 932.7 eV (Cu $2p_{3/2}$), corresponding to Cu^0 and/or Cu^+ species.[51,52] The presence of a small satellite

peak at ca. 945 eV revealed the existence of a Cu^{2+} contribution, which accounted for less than 10 % of the total measured copper. This contribution may result from a partial surface oxidation upon exposure to ambient atmosphere.[53] The Cu $L_3M_{4,5}M_{4,5}$ Auger spectrum was analyzed to differentiate between Cu^0 and Cu^+ components. As displayed in Figure 2.2f, the Cu LMM signal could be fitted assuming a main Cu_2S component and a minor CuO contribution[54,55] accounting for *ca.* 10 % of the total Cu, in agreement with the deconvolution of the Cu 2p region. We speculate that Cu^{2+} ions within $Cu(OH)_2$ are first reduced by S^{2-} to Cu^+ of Cu_2O (eq. 2.1),[56] and then an anion exchange between O^{2-} and S^{2-} (eq. 2.2) takes place, since the solubility constant of Cu_2S (K_{sp} = 2.5 ×10^{-48}) is much lower than that of Cu_2O (K_{sp} = 2.0 ×10^{-15}).[57,58]

$$2Cu(OH)_2 + S^{2-} \rightarrow Cu_2O + S\downarrow + 2OH^- + H_2O \qquad \text{eq. 2.1}$$

$$Cu_2O + S^{2-} + H_2O \rightarrow Cu_2S + 2OH^- \qquad \text{eq. 2.2}$$

Besides, the K_{sp} of CuO (4.37×10^{-21}) [59] is much higher than that of Cu_2S, thus the initial formation of a CuO layer due to air oxidation or dehydration of some $Cu(OH)_2$ would also be transformed to Cu_2S via the anion exchange as shown in eq. 2.3. [60]

$$2CuO + 2S^{2-} + 2H_2O \rightarrow Cu_2S + S\downarrow + 4OH^- \qquad \text{eq. 2.3}$$

The S 2p XPS spectrum displayed two well-defined doublets at 162.2 eV (S $2p_{3/2}$) and 169.1 eV (S $2p_{3/2}$) that were assigned to lattice S in Cu_2S and to sulfate species arising from the surface oxidation of the material, respectively.[53,61–66] Sulfates accounted for *ca.* 14 % of the total amount of sulfur detected.

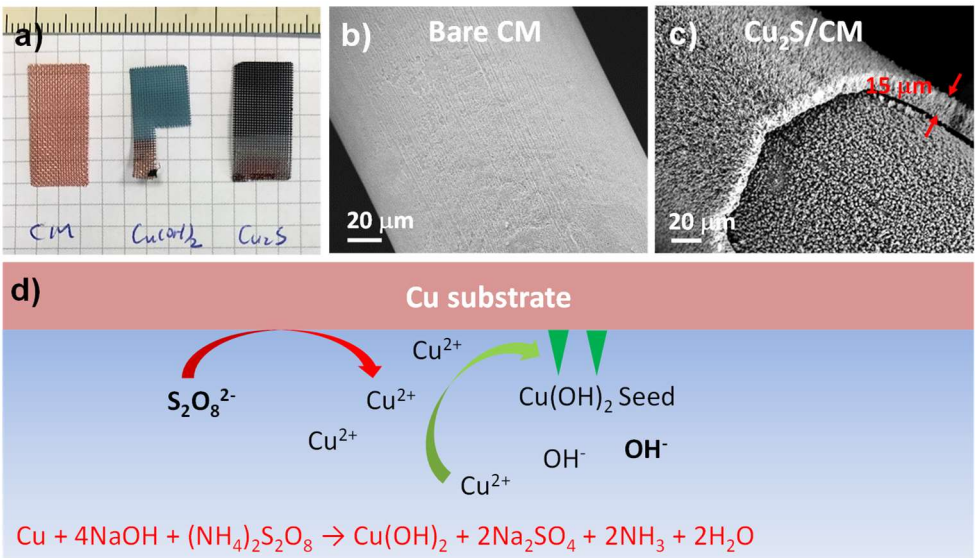

Figure 2.1. (a) Photograph of blank bare CM (left), $Cu(OH)_2$/CM (middle) and as-prepared Cu_2S/CM (right). (b) SEM image of bare CM. (c) SEM image of a cracked Cu_2S/CM. It can be easily seen that the layer thickness and thus the length of the Cu_2S NWs was ca. 15 μm. (d) Schematic diagram of the growth of $Cu(OH)_2$ NWs on CM.

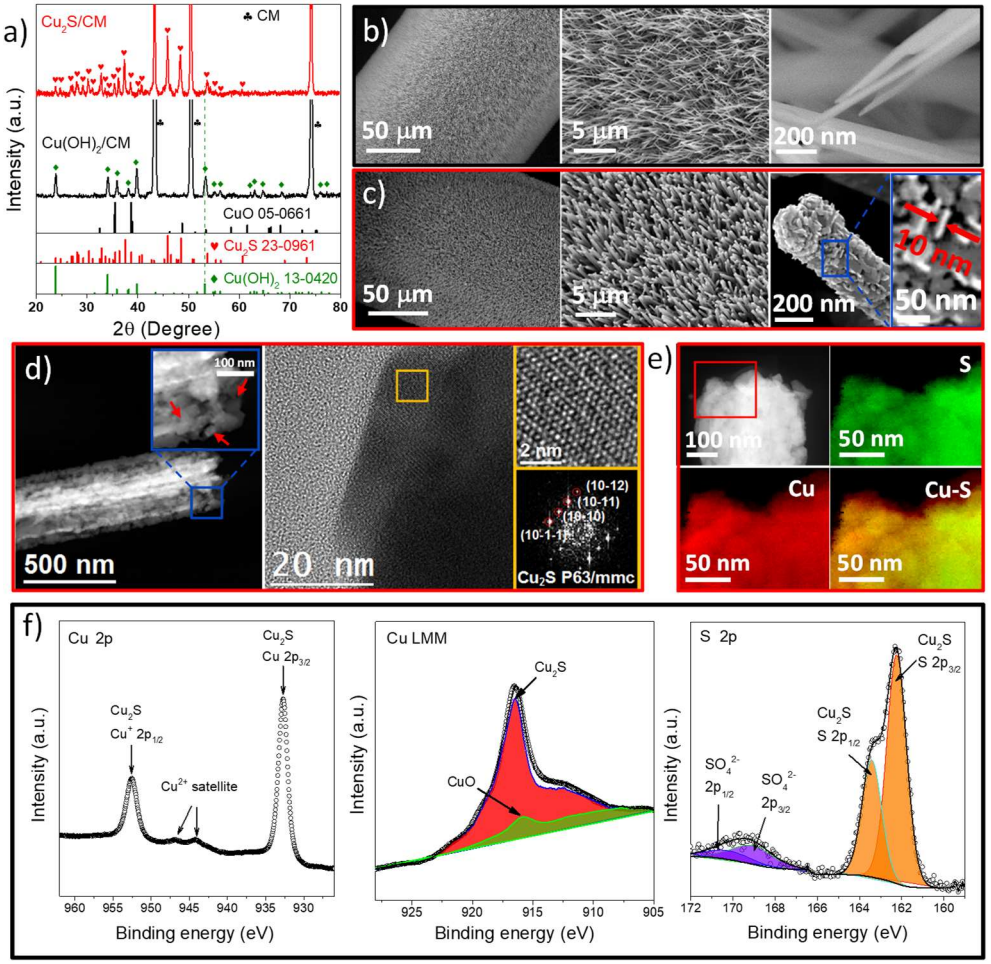

Figure 2.2. (a) XRD patterns of $Cu(OH)_2$/CM and Cu_2S/CM. (b,c) SEM images of (b) $Cu(OH)_2$/CM and (c) Cu_2S/CM. (d) HAADF STEM and HRTEM micrographs of a Cu_2S NW. Arrows point at single nanoflakes used to determine their size. From the crystalline domain displayed, the Cu_2S lattice fringe distances were measured to be 0.236 nm, 0.296 nm, 0.342 nm and 0.311 nm, at 18.65º, 45.93º and 72.42º, which was interpreted as the hexagonal Cu_2S phase visualized along its [-12-10] zone axis. (e) HAADF STEM micrograph and EELS chemical composition maps obtained from the red squared area of the HAADF STEM micrograph: Individual Cu $L_{2,3}$-edges at 931 eV (red) and S $L_{2,3}$-edges at 165 eV (green) as well as its composite. (f) Cu 2p, Cu LMM and S 2p regions of the XPS spectrum of Cu_2S/CM.

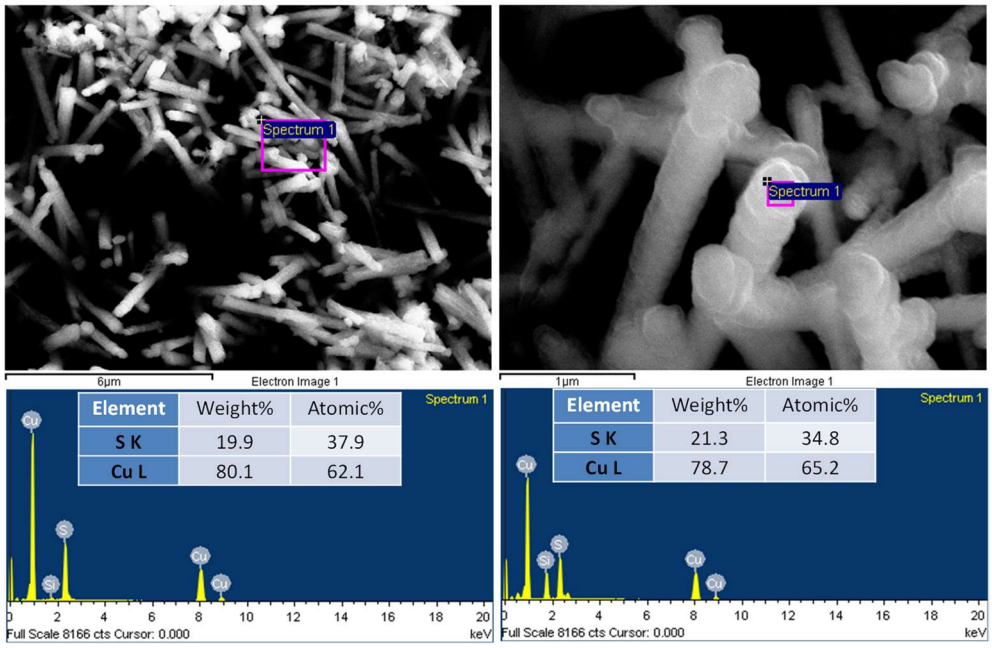

Figure 2.3. SEM micrographs and EDX spectra of as-prepared Cu_2S NWs scratched from CM and supported on silicon.

Cu_2S/CM electrodes were cycled in the potential range 0-0.8 V *vs.* Hg/HgO at a scan rate of 100 mV/s while immersed in a 1 M KOH electrolyte solution. During the initial 50 CV cycles, a drastic change of electrochemical performance was observed (Figure 2.4a). The first several CVs provided a relatively linear dependence of the current density with the applied potential. This current density rapidly decreased with the cycle number, pointing at an intense chemical transformation of the working electrode. After 200 cycles, the electrochemical response was stabilized (Figure 2.4b-d). Figure 2.4e displays a series of quasi-stationary CVs measured at a slow scan rate of 5 mV/s on the initial Cu_2S/CM and after 50, 100 and 200 CV cycles (Cu_2S/CM_50CVs; Cu_2S/CM_100CVs; Cu_2S/CM_200CVs). High oxidation currents were obtained from the initial Cu_2S/CM electrodes and only after *ca.* 200 CVs a conventional and relatively stable OER curve was measured (Figure 2.4e, f).

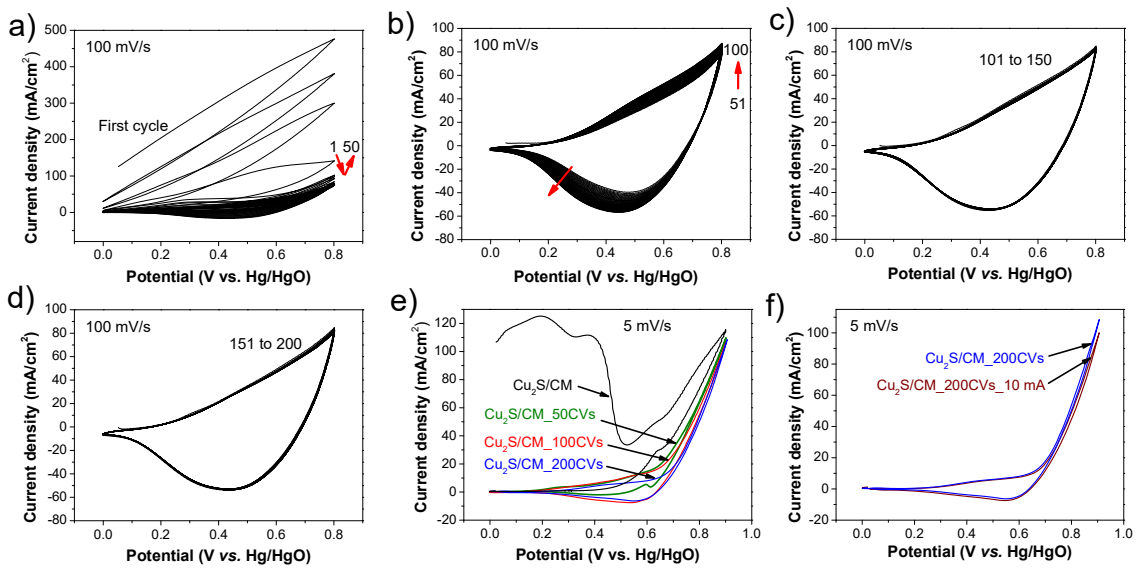

Figure 2.4. (a-d) Multiple CVs of Cu_2S/CM at a scan rate of 100 mV/s: (a) 1-50 cycles; (b) 151-100 cycles; (c) 101-150; (d) 151-200. (e, f) Quasi-stationary polarization CVs obtained at 5 mV/s of Cu_2S/CM: (c) after different activation CVs at 100 mV/s, and (d) after 200 CVs at 100 mV/s and before/after further chronopotentiometry measurement at a geometric current density of 10 mA/cm^2 for 10000 s.

SEM analysis of Cu_2S/CM electrodes showed that under OER conditions, the initial Cu_2S NWs developed thin nanofibers that interconnected into networks after 50 CVs (Figure 2.5a-b). After 100 CVs, nanofibers had grouped into bundles, which evolved again into nanoflake-based NWs as cycling continued (Figure 2.5c-d). Stable NWs obtained after *ca.* 200 CVs were slightly thicker than the initial ones, *ca.* 400 nm, conserved a similar length, *ca.* 15 μm, and were composed of slightly larger nanoflakes (*ca.* 150 nm in diameter, *ca.* 10 nm in thickness) that grouped less compactly than in the original Cu_2S NWs, thus providing a more porous NW structure.

XRD analysis demonstrated the initial Cu_2S to be transformed into $Cu(OH)_2$ after 50 CVs, and to have evolved to CuO after 200 CVs at 100 mV/s (Figure 2.5e). To track the composition evolution in more detail, *in-situ* Raman spectroscopy was performed on freshly prepared Cu_2S/CM samples after 10, 20, 50, 100, and 200 CVs at 100 mV/s. As shown in Figure 2.5f, the initial Cu_2S/CM exhibited two characteristic Raman peaks at 266 cm^{-1} (Cu–S bond)[67,68] and 472 cm^{-1} (S–S bond),[67,68] that corresponded to Cu_2S. A similar spectrum was obtained after 10 CVs. After 20 CVs, the intensity of the main peak at 472 cm^{-1} dramatically decreased and new peaks appeared. After 50 CVs, Raman spectra evidenced the presence of $Cu(OH)_2$, with two characteristic peaks at 290 cm^{-1} and 488 cm^{-1}.[69] An additional weak peak at 633 cm^{-1} could be assigned to the presence

of a copper oxide phase.[69] After extensive cycling, the initial Cu_2S/CM had completely transformed to CuO, which displayed three characteristic Raman peaks at 290 cm^{-1} (Cu–O bond, A_g phonon mode),[69] 340 cm^{-1} (Cu–O bond, B_{1g} phonon mode),[69,70] and 623 cm^{-1} (Cu–O bond, B_{2g} phonon mode).[69,70]

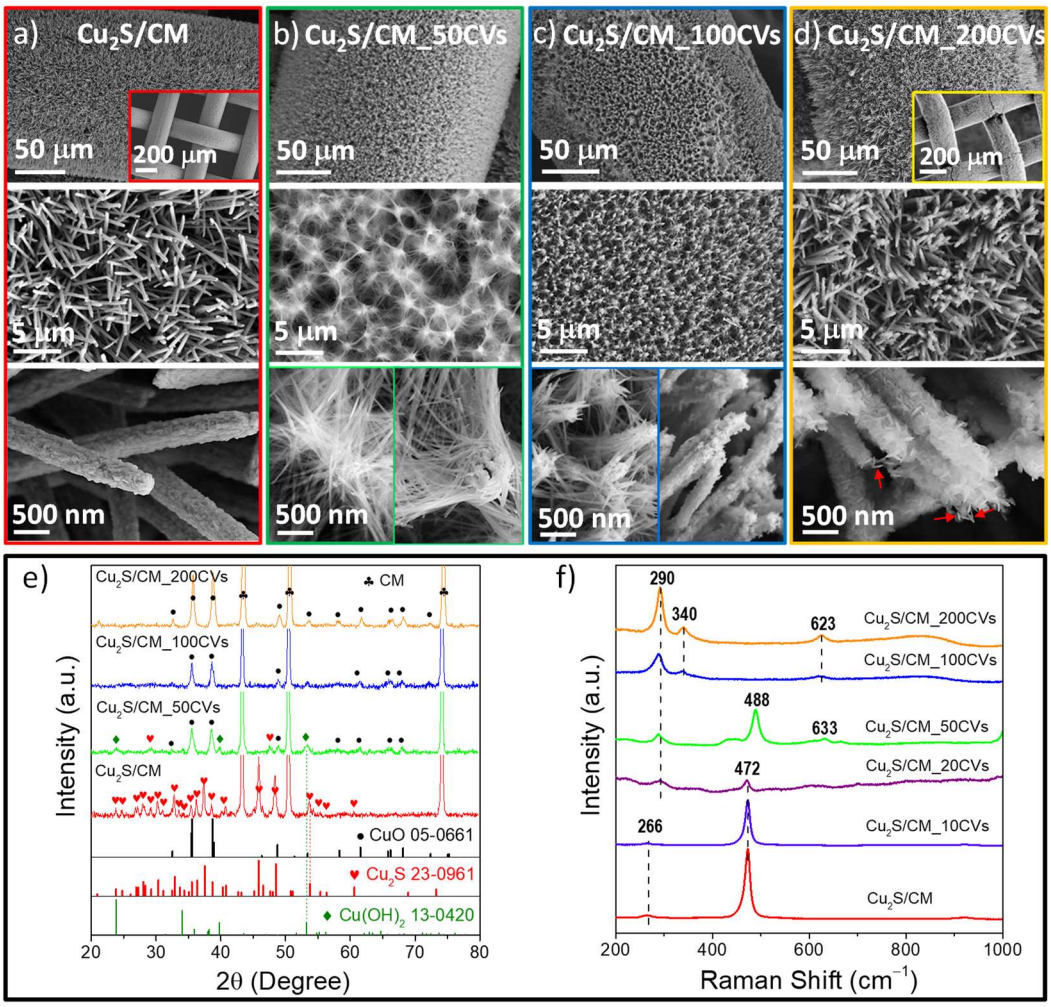

Figure 2.5. (a-d) SEM micrographs of as-prepared Cu_2S/CM after different numbers of CVs at a scan rate of 100 mV/s: (a) initial; (b) after 50 CVs; (c) after 100 CVs; (d) after 200 CVs. Arrows point at single nanoflakes used to determine their size. (e) XRD patterns of as-prepared Cu_2S/CM and after a different number of CVs at a scan rate of 100 mV/s. (f) *In-situ* Raman spectra of as-prepared Cu_2S/CM and after 10, 20, 50, 100, and 200 CVs at 100 mV/s.

A fresh Cu_2S/CM was cycled for 50 CV at 100 mV/s and afterward operated at a current density of 10 mA/cm^2 for 10000 s within a 1M KOH water solution. After these two steps, Cu_2S had fully transformed into CuO (Figure 2.6a). SEM characterization showed the surface morphology of the final material to consist in nanoflake-based NWs as those obtained after extensive cycling (Figure 2.6b-d). XPS analysis further confirmed the evolution from Cu_2S to CuO after the two steps. A shift of the Cu 2p doublet to higher

binding energies, from 932.7 eV to 933.6 eV (Cu $2p_{3/2}$), was associated to the Cu^{+} to Cu^{2+} oxidation (Figure 2.6e). According to XPS analysis (Figure 2.6e, Table 2.1), the initial Cu_2S/CM sample contained 90 % of Cu_2S and 10 % CuO ascribed to surface oxidation as aforementioned. This composition changed to 70 % $Cu(OH)_2$, 12 % CuO and 18 % Cu_2S after 50 CVs and to 100 % CuO after additional operation at 10 mA/cm^2 for 10000 s. Besides, the S 2p peak intensity decreased drastically after operation at 10 mA/cm^2 for 10000 s, corroborating the chemical transformation of Cu_2S to CuO. Interestingly, small amounts of S remained after long term operation, *ca.* 10 % with respect to Cu. The relative amount of sulfate with respect to the total amount of S significantly increased during OER operation, up to a 70 % of the total detected sulfur.[42,66]

Table 5.1. Components calculated from XPS and AES (Auger electron spectroscopy) spectra.

Sample Identifier	Atomic Concentration (Photoelectron peaks)					Atomic Concentration (Auger peaks)		
	Cu^{+} (Cu_2S)	Cu^{2+} ($Cu(OH)_2$)	Cu^{2+} (CuO)	SO_4^{2-} /S^{2-}	Cu /S^{2-}	Cu^{+} (Cu_2S)	Cu^{2+} ($Cu(OH)_2$)	Cu^{2+} (CuO)
Cu_2S/CM	90 %	-	10 %	14.5 % / 85.5 %	63.5 % / 36.5 %	89.2 %	-	10.8 %
Cu_2S/CM_50 CVs	18.1 %	69.6 %	12.3 %	56.6 % / 43.4 %	86.1 % / 13.9 %	10.9 %	74.6 %	13.5 %
Cu_2S/CM_50CVs _10 mA@10^4 s	-	-	100 %	70.2 % / 29.8 %	96.2 % / 3.8 %	-	22.7 %	77.3 %

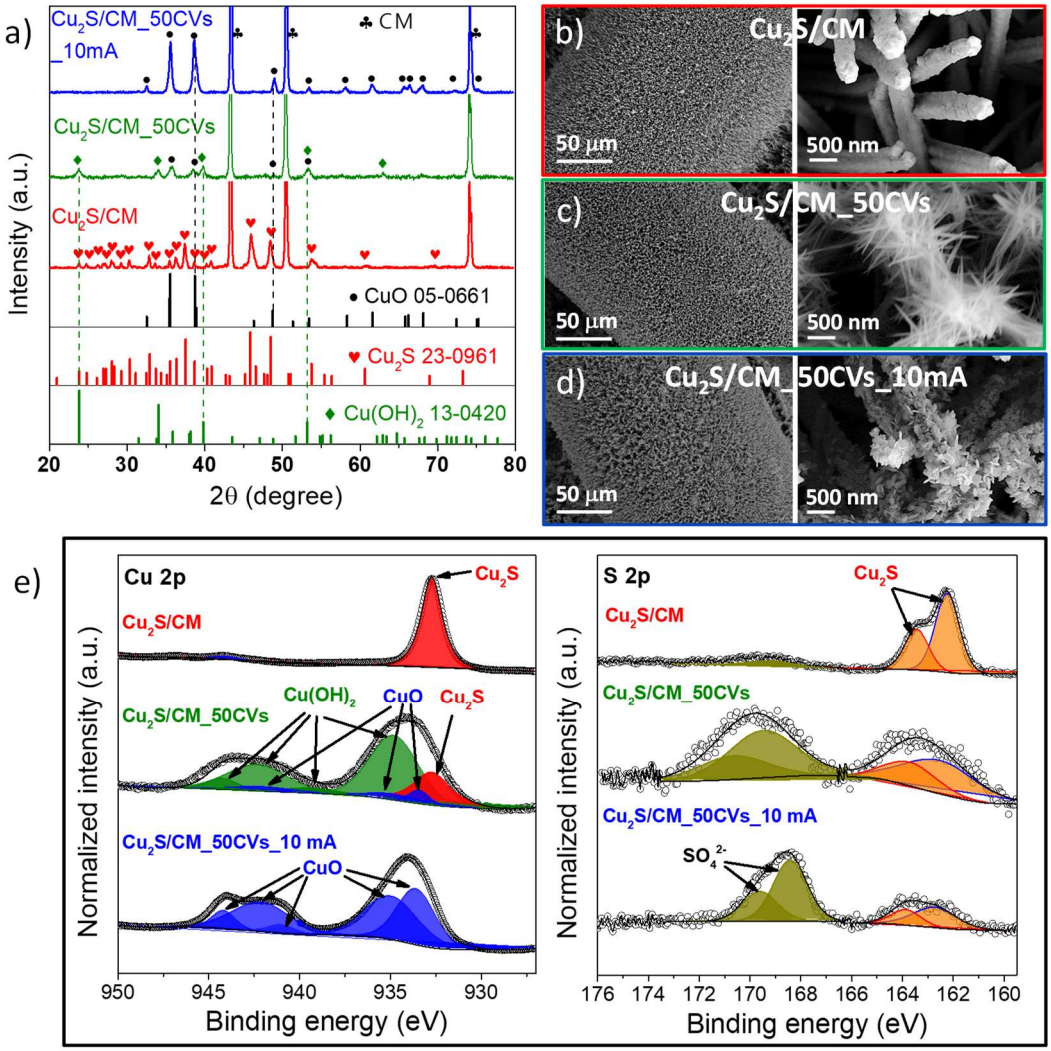

Figure 2.6. (a) XRD patterns and (b-d) SEM images of fresh Cu_2S/CM, after 50 CVs at a scan rate of 100 mV/s (Cu_2S/CM_50CVs), and after additional operation at 10 mA for 10000s (Cu_2S/CM_50CVs_10mA). (e) Normalized Cu 2p region and S 2p region of the XPS spectra of Cu_2S/CM, Cu_2S/CM_50CVs and Cu_2S/CM_50CVs_10mA samples.

EELS compositional maps showed a homogeneous distribution of Cu and oxygen throughout the grown nanostructures (Figure 2.7a, e). HRTEM characterization further confirmed the formation of $Cu(OH)_2$ after 50 CVs (Figure 2.7b), with the additional presence of CuO (Figure 2.7c) and Cu_2O minor phases (Figure 2.7d). We associated the appearance of Cu_2O on the HRTEM analysis to the reduction of CuO under the electron beam, consistently with previous reports.[71] After long-term operation at 10 mA/cm^2. HRTEM characterization displayed the presence of CuO as the main phase (Figure 2.7f), which matched well with results obtained by XRD.

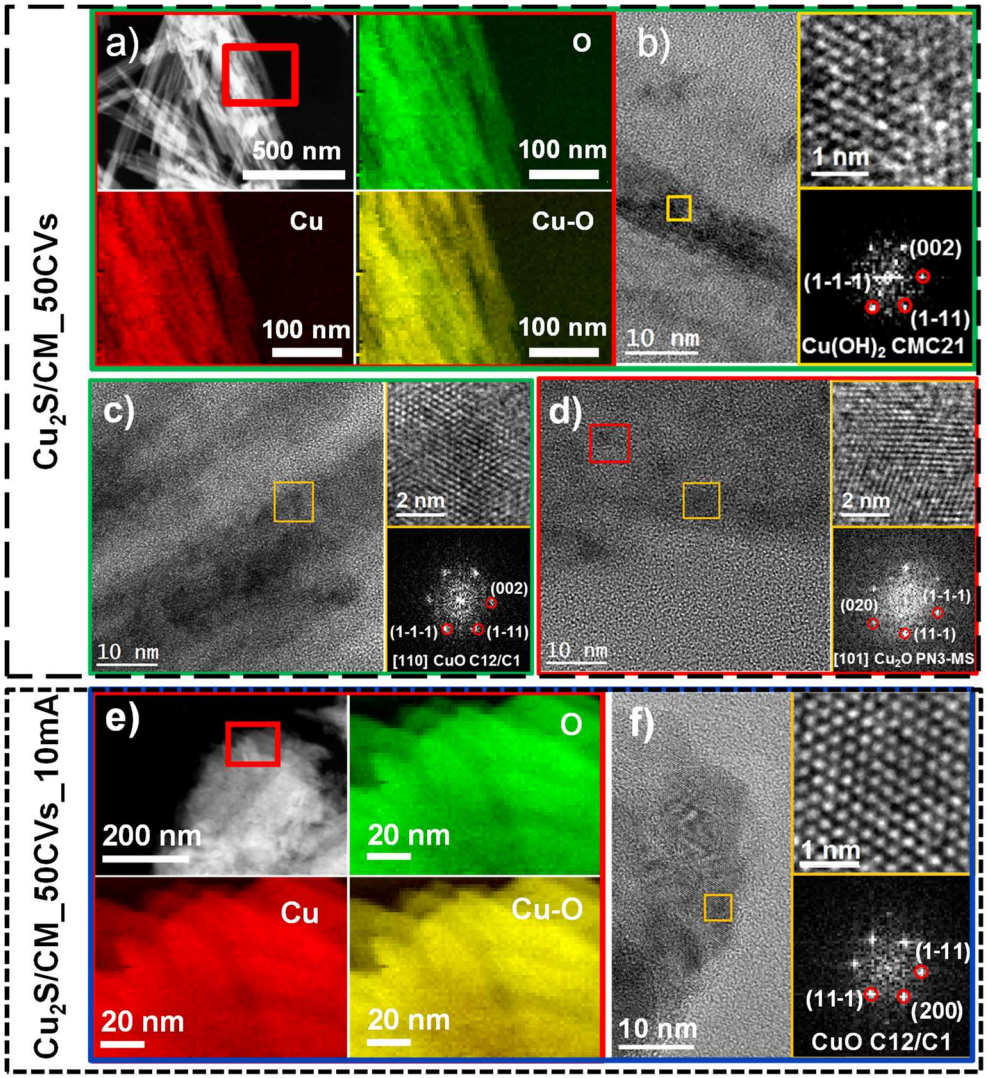

Figure 2.7. (a) EELS chemical composition maps obtained from the red squared area in the HAADF STEM micrograph of Cu_2S/CM_50CVs. Individual Cu $L_{2,3}$-edges at 931 eV (red) and O K-edges at 532 eV (green) as well as their composites of Cu-O. (b) HRTEM micrograph of a Cu_2S/CM_50CVs NW, detail of the orange squared region and its corresponding power spectrum visualized along its [110] zone axis. (c, d) HRTEM micrograph, detail of the squared region and its corresponding power spectrum of two different areas of sample Cu_2S/CM_50CVs. (e) EELS chemical composition maps obtained from the red squared area in the HAADF STEM micrograph of Cu_2S/CM_50CVs_10mA. (f) HRTEM micrograph of a Cu_2S/CM_50CVs_10mA NW, detail of the orange squared region and its corresponding power spectrum visualized along its [011] zone axis.

A fresh Cu_2S/CM was operated in a 1M KOH solution at 10 mA/cm^2 for 10000 s without CV preconditioning (Figure 2.8). Chronopotentiometry curves (Figure 2.8a) showed the potential required to maintain 10 mA/cm^2 to increase drastically during the initial *ca.* 2000 s, and to stay stable at longer operation times. Initially, no bubbles evolved from the working electrode. However, distinct bubbles started to appear after *ca.* 2000 s.

During this time, the initial black CM surface changed to slightly green, which we attributed to the formation of $Cu(OH)_2$, to later become black again. XRD analysis showed the final material to consist in CuO (Figure 2.8d). SEM analysis showed the final surface to consist on flaked NWs as those obtained after cycling, but presenting more cracks than when the electrode was pre-cycled (Figure 2.8e, f). After 10000 s operation, CuO/CM was cycled at 5 mV/s, showing an overpotential of 378 mV ($\eta_{corrected}$ = 336 mV) when delivering a geometric current density of 10 mA/cm^2 (Figure 2.8b).

According to previous reports, the Cu^{2+}-Cu^{3+} redox is at the basis of the OER mechanism on CuO/CM electrodes, being Cu^{3+} species the catalytically active sites for oxygen evolution.[72–74] The cathodic peak at *ca.* 1.52 V (0.59 V *vs.* Hg/HgO) obtained on the OER curve of Cu_2S-derived CuO/CM (Figure 2.8b), was attributed to the reduction of Cu^{3+} to Cu^{2+}.[72–74] The anodic peak corresponding to the oxidation of Cu^{2+}/Cu^{3+} that should appear at *ca.* 0.7 V *vs.* Hg/HgO[74] was not visible in our CVs due to its overlap with the high OER current density. The following mechanism, involving the intermediates OH, OOH, O and O_2 adsorbed on an active site M, was proposed for OER in CuO: [72,75]

$$M + OH^- \rightarrow M\text{-}OH + e^-$$

$$M\text{-}OH + OH^- \rightarrow M\text{-}O + H_2O + e^-$$

$$M\text{-}O + OH^- \rightarrow M\text{-}OOH + e^-$$

$$M\text{-}OOH + OH^- \rightarrow M\text{-}OO + H_2O + e^-$$

$$M\text{-}OO \rightarrow M + O_2$$

The generation of M-OH or M-OOH is the crucial step in the formation of O_2 and in the extensive oxidation of Cu_2S to $Cu(OH)_2$ and CuO. Being CuO more thermodynamically stable than $Cu(OH)_2$, $K_{sp\ CuO} = 4.37 \times 10^{-21}$ *vs.* $K_{sp\ Cu(OH)2} = 4.57 \times 10^{-20}$, CuO/CM is the final composition after relatively long operation of Cu_2S/CM under OER conditions.[59]

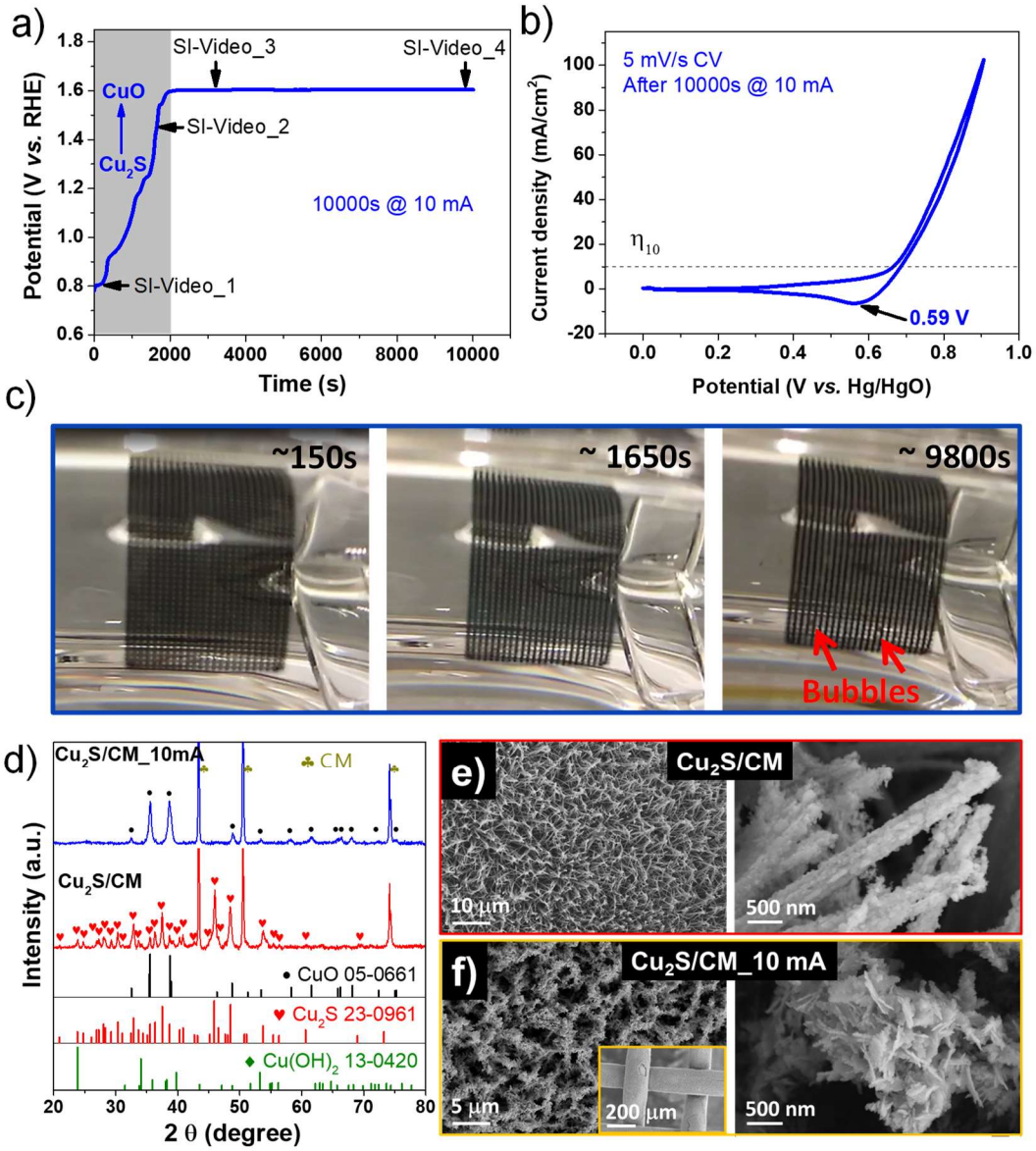

Figure 2.8. (a) Chronopotentiometry curve of Cu_2S/CM at a geometric current density of 10 mA/cm^2 in 1 M KOH. No CV preconditioning was performed on this sample. (b) Quasi-stationary OER polarization CV at a scan rate of 5 mV/s of Cu_2S/CM after 10000 s at 10 mA. (c) Video frames of a Cu_2S/CM working electrode showing the evolution of bubbles after 9800 s OER operation. (d) XRD patterns and SEM images of Cu_2S/CM before (e) and after (f) chronopotentiometry measurement at a geometric current density of 10 mA/cm^2 for 10000 s. Electrolyte: 1 M KOH.

To compare the OER performance of Cu_2S-derived CuO/CM, additional $Cu(OH)_2$/CM were produced by oxidizing CM in a NaOH/APS solution, and additional CuO/CM electrodes were obtained by annealing $Cu(OH)_2$/CM under argon (CuO/CM_AN, see experimental section for details). $Cu(OH)_2$/CM layers directly obtained from the immersion of CM into a NaOH/APS solution contained free standing faceted NWs as described above. The morphology of these $Cu(OH)_2$ faceted NWs was

preserved for several dozens of CVs, but cracks started to appear after 100 CVs (Figure 2.9a-d). XRD analysis showed $Cu(OH)_2$ NWs to partially transform into CuO after 150 CVs (Figure 2.10). Notice the conversion of $Cu(OH)_2$ NWs directly grown of the surface of CM was much slower than that of $Cu(OH)_2$ NWs derived from Cu_2S NWs. We associate this experimental result to the much better crystallinity of the former and to the low concentration of grain boundaries in $Cu(OH)_2$ NWs directly grown from CM. Besides, CuO/CM_AN electrodes displayed the presence of smooth NWs (Figure 2.9e), which appeared attached together after 50 CVs (Figure 2.9f). After additional cycles, CuO NWs started to break, and after long term chronopotentiometric measurements they detached from CM (Figure 2.9g, h). It should be noticed that directly formed $Cu(OH)_2$/CM and CuO/CM_AN electrodes did not display the same dramatic evolution of the CVs obtained for Cu_2S/CM during the first several cycles (Figure 2.11).

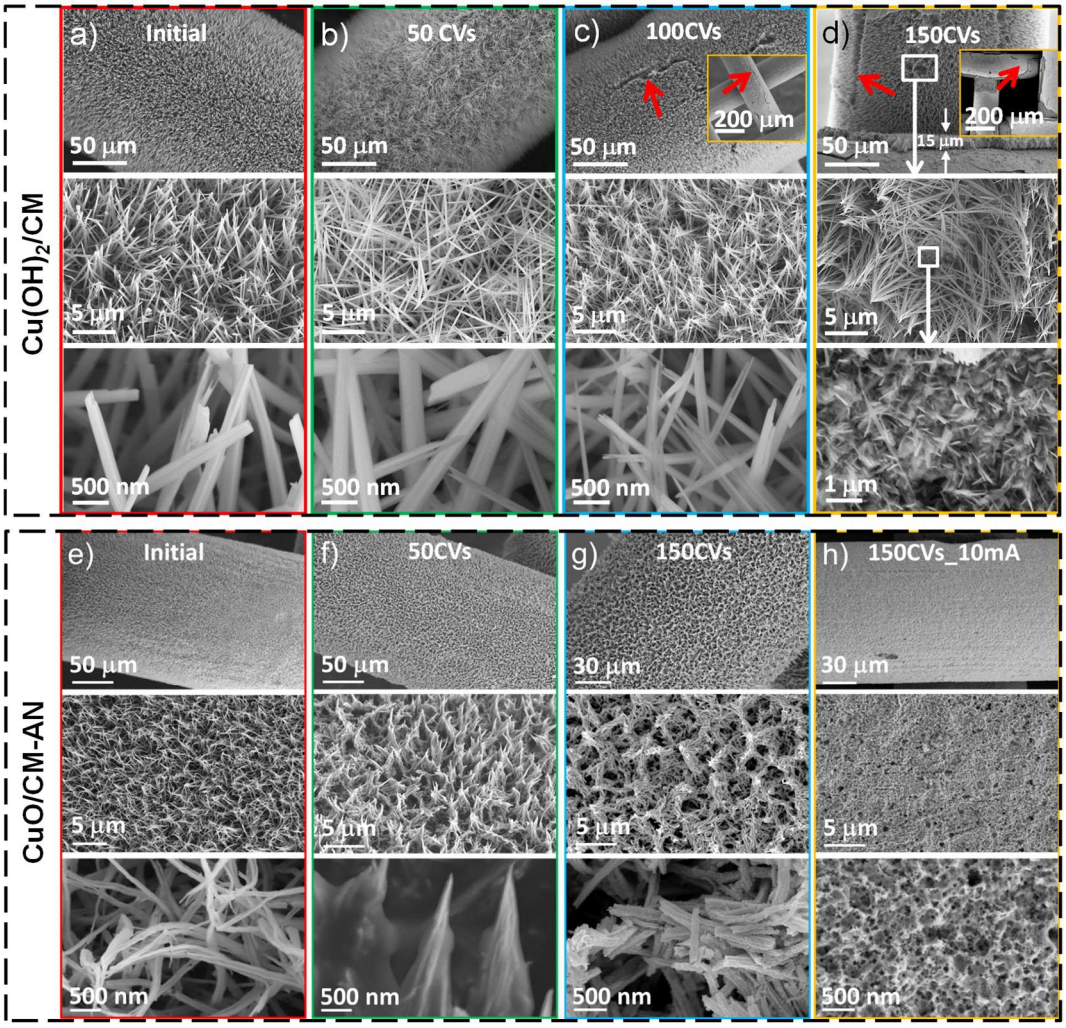

Figure 2.9. SEM images of precursor $Cu(OH)_2$/CM after different CV cycles activation at can rate of 100 mV/s: (a) initial; (b) after 50 CVs; (c) after 100 CVs; (d) after 150 CVs. The red arrows

in (c) and (d) point at cracks. SEM images of as-prepared CuO/CM-AN after different CV cycles activation at can rate of 100 mV/s: (e) initial; (f) after 50 CVs; (g) after 150 CVs; (h) after 150 CVs and chronopotentiometry measurement at a geometric current density of 10 mA/cm^2 for 10000 s.

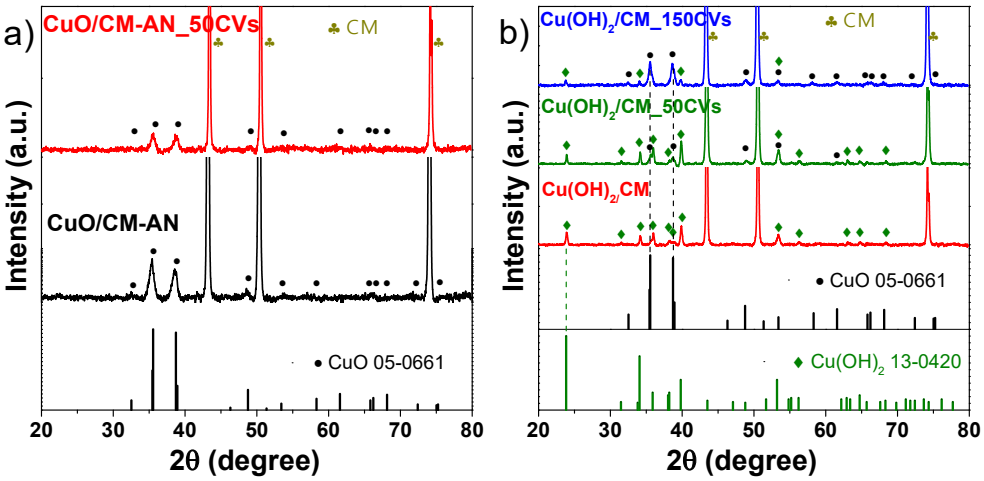

Figure 2.10. XRD patterns of (a) CuO/CM-AN and (b) $Cu(OH)_2$/CM before and after different CV cycles activation. Scan rate: 100 mV/s. Electrolyte: 1 M KOH.

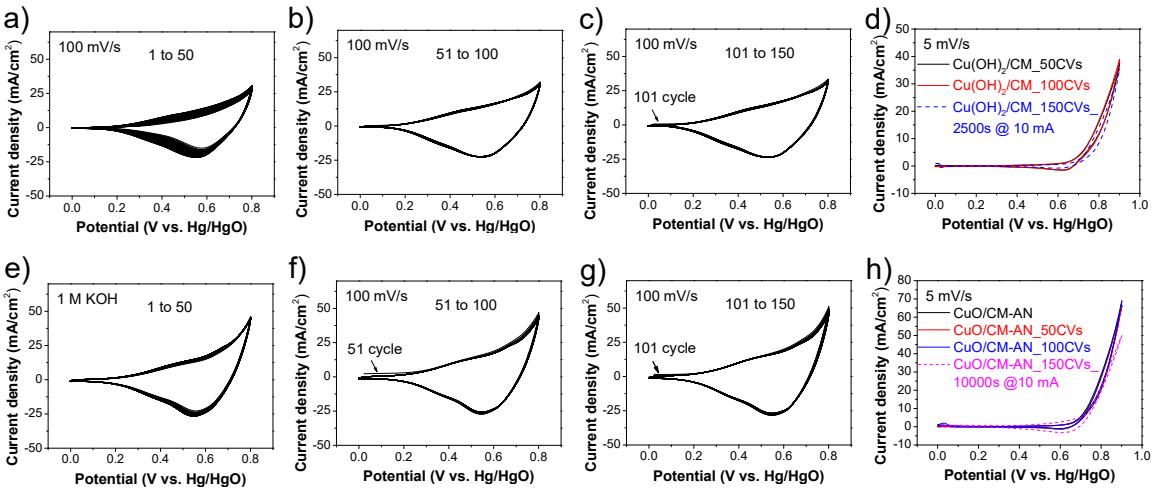

Figure 2.11. Multiple CV curves of precursor $Cu(OH)_2$/CM: (a) 1-50 cycles; (b) 51-100 cycles; (c) 101-150 cycles. Scan rate: 100 mV/s. (d) Quasi-stationary polarization CV curves of $Cu(OH)_2$/CM: before/after different CV cycles activation and after chronopotentiometry measurement at a geometric current density of 10 mA/cm^2. Scan rate: 5 mV/s. Electrolyte: 1 M KOH. Multiple CV curves of CuO/CM-AN annealed from precursor $Cu(OH)_2$/CM: (e) 1-50 cycles; (f) 51-100 cycles; (g) 101-150 cycles. Scan rate: 100 mV/s. (h) Quasi-stationary polarization CV curves of CuO/CM-AN before/after different CV cycles activation and after chronopotentiometry measurement at a geometric current density of 10 mA/cm^2. Scan rate: 5 mV/s. Electrolyte: 1 M KOH.

Figure 2.12a displays quasi-stationary polarization CV curves from CM and from directly obtained $Cu(OH)_2$/CM_100 CVs, CuO/CM-AN_100 CVs, and Cu_2S-derived CuO/CM_200 CVs at a scan rate of 5 mV/s. Bare CM showed very poor activity toward OER, requiring an overpotential of 526 mV to deliver a geometric current density of 10 mA/cm^2. Cu_2S-derived CuO/CM required 380 mV ($\eta_{corrected}$ = 338 mV) to reach 10 mA/cm^2, well below the overpotential required by $Cu(OH)_2$/CM_100 CVs (η = 484 mV) and CuO/CM_100 CVs (η = 441 mV). Cu_2S-derived CuO/CM electrodes also displayed much lower Tafel slopes, 96 mV/dec, than the other electrodes measured (Figure 2.12b-c), suggesting a more favorable OER kinetics.

ECSA and EIS measurements were carried out to further understand the improved OER activity of Cu_2S-derived CuO/CM electrodes. The relative ECSA was estimated through measurement of the double-layer capacitances (C_{dl}) at the solid/liquid interface.[76] As shown in Figure 2.13a, b, C_{dl} values for Cu_2S/CM_100CVs and CuO/CM-AN_100 CVs were calculated as 93 and 47 mF/cm^2, while their ECSA were caculated as 2325 and 1175, respectively (See Experimental section for details). This result suggested a much higher surface roughness for Cu_2S-derived CuO/CMs than directly obtained CuO/CM-AN (Figures 2.13a, b, 2.12d).

Nyquist plots of the impedance response measured at 0.68 V *vs.* Hg/HgO of Cu_2S/CM_200CVs and CuO/CM-AN_100CVs are shown in Figure 2.12e. Qualitatively speaking, Cu_2S/CM_200CVs exhibited a smaller semicircle radius compared with that of CuO/CM-AN_100CVs, indicating a smaller charge transfer resistance.[77,78] Impedance responses were fitted with an equivalent circuit containing a series resistance R_S, a charge transfer resistance R_{ct}, and a constant phase element CPE (Figure 2.12e, inset).[77,79,80] Fitting results unambiguously revealed a clearly enhanced charge transfer process on Cu_2S/CM_200CVs, with a R_{ct} of 146 Ω, than on CuO/CM-AN_100CVs, with an order of magnitude higher R_{ct}, 1288 Ω.

As shown in Figure 2.12f, the overpotential required by Cu_2S-derived CuO/CM electrodes to deliver a geometric current density of 10 mA/cm^2 remained unchanged after 10000 s. Besides, no obvious change on CV behavior occurred after long-term stability test (Figure 2.4f), indicating remarkable stable electrochemical activity toward OER. On the other hand, the overpotential of $Cu(OH)_2$/CM_100CVs electrode clearly increased from the very beginning of the durability test, manifesting a moderate stability for water

electrolysis. As for the CuO/CM-AN_100CVs electrode, it showed a good stability in the initial *ca.* 2000 s, but after this time period, the overpotential strongly increased, which we associated with the detachment of CuO from the CM (Figure 2.9h).

To study the influence of possible electrolyte change due to leaching of sulfides from Cu_2S during the longterm test, quasi-stationary CVs without/with a fresh electrolyte were obtained to compare OER performances. As can be seen in Figure 2.13c, there is a slight increase of the performance using fresh electrolyte, demonstrating the electrolyte after longterm test would not lead to an improvement of performance. Besides, ECSA-normalized current density of Cu_2S-derived CuO did not display significant differences compared with that of annealed CuO, indicating the increased amount of surface active sites is the main parameter behind OER enhancement (Figure 2.13d).

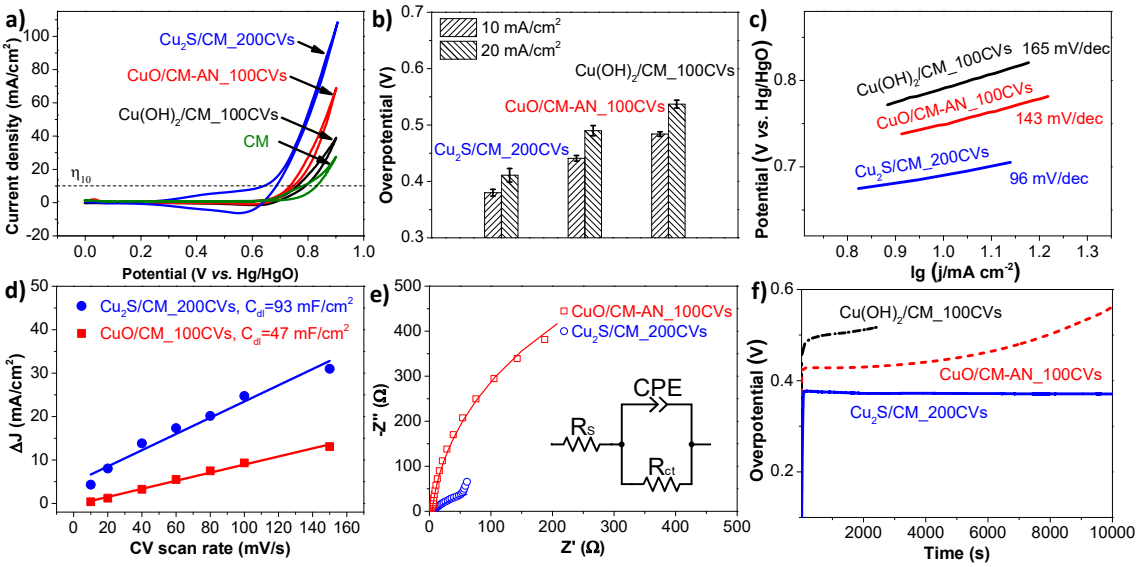

Figure 2.12. OER activity of $Cu(OH)_2$/CM_100CVs (**Black line**), CuO/CM-AN_100CVs (**Red line**) and Cu_2S/CM_200CVs (**Blue line**) in 1.0 M KOH. (a) Quasi-stationary CVs at a scan rate of 5 mV/s. (b) OER overpotential at 10 mA/cm^2 and 20 mV/cm^2. (c) Tafel curves. (d) Capacitive current densities at 1.27 V *vs.* RHE as a function of the scan rate. (e) Nyquist plots of the impedances including the fitted curves and equivalent circuit. (f) Chronopotentiometric curves at a constant current density of 10 mA/cm^2.

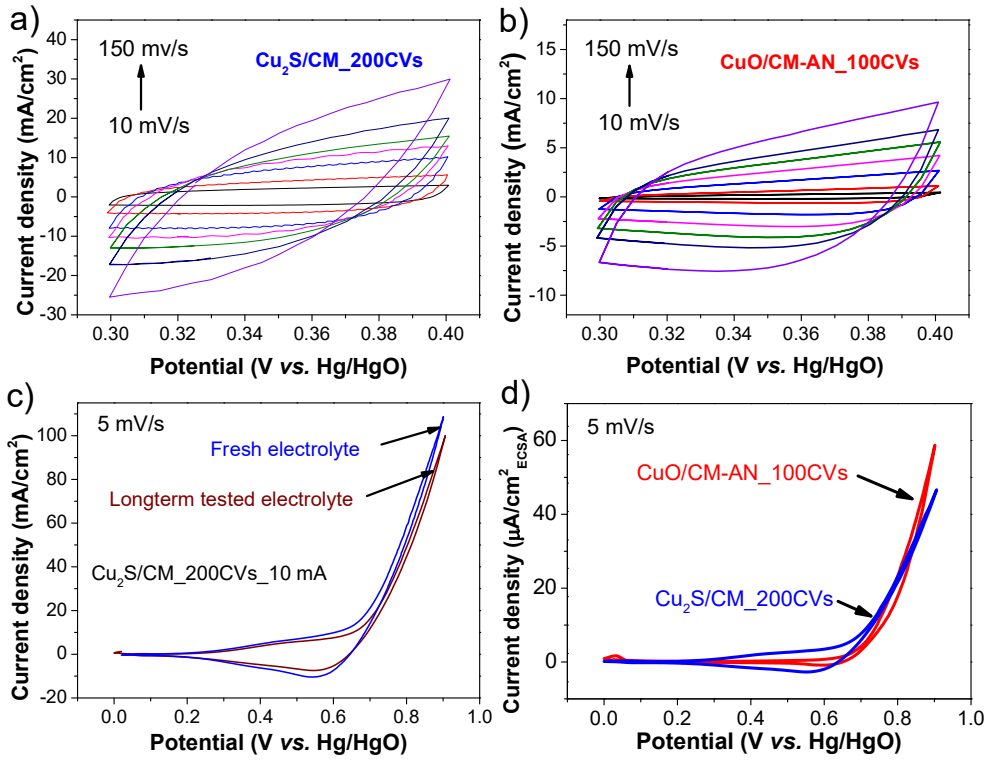

Figure 2.13. Cyclic voltammograms of (a) Cu_2S/CM_200CVs and (b) CuO/CM-AN_100CVs at scan rates of 10, 20, 40, 60, 80, 100, and 150 mV/s. (c) Quasi-stationary polarization CV curves of Cu_2S/CM-200CVs after longterm test of 10000 s at 10 mA/cm^2 before/after using fresh electrolyte. (d) ECSA normalized quasi-stationary CVs for Cu_2S/CM_200CVs and CuO/CM-AN_100CVs. Scan rate: 5 mV/s. Electrolyte: 1 M KOH.

To improve the catalytic performance of Cu_2S-derived CuO/CM, the CM was replaced by a CF, which provided a larger surface area. CV curves measured from Cu_2S/CF displayed a similar evolution in the first several cycles, indicating the transition from Cu_2S/CF to CuO/CF via $Cu(OH)_2$/CF intermediate (Figure 2.14a-f). This result was confirmed by XRD and SEM analysis that displayed a similar structural and morphology evolution as that described for Cu_2S/CM (Figure 2.15a, d and 2.14g). OER performance was improved after CV activation, reaching an overpotential down to 328 mV ($\eta_{corrected}$ = 286 mV) to deliver a geometric current density of 10 mA/cm^2, and a Tafel slope of 87 mV/dec (Figure 2.15b). A remarkable durability for 16 h was also measured (Figure 2.15c and inset). These results place Cu_2S-derived CuO/CF among the best Cu-based OER catalysts, with even better performance than numerous nickel/cobalt-based catalysts previously reported (Table 2.2).

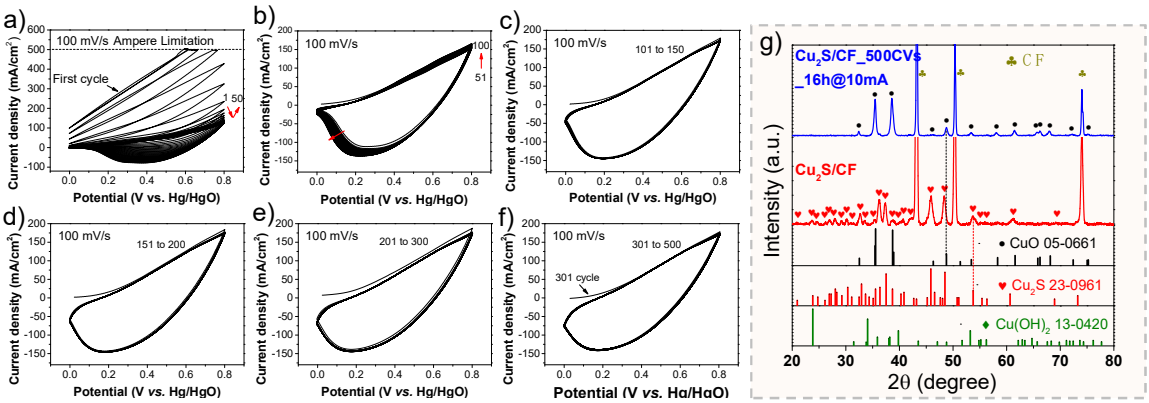

Figure 2.14. Multiple CV curves of as-prepared Cu_2S/CF: (a) 1-50 cycles; (b) 51-100 cycles; (c) 101-150 cycles; (d) 151-200 cycles; (e) 201-300 cycles; (f) 301-500 cycles. (g) XRD patterns of Cu_2S/CF before and after 500CVs activation and further chronopotentiometry measurement at a geometric current density of 10 mA/cm^2 for 16 h. Electrolyte: 1 M KOH.

This outstanding performance was associated to several advantages of the Cu_2S-derived electrocatalyst, namely: a) Improved adhesion of the active layer to copper when mediating an intermediate sulfurization step; b) Increased surface area associated with the nanostructuration of the NWs; c) Lower charge transfer resistance associated with the higher surface area and the larger density or higher activity of the newly formed catalytic sites; d) the presence of additional oxidized sulfate on the surface. In this last direction, recent reports indicated that in metal sulfides, oxidized S species can remain on the surface for a long period of time and are favorable for OER catalytic activity by tuning the adsorption free energy of the reaction intermediates on the metal sites.[42–45]

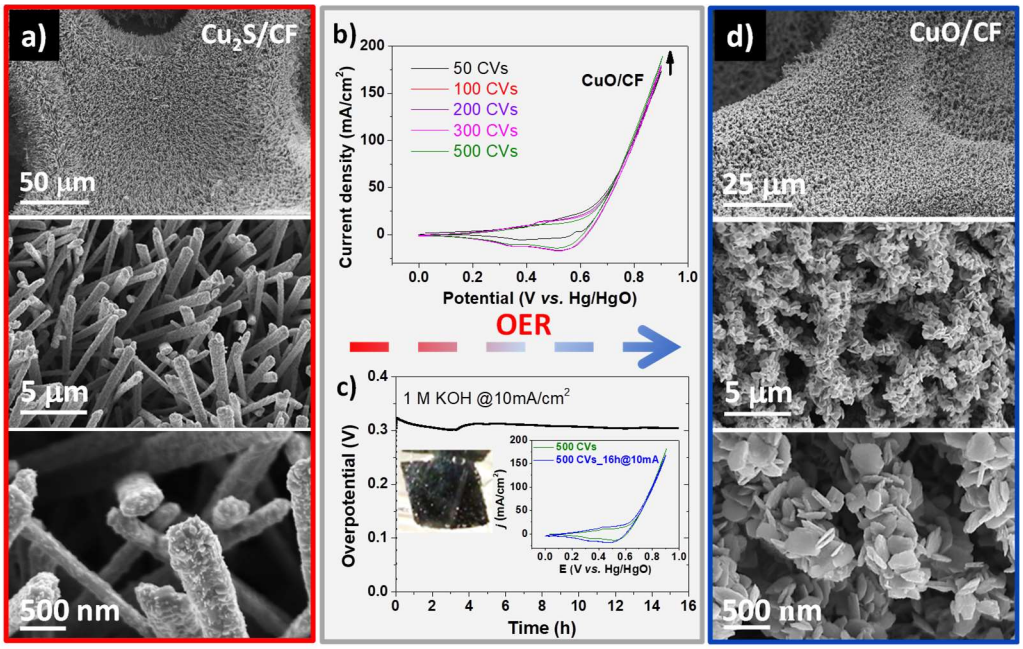

Figure 2.15. (a) SEM images of Cu_2S/CF before electrochemical tests. (b) Quasi-stationary OER polarization curves at a scan rate of 5 mV/s from Cu_2S/CF electrodes after different CV activation cycles. (c) Long term chronopotentiometric curve at a constant current density of 10 mA/cm^2; Inset photograph shows oxygen bubbles evolving from the working electrode during OER (see SI-Video_5 for more details). Inset graph shows the quasi-stationary OER polarization CV before and after chronopotentiometry. (d) SEM images of Cu_2S-derived CuO/CF after chronopotentiometry.

Table 5.2. Comparisons of OER activity of some reported Cu-based electrocatalysts (light yellow shading) and nickel/cobalt-based electrocatalysts (light blue shading).

Catalysts	Overpotential (j=10mA/cm^2), mV	Overpotential (j=20mA/cm^2), mV	Tafel slope, mV/dec	Electrolyte	Ref.
CuO/CF-EOT	286	355	87	1.0 M KOH	This work
CuO/CM-EOT	338	411	96		
Cu_2S/CF	290	336	101	1.0 M KOH	53
CuS/C	586	-	82	Phosphate buffer/ pH=13	52
Cu_2S/C	428	-	63		
$Cu(OH)_2$:$Fe(OH)_3$/CF	365	-	42	1.0 M KOH	46
$Cu(OH)_2$ nanowires/Cu foil	530	-	86	0.1 M KOH	81
Cu@CuO/C	340	-	156	1.0 M KOH	82
CuO/Stainless steel	350	-	59	1.0 M KOH	83
Cu_2O@C	330	360	63	1.0 M KOH	84
CuO/Cu_2O/Cu plate	290	340	64	1.0 M KOH	85
Cu_2O-Cu/Cu foam	~350	-	67.52	1.0 M KOH	86
$CuFe_2O_4$ NFs	440	-	82.15	1.0 M KOH	87
Cu_3P NWAs/Cu foam	315	-	74.8	1.0 M KOH	88
Cu_3P/Cu mesh	380	390	-	1.0 M KOH	89
Cu_3P microsheets/Ni foam	290	-	84	1.0 M KOH	90
Cu_3P/Ni foam	~320	-	54	1.0 M KOH	91
$Co_{0.6}Fe_{0.4}P$-1.125	297	-	48	1.0 M KOH	36
CoNi(OH)x	280	-	77	1.0 M KOH	92
NiCo-LDH	314	-	77	1.0 M KOH	93
CoNC@MoS_2/CNF	350	-	51.9	1.0 M KOH	94
$Co_{0.37}Ni_{0.26}Fe_{0.37}O$-ECT	232	-	37.6	1.0 M KOH	95
Co@Co_9S_8-180	350	-	55	1.0 M KOH	25
Co_9S_8@MoS_2	342	-	94	1.0 M KOH	96
Ni_3S_2/Ni foam	260	290	-	1.0 M KOH	97
$Ni_{0.6}Co_{1.4}P$	300	-	80	1.0 M KOH	17

2.5 Conclusions

In summary, we reported on the chemical, structural and morphological *in-situ* transformation of Cu_2S/CM into CuO/CM during OER via $Cu(OH)_2$ intermediate. Cu_2S-derived CuO/CM displayed enhanced electrochemical OER activity than its precursor $Cu(OH)_2$/CM and CuO/CM-AN directly obtained from the $Cu(OH)_2$/CM annealing. Cu_2S-derived CuO/CF displayed an overpotential of 286 mV to deliver a geometric current density of 10 mA/cm^2, surpassing most Cu-based OER electrocatalysts previously reported. Improved performance with respect to CuO produced from the annealing of $Cu(OH)_2$ NWs was associated to: i) a more stable attachment of the active layer to the current collector; ii) a higher surface area; iii) a lower charge transfer resistance; iv) the presence of sulfate ions that may facilitate the OER process by tuning the adsorption free energy of reaction intermediates. We believe this work provides insights for the fabrication of more effective metal oxide OER catalysts using a simple electrochemical oxidation process. This strategy may be also extended to other sulfides and chalcogenides, and even to phosphide and nitride catalysts. Additionally, based on these results, we suggest the necessity to reconsider the chemical composition and associated OER performance of previously reported sulfide OER catalysts in alkaline media.

2.6 References

(1) Cabán-Acevedo, M.; Stone, M. L.; Schmidt, J. R.; Thomas, J. G.; Ding, Q.; Chang, H. C.; Tsai, M. L.; He, H.; Jin, S. Efficient Hydrogen Evolution Catalysis Using Ternary Pyrite-Type Cobalt Phosphosulphide. *Nat. Mater.* **2015**, *14* (12), 1245–1251.

(2) Jin, S. Are Metal Chalcogenides, Nitrides, and Phosphides Oxygen Evolution Catalysts or Bifunctional Catalysts? *ACS Energy Lett.* **2017**, *2* (8), 1937–1938.

(3) Wang, H.-F.; Tang, C.; Zhang, Q. A Review of Precious-Metal-Free Bifunctional Oxygen Electrocatalysts: Rational Design and Applications in Zn−Air Batteries. *Adv. Funct. Mater.* **2018**, *28* (46), 1803329.

(4) Zou, X.; Goswami, A.; Asefa, T. Efficient Noble Metal-Free (Electro)Catalysis of Water and Alcohol Oxidations by Zinc-Cobalt Layered Double Hydroxide. *J. Am. Chem. Soc.* **2013**, *135* (46), 17242–17245.

(5) Li, D.; Baydoun, H.; Verani, C. N.; Brock, S. L. Efficient Water Oxidation Using CoMnP Nanoparticles. *J. Am. Chem. Soc.* **2016**, *138* (12), 4006–4009.

(6) Gao, R.; Li, G. D.; Hu, J.; Wu, Y.; Lian, X.; Wang, D.; Zou, X. In Situ Electrochemical Formation of NiSe/NiO_x Core/Shell Nano-Electrocatalysts for Superior Oxygen Evolution Activity. *Catal. Sci. Technol.* **2016**, *6* (23), 8268–8275.

(7) Dutta, A.; Samantara, A. K.; Dutta, S. K.; Jena, B. K.; Pradhan, N. Surface-Oxidized Dicobalt Phosphide Nanoneedles as a Nonprecious, Durable, and Efficient OER Catalyst. *ACS Energy Lett.* **2016**, *1* (1), 169–174.

(8) Zhang, J.; Wang, T.; Pohl, D.; Rellinghaus, B.; Dong, R.; Liu, S.; Zhuang, X.; Feng, X. Interface Engineering of MoS_2/Ni_3S_2 Heterostructures for Highly Enhanced Electrochemical Overall-Water-Splitting Activity. *Angew. Chem. Int. Ed.* **2016**, *55* (23), 6702–6707.

(9) Song, F.; Schenk, K.; Hu, X. A Nanoporous Oxygen Evolution Catalyst Synthesized by Selective Electrochemical Etching of Perovskite Hydroxide $CoSn(OH)_6$ Nanocubes. *Energy Environ. Sci.* **2016**, *9* (2), 473–477.

(10) Jia, X.; Zhao, Y.; Chen, G.; Shang, L.; Shi, R.; Kang, X.; Waterhouse, G. I. N.; Wu, L. Z.; Tung, C. H.; Zhang, T. Ni_3FeN Nanoparticles Derived from Ultrathin NiFe-Layered Double Hydroxide Nanosheets: An Efficient Overall Water Splitting Electrocatalyst. *Adv. Energy Mater.* **2016**, *6* (10), 1502585.

(11) Jin, Y.; Wang, H.; Li, J.; Yue, X.; Han, Y.; Shen, P. K.; Cui, Y. Porous MoO_2 Nanosheets as Non-Noble Bifunctional Electrocatalysts for Overall Water Splitting. *Adv. Mater.* **2016**, *28* (19), 3785–3790.

(12) Yan, X.; Li, K.; Lyu, L.; Song, F.; He, J.; Niu, D.; Liu, L.; Hu, X.; Chen, X. From Water Oxidation to Reduction: Transformation from $Ni_xCo_{3-x}O_4$ Nanowires to NiCo/$NiCoO_x$ Heterostructures. *ACS Appl. Mater. Interfaces* **2016**, *8* (5), 3208–3214.

(13) Liu, Y.; Liang, X.; Gu, L.; Zhang, Y.; Li, G. D.; Zou, X.; Chen, J. S. Corrosion Engineering towards Efficient Oxygen Evolution Electrodes with Stable Catalytic Activity for over 6000 Hours. *Nat. Commun.* **2018**, *9* (1), 2609.

(14) McCrory, C. C. L.; Jung, S.; Ferrer, I. M.; Chatman, S. M.; Peters, J. C.; Jaramillo, T. F. Benchmarking Hydrogen Evolving Reaction and Oxygen Evolving Reaction

Electrocatalysts for Solar Water Splitting Devices. *J. Am. Chem. Soc.* **2015**, *137* (13), 4347–4357.

(15) Browne, M. P.; Sofer, Z.; Pumera, M. Layered and Two Dimensional Metal Oxides for Electrochemical Energy Conversion. *Energy Environ. Sci.* **2019**, *12* (1), 41–58.

(16) He, P.; Yu, X. Y.; Lou, X. W. D. Carbon-Incorporated Nickel–Cobalt Mixed Metal Phosphide Nanoboxes with Enhanced Electrocatalytic Activity for Oxygen Evolution. *Angew. Chem. Int. Ed.* **2017**, *56* (14), 3897–3900.

(17) Qiu, B.; Cai, L.; Wang, Y.; Lin, Z.; Zuo, Y.; Wang, M.; Chai, Y. Fabrication of Nickel–Cobalt Bimetal Phosphide Nanocages for Enhanced Oxygen Evolution Catalysis. *Adv. Funct. Mater.* **2018**, *28* (17), 1706008.

(18) Yu, X. Y.; Feng, Y.; Guan, B.; Lou, X. W. D.; Paik, U. Carbon Coated Porous Nickel Phosphides Nanoplates for Highly Efficient Oxygen Evolution Reaction. *Energy Environ. Sci.* **2016**, *9* (4), 1246–1250.

(19) Xu, K.; Chen, P.; Li, X.; Tong, Y.; Ding, H.; Wu, X.; Chu, W.; Peng, Z.; Wu, C.; Xie, Y. Metallic Nickel Nitride Nanosheets Realizing Enhanced Electrochemical Water Oxidation. *J. Am. Chem. Soc.* **2015**, *137* (12), 4119–4125.

(20) Wang, Y.; Liu, D.; Liu, Z.; Xie, C.; Huo, J.; Wang, S. Porous Cobalt-Iron Nitride Nanowires as Excellent Bifunctional Electrocatalysts for Overall Water Splitting. *Chem. Commun.* **2016**, *52* (85), 12614–12617.

(21) Wang, Y.; Zhang, B.; Pan, W.; Ma, H.; Zhang, J. 3 D Porous Nickel–Cobalt Nitrides Supported on Nickel Foam as Efficient Electrocatalysts for Overall Water Splitting. *ChemSusChem* **2017**, *10* (21), 4170–4177.

(22) Wang, Y.; Xie, C.; Liu, D.; Huang, X.; Huo, J.; Wang, S. Nanoparticle-Stacked Porous Nickel-Iron Nitride Nanosheet: A Highly Efficient Bifunctional Electrocatalyst for Overall Water Splitting. *ACS Appl. Mater. Interfaces* **2016**, *8* (29), 18652–18657.

(23) Hou, Y.; Lohe, M. R.; Zhang, J.; Liu, S.; Zhuang, X.; Feng, X. Vertically Oriented Cobalt Selenide/NiFe Layered-Double-Hydroxide Nanosheets Supported on Exfoliated Graphene Foil: An Efficient 3D Electrode for Overall Water Splitting. *Energy Environ. Sci.* **2016**, *9* (2), 478–483.

(24) Xu, R.; Wu, R.; Shi, Y.; Zhang, J.; Zhang, B. Ni_3Se_2 Nanoforest/Ni Foam as a Hydrophilic, Metallic, and Self-Supported Bifunctional Electrocatalyst for Both H_2 and O_2 Generations. *Nano Energy* **2016**, *24*, 103–110.

(25) Xiong, D.; Zhang, Q.; Thalluri, S. M.; Xu, J.; Li, W.; Fu, X.; Liu, L. One-Step Fabrication of Monolithic Electrodes Comprising Co_9S_8 Particles Supported on Cobalt Foam for Efficient and Durable Oxygen Evolution Reaction. *Chem. - A Eur. J.* **2017**, *23* (36), 8749–8755.

(26) Dong, B.; Zhao, X.; Han, G. Q.; Li, X.; Shang, X.; Liu, Y. R.; Hu, W. H.; Chai, Y. M.; Zhao, H.; Liu, C. G. Two-Step Synthesis of Binary Ni-Fe Sulfides Supported on Nickel Foam as Highly Efficient Electrocatalysts for the Oxygen Evolution Reaction. *J. Mater. Chem. A* **2016**, *4* (35), 13499–13508.

(27) Zhu, W.; Yue, X.; Zhang, W.; Yu, S.; Zhang, Y.; Wang, J.; Wang, J. Nickel Sulfide Microsphere Film on Ni Foam as an Efficient Bifunctional Electrocatalyst for Overall Water Splitting. *Chem. Commun.* **2016**, *52* (7), 1486–1489.

(28) Ma, X.; Zhang, W.; Deng, Y.; Zhong, C.; Hu, W.; Han, X. Phase and Composition Controlled Synthesis of Cobalt Sulfide Hollow Nanospheres for Electrocatalytic Water Splitting. *Nanoscale* **2018**, *10* (10), 4816–4824.

(29) Huynh, M.; Bediako, D. K.; Nocera, D. G. A Functionally Stable Manganese Oxide Oxygen Evolution Catalyst in Acid. *J. Am. Chem. Soc.* **2014**, *136* (16), 6002–6010.

(30) Ryu, J.; Jung, N.; Jang, J. H.; Kim, H. J.; Yoo, S. J. In Situ Transformation of Hydrogen-Evolving CoP Nanoparticles: Toward Efficient Oxygen Evolution Catalysts Bearing Dispersed Morphologies with Co-Oxo/Hydroxo Molecular Units. *ACS Catal.* **2015**, *5* (7), 4066–4074.

(31) Reddy, N. K.; Winkler, S.; Koch, N.; Pinna, N. Electrochemical Water Oxidation of Ultrathin Cobalt Oxide-Based Catalyst Supported onto Aligned ZnO Nanorods. *ACS Appl. Mater. Interfaces* **2016**, *8* (5), 3226–3232.

(32) Zhu, Y.; Chen, H. C.; Hsu, C. S.; Lin, T. S.; Chang, C. J.; Chang, S. C.; Tsai, L. D.; Chen, H. M. Operando Unraveling of the Structural and Chemical Stability of P-Substituted $CoSe_2$ Electrocatalysts toward Hydrogen and Oxygen Evolution Reactions in Alkaline Electrolyte. *ACS Energy Lett.* **2019**, *4* (4), 987–994.

(33) Feng, X.; Jiao, Q.; Liu, T.; Li, Q.; Yin, M.; Zhao, Y.; Li, H.; Feng, C.; Zhou, W. Facile Synthesis of Co_9S_8 Hollow Spheres as a High-Performance Electrocatalyst for the Oxygen Evolution Reaction. *ACS Sustain. Chem. Eng.* **2018**, *6* (2), 1863–1871.

(34) Wygant, B. R.; Kawashima, K.; Mullins, C. B. Catalyst or Precatalyst? The Effect of Oxidation on Transition Metal Carbide, Pnictide, and Chalcogenide Oxygen Evolution Catalysts. *ACS Energy Lett.* **2018**, *3* (12), 2956–2966.

(35) Mabayoje, O.; Shoola, A.; Wygant, B. R.; Mullins, C. B. The Role of Anions in Metal Chalcogenide Oxygen Evolution Catalysis: Electrodeposited Thin Films of Nickel Sulfide as "Pre-Catalysts." *ACS Energy Lett.* **2016**, *1* (1), 195–201.

(36) Lian, Y.; Sun, H.; Wang, X.; Qi, P.; Mu, Q.; Chen, Y.; Ye, J.; Zhao, X.; Deng, Z.; Peng, Y. Carved Nanoframes of Cobalt-Iron Bimetal Phosphide as a Bifunctional Electrocatalyst for Efficient Overall Water Splitting. *Chem. Sci.* **2019**, *10* (2), 464–474.

(37) Xu, J.; Li, J.; Xiong, D.; Zhang, B.; Liu, Y.; Wu, K. H.; Amorim, I.; Li, W.; Liu, L. Trends in Activity for the Oxygen Evolution Reaction on Transition Metal (M = Fe, Co, Ni) Phosphide Pre-Catalysts. *Chem. Sci.* **2018**, *9* (14), 3470–3476.

(38) Zhang, Y.; Ouyang, B.; Xu, J.; Jia, G.; Chen, S.; Rawat, R. S.; Fan, H. J. Rapid Synthesis of Cobalt Nitride Nanowires: Highly Efficient and Low-Cost Catalysts for Oxygen Evolution. *Angew. Chem. Int. Ed.* **2016**, *55* (30), 8670–8674.

(39) Li, W.; Gao, X.; Xiong, D.; Xia, F.; Liu, J.; Song, W. G.; Xu, J.; Thalluri, S. M.; Cerqueira, M. F.; Fu, X.; Liu, L. Vapor-Solid Synthesis of Monolithic Single-Crystalline CoP Nanowire Electrodes for Efficient and Robust Water Electrolysis. *Chem. Sci.* **2017**, *8* (4), 2952–2958.

(40) Liu, Y.; Li, Q.; Si, R.; Li, G.-D.; Li, W.; Liu, D.-P.; Wang, D.; Sun, L.; Zhang, Y.; Zou, X. Coupling Sub-Nanometric Copper Clusters with Quasi-Amorphous Cobalt Sulfide Yields Efficient and Robust Electrocatalysts for Water Splitting Reaction. *Adv. Mater.* **2017**, *29* (13), 1606200.

(41) Xu, X.; Song, F.; Hu, X. A Nickel Iron Diselenide-Derived Efficient Oxygen-Evolution Catalyst. *Nat. Commun.* **2016**, *7* (1), 12324.

(42) Souleymen, R.; Wang, Z.; Qiao, C.; Naveed, M.; Cao, C. Microwave-Assisted Synthesis of Graphene-like Cobalt Sulfide Freestanding Sheets as an Efficient Bifunctional Electrocatalyst for Overall Water Splitting. *J. Mater. Chem. A* **2018**, *6* (17), 7592–7607.

(43) Wu, Z.; Huang, L.; Liu, H.; Wang, H. Element-Specific Restructuring of Anion- and Cation-Substituted Cobalt Phosphide Nanoparticles under Electrochemical Water-Splitting Conditions. *ACS Catal.* **2019**, *9* (4), 2956–2961.

(44) Wang, T.; Nam, G.; Jin, Y.; Wang, X.; Ren, P.; Kim, M. G.; Liang, J.; Wen, X.; Jang, H.; Han, J.; Huang, Y.; Li, Q.; Cho, J. NiFe (Oxy) Hydroxides Derived from NiFe Disulfides as an Efficient Oxygen Evolution Catalyst for Rechargeable Zn–Air Batteries: The Effect of Surface S Residues. *Adv. Mater.* **2018**, *30* (27), 1800757.

(45) Legrand, D. L.; Nesbitt, H. W.; Bancroft, G. M. X-Ray Photoelectron Spectroscopic Study of a Pristine Millerite (NiS) Surface and the Effect of Air and Water Oxidation. *Am. Mineral.* **1998**, *83* (11-12 PART 1), 1256–1265.

(46) Hou, C. C.; Wang, C. J.; Chen, Q. Q.; Lv, X. J.; Fu, W. F.; Chen, Y. Rapid Synthesis of Ultralong $Fe(OH)_3$:$Cu(OH)_2$ Core-Shell Nanowires Self-Supported on Copper Foam as a Highly Efficient 3D Electrode for Water Oxidation. *Chem. Commun.* **2016**, *52* (100), 14470–14473.

(47) Kang, J.; Sheng, J.; Xie, J.; Ye, H.; Chen, J.; Fu, X. Z.; Du, G.; Sun, R.; Wong, C. P. Tubular $Cu(OH)_2$ Arrays Decorated with Nanothorny Co-Ni Bimetallic Carbonate Hydroxide Supported on Cu Foam: A 3D Hierarchical Core-Shell Efficient Electrocatalyst for the Oxygen Evolution Reaction. *J. Mater. Chem. A* **2018**, *6* (21), 10064–10073.

(48) C. L. McCrory, C.; Jung, S.; C. Peters, J.; F. Jaramillo, T. Benchmarking Heterogeneous Electrocatalysts for the Oxygen Evolution Reaction. *J. Am. Chem. Soc.* **2013**, *135* (45), 16977–16987.

(49) Liu, X.; Cui, S.; Sun, Z.; Ren, Y.; Zhang, X.; Du, P. Self-Supported Copper Oxide Electrocatalyst for Water Oxidation at Low Overpotential and Confirmation of Its Robustness by Cu K-Edge X-Ray Absorption Spectroscopy. *J. Phys. Chem. C* **2016**, *120* (2), 831–840.

(50) Zhu, S.; Wang, Z.; Huang, F.; Zhang, H.; Li, S. Hierarchical $Cu(OH)_2$@$Ni_2(OH)_2CO_3$ Core/Shell Nanowire Arrays: In Situ Grown on Three-Dimensional Copper Foam for High-Performance Solid-State Supercapacitors. *J. Mater. Chem. A* **2017**, *5* (20), 9960.

(51) Wang, P.; Qiao, M.; Shao, Q.; Pi, Y.; Zhu, X.; Li, Y.; Huang, X. Phase and Structure Engineering of Copper Tin Heterostructures for Efficient Electrochemical Carbon Dioxide Reduction. *Nat. Commun.* **2018**, *9* (1), 4933.

(52) An, L.; Zhou, P.; Yin, J.; Liu, H.; Chen, F.; Liu, H.; Du, Y.; Xi, P. Phase Transformation Fabrication of a Cu_2S Nanoplate as an Efficient Catalyst for Water Oxidation with Glycine. *Inorg. Chem.* **2015**, *54* (7), 3281–3289.

(53) He, L.; Zhou, D.; Lin, Y.; Ge, R.; Hou, X.; Sun, X.; Zheng, C. Ultrarapid in Situ Synthesis of Cu_2S Nanosheet Arrays on Copper Foam with Room-Temperature-Active Iodine Plasma for Efficient and Cost-Effective Oxygen Evolution. *ACS Catal.* **2018**, *8* (5), 3859–3864.

(54) Biesinger, M. C. Advanced Analysis of Copper X-Ray Photoelectron Spectra. *Surf. Interface Anal.* **2017**, *49* (13), 1325–1334.

(55) Larson, P. E. X-Ray Induced Photoelectron and Auger Spectra of Cu, CuO, Cu_2O, and Cu_2S Thin Films. *J. Electron Spectros. Relat. Phenomena* **1974**, *4* (3), 213–218.

(56) Zhou, C.; Li, H.; Lin, J.; Hou, K.; Yang, Z.; Pi, P.; Xu, S.; Wen, X.; Cheng, J. Matchstick-Like $Cu_2S@Cu_xO$ Nanowire Film: Transition of Superhydrophilicity to Superhydrophobicity. *J. Phys. Chem. C* **2017**, *121* (36), 19716–19726.

(57) Minguez-Bacho, I.; Courté, M.; Fan, H. J.; Fichou, D. Conformal Cu_2S-Coated Cu_2O Nanostructures Grown by Ion Exchange Reaction and Their Photoelectrochemical Properties. *Nanotechnology* **2015**, *26* (18), 1–10.

(58) Jiang, Y.; Zhang, X.; Ge, Q. Q.; Yu, B. Bin; Zou, Y. G.; Jiang, W. J.; Hu, J. S.; Song, W. G.; Wan, L. J. Engineering the Interfaces of $ITO@Cu_2S$ Nanowire Arrays toward Efficient and Stable Counter Electrodes for Quantum-Dot-Sensitized Solar Cells. *ACS Appl. Mater. Interfaces* **2014**, *6* (17), 15448–15455.

(59) Pichtel, J. Solubility Product Constants at 25°C http://www.aqion.de/site/16. (accessed Feb 21, 2020)

(60) Zhang, X.; Guo, Y.; Zhang, P.; Wu, Z.; Zhang, Z. Superhydrophobic $CuO@Cu_2S$ Nanoplate Vertical Arrays on Copper Surfaces. *Mater. Lett.* **2010**, *64* (10), 1200–1203.

(61) Kuo, C. H.; Chu, Y. T.; Song, Y. F.; Huang, M. H. Cu_2O Nanocrystal-Templated Growth of Cu_2S Nanocages with Encapsulated Au Nanoparticles and in-Situ Transmission X-Ray Microscopy Study. *Adv. Funct. Mater.* **2011**, *21* (4), 792–797.

(62) Fan, M.; Gao, R.; Zou, Y. C.; Wang, D.; Bai, N.; Li, G. D.; Zou, X. An Efficient Nanostructured Copper(I) Sulfide-Based Hydrogen Evolution Electrocatalyst at Neutral PH. *Electrochim. Acta* **2016**, *215*, 366–373.

(63) Folmer, J. C. W.; Jellinek, F. The Valence of Copper in Sulphides and Selenides: An X-Ray Photoelectron Spectroscopy Study. *J. Less-Common Met.* **1980**, *76* (1–2), 153–162.

(64) Nayak, A.; Tsuruoka, T.; Terabe, K.; Hasegawa, T.; Aono, M. Switching Kinetics of a Cu_2S-Based Gap-Type Atomic Switch. *Nanotechnology* **2011**, *22* (23), 235201.

(65) Laajalehto, K.; Kartio, I.; Nowak, P. XPS Study of Clean Metal Sulfide Surfaces. *Appl. Surf. Sci.* **1994**, *81* (1), 11–15.

(66) Yang, Y.; Luan, X.; Dai, X.; Zhang, X.; Qiao, H.; Zhao, H.; Yong, J.; Yu, L.; Han, J.; Zhang, J. Partially Sulfurated Ultrathin Nickel-Iron Carbonate Hydroxides Nanosheet Boosting the Oxygen Evolution Reaction. *Electrochim. Acta* **2019**, *309*, 57–64.

(67) Minceva-Sukarova, B.; Najdoski, M.; Grozdanov, I.; Chunnilall, C. J. Raman Spectra of Thin Solid Films of Some Metal Sulfides. *J. Mol. Struct.* **1997**, *410–411*, 267–270.

(68) Milekhin, A. G.; Yeryukov, N. A.; Sveshnikova, L. L.; Duda, T. A.; Rodyakina, E. E.; Gridchin, V. A.; Sheremet, E. S.; Zahn, D. R. T. Combination of Surface- and Interference-Enhanced Raman Scattering by CuS Nanocrystals on Nanopatterned Au Structures. *Beilstein J. Nanotechnol.* **2015**, *6* (1), 749–754.

(69) Hamilton, J. C. In Situ Raman Spectroscopy of Anodic Films Formed on Copper and Silver in Sodium Hydroxide Solution. *J. Electrochem. Soc.* **2006**, *133* (4), 739.

(70) Chou, M. H.; Liu, S. B.; Huang, C. Y.; Wu, S. Y.; Cheng, C. L. Confocal Raman Spectroscopic Mapping Studies on a Single CuO Nanowire. *Appl. Surf. Sci.* **2008**, *254* (23), 7539–7543.

(71) Long, N. J.; Petford-Long, A. K. In-Situ Electron-Beam-Induced Reduction of CuO: A Study of Phase Transformations in Cupric Oxide. *Ultramicroscopy* **1986**, *20* (1–2), 151.

(72) Deng, Y.; Handoko, A. D.; Du, Y.; Xi, S.; Yeo, B. S. In Situ Raman Spectroscopy of Copper and Copper Oxide Surfaces during Electrochemical Oxygen Evolution Reaction: Identification of Cu^{III} Oxides as Catalytically Active Species. *ACS Catal.* **2016**, *6* (4), 2473–2481.

(73) Miller, B. Split-Ring Disk Study of the Anodic Processes at a Copper Electrode in Alkaline Solution. *J. Electrochem. Soc.* **1969**, *116* (12), 1675.

(74) Reyter, D.; Odziemkowski, M.; Bélanger, D.; Roué, L. Electrochemically Activated Copper Electrodes. *J. Electrochem. Soc.* **2007**, *154* (8), K36.

(75) Fan, K.; Zou, H.; Lu, Y.; Chen, H.; Li, F.; Liu, J.; Sun, L.; Tong, L.; Toney, M. F.; Sui, M.; Yu, J. Direct Observation of Structural Evolution of Metal Chalcogenide in Electrocatalytic Water Oxidation. *ACS Nano* **2018**, *12* (12), 12369–12379.

(76) Lu, X.; Zhao, C. Electrodeposition of Hierarchically Structured Three-Dimensional Nickel-Iron Electrodes for Efficient Oxygen Evolution at High Current Densities. *Nat. Commun.* **2015**, *6* (1), 6616.

(77) Zuo, Y.; Liu, Y.; Li, J.; Du, R.; Yu, X.; Xing, C.; Zhang, T.; Yao, L.; Arbiol, J.; Llorca, J.; Sivula, K.; Guijarro, N.; Cabot, A. Solution-Processed Ultrathin SnS_2-Pt Nanoplates for Photoelectrochemical Water Oxidation. *ACS Appl. Mater. Interfaces* **2019**, *11* (7), 6918–6926.

(78) Zhu, X.; Guijarro, N.; Liu, Y.; Schouwink, P.; Wells, R. A.; Le Formal, F.; Sun, S.; Gao, C.; Sivula, K. Spinel Structural Disorder Influences Solar-Water-Splitting Performance of $ZnFe_2O_4$ Nanorod Photoanodes. *Adv. Mater.* **2018**, *30* (34), 1801612.

(79) Liu, Y.; Le Formal, F.; Boudoire, F.; Yao, L.; Sivula, K.; Guijarro, N. Insights into the Interfacial Carrier Behaviour of Copper Ferrite ($CuFe_2O_4$) Photoanodes for Solar Water Oxidation. *J. Mater. Chem. A* **2019**, *7* (4), 1669–1677.

(80) Liu, Y.; Le Formal, F.; Boudoire, F.; Guijarro, N. Hematite Photoanodes for Solar Water Splitting: a Detailed Spectroelectrochemical Analysis on the pH-Dependent Performance. *ACS Appl. Energy Mater.* **2019**, *2* (9), 6825-6833.

(81) Hou, C. C.; Fu, W. F.; Chen, Y. Self-Supported Cu-Based Nanowire Arrays as Noble-Metal-Free Electrocatalysts for Oxygen Evolution. *ChemSusChem* **2016**, *9* (16), 2069–2073.

(82) Wu, J. X.; He, C. T.; Li, G. R.; Zhang, J. P. An Inorganic-MOF-Inorganic Approach to Ultrathin CuO Decorated Cu-C Hybrid Nanorod Arrays for an Efficient Oxygen Evolution Reaction. *J. Mater. Chem. A* **2018**, *6* (39), 19176–19181.

(83) Pawar, S. M.; Pawar, B. S.; Hou, B.; Kim, J.; Aqueel Ahmed, A. T.; Chavan, H. S.; Jo, Y.; Cho, S.; Inamdar, A. I.; Gunjakar, J. L.; Kim, H.; Cha, S. N.; Im, H. Self-Assembled Two-Dimensional Copper Oxide Nanosheet Bundles as an Efficient Oxygen Evolution Reaction (OER) Electrocatalyst for Water Splitting Applications. *J. Mater. Chem. A* **2017**, *5* (25), 12747–12751.

(84) Zhang, H.; Zhang, Z.; Li, N.; Yan, W.; Zhu, Z. Cu_2O@C Core/Shell Nanoparticle as an Electrocatalyst for Oxygen Evolution Reaction. *J. Catal.* **2017**, *352*, 239–245.

(85) Huan, T. N.; Rousse, G.; Zanna, S.; Lucas, I. T.; Xu, X.; Menguy, N.; Mougel, V.; Fontecave, M. A Dendritic Nanostructured Copper Oxide Electrocatalyst for the Oxygen Evolution Reaction. *Angew. Chem. Int. Ed.* **2017**, *56* (17), 4792–4796.

(86) Xu, H.; Feng, J. X.; Tong, Y. X.; Li, G. R. Cu_2O-Cu Hybrid Foams as High-Performance

Electrocatalysts for Oxygen Evolution Reaction in Alkaline Media. *ACS Catal.* **2017**, *7* (2), 986–991.

(87) Li, M.; Xiong, Y.; Liu, X.; Bo, X.; Zhang, Y.; Han, C.; Guo, L. Facile Synthesis of Electrospun MFe_2O_4 (M = Co, Ni, Cu, Mn) Spinel Nanofibers with Excellent Electrocatalytic Properties for Oxygen Evolution and Hydrogen Peroxide Reduction. *Nanoscale* **2015**, *7* (19), 8920–8930.

(88) Du, J.; Li, F.; Wang, Y.; Zhu, Y.; Sun, L. Cu_3P/CuO Core-Shell Nanorod Arrays as High-Performance Electrocatalysts for Water Oxidation. *ChemElectroChem* **2018**, *5* (15), 2064–2068.

(89) Wei, S.; Qi, K.; Jin, Z.; Cao, J.; Zheng, W.; Chen, H.; Cui, X. One-Step Synthesis of a Self-Supported Copper Phosphide Nanobush for Overall Water Splitting. *ACS Omega* **2016**, *1* (6), 1367–1373.

(90) Hao, J.; Yang, W.; Huang, Z.; Zhang, C. Superhydrophilic and Superaerophobic Copper Phosphide Microsheets for Efficient Electrocatalytic Hydrogen and Oxygen Evolution. *Adv. Mater. Interfaces* **2016**, *3* (16), 1600236.

(91) Han, A.; Zhang, H.; Yuan, R.; Ji, H.; Du, P. Crystalline Copper Phosphide Nanosheets as an Efficient Janus Catalyst for Overall Water Splitting. *ACS Appl. Mater. Interfaces* **2017**, *9* (3), 2240–2248.

(92) Li, S.; Wang, Y.; Peng, S.; Zhang, L.; Al-Enizi, A. M.; Zhang, H.; Sun, X.; Zheng, G. Co-Ni-Based Nanotubes/Nanosheets as Efficient Water Splitting Electrocatalysts. *Adv. Energy Mater.* **2016**, *6* (3), 1501661.

(93) Sun, S.; Lv, C.; Hong, W.; Zhou, X.; Wu, F.; Chen, G. Dual Tuning of Composition and Nanostructure of Hierarchical Hollow Nanopolyhedra Assembled by NiCo-Layered Double Hydroxide Nanosheets for Efficient Electrocatalytic Oxygen Evolution. *ACS Appl. Energy Mater.* **2019**, *2* (1), 312–319.

(94) Ji, D.; Peng, S.; Fan, L.; Li, L.; Qin, X.; Ramakrishna, S. Thin MoS_2 Nanosheets Grafted MOFs-Derived Porous Co-N-C Flakes Grown on Electrospun Carbon Nanofibers as Self-Supported Bifunctional Catalysts for Overall Water Splitting. *J. Mater. Chem. A* **2017**, *5* (45), 23898–23908.

(95) Chen, W.; Wang, H.; Li, Y.; Liu, Y.; Sun, J.; Lee, S.; Lee, J. S.; Cui, Y. In Situ Electrochemical Oxidation Tuning of Transition Metal Disulfides to Oxides for Enhanced Water Oxidation. *ACS Cent. Sci.* **2015**, *1* (5), 244–251.

(96) Bai, J.; Meng, T.; Guo, D.; Wang, S.; Mao, B.; Cao, M. Co_9S_8@MoS_2 Core-Shell Heterostructures as Trifunctional Electrocatalysts for Overall Water Splitting and Zn-Air Batteries. *ACS Appl. Mater. Interfaces* **2018**, *10* (2), 1678–1689.

(97) Feng, L. L.; Yu, G.; Wu, Y.; Li, G. D.; Li, H.; Sun, Y.; Asefa, T.; Chen, W.; Zou, X. High-Index Faceted Ni_3S_2 Nanosheet Arrays as Highly Active and Ultrastable Electrocatalysts for Water Splitting. *J. Am. Chem. Soc.* **2015**, *137* (44), 14023–14026

Chapter 3

Solution-Processed Ultrathin SnS_2-Pt Nanoplates for Photoelectrochemical Water Oxidation

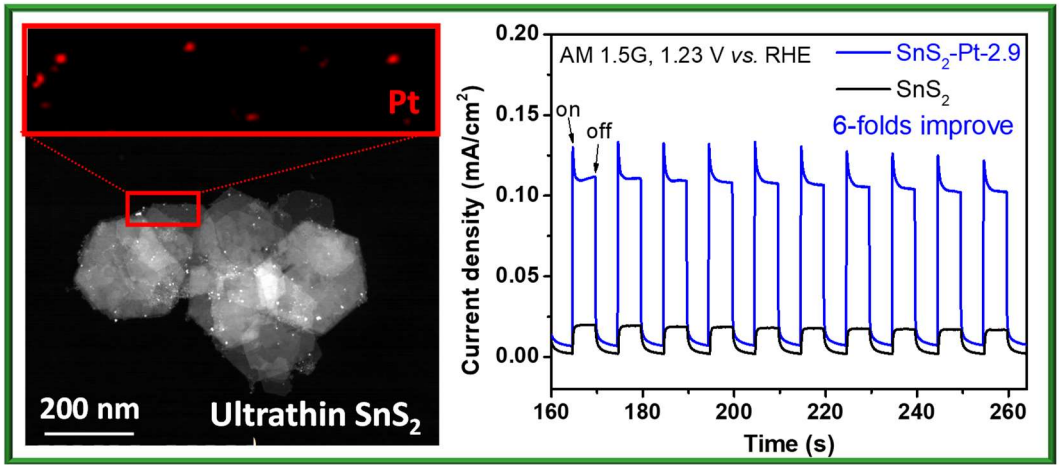

3.1 Abstract

Tin disulfide (SnS_2) is attracting significant interest due to the abundance of its elements and its excellent optoelectronic properties in part related to its layered structure. In this work, we detail the preparation of ultrathin SnS_2 nanoplates (NPLs) through a hot-injection solution-based process. Subsequently, Pt was grown on their surface via *in-situ* reduction of a Pt salt. The photoelectrochemical (PEC) performance of such nanoheterostructures as photoanode toward water oxidation was afterward tested. Optimized SnS_2-Pt photoanodes provided significantly higher photocurrent densities than bare SnS_2 and SnS_2-based photoanodes previously reported. Mott-Schottky analysis and PEC impedance spectroscopy (PEIS) were used to analyze in more detail the effect of Pt on the PEC performance. From these analyses, we attribute the enhanced activity of the SnS_2-Pt photoanodes here reported to a combination of the very thin SnS_2 NPLs and the proper electronic contact between Pt nanoparticles (NPs) and SnS_2.

3.2 Introduction

The conversion of solar energy into electric power or solar fuels such as hydrogen is a particularly relevant economic and social challenge.[1] Toward this goal, since the report by Fujishima and Honda,[2] photoelectrochemical (PEC) water splitting has become a promising route to produce environmentally friendly and potentially cost-effective hydrogen through the absorption and conversion of solar energy by a suitable semiconductor.[3,4]

Owing to its composition, SnS_2, an indirect bandgap n-type semiconductor with a gap energy of 2.18−2.44 eV,[5] has been proposed as a potentially advantageous absorber material free of rare, costly and toxic elements. SnS_2 displays a characteristic 2D hexagonal structure with tin atoms sandwiched between two close-packed sulfur atoms, and with the adjacent sandwiches being held together by weak Van der Waals forces. Such layered material has been used in a range of applications, including batteries,[6–8] photocatalysis,[5] sensors[9] and FETs.[10] Surprisingly, taking into account its well-fitted properties, the use of SnS_2 for PEC water oxidation has been not thoroughly investigated.

The main flaws of SnS_2 are a relatively low electrical conductivity and a moderate absorption coefficient in the visible part of the solar spectrum, what limits its photoactivity.[11] To solve these limitations, a number of strategies have been developed: i) introduce extrinsic dopants to adjust the SnS_2 band gap and modulate its charge carrier concentration;[12–14] ii) introduce co-catalysts on the surface of SnS_2 to enhance its activity, e.g. Pt;[15–25] and iii) reduce the SnS_2 thickness taking into account that thin SnS_2 nanosheets with exposed (001) facets display higher photocatalytic activities.[26–28]

In this last direction, several methods have been used to prepare SnS_2 nanostructures with a variety of morphologies, trying to maximize the exposed surface:[6,7,9] e.g. nanoflakes,[29] nanowires,[30] nanoleaves[31] and microspheres[8]. A particularly interesting example is the exfoliation of SnS_2 bulk powders into single-layers, which showed a promising although still moderate performance in PEC water splitting.[32] This approach had, as main drawback, its relatively low production throughput due to the long processing time and low yield.

Herein, we present a simple solution-based route to produce (001)-faceted SnS_2 NPLs. These NPLs are loaded with Pt NPs via an *in-situ* reduction process. The resulting SnS_2-Pt heterostructures are used as photoanode here for PEC water oxidation under

simulated sun light. The performance of this new material is further characterized using Mott-Schottky analysis and PEIS.

3.3 Experimental Section

3.3.1 Chemicals

All chemicals were used as received, without additional purification. Tin(IV) chloride pentahydrate ($SnCl_4 \cdot 5H_2O$, 98%), sulfur powder (99.8%), tetrahydrofuran (THF, ≥99%), 1,2-hexadecanediol (90%), 1,2-dichlorobenzene (DCB, 99%) and diphenyl ether (≥99%) were purchased from Sigma-Aldrich. Platinum(II) acetylacetonate (98%), oleylamine (OAm, 80-90%) and oleic acid (OAc, 70%) were purchased from Acros. 1-Octadecene (ODE, 90%) was purchased from Alfa-Aesar. Toluene, hexane, isopropanol and ethanol were of analytical grade and obtained from various sources. All the aqueous solutions were prepared using Milli-Q water (18.2 MΩ·cm).

3.3.2 Synthesis of SnS_2 Nanoplates

In a typical synthesis, $SnCl_4 \cdot 5H_2O$ (2 mmol) was dissolved in THF (1 mL) in a 50 mL three-neck round flask. ODE (16 mL), OAc (4 mL) and OAm (2 mL) were then added and stirred at room temperature for 10 min. A syringe inserted into the solution was used to bubble Ar. The solution was then heated up to 140 °C and kept at this temperature for 1h to remove low boiling-point impurities. Then the obtained clear brown solution was heated to 220 °C. At this temperature, 4 mL of a S-OAm stock solution, pre-prepared by dissolving sulfur powder (4 mmol) into OAm (4 mL) under sonication, was quickly injected into the reaction flask with a syringe. The mixture was maintained at this temperature for 1h and afterward quickly cooled down using a cold water bath. The resulted product was centrifuged at 6000 rpm for 4 mins after adding toluene (15 mL), and then washed three times with toluene and ethanol by dispersion-precipitation cycles. The obtained pale yellow product was dried under vacuum for its posterior use and characterization. Around 280 mg of material was obtained in each batch, which corresponded to a 80 % material yield after purification.

3.3.3 Synthesis of SnS_2-Pt Nanoheterostructures

Phenyl ether (10 mL), 1,2-hexadecanediol (43 mg), OAm (0.2 mL) and OAc (0.2 mL) were loaded into a 25 mL three-neck reaction flask and kept at 140 °C for 30 min with Ar

bubbling through a syringe. Depending on the relative SnS_2/Pt ratio targeted, 2 mg (SnS_2-Pt-2), 5 mg (SnS_2-Pt-5), 10 mg (SnS_2-Pt-10), or 20 mg (SnS_2-Pt-20) of platinum(II) acetylacetonate was added into a SnS_2 dispersion containing 100 mg of SnS_2 NPs (containing ca. 20 % organics) within 4 mL of DCB. These values correspond to a nominal molar concentration of 1.2 % (SnS_2-Pt-1.2), 2.9 % (SnS_2-Pt-2.9), 5.8 % (SnS_2-Pt-5.8) and 11.6 % (SnS_2-Pt-11.6), respectively. The solution was then sonicated at 45 °C for 30 mins to homogenize. This mixture was quickly injected into the reaction flask at 200 °C and maintained at this temperature for 10 mins. A cold water bath was then used to quench the reaction. The product was washed with hexane and ethanol by multiple dispersion-precipitation cycles.

3.3.4 Ligand Exchange

The native organic ligands were displaced from the NP surface using a NH_4SCN solution.[33] Briefly, 10 mL of a hexane solution containing the NPs (5 mg/mL in hexane) was mixed with 5 mL of 0.13 M NH_4SCN solution (0.5 g NH_4SCN in 50 mL acetone). The mixture was then shacked for several minutes with a vortex and finally centrifuged out at 4000 rpm for 3 mins. The resulted product was further washed with 10 mL acetone twice to remove residual NH_4SCN.

3.3.5 Sample Characterization

Powder X-ray diffraction (XRD) patterns were obtained on a Bruker AXS D8 ADVANCE X-ray diffractometer (Bruker, Karlsruhe, Germany) operating at 40 kV and 40 mA with Ni-filtered (2 μm thickness) Cu Kα1 radiation (λ = 1.5406 Å). Transmission electron microscopy (TEM) characterization was carried out on a ZEISS LIBRA 120 (Carl Zeiss, Jena, Germany), operating at 120 kV. High-resolution TEM (HRTEM) images were obtained using a field emission gun FEI Tecnai F20 microscope at 200 kV with a point-to-point resolution of 0.19 nm. High angle annular dark-field (HAADF) STEM was combined with electron energy loss spectroscopy (EELS) in the Tecnai microscope by using a GATAN QUANTUM filter. For TEM characterization, samples were prepared by drop casting a solution of NPs on a 200 mesh copper grid. SEM analysis was done in a ZEISS Auriga microscope (Carl Zeiss, Jena, Germany) with an energy dispersive X-ray spectroscopy (EDX) detector at 20 kV to study composition. X-ray photoelectron spectroscopy (XPS) was carried out on a SPECS system (SPECS GmbH,

Berlin, Germany) equipped with an Al anode XR50 source operating at 150 mW and a Phoibos 150 MCD-9 detector (SPECS GmbH, Berlin, Germany). The pressure in the analysis chamber was kept below 10^{-7} Pa. Data processing was performed with the CasaXPS program (Casa Software Ltd., UK). Binding energy (BE) values were centered by using the C 1s peak at 284.8 eV. Fourier transform infrared spectroscopy (FTIR) was performed on an Alpha Bruker FTIR spectrometer with a platinum attenuated total reflectance (ATR) single reflection module. FTIR data were typically averaged over 24 scans. UV-Vis absorption spectra were recorded on a PerkinElmer LAMBDA 950 UV-Vis spectrophotometer (PerkinElmer,Walthham, MA, USA). Steady state photoluminescence (PL) spectra were recorded on a high resolution photoluminescence spectrofluorometer (Horiba Jobin Yvon Fluorolog-3).

3.3.6 Photoelectrochemical Measurements

PEC characterization was performed in a three-electrode system using an electrochemical workstation (Metrohm Autolab). A Pt mesh (2 cm^2 surface area) and Ag/AgCl (3.3 M KCl) were used as the counter and reference electrodes, respectively. To prepare the working electrode, 2 mg of NPs and Nafion (20 μL, 5wt%) were dispersed in water-isopropanol (0.4 mL) with a volume ratio of 3:1 by sonicating 1h until obtaining a homogeneous ink. Depending on the amount of catalyst we wanted to test, 50 μL-300 μL ink was drop casted onto an FTO (fluorine doped tin oxide, 1cm × 1.8cm) substrate and then annealed at 200 °C for 20 min after solvent evaporation. Before deposition, the FTO glass was washed with acetone-isopropanol (1-1 volume), ethanol, and then deionized water. After ink deposition, part of the material was wiped out from the FTO substrate to leave a clean area for electrical connection. An active area of 1cm x 1cm was left for PEC tests. An aqueous solution of Na_2SO_4 (0.5 M, pH = 7) was used as the electrolyte. The electrolyte was purged with Ar for 30 min prior to the measurement. The incident light source was provided by 8 radially distributed 35 W xenon lamps, providing a total irradiance power on the sample of ca. 100 mW/cm^2. The following formula was used to convert the potentials to the reversible hydrogen electrode (RHE) standard scale:

$$E \text{ vs. RHE} = E_{Ag/AgCl} + E^{o}_{Ag/AgCl} + 0.059 \times pH = E_{Ag/AgCl} + 0.623 \text{ (V)}$$

For PEIS measurements, the frequency was swept from 1 MHz to 50 mHz with a sinusoidal amplitude of 25 mV under the same conditions used for photocurrent measurements. An equivalent circuit modeling software ZView (Scribner Associates)

was used to fit the PEIS data. Mott-Schottky analysis was performed under dark conditions.

3.4 Results and discussion

SnS_2 NPs were produced from the reaction of tin chloride with elemental sulfur dissolved in OAm at 220 °C (see experimental section for details). Figure 3.1 shows representative TEM and SEM micrographs of the SnS_2 NPs produced following this synthesis procedure. SnS_2 NPs displayed hexagonal plate-like geometry with a diameter of around 150 nm and a thickness of ca. 6 nm (Figure 3.1a,b). Such NPLs were much thinner than previously reported solution-processed SnS_2 NPs.[29,34–36] XRD patterns showed the SnS_2 NPLs to have a hexagonal phase and pointed at the (001) facet as the dominantly exposed (Figure 3.1c). HRTEM characterization confirmed SnS_2 NPLs to have a hexagonal crystallographic phase (space group =P-3m1) with a=b=3.6460 Å, c=5.8960 Å, and revealed them to be ~10 layers thick along the [001] direction. Additional EELS chemical composition analysis (Figure 3.1e) showed a uniform distribution of Sn and S through the whole SnS_2 NPL.

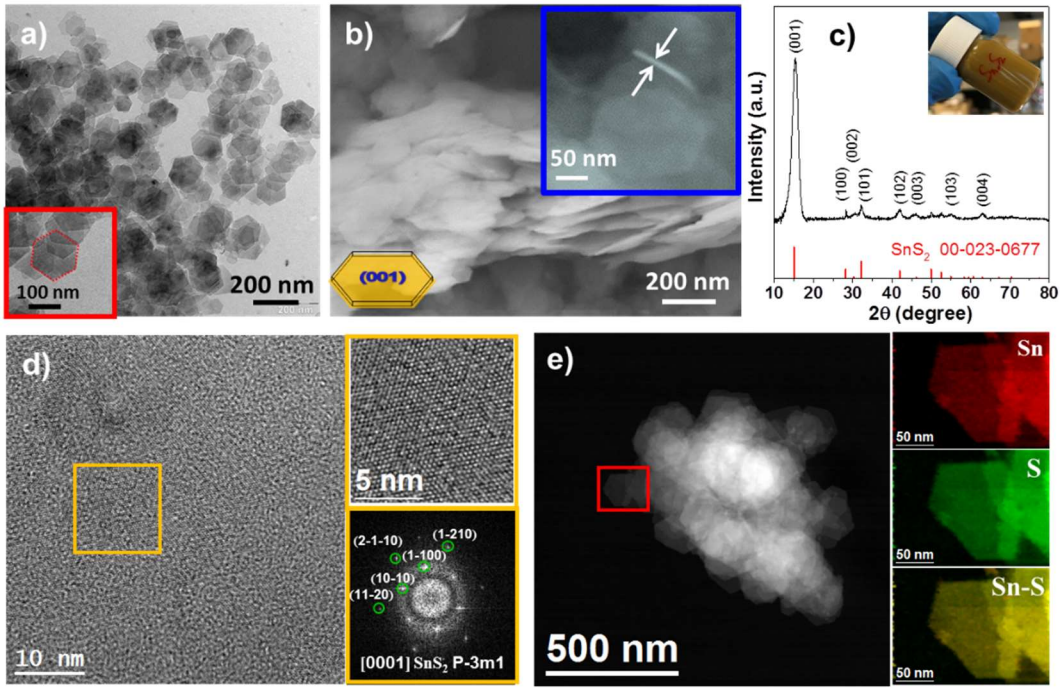

Figure 3.1. (a) TEM micrograph of the hexagonal SnS_2 NPLs produced from the detailed experimental procedure. (b) SEM micrograph of the SnS_2 NPLs. Inset shows a NPL oriented normal to the substrate, which was used to measure a NPL thickness of 6 nm. (c) XRD pattern of the dried SnS_2 NPLs, including the SnS_2 JCPDS 00-023-0677 reference pattern. Inset shows an optical image of the SnS_2 NPLs solution. (d) HRTEM micrographs and selected area electron

diffraction (SAED) pattern of a SnS_2 NPL. SnS_2 lattice fringe distances were measured to be 0.181 nm, 0.180 nm, 0.157 and 0.181 nm, at 60.56º, 90.52º and 120.32º, which was interpreted as the hexagonal SnS_2 phase, visualized along its [0001] zone axis. (e) STEM micrograph and EELS chemical composition maps from the red squared area: Sn $M_{4,5}$-edges at 485 eV (red), S $L_{2,3}$-edges at 165 eV (green).

The process of formation of SnS_2 NPLs was analyzed through the XRD characterization of the product precipitated from aliquots extracted at different reaction times (Figure 3.2a,b). We observed that after few minutes reaction, mainly S was present in the precipitated powder, obtained from the reversible reaction of formation of oleylammonium polysulfides from the reaction of sulfur and OAm (Figure 3.2c).[37,38] With time, SnS_2 was directly formed and S was gradually consumed along the 1h reaction. Sulfur could react with Sn(IV)-OAm directly, or in the form of oleylammonium polysulfices. We actually believe that both reactions took place simultaneously. No Sn-S intermediate phase could be detected.

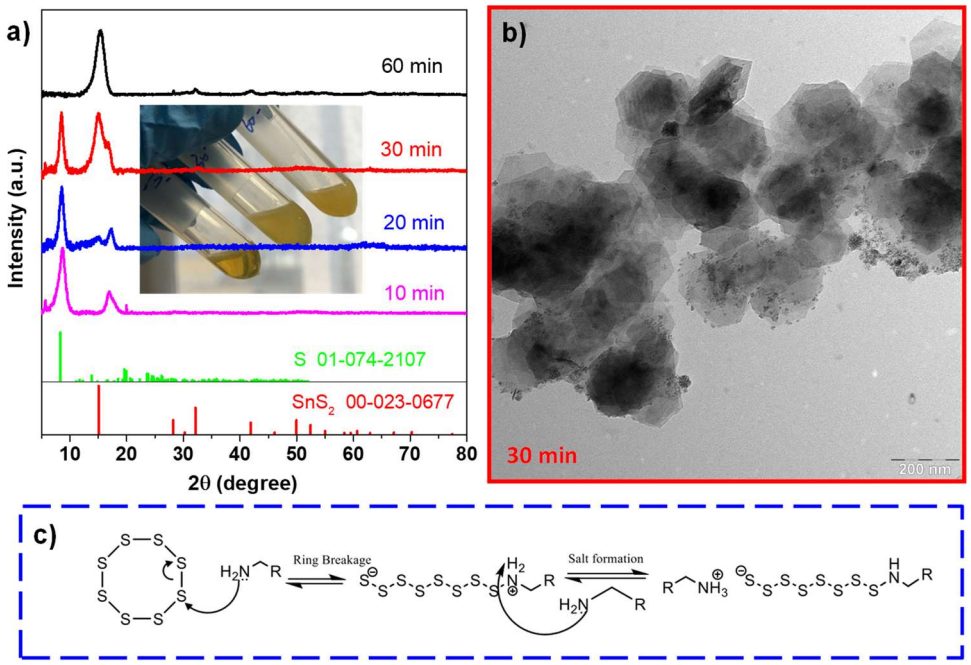

Figure 3.2. (a) XRD patterns of products obtained at different reaction time. Inset image shows the product obtained at 220 ºC for 10 min,30 min, 60 min and dispersed in hexane. (b) SEM image of product obtained after 30 min reaction time. (c) Proposed mechanism for the formation of oleylammonium polysulfide salt.

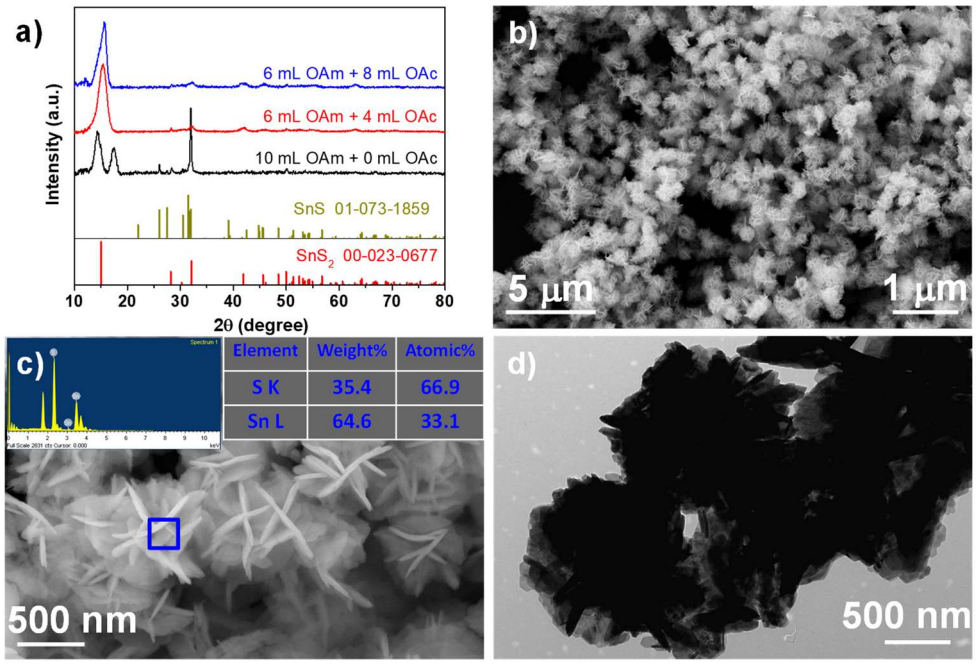

Figure 3.3. (a) XRD patterns of products obtained from different volumes of OAm and OAc. (b-(c) SEM and (d) TEM images of products obtained in the absence of OAm. Inset in (c) shows the EDX spectrum and the obtained elements content. We can obviously see here that without OAm presence, large flower-like SnS_2 crystals were formed.

The influence of the OAc/OAm ratio was analyzed through the XRD and TEM characterization of the products obtained under different amounts of these two surfactants (Figure 3.3a). Pure OAm resulted in the formation of both SnS and SnS_2 phases due to the partial reduction of the Sn^{4+} precursor by OAm. Only with the addition of a sufficient amount of OAc, pure SnS_2 phase could be formed. When no OAm was added, the Sn precursor could not be totally dissolved in the ODE-OAc initial solution. Under these conditions, large (~1 µm) flower-like SnS_2 structures were formed at 220 °C, after injecting the sulfur precursor (S-ODE in this case), as observed from representative SEM and TEM micrographs in Figure 3.3b-d. The microstructures of SnS_2 samples show difference with/without OAm addition because OAm was not only necessary to bring Sn and S into the solution, but it also played a role as surfactant promoting the asymmetric growth of SnS_2 into NPLs, probably by preferential binding at (001) facets, and preventing the NPLs aggregation. Without OAm, urchin-like structures were obtained (Figure 3.3b,c). On the other hand, OAc facilitated the formation of the SnS_2 phase.[34] With no OAc, a mixture of SnS_2 and SnS phases was systematically obtained (Figure 3.3a).

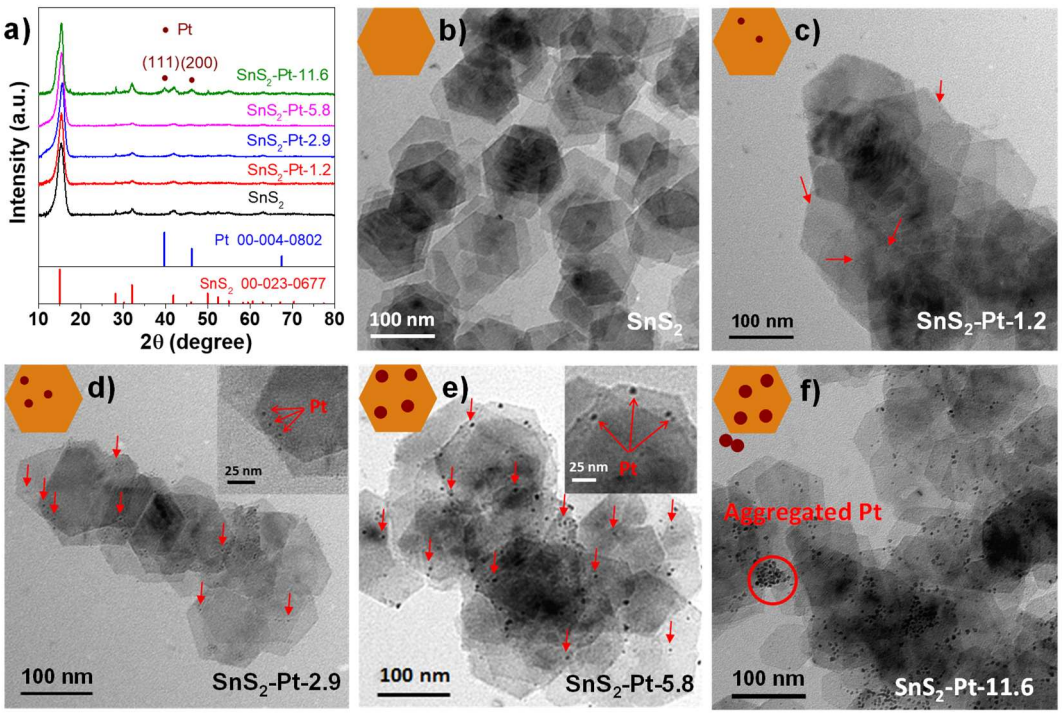

Figure 3.4. (a) XRD patterns of SnS_2-Pt nanoheterostructures. TEM images of (b) SnS_2 NPLs and SnS_2-Pt nanoheterostructures with increasing amounts of (c) Pt: 1.2 mol%, d) 2.9 mol%, (e) 5.8 mol% and (f) 11.6 mol%.

SnS_2-Pt nanoheterostructures were produced by the growth of Pt nanodomains on the surface of preformed SnS_2 NPLs through the reduction of Pt(II) acetylacetonate (see experimental section for details). EDX analyses showed the final Pt concentration on the SnS_2 NPL surface to follow the nominal precursor ratios, pointing at a high yield of Pt deposition. XRD analyses showed the Pt metallic peaks at high Pt concentration, but no additional phase (Figure 3.4a). When increasing the nominal amount of Pt, from 1.2%, to 2.9% and 5.8%, the diameter of the Pt domains in the SnS_2-Pt nanoheterostructures increased from ~1 nm, to ~3 nm and ~5 nm (Figure 3.4b-d), respectively. Pt nanodomains were found uniformly distributed on the NPLs surface. However, at higher Pt concentrations, e.g. when introducing a nominal 11.6% of Pt (Figure 3.4f), the Pt size did not significantly further increase with respect to SnS_2-Pt-5.8 but some Pt aggregation started to occur. HRTEM and EELS chemical compositional maps further confirmed the homogeneous distribution of Pt NPs through the SnS_2 surface and their average crystal domain size (Figure 3.5).

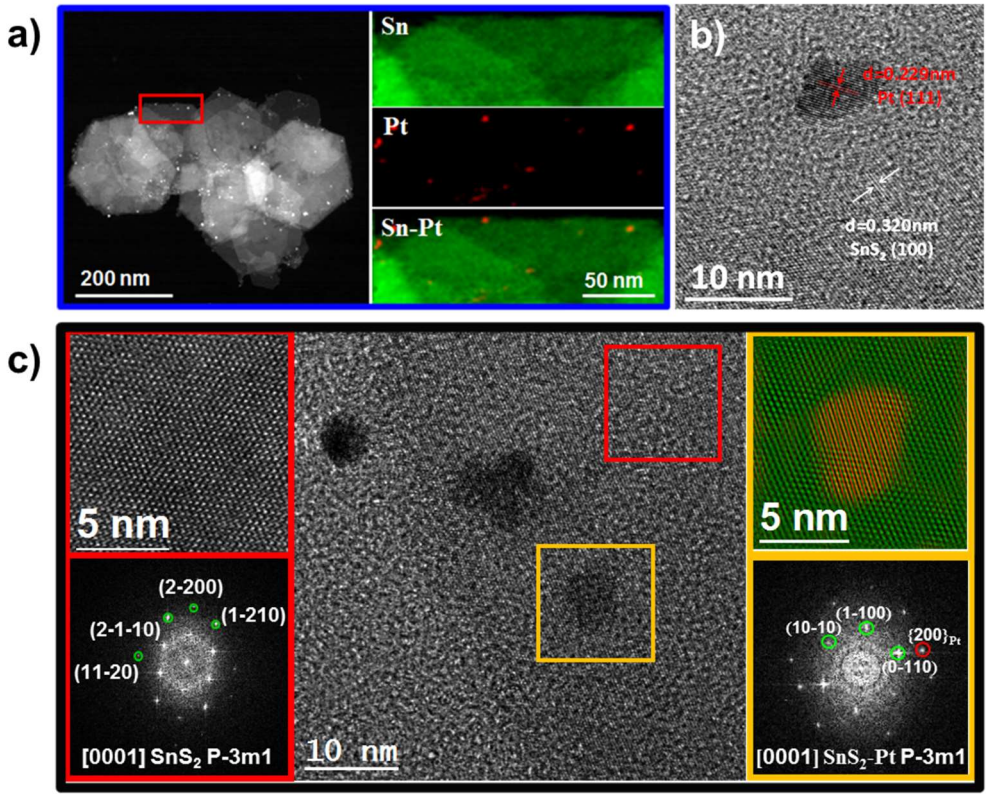

Figure 3.5. (a) STEM micrograph of SnS_2-Pt-5.8 NPLs and EELS chemical composition maps from the red squared area: Sn $M_{4,5}$-edges at 485 eV (green), Pt $M_{4,5}$-edges at 2122 eV (red). (b) HRTEM lattice image of SnS_2-Pt-5.8 nanoheterostructures. (c) HRTEM micrograph of a SnS_2-Pt-5.8 NPL and details of the red and orange squared regions with their corresponding power spectrum. The SnS_2 NPL (red square) displayed the SnS_2 hexagonal phase (space group =P-3m1) with a=b=3.6460 Å, c=5.8960 Å in its [0001] zone axis. Detail of the orange squared region and its corresponding power spectrum further revealed a reflection corresponding to the {200} Pt planes. A frequency filtered image where the corresponding lattice fringes in green (SnS_2) and red (Pt) was overlapped is also presented.

XPS analyses provided slightly higher Pt concentrations than those nominally introduced and measured by EDX. As an example, the Pt concentration in the sample with a nominal composition of 2.9% was 3.8 mol% (Figure 3.6b). As expected, XPS analysis showed the Pt to be in a metallic state. The Sn:S ratio was found at 0.6, which also pointed at a slightly Sn-rich surface. XPS analysis of bare SnS_2 (Figure 3.6a) showed the same Sn/S atomic ratio, 0.6, proving the addition of Pt not to affect the SnS_2 composition. The Sn-rich surface could be ascribed to an intrinsically off-stoichiometry of SnS_2 surfaces, particularly (001) facets, or to a slight oxidation of the SnS_2 NPLs that had been exposed to air. Nevertheless, only one chemical environment was identified for Sn in both SnS_2 and SnS_2-Pt samples, and this was compatible with a Sn^{4+} chemical state in a SnS_2 environment.

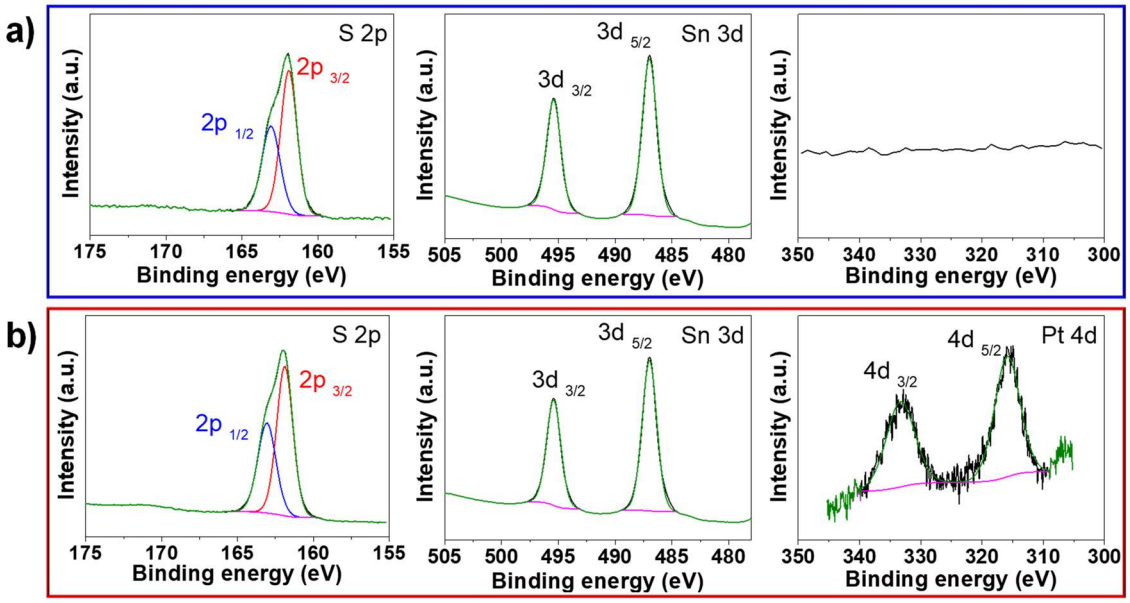

Figure 3.6. XPS spectra of (a) SnS_2 NPLs and (b) SnS_2-Pt-2.9 nanoheterostructures.

To promote an efficient transport of charge carriers within SnS_2-Pt NPL-based films, before film preparation, original insulating organic ligands were removed using a 0.13 M NH_4SCN solution (see experimental section for details). After ligand exchange, samples could not be re-dispersed in non-polar solvents such as hexane. Additionally, the bands corresponding to the C–H signal of OAm and OAc (2851-2923 cm^{-1}) completely disappeared from the FTIR spectrum (Figure 3.7), which indicated the effective removal of organic ligands from the NC surface. Subsequently, SnS_2-Pt NPLs were drop-casted on FTO substrates to test their performance as photoanode for PEC oxygen evolution.

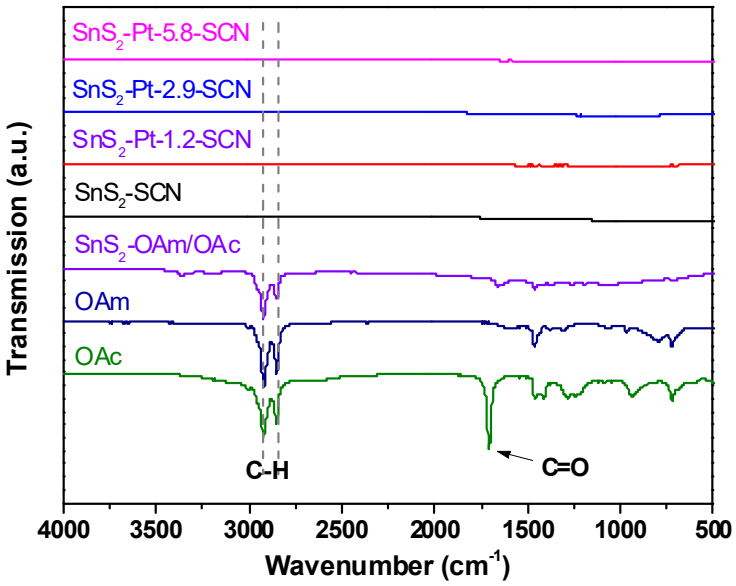

Figure 3.7. FTIR spectra of pure OAm, OAc, as-produced SnS_2 NPLs (SnS_2-OAm/OAc) and SnS_2-Pt nanoheterostructures after ligand exchange with NH_4SCN solution (SnS_2-Pt-1.2, 2.9, 5.8-SCN).

All samples showed activity toward PEC water oxidation under simulated solar light (Figure 3.8). Figure 3.8a and 3.8b display the I-V curves and transient photocurrent (external bias of 1.23 V *vs.* RHE) under chopped visible-light illumination. As expected, the addition of Pt increased the PEC activity, being the SnS_2-Pt-2.9 photoanode the one providing the highest photocurrent densities. The values obtained with this catalyst were superior to most SnS_2-based photocatalysts previously reported (Table 3.1), particularly when compared with materials deposited from solution on top of FTO/ITO substrate (see Ref. 5, 11, 44). Although SnS_2-based materials directly grown from a conducting substrate like FTO (Ref. 47, 48) and Ti foil (Ref. 49), generally showed an improved contact between sample materials and current-collector and a related lower contact resistance.

When increasing the Pt loading, the PEC current density at 1.23 V *vs.* RHE increased from 16.84 $\mu A/cm^2$ for SnS_2, to 112 $\mu A/cm^2$ for SnS_2-Pt-2.9, to later decrease at higher Pt concentrations, e.g. 36.18 $\mu A/cm^2$ for SnS_2-Pt-5.8. The reduced photocurrent at high Pt loading was associated to: 1) a poor electronic/catalytic properties of the Pt with increased particle size; 2) the excessive electron-hole recombination centers resulting from higher Pt loading, thereby limiting the extraction of electrons with the external bias;[39] 3) a strong light absorbance by Pt that partially shadowed the semiconductor from the light.[40] Photoresponse times were on the order of 0.1 s for all samples, indicating a relatively rapid charge transport toward the substrate. The SnS_2-Pt-2.9 photoanode displayed transient spikes that increased with the photocurrent. These spikes were typically attributed to the charge accumulation and recombination at the interface, evidencing limitations on the charge transfer process to the electrolyte.[41–43]

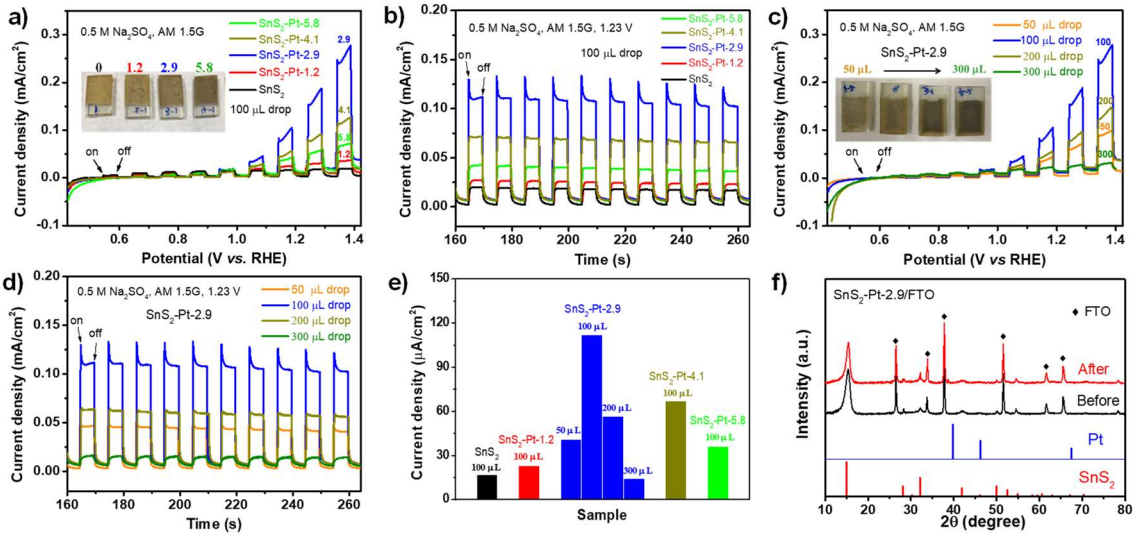

Figure 3.8. (a) Linear sweep voltammogram curves under chopped AM 1.5G illumination for PECs. (b) Corresponding amperometric i-t curves under chopped illumination at an applied potential of 1.23 V *vs.* RHE (0.6 V *vs.* Ag/AgCl, 3.3 M KCl). (c) Linear sweep voltammogram curves under AM 1.5G illumination of SnS_2-Pt-2.9 layers with different material amounts. (d) Amperometric i-t curves from films of different thicknesses produced from different ink amounts. (e) Comparison of the PEC performance obtained from different samples. (f) XRD patterns of SnS_2-Pt-2.9 on FTO substrate before and after PEC tests.

The amount of catalyst used to produce the film had a notable influence on the photocurrent response (Figure 3.8c, d). Excess amounts of catalysts resulted in a low illumination of the material close to the electrodes, where a more efficient charge extraction takes place. On the contrary, too small amounts limit the total surface area available for PEC oxygen evolution, also resulting in lower photocurrents (Figure 3.8e). XRD (Figure 3.8f), SEM and TEM (Figure 3.9) characterization demonstrated that no crystallographic phase change took place during PEC measurements.

Long term stability of the SnS_2-Pt-2.9 photoanode was tested under chopped simulated solar light (on/off every 10 s). The results showed that around 60 % of the initial current density was preserved after 2000 s and then became almost steady, indicating an acceptable stability (Figure 3.10a). Bubbles could be easily seen around the photoanode and Pt mesh, which was respectively ascribed to the O_2 and H_2 generation from water during test, as well as the inside wall of the PEC cell (Figure 3.10b).

Table 2.1. Comparisons of Different SnS_2-based photocatalysts on photoelectrochemical water splitting

Catalyst material	Synthesis method	Load method	Electrolyte	Reference electrode	Bias/*vs* RHE	Photocurrent	Ref.
SnS_2-Pt-2.9	Hot-injection	Drop casting, 1 cm^2/FTO	0.5M Na_2SO_4	Ag/AgCl	1.23 V	112 μA/cm^2	This work
SnS_2 nanoplates	Hot-injection	Drop casting, 1 cm^2/FTO	0.5M Na_2SO_4	Ag/AgCl	1.23 V	18 μA/cm^2	This work
SnS_2 nanosheets	Hydrothermal	Drop casting, 1.5 mg/1 cm^2/ITO	0.5M Na_2SO_4	SCE	1.46 V	11.7 μA/cm^2	5
Ag_2S(8wt%)/SnS_2 composite	Hydrothermal + Ion exchange	Spin coating, 1 cm^2/ITO	0.5M Na_2SO_4	Ag/AgCl	1.33 V	13.99 μA/cm^2	11
BiOCl/SnS_2 hollow spheres	Hydrothermal	Spray, 6 cm^2/FTO	0.1M Na_2SO_4	SCE	1.36 V	40 μA/cm^2	44
SnS_2/g-C_3N_4 Nanosheets	Sintering + Chemical precipitation	Spin coating, 1 cm^2/FTO	0.1M Na_2SO_4	Ag/AgCl	1.43 V	13.66 μA/cm^2	45
ZnS-SnS_2 porous nanosheets	Hydrothermal + Chemical precipitation	/	0.5M Na_2SO_4	SCE	1.66 V	12 μA/cm^2	46
Hierarchical CdS Nanorod/SnSx Nanosheet	Hydrothermal + Annealing	As-sythesized electrode	0.5M Na_2SO_4	Ag/AgCl	1.23 V	1.59 mA/cm^2	47
SnS_2/FTO	Wet-chemical method + Annealing	As-sythesized electrode	1M Na_2SO_4	Ag/AgCl	1.43 V	1.23 mA/cm^2	48
SnS_2/TiO_2 nanotube arrays/Ti	Solvothermal + Annealing	As-sythesized electrode	0.5M Na_2SO_4	SCE	1.16 V	1.05 mA/cm^2	49

*The following formula was used to convert the potentials listed above to the reversible hydrogen electrode (RHE) standard scale: E vs. RHE = E_{Ref}+ E^o_{Ref} + 0.059 × pH

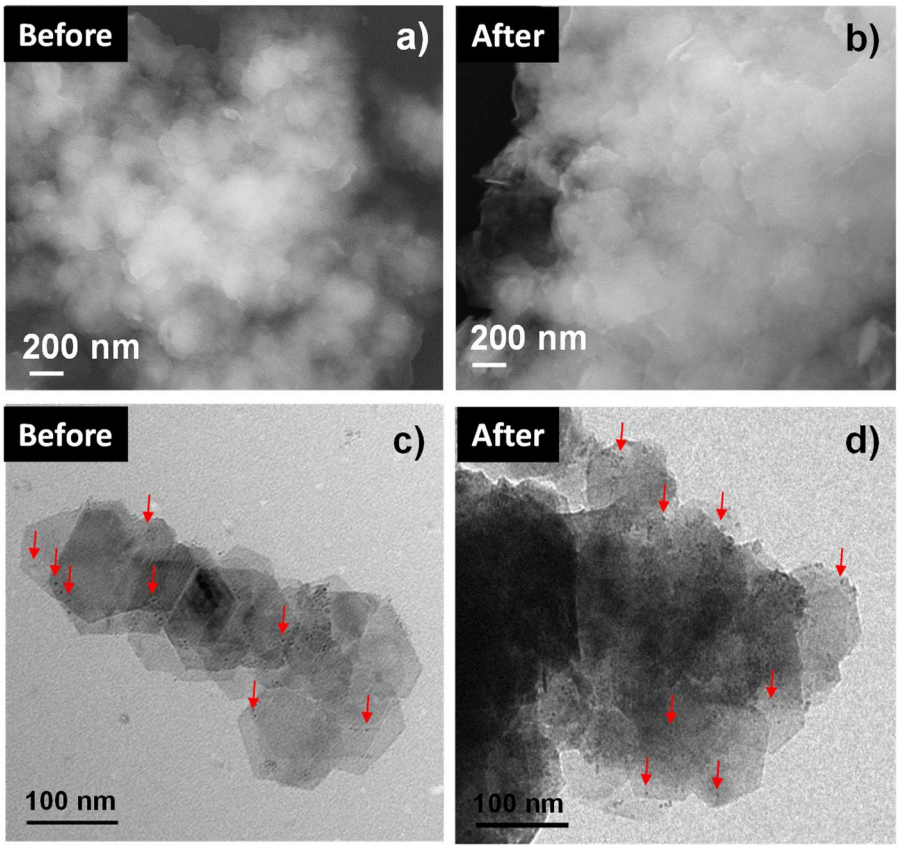

Figure 3.9. SEM images (a,b) and TEM images (c,d) of sample SnS_2-Pt-2.9 before (a,c) and after (b,d) PEC test.

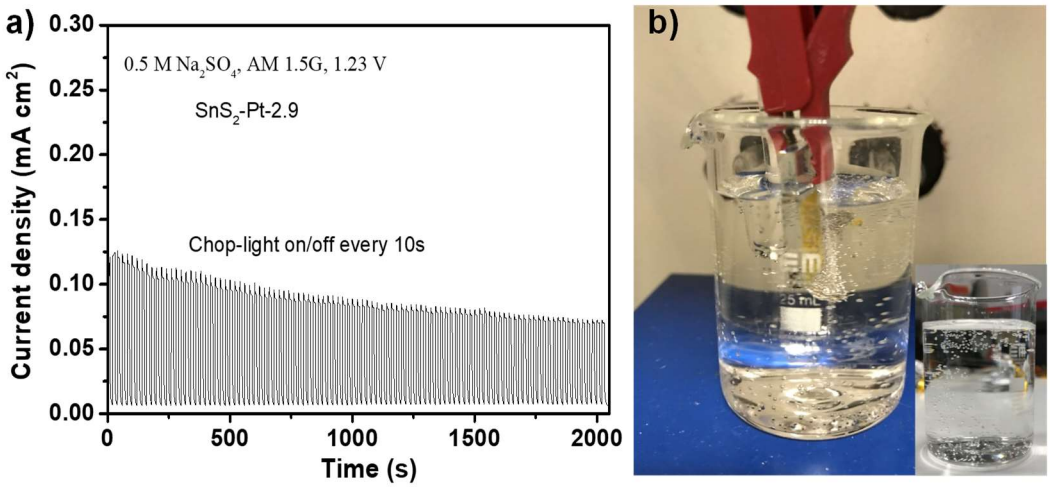

Figure 3.10. (a) Long term stability of sample SnS_2-Pt-2.9 after 2000s test on chop light. (b) Optical image of photoelectrochemical cell after test. Some bubbles are clear to see, which are probably released H_2 and O_2 splitted from water during test.

To gain insight into the charge carrier behavior at the semiconductor-liquid interface, PEIS measurements were carried out. Figure 3.11 shows the Nyquist plots corresponding to the SnS_2-based anodes containing increasing amounts of Pt. At first sight, the decrease in the diameter of the semi-arc with the increased Pt loading suggested a decrease in the film resistance (Figure 3.11a). A quantitative analysis of the electrochemical properties of the electrodes was attempted by fitting the Nyquist plots with equivalent circuits.[50] Given the components and processes assumed to occur in these electrodes, we considered a general equivalent circuit containing a series resistance (R_s) and three RC components with the following contributions (Figure 3.11b): i) capacitance of the bulk SnS_2 (C_{bulk}) and resistance of hole trapping to the surface states (R_{trap}); ii) capacitance of the surface states (C_{ss}) and resistance for charge transfer to the electrolyte through the surface states ($R_{ct,ss}$); and iii) charge transfer resistance from the valence band to Pt particles ($R_{ct,bulk}$), capacitance associated to the surface Pt particles (C_{Pt}) and charge transfer resistance from Pt particles to the electrolyte ($R_{ct,Pt}$). The Bode plot (Figure 3.11e) obtained for the different samples displayed a broad band, probably composed by two nearby peaks, indicating that a two-time constant equivalent circuit could describe sufficiently well the impedance response. Therefore, two simplified equivalent circuits (Figure 3.11c,d) were used to fit the Nyquist plots.[51] For the sake of the analysis, the electrochemical parameters extracted from the fitting were plotted as a function of Pt loading in Figure 3.11f. In terms of the charge transfer resistance, bare SnS_2 and SnS_2-Pt-1.2 presented very high values, which resulted in low photocurrents. When the Pt loading increased (SnS_2-Pt-2.9 and SnS_2-Pt-5.8), the charge transfer resistance at the surface dropped dramatically, evidencing the improved catalytic activity provided by the Pt NPs. It is worth noting that $R_{ct,bulk}$ (R_{trap}) values are much lower than those of $R_{ct,Pt}$ ($R_{ct,ss}$), which was a sign that charge transfer was limited by the electrode/electrolyte interface instead of bulk. Interestingly, it was found that the lowest charge transfer resistance was achieved for SnS_2-Pt-2.9, in good agreement with the best performance obtained for this material. Further increase of the Pt loading led to an increase in C_{Pt} and $R_{ct,bulk}$, whereas $R_{ct,Pt}$ remained virtually unchanged. These findings suggest that the decreased performance for high Pt loading (Figure 3.8a) did not originate from a deterioration of the catalytic activity of the Pt overlayer since $R_{ct,Pt}$ barely changed, but potentially from a worse charge transfer from the SnS_2 to the larger Pt NPs, given the increased $R_{ct,bulk}$. Likewise, the larger C_{Pt} could be accounted for by the increased coverage and size of the Pt nanoparticles. To

provide more details about the water oxidation mechanism on SnS_2-Pt nanoheterostructures, EIS was carried out in the dark and under illumination on a representative SnS_2-Pt-2.9 photoanode (Figure 3.11g). Data extracted from fitting is displayed in inset of Figure 3.11g. First, the value of $R_{ct,bulk}$ in the dark (around 2.8 kΩ) is higher than that under illumination (1.9 kΩ). This is not surprising given that under illumination the increased carrier density will decrease the film resistance. Second, the value of $R_{ct,Pt}$ decreases significantly under illumination which is consistent with the increased current. Indeed, the negligible faradaic dark current suggests that charges at this applied potential are unable to drive the water oxidation reaction, whereas under illumination the more oxidizing holes can successfully trigger the interfacial reaction. Third, the value of C_{Pt} increases under illumination, which could be accounted for by the role of Pt as a reservoir of photogenerated holes at the interface. This result together with the increased photocurrent observed when coating SnS_2 with Pt provides compelling evidence that water oxidation occurs primarily via Pt sites rather than through the valence band of SnS_2. Similar behavior has also been found on other photoanodes such as hematite[52] and copper ferrite[53]. Additionally, Mott-Schottky analysis was performed on two representative samples, bare SnS_2 and SnS_2-Pt-2.9, under dark conditions. A Randles circuit was used to extract C_{bulk} from impedance response to construct Mott-Schottky plot in Figure 3.11h. The positive slope of the C^{-2}-E plots indicated that both bare SnS_2 and SnS_2-Pt-2.9 are n-type semiconductors.[52,53] The introduction of an optimal Pt loading positively shifted the flat band potential (V_{fb}) from 0.24 V to 0.14 V vs RHE. This implied a better photocurrent onset potential for SnS_2-Pt-2.9 and was consistent with Gong and co-workers reporting on surface modified hematite photoanodes.[54]

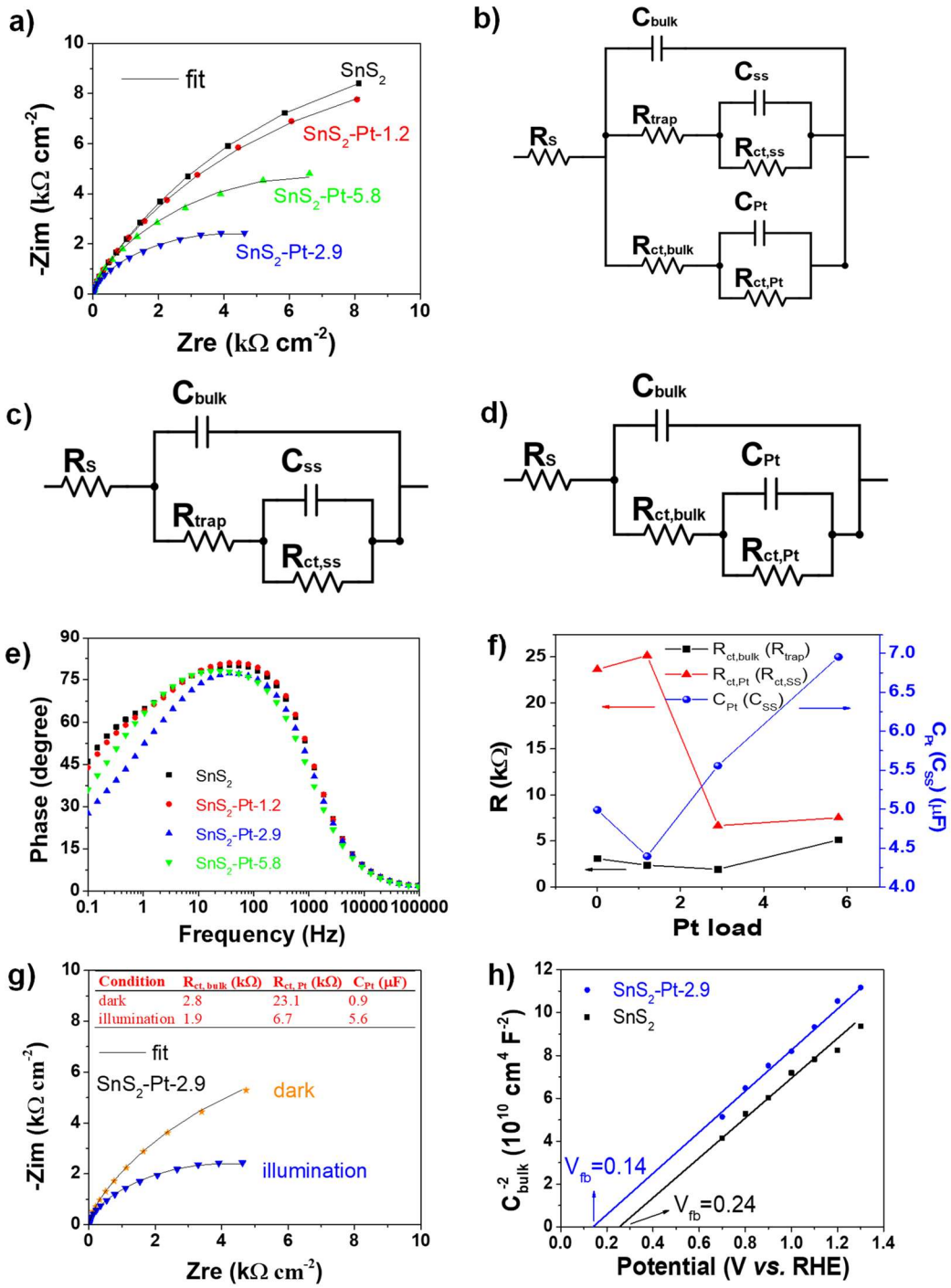

Figure 3.11. (a) Nyquist plots measured under simulated sunlight irradiation with correspoding fitting curves of the bare SnS_2 and SnS_2-Pt nano-heterocomposites at a bias of 0.6 V (*vs* Ag/AgCl). (b) Proposed full equivalent circuit used for interpretation of SnS_2-Pt photoanode. Simplified equivalent circuit used for fitting impedance response of SnS_2 (c) without and (d) with Pt loading. (e) Corresponding bode plots measured under simulated sunlight irradiation of electrodes based on bare SnS_2 and SnS_2-Pt nanoheterostructures at a bias of 0.6 V (*vs* Ag/AgCl). (f) $R_{ct,bulk}$, $R_{ct,ss}/R_{ct,Pt}$ and C_{SS}/C_{Pt} values fit from impedance response of SnS_2 photoanode as a function of Pt loading. (g) Nyquist plots measured under dark/illumination with correspoding fitting curves of the SnS_2-Pt-2.9 nano-heterocomposites at a bias of 0.6 V (*vs* Ag/AgCl). (h) Mott–Schottky plots of SnS_2 NPLs and SnS_2-Pt-2.9 nanoheterostructures measured in the dark.

To further investigate the recombination behavior of photoinduced electron-hole pairs in bare SnS_2 and SnS_2-Pt-2.9 nanoheterostructures, PL spectra were measured. The PL measurements of bare SnS_2 and SnS_2-Pt-2.9 nanoheterostructure were carried out under the excitation wavelength of 390 nm. As shown in the PL spectra (Figure 3.12a), bare SnS_2 exhibited the radiative interband recombination peak at 543 nm, which was consistent with the SnS_2 band gap (2.25 eV, Figure 3.12b). In addition, an emission shoulder appeared at 455 nm, which we related to the radiative recombination of exciton absorption.[35] Compared with the PL intensity of bare SnS_2, a significantly decreased PL emission, especially for the emission from radiative interband recombination, was observed for SnS_2-Pt-2.9 nanoheterostructures. These results demonstrate that a reduced photogenerated hole-electron recombination existed in SnS_2 photoanodes, assigned to the facilitated charge separation by the introduction of Pt. The suppressed charge recombination in SnS_2 photoanode benefited achieving high photocurrent responses.

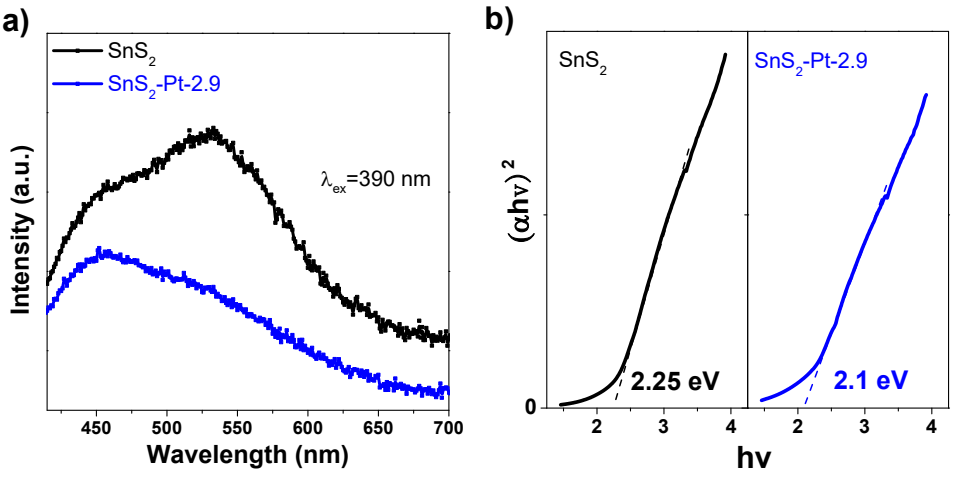

Figure 3.12. (a) Photoluminescence plots of SnS_2 NPLs and SnS_2-Pt-2.9 nanoheterostructures. (b) Bandgap of SnS_2 nanoplates and SnS_2-Pt nanoheterostructures extrapolated from the plot of $(\alpha h\nu)^2$ as a function of photon energy.

A simplified PEC water oxidation mechanism on SnS_2-Pt nanoheterostructures is summarized in Figure 3.13. As shown in Figure 3.13a, photogenerated electrons from SnS_2 NPLs are transferred to the FTO and from it to the Pt mesh for H_2 evolution. Photogenerated holes are injected from the SnS_2 NPLs to the OH^- groups through the Pt nanodomains. The flow direction of electrons and holes is schematized in the energy-band diagram in Figure 3.13b. We consider the SnS_2 conduction band minimum (CBM) of SnS_2 to be 0.1 V above the flat band potential (0.24 V vs NHE for SnS_2 as measured from M-S).[55] Therefore, the CBM of SnS_2 without external bias was around 0.14 V vs

NHE. Under a positive bias, the CB and VB shifted toward positive values, facilitating the photogenerated holes transfer to OH^- groups in solution through Pt domains. On the other hand, the photogenerated electrons transferred to the counter electrode (a Pt mesh) to reduce H^+ into H_2. A relatively fast separation of the photogenerated charge carriers reduced opportunity of charge recombination thus promoting performance in SnS_2-Pt nanoheterostructures compared with SnS_2 NPLs. Pt NPs played a significant role in electron-hole separation and facilitating charge transfer to the hydroxyl groups, thus resulting in a superior performance of SnS_2-Pt nanoheterostructures when compared with bare SnS_2. However, a clear deterioration of the performance was observed when larger Pt NPs were deposited. Overall, these results suggest that new strategies, capable of decoupling both particle size and coverage during the Pt deposition, would be essential to further enhance the performance of this system, targeting a narrow size distribution for the Pt NPs and a high coverage.

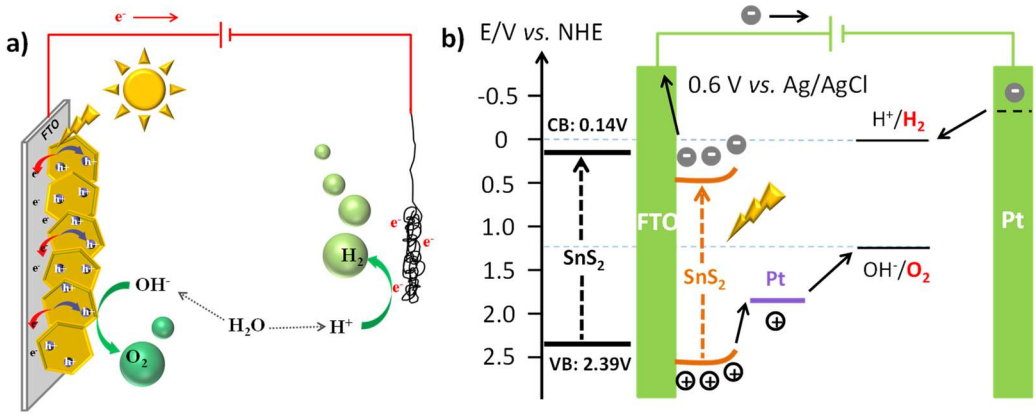

Figure 3.13. (a) Cartoon and (b) Energy band schematic diagram of SnS_2-Pt nanoheterostructures for water oxidation in a PEC cell.

3.5 Conclusions

In summary, ultrathin SnS_2 NPLs were produced via colloidal hot injection synthesis route, and the roles of surfactant OAm and OAc were investigated. Subsequently, metallic Pt was uniformly deposited on the surface via an *in-situ* reduction method. Such SnS_2-Pt nanoheterostructures showed significantly enhanced PEC current response under simulated sunlight compared to bare SnS_2 NPLs. The decreased performance observed for high Pt loadings appeared to be related to a deterioration of the charge transfer from the SnS_2 to the larger Pt NPs according to the PEIS data. The intimate contact between Pt NPs and SnS_2 NPLs was the key to obtain a useful semiconductor-noble metal synergetic effect through an efficient charge transfer of the photogenerated carriers from the semiconductor to the metal to promote solar energy conversion.

3.6 References

(1) Grätzel, M. Photoelectrochemical Cells. *Nature* **2001**, *414* (6861), 338–344.

(2) FUJISHIMA, A.; HONDA, K. Electrochemical Photolysis of Water at a Semiconductor Electrode. *Nature* **1972**, *238* (5358), 37–38.

(3) Wang, L.; Wang, W.; Chen, Y.; Yao, L.; Zhao, X.; Shi, H.; Cao, M.; Liang, Y. Heterogeneous P-N Junction CdS/Cu_2O Nanorod Arrays: Synthesis and Superior Visible-Light-Driven Photoelectrochemical Performance for Hydrogen Evolution. *ACS Appl. Mater. Interfaces* **2018**, *10* (14), 11652–11662.

(4) Fang, Z.; Hao, S.; Long, L.; Fang, H.; Qiang, T.; Song, Y. The Enhanced Photoelectrochemical Response of $SnSe_2$ Nanosheets. *CrystEngComm* **2014**, *16* (12), 2404–2410.

(5) Yu, J.; Xu, C.-Y.; Ma, F.-X.; Hu, S.-P.; Zhang, Y.-W.; Zhen, L. Monodisperse SnS_2 Nanosheets for High-Performance Photocatalytic Hydrogen Generation. *ACS Appl. Mater. Interfaces* **2014**, *6* (24), 22370–22377.

(6) Seo, J.; Jang, J.; Park, S.; Kim, C.; Park, B.; Cheon, J. Two-Dimensional SnS_2 Nanoplates with Extraordinary High Discharge Capacity for Lithium Ion Batteries. *Adv. Mater.* **2008**, *20* (22), 4269–4273.

(7) Jana, M. K.; Rajendra, H. B.; Bhattacharyya, A. J.; Biswas, K. Green Ionothermal Synthesis of Hierarchical Nanostructures of SnS_2 and Their Li-Ion Storage Properties. *CrystEngComm* **2014**, *16* (19), 3994.

(8) Zai, J.; Wang, K.; Su, Y.; Qian, X.; Chen, J. High Stability and Superior Rate Capability of Three-Dimensional Hierarchical SnS_2 Microspheres as Anode Material in Lithium Ion Batteries. *J. Power Sources* **2011**, *196* (7), 3650–3654.

(9) Ou, J. Z.; Ge, W.; Carey, B.; Daeneke, T.; Rotbart, A.; Shan, W.; Wang, Y.; Fu, Z.; Chrimes, A. F.; Wlodarski, W.; Wlodarski, W.; Russo, S. P.; Li, Y. X.; Kalantar-zadeh, K. Physisorption-Based Charge Transfer in Two-Dimensional SnS_2 for Selective and Reversible NO_2 Gas Sensing. *ACS Nano* **2015**, *9* (10), 10313–10323.

(10) Su, G.; Hadjiev, V. G.; Loya, P. E.; Zhang, J.; Lei, S.; Maharjan, S.; Dong, P.; M. Ajayan, P.; Lou, J.; Peng, H. Chemical Vapor Deposition of Thin Crystals of Layered Semiconductor SnS_2 for Fast Photodetection Application. *Nano Lett.* **2015**, *15* (1), 506–513.

(11) Liu, Y.; Geng, P.; Wang, J.; Yang, Z.; Lu, H.; Hai, J.; Lu, Z.; Fan, D.; Li, M. In-Situ Ion-Exchange Synthesis Ag_2S Modified SnS_2 Nanosheets toward Highly Photocurrent Response and Photocatalytic Activity. *J. Colloid Interface Sci.* **2018**, *512*, 784–791.

(12) An, X.; Yu, J. C.; Tang, J. Biomolecule-Assisted Fabrication of Copper Doped SnS_2 Nanosheet–reduced Graphene Oxide Junctions with Enhanced Visible-Light Photocatalytic Activity. *J. Mater. Chem. A* **2014**, *2* (4), 1000–1005.

(13) Wahnón, P.; Conesa, J. C.; Palacios, P.; Lucena, R.; Aguilera, I.; Seminovski, Y.; Fresno, F. V-Doped SnS_2: A New Intermediate Band Material for a Better Use of the Solar Spectrum. *Phys. Chem. Chem. Phys.* **2011**, *13* (45), 20401.

(14) Hu, K.; Wang, D.; Zhao, W.; Gu, Y.; Bu, K.; Pan, J.; Qin, P.; Zhang, X.; Huang, F. Intermediate Band Material of Titanium-Doped Tin Disulfide for Wide Spectrum Solar Absorption. *Inorg. Chem.* **2018**, *57* (7), 3956–3962.

(15) Zhang, Z.; Shao, C.; Li, X.; Sun, Y.; Zhang, M.; Mu, J.; Zhang, P.; Guo, Z.; Liu, Y. Hierarchical Assembly of Ultrathin Hexagonal SnS_2 Nanosheets onto Electrospun TiO_2 Nanofibers: Enhanced Photocatalytic Activity Based on Photoinduced Interfacial Charge Transfer. *Nanoscale* **2013**, *5* (2), 606–618.

(16) Christoforidis, K. C.; Sengele, A.; Keller, V.; Keller, N. Single-Step Synthesis of SnS_2 Nanosheet-Decorated TiO_2 Anatase Nanofibers as Efficient Photocatalysts for the Degradation of Gas-Phase Diethylsulfide. *ACS Appl. Mater. Interfaces* **2015**, *7* (34), 19324–19334.

(17) Zhang, Z.; Huang, J.; Zhang, M.; Yuan, Q.; Dong, B. Ultrathin Hexagonal SnS_2 Nanosheets Coupled with G-C_3N_4 Nanosheets as 2D/2D Heterojunction Photocatalysts toward High Photocatalytic Activity. *Appl. Catal. B Environ.* **2015**, *163*, 298–305.

(18) Zhang, Y. C.; Du, Z. N.; Li, K. W.; Zhang, M.; Dionysiou, D. D. High-Performance Visible-Light-Driven SnS_2 /SnO_2 Nanocomposite Photocatalyst Prepared via In Situ Hydrothermal Oxidation of SnS_2 Nanoparticles. *ACS Appl. Mater. Interfaces* **2011**, *3* (5), 1528–1537.

(19) Ahn, C. W.; Borse, P. H.; Kim, J. H.; Kim, J. Y.; Jang, J. S.; Cho, C.-R.; Yoon, J.-H.; Lee, B.; Bae, J.-S.; Kim, H. G.; Lee, J. S.. Effective Charge Separation in Site-Isolated Pt-Nanodot Deposited $PbTiO_3$ Nanotube Arrays for Enhanced Photoelectrochemical Water Splitting. *Appl. Catal. B Environ.* **2018**, *224*, 804–809.

(20) Yu, J.; Qi, L.; Jaroniec, M. Hydrogen Production by Photocatalytic Water Splitting over Pt/TiO_2 Nanosheets with Exposed (001) Facets. *J. Phys. Chem. C* **2010**, *114* (30), 13118–13125.

(21) Zhang, J.; Yu, Z.; Gao, Z.; Ge, H.; Zhao, S.; Chen, C.; Chen, S.; Tong, X.; Wang, M.; Zheng, Z.;Qin, Y. Porous TiO_2 Nanotubes with Spatially Separated Platinum and CoO_x Cocatalysts Produced by Atomic Layer Deposition for Photocatalytic Hydrogen Production. *Angew. Chem. Int. Ed.* **2017**, *56* (3), 816–820.

(22) Qu, Q.; Pan, G.-L.; Lin, Y.-T.; Xu, C.-W. Boosting the Electrocatalytic Performance of Pt, Pd and Au Embedded within Mesoporous Cobalt Oxide for Oxygen Evolution Reaction. *Int. J. Hydrogen Energy* **2018**, *43* (31), 14252–14264.

(23) Li, Z.; Shi, S.; Zhong, Q.; Zhang, C.; Xu, C. Pt-Mn_3O_4/C as Efficient Electrocatalyst for Oxygen Evolution Reaction in Water Electrolysis. *Electrochim. Acta* **2014**, *146*, 119–124.

(24) Warwick, M. E. A.; Barreca, D.; Bontempi, E.; Carraro, G.; Gasparotto, A.; Maccato, C.; Kaunisto, K.; Ruoko, T.-P.; Lemmetyinen, H.; Sada, C.; Gönüllü, Y.; Mathur, S. Pt-Functionalized Fe_2O_3 Photoanodes for Solar Water Splitting: The Role of Hematite Nano-Organization and the Platinum Redox State. *Phys. Chem. Chem. Phys.* **2015**, *17* (19), 12899–12907.

(25) Liu, G.; Qiu, Y.; Wang, Z.; Zhang, J.; Chen, X.; Dai, M.; Jia, D.; Zhou, Y.; Li, Z.; Hu, P. Efficiently Synergistic Hydrogen Evolution Realized by Trace Amount of Pt-Decorated Defect-Rich SnS_2 Nanosheets. *ACS Appl. Mater. Interfaces* **2017**, *9* (43), 37750–37759.

(26) Wei, R.; Hu, J.; Zhou, T.; Zhou, X.; Liu, J.; Li, J. Ultrathin SnS_2 Nanosheets with Exposed {0 0 1} Facets and Enhanced Photocatalytic Properties. *Acta Mater.* **2014**, *66*, 163–171.

(27) Zhou, M.; Lou, X. W. (David); Xie, Y. Two-Dimensional Nanosheets for Photoelectrochemical Water Splitting: Possibilities and Opportunities. *Nano Today* **2013**, *8* (6), 598–618.

(28) Li, M.; Liu, E.; Hu, H.; Ouyang, S.; Xu, H.; Wang, D. Surfactant-Free Synthesis of Single Crystalline SnS_2 and Effect of Surface Atomic Structure on the Photocatalytic Property. *Int. J. Photoenergy* **2014**, *2014*, 1–7.

(29) Feng, J.; Chen, J.; Geng, B.; Feng, H.; Li, H.; Yan, D.; Zhuo, R.; Cheng, S.; Wu, Z.; Yan, P. Two-Dimensional Hexagonal SnS_2 Nanoflakes: Fabrication, Characterization, and Growth Mechanism. *Appl. Phys. A* **2011**, *103* (2), 413–419.

(30) Yella, A.; Mugnaioli, E.; Panthöfer, M.; Therese, H. A.; Kolb, U.; Tremel, W. Bismuth-Catalyzed Growth of SnS_2 Nanotubes and Their Stability. *Angew. Chem. Int. Ed.* **2009**, *48* (35), 6426–6430.

(31) Ma, D.; Zhou, H.; Zhang, J.; Qian, Y. Controlled Synthesis and Possible Formation Mechanism of Leaf-Shaped SnS_2 Nanocrystals. *Mater. Chem. Phys.* **2008**, *111* (2–3), 391–395.

(32) Sun, Y.; Cheng, H.; Gao, S.; Sun, Z.; Liu, Q.; Liu, Q.; Lei, F.; Yao, T.; He, J.; Wei, S.;Xie, Y. Freestanding Tin Disulfide Single-Layers Realizing Efficient Visible-Light Water Splitting. *Angew. Chem. Int. Ed.* **2012**, *51* (35), 8727–8731.

(33) Fafarman, A. T.; Koh, W.; Diroll, B. T.; Kim, D. K.; Ko, D.-K.; Oh, S. J.; Ye, X.; Doan-Nguyen, V.; Crump, M. R.; Reifsnyder, D. C.; Christopher B. M.,; Cherie R. K.. Thiocyanate-Capped Nanocrystal Colloids: Vibrational Reporter of Surface Chemistry and Solution-Based Route to Enhanced Coupling in Nanocrystal Solids. *J. Am. Chem. Soc.* **2011**, *133* (39), 15753–15761.

(34) Zhang, Y.; Lu, J.; Shen, S.; Xu, H.; Wang, Q. Ultralarge Single Crystal SnS Rectangular Nanosheets. *Chem. Commun.* **2011**, *47* (18), 5226-5228.

(35) Du, Y.; Yin, Z.; Rui, X.; Zeng, Z.; Wu, X.-J.; Liu, J.; Zhu, Y.; Zhu, J.; Huang, X.; Yan, Q.; Zhang, H. A Facile, Relative Green, and Inexpensive Synthetic Approach toward Large-Scale Production of SnS_2 Nanoplates for High-Performance Lithium-Ion Batteries. *Nanoscale* **2013**, *5* (4), 1456-1459.

(36) Mishra, R. K.; Baek, G. W.; Kim, K.; Kwon, H.-I.; Jin, S. H. One-Step Solvothermal Synthesis of Carnation Flower-like SnS_2 as Superior Electrodes for Supercapacitor Applications. *Appl. Surf. Sci.* **2017**, *425*, 923–931.

(37) Davis, R. E.; Nakshbendi, H. F. Sulfur in Amine Solvents. *J. Am. Chem. Soc.* **1962**, *84* (11), 2085–2090.

(38) Lynch, M. An Investigation of Solutions of Sulfur in Oleylamine by Raman Spectroscopy and Their Relation to Lead Sulfide Quantum Dot Synthesis. *Undergrad. Honor. Theses* **2017**. https://scholar.colorado.edu/honr_theses/1389.

(39) Jia, Y.; Yang, Y.; Guo, Y.; Guo, W.; Qin, Q.; Yang, X.; Guo, Y. Simulated Sunlight Photocatalytic Degradation of Aqueous P-Nitrophenol and Bisphenol A in a Pt/BiOBr Film-Coated Quartz Fiber Photoreactor. *Dalt. Trans.* **2015**, *44* (20), 9439–9449.

(40) Serrano, D. P.; Calleja, G.; Pizarro, P.; Gálvez, P. Enhanced Photocatalytic Hydrogen Production by Improving the Pt Dispersion over Mesostructured TiO_2. *Int. J. Hydrogen Energy* **2014**, *39* (10), 4812–4819.

(41) Wang, Z.; Wang, H.; Liu, B.; Qiu, W.; Zhang, J.; Ran, S.; Huang, H.; Xu, J.; Han, H.; Chen, D.;Shen, G. Transferable and Flexible Nanorod-Assembled TiO_2 Cloths for Dye-Sensitized Solar Cells, Photodetectors, and Photocatalysts. *ACS Nano* **2011**, *5* (10), 8412–8419.

(42) Ye, H.; Park, H. S.; Akhavan, V. A.; Goodfellow, B. W.; Panthani, M. G.; Korgel, B. A.; Bard, A. J. Photoelectrochemical Characterization of $CuInSe_2$ and $Cu(In_{1-x}Ga_x)Se_2$ Thin Films for Solar Cells. *J. Phys. Chem. C* **2011**, *115* (1), 234–240.

(43) Hickey, S. G.; Waurisch, C.; Rellinghaus, B.; Eychmüller, A. Size and Shape Control of Colloidally Synthesized IV−VI Nanoparticulate Tin(II) Sulfide. *J. Am. Chem. Soc.* **2008**, *130* (45), 14978–14980.

(44) Meng, H.; Wang, T.; Yu, X.; Zhu, Y.; Zhang, Y. BiOCl/SnS_2 hollow Spheres for the Photocatalytic Degradation of Waste Water. *RSC Adv.* **2015**, *5* (129), 107088–107097.

(45) Liu, Y.; Chen, P.; Chen, Y.; Lu, H.; Wang, J.; Yang, Z.; Lu, Z.; Li, M.; Fang, L. In Situ Ion-Exchange Synthesis of SnS_2/g-C_3N_4 nanosheets Heterojunction for Enhancing Photocatalytic Activity. *RSC Adv.* **2016**, *6* (13), 10802–10809.

(46) Wang, L.; Jin, G.; Shi, Y.; Zhang, H.; Xie, H.; Yang, B.; Sun, H. Co-Catalyst-Free ZnS-SnS_2 porous Nanosheets for Clean and Recyclable Photocatalytic H_2 generation. *J. Alloys Compd.* **2018**, *753*, 60–67.

(47) Fu, Y.; Cao, F.; Wu, F.; Diao, Z.; Chen, J.; Shen, S.; Li, L. Phase-Modulated Band Alignment in CdS Nanorod/SnS_x Nanosheet Hierarchical Heterojunctions toward Efficient Water Splitting. *Adv. Funct. Mater.* **2018**, *28* (16), 1706785.

(48) Chen, H.; Lyu, M.; Zhang, M.; Feron, K.; Searles, D. J.; Dargusch, M.; Yao, X.; Wang, L. Switched Photocurrent on Tin Sulfide-Based Nanoplate Photoelectrodes. *ChemSusChem* **2017**, *10* (4), 670–674.

(49) Mu, J.; Miao, H.; Liu, E.; Feng, J.; Teng, F.; Zhang, D.; Kou, Y.; Jin, Y.; Fan, J.; Hu, X. Enhanced Light Trapping and High Charge Transmission Capacities of Novel Structures for Efficient Photoelectrochemical Water Splitting. *Nanoscale* **2018**, *10* (25), 11881–11893.

(50) Zhu, X.; Guijarro, N.; Liu, Y.; Schouwink, P.; Wells, R. A.; Le Formal, F.; Sun, S.; Gao, C.; Sivula, K. Spinel Structural Disorder Influences Solar-Water-Splitting Performance of $ZnFe_2O_4$ Nanorod Photoanodes. *Adv. Mater.* **2018**, *30* (34), 1801612.

(51) Klahr, B.; Gimenez, S.; Fabregat-Santiago, F.; Bisquert, J.; Hamann, T. W. Photoelectrochemical and Impedance Spectroscopic Investigation of Water Oxidation with "Co–Pi"-Coated Hematite Electrodes. *J. Am. Chem. Soc.* **2012**, *134* (40), 16693–16700.

(52) Klahr, B.; Gimenez, S.; Fabregat-Santiago, F.; Hamann, T.; Bisquert, J. Water Oxidation at Hematite Photoelectrodes: The Role of Surface States. *J. Am. Chem. Soc.* **2012**, *134* (9), 4294–4302.

(53) Liu, Y.; Le Formal, F.; Boudoire, F.; Yao, L.; Sivula, K.; Guijarro, N. Insights into the Interfacial Carrier Behaviour of Copper Ferrite ($CuFe_2O_4$) Photoanodes for Solar Water Oxidation. *J. Mater. Chem. A* **2019**, *7*, 1669-1677

(54) Dang, K.; Wang, T.; Li, C.; Zhang, J.; Liu, S.; Gong, J. Improved Oxygen Evolution Kinetics and Surface States Passivation of Ni-Bi Co-Catalyst for a Hematite Photoanode. *Engineering* **2017**, *3* (3), 285–289.

(55) Matsumoto, Y.; Omae, M.; Watnabe, I.; Sato, E. Photoelectrochemical Properties of the Zn-Ti-Fe Spinel Oxides. *J. Electrochem. Soc.* **1986**, *133* (4), 711.

Chapter 4

A SnS_2 Molecular Precursor for Conformal Nanostructured Coatings

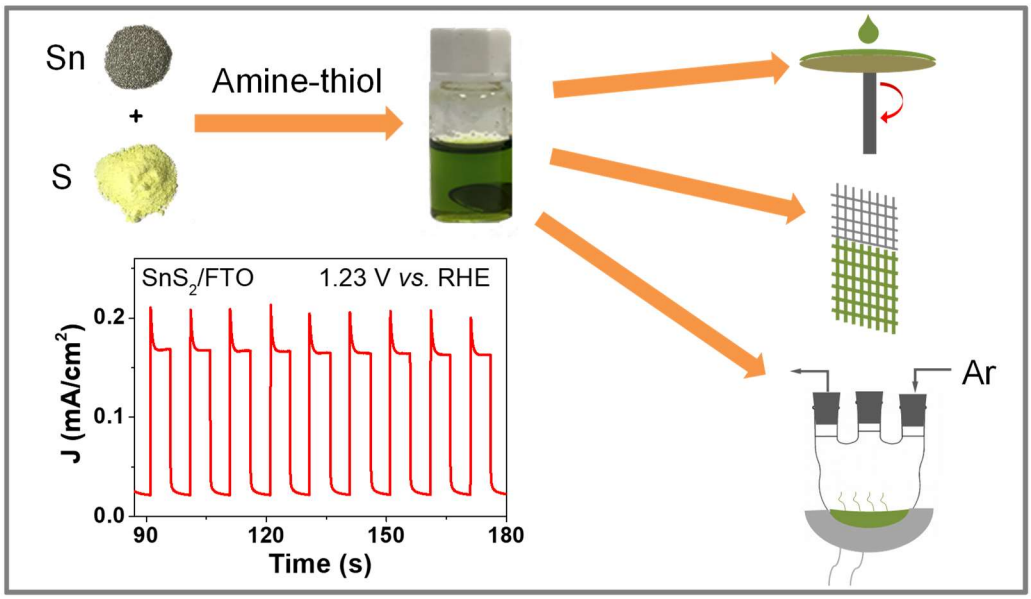

4.1 Abstract

We present a simple, versatile and scalable procedure to produce SnS_2 nanostructured layers based on an amine/thiol-based molecular ink. The ratios amine/thiol and Sn/S, and the reaction conditions are systematically investigated to produce phase-pure SnS_2 planar and conformal layers with a tremella-like SnS_2 morphology. Such nanostructured layers are characterized by excellent photocurrent densities. The same strategy can be used to produce SnS_2-graphene composites by simply introducing graphene oxide (GO) into the initial solution. Conveniently, the solvent mixture is able to simultaneously dissolve the Sn and Se powders and reduce the GO. Besides, $SnS_{2-x}Se_x$ ternary coatings and phase pure $SnSe_2$ can be easily produced by simply incorporating proper amounts of Se into the initial ink formulation. Finally, the potential of this precursor ink to produce gram scale amounts of unsupported SnS_2 is investigated.

4.2 Introduction

The production of planar and conformal nanostructured layers with high surface areas and porosity using simple, rapid, cost-effective and scalable processes that are neither energy nor labor intensive is a topic of major relevance.[1–3] Toward this goal, solution-based strategies based on the decomposition, assembly and/or deposition of salts, molecular precursors or colloidal nanoparticles offer obvious advantages over physical and chemical vacuum-based technologies.[4] However, the use of salts generally leads to the incorporation of large amounts of impurities in the final material and may result in inhomogeneous layer compositions. Besides, nanoparticle-based inks suffer from suspension stability and result in layers characterized by inadequate interphases with the support, with poor charge transfer and feeble mechanical stability, *i.e.* present delamination issues.[5–11] On the other hand, molecular precursors generally provide a homogeneous mixing of the precursor elements that ensures a uniform layer composition without impurities. Additionally, the crystallization of the material post deposition can considerably improve charge transfer/transport properties and layer adherence.[2]

In 2004, Mitzi and coworkers reported the use of hydrazine to produce a molecular ink from the dissolution of bulk SnS_2 and $SnSe_2$ in the presence of excess elemental chalcogen.[12] The process was facilitated by the *in-situ* reduction of the elemental chalcogen to produce chalcogenide anions that subsequently started a series of nucleophilic reactions with the bulk chalcogenide, breaking it down to eventually yield soluble molecular metal chalcogenide species.[12] The obtained molecular inks could then be spin-coated and thermally annealed at 350 °C to yield phase-pure $SnS_{2-x}Se_x$ thin films with high charge carrier mobility.[12] After this pioneer report, the hydrazine route was demonstrated effective in producing a plethora of chalcogenides, including $GeSe_2$,[13] $Cu_{1.9}S$,[14] In_2Se_3,[15] ZnTe,[16] In_2Te_3,[17] GeSbSe[18], $CuInSe_2$[19], and $CuInTe_2$[17]. The use of hydrazine finds advantages on its high reduction power, small size, volatility and on leaving no carbon residue. However, hydrazine is highly toxic and explosive, thus it is not convenient for scale-up and commercial applications.[20]

To avoid the disadvantages of hydrazine, the Brutchey group demonstrated a binary solvent mixture based on ethanedithiol (Edt) and ethylenediamine (En), named the ¨alkahest solvent¨, to dissolve and recover several V_2VI_3 chalcogenides, including As_2S_3, As_2Se_3, As_2Te_3, Sb_2S_3, Sb_2Se_3, Sb_2Te_3, Bi_2S_3, Bi_2Se_3 and Bi_2Te_3,[21] at room

temperature and ambient pressure, under air atmosphere and in just few minutes.[21,22] This amine-thiol solution system dissolves the bulk chalcogen through an amine-catalyzed reaction resulting in alkyl di-, tri-, and tetrachalcogens while -SR species bind to the metal ions.[20,21,23] Various combinations of mono- or dithiols with primary mono- and/or diamines, as well as different amine/thiol ratios have been used to dissolve a plethora of metal and chalcogen precursor materials[20,24,25]. As an example, Cu, Zn, Sn, and In are soluble in butylamine and Edt;[26] M_aX_n (M = Cu^+, Cu^{2+}, Zn^{2+}, Sn^{2+}, In^{3+}, Ga^{3+}; X = Cl^-, $acac^-$, OAc^-, O^{2-}) can be easily dissolved in a mixture of hexylamine and propanethiol; and M_bY_n (M = Cu^+, Cu^{2+}, Sn^{2+}, In^{3+}; Y = S^{2-}, Se^{2-}) are highly soluble in hexylamine and Edt.[27] In the amine-thiol system, the main difficulty to prepare a phase pure material is to find the proper amine and thiol mixture, their ratio and reaction conditions to crystallize the targeted product in the desired phase, preventing the formation of unwanted secondary phases.

SnS_2 is an indirect n-type semiconductor that is attracting significant interest as absorber material for solar energy conversion due to the abundance of its constituting elements and its excellent optoelectronic properties in part related to its layered structure. To prepare SnS_2 different methods have been put forward, including hydrothermal,[28–30] hot-injection,[31–33] heat-up,[34,35] exfoliation,[36–38] and chemical vapor deposition.[39–41] Sn has been also dissolved in 10/1 of En/Edt to recover SnS,[42] but the production of pure SnS_2 by this method has been so far elusive.

Herein, we present a simple route based on a molecular ink to produce phase pure SnS_2 from a Edt and En mixture. The ratio of Sn/S, En/Edt and the annealing process are investigated to define the optimal conditions to recover pure SnS_2 planar and conformal layers. We additionally study the production of ternary $SnS_{2-x}Se_x$ and phase pure $SnSe_2$, the one step production of composite of SnS_2/reduced graphene oxide (SnS_2/rGO) composites and the photocatalytic properties of the produced layers.

4.3 Experimental Section

4.3.1 Chemicals

All chemicals were used as received, without additional purification. Sn powder (99+ %), S powder (99.98 %), En (99.5+ %), Edt (98+ %) were purchased from Sigma-Aldrich. Se

powder (99.5+ %) was purchased from Acros Organics. All chemical manipulation and material preparation processes were carried out in an argon-filled glove box.

4.3.2 Ink Preparation

Tin and sulfur elemental powders, other than their salts, were selected as solutes to avoid any potential counterion contamination. To prepare a Sn-S molecular ink, elemental Sn (0.5 mmol) and S (1.5 mmol) powders were weighted and transferred into a glass vial (4 mL). En (2 mL) and Edt (0.1 mL) were sequentially added into the vial. The mixture was then stirred at 750 rpm and heated to 70 °C and kept at this temperature for 30 min to get an optical transparent green ink solution. To study the influence of ratio between En and Edt, different amount of Edt was used, while En amount kept unchanged. To study the influence of sulfur amount, we used different amount of sulfur.

4.3.3 Recovery of Semiconductor Film on Planar Glass Slides

Typically, 0.1 mL of molecular ink was drop casted on a microscope glass slide (~1×1 cm^2), and then the deposited substrate was heated on a hot plate (Corning, PC400D) at 200 °C to dry the ink. The dried precursor film was afterward annealed at 320 °C on the hotplate for 30 min. These operations were conducted in the argon-filled glovebox. The obtained film was scraped off of the substrate for posterior characterization by XRD, SEM and HRTEM.

4.3.4 Recovery of Semiconductor Film on FTO-coated Glass Slides

20 μL of molecular ink was drop casted on the surface of FTO with an active area of 1cm×1cm (an additional area of 1cm×1cm was covered by the high-temperature bearable tape to leave a clean area for electrical connection). The tip of the pipette-pipe was used to pull the solution in order to produce a uniform coverage (in this operation, the tip shouldn't touch the FTO surface), after then dried at 200 °C and finally annealed on the hot plate at 320 °C for 30 min.

4.3.5 Recovery of Semiconductor Film on Stainless Steel and Carbon Cloth

Typically, a piece of pre-cleaned stainless steel (SS) was firstly heated on the hot plate at 200 °C for several minutes, then quickly immerse into molecular ink and hold for 30 s. The wet SS was then held by a tweezer and put close to the surface of the hot plate to dry, after then annealed in Ar filled tubular furnace at 320 °C for 30 min with a temperature

ramp of 3 °C/min. SS was preheated to decrease the local viscosity of the molecular ink close to the SS surface, and thus facilitate it diffusion through the porous electrode structure. The heated support also promoted the film drying and facilitated the formation of more uniform coatings.

To coat carbon cloth (CC) with a SnS_2 layer, 40 μL of molecular ink was evenly drop casted on two sides of a 1x1 cm^2 CC using the tip of the pipette to spread the precursor solution and then put close to the surface of the hot plate to dry, subsequently annealed in Ar filled tubular furnace at 320 °C for 30 min with a temperature ramp of 3 °C/min.

4.3.6 Recovery of SnS_2/rGO Composites

GO was produced by the Hummers method as originally presented by Kovtyukhova.[62] In the next step, 10 mg of GO was added together with Sn powder and S powder to formulate the Sn-S molecular ink. The same ratios of Sn/S and En/Edt and dissolution and annealing times and temperatures as used in conventional inks were used to recover SnS_2/rGO composite layers.

4.3.7 Recovery of $SnS_{2-x}Se_x$

A proper amount of elemental Se powder was introduced in the initial mixture in replacement of the same molar amount of S powder. The dissolution time was adjusted to make sure that all the precursor powders were dissolved and an optical transparent molecular solution was obtained. Dissolution time was typically 30 min for SnS_2 and increased up to 80 min with Se amount increasing. Dissolution temperature was set at 70 ºC in all cases. The same drying and annealing steps used to recover pure-phase SnS_2 were used to recover $SnS_{2-x}Se_x$, except that the annealing time was increase to 60 min.

To coat $SnS_{2-x}Se_x$ on FTO for posterior PEC measurements, we noticed that the recovered $SnS_{2-x}Se_x$, especially $SnSe_2$, using the same spin coating method as we did on SnS_2/FTO showed almost no i-t response. We attributed this result to the $SnSe_2$ layer being too thick. Notice $SnSe_2$ has a much lower band gap and thus absorbs light much more strongly, thus thinner layers are required. Too thick layers prevent light from arriving to the semiconductor-electrode interphase and decrease performance. We thus used the spin coating method to produce thinner layers, and kept all the deposition process the same to make the results comparable.

4.3.8 Recovery of Large-scaled Powder

5 mL of Sn-S molecular ink was injected into a 50 mL three-neck flask preheated 300 °C and containing an Ar atmosphere. A safety flask containing water/ethanol was used to collect the gas/vapor emanated from the ink solution. Upon ink injection, temperature decreased to ~200 °C and then increased slowly to 300 °C. The flask was kept at this temperature for additional 10 min to obtain a dry powder. The powder was then grinded and annealed in tubular furnace under Ar atmosphere at 350 °C for 2 hours with a ramp rate of 3 °C/min or lower. The annealed powder was washed using CS_2 and ethanol by sonication to remove the potential sulfur residues. The sample was finally dried for posterior characterizations and use. It should be noted that we injected the precursor solution very fast in order to make the heating process more uniform and synthesis more repeatable, and thus minimizing the difference among different batches.

4.3.9 Sample Characterization

XRD patterns were obtained on a Bruker AXS D8 ADVANCE X-ray diffractometer (Bruker, Karlsruhe, Germany) operating at 40 kV and 40 mA with Ni-filtered (2 μm thickness) Cu Kα1 radiation (λ = 1.5406 Å). TEM characterization was carried out on a ZEISS LIBRA 120 (Carl Zeiss, Jena, Germany), operating at 120 kV. HRTEM images were obtained using a field emission gun FEI Tecnai F20 microscope at 200 kV with a point-to-point resolution of 0.19 nm. For TEM characterization, samples were prepared by peeling off directly from glass slide and drop casting their ethanol solutions onto a 200 mesh copper grid. SEM analysis was done in a ZEISS Auriga microscope (Carl Zeiss, Jena, Germany) with an EDX detector at 20 kV to study composition. XPS was carried out on a SPECS system (SPECS GmbH, Berlin, Germany) equipped with an Al anode XR50 source operating at 150 W and a Phoibos 150 MCD-9 detector (SPECS GmbH, Berlin, Germany). The pressure in the analysis chamber was kept below 10^{-7} Pa. Data processing was performed with the CasaXPS program (Casa Software Ltd., UK). Binding energy (BE) values were centered by using the C 1s peak at 284.8 eV. TG analysis was carried out using a PerkinElmer Diamond TG/DTA instrument (PerkinElmer, Walthham, MA, USA). For TG analysis, a proper amount of molecular ink was dried on a glass slide at 200 °C and scratched out after cooling down and ~20 mg of the dried gel powder was collected and loaded into a ceramic pan. Measurements were carried out in an Ar atmosphere from room temperature to 700 °C at a heating rate of 5 °C/min. FTIR was

performed on an Alpha Bruker FTIR spectrometer with a platinum attenuated total reflectance (ATR) single reflection module. FTIR data were typically averaged over 24 scans. UV-vis absorption spectra were acquired with a PerkinElmer LAMBDA 950 UV-vis spectrophotometer equipped with an integrating sphere. For FTIR and UV-vis analysis, films were produced by spin coating on glass substrates instead of drop-casting.

4.3.10 Photoelectrochemical Measurements

PEC characterization was performed in a three-electrode system using an electrochemical workstation (Metrohm Autolab). A Pt mesh (2 cm^2 surface area) and Ag/AgCl (3.3 M KCl) were used as the counter and reference electrodes, respectively. $SnS_{2-x}Se_x$ films deposited on FTO were used as working electrode. Before film deposition, the FTO glass was washed with acetone-isopropanol (1-1 volume), ethanol, and then deionized water. An aqueous solution of Na_2SO_4 (0.5 M, pH = 7) was used as the electrolyte. Relatively thick SnS_2 films deposited by drop casting were used to test the SnS_2 PEC performance. On the other hand, thinner films produced by spin coating were used to the $SnSe_2$ performance owing to the higher light absorption capability of this material associated to its lower band gap. The electrolyte was purged with Ar for 30 min prior to the measurement. The incident light source was provided by 8 radially distributed 35 W xenon lamps, providing a total irradiance power on the sample of ca. 100 mW/cm^2. The following formula was used to convert the potentials to the RHE standard scale:

$$E \textit{ vs. } RHE = E_{Ag/AgCl} + E^{o}_{Ag/AgCl} + 0.059 \times pH = E_{Ag/AgCl} + 0.623 \text{ (V)}$$

4.4 Results and Discussion

In our first attempts to produce SnS_2, stoichiometric molar amounts of sulfur and tin powders (Sn/S=1/2) were dissolved in a volume ratio En/Edt=10/1 at 70 ºC for 1h to obtain an optically clear pale yellow solution. The precursor ink was coated onto a glass substrate and the obtained film was annealed at 320 °C for 30 min. Upon annealing, the layer turned grey yellow. Scanning electron microscope (SEM) characterization showed the layer to contain a large density of quasi-spherical flower-like structures (Figure 4.1a), but powder X-ray diffraction (XRD) analysis identified the main crystal phase of the obtained material as SnS (Figure 4.1b), with only a minor amount of SnS_2 (Figure 4.1b).

The precursor solution was modified by incorporating an additional amount of sulfur (Sn/S=1/3) to correct for the low quantity of this element in the final layer. This precursor

solution displayed a much more intense yellow color (Figure 4.1c). XRD analyses of the layers produced from the coating and posterior annealing of this precursor ink showed a notable increase of the amount of SnS_2, but SnS impurity peaks were still evident. Besides, the structure of the obtained film changed from the quasi-spherical flowers to tremella-like particles (Figure 4.1d). Similar results were obtained when instead of increasing the amount of sulfur, we decreased the concentration of Edt in the initial solution (Sn/S=1/2; En/Edt=20/1). This precursor solution decomposed into tremella-like structures with a main SnS_2 phase and a residual SnS component (Figure 4.1b,e).

To further adjust the stoichiometry and crystal phase of the final layer, we simultaneously increased the amount of sulfur (Sn/S=1/3) and reduced the amount of Edt (En/Edt=20/1). Using this new precursor solution (Sn/S=1/3, En/Edt=20/1), which displayed a green color (Figure 4.1c), phase-pure tremella-like SnS_2 could be finally recovered (Figure 4.1b,f). Energy dispersive X-ray spectroscopy (EDX) analysis further confirmed the composition of the obtained layer to be consistent with stoichiometric SnS_2 (Table 4.1).

Generally, lower amounts of Edt favored the formation of the SnS_2 phase over SnS. Pure SnS_2 could be obtained with Edt contents of En/Edt=20/1 or lower when using an excess of S, Sn/S≤1/3 (Figures 4.2a and 4.3). However, without Edt, the Sn and S powder mixture could not be fully dissolved (Figure 4.2b, 4.3) and no SnS_2 could be recovered. On the amine side, replacing En by hexylamine or butylamine did not allow the dissolution of proper amounts of Sn and S (Figure 4.4).

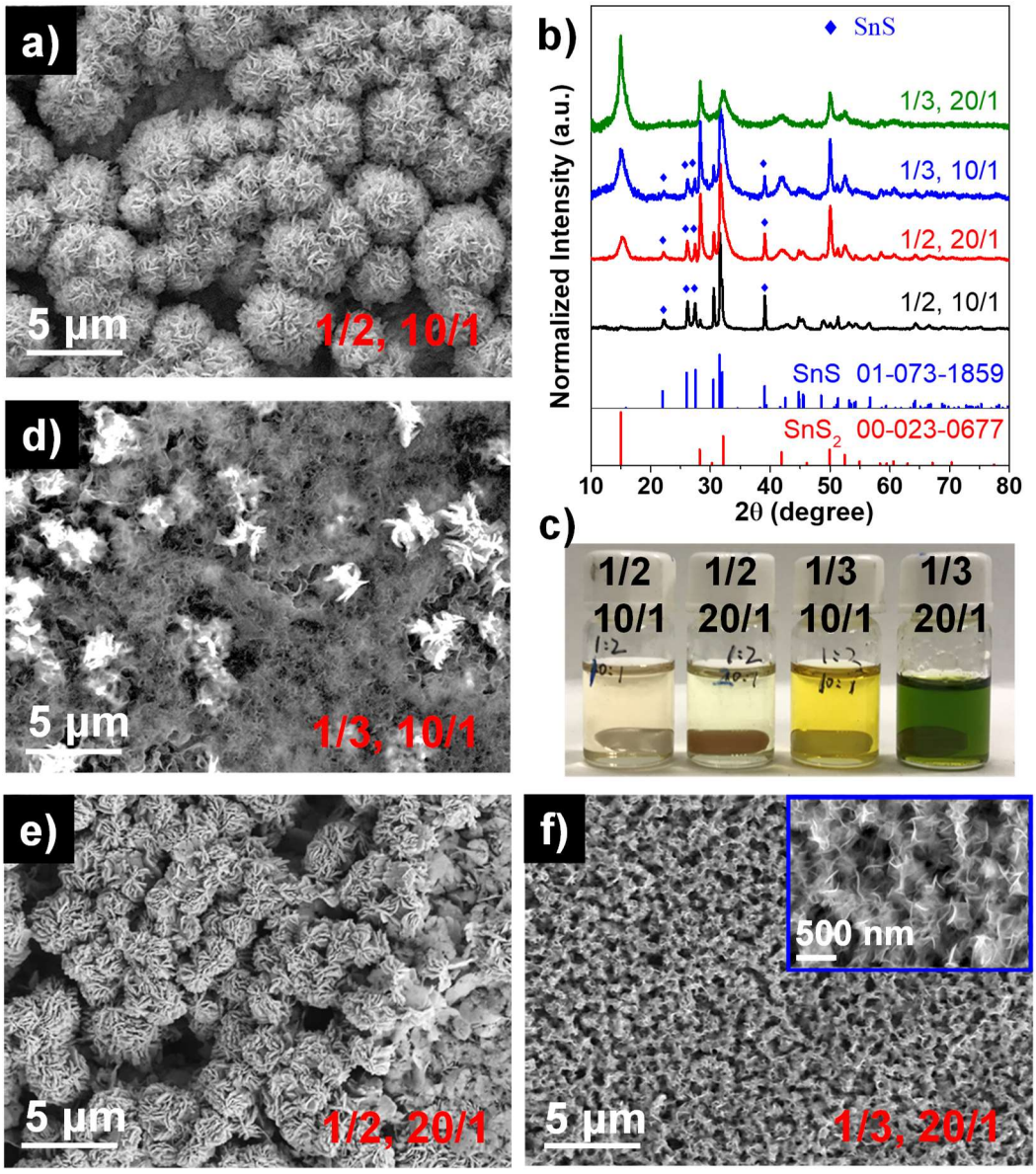

Figure 4.1. (a) SEM micrograph of the material recovered after annealing a layer produced from an ink containing a molar ratio Sn/S=1/2 and a volume ratio En/Edt=10/1. (b) XRD patterns of materials obtained after annealing layers produced from inks containing different Sn/S (1/2 or 1/3) and En/Edt ratios (10/1 or 20/1), as specified. (c) Optical photographs of molecular inks obtained by dissolving different Sn/S (1/2 or 1/3) and En/Edt ratios (10/1 or 20/1), as specified. (d-f) SEM micrographs of materials obtained after annealing layers produced from different Sn/S (1/2 or 1/3) and En/Edt ratios (10/1 or 20/1), as specified. Inks were formulated by dissolving the proper Sn and S ratios in En/Edt mixtures at 70 ºC for 1 h. Annealing conditions: 320 ºC, 30 min.

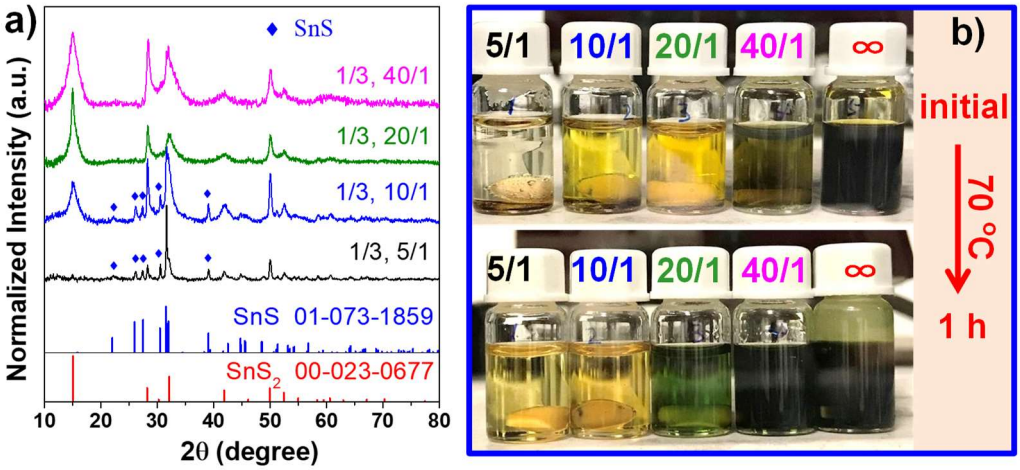

Figure 4.2. (a) XRD patterns of sample recovered after annealing layers produced from inks containing different ratios En/Edt (from 5/1 to 40/1), as specified (b) Optical photographs of SnS_2 molecular inks prepared with different ratios En/Edt (from 5/1 to 40/1) before and after heating at 70 °C for 1 h, as specified. Ink formulation parameters: Sn/S=1/3, 70 ºC, 1 h. Annealing conditions: 320 ºC, 30 min.

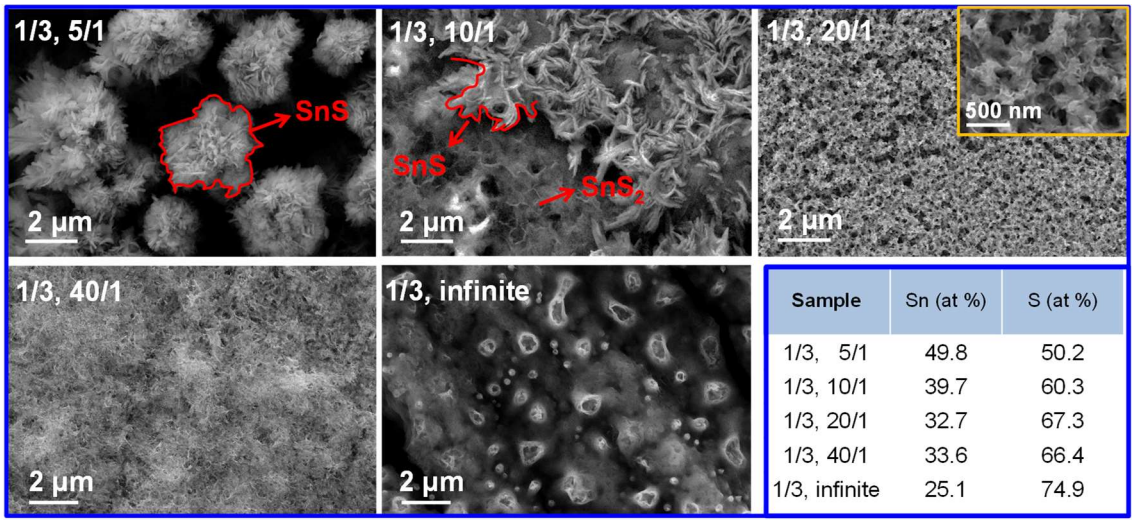

Sample	Sn (at %)	S (at %)
1/3, 5/1	49.8	50.2
1/3, 10/1	39.7	60.3
1/3, 20/1	32.7	67.3
1/3, 40/1	33.6	66.4
1/3, infinite	25.1	74.9

Figure 4.3. SEM images and large-area EDX data of samples recovered from molecular inks with different volume ratio of En/Edt, from 5/1 to infinite. Ink synthesis parameters: Sn/S=1/3, 70 ºC, 1h.

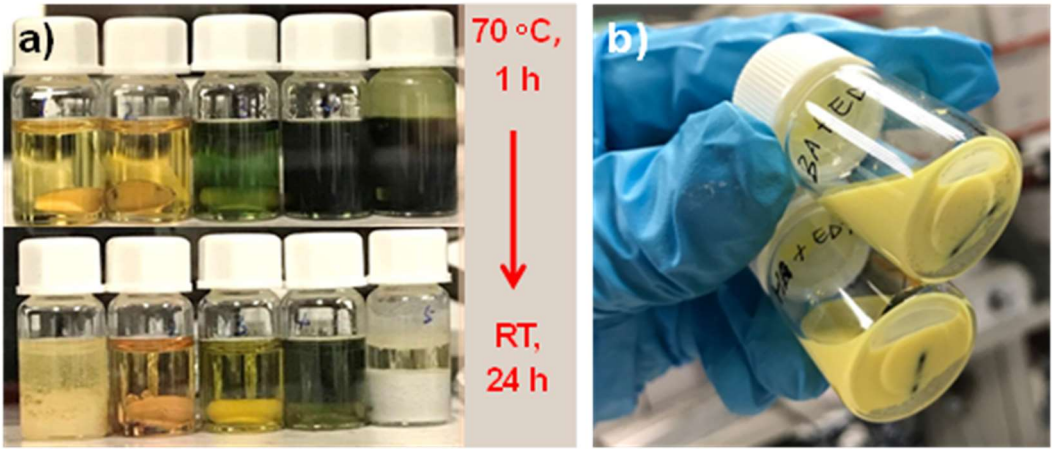

Figure 4.4. (a) Optical photographs of SnS_2 molecular inks formulated using different En/Edt volume ratios and cooled down to RT after 24 h at 70 ºC. (b) Ink obtained using butylamine and hexylamine instead of En. Ink synthesis parameters: Sn/S=1/3, 70 ºC, 1h.

Table 4.1. Large-area EDX composition of samples recovered from molecular inks with different volume ratios of Sn/S and En/Edt. Ink formulation parameters: 70 ºC, 1h.

Sample	Sn (at %)	S (at %)
1/2, 10/1	48.8	51.3
1/2, 20/1	45.9	54.1
1/3, 10/1	43.7	56.3
1/3, 20/1	32.8	67.2

Table 4.2. XRD crystal phases obtained from inks prepared by different solvent mixtures and different dissolution times. Ink formulation parameters: Sn/S=1/3, 70ºC, 1h.

Sample	Dissolution time @ 70 ºC	XRD phase
1/3, 5/1	~ 5 min	SnS
1/3, 10/1	~ 12 min	SnS+SnS_2
1/3, 20/1	~ 20 min	SnS_2
1/3, 40/1	~ 80 min	SnS_2

The higher the Edt concentration, the lower the time required to obtain an optically clear ink (Table 4.2). When using dissolution times in the range between 20 min and 1 h, no major effect was observed on the phase and structure of the produced material. However, when increasing the dissolution time, the SnS phase appeared even when using

the previously defined as proper precursor compositions: Sn/S=1/3, En/Edt=20/1 (Figure 4.5a). EDX analysis further confirmed the Sn/S ratio of the annealed material to increase with the time of preparation of the precursor solution (Table 4.3). Additionally, the color of the ink also faded with the dissolution time (Figure 4.5b). Besides, the morphology of the final material turned toward sunflower-like structures when dissolution time increased to 3 h and above (Figure 4.6). We hypothesize that all these observations were associated with a sulfur loss during ink formulation. This loss was in the form of H_2S that was produced by the reaction of elemental sulfur with amine,[43,44] To prove this hypothesis, we added an additional amount (0.5 mmol) of sulfur powder into a SnS_2 molecular ink after 6 h at 70 ºC. This ink was mixed for additional 30 min to dissolve the added sulfur. After this time, the intense green color was recovered, and pure SnS_2 phase with a tremella morphology was obtained after annealing (Figure 4.7).

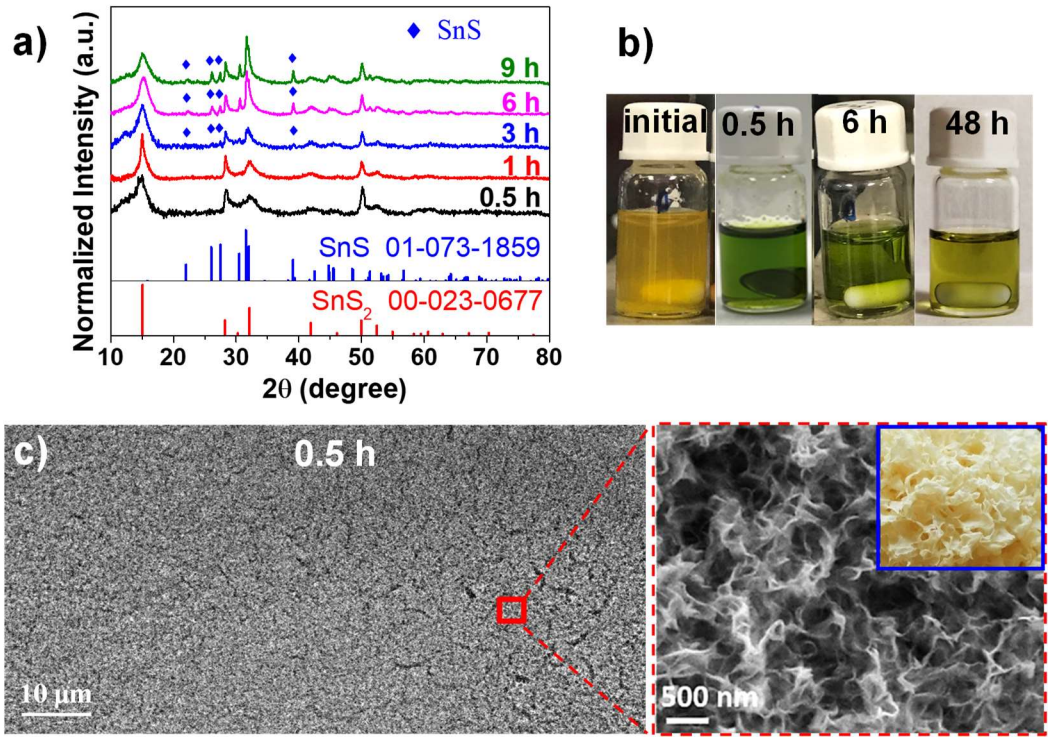

Figure 4.5. (a) XRD patterns of samples recovered after annealing the layers obtained from molecular inks prepared after different dissolution times from 0.5 h to 9 h, as noted; (b) Optical photos of respective molecular inks before and after heating at 70 °C for varied range of times. Ink composition and dissolution temperature: Sn/S=1/3, En/Edt=20/1, 70 ºC. (c) Large area SEM micrograph and higher magnification image of sample recovered from the annealing of a layer produced from a standard ink: Sn/S=1/3, En/Edt=20/1, 70 ºC, 0.5 h dissolution time. Inset shows optical photograph of the tremella fungus.

Table 4.3. Large-area EDX composition of sample recovered from molecular inks prepared at different dissolution times, from 0.5 h to 6 h. Ink formulation parameters: Sn/S=1/3, En/Edt=20/1, 70 ºC.

Sample	Sn (at %)	S (at %)
0.5 h	32.6	67.4
1 h	32.6	67.4
3 h	38.9	61.1
6 h	39.1	60.9

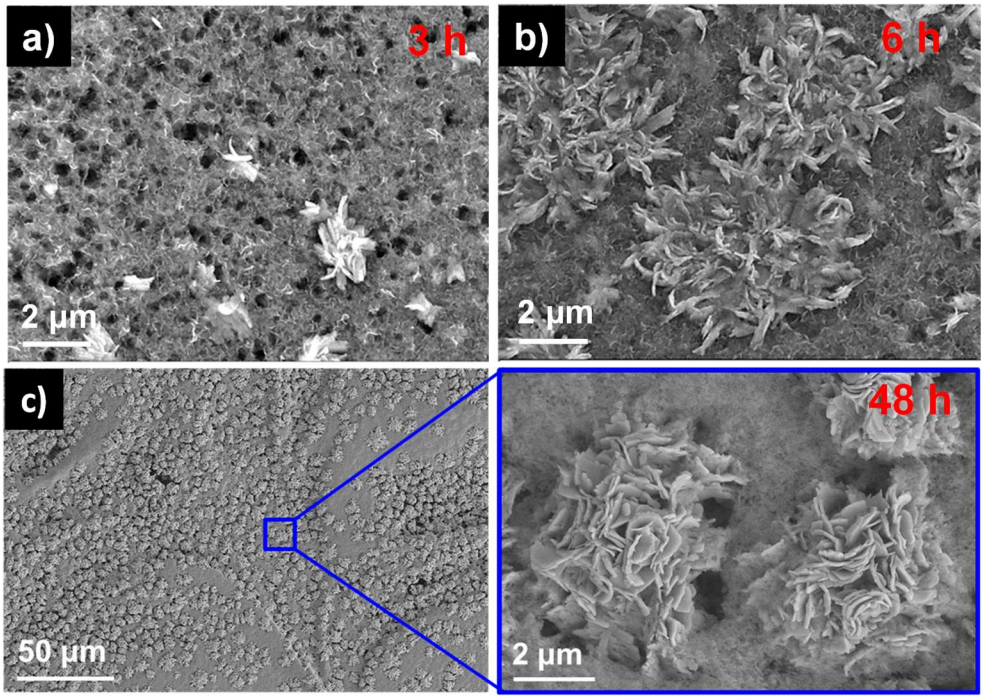

Figure 4.6. (a-c) SEM images of sample recovered from molecular inks prepared using different dissolution times, from 3 h to 48 h. Ink synthesis parameters: Sn/S=1/3, En/Edt=20/1, 70 ºC.

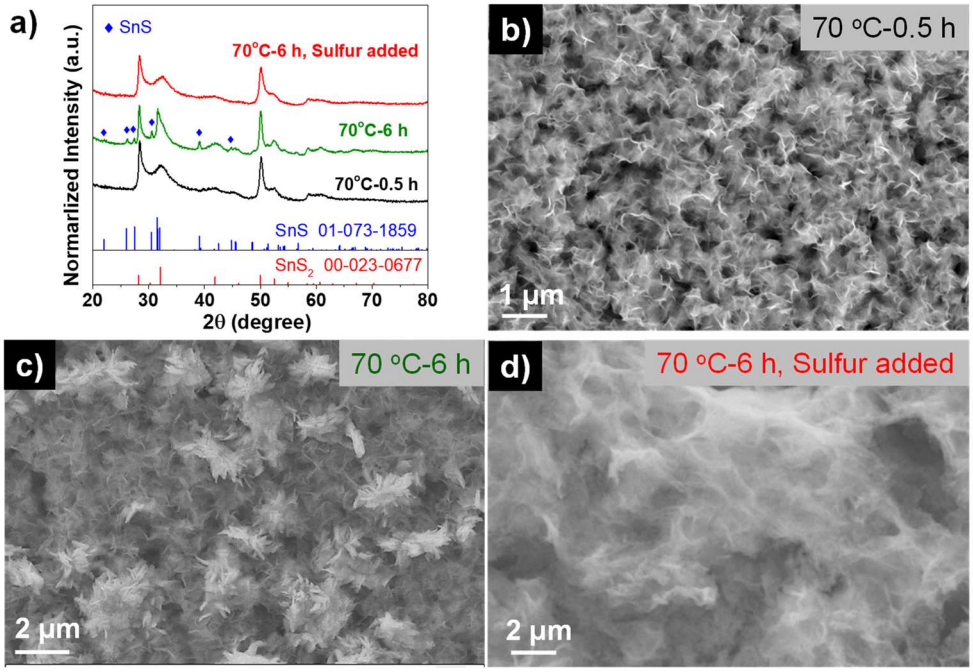

Figure 4.7. (a) XRD patterns and (b-d) SEM images of sample recovered from molecular inks before/after adding additional sulfur powder at 70 ºC, 6 h. Ink synthesis parameters: Sn/S=1/3, En/Edt=20/1.

When applying no heat, a suitable ink could be prepared by dissolving proper amounts of Sn and S (Sn/S=1/3) in En/Edt=20/1 at ambient temperature for 6 h. In this condition, no significant loss of sulfur was detected and pure SnS_2 could be recovered after annealing (Figure 4.8). Overall, to optimize time and ensure a proper product phase with tremella like morphology (Figure 4.5a,c), we fixed the ink preparation time at 30 min, dissolution temperature at 70 ºC, the element ratio at Sn/S=1/3 and the solvent ratio at En/Edt=20/1.

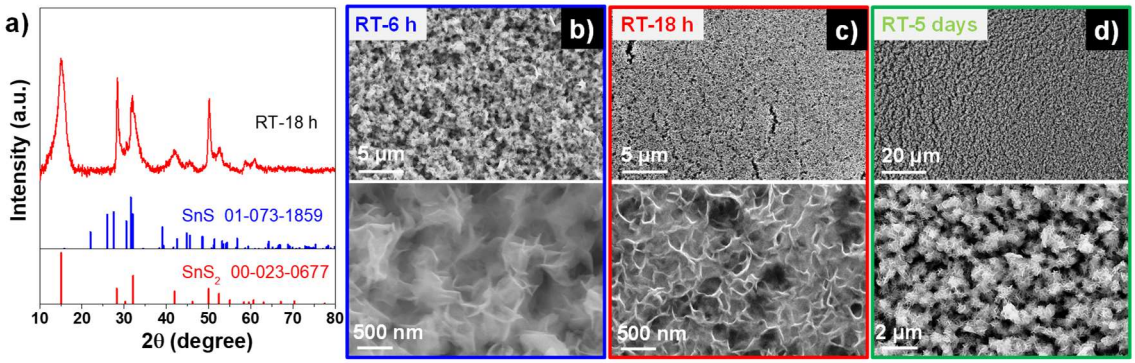

Figure 4.8. (a) XRD pattern and (b-d) SEM images of samples recovered from molecular inks obtained at room temperature after different dissolution times. Ink synthesis parameters: Sn/S=1/3, En/Edt=20/1.

Thermogravimetric (TG) analysis of the yellowish gel-like paste collected after drying the conventional ink at 200 ºC (Figure 4.9a) displayed a two-step mass loss in the temperature range 200-300 ºC. These steps were associated with the ink decomposition and overall accounted for ca. 65 wt% of the initial mass. At temperatures above 500 ºC an additional mass loss, associated with the sulfur evaporation, was observed. Fourier transform infrared spectroscopy (FTIR, Figure 4.9b) corroborated the loss of organics after annealing the material at 320 ºC for 30 min, as evidenced by the complete loss of strong ν(N-H)/ν(O-H) and ν(C-H) stretching bands originating from the solvent mixture. The absence of bands corresponding to the ν(S-H) thiol group at 2560 cm^{-1} implies that Edt is fully deprotonated by En.[42]

EDX elemental mapping of the films obtained from the deposition and annealing of the conventional ink showed a uniform distribution of S and Sn (Figure 4.10a). High-resolution transmission electron microscopy (HRTEM) micrographs confirmed the SnS_2 hexagonal phase (space group = P63mc) with a=b=3.6450 Å, c=11.8020 Å (Figure 4.9d, 4.10b). HRTEM analysis reported in Figure 4.9d shows the overlapping of two 2 different [0001]-oriented nanosheets. The power spectrum (Fast Fourier Transform) applied to the HRTEM image with the applied reciprocal space frequency (structural) filtering showed the presence of a 21º rotation between the overlapping nanosheets (Figure 4.9d). These results confirmed the pileup of different nanosheets, consistently with SEM results. UV-vis analysis of recovered SnS_2 films (Figure 4.9c) showed their bandgap to be around 2.5 eV, which is consistent with the relatively wide range of optical bandgaps reported for SnS_2.[41,45] The small deviation on the experimental band gap values measured here with respect to theoretical SnS_2 values can be ascribed to the reduced thickness of the produced SnS_2 layer (Figure 4.1f, 4.9c and 4.9d), consistently with previous report.[46]

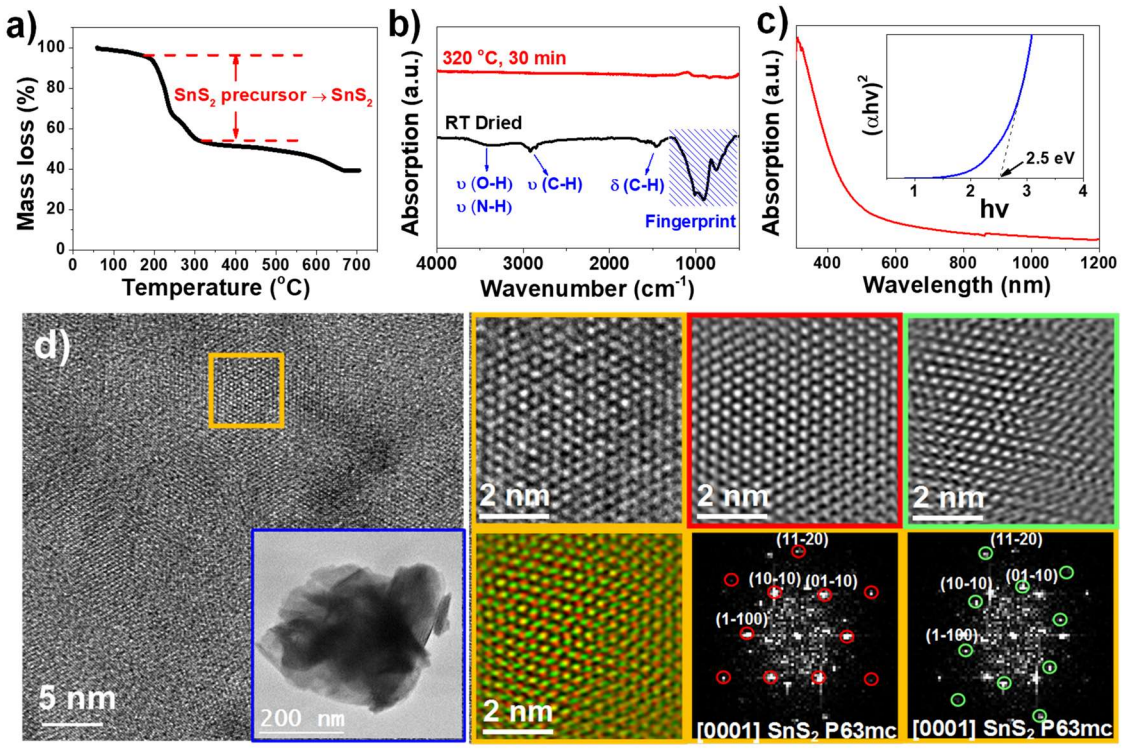

Figure 4.9. SnS_2 recovered from a conventional molecular ink: (a) TG profile of a SnS_2 molecular ink after drying at 200 ºC. (b) FTIR spectra of a SnS_2 molecular ink dried at room temperature and of the material recovered after annealing at 320 ºC for 30 min. (c) UV-Vis spectrum of the material recovered after annealing at 320 ºC for 30 min. (d) HRTEM micrograph of the material recovered after annealing at 320 ºC for 30 min, detail of the orange squared region and its corresponding power spectrum. From the analyzed crystalline domain, the SnS_2 lattice fringe distances were measured to be 0.316 nm, 0.314 nm, 0.310 and 0.181 nm, at 62.65, 123.67 and 94.00º, which could be interpreted as the hexagonal SnS_2 phase, visualized along its [0001] zone axis. Green and yellow squared images correspond to the reciprocal space frequency filtered reconstructed images corresponding to each individual overlapping nanosheet, as extracted from the orange squared region. The spots used in the frequency reconstruction have been circled in red and green, respectively, in the power spectra provided below.

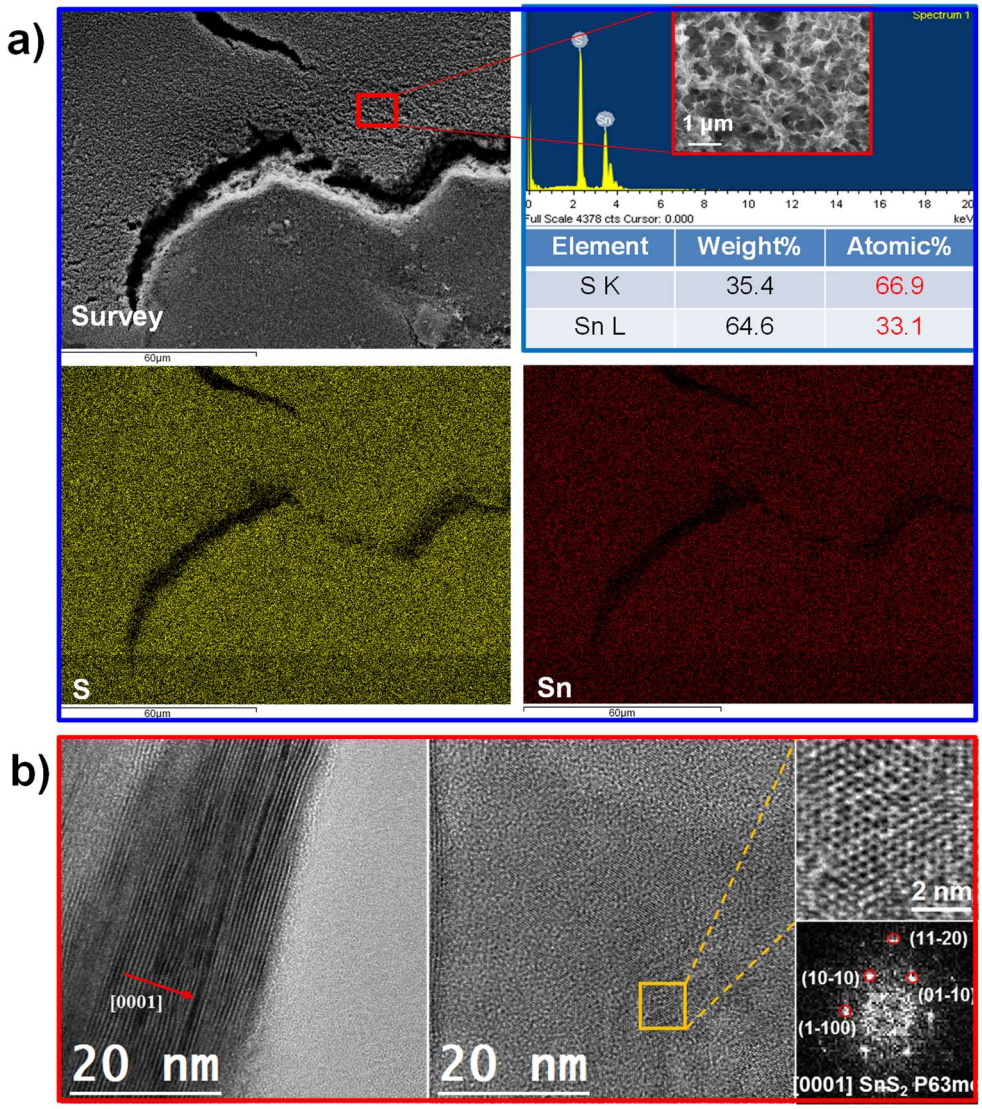

Figure 4.10. (a) SEM-EDX mapping and (b) HRTEM micrograph of a SnS_2 layer recovered from the conventional molecular ink. Ink synthesis parameters: Sn/S=1/3, En/Edt=20/1, 70 ºC, 0.5 h.

To study the photocatalytic properties of SnS_2 tremella layers obtained from the molecular ink, the ink was deposited on fluorine doped tin oxide (FTO)-coated glass substrates by drop casting. The annealed layer was used as anode in a photoelectrochemical (PEC) cell for water splitting. XRD and SEM analysis confirmed the phase and structure of the SnS_2 to be maintained when depositing the ink over FTO instead of glass (Figure 4.11a-d). Using these SnS_2 layers, current densities reaching up to ~160 µA/cm^2 (1.23 V *vs.* RHE) were measured (Figure 4.11e,f). This performance was well above that of previously reported bare SnS_2 photoanodes,[47] and even better than some SnS_2 samples incorporating co-catalysts.[48–52] We ascribed this excellent photocurrents to: 1) the tremella morphology that provided a larger interface area with

the electrolyte and effective paths for the solution diffusion; 2) the intimate contact of the SnS_2 absorber with the FTO current collector, thus decreasing the interphase electrical resistance and facilitating the transfer of photogenerated charges from the SnS_2 photocatalyst films to the FTO.

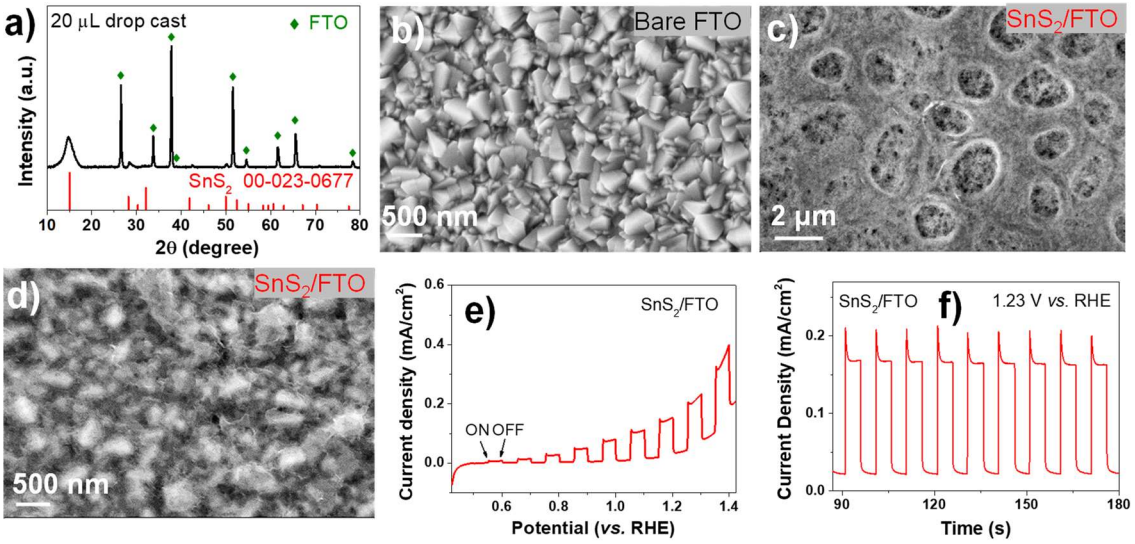

Figure 4.11. SnS_2 film recovered on FTO from a conventional molecular ink. (a) XRD pattern; (b) SEM image of bare FTO. (c-d) SEM images of recovered tremella-like SnS_2/FTO by drop casting. (e) Linear sweep voltammogram and (f) amperometric i-t curve at 1.23 V vs RHE of a SnS_2/FTO sample under chopped illumination. RHE: reversible hydrogen electrode.

We further investigated the conformal coating of SnS_2 on different substrates. As an example, stainless steel (SS) meshes were coated through a quick immersion of the preheated support on the molecular ink and the posterior drying and annealing of the obtained film (see experimental section for details). Using this simple procedure, homogeneous layers of nanostructured SnS_2 could be coated on the surface of SS meshes as observed by SEM, EDX and SEM mapping (Figures 4.12). Notice that since the mixture of En/Edt has a high metal dissolution power, the coating of Ni and Cu foams/meshes using this ink inevitably resulted in Ni or Cu contamination in the final SnS_2 layer. As an alternative, instead of SS, corrosion-free carbon cloth (CC) was used as current collector. Figure 4.13 displays SEM micrographs of bare and SnS_2-coated CCs.

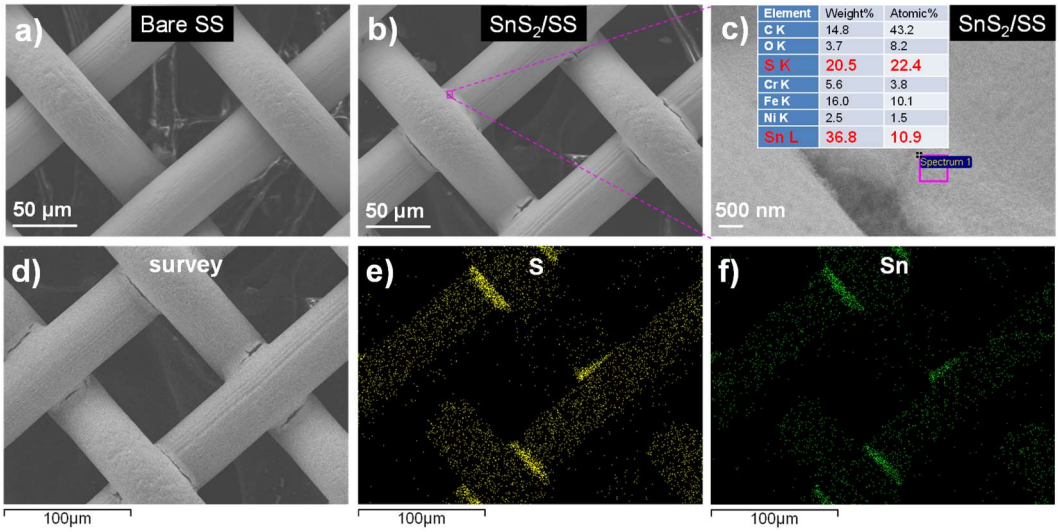

Figure 4.12. SEM images of (a) bare stainless steel mesh and (b,c) SnS_2-coated stainless steel mesh. (d-f) EDX mapping of SnS_2-coated stainless steel mesh.

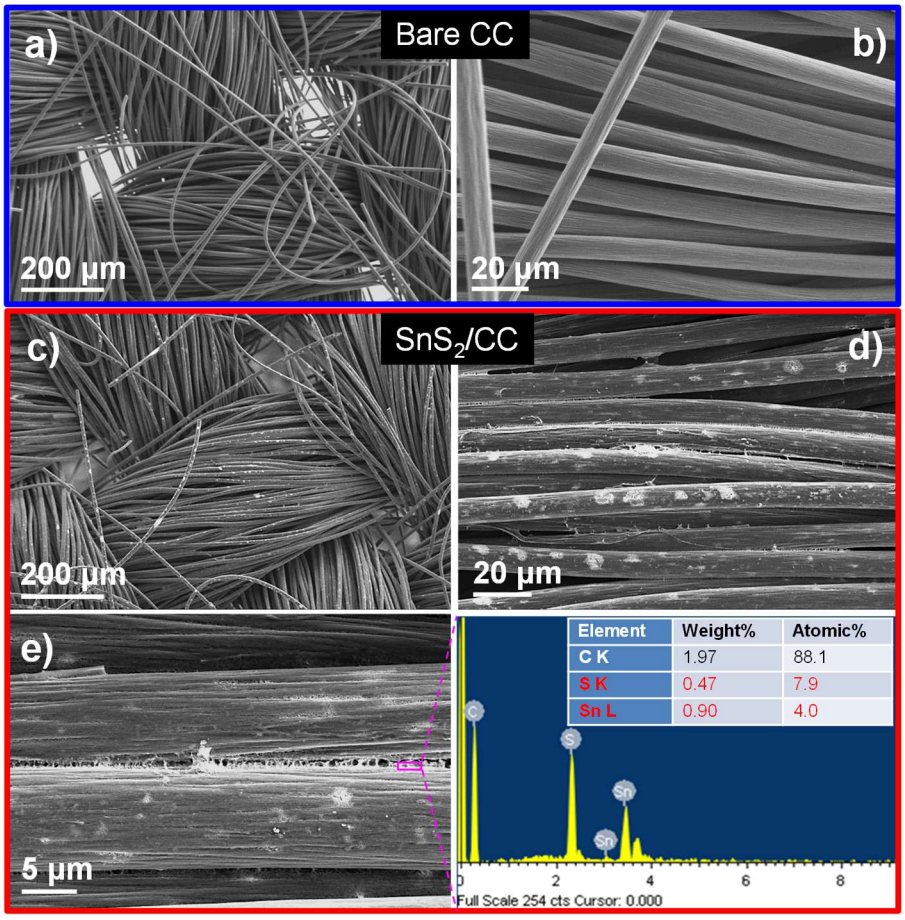

Figure 4.13. SEM images of (a-b) bare carbon cloth; (c-d) SnS_2-coated carbon cloth. Ink synthesis parameters: Sn/S=1/3, En/Edt=20/1, 70 ºC-30 min. Annealing parameters: 320 ºC, 30 min, 3 ºC/min.

A different strategy was used to coat graphene flakes. GO produced by the Hummers method was introduced in the precursor solution. During the ink formulation, simultaneously to the dissolution of Sn and S powders, GO was reduced by the amine,[53,54] yielding an ink containing a mixture of Sn-S molecular precursor and rGO. This composite ink could be used to coat virtually any substrate with SnS_2/rGO composite layers using the above coating and annealing steps (Figure 4.14).

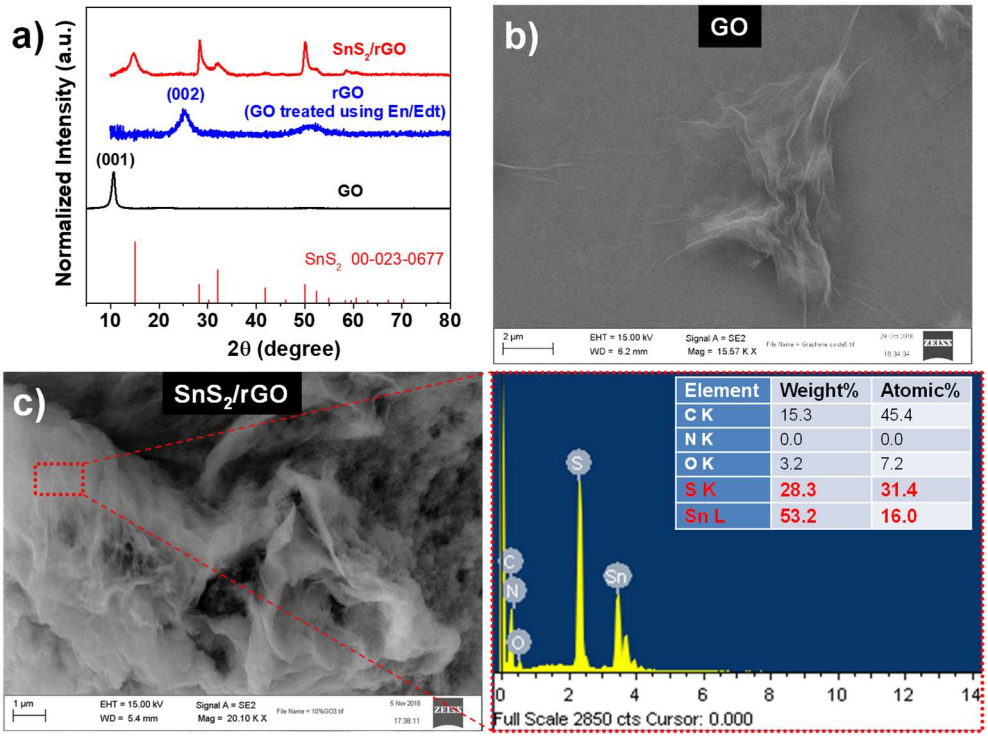

Figure 4.14. (a) XRD pattern of GO, rGO treated with the En/EdT solvent mixture and SnS_2-coated rGO; b) SEM micrograph of initial GO. (c-d) SEM image and EDX composition of SnS_2/rGO composite recovered after annealing a layer produced from an ink prepared by adding GO in the initial elemental mixture. XRD data demonstrated that the original GO was reduced to rGO by En/Edt (20/1, 70 ºC, 0.5 h).

We used the same strategy to produce $SnS_{2-x}Se_x$ coatings with controlled S/Se ratios, by simply adding the proper amount of Se in the precursor solution (see experimental section for details). As can be seen in Figure 4.15a, an obvious XRD peak shift towards lower angle occurred when Se ratio increased from 0 to 100 %, indicating the Se ion entered within the crystal structure. No impurity peaks were detected, even when pure $SnSe_2$ was recovered. The phase purity obtained in the present work was in contrast with results obtained by McCarthy et al., who systematically obtained sulfide impurities when attempting to produce pure $CoSe_2$.[55] Differences are associated with the very little amount

of Edt used in the present work. Figure 4.15b shows how the color of the precursor solution changed from green to dark brown with the selenium dosage increase and also how the color of spin-coated thin-film changed after annealing. SEM-EDX data (Table 4.4) demonstrated the sum of Se and S to be always around 67 %, while the tin composition was around 33 %, confirming that Se ions occupied the position of S within $SnS_{2-x}Se_x$ ternary chalcogenides. SEM analysis further showed the tremella-like morphology to change into sheet-like with the addition of Se (Figure 4.15c). Additionally, the band gap energy decreased from 2.50 eV (SnS_2) to 1.65 eV ($SnSe_2$) with Se incorporation (Figure 4.15d).

$SnS_{2-x}Se_x$/FTO electrodes displayed a negative photoconductivity at -0.1 V *vs.* Ag/AgCl. Among the samples containing Se, the highest photocurrents were measured from $SnSe_2$/FTO photoelectrodes, reaching up to 10 μA/cm^2 at -0.1 V *vs.* Ag/AgCl (Figure 4.16).

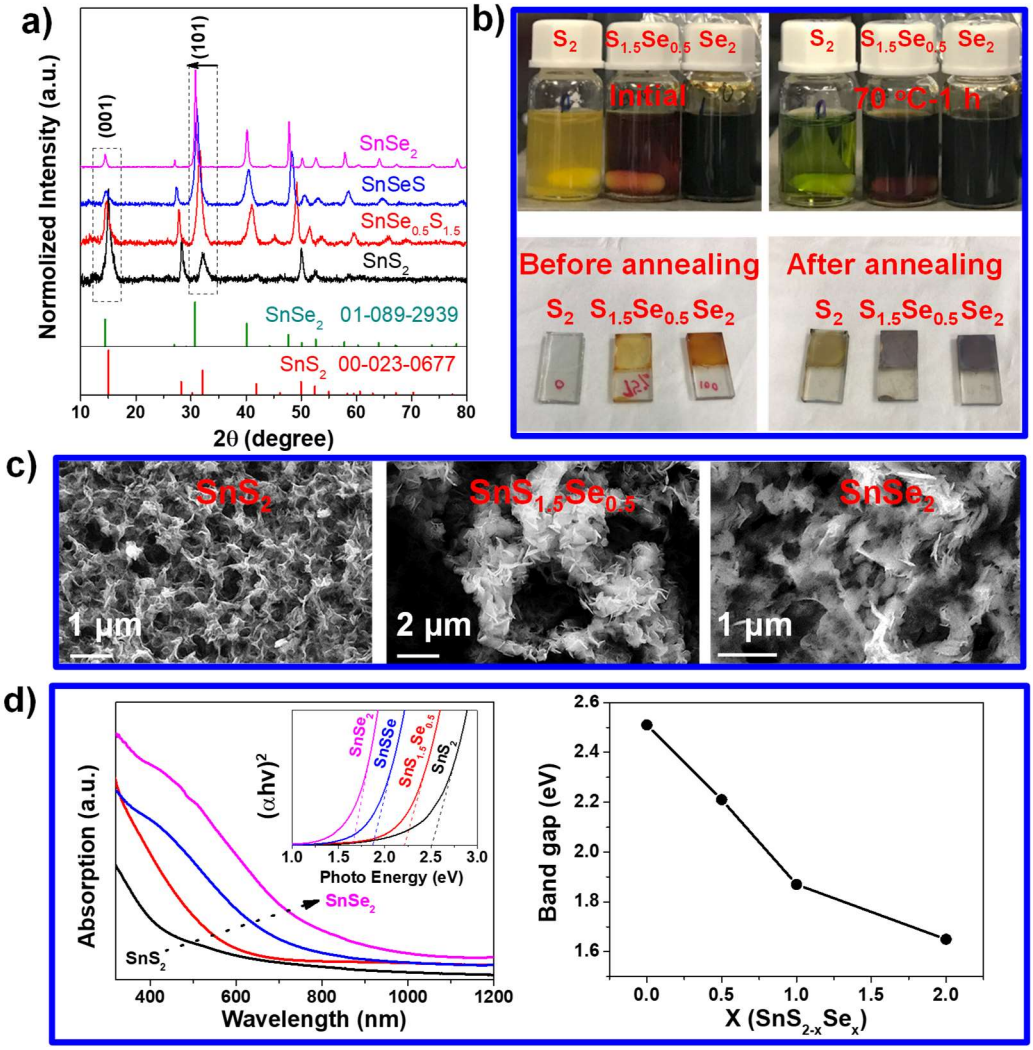

Figure 4.15. $SnS_{2-x}Se_x$ ternary chalcogenides obtained from the annealing for layers produced from inks containing different S/Se ratios: (a) XRD patterns; (b) optical photograph of $SnS_{2-x}Se_x$ molecular inks obtained at 70 ºC, 1 h and $SnS_{2-x}Se_x$/FTO layers before and after annealing; (c) SEM micrographs; d) UV-Vis spectra.

Table 4.4. Large-area EDX composition of $SnS_{2-x}Se_x$ sample recovered from molecular ink prepared using different Se content from x=0 to x=2. Ink formulation parameters: Sn/(S+Se)=1/3, En/Edt=20/1, 70 ºC.

Sample/nominal	Sn (at %)	Se (at %)	S (at %)
SnS_2	32.8	0	67.2
$SnS_{1.5}Se_{0.5}$	32.0	31.2	36.8
SnSSe	32.1	53.1	14.8
$SnSe_2$	33.6	66.4	0

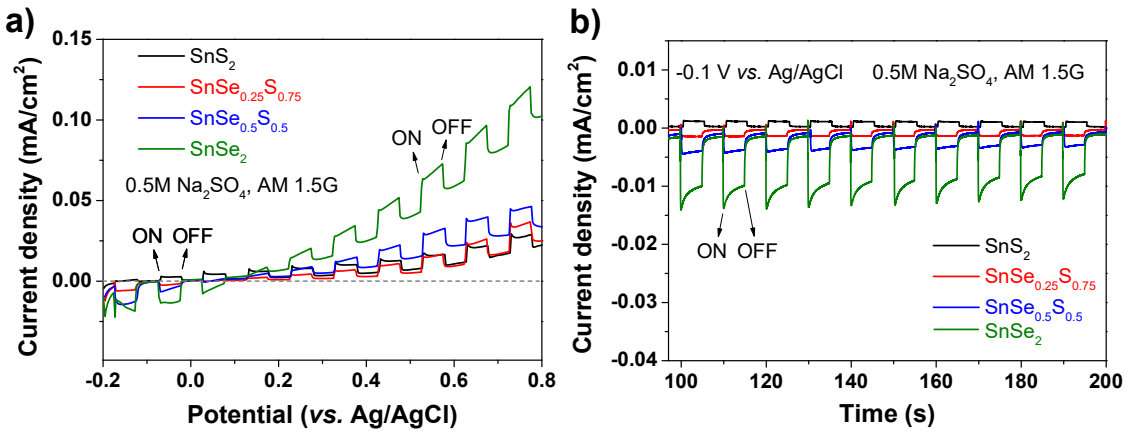

Figure 4.16. (a) Linear sweep voltammogram and (b) Amperometric i-t curves of sample $SnS_{2-x}Se_x$/FTO obtained by spin coating technique after annealing.

We additionally studied the potential of this precursor ink to produce gram scale amounts of unsupported particles, which can be potentially used in catalysis [36], batteries,[8] photodetectors,[56] sensors,[57] field-effect transistor devices,[58] etc. With this aim, large amounts of SnS_2 molecular ink (5 mL) were decomposed inside a heated flask (see experimental section and Figure 4.17a for details). After annealing, a gray powder was collected, which turned gray-yellow after washing. XRD analysis showed the powder to be phase pure SnS_2 (Figure 4.17b). X-ray photoelectron spectroscopy (XPS) analysis showed the Sn 3d region to display a unique doublet at 495.9 eV (Sn $3d_{3/2}$) and 487.5 eV (Sn $3d_{5/2}$), associated with Sn^{4+} within the SnS_2 lattice, [59-61] while the S 2p region showed a doublet at 163.5 eV (S $2p_{1/2}$) and 162.3 eV (S $2p_{3/2}$), ascribed to S^{2-} in the SnS_2 lattice

[60,61] (Figure 4.17c). Besides, SEM-EDX data in Figure 4.17d further confirmed that the composition of Sn/S was ca. 1/2, consistent with stoichiometric SnS_2. Interestingly, the powder displayed a flake-like morphology in contrast to the tremella-like particles recovered on substrates, which was ascribed to the additional growth of the crystals recovered in powder form associated with the larger amount of available precursor.

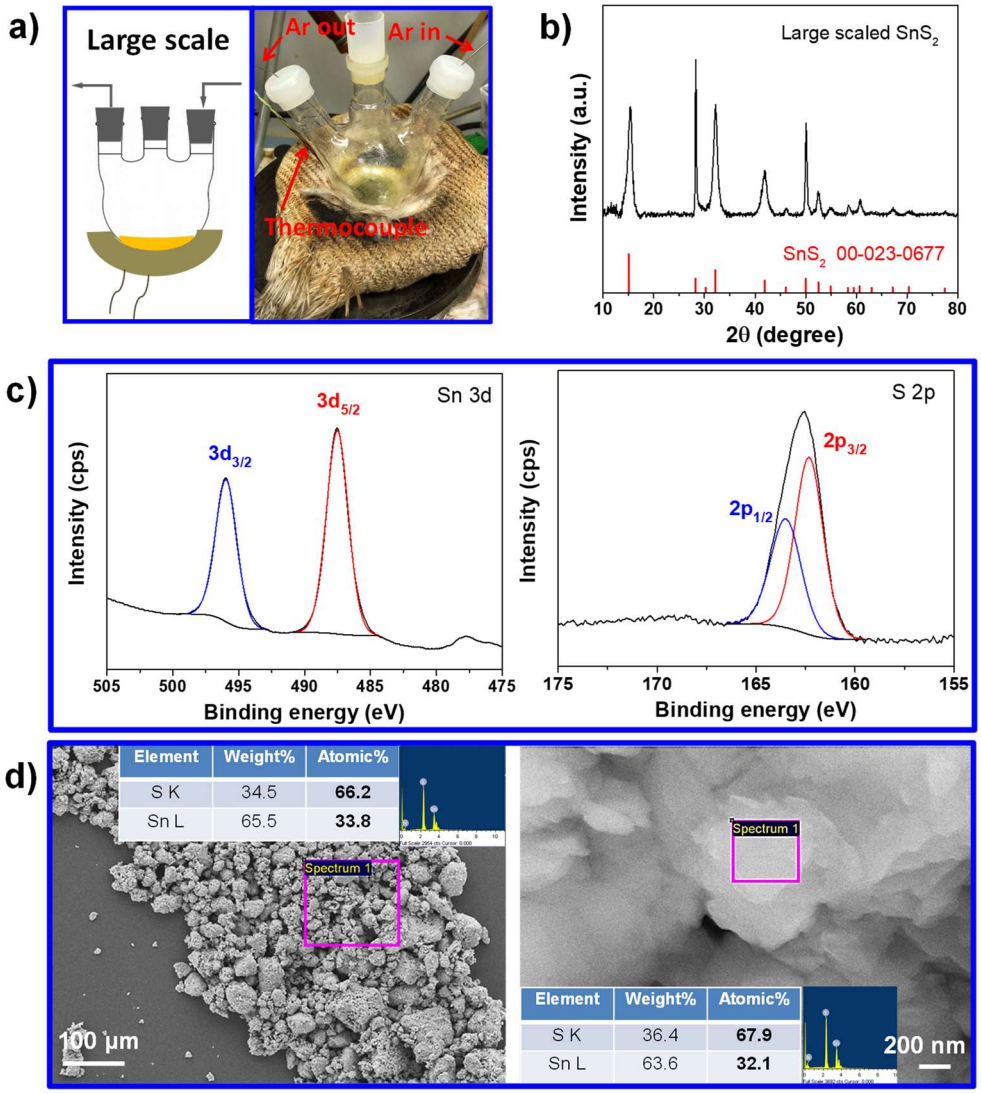

Figure 4.17. Large-scale SnS_2 powder recovering from the SnS_2 molecular ink: (a) scheme and photograph of a three-neck flask used; (b) XRD pattern; (c) XPS spectra of Sn 3d region and S 2p regions; (d) SEM micrographs and EDX data.

Regarding to the composition of SnS_2 precursor, recent works indicate that elemental metals dissolved in an amine-thiol mixture form thiolatochalgenometallate anions, such as bis(1,2-ethanedithiolate)tin(II) when dissolving Sn metal in En/Edt [42] and bis(1,2-ethanedithiolate)-indium(III) when dissolving In metal in hexylamine/Edt.[63] These anions are counterbalanced by enH^+ cations, which can be shown as following structure:

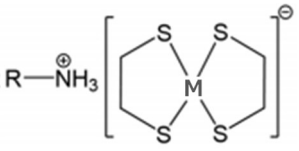

M = In, Sn

The dissolution of bulk sulfur in amine-thiol mixture has been investigated previously. Vineyard et al. reported the mechanism for the dissolution of bulk sulfur by amine-thiol mixtures,[22] which was proposed to occur via an amine-catalyzed reaction resulting in alkyl di-, tri-, and tetrasulfides. In this reaction, the amine deprotonates the thiol and the resulting nucleophilic thiolate reacts with the bulk sulfur (in the form of 8-membered rings) to create alkyl hydrogen polysulfide chains that further iteratively react with thiolate molecules to produce a mixture of smaller polysulfide products. The proposed mechanism for the base-catalyzed thiol-sulfur reaction is shown as follows:

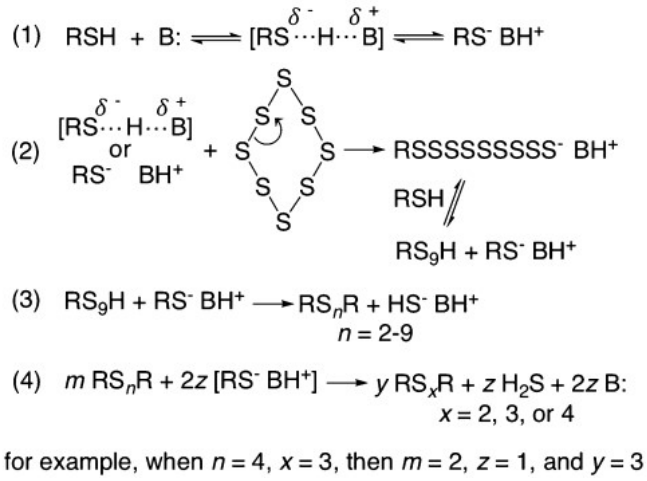

Combining the aforementioned dissolution mechanism of Sn metal and bulk sulfur in amine-thiol mixture, we hypothesis the composition of SnS_2 molecular precursor in our work as below:

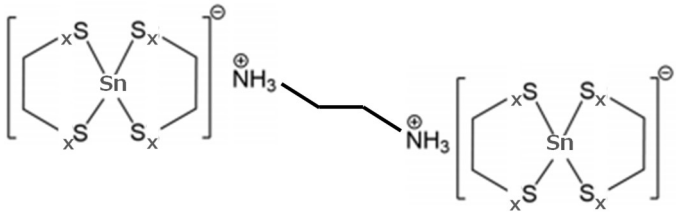

x = 2, 3 or 4

4.5 Conclusions

In summary, a Sn-S molecular ink was produced by dissolving Sn and S elemental powders in an amine/thiol co-solvent. The decomposition and annealing of this ink at 320 ºC for 30 min resulted in the formation of nanostructured tin sulfide. Pure SnS_2 layers with a tremella morphology were obtained using an ink containing an elemental ratio Sn/S=1/3 and a solvent ratio En/Edt=20/1. A loss of sulfur in the form of H_2S gas during dissolution was identified as the reason behind the presence of SnS impurities in inks produced using too long dissolution times. This molecular ink could be applied to produce planar and conformal SnS_2 nanostructured layer on conductive substrates, such as FTO, SS and CC. SnS_2/FTO photoanodes provided outstanding photocurrent densities under illumination with simulated solar light. Besides, SnS_2/rGO composites and $SnS_{2-x}Se_x$ were easily synthesized using the same strategy by simply introducing GO and Se powder in the initial precursor solution.

4.6 References

(1) McCarthy, C. L.; Webber, D. H.; Schueller, E. C.; Brutchey, R. L. Solution-Phase Conversion of Bulk Metal Oxides to Metal Chalcogenides Using a Simple Thiol-Amine Solvent Mixture. *Angew. Chem. Int. Ed.* **2015**, *54* (29), 8378–8381.

(2) Vayssieres, L.; Beermann, N.; Lindquist, S. E.; Hagfeldt, A. Controlled Aqueous Chemical Growth of Oriented Three-Dimensional Crystalline Nanorod Arrays: Application to Iron(III) Oxides. *Chem. Mater.* **2001**, *13* (2), 233–235.

(3) McCarthy, C. L.; Brutchey, R. L. Preparation of Electrocatalysts Using a Thiol-Amine Solution Processing Method. *Dalton Transactions*. **2018**, *47*, 5137–5143.

(4) Mitzi, D. B. *Solution Processing of Inorganic Materials*; John Wiley & Sons: Hoboken, NJ, 2009.

(5) Li, J.; Luo, Z.; Zuo, Y.; Liu, J.; Zhang, T.; Tang, P.; Arbiol, J.; Llorca, J.; Cabot, A. NiSn Bimetallic Nanoparticles as Stable Electrocatalysts for Methanol Oxidation Reaction. *Appl. Catal. B Environ.* **2018**, *234*, 10–18.

(6) Li, J.; Zuo, Y.; Liu, J.; Wang, X.; Yu, X.; Du, R.; Zhang, T.; Infante-Carrió, M. F.; Tang, P.; Arbiol, J.; Llorca, J.; Luo, Z.; Cabot, A. Superior methanol electrooxidation performance of (110)-faceted nickel polyhedral nanocrystals. *J. Mater. Chem. A* **2019**, *7,* 22036-22043.

(7) Li, Y.; Meng, J.; Yu, Z.; Li, Y. PdS-Modified CdS/NiS Composite as an Efficient Photocatalyst for H_2 evolution in Visible Light. *Catal. Today* **2014**, *225*, 136–141.

(8) Liu, Y.; Kang, H.; Jiao, L.; Chen, C.; Cao, K.; Wang, Y.; Yuan, H. Exfoliated-SnS_2 Restacked on Graphene as a High-Capacity, High-Rate, and Long-Cycle Life Anode for Sodium Ion Batteries. *Nanoscale* **2015**, *7*, 1325–1332.

(9) Zuo, Y.; Ni, J.; Song, J.; Niu, H.; Mao, C.; Zhang, S.; Shen, Y. Synthesis of Co_3O_4/NiO nanofilms and their enhanced electrochemical performance for supercapacitor application. *Appl. Surf. Sci.* **2016**, *370*, 528-535.

(10) Li, J.; Luo, Z.; He, F.; Zuo, Y.; Zhang, C.; Liu, J.; Yu, X.; Du, R.; Zhang, T.; Infante-Carrió, M. F.; Tang, P.; Arbiol, J.; Llorca, J.; Cabot, A. Colloidal Ni-Co-Sn nanoparticles as efficient electrocatalysts for the methanol oxidation reaction. *J. Mater. Chem. A* **2018**, *6*, 22915-22924.

(11) Chlistunoff, J.; Sansiñena, J. M. On the Use of Nafion® in Electrochemical Studies of Carbon Supported Oxygen Reduction Catalysts in Aqueous Media. *J. Electroanal. Chem.* **2016**, *780*, 134–146.

(12) Mitzi, D. B.; Kosbar, L. L.; Murray, C. E.; Copel, M.; Afzali, A. High-Mobility Ultrathin Semiconducting Films Prepared by Spin Coating. *Nature* **2004**, *428*, 299–303.

(13) Mitzi, D. B. Synthesis, Structure, and Thermal Properties of Soluble Hydrazinium Germanium(IV) and Tin(IV) Selenide Salts. *Inorg. Chem.* **2005**, *44* (10), 3755–3765.

(14) Mitzi, D. B. $N_4H_9Cu_7S_4$: A Hydrazinium-Based Salt with a Layered Cu_7S_4- Framework. *Inorg. Chem.* **2007**, *46* (3), 926–931.

(15) Mitzi, D. B.; Copel, M.; Chey, S. J. Low-Voltage Transistor Employing a High-Mobility Spin-Coated Chalcogenide Semiconductor. *Adv. Mater.* **2005**, *17* (10), 1285–1289.

(16) Mitzi, D. B. Polymorphic One-Dimensional $(N_2H_4)_2ZnTe$: Soluble Precursors for the Formation of Hexagonal or Cubic Zinc Telluride. *Inorg. Chem.* **2005**, *44* (20), 7078–7086.

(17) Mitzi, D. B.; Copel, M.; Murray, C. E. High-Mobility p-Type Transistor Based on a Spin-Coated Metal Telluride Semiconductor. *Adv. Mater.* **2006**, *18* (18), 2448–2452.

(18) Milliron, D. J.; Raoux, S.; Shelby, R. M.; Jordan-Sweet, J. Solution-Phase Deposition and Nanopatterning of GeSbSe Phase-Change Materials. *Nat. Mater.* **2007**, *6*, 352–356.

(19) Milliron, D. J.; Mitzi, D. B.; Copel, M.; Murray, C. E. Solution-Processed Metal Chalcogenide Films for p-Type Transistors. *Chem. Mater.* **2006**, *18* (3), 587–590.

(20) McCarthy, C. L.; Brutchey, R. L. Solution Processing of Chalcogenide Materials Using Thiol-Amine "Alkahest" Solvent Systems. *Chem. Commun.* **2017**, *53*, 4888–4902.

(21) Webber, D. H.; Brutchey, R. L. Alkahest for V_2VI_3 Chalcogenides: Dissolution of Nine Bulk Semiconductors in a Diamine-Dithiol Solvent Mixture. *J. Am. Chem. Soc.* **2013**, *135* (42), 15722–15725.

(22) Vineyard, B. D. Versatility and the Mechanism of the N-Butyl-Amine-Catalyzed Reaction of Thiols with Sulfur. *J. Org. Chem.* **1967**, *32* (12), 3833–3836.

(23) Lin, Z.; He, Q.; Yin, A.; Xu, Y.; Wang, C.; Ding, M.; Cheng, H. C.; Papandrea, B.; Huang, Y.; Duan, X. Cosolvent Approach for Solution-Processable Electronic Thin Films. *ACS Nano* **2015**, *9* (4), 4398–4405.

(24) Zhao, X.; Zhang, R.; Handwerker, C.; Agrawal, R. The Potential of Amine-Thiol Based Solution Processing for Chalcogenide Photovoltaics. In *2016 IEEE 43rd Photovoltaic Specialists Conference (PVSC)*; IEEE, **2016**, 0542–0544.

(25) Agrawal, R.; Zhang, R.; Walker, B. C.; Handwerker, C. Homogeneous Precursor Formation Method and Device Thereof. US 9738799 B2, August 12, 2015.

(26) Zhang, R.; Cho, S.; Lim, D. G.; Hu, X.; Stach, E. A.; Handwerker, C. A.; Agrawal, R. Metal–Metal Chalcogenide Molecular Precursors to Binary, Ternary, and Quaternary Metal Chalcogenide Thin Films for Electronic Devices. *Chem. Commun.* **2016**, *52*, 5007–5010.

(27) McCarthy, C. L.; Brutchey, R. L. Solution Processing of Chalcogenide Materials Using Thiol-Amine "Alkahest" Solvent Systems. *Chem. Commun.* **2017**, *53*, 4888–4902.

(28) Lei, Y. M.; Zhou, J.; Chai, Y. Q.; Zhuo, Y.; Yuan, R. SnS_2 Quantum Dots as New Emitters with Strong Electrochemiluminescence for Ultrasensitive Antibody Detection. *Anal. Chem.* **2018**, *90* (20), 12270–12277.

(29) Giri, B.; Masroor, M.; Yan, T.; Kushnir, K.; Carl, A. D.; Doiron, C.; Zhang, H.; Zhao, Y.; McClelland, A.; Tompsett, G. A.; Wang, D. W.; Grimm, R. L.; Titova, L. V.; Rao, P. M. Balancing Light Absorption and Charge Transport in Vertical SnS_2 Nanoflake Photoanodes with Stepped Layers and Large Intrinsic Mobility. *Adv. Energy Mater.* **2019**, *9* (31), 1901236.

(30) Meng, L.; Wang, S.; Cao, F.; Tian, W.; Long, R.; Li, L. Doping-Induced Amorphization, Vacancy, and Gradient Energy Band in SnS_2 Nanosheet Arrays for Improved Photoelectrochemical Water Splitting. *Angew. Chem. Int. Ed.* **2019**, *58* (20), 6761–6765.

(31) Du, Y.; Yin, Z.; Rui, X.; Zeng, Z.; Wu, X. J.; Liu, J.; Zhu, Y.; Zhu, J.; Huang, X.; Yan, Q.; Zhang, H. A Facile, Relative Green, and Inexpensive Synthetic Approach toward Large-Scale Production of SnS_2 nanoplates for High-Performance Lithium-Ion Batteries. *Nanoscale* **2013**, *5*, 1456–1459.

(32) Zhang, Y.; Lu, J.; Shen, S.; Xu, H.; Wang, Q. Ultralarge Single Crystal SnS Rectangular Nanosheets. *Chem. Commun.* **2011**, *47* , 5226–5228.

(33) Yin, D.; Liu, Y.; Dun, C.; Carroll, D. L.; Swihart, M. T. Controllable Colloidal Synthesis of Anisotropic Tin Dichalcogenide Nanocrystals for Thin Film Thermoelectrics. *Nanoscale* **2018**, *10*, 2533–2541.

(34) Chakrabarti, A.; Lu, J.; McNamara, A. M.; Kuta, L. M.; Stanley, S. M.; Xiao, Z.; Maguire, J. A.; Hosmane, N. S. Tin(IV) Sulfide: Novel Nanocrystalline Morphologies. *Inorganica Chim. Acta* **2011**, *374* (1), 627–631.

(35) Zhang, Y. C.; Du, Z. N.; Li, S. Y.; Zhang, M. Novel Synthesis and High Visible Light Photocatalytic Activity of SnS_2 Nanoflakes from $SnCl_2{\cdot}2H_2O$ and S Powders. *Appl. Catal. B Environ.* **2010**, *95*, 153–159.

(36) Sun, Y.; Cheng, H.; Gao, S.; Sun, Z.; Liu, Q.; Liu, Q.; Lei, F.; Yao, T.; He, J.; Wei, S.; Xie, Y. Freestanding Tin Disulfide Single-Layers Realizing Efficient Visible-Light Water Splitting. *Angew. Chem. Int. Ed.* **2012**, *51* (35), 8727–8731.

(37) Chen, H.; Chen, Y.; Zhang, H.; Zhang, D. W.; Zhou, P.; Huang, J. Suspended SnS_2 Layers by Light Assistance for Ultrasensitive Ammonia Detection at Room Temperature. *Adv. Funct. Mater.* **2018**, *28* (20), 1801035.

(38) Ying, H.; Li, X.; Wu, Y.; Yao, Y.; Xi, J.; Su, W.; Jin, C.; Xu, M.; He, Z.; Zhang, Q. High-Performance Ultra-Violet Phototransistors Based on CVT-Grown High Quality SnS_2 Flakes. *Nanoscale Adv.* **2019**, *1*, 3973–3979.

(39) Shao, G.; Xue, X. X.; Zhou, X.; Xu, J.; Jin, Y.; Qi, S.; Liu, N.; Duan, H.; Wang, S.; Li, S.; Ouzounian, M; Hu, T. S.; Luo, J; Liu, S; Feng, Y. Shape-Engineered Synthesis of Atomically Thin 1T-SnS_2 Catalyzed by Potassium Halides. *ACS Nano* **2019**, *13* (7), 8265–8274.

(40) Xu, L.; Zhang, P.; Jiang, H.; Wang, X.; Chen, F.; Hu, Z.; Gong, Y.; Shang, L.; Zhang, J.; Jiang, K.; Chu, J. H. Large-Scale Growth and Field-Effect Transistors Electrical Engineering of Atomic-Layer SnS_2. *Small* **2019**, *15* (46), 1904116.

(41) Mattinen, M.; King, P. J.; Khriachtchev, L.; Meinander, K.; Gibbon, J. T.; Dhanak, V. R.; Räisänen, J.; Ritala, M.; Leskelä, M. Low-Temperature Wafer-Scale Deposition of Continuous 2D SnS_2 Films. *Small* **2018**, *14* (21), 1800547.

(42) Buckley, J. J.; McCarthy, C. L.; Del Pilar-Albaladejo, J.; Rasul, G.; Brutchey, R. L. Dissolution of Sn, SnO, and SnS in a Thiol-Amine Solvent Mixture: Insights into the Identity of the Molecular Solutes for Solution-Processed SnS. *Inorg. Chem.* **2016**, *55* (6), 3175–3180.

(43) Thomson, J. W.; Nagashima, K.; Macdonald, P. M.; Ozin, G. A. From Sulfur−Amine Solutions to Metal Sulfide Nanocrystals: Peering into the Oleylamine-Sulfur Black Box. *J. Am. Chem. Soc.* **2011**, *133* (13), 5036–5041.

(44) Kim, E. T.; Chung, W. J.; Lim, J.; Johe, P.; Glass, R. S.; Pyun, J.; Char, K. One-Pot Synthesis of PbS NP/Sulfur-Oleylamine Copolymer Nanocomposites via the Copolymerization of Elemental Sulfur with Oleylamine. *Polym. Chem.* **2014**, *5*, 3617–3623.

(45) Ye, G.; Gong, Y.; Lei, S.; He, Y.; Li, B.; Zhang, X.; Jin, Z.; Dong, L.; Lou, J.; Vajtai, R.; Zhou, W.; Ajayan, P. M. Synthesis of Large-Scale Atomic-Layer SnS_2 through Chemical Vapor Deposition. *Nano Res.* **2017**, *10*, 2386–2394.

(46) Mukhokosi, E. P.; Krupanidhi, S. B.; Nanda, K. K. Band Gap Engineering of Hexagonal $SnSe_2$ Nanostructured Thin Films for InfraRed Photodetection. *Sci. Rep.* **2017**, *7*, 15215.

(47) Yu, J.; Xu, C. Y.; Ma, F. X.; Hu, S. P.; Zhang, Y. W.; Zhen, L. Monodisperse SnS_2 Nanosheets for High-Performance Photocatalytic Hydrogen Generation. *ACS Appl. Mater. Interfaces* **2014**, *6* (24), 22370–22377.

(48) Liu, Y.; Chen, P.; Chen, Y.; Lu, H.; Wang, J.; Yang, Z.; Lu, Z.; Li, M.; Fang, L. In Situ Ion-Exchange Synthesis of SnS_2/g-C_3N_4 Nanosheets Heterojunction for Enhancing Photocatalytic Activity. *RSC Adv.* **2016**, *6*, 10802–10809.

(49) Meng, H.; Wang, T.; Yu, X.; Zhu, Y.; Zhang, Y. BiOCl/SnS_2 hollow Spheres for the Photocatalytic Degradation of Waste Water. *RSC Adv.* **2015**, *5*, 107088–107097.

(50) Liu, Y.; Geng, P.; Wang, J.; Yang, Z.; Lu, H.; Hai, J.; Lu, Z.; Fan, D.; Li, M. In-Situ Ion-Exchange Synthesis Ag_2S Modified SnS_2 nanosheets toward Highly Photocurrent Response and Photocatalytic Activity. *J. Colloid Interface Sci.* **2018**, *512*, 784–791.

(51) Wang, L.; Jin, G.; Shi, Y.; Zhang, H.; Xie, H.; Yang, B.; Sun, H. Co-Catalyst-Free ZnS-SnS_2 porous Nanosheets for Clean and Recyclable Photocatalytic H_2 generation. *J. Alloys Compd.* **2018**, *753*, 60–67.

(52) Zuo, Y.; Liu, Y.; Li, J.; Du, R.; Yu, X.; Xing, C.; Zhang, T.; Yao, L.; Arbiol, J.; Llorca, J.; Sivula, K.; Guijarro, N.; Cabot; A. Solution-Processed Ultrathin SnS_2-Pt Nanoplates for Photoelectrochemical Water Oxidation. *ACS Appl. Mater. Interfaces* **2019**, *11* (7), 6918–6926.

(53) Huang, H. H.; De Silva, K. K. H.; Kumara, G. R. A.; Yoshimura, M. Structural Evolution of Hydrothermally Derived Reduced Graphene Oxide. *Sci. Rep.* **2018**, *8* , 6849.

(54) Li, X.; Hao, Z.; Zhang, F.; Li, H. Reduced Graphene Oxide-Immobilized Tris(Bipyridine)Ruthenium(II) Complex for Efficient Visible-Light-Driven Reductive Dehalogenation Reaction. *ACS Appl. Mater. Interfaces* **2016**, *8* (19), 12141–12148.

(55) McCarthy, C. L.; Downes, C. A.; Schueller, E. C.; Abuyen, K.; Brutchey, R. L. Method for the Solution Deposition of Phase-Pure $CoSe_2$ as an Efficient Hydrogen Evolution Reaction Electrocatalyst. *ACS Energy Lett.* **2016**, *1* (3), 607–611.

(56) Fu, X.; Ilanchezhiyan, P.; Mohan Kumar, G.; Cho, H. D.; Zhang, L.; Chan, A. S.; Lee, D. J.; Panin, G. N.; Kang, T. W. Tunable UV-Visible Absorption of SnS_2 Layered Quantum Dots Produced by Liquid Phase Exfoliation. *Nanoscale* **2017**, *9*, 1820–1826.

(57) Lee, K. T.; Liang, Y. C.; Lin, H. H.; Li, C. H.; Lu, S. Y. Exfoliated SnS_2 Nanoplates for Enhancing Direct Electrochemical Glucose Sensing. *Electrochim. Acta* **2016**, *219*, 241–250.

(58) Huang, Y.; Sutter, E.; Sadowski, J. T.; Cotlet, M.; Monti, O. L. A.; Racke, D. A.; Neupane, M. R.; Wickramaratne, D.; Lake, R. K.; Parkinson, B. A.; Sutter, P. Tin Disulfide-an Emerging Layered Metal Dichalcogenide Semiconductor: Materials Properties and Device Characteristics. *ACS Nano* **2014**, *8* (10), 10743–10755.

(59) Jiang, Y.; Wei, M.; Feng, J.; Ma, Y.; Xiong, S. Enhancing the Cycling Stability of Na-Ion Batteries by Bonding SnS_2 Ultrafine Nanocrystals on Amino-Functionalized Graphene Hybrid Nanosheets. *Energy Environ. Sci.* **2016**, *9*, 1430–1438.

(60) Li, X.; Sun, X.; Gao, Z.; Hu, X.; Ling, R.; Cai, S.; Zheng, C.; Hu, W. A Simple One-Pot Strategy for Synthesizing Ultrafine SnS_2 Nanoparticle/Graphene Composites as Anodes for Lithium/Sodium-Ion Batteries. *ChemSusChem* **2018**, *11* (9), 1549–1557.

(61) Yang, Z.; Zhang, P.; Wang, J.; Yan, Y.; Yu, Y.; Wang, Q.; Liu, M. Hierarchical Carbon@SnS_2 Aerogel with “Skeleton/Skin” Architectures as a High-Capacity, High-

Rate Capability and Long Cycle Life Anode for Sodium Ion Storage. *ACS Appl. Mater. Interfaces* **2018**, *10* (43), 37434–37444.

(62) Kovtyukhova, N. I.; Ollivier, P. J.; Martin, B. R.; Mallouk, T. E.; Chizhik, S. A.; Buzaneva, E. V.; Gorchinskiy, A. D. Layer-by-Layer Assembly of Ultrathin Composite Films from Micron-Sized Graphite Oxide Sheets and Polycations. *Chem. Mater.* **1999**, *11* (3), 771–778.

(63) Zhao, X.; Deshmukh, S. D.; Rokke, D. J.; Zhang, G.; Wu, Z.; Miller, J. T.; Agrawal, R. Investigating Chemistry of Metal Dissolution in Amine-Thiol Mixtures and Exploiting It toward Benign Ink Formulation for Metal Chalcogenide Thin Films. *Chem. Mater*. **2019**, *31* (15), 5674−5682.

Chapter 5

SnS_2/g-C_3N_4/Graphite Nanocomposites as Durable Lithium-Ion Battery Anode with High Pseudocapacitance Contribution

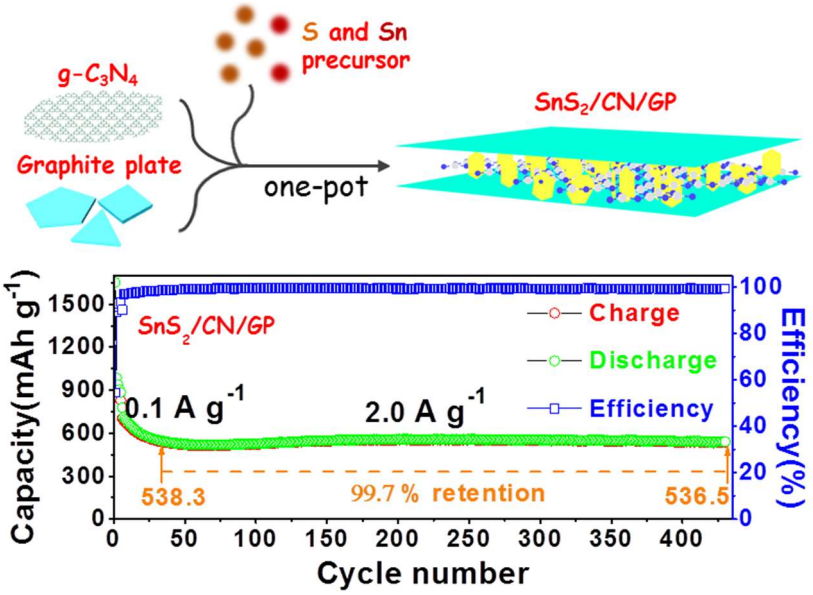

5.1 Abstract

Tin disulfide is a promising anode material for Li-ion batteries (LIBs) owing to its high theoretical capacity and the abundance of its composing elements. However, bare SnS_2 suffers from low electrical conductivity and large volume expansion, which results in poor rate performance and cycling stability. Herein, we present a solution-based strategy to grow SnS_2 nanostructures within a matrix of porous g-C_3N_4 (CN) and high electrical conductivity graphite plates (GPs). We test the resulting nanocomposite as anode in LIBs. First, SnS_2 nanostructures with different geometries are tested, to find out that thin SnS_2 nanoplates (SnS_2-NPLs) provide the highest performances. Such SnS_2-NPLs, incorporated into hierarchical SnS_2/CN/GP nanocomposites, display excellent rate capabilities (536.5 mAh g^{-1} at 2.0 A g^{-1}) and an outstanding stability (~99.7 % retention

after 400 cycles), which are partially associated with a high pseudocapacitance contribution (88.8 % at 1.0 mV s^{-1}). The excellent electrochemical properties of these nanocomposites are ascribed to the synergy created between the three nanocomposite components: i) thin SnS_2-NPLs provide a large surface for rapid Li-ion intercalation and a proper geometry to stand volume expansions during lithiation/delithiation cycles; ii) porous CN prevents SnS_2-NPLs aggregation, habilitates efficient channels for Li-ion diffusion and buffer stresses associated to SnS_2 volume changes; and iii) conductive GPs allow an efficient charge transport.

5.2 Introduction

Lithium-ion batteries (LIBs) are widely commercialized for portable applications owing to their notable volumetric energy density and their flexible and lightweight design. However, commercial devices suffer from low stability, and their potential energy densities and charging rates are far from those potentially attained by LIBs, which leaves plenty of room for improvement of their design and components, particularly of their anode materials.[1-3] Commercial LIBs use graphite anodes, which provide a modest theoretical energy density, 372 mAh g^{-1},[4,5] and are far away from the requirements of the next generation of high-energy and high-power LIBs.[6] Therefore, alternative anodes based on Si,[7,8] Ge [9,10] or Sn[11-13] are being actively developed.

Among the different materials able to intercalate or react with Li^+, sulfides and particularly SnS_2 are especially interesting due to the abundance of its elements and the ability to simultaneously interact with Li^+ through two different bulk mechanisms: Li-S reaction and Sn-Li alloying. SnS_2 anodes have a potential capacity of 1231 mAh g^{-1} ascribed to the combination of the Li-S reaction ($SnS_2 + 4Li^+ + 4e^- \rightarrow Sn + 2Li_2S$, 586 mAh g^{-1} capacity contribution)[14] and the Sn-Li alloying/dealloying reaction ($Sn + 4.4Li^+ + 4.4e^- \rightarrow Li_{4.4}Sn$, 645 mAh g^{-1} capacity contribution).[15,16] Besides, oxides and chalcogenides may provide a significant additional energy storage capacity contribution in the form of a rapid surface-related pseudocapacity.[3,17,18]

SnS_2 displays a two-dimensional (2D) hexagonal structure with layers of tin atoms sandwiched between two close-packed layers of sulfur atoms. Adjacent sandwiches, separated a distance of 0.59 nm, are hold together by Van der Waals forces.[19-21] This layered structure allows for the effective and fast diffusion of Li^+ (0.076 nm) to interact with Sn and S. However, during charge/discharge processes, SnS_2 suffers from huge

volumetric changes in large part related to the expansion/contraction in the c direction, i.e. across the planes, its softer crystallographic direction. This volumetric changes may result in the pulverization and detachment of the material from the current collector.[22-24] Additionally, the low electrical conductivity of SnS_2 provides a poor rate performance. These limitations lead to a deficient cyclability, especially at high current densities.[25-28]

To overcome its flaws as anode material in LIBs, SnS_2 needs to be nanostructured [29-32] and combined with high surface area materials, e.g. carbon-based networks, to improve dispersion and simultaneously provide the necessary paths for electrolyte diffusion and electron transport.[33-35] Graphene is considered as one of the best materials for these last roles,[25,36] owing to its large surface, extraordinary electrical conductivity, and convenient flexibility that allows accommodating the conductive network to the volume expansion of the active material.[37] Graphene can interact with Li^+ itself, delivering additional storage capacity. To maximize this interaction, graphene can be doped with large concentrations of N atoms which interact more efficiently with Li^+ due to the higher electronegativity of nitrogen compared with carbon.[38-40] In this direction, graphitic carbon nitride (g-C_3N_4, CN) is regarded as the analogue to graphite with the highest level of nitrogen, and thus may provide a significant Li^+ storage capacity.[6,41,42] CN also has a 2D layered structure in which p-conjugated graphitic planes are composed by alternate arrangements of sp2 hybridized carbon and nitrogen atoms.[43,44] Advantageously, CN can be easily produced in a scalable way by the thermal decomposition of urea at moderate temperatures.[45,46] However, such CN is usually characterized by a low electrical conductivity due to an intrinsic porous microstructure.[41,47] Thus a highly conductive material needs to be additionally introduced to provide the necessary paths for electron transport.

Herein, we combine SnS_2 nanostructures with high surface area and porous CN and high electrical conductivity graphite plates (GPs) in hierarchical nanocomposites, and analyze their performance as anode material in LIBs. We initially identify the SnS_2 nanostructure geometry providing better electrochemical performance by producing and testing SnS_2 particles with different shapes. The better performing SnS_2 nanostructure is then combined with porous CN, which we demonstrate is able to improve to some extent the electrode cycling stability. Finally, we analyze the effect of additionally incorporating conductive GP into the mixture to further improve performance.

5.3 Experimental Section

5.3.1 Chemicals

Tin(IV) chloride pentahydrate ($SnCl_4 \cdot 5H_2O$, 98 %), sulfur powder (99.8 %), tetrahydrofuran (THF, ≥99 %), and GP (99 % carbon basis, -325 mesh) were purchased from Sigma-Aldrich. 1-octadecene (ODE, 90 %) was purchased from Alfa-Aesar. Oleylamine (OAm, 80-90 %), oleic acid (OAc, 70 %), and urea (99 %) were purchased from Acros. Super P, polyvinylidene fluoride (PVDF) and porous polypropylene film (Celgard2400) were purchased from Shenzhen Kejing Star Technology Co. LTD. N-methy1-2-pyrrolidone (NMP, 99 %), ethylene carbonate (EC), diethylcarbonate (DEC) and fluoro ethylenecarbonate (FEC) were purchased from Aladdin. Toluene, hexane, isopropanol and ethanol were of analytical grade and obtained from various sources. GPs were cleaned using diluted HCl and ethanol under sonication. All other chemicals were used as received, without additional purification. Aqueous solutions were prepared using Milli-Q water (DW, 18.2 MΩ·cm).

5.3.2 Synthesis of SnS_2 Nanostructures, SnS_2/CN and SnS_2/CN/GP Nanocomposites

Plate- and flower-shaped SnS_2 nanostructures were produced following our recently reported protocol.[21] Briefly, to prepare SnS_2 nanoplates (SnS_2-NPLs), $SnCl_4 \cdot 5H_2O$ (2 mmol), ODE (16 mL), OAc (4 mL), OAm (2 mL) and THF (1 mL) were added into a three-neck round flask (50 mL). The solution was stirred using a magnetic stirring bar and a syringe was inserted into the solution to bubble Ar. The solution was then heated up to 140 °C and kept at this temperature for 1h to remove low boiling-point impurities. Then the obtained brown transparent solution was heated to 220 °C. At this temperature, 4 mL of S-OAm stock solution, prepared by dissolving sulfur powder (4 mmol) into OAm (4 mL) under sonication, were quickly injected into the reaction flask with a syringe. The solution was maintained at 220 ºC for 1h after S source injection and afterward quickly cooled down using a cold-water bath. The resulted product was centrifuged at 6000 rpm for 4 mins after adding toluene (15 mL), and then washed three times with toluene and ethanol by dispersion-precipitation cycles. The obtained yellow products (~80 % yield for SnS_2-NPL) were dried under vacuum for posterior use and characterization.

SnS_2 microflowers (SnS_2-MFL) were prepared in the same way, but replacing OAm with ODE. The S-ODE stock solution was prepared by dissolving sulfur powder (4 mmol) into ODE (4 mL) under Ar at 180 ºC in a 25 mL flask.

SnS_2/CN and SnS_2/CN/GP nanocomposites were prepared by adding CN (25 mg) and eventually GP (25 mg) into the reaction mixture containing enough Sn and S precursor to nominally yield 2 mmol SnS_2. The ratio of CN and SnS_2 was selected taking into account previous works,[6,35] and the same amount of GP was introduced to compensate for the decreased electrical conductivity upon CN addition. 25 mg of CN corresponded to a nominal concentration of ~8.5 wt% with respect to SnS_2. The precursor solution was initially stirred for 30 min at room temperature to ensure a proper dispersion of the carbon-based materials. The exact same reaction conditions used to prepare unsupported SnS_2 nanostructures were applied to prepare SnS_2/CN and SnS_2/CN/GP nanocomposites**.**

5.3.3 Synthesis of CN

CN was prepared according to a method reported previously with some modification.[45,46] Briefly, 2 g of urea was placed in a crucible with a loosely closed lid, and heated to 550 °C at a rate of 5 °C/min for 4 h in a tubular furnace with air flow. The obtained light yellow product was collected after cooling down to room temperature and grounded into powder. To hydrolyze the bulk CN in alkaline conditions, 500 mg of as-synthesized powder was mixed with 20 mL of NaOH solution (3 M in DW). The mixture was stirred at 70 °C for 8 h. The obtained hydrolyzed CN was washed using water/ethanol and collected using centrifugation for three times. The product was finally dried under vacuum and stored until further use**.**

5.3.4 Ligand Removal (LR)

Native organic ligands were removed from the SnS_2 surface according to previously published reports.[48,49] Briefly, SnS_2 particles were dispersed in a vial containing a solution of 0.8 mL hydrazine and 25 mL acetonitrile. The mixture was then stirred for 4 h at room temperature and subsequently collected by centrifugation. The resulted product was further washed with acetonitrile and centrifuged at 2000 rpm for additional 2 times. Ligand-removed products were collected and stored in Ar atmosphere after drying under vacuum at room temperature.

5.3.5 Sample Characterization

Powder X-ray diffraction (XRD) patterns were obtained on a Bruker AXS D8 ADVANCE X-ray diffractometer operating at 40 kV and 40 mA with Ni-filtered (2 μm thickness) Cu Kα1 radiation (λ = 1.5406 Å). X-ray photoelectron spectroscopy (XPS) was carried out on a SPECS system equipped with an Al anode XR50 source operating at 150 W and a Phoibos 150 MCD-9 detector. The pressure in the analysis chamber was kept below 10^{-7} Pa. Data processing was performed with the CasaXPS program. Binding energy (BE) values were centered by using the C 1s peak at 284.8 eV. SEM analysis was carried out in a ZEISS Auriga microscope with an energy dispersive X-ray spectroscopy (EDX) detector at 20 kV to study composition. Transmission electron microscopy (TEM) characterization was carried out on a ZEISS LIBRA 120, operating at 120 kV. High-resolution TEM (HRTEM) images were obtained using a field emission gun FEI Tecnai F20 microscope at 200 kV with a point-to-point resolution of 0.19 nm. High angle annular dark-field (HAADF) STEM was combined with electron energy loss spectroscopy (EELS) in the Tecnai microscope by using a GATAN QUANTUM filter. For TEM characterization, samples were prepared by drop casting a dispersion containing the material on a 200 mesh copper grid. Thermogravimetric (TG) analyses were performed using a PerkinElmer Diamond TG/DTA instrument. Samples were measured in air at a heating rate of 5 ºC/min from ambient temperature to 800 ºC. Fourier transform infrared spectroscopy (FTIR) was performed on an Alpha Bruker FTIR spectrometer with a platinum attenuated total reflectance (ATR) single reflection module. FTIR data were typically averaged over 24 scans.

5.3.6 Electrochemical Measurements

To evaluate the electrochemical performance of the materials, 80 wt% of sample, 10 wt% Super P, and 10 wt% PVDF were mixed together in an appropriate amount of NMP to form a homogenous slurry. Subsequently, the resultant flowing slurry was coated on Cu foil and dried in a vacuum oven at 80 ºC for 24 h. The foil was then cut into disks with a diameter of 12 mm. The mass of active material was estimated to be *ca.* 1.0 mg/cm^2. To test the performance of obtained electrodes, half cells were constructed in an argon-filled glove-box (H_2O and O_2 < 0.1 ppm) using Celgard2400 as separator, and $LiPF_6$ solution (1 M) in EC/DEC (1:1 volume) with 5 wt% FEC as the electrolyte. Galvanostatic charge-discharge curves of the assembled cells were measured at different current densities in

the voltage range of 0.01-3.0 V versus Li^+/Li on a battery test system (CT2001A, LAND). Cyclic voltammetry (CV) measurements were respectively performed with an electrochemical workstation (Gamry Interface 1000) in the voltage range from 0.01-3.0V and the scan rate from 0.1 to 1mV s^{-1}. Electrochemical impedance spectroscopy (EIS) tests were performed in a scanning frequency range from 100 kHz to 10 mHz using a sinusoidal voltage with amplitude of 5 mV.

5.4 Results and Discussion

Figure 5.1 shows electron microscopy micrographs of SnS_2 nsnostructures, CN and GP. Following the above detailed procedure, SnS_2-NPLs with ~200 nm in diameter and ~10 nm thickness, and ~1 μm SnS_2-MFLs were produced (Figures 5.1a and 5.1b).[21] CN showed a graphene-like flexible morphology with high porosity (Figure 5.1c and inset) and GP was characterized by a surface-smooth thick plate morphology (Figure 5.1d). Figure 5.1e shows a SEM micrograph of a SnS_2-NPL/CN/GP nanocomposite formed by growing SnS_2-NPLs in the presence of CN and GP. Notice that the morphology of CN and GP was not modified during the synthesis process, although their particle size was slightly reduced as they were probably fragmented during agitation. Besides, the presence of CN and GP in the reaction mixture did not significantly change the size and morphology of the obtained SnS_2-NPLs. Additional SEM micrographs of SnS_2/CN and SnS_2/CN/GP nanocomposites obtained from SnS_2-NPLs and SnS_2-MFLs can be found in Figure 5.2, demonstrating the presence of SnS_2 in all the nanocomposites.

Figure 5.1f shows the XRD patterns of SnS_2-NPLs, SnS_2-MFLs, CN and GP. XRD patterns of the SnS_2/CN/GP composites can be found on Figure 5.3a. XRD patterns of GP and CN displayed two characteristic peaks, corresponding to the (002) and (004) crystallographic planes for GP and the (100) and (002) for CN. The XRD pattern of SnS_2 could be indexed with the hexagonal berndtite SnS_2 structure (JCPDS# 23-0677). The high intensity ratio between (001) and (101) XRD peaks for SnS_2-NPL in comparison with SnS_2-MFL, pointed at the highly asymmetric morphology of SnS_2-NPL with largely exposed {001} facets. The XRD pattern of SnS_2/CN/GP was also indexed with the berndtite SnS_2 structure, with the two additional peaks of GP. The diffraction peaks of CN were not visible in the XRD pattern of SnS_2/CN/GP because of their low intensity and their partial overlap with those of SnS_2. HRTEM micrographs (Figure 5.3b) confirmed the hexagonal structure of SnS_2 NPLs (space group = P-3M1).

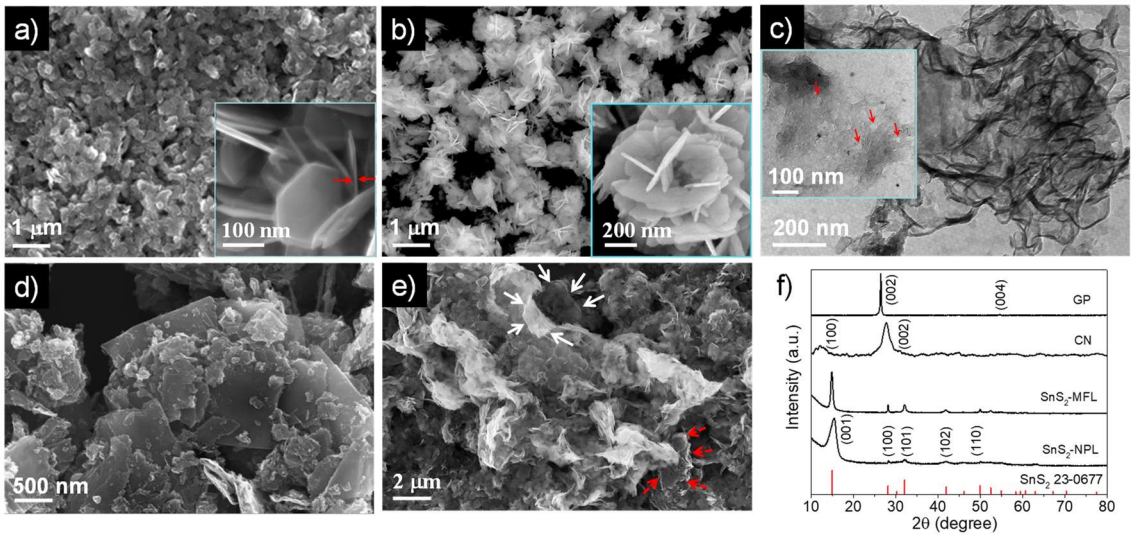

Figure 5.1. (a) SEM micrograph of SnS_2-NPLs. b) SEM micrograph of SnS_2-MFLs. c) TEM micrograph of CN. In the inset, arrows point out at the presence of pores/holes. d) SEM micrograph of GP. e) SEM micrograph of a SnS_2-NPL/CN/GP composite. White arrows point at a CN structure. Red arrows point at GPs. f) XRD pattern of SnS_2-NPLs, SnS_2-MFLs, CN and GP.

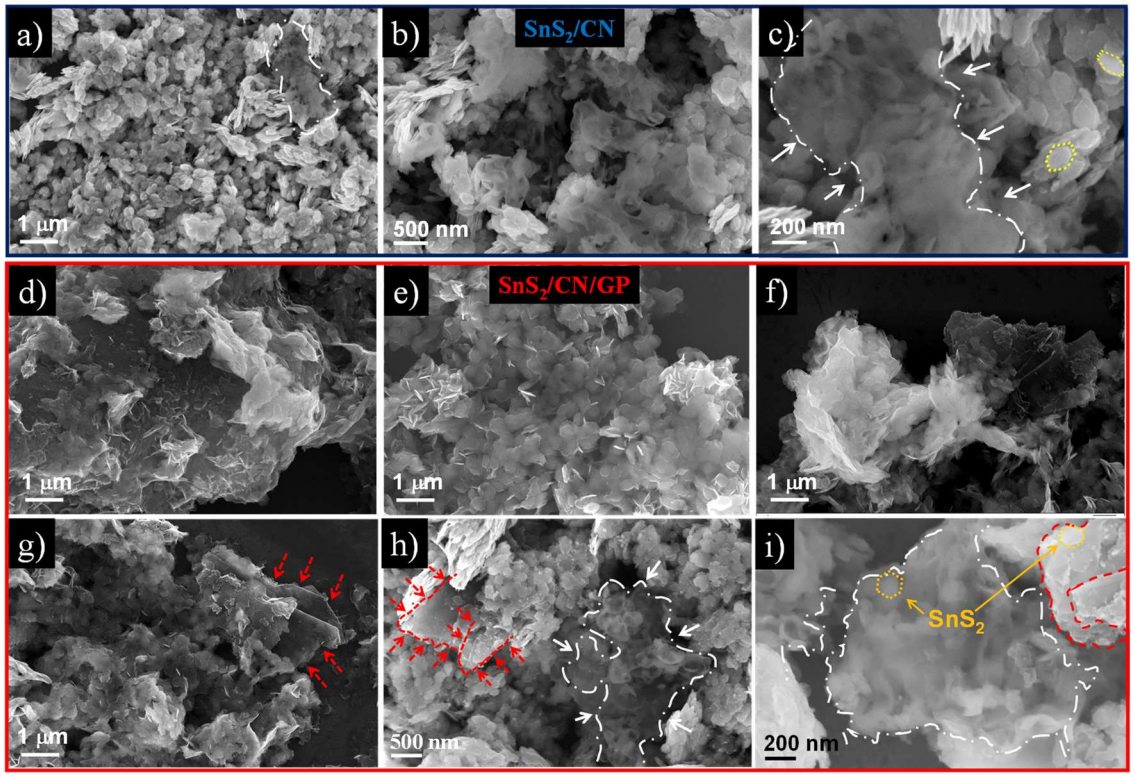

Figure 5.2. SEM images with different magnification of (a-c) SnS_2/CN; (d-i) additional SnS_2/CN/GP hybrid. The white dash-dot line/solid arrows indicate CN, while the red dash line and arrows indicate GP.

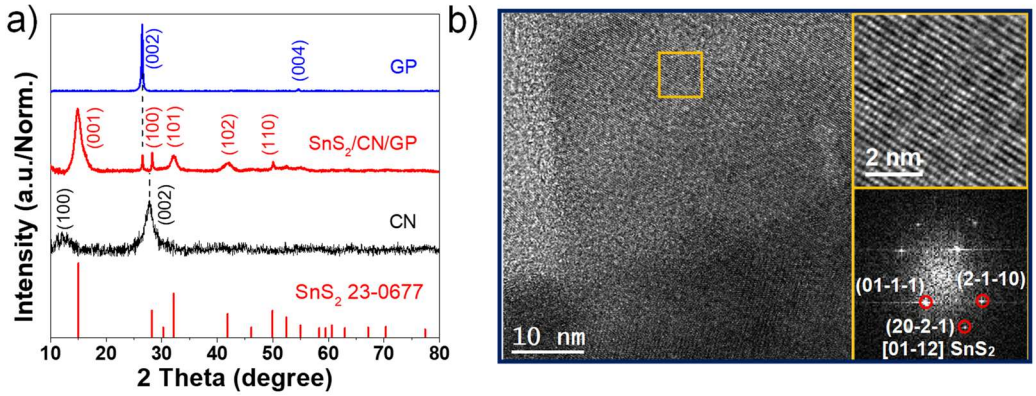

Figure 5.3. a) XRD patterns of SnS_2/CN/GP nanocomposite and bare CN, GP. b) HRTEM of SnS_2 in SnS_2/CN/GP nanocomposite. Detail of the orange squared region and its corresponding power spectrum revealed that this nanostructure had a crystal phase assigned to the SnS_2 hexagonal phase (space group = P-3M1). From the crystalline domain, the SnS_2 lattice fringe distances were measured to be 0.150 nm, 0.181nm and 0.274 nm, at 32.81º and 55.36º which could be interpreted as the hexagonal SnS_2 phase, visualized along its [01-12] zone axis.

Figure 5.4a displays SEM-EDX maps of the different elements within SnS_2/CN/GP, showing a homogenous distribution of the different components within the composite. EDX analysis systematically showed the SnS_2 composition to be slightly sulfur rich, with an everage elemental ratio of S/Sn = 2.06 (Figure 5.5). Nevertheless, the measured differences with respect to the stoichiometric ratio were within the experimental error of the technique. EELS elemental maps revealed a homogenous distribution of N at the nanometer level, proving CN nanosheets to ubiquitously support/wrap SnS_2 nanostructures (Figure 5.4b).

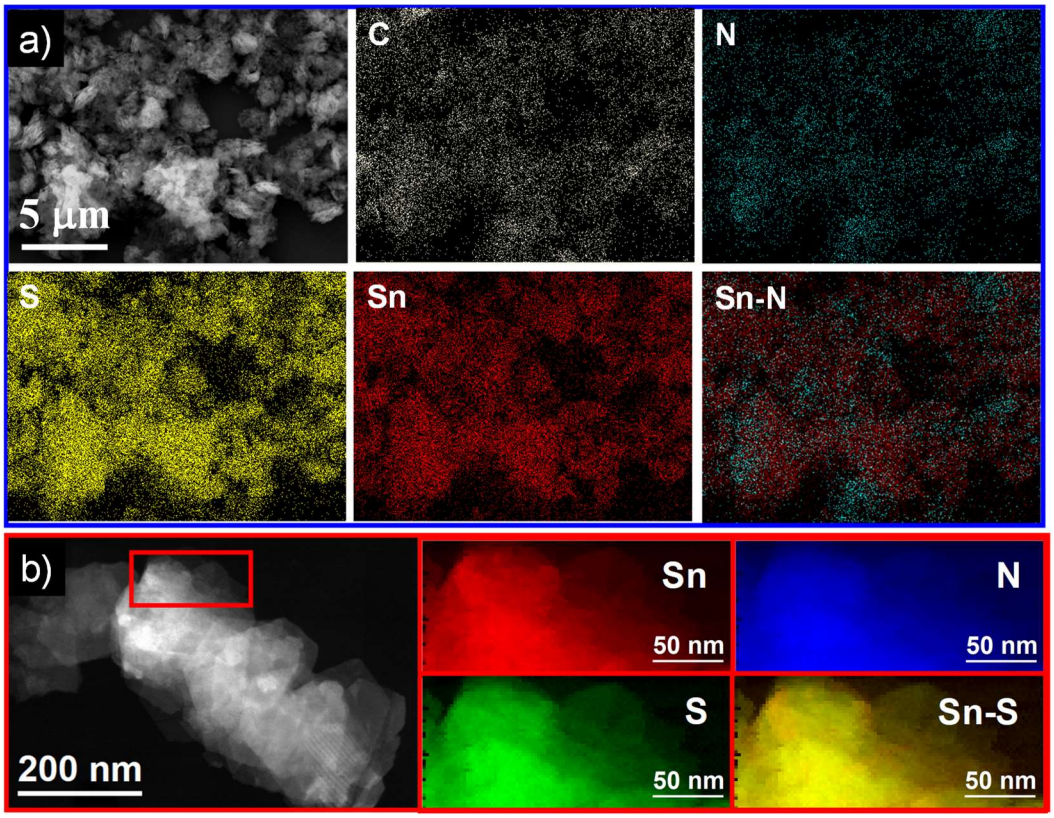

Figure 5.4. (a) SEM micrograph and EDX elemental maps of a SnS_2/CN/GP composite. (b) STEM micrograph of a SnS_2/CN/GP composite and EELS chemical composition maps obtained from the red squared area in the STEM micrograph.

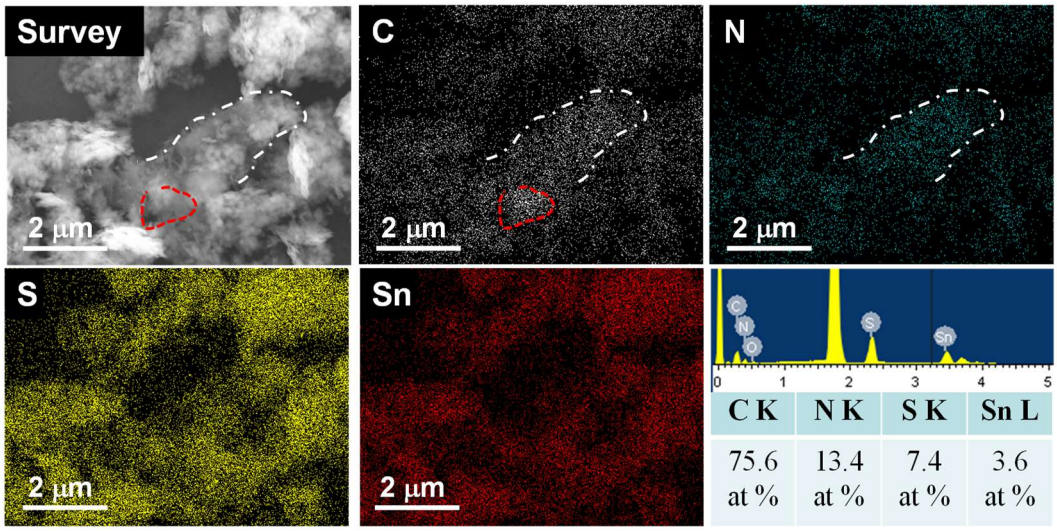

Figure 5.5. Additional SEM-EDX mapping of SnS_2/CN/GP and its corresponding quantitative EDX result. Red dash line indicates the GP, while the white dash-dot line indicates the CN.

The bulk content of CN, GP and SnS_2 within SnS_2/CN/GP composites was measured using TGA (Figure 5.6). Upon heating the sample up to 800 ºC in the presence of oxygen,

the composite displayed a total weight loss of 34 %. This weight loss was ascribed to the oxidative dissociation of GP and CN, the oxidation of SnS_2 to SnO_2 and the removal of surface ligands.[50] TGA of SnS_2-NPLs provided a final mass of SnO_2 of a 77 % with respect to the initial amount of material analyzed, which corresponded to an initial content of SnS_2 in the SnS_2-NPLs sample of 93.4 %. We hypothesize the remaining 6.6 wt% to be associated with surface organic ligands. From the weight decrease measured in SnS_2/CN/GP composites (66 % SnO_2 remaining, which corresponds to 80.1 % initial SnS_2), and assuming the same ratio of organic ligands as in SnS_2-NPLs, the total amount of CN and GP with respect to SnS_2 was estimated at a 17.7 % (14.2 wt%/80.1 wt%), which was close to the nominal 17.1 % [50 mg/(183*2*80%) mg].

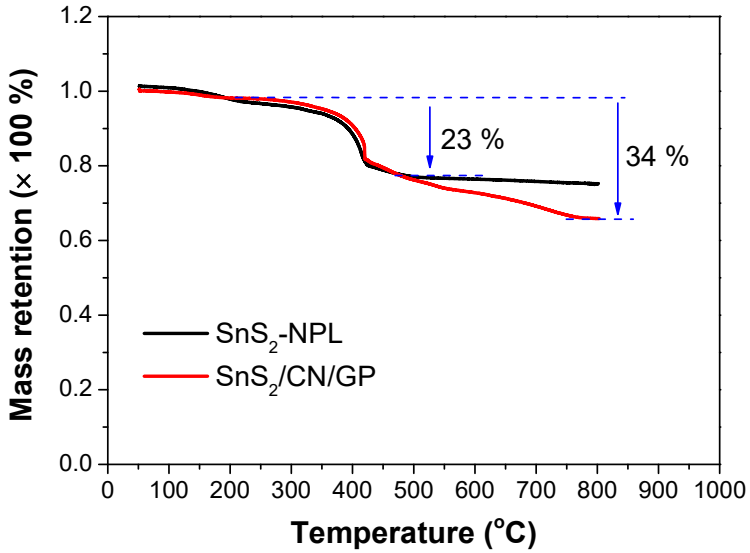

Figure 5.6. TG curves of SnS_2-NPL and SnS_2/CN/GP tested from ambient temperature to 800 °C under air atmosphere.

SnS_2/CN/GP nanocomposites were treated with a mixture of hydrazine and acetonitrile to remove the surface ligands from the final composites (see Experimental section for details).[48,49] FTIR analyses confirmed the successful ligand removal from the material (Figure 5.7).

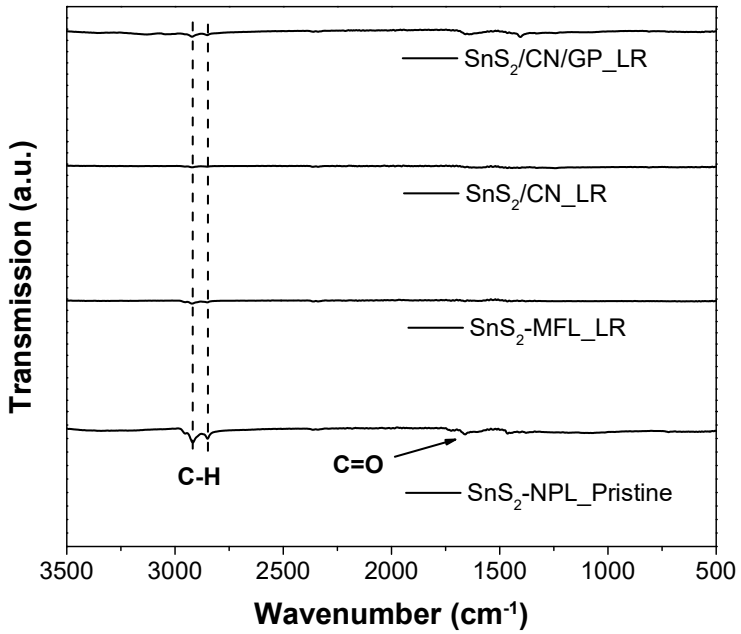

Figure 5.7. FTIR spectra of samples before (Pristine) and after (LR) ligand removal.

XPS analysis of SnS_2-based composites after hydrazine treatment showed the surface of the final material to be partially reduced (Figure 5.8). Two chemical environments were clearly visible in the Sn 3d XPS spectrum (Figure 5.8a) of the SnS_2/CN/GP composites. The first doublet (Sn $3d_{5/2}$ at 487.1 eV) was associated with Sn^{4+},[51,52] and the second doublet (Sn $3d_{5/2}$ at 485.8 eV) with Sn^{2+}.[53,54] From the peak intensities, we estimated the ratio of the two chemical states to be ca. $Sn^{2+}/Sn^{4+} = 0.3$. Similarly, the XPS spectrum of the S 2p region (Figure 5.8b) of the SnS_2/CN/GP composites was fitted with two doubles. The first was located at 162.1 eV (S $2p_{3/2}$) and 163.3 eV (S $2p_{1/2}$), and it was associated with S^{2-} in the SnS_2 lattice.[51,52,55] A second S 2p doublet was fitted at 160.7 eV (S $2p_{3/2}$) and 161.8 eV (S $2p_{1/2}$), and it was associated with S^{2-} within SnS.[53,54] As measured by XPS, the surface ratio $SnS/SnS_2 = 0.4$. The N 1s spectrum of SnS_2/CN/GP (Figure 5.8c) showed three peaks at BEs of 398.2 eV, 399.2 eV and 401.0 eV, which were assigned to N-(C-N=C), tertiary nitrogen N-(C)3 group and C-N-H of CN, respectively.[56,57] Finally, the C 1s spectrum (Figure 5.8d) showed 2 to 3 characteristic peaks corresponding to carbon within CN and graphitic carbon.[58] No clear evidence of chemical bonding between CN, GP and SnS_2 could be obtained by XPS.

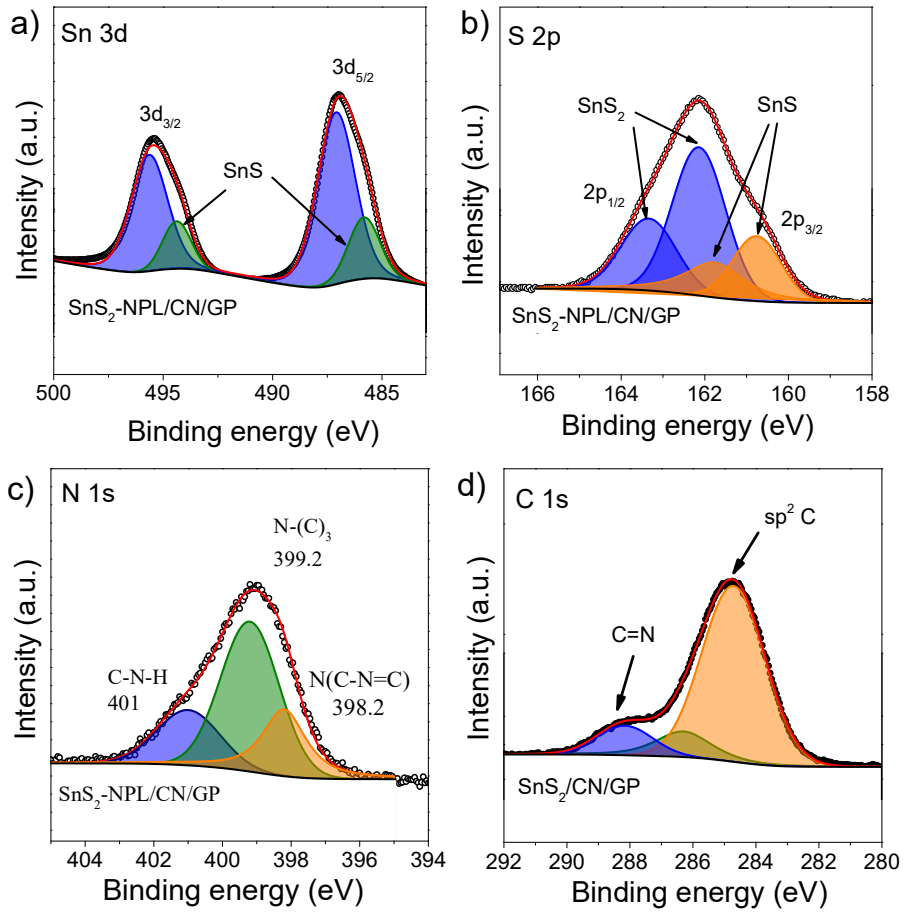

Figure 5.8. XPS spectra of (a) Sn 3d region; (b) S 2p region; (c) N 1s region and (d) C 1s region of SnS_2/CN/GP.

The electrochemical behavior of SnS_2-based LIB anodes was initially investigated using CV with a scan rate of 0.1 mV s^{-1} in the voltage window 0.01-3 V vs. Li^+/Li. To determine the best performing SnS_2 nanostructure geometry, SnS_2-NPL and SnS_2-MFL were initially compared. Figure 5.9a shows results obtained from a SnS_2-NPL electrode. The first sweep displayed three clear cathodic current peaks at ~1.8 V, ~1.1 V and ~0.15 V. The peak at ~1.8 V disappeared in the following cycles, and it was assigned to lithium insertion in the layered SnS_2 without phase decomposition (equation 5.1).[52,59,60] The strong peak at ~1.1 V was attributed to the decomposition of SnS_2 (equation 5.2), the formation of Li_2S and Sn metal (equation 5.3), and the growth of the solid electrolyte interface (SEI) layer.[52,61,62] The intensity of this peak decreased and was shifted to ~1.3 V in subsequent cycles.[52,63] The cathodic peak at ~0.15 V corresponded to the reaction between metallic Sn and Li^+ (equation 5.4). [61,63] Anodic peaks at ~0.5 V, ~1.25 V, and ~1.8 V were related to the dealloying reaction of $Li_{4.4}Sn$ to metallic Sn, the partial deinsertion reaction of Li^+ from Li_xSnS_2 to form SnS_2, and the oxidation of metallic Sn

to SnS_2, respectively.[22,64-66] In addition, the anodic peak at ~2.35 V was assigned to the transformation of unreacted Li_2S to polysulfides.[67,68] Very similar CV profiles were obtained for SnS_2-MFL anodes (Figure 5.9b). The aforementioned electrochemical reactions between SnS_2 and lithium ions during charge-discharge processes are outlined as follows:

$$SnS_2 + xLi^+ + xe^- \rightarrow Li_xSnS_2 \qquad \text{eq. 5.1}$$

$$Li_xSnS_2 + (4\text{-}x)Li^+ + (4\text{-}x)e^- \rightarrow 2Li_2S + Sn \qquad \text{eq. 5.2}$$

$$SnS_2 + 4Li^+ + 4e^- \rightarrow Sn + 2Li_2S \qquad \text{eq. 5.3}$$

$$Sn + 4.4Li^+ + 4.4e^- \rightarrow Li_{4.4}Sn \qquad \text{eq. 5.4}$$

Galvanostatic charge-discharge curves of the SnS_2-NPL and SnS_2-MFL electrodes were performed in the voltage range of 0.01-3.0 V *vs.* Li^+/Li at a current density of 0.1 A g^{-1} (Figure 5.9c,d). Similar profiles were obtained for SnS_2-based electrodes with different particle geometries. The initial irreversible capacity loss was mainly associated with the decomposition of electrolyte on the surface of active particles to form the SEI layer among other possible irreversible processes (Figure 5.9c,d).[69,70]

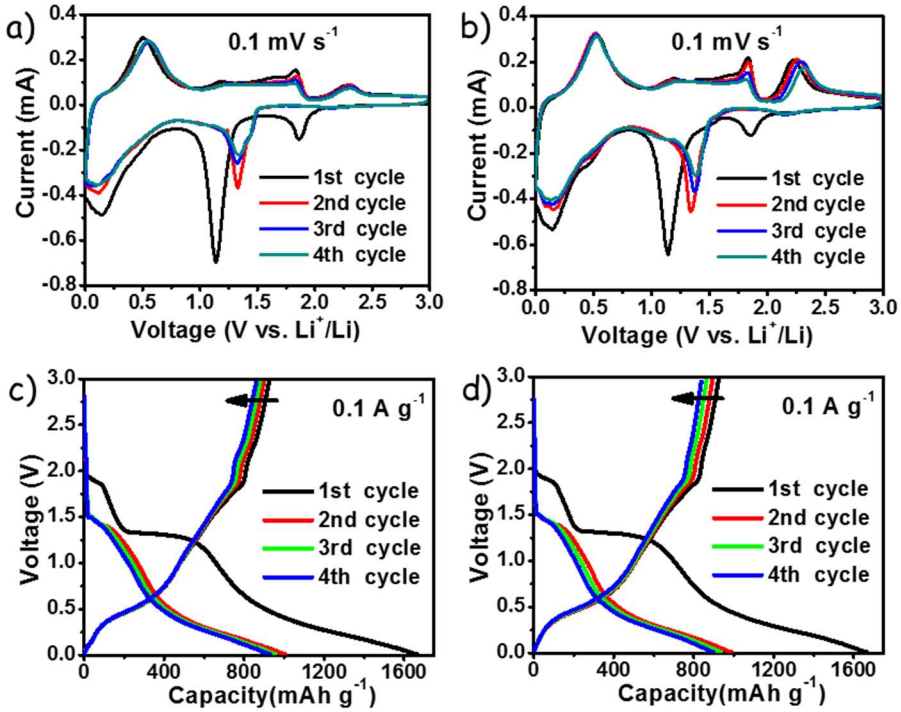

Figure 5.9. Initial four CV curves obtained at a scan rates of 0.1 mV s^{-1} on electrodes of (a) SnS_2-NPL; (b) SnS_2-MFL. Initial four galvanostatic charge-discharge curves obtained at a current density of 0.1 A g^{-1} on electrodes of (c) SnS_2-NPL; (d) SnS_2-MFL.

As shown in Figure 5.10, SnS_2-NPL electrodes provided significantly better rate capacity performance than SnS_2-MFL, with a lower loss of reversible capacity as the current density increased. SnS_2-NPL electrodes delivered a capacity of ~380 mAh g^{-1} after increasing a 50 fold the current density, from 0.1 A g^{-1} to 5.0 A g^{-1}, ~59 % of the initial capacity was recovered when the current density decreased back to 0.1 A g^{-1}. By contrast, SnS_2-MFL electrodes delivered a lower capacity of only ~70 mAh g^{-1} and ~17 % recovery. These results pointed at SnS_2-NPL as the best SnS_2 nanostructure geometry to be used as LIB anode material. Therefore, additional work was carried out using SnS_2-NPLs.

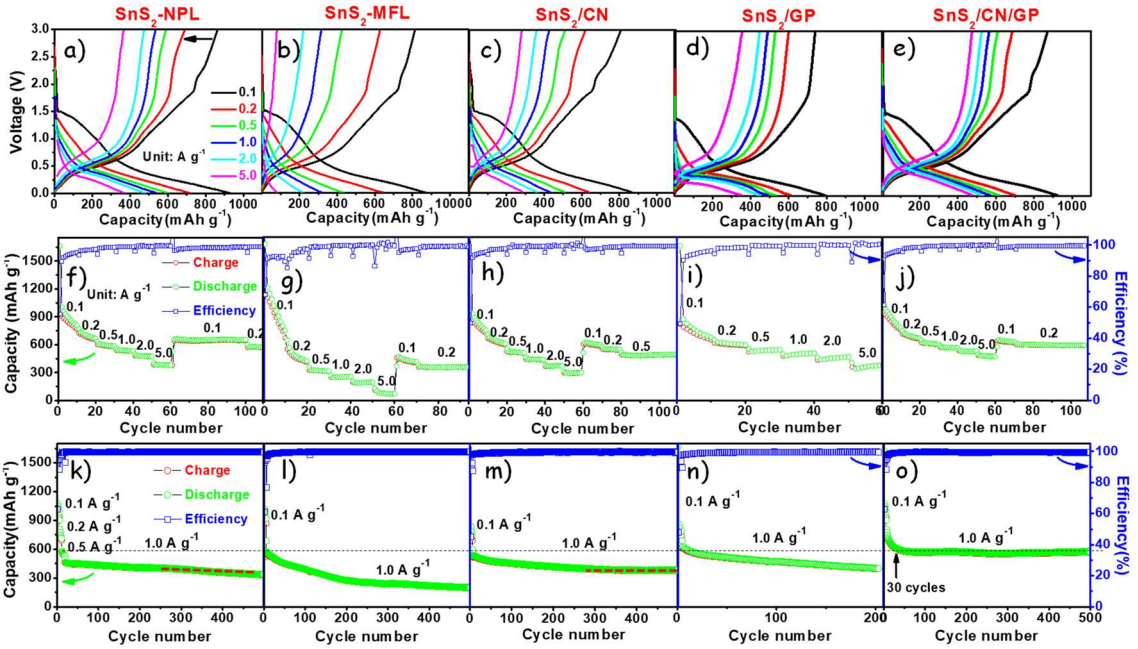

Figure 5.10. Li-ion storage performance of different electrodes as displayed on the top. (a-e) Rate performance and (f-j) charge-discharge curves at 0.1, 0.2, 0.5, 1.0, 2.0 and 5.0 A g^{-1}. (k-o) Charge-discharge capacity and related efficiency curves over 500 cycles at a current density of 1.0 A g^{-1}.

Figure 5.11a,b displays CV data obtained from electrodes based on SnS_2/CN and SnS_2/CN/GP nanocomposites. The first CV cycle of SnS_2/CN and SnS_2/CN/GP electrodes displayed similar CV profiles as those obtained for SnS_2 electrodes, except that SnS_2/CN/GP electrodes showed stronger intensity peaks related to conversion and alloying reactions, indicating a better cycling performance. Figure 5.11c,d shows the galvanostatic charge-discharge performance of electrodes based on SnS_2/CN and SnS_2/CN/GP in the voltage range of 0.01-3.0 V *vs.* Li^+/Li at a current density of 0.1 A g^{-1} (Figure 5.11c,d). The initial irreversible capacity loss can be ascribed to the formation of the SEI layer.[69,70]

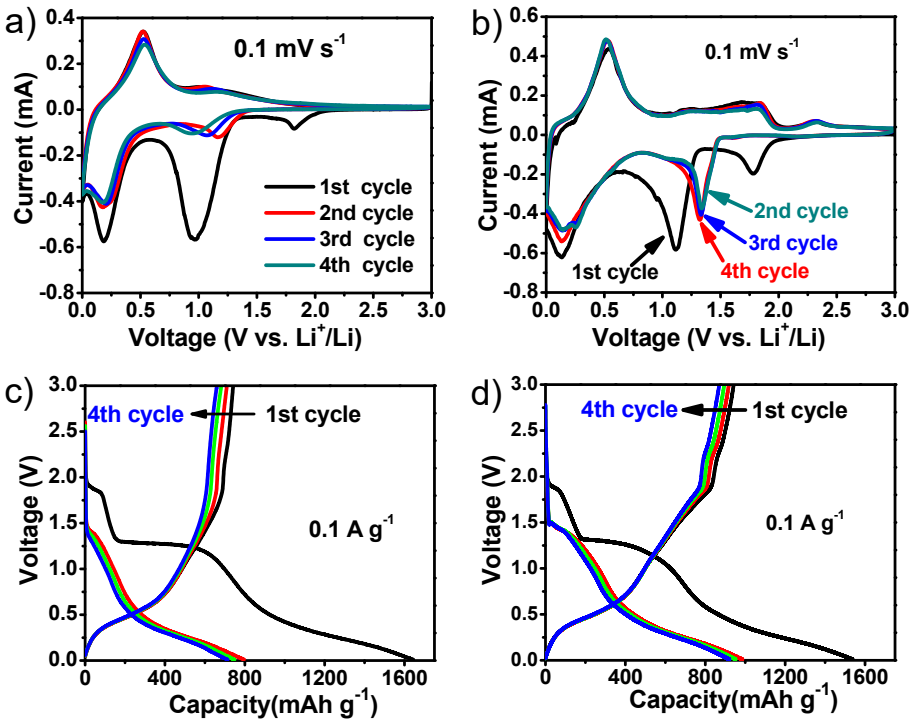

Figure 5.11. Initial four CV cycles obtained from different electrodes of (a) SnS_2/CN; (b) SnS_2/CN/GP in the voltage window 0.01-3.0 V *vs.* Li^+/Li at the same scan rate of 0.1 mV s^{-1}. Initial four galvanostatic charge-discharge curves at 0.1 A g^{-1} for the electrode of (c) SnS_2/CN; (d) SnS_2/CN/GP.

The rate performance, charge-discharge curves and charge-discharge capacity change as a function of the cycle number of electrodes based on SnS_2/CN, SnS_2/GP and SnS_2/CN/GP were further analyzed to assess their activity and stability (Figure 5.10). SnS_2/CN/GP electrodes provided better rate capacity performance than SnS_2/CN, SnS_2/GP and SnS_2 electrodes, with reversible capacities moderately decreasing as the current densities increased. Namely, SnS_2/CN/GP electrodes delivered a capacity of ~470 mAh g^{-1} after increasing the current density from 0.1 A g^{-1} to 5.0 A g^{-1}, and ~74 % of the initial capacity was recovered when the current density decreased back to 0.1 A g^{-1}. By contrast, SnS_2/CN and SnS_2-NPL electrodes delivered lower capacities of ~280 mAh g^{-1} (~68 % recovery) and ~380 mAh g^{-1} (~59 % recovery), respectively.

The charge-discharge capability of the electrodes based on bare SnS_2 notably decreased with the cycling process, which was attributed to the progressive disconnection of the particles from the current collector associated to the large volume change during Li^+ insertion/deinsertion.[71-73] The poor electrical conductivity of SnS_2 rendered an inhomogeneous reaction with Li^+, resulting in a non-uniform volumetric changes that created additional stress. This stress promoted cracking of the particles and it thus resulted

in a larger degradation of capacity. This drawback was particularly severe at higher current densities of charge-discharge, thus deteriorating the rate performance.[71] On the other hand, the presence of CN allowed to maintain the capacity after activation, which we associated to the role played by CN as spacer to accommodate the volumetric expansion within SnS_2 and to alleviate the detachment of the SnS_2-NPL.[73-75] Besides, the interconnected porous structure of CN could provide continuous paths for Li-ion diffusion to the active material.[75-77]

SnS_2/CN/GP composites demonstrated even better stability towards Li-ion charge-discharge processes, with a capacity of 571 mAh g^{-1} (~99.3 % capacity retention) and 99.4 % coulombic efficiency at 1.0 A g^{-1} for 470 cycles (from 30 cycles to 500 cycles), performing much better than SnS_2, SnS_2/CN and SnS_2/GP electrodes. Focusing on the effect of CN and GP, the SnS_2/CN electrode showed improved cycling stability compared with bare SnS_2-NPL, but the SnS_2/GP electrode showed worse stability. On the other hand, the addition of GP provided a better rate performance and a higher starting capacity than adding CN at a charge-discharge current density of 1 A g^{-1} (Figure 5.10h,i,m,n). We thus attributed the improved charge-discharge performance, especially the capacity stability, to the porous CN preventing SnS_2-NPLs aggregation and the improved charge transport with the incorporation of high electrical conductivity GPs. Besides, the changed SEI interface due to the addition of GP could also contribute.[78,79]

Figure 5.12a displays EIS data obtained from electrodes containing SnS_2-NPLs and SnS_2/CN/GP. Impedance responses were fitted with an equivalent circuit containing a series resistance R_s, an electrode surface resistance R_{surf} composed by the charge transfer resistance R_{ct} and the SEI resistance R_{SEI}, and a constant phase element CPE (Figure 5.12a, inset).[21,80] Fitting results clearly revealed an enhanced charge transfer process on SnS_2/CN/GP electrodes, with a much lower R_{surf}, 110 Ω, when compared with SnS_2, 290.8 Ω. This result was consistent with the faster charge transfer and charge-discharge kinetics.

Figure 5.12b shows the charge-discharge capacity and related efficiency of a SnS_2/CN/GP electrode during long-term charge-discharge cycling at a high current density of 2.0 A g^{-1}. The electrodes displayed an outstanding capacity retention of ~99.7 % and a coulombic efficiency of 99.3 % after 400 charge-discharge cycles (comparing cycles 30th and 430th, Table 5.1). While SnS_2 and SnS_2/CN electrodes displayed a very fast initial capacity decay due to the partially irreversible conversion reaction (equation

5.3),[81,82] the SnS_2/CN/GP electrode exhibited a capacity decay that extended during the initial 30 cycles. According to recent reports, we ascribed this relatively extended decay to the decomposition of the electrolyte catalyzed by GP.[78,79]

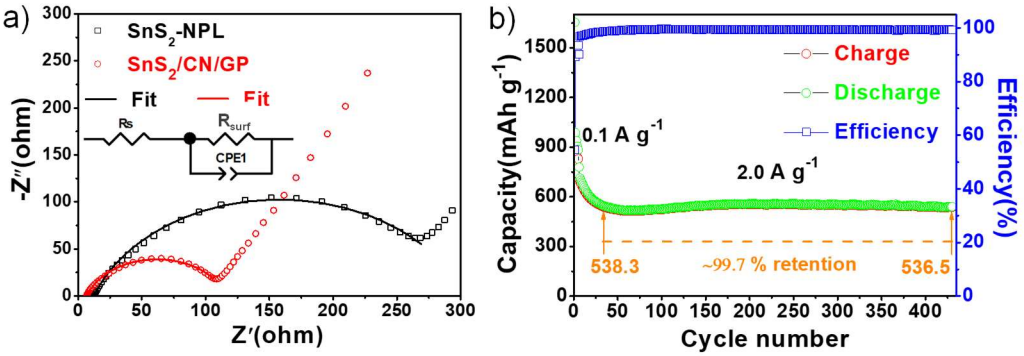

Figure 5.12. (a) Nyquist plots of the EIS data obtained from SnS_2-NPL and SnS_2/CN/GP electrodes. (b) Charge-discharge capacity and related efficiency curves of an SnS_2/CN/GP electrode over 430 cycles at a current density of 2.0 A g^{-1}. The electrode was initially activated at 0.1 A g^{-1} for 5 cycles.

Table 5.1. Comparison of cycling performance of SnS_2/CN/GP with previously reported SnS_2 based materials anodes for LIB

Materials	Performance	Retention	Reference
SnS_2 NPLs	521 mAh g^{-1} after 50 cycles at 100 mA g^{-1}	~90.0 %	*Electrochim. Acta, 2013, 112, 439-447*
SnS_2 flower-like hierarchical structures	549.5 mAh g^{-1} after 100 cycles at 100 mA g^{-1}	60 %	*J. Power Sources, 2013, 239, 89-93*
SnS_2 nanosheets	436.5 mAh g^{-1} after 100 cycles at 100 mA g^{-1}	~55 %	*Electrochim. Acta, 2015, 184, 239-249*
SnS_2@PANI NPLs	731 mAh g^{-1} after 80 cycles at 0.1 A g^{-1}	75.4 %	*J. Mater. Chem. A, 2015, 3, 3659-3666*
SnS_2@nitrogen-doped graphene sheets	914 mAh g^{-1} after 150 cycles at 0.8 A g^{-1}	~74 %	*J. Mater. Chem. A, 2016, 4, 10719-10726*
Tucked flower-like SnS_2/Co_3O_4	715 mAh g^{-1} after 100 cycles at 0.1 A g^{-1}	~72 %	*Electrochim. Acta, 2016, 190, 843-851*
rGO/SnS_2/TiO_2	485 mAh g^{-1} after 200 cycles at 0.5 A g^{-1}	~96 %	*J. Mater. Chem. A, 2017, 5, 25056-25063*
Carbon coated SnS_2 nanoplate	800 mAh g^{-1} after 300 cycles at 0.5 A g^{-1}	~84 %	*ACS Appl. Mater. Inter., 2017, 9, 35880-35887*
Carbon coated SnS_2 nanosheet assemblies	915 mAh g^{-1} after 300 cycles at 1.0 A g^{-1}	~99 %	*J. Mater. Chem. A, 2017, 5, 25618-25624*
MoO_3/SnS_2 core-shell nanowires	504 mAh g^{-1} after 100 cycles at 0.1 A g^{-1}	~52 %	*Phys.Chem.Chem.Phys., 2018, 20, 17171-17179*

SnS_2 nanosheets confined in nitrogen doped graphene	763 mAh g^{-1} after 200 cycles at 0.5 A g^{-1}	~70 %	*Chem. Commun., 2018, 54, 8379-8382*
Graphene@SnS_2 nanocomposites	664 mAh g^{-1} after 200 cycles at 300 mA g^{-1}	-	*ACS Appl. Mater. Interfaces, 2019, 11, 22314-22322*
H-TiO_2@SnS_2@PPy	584.9 mAh g^{-1} after 1000 cycles at 2.0 A g^{-1}	~92.3%	*Angew. Chem. Int. Ed. 2019, 58, 811-815*
SnS_2 nanoflowers @ reduced graphene oxide	525 mAh g^{-1} after 200 cycles at 0.5 C	~100 % (160 cycles)	*J. Alloys Compd, 2019, 794, 285-293*
SnS_2 nanoflower/g-C_3N_4	444.7 mAh g^{-1} after 100 cycles at 100 mA g^{-1}	~70 %	*Electrochim. Acta, 2019, 293, 408-418*
SnS_2/CN/GP	**571 mAh g^{-1} after 470 cycles at 1.0 A g^{-1}; 536.5 mAh g^{-1} after 400 cycles at 2.0 A g^{-1}**	**~99.3 %; ~99.7 %**	**This work**

To understand the reaction kinetics of the SnS_2/CN/GP electrode during charge-discharge cycling, CV measurements under different scan rates in the potential range of 0.01-3.0 V *vs.* Li^+/Li were carried out. As shown in Figure 5.13a, the anodic peak at 0.72 V and cathodic peak at 1.17 V increased with scan rate from 0.1 to 1.0 mV s^{-1}. The measured current (i) should increase with a power of the scan rate (ν): [3,48,83-85]

$$i = a\,\nu^{\,b} \qquad \text{eq. 5.5}$$

$$\log i = b \cdot \log \nu + \log a \qquad \text{eq. 5.6}$$

in which a and b are adjustable constants related to the reaction process. According to previous reports,[3,48,84,86,87] b = 1 corresponds to an ideal capacitive behavior, while b = 0.5 indicates a diffusion-controlled process. Generally, the capacitive behavior is particular attractive, since it is a much faster and stable process to provide relatively good rate performance and long cycle life, compared with the diffusion process.[3] Based on equation 6, the b value could be calculated by a liner fit of log i against log ν, as shown in Figure 5.13b. For SnS_2/CN/GP electrodes, b values of 0.80 and 0.67 were calculated at 0.72 V and 1.17 V, respectively. b values above 0.5 were consistent with a fast kinetics resulting from a significant pseudocapacitive contribution.

Total capacity at a giving scan rate was divided into a diffusion-controlled ($k_1 \nu^{1/2}$) and a capacitor-like ($k_2\nu$) contribution:

$$i\,(V) = k_1 \nu^{1/2} + k_2\nu \qquad \text{eq. 5.7}$$

Thus:

$$i\,(V)/\nu^{1/2} = k_1 + k_2\nu^{1/2} \qquad \text{eq. 5.8}$$

Then, k_1 and k_2 values could be calculated by plotting $i(V)/\nu^{1/2}$ versus $\nu^{1/2}$.[3,48,83,85,88] We took 0.1 V as the interval to calculate k_1 and k_2 in the potential range of 0.01-3.0 V. At each fixed voltage, the sweep rate and the corresponding current from Figure 5.13a were plotted according to equation 5.8. The resulting straight line enabled us to determine k_1 and k_2 for different voltages from the y-axis intercept point and the slope, respectively. Results at two different potentials, 0.5 V and 1.0 V, are plotted in Figure 5.13c. Figure 5.13d displays the $k_2\nu$ contribution at each potential. For different scan rate, different percentages of the red region/total current contribution were calculated, as displayed in Figure 5.13e. Figures 5.13d and 5.13e show the capacitive contribution to the total capacity. It should be noted that this method to determine the k_1 and k_2 values is not precise at the voltages that have the capacitive current as the principal contribution (b ~ 0.8 - 1.0).[89] This explains why the capacitive contribution is slightly higher than 100 % at some voltages in Figure 5.13d, such as at 1.0 V. Very high pseudocapacitive contributions of 65.3 %, 69.4 %, 75.6 %, 82.5 % and 88.8 % at scan rates of 0.1, 0.2, 0.4, 0.7 and 1.0 mV s^{-1}, respectively, were obtained (Figure 5.13e). Electrodes based on SnS_2-NPL, SnS_2-MFL and SnS_2/CN showed lower pseudocapacitive contributions than those of SnS_2/CN/GP electrodes at all scan rates measured (Figure 5.14). The high pesudocapacitance of SnS_2/CN/GP electrodes was in large part related to their large surface areas derived from their hierarchical structure. Besides, the heterojunction between surface SnS and inner SnS_2 could facilitate the charge transfer,[90] accelerating the charge-transfer kinetics and resulting in a better electrochemical performance.[91]

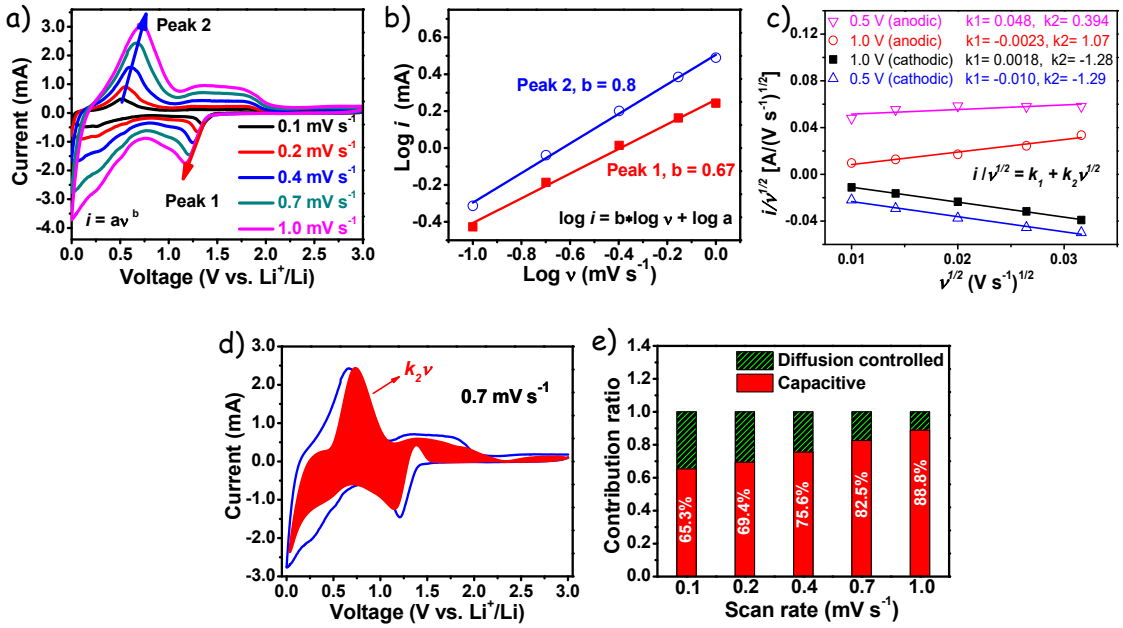

Figure 5.13. Li-ion storage performance of a SnS_2/CN/GP electrode: (a) CV curves at the scan rates of 0.1, 0.2, 0.4, 0.7, and 1.0 mV s^{-1}. (b) Linear fit of the logarithmic dependence between peak current density and scan rate at the anodic peak of 0.72 V and cathodic peak of 1.17 V. (c) Fitted k_1 and k_2 at 0.5 V and 1.0 V using equation 8. (d) Capacitive contribution (red region) to the total current contribution at 0.7 mV s^{-1}. (e) Normalized capacitive and diffusion-controlled contribution at the scan rates of 0.1, 0.2, 0.4, 0.7, and 1.0 mV s^{-1}.

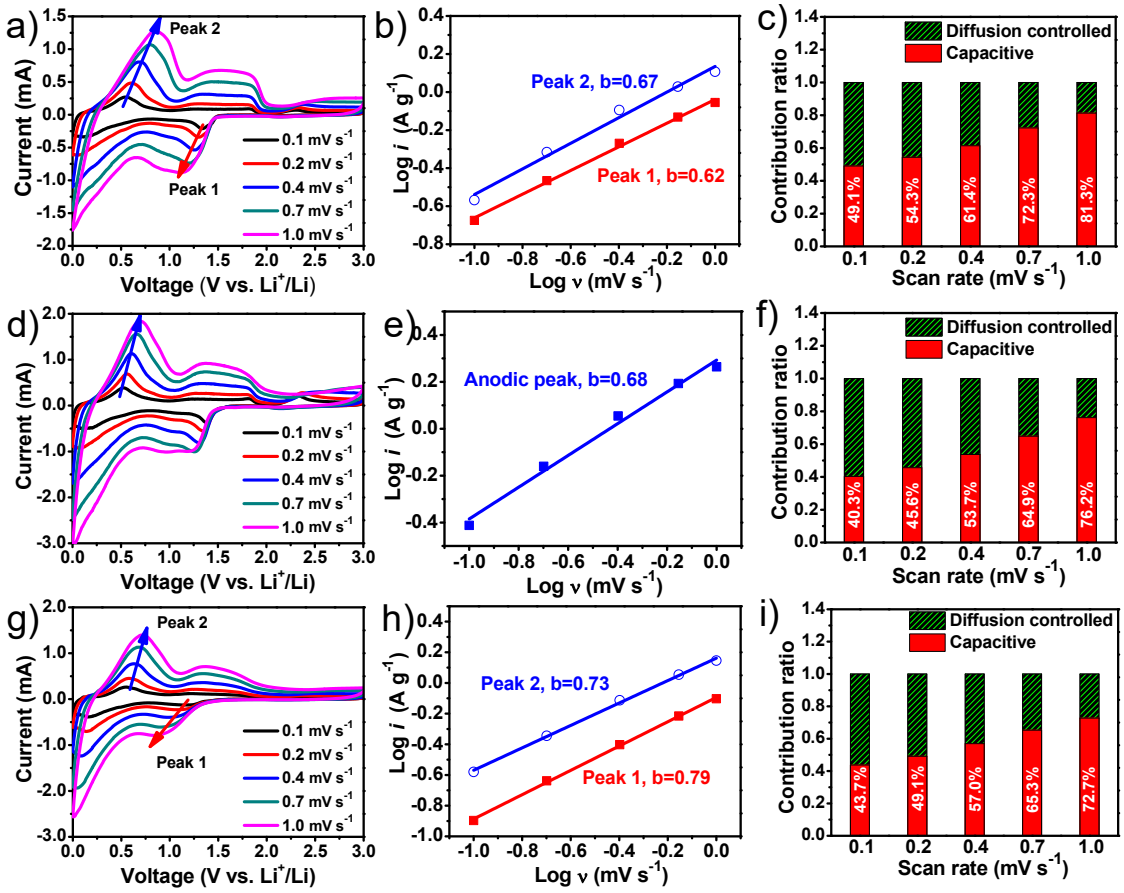

Figure 5.14. Li-ion storage performance of electrode of: (a-c) SnS_2/CN, (d-f) SnS_2-NPL, and (g-i) SnS_2-MFL: (a,d,g) CV curves at the scan rates of 0.1, 0.2, 0.4, 0.7, and 1.0 mV/s; (b,e,h) Logarithmic dependence between peak current density and scan rate at the respective anodic peak and cathodic peak; (c,f,i) Normalized capacitive and diffusion-controlled contribution at the scan rates of 0.1, 0.2, 0.4, 0.7, and 1.0 mV/s.

Overall, based on the aforementioned analyses, the excellent performance of SnS_2/CN/GP anodes in LIBs was attributed to their hierarchical structure, which simultaneously allowed a large dispersion of the nanometric active material, a large porosity for electrolyte diffusion and a high electrical conductivity network for electron injection and extraction: 1) The small and thin SnS_2 NPLs provided more active sites than SnS_2 MFL, and a larger interface with the electrolyte, CN and GP, favoring Li reaction and intercalation kinetics;[92,93] 2) The highly porous and ultrathin CN provided suitable channels for Li-ions to rapidly diffuse through the electrode, and thus facilitate the electrochemical reaction. This effect was particularly important at high charge/discharge current densities; 3) The randomly distributed CN within the SnS_2-NPL matrix acted as "cushion" and "spacer" to buffer the strain from volume changes, preventing the aggregation and detachment of SnS_2 during cycling; 4) GP provided avenues for efficient charge transport.

5.5 Conclusions

We developed a facile strategy to produce hierarchical SnS_2/CN/GP composites using SnS_2-NPL as active materials, porous CN to provide avenues for electrolyte diffusion and ease the volumetric expansion of SnS_2, and GP as "highways" for charge transport. Benefiting from this hierarchical structure and synergistic effects, an efficient ion/charge transportation and excellent lithium storage performance was achieved, with a capacity of 536.5 mAh g^{-1} and retention of ~99.7 % at a current density of 2.0 A g^{-1} after 400 cycles, and a high pseudocapacitance contribution of 88.8 % at a sweep rate of 1.0 mV s^{-1}. The hierarchical architecture here proposed can be used to promote performance in other energy storage devices.

5.6 References

(1) Martinet, S. Nanomaterials for Rechargeable Lithium Batteries. *Nanosci. Technol.* **2016**, *47* (16), 471–512.

(2) Obrovac, M. N.; Chevrier, V. L. Alloy Negative Electrodes for Li-Ion Batteries. *Chem. Rev.* **2014**, *114* (23), 11444–11502.

(3) Li, J.; Xu, X.; Luo, Z.; Zhang, C.; Zuo, Y.; Zhang, T.; Tang, P.; Infante-Carrió, M. F.; Arbiol, J.; Llorca, J.; Liu, J.; Cabot, A. Co–Sn Nanocrystalline Solid Solutions as Anode Materials in Lithium-Ion Batteries with High Pseudocapacitive Contribution. *ChemSusChem* **2019**, *12* (7), 1451–1458.

(4) Ding, L. X.; Li, G. R.; Wang, Z. L.; Liu, Z. Q.; Liu, H.; Tong, Y. X. Porous Ni@Pt Core-Shell Nanotube Array Electrocatalyst with High Activity and Stability for Methanol Oxidation. *Chem. - A Eur. J.* **2012**, *18* (27), 8386–8391.

(5) Kaskhedikar, N. A.; Maier, J. Lithium Storage in Carbon Nanostructures. *Adv. Mater.* **2009**, *21* (25–26), 2664–2680.

(6) Li, X.; Feng, Y.; Li, M.; Li, W.; Wei, H.; Song, D. Smart Hybrids of Zn_2GeO_4 Nanoparticles and Ultrathin G-C_3N_4 Layers: Synergistic Lithium Storage and Excellent Electrochemical Performance. *Adv. Funct. Mater.* **2015**, *25* (44), 6858–6866.

(7) Hu, Y. S.; Demir-Cakan, R.; Titirici, M. M.; Müller, J. O.; Schlögl, R.; Antonietti, M.; Maier, J. Superior Storage Performance of a Si@SiO_x/C Nanocomposite as Anode Material for Lithium-Ion Batteries. *Angew. Chem. Int. Ed.* **2008**, *47* (9), 1645–1649.

(8) Chan, C. K.; Peng, H.; Liu, G.; McIlwrath, K.; Zhang, X. F.; Huggins, R. A.; Cui, Y. High-Performance Lithium Battery Anodes Using Silicon Nanowires. *Nat. Nanotechnol.* **2008**, *3* (1), 31–35.

(9) Wang, X. L.; Han, W. Q.; Chen, H.; Bai, J.; Tyson, T. A.; Yu, X. Q.; Wang, X. J.; Yang, X. Q. Amorphous Hierarchical Porous GeO_x as High-Capacity Anodes for Li Ion Batteries with Very Long Cycling Life. *J. Am. Chem. Soc.* **2011**, *133* (51), 20692–20695.

(10) Kim, H.; Son, Y.; Park, C.; Cho, J.; Choi, H. C. Catalyst-Free Direct Growth of a Single to a Few Layers of Graphene on a Germanium Nanowire for the Anode Material of a Lithium Battery. *Angew. Chem. Int. Ed.* **2013**, *52* (23), 5997–6001.

(11) Guo, W.; Wang, Y.; Li, Q.; Wang, D.; Zhang, F.; Yang, Y.; Yu, Y. SnO_2@C@VO_2 Composite Hollow Nanospheres as an Anode Material for Lithium-Ion Batteries. *ACS Appl. Mater. Interfaces* **2018**, *10* (17), 14993–15000.

(12) Abouali, S.; Akbari Garakani, M.; Kim, J. K. Ultrafine SnO_2 Nanoparticles Encapsulated in Ordered Mesoporous Carbon Framework for Li-Ion Battery Anodes. *Electrochim. Acta* **2018**, *284*, 436–443.

(13) Liu, Y.; Yu, X. Y.; Fang, Y.; Zhu, X.; Bao, J.; Zhou, X.; Lou, X. W. (David). Confining SnS_2 Ultrathin Nanosheets in Hollow Carbon Nanostructures for Efficient Capacitive Sodium Storage. *Joule* **2018**, *2* (4), 725–735.

(14) Wang, Y.; Huang, L.; Li, B.; Shang, J.; Xia, C.; Fan, C.; Deng, H.-X.; Wei, Z.; Li, J. Composition-Tunable 2D $SnSe_{2(1-x)}S_{2x}$ Alloys towards Efficient Bandgap Engineering and High Performance (Opto)Electronics. *J. Mater. Chem. C* **2017**, *5*, 84–90.

(15) Yin, L.; Cheng, R.; Song, Q.; Yang, J.; Kong, X.; Huang, J.; Lin, Y.; Ouyang, H. Construction of Nanoflower SnS_2 Anchored on G-C_3N_4 Nanosheets Composite as Highly Efficient Anode for Lithium Ion Batteries. *Electrochim. Acta* **2019**, *293*, 408–418.

(16) Wang, J. G.; Sun, H.; Liu, H.; Jin, D.; Zhou, R.; Wei, B. Edge-Oriented SnS_2 Nanosheet Arrays on Carbon Paper as Advanced Binder-Free Anodes for Li-Ion and Na-Ion Batteries. *J. Mater. Chem. A* **2017**, *5* (44), 23115–23122.

(17) Cook, J. B.; Kim, H. S.; Lin, T. C.; Lai, C. H.; Dunn, B.; Tolbert, S. H. Pseudocapacitive Charge Storage in Thick Composite MoS_2 Nanocrystal-Based Electrodes. *Adv. Energy Mater.* **2017**, *7* (2), 201601283.

(18) Zhao, Y.; Pang, Q.; Meng, Y.; Gao, Y.; Wang, C.; Liu, B.; Wei, Y.; Du, F.; Chen, G. Self-Assembled CoS Nanoflowers Wrapped in Reduced Graphene Oxides as the High-Performance Anode Materials for Sodium-Ion Batteries. *Chem. - A Eur. J.* **2017**, *23* (53), 13150–13157.

(19) Johny, J.; Sepulveda-Guzman, S.; Krishnan, B.; Avellaneda, D.; Shaji, S. Facile and Fast Synthesis of SnS_2 Nanoparticles by Pulsed Laser Ablation in Liquid. *Appl. Surf. Sci.* **2018**, *435*, 1285–1295.

(20) Fan, L.; Li, X.; Song, X.; Hu, N.; Xiong, D.; Koo, A.; Sun, X. Promising Dual-Doped Graphene Aerogel/SnS_2 Nanocrystal Building High Performance Sodium Ion Batteries. *ACS Appl. Mater. Interfaces* **2018**, *10* (3), 2637–2648.

(21) Zuo, Y.; Liu, Y.; Li, J.; Du, R.; Yu, X.; Xing, C.; Zhang, T.; Yao, L.; Arbiol, J.; Llorca, J.; Sivula, K.; Guijarro, N.; Cabot, A. Solution-Processed Ultrathin SnS_2-Pt Nanoplates for Photoelectrochemical Water Oxidation. *ACS Appl. Mater. Interfaces* **2019**, *11* (7), 6918–6926.

(22) Wu, L.; Zheng, J.; Wang, L.; Xiong, X.; Shao, Y.; Wang, G.; Wang, J. H.; Zhong, S.; Wu, M. PPy-Encapsulated SnS_2 Nanosheets Stabilized by Defects on a TiO_2 Support as a Durable Anode Material for Lithium-Ion Batteries. *Angew. Chem. Int. Ed.* **2019**, *58* (3), 811–815.

(23) Zhao, B.; Chen, F.; Wang, Z.; Huang, S.; Jiang, Y.; Chen, Z. Lithiation-Assisted Exfoliation and Reduction of SnS_2 to SnS Decorated on Lithium-Integrated Graphene for Efficient Energy Storage. *Nanoscale* **2017**, *9* (45), 17922–17932.

(24) Chen, X.; Huang, Y.; Zhang, K.; Feng, X. S.; Wang, M. Synthesis and High-Performance of Carbonaceous Polypyrrole Nanotubes Coated with SnS_2 Nanosheets Anode Materials for Lithium Ion Batteries. *Chem. Eng. J.* **2017**, *330*, 470–479.

(25) Tang, H.; Qi, X.; Han, W.; Ren, L.; Liu, Y.; Wang, X.; Zhong, J. SnS_2 Nanoplates Embedded in 3D Interconnected Graphene Network as Anode Material with Superior Lithium Storage Performance. *Appl. Surf. Sci.* **2015**, *355*, 7–13.

(26) Shang, H.; Zuo, Z.; Li, L.; Wang, F.; Liu, H.; Li, Y.; Li, Y. Ultrathin Graphdiyne Nanosheets Grown In Situ on Copper Nanowires and Their Performance as Lithium-Ion Battery Anodes. *Angew. Chem. Int. Ed.* **2018**, *57* (3), 774–778.

(27) Luo, B.; Hu, Y.; Zhu, X.; Qiu, T.; Zhi, L.; Xiao, M.; Zhang, H.; Zou, M.; Cao, A.; Wang, L. Controllable Growth of SnS_2 Nanostructures on Nanocarbon Surfaces for Lithium-Ion and Sodium-Ion Storage with High Rate Capability. *J. Mater. Chem. A* **2018**, *6* (4), 1462–1472.

(28) Wang, J. G.; Sun, H.; Liu, H.; Jin, D.; Liu, X.; Li, X.; Kang, F. Triaxial Nanocables of Conducting Polypyrrole@SnS_2@Carbon Nanofiber Enabling Significantly Enhanced Li-Ion Storage. *ACS Appl. Mater. Interfaces* **2018**, *10* (16), 13581–13587.

(29) Guan, D.; Li, J.; Gao, X.; Xie, Y.; Yuan, C. Growth Characteristics and Influencing Factors of 3D Hierarchical Flower-like SnS_2 Nanostructures and Their Superior Lithium-Ion Intercalation Performance. *J. Alloys Compd.* **2016**, *658*, 190–197.

(30) Bhaskar, A.; Deepa, M.; Rao, T. N. Tin Disulfide Nanoflowers versus Nanosheets as Anodes in Lithium-Ion Batteries: How the Nanostructure Controls Performance. *Electrochim. Acta* **2015**, *184*, 239–249.

(31) Du, Y.; Yin, Z.; Rui, X.; Zeng, Z.; Wu, X. J.; Liu, J.; Zhu, Y.; Zhu, J.; Huang, X.; Yan, Q.; Zhang, H. A Facile, Relative Green, and Inexpensive Synthetic Approach toward Large-Scale Production of SnS_2 nanoplates for High-Performance Lithium-Ion Batteries. *Nanoscale* **2013**, *5* (4), 1456–1459.

(32) Wang, Y.; Li, H.; He, P.; Hosono, E.; Zhou, H. Nano Active Materials for Lithium-Ion Batteries. *Nanoscale* **2010**, *2* (8), 1294–1305.

(33) Tang, J.; Zhong, X.; Li, H.; Li, Y.; Pan, F.; Xu, B. In-Situ and Selectively Laser Reduced Graphene Oxide Sheets as Excellent Conductive Additive for High Rate Capability $LiFePO_4$ Lithium Ion Batteries. *J. Power Sources* **2019**, *412*, 677–682.

(34) Yao, W.; Wu, S.; Zhan, L.; Wang, Y. Two-Dimensional Porous Carbon-Coated Sandwich-like Mesoporous SnO_2/Graphene/Mesoporous SnO_2 Nanosheets towards High-Rate and Long Cycle Life Lithium-Ion Batteries. *Chem. Eng. J.* **2019**, *361*, 329–341.

(35) Guo, A.; Chen, E.; Wygant, B. R.; Heller, A.; Mullins, C. B. Lead Oxide Microparticles Coated by Ethylenediamine-Cross-Linked Graphene Oxide for Lithium Ion Battery Anodes. *ACS Appl. Energy Mater.* **2019**, *2* (5), 3017–3020.

(36) Zhang, L.; Huang, Y.; Zhang, Y.; Fan, W.; Liu, T. Three-Dimensional Nanoporous Graphene-Carbon Nanotube Hybrid Frameworks for Confinement of SnS_2 Nanosheets: Flexible and Binder-Free Papers with Highly Reversible Lithium Storage. *ACS Appl. Mater. Interfaces* **2015**, *7* (50), 27823–27830.

(37) Chang, K.; Wang, Z.; Huang, G.; Li, H.; Chen, W.; Lee, J. Y. Few-Layer SnS_2/Graphene Hybrid with Exceptional Electrochemical Performance as Lithium-Ion Battery Anode. *J. Power Sources* **2012**, *201*, 259–266.

(38) Cai, D.; Wang, S.; Lian, P.; Zhu, X.; Li, D.; Yang, W.; Wang, H. Superhigh Capacity and Rate Capability of High-Level Nitrogen-Doped Graphene Sheets as Anode Materials for Lithium-Ion Batteries. *Electrochim. Acta* **2013**, *90*, 492–497.

(39) Wu, Z. S.; Ren, W.; Xu, L.; Li, F.; Cheng, H. M. Doped Graphene Sheets as Anode Materials with Superhigh Rate and Large Capacity for Lithium Ion Batteries. *ACS Nano* **2011**, 5, 5463–5471.

(40) Yoo, E.; Nakamura, J.; Zhou, H. N-Doped Graphene Nanosheets for Li-Air Fuel Cells under Acidic Conditions. *Energy Environ. Sci.* **2012**, *5* (5), 6928–6932.

(41) Fu, Y.; Zhu, J.; Hu, C.; Wu, X.; Wang, X. Covalently Coupled Hybrid of Graphitic Carbon Nitride with Reduced Graphene Oxide as a Superior Performance Lithium-Ion Battery Anode. *Nanoscale* **2014**, *6* (21), 12555–12564.

(42) Zhang, Y.; Thomas, A.; Antonietti, M.; Wang, X. Activation of Carbon Nitride Solids by Protonation: Morphology Changes, Enhanced Ionic Conductivity, and Photoconduction Experiments. *J. Am. Chem. Soc.* **2009**, *131* (1), 50–51.

(43) Zhu, J.; Xiao, P.; Li, H.; Carabineiro, S. A. C. Graphitic Carbon Nitride: Synthesis, Properties, and Applications in Catalysis. *ACS Appl. Mater. Interfaces* **2014**, *6* (19), 16449–16465.

(44) Ong, W. J.; Tan, L. L.; Ng, Y. H.; Yong, S. T.; Chai, S. P. Graphitic Carbon Nitride (g-C_3N_4)-Based Photocatalysts for Artificial Photosynthesis and Environmental Remediation: Are We a Step Closer to Achieving Sustainability? *Chem. Rev.* **2016**, *116* (12), 7159–7329.

(45) Fan, X.; Zhang, L.; Cheng, R.; Wang, M.; Li, M.; Zhou, Y.; Shi, J. Construction of Graphitic C_3N_4-Based Intramolecular Donor-Acceptor Conjugated Copolymers for Photocatalytic Hydrogen Evolution. *ACS Catal.* **2015**, *5* (9), 5008–5015.

(46) An, X.; Hu, C.; Lan, H.; Liu, H.; Qu, J. Strongly Coupled Metal Oxide/Reassembled Carbon Nitride/Co-Pi Heterostructures for Efficient Photoelectrochemical Water Splitting. *ACS Appl. Mater. Interfaces* **2018**, *10* (7), 6424–6432.

(47) Zheng, Y.; Liu, J.; Liang, J.; Jaroniec, M.; Qiao, S. Z. Graphitic Carbon Nitride Materials: Controllable Synthesis and Applications in Fuel Cells and Photocatalysis. *Energy Environ. Sci*. **2012**, *5*, 6717–6731.

(48) Li, J.; Xu, X.; Luo, Z.; Zhang, C.; Yu, X.; Zuo, Y.; Zhang, T.; Tang, P.; Arbiol, J.; Llorca, J.; Liu, J.; Cabot, A. Compositionally Tuned Ni_xSn Alloys as Anode Materials for Lithium-Ion and Sodium-Ion Batteries with a High Pseudocapacitive Contribution. *Electrochim. Acta* **2019**, *304*, 246–254.

(49) He, M.; Walter, M.; Kravchyk, K. V.; Erni, R.; Widmer, R.; Kovalenko, M. V. Monodisperse SnSb Nanocrystals for Li-Ion and Na-Ion Battery Anodes: Synergy and Dissonance between Sn and Sb. *Nanoscale* **2015**, *7* (2), 455–459.

(50) Mei, L.; Xu, C.; Yang, T.; Ma, J.; Chen, L.; Li, Q.; Wang, T. Superior Electrochemical Performance of Ultrasmall SnS_2 nanocrystals Decorated on Flexible RGO in Lithium-Ion Batteries. *J. Mater. Chem. A* **2013**, *1*, 8658–8664.

(51) Sun, W.; Rui, X.; Yang, D.; Sun, Z.; Li, B.; Zhang, W.; Zong, Y.; Madhavi, S.; Dou, S.; Yan, Q. Two-Dimensional Tin Disulfide Nanosheets for Enhanced Sodium Storage. *ACS Nano* **2015**, *9* (11), 11371–11381.

(52) Yin, L.; Cheng, R.; Song, Q.; Yang, J.; Kong, X.; Huang, J.; Lin, Y.; Ouyang, H. Construction of Nanoflower SnS_2 Anchored on G-C_3N_4 Nanosheets Composite as Highly Efficient Anode for Lithium Ion Batteries. *Electrochim. Acta* **2019**, *293*, 408–418.

(53) Rauf, A.; Arif Sher Shah, M. S.; Lee, J. Y.; Chung, C. H.; Bae, J. W.; Yoo, P. J. Non-Stoichiometric SnS Microspheres with Highly Enhanced Photoreduction Efficiency for Cr(VI) Ions. *RSC Adv.* **2017**, *7* (49), 30533–30541.

(54) Choi, H.; Lee, J.; Shin, S.; Lee, J.; Lee, S.; Park, H.; Kwon, S.; Lee, N.; Bang, M.; Lee, S. B.; Jeon, H. Fabrication of High Crystalline SnS and SnS_2 Thin Films, and Their Switching Device Characteristics. *Nanotechnology* **2018**, *29* (21), 215201

(55) Zheng, P.; Dai, Z.; Zhang, Y.; Dinh, K. N.; Zheng, Y.; Fan, H.; Yang, J.; Dangol, R.; Li, B.; Zong, Y.; Yan, Q.; Liu, X. Scalable Synthesis of SnS_2/S-Doped Graphene Composites for Superior Li/Na-Ion Batteries. *Nanoscale* **2017**, *9* (39), 14820–14825.

(56) Cao, S.; Yu, J. G-C_3N_4-Based Photocatalysts for Hydrogen Generation. *Journal of Physical Chemistry Letters*. **2014**, *5,* 2101–2107.

(57) Zhang, Z.; Huang, J.; Zhang, M.; Yuan, Q.; Dong, B. Ultrathin Hexagonal SnS_2 Nanosheets Coupled with G-C_3N_4 Nanosheets as 2D/2D Heterojunction Photocatalysts toward High Photocatalytic Activity. *Appl. Catal. B Environ.* **2015**, *163*, 298–305.

(58) Jing, L.; Xu, Y.; Chen, Z.; He, M.; Xie, M.; Liu, J.; Xu, H.; Huang, S.; Li, H. Different Morphologies of SnS_2 Supported on 2D G-C_3N_4 for Excellent and Stable Visible Light Photocatalytic Hydrogen Generation. *ACS Sustain. Chem. Eng.* **2018**, *6* (4), 5132–5141.

(59) Wang, G.; Peng, J.; Zhang, L.; Zhang, J.; Dai, B.; Zhu, M.; Xia, L.; Yu, F. Two-Dimensional SnS_2@PANI Nanoplates with High Capacity and Excellent Stability for Lithium-Ion Batteries. *J. Mater. Chem. A* **2015**, *3* (7), 3659–3666.

(60) Jiang, Y.; Feng, Y.; Xi, B.; Kai, S.; Mi, K.; Feng, J.; Zhang, J.; Xiong, S. Ultrasmall SnS_2 Nanoparticles Anchored on Well-Distributed Nitrogen-Doped Graphene Sheets for Li-Ion and Na-Ion Batteries. *J. Mater. Chem. A* **2016**, *4* (27), 10719–10726.

(61) Luo, B.; Hu, Y.; Zhu, X.; Qiu, T.; Zhi, L.; Xiao, M.; Zhang, H.; Zou, M.; Cao, A.; Wang, L. Controllable Growth of SnS_2 Nanostructures on Nanocarbon Surfaces for Lithium-Ion and Sodium-Ion Storage with High Rate Capability. *J. Mater. Chem. A* **2018**, *6* (4), 1462–1472.

(62) Wang, J. G.; Sun, H.; Liu, H.; Jin, D.; Zhou, R.; Wei, B. Edge-Oriented SnS_2 Nanosheet Arrays on Carbon Paper as Advanced Binder-Free Anodes for Li-Ion and Na-Ion Batteries. *J. Mater. Chem. A* **2017**, *5* (44), 23115–23122.

(63) Sher Shah, M. S. A.; Park, A. R.; Rauf, A.; Hong, S. H.; Choi, Y.; Park, J.; Kim, J.; Kim, W. J.; Yoo, P. J. Highly Interdigitated and Porous Architected Ternary Composite of SnS_2 , g-C_3N_4, and Reduced Graphene Oxide (RGO) as High Performance Lithium Ion Battery Anodes. *RSC Adv.* **2017**, *7* (6), 3125–3135.

(64) Bhaskar, A.; Deepa, M.; Rao, T. N. Tin Disulfide Nanoflowers versus Nanosheets as Anodes in Lithium-Ion Batteries: How the Nanostructure Controls Performance. *Electrochim. Acta* **2015**, *184*, 239–249.

(65) Zai, J.; Wang, K.; Su, Y.; Qian, X.; Chen, J. High Stability and Superior Rate Capability of Three-Dimensional Hierarchical SnS_2 Microspheres as Anode Material in Lithium Ion Batteries. *J. Power Sources* **2011**, *196* (7), 3650–3654.

(66) Kim, T. J.; Kim, C.; Son, D.; Choi, M.; Park, B. Novel SnS_2-Nanosheet Anodes for Lithium-Ion Batteries. *J. Power Sources* **2007**, *167* (2), 529–535.

(67) Song, M. K.; Zhang, Y.; Cairns, E. J. A Long-Life, High-Rate Lithium/Sulfur Cell: A Multifaceted Approach to Enhancing Cell Performance. *Nano Lett.* **2013**, *13* (12), 5891–5899.

(68) Ji, X.; Evers, S.; Black, R.; Nazar, L. F. Stabilizing Lithium-Sulphur Cathodes Using Polysulphide Reservoirs. *Nat. Commun.* **2011**, *2* (1), 325.

(69) Liu, Y.; Yu, X. Y.; Fang, Y.; Zhu, X.; Bao, J.; Zhou, X.; Lou, X. W. (David). Confining SnS_2 Ultrathin Nanosheets in Hollow Carbon Nanostructures for Efficient Capacitive Sodium Storage. *Joule* **2018**, *2* (4), 725–735.

(70) Zhou, X.; Yu, L.; Yu, X. Y.; Lou, X. W. D. Encapsulating Sn Nanoparticles in Amorphous Carbon Nanotubes for Enhanced Lithium Storage Properties. *Adv. Energy Mater.* **2016**, *6* (22), 1601177.

(71) Zhang, Z.; Zhao, H.; Du, Z.; Chang, X.; Zhao, L.; Du, X.; Li, Z.; Teng, Y.; Fang, J.; Świerczek, K. (101) Plane-Oriented SnS_2 Nanoplates with Carbon Coating: A High-Rate and Cycle-Stable Anode Material for Lithium Ion Batteries. *ACS Appl. Mater. Interfaces* **2017**, *9* (41), 35880–35887.

(72) Feng, L. L.; Yu, G.; Wu, Y.; Li, G. D.; Li, H.; Sun, Y.; Asefa, T.; Chen, W.; Zou, X. High-Index Faceted Ni_3S_2 Nanosheet Arrays as Highly Active and Ultrastable Electrocatalysts for Water Splitting. *J. Am. Chem. Soc.* **2015**, *137* (44), 14023–14026.

(73) Zhang, L.; Huang, Y.; Zhang, Y.; Fan, W.; Liu, T. Three-Dimensional Nanoporous Graphene-Carbon Nanotube Hybrid Frameworks for Confinement of SnS_2 Nanosheets: Flexible and Binder-Free Papers with Highly Reversible Lithium Storage. *ACS Appl. Mater. Interfaces* **2015**, *7* (50), 27823–27830.

(74) Li, X.; Feng, Y.; Li, M.; Li, W.; Wei, H.; Song, D. Smart Hybrids of Zn_2GeO_4 Nanoparticles and Ultrathin G-C_3N_4 Layers: Synergistic Lithium Storage and Excellent Electrochemical Performance. *Adv. Funct. Mater.* **2015**, *25* (44), 6858–6866.

(75) Shi, M.; Wu, T.; Song, X.; Liu, J.; Zhao, L.; Zhang, P.; Gao, L. Active Fe_2O_3 Nanoparticles Encapsulated in Porous G-C_3N_4/Graphene Sandwich-Type Nanosheets as a Superior Anode for High-Performance Lithium-Ion Batteries. *J. Mater. Chem. A* **2016**, *4* (27), 10666–10672.

(76) Zhao, Z.; Sun, Y.; Dong, F. Graphitic Carbon Nitride Based Nanocomposites: A Review. *Nanoscale* **2015**, *7* (1), 15–37.

(77) Duan, J.; Chen, S.; Jaroniec, M.; Qiao, S. Z. Porous C_3N_4 Nanolayers@n-Graphene Films as Catalyst Electrodes for Highly Efficient Hydrogen Evolution. *ACS Nano* **2015**, *9* (1), 931–940.

(78) Liu, W; Xia, Y.; Wang, W.; Wang, Y.; Jin, J.; Chen, Y.; Paek, E.; Mitlin, D. Pristine or Highly Defective? Understanding the Role of Graphene Structure for Stable Lithium Metal Plating, *Adv. Energy Mater*. **2019**, *9,* 1802918.

(79) Liu, W.; Li, H.; Jin, J.; Wang, Y.; Zhang, Z.; Chen, Z.; Wang, Q.; Chen, Y.; Paek, E.; Mitlin, D. Synergy of Epoxy Chemical Tethers and Defect-Free Graphene in Enabling Stable Lithium Cycling of Silicon Nanoparticles, *Angew. Chem. Int. Ed*. **2019**, *58*, 16743-16753.

(80) Zuo, Y.; Liu, Y.; Li, J.; Du, R.; Han, X.; Zhang, T.; Arbiol, J.; Divins, N. J.; Llorca, J.; Guijarro, N.; Sivula, K.; Cabot, A. In Situ Electrochemical Oxidation of Cu_2S into CuO Nanowires as a Durable and Efficient Electrocatalyst for Oxygen Evolution Reaction. *Chem. Mater*. **2019**, *31*, 7732-7743.

(81) Wei, E.; Jia, F. F.; Wang, K. F.; Qu, P. SnS_2/graphene nanocomposite: a high rate anode material for lithium ion battery. *Chinese Chem. Lett.* **2017**, *28*, 324–328.

(82) Yin, K.; Zhang, M.; Hood, Z. D.; Pan, J.; Meng, Y. S.; Chi, M. Self-Assembled Framework Formed During Lithiation of SnS_2 Nanoplates Revealed by In Situ Electron Microscopy. *Accounts Chem. Res.* **2017**, *50*, 1513–1520.

(83) Augustyn, V.; Simon, P.; Dunn, B. Pseudocapacitive Oxide Materials for High-Rate Electrochemical Energy Storage. *Energy Environ. Sci*. **2014**, *7*, 1597–1614.

(84) Yang, L.; Li, X.; He, S.; Du, G.; Yu, X.; Liu, J.; Gao, Q.; Hu, R.; Zhu, M. Mesoporous Mo_2C/N-Doped Carbon Heteronanowires as High-Rate and Long-Life Anode Materials for Li-Ion Batteries. *J. Mater. Chem. A* **2016**, *4* (28), 10842–10849.

(85) Xu, X.; Liu, J.; Liu, Z.; Shen, J.; Hu, R.; Liu, J.; Ouyang, L.; Zhang, L.; Zhu, M. Robust Pitaya-Structured Pyrite as High Energy Density Cathode for High-Rate Lithium Batteries. *ACS Nano* **2017**, *11* (9), 9033–9040.

(86) Xu, X.; Liu, J.; Liu, J.; Ouyang, L.; Hu, R.; Wang, H.; Yang, L.; Zhu, M. A General Metal-Organic Framework (MOF)-Derived Selenidation Strategy for In Situ Carbon-Encapsulated Metal Selenides as High-Rate Anodes for Na-Ion Batteries. *Adv. Funct. Mater.* **2018**, *28* (16), 1707573.

(87) Liu, T.-C. Behavior of Molybdenum Nitrides as Materials for Electrochemical Capacitors. *J. Electrochem. Soc.* **1998**, *145* (6), 1882.

(88) Zhang, K.; Park, M.; Zhou, L.; Lee, G. H.; Shin, J.; Hu, Z.; Chou, S. L.; Chen, J.; Kang, Y. M. Cobalt-Doped FeS_2 Nanospheres with Complete Solid Solubility as a High-Performance Anode Material for Sodium-Ion Batteries. *Angew. Chem. Int. Ed.* **2016**, *55* (41), 12822–12826.

(89) Wang, J.; Polleux, J.; Lim, J.; Dunn, B. Pseudocapacitive Contributions to Electrochemical Energy Storage in TiO_2 (Anatase), *J. Phys. Chem. C*, **2017**, *111* (40), 14925-14931.

(90) Sun, Q.; Xie, J. X.; Hao, J. Y.; Zheng, S. L.; Wang, P.; Wang, T. T.; Fang, H. T.; Wang, Y. SnS_2/SnS p–n heterojunctions with an accumulation layer for ultrasensitive roomtemperature NO_2 detection, *Nanoscale*, **2019**, *11*, 13741–13749.

(91) Hu. M. X.; Zhang, H. W.; Yang, L.; Lv, R. T. Ultrahigh rate sodium-ion storage of SnS/SnS_2 heterostructures anchored on S-doped reduced graphene oxide by ion-assisted growth, *Carbon*, **2019**, *143*, 21-29.

(92) Liu, S.; Lu, X.; Xie, J.; Cao, G.; Zhu, T.; Zhao, X. Preferential C-Axis Orientation of Ultrathin SnS_2 Nanoplates on Graphene as High-Performance Anode for Li-Ion Batteries. *ACS Appl. Mater. Interfaces* **2013**, *5* (5), 1588–1595.

(93) Seo, J. W.; Jang, J. T.; Park, S. W.; Kim, C.; Park, B.; Cheon, J. Two-Dimensional SnS_2 Nanoplates with Extraordinary High Discharge Capacity for Lithium Ion Batteries. *Adv. Mater.* **2008**, *20* (22), 4269–4273.

Results

In this thesis, an *in-situ* synthesis method was applied to prepare nanostructured Cu_2S arrays on metallic copper substrate, a solution-based colloidal synthesis method was used to produce nanostructured SnS_2 NPs with plate- and flower-like morphology, and an amine-thiol dissolution-recovery process was applied to produce nanostructured SnS_2 coating layers with tremella-like morphology. The energy-related applications such as electrochemical water splitting, photoelectrochemical water splitting and lithium-ion storage have been evaluated accordingly using the produced materials. The main results are:

1) Nanostructured Cu_2S nanorod arrays was *in-situ* produced on the surface of copper mesh (CM). We learned that the Cu_2S/CM was *in-situ* changed to CuO/CM during the OER via $Cu(OH)_2$ intermediate, and the chemical, structural and morphological transformation has been characterized. Electrochemical OER activity was tested, and the results showed that Cu_2S-derived CuO/CM displayed enhanced performance than its precursor $Cu(OH)_2$/CM and CuO/CM-AN directly obtained from the $Cu(OH)_2$/CM annealing, in terms of both activity and stability. Copper foam (CF) can be introduced to replace CM and the Cu_2S-derived CuO/CF displayed an overpotential of 286 mV to deliver a geometric current density of 10 mA/cm^2, well above those of most Cu-based OER electrocatalysts reported previously.

2) Nanostructured SnS_2-Pt heterostructure was produced for photoelectrochemical water splitting. We detailed the preparation of ultrathin SnS_2 nanoplates (NPLs) through a hot-injection process, during which the roles of surfactant OAm and OAc were investigated. Subsequently, metallic Pt nanoparticles (NPs) were uniformly deposited on the SnS_2 surface via an *in-situ* reduction method. PEC measurements demonstrated that optimized SnS_2-Pt photoanodes showed significantly enhanced PEC current response under simulated sunlight compared to bare SnS_2 NPLs. Mott-Schottky analysis and PEC impedance spectroscopy (PEIS) were used to analyze in more detail the effect of Pt on the PEC performance.

3) Nanostructured tremella-like SnS_2 coating layers based on an amine-thiol co-solvent was produced. The ratios of amine/thiol, Sn/S, and the reaction conditions were

systematically investigated. A loss of sulfur in the H_2S gas form during dissolution was identified as the reason behind the presence of SnS impurities in inks produced using too long dissolution time. This molecular ink could be applied to produce planar and conformal SnS_2 nanostructured layer on conductive substrates like FTO, stainless steel and carbon cloth. The produced SnS_2/FTO photoanodes were evaluated as an example and outstanding photocurrent densities were seen under simulated solar light illumination. Besides, SnS_2/rGO composites, $SnS_{2-x}Se_x$ and even phase-pure $SnSe_2$ could be easily synthesized using the same strategy by simply introducing GO and Se powder in the initial precursor solution. Finally, the potential of this molecular precursor ink to produce gram scale amounts of unsupported SnS_2 is investigated.

4) Nanostructured hierarchical SnS_2/g-C_3N_4/graphite (SnS_2/CN/GP) composites were produced using one-pot hot-injection approach. First, SnS_2 nanostructures with different morphologies were tested, to learn that thin SnS_2-NPLs provide the highest performances towards LIB application. Such hierarchical SnS_2/CN/GP composites, using SnS_2-NPL as active materials, porous CN to provide avenues for electrolyte diffusion and ease the volumetric expansion of SnS_2, and GP as "highways" for charge transport, displayed excellent rate capabilities (536.5 mAh g^{-1} at 2.0 A g^{-1}) and an outstanding stability (~99.7 % retention after 400 cycles), which are partially associated with a high pseudocapacitance contribution (88.8 % at 1.0 mV s^{-1}). The excellent electrochemical properties of these nanocomposites can be ascribed to the synergy created between the three components.

Discussion of Results

As the best solution to relieve the increasing energy crisis, the exploitation on renewable energy sources, such as wind and solar energy, has significantly caught the attention of scientists. The main difficulty within the direct application of renewable energy sources is the intermittence issue. Hence, to store the renewable energy directly or the surplus energy, mainly produced as electricity from renewable energy sources, into chemical fuels, such as H_2, or batteries and then convert it back when needed in future becomes really meaningful.

To convert the renewable energy into stable chemical fuels or to store it in batteries, we need suitable materials to efficiently perform the electrochemical energy conversion processes. These materials need to be based on abundant elements and cost effective because they are going to be applied to very widely deployed technologies. They also need to be stable, have a notable electrical conductivity and a high surface area to interact with the media, and in some particular technologies need to show catalytic properties and have a proper band gap to harvest solar energy.

Noble metals are widely used as catalysts in some applications due to their excellent activity. Nevertheless, the rare and expensive feature has limited their direct application in industry. As other metals generally are not stable under operation conditions, the stable metal oxides have been selected in some cases. However, metal oxides generally demonstrate too low electrical conductivities due to low mobilities associated to their relatively high bond ionicity. Besides, metal oxides generally possess too large band gaps to absorb the main part of the solar spectrum, demonstrating less feasibility as solar photocatalysts. Last but not the least, metal oxides are difficult to synthesize with controlled parameters at the nanoscale, indicating less processability in reactions related to size/shape-dependence.

Metal chalcogenides may be an excellent alternative to metals and metal oxides. Compared with metal oxides, their more covalent bonds provide higher charge carrier mobilities, and thus better electrical conductivities, and lower band gaps for solar energy conversion. Among chalcogens, sulfur is the most abundant and low cost and metal sulfides are more stable than metal selenides and tellurides, although not fully stable as

we have seen during this thesis. In terms of the metal, copper is very interesting and a good example to illustrate the group of transition metal sulfides. Beside transition metals, Sn is an excellent element to illustrate the other metals. The single metal sulfides may demonstrate limited/unsatisfied performance towards electrochemical energy conversion processes in many cases. For this reason, rational strategies/treatments should be adopted to optimize their performances towards the respective applications undertaken, as illustrated by the results in this thesis.

The results section started by presenting a new method to produce high efficiency OER catalyst based on suitable metal sulfides. As shown in the thesis, the as-synthesized Cu_2S was transformed into CuO during the OER operation via an intermediate of $Cu(OH)_2$. This transformation happened due to the Cu_2S not being thermodynamic stable compared to CuO. The *in-situ* transformation of catalyst during electrocatalytic applications has been reported in some previous works, not only limited to OER process, but also within other electrochemical reactions where high positive/negative potentials are applied, such as HER, CO_2 reduction, methanol oxidation reaction, *etc*. Generally, the *in-situ* transformation is always treated as a phenomenon along with the reaction processes, and thus its merit for synthesis has been underestimated, and even disregarded in most recent reports. The key contribution of this work presented in the thesis is that the advantage of the *in-situ* transformation could be taken to produce high-performed OER catalysts, as shown in this work that the CuO obtained via the *in-situ* transformation demonstrated much better performance comparing to the directly produced CuO. The enhanced activity was mainly ascribed to the much larger electrochemical surface area. Besides, the improved adhesion of the *in-situ* transformed layer on Cu substrate, and the presence of additional oxidized sulfate on the catalyst surface could also contribute. Based on this work, OER catalysts derived from other metal sulfides, such as NiS, CoS, SnS, *etc* are interesting to exploit.

Metal sulfides are also excellent candidates to harvest and exploit solar energy, which is one of the most important renewable energy sources. In this direction, nanostructured SnS_2 nanoplate (NPL) and microflower (MFL) with a suitable band gap of around 2.2 eV were produced using a colloidal hot-injection approach. Ultrathin SnS_2-NPL was selected to be the investigation target, taking into account that thin SnS_2 nanosheets with exposed (001) facets display excellent photocatalytic activities as

reported previously. This bare SnS_2-NPL was deposited onto pre-cleaned FTO glass after suitable ligand removal treatment (to promote an efficient transport of charge carriers), and tested for PEC water oxidation. However, the performance was not outstanding, with a current density of 18 $\mu A/cm^2$. This unsatisfying performance was ascribed to the fast recombination of electron-hole excited on the SnS_2-NPL surface by simulated sunlight. To improve the system, metallic Pt nanodomains were *in-situ* grown on the surface of SnS_2-NPL. The optimal amount of Pt was SnS_2-Pt-2.9 resulting in the best-performing photoanode (112 $\mu A/cm^2$). This high performance was ascribed to a useful semiconductor-noble metal synergetic effect through an efficient charge transfer of the photogenerated carriers from the semiconductor to the metal to promote solar energy conversion. No transformation/change on SnS_2 has been found using characterizations of XPS and XRD after long-term test, which can be due to the potential applied (1.23 V *vs* RHE) and/or photocurrent generated not being high enough. This work suggests that a new strategy, capable of decoupling both particle size and coverage during the co-catalyst deposition, would be essential to further enhance the performance of this system.

Similarly, this strategy can be also applied to design anode materials towards Li-ion storage, except that the co-catalyst needs to be changed to other proper components accordingly. As is known, Sn contained SnS_2 could be a promising candidate of Li-ion battery (LIB) anodes apart from being a photocatalyst. Besides, the structure at nanoscale of anode materials could influence their performance towards Li-ion storage. In this direction, the SnS_2 with different morphologies towards LIB application should be interesting to investigate. Therefore, the SnS_2-NPL and SnS_2- MFL have been studied as LIB anodes and compared on performance. Results showed that the SnS_2-NPL displayed better Li-ion storage behavior, however, still not satisfying rate capacity and stability. This moderate performance towards LIB on single SnS_2-NPLs should be ascribed to the low electrical conductivity (as demonstrated by the electrochemical impedance spectroscopy) and large volume expansion according to previous works. To solve this issue, "separator", especially with porous feature such as g-C_3N_4 (CN) demonstrated herein, could added into SnS_2-NPL to prevent the SnS_2 from aggregation and also provide additional routes for Li-ion transport. The decreased electric conductivity resulted from "separator" addition could be compensated by adding highly conductive additive, such as conventional graphite carbon plate (GP) adopted herein, to provide avenues for efficient charge transport. This well-designed hierarchical SnS_2/CN/GP finally demonstrated an

excellent performance towards Li-ion storage due to the synergistic effects creating between these three components. This kind of hierarchical architecture can be also used to promote performance in other energy storage devices.

Even though the optimal SnS_2-Pt heterostructure aforementioned presented acceptable performance towards PEC water splitting, its stability under working conditions was still not that excellent (60 % retaining of photocurrent after 2000 s), which could be due to the peel-off of catalyst from the FTO surface. To solve this problem, a molecular ink of SnS_2 was developed to recover layer/particle of SnS_2 directly on suitable substrate surfaces. According to previous reports, hydrazine, initially adopted by Mitzi group, has been well-developed to produce molecular ink of metal sulfides and recover the corresponding layers/particles. However, hydrazine is highly toxic and explosive, and thus it is not convenient for scale-up and commercial applications. Based on this, the binary solvent mixture based on ethanedithiol (Edt) and ethylenediamine (En) to produce molecular ink put forwarded by Brutchey group several years ago could be a better option. In the amine-thiol system, the main difficulty to prepare a phase pure material is to find the proper amine and thiol mixture, their ratio and reaction conditions to crystallize the targeted product in the desired phase, preventing the formation of unwanted secondary phases. In this direction, a series of investigations have been done and the results demonstrated that the ratios amine/thiol and Sn/S, and the reaction conditions (reaction time, temperature) indeed significantly influenced the composition of recovered layers, containing extra impurity phase of SnS in most cases. Ternary $SnS_{2-x}Se_x$, phase pure $SnSe_2$, SnS_2/reduced graphene oxide (SnS_2/rGO) composites, and even large-scaled SnS_2 powder were successfully produced, demonstrating the versatility of this SnS_2 molecular ink. The recovered SnS_2 layer on FTO surface outperformed SnS_2-NPL and even SnS_2-Pt-2.8, towards PEC water splitting, with a stable photocurrent density of around 160 $\mu A/cm^2$, indicating the advance of the recovered SnS_2 layer directly on conductive substrate. The SnS_2 layer could be well-recovered on the surface of substrates like stainless steel and carbon cloth, however, it was unsuccessful on convention metallic substrates, such as foam/mesh of Ni and Cu, demonstrating the drawback of this molecular ink towards layer deposition on substrates with less anticorrosive ability.

From the discussion above, it could be seen that the results obtained from the four research works published have a close relation. The well-performed OER catalyst of CuO

derived from *in-situ* synthesized Cu_2S demonstrated the great potential and advance of a new strategy to take metal sulfides as "pre-catalysts". However, the single metal sulfides, in many cases, need to be cooperated with other components, either served as co-catalysts on the surface of metal sulfides or hybrid additives to rationally tune the transport process of carriers, ions or both together, to reach an enhanced activity towards electrochemical energy conversion processes, such as SnS_2-Pt-2.9 system for PEC water splitting and SnS_2/CN/GP for Li-ion storage. As for the preparation of working electrodes, the posterior deposition operation of prepared electrocatalysts, usually evolving the addition of conductive and binding materials, onto conductive substrates has its drawback of peel-off issue. Thus so the recovery of catalyst layers on substrates directly could be very attractive. The investigation on recovery of SnS_2 layer on different substrates from its corresponding molecular ink in this thesis has well-demonstrated the advance of this approach.

Based on all the results shown in this thesis, nanostructured metal sulfides, with rational design of synthesis routes, posterior treatments and combination with suitable additive components if necessary, could be the promising candidates for electrochemical energy conversion processes. Persistent endeavors on improving the activity towards energy conversion process especially based on those non-toxic, low cost metal sulfides could be appealed.

Conclusions

In this thesis, four nanostructured electrocatalysts based on metal sulfides of Cu_2S and SnS_2 have been rationally developed and their applications in various electrochemical energy conversion processes have been investigated. From these investigations we reached the following conclusions: *1)* the *in-situ* electrochemical oxidation of metal sulfides studied on Cu_2S could be an excellent method to produce electrocatalysts with high-activity towards oxygen evolution reaction; *2)* Nanostructuring metal sulfides with particular shapes and subsequently depositing optimal nanodomains as co-catalyst could be a good approach to improve the utilization efficiency of solar energy in PEC water splitting, as indicated in this thesis that the nanostructured SnS_2 nanoplates with suitable Pt nanodomains deposition showed the best performance among the tested samples. Similarly, the rational combination of nanostructured metal sulfide, separator and conductive components could be applied to overcome the issue of low electrical conductivity and large volume expansion on those metal sulfides towards Li-ion battery storage and thus to obtain an excellent performance, as shown in the thesis that SnS_2/g-C_3N_4/graphite demonstrated both excellent rate capability and outstanding stability as Li-ion battery anode; *3)* To produce the catalytic layers directly on suitable conducting substrates could be a good solution to avoid the peel-off issue during the catalytic process resulting from the less adhesive ability from post-deposition of electrocatalysts. In this direction, the recovery of metal sulfide layer from its corresponding molecular ink, such as SnS_2 molecular ink, becomes promising, and its versatility to produce layers on different substrates can be expected.

Overall, the metal sulfides are promising to be applied for electrochemical energy conversion. In some cases, the metal sulfides may be taken as “pre-catalysts” to *in-situ* prepare catalysts of their corresponding metal oxides/oxyhydroxides in oxidation conditions or metallic metal in reduction conditions. Remember the *in-situ* transformation can be taken advantage of and it should be highly aware. In many cases, the single metal sulfides may demonstrate limited/unsatisfied performance, in this direction, reasonable optimizations/treatments could be applied according to the applications undertaken. The nanostructuring engineering on metal sulfides and also combining suitable additive components could be very useful herein to design well-performed electrocatalysts.

Outlook

In this thesis, four nanostructured materials based on SnS_2 and Cu_2S were produced and their applications towards electrochemical energy conversion have been studied. There are still some problems and challenges related to the energy conversion applications of metal sulfide need to be solved based on the completed results, and these issues should be concerned in the future work, and subsequent endeavor is required.

1) Regarding to the electrochemical water splitting, it is significant to determine the real active sites during/after the electrocatalytic process, and be aware of the advantages/benefits of *in-situ* transformed catalysts from "pre-catalysts". These "pre-catalysts" include but are not limited to metal sulfides, and can be extended to metal of carbides, pnictides, phosphides and other chalcogenides, as well as other electrochemical applications related to redox process like electrochemical CO_2 reduction. To better unveil the transformation and intrinsic catalytic mechanism is meaningful to understand the reason behind the change of catalytic activity, and therefore the *in-situ* techniques to monitor the surface features and molecules of catalyst are necessary.

2) Regarding to the photoelectrochemical water splitting, the improvement of photocurrent to mA scale of photoelectrodes based on metal sulfide with none or less noble metal participation is necessary for the posterior application in industry. In this direction, to develop photoelectrodes with rational tandem from components becomes crucial, where the band gap engineering related to theoretical calculation should be involved. Regarding to the synthesis, the further investigation on synthesis of molecular ink using odorless solvent mixture could also be an issue to be addressed.

3) Regarding to the lithium-ion battery, the higher capacity and durable stability is further appealed to undertake. In this direction, *in-situ* characterization of ion intercalation would be extremely helpful to provide suggestions to further optimize the electrode materials. As for the synthetic route, the *in-situ* synthesis/deposition with low-cost procedure and large-scale capability involving thickness control could be a promising option, since the excellent LIB performance due to short diffusion lengths, good electron transport and less charge recombination can be thus obtained.

Curriculum Vitae

Yong Zuo

Address: Catalonia Institute for Energy Research, Barcelona, Spain

Mobile Phone: +34 666 059 587 Google scholar: click here

E-mail: yongzuo16@gmail.com

Nationality: People's Republic of China

EDUCATION

2016.10-2020.6, **PhD student** (Supervisor: Prof. Andreu Cabot)

Universitat de Barcelona, Catalonia Institute for Energy Research, Barcelona, Spain

Major: Nanoscience

Key words: Colloidal synthesis, photocatalysis, electrocatalysis, water splitting, CO2RR

2019.7-2019.9, **Visiting PhD student** (Supervisor: Prof. Raffaella Buonsanti)

École Polytechnique Fédérale de Lausanne (EPFL), School of Basic Science, Sion, Switzerland

2013.9-2016.6, **Master** (Supervisor: Prof. Ji-Ming Song)

Major: Applied Chemistry

Anhui University, School of Chemistry & Chemical Engineering

2009.9-2011.7 & 2012.9-2013.6, **Bachelor**

Major: Chemical Engineering & Technology

Ningxia University, School of Chemistry & Chemical Engineering, Yin Chuan, China.

GPA: 3.49/4.0

2011.9-2012.7, **Exchange student** (1/72)

Jilin University, School of Chemistry, Chang Chun, China.

ACADEMIC RESEARCH EXPERIENCE

2019.7- present, Colloidal synthesis of herterostructured metal/metal phosphide for CO2RR.

2018.6-2019.6, Investigation on in-situ electrochemical oxidation of metal chacoginides into metal oxides as a durable and efficient electrocatalyst for water splitting.

2017.3-2019.1, A versatile solution to produce phase-pure SnS_2 and SnS_2-based electrocatalysts from molecular ink for photoelectrochemical water splitting.

2016.10-2018.5, Solution-processed ultrathin SnS_2-Pt nanoplates for photoelectrochemical water oxidation.

2016.10-2017.12, Precise engineering of colloidal interband photocatalysts for photoelectochemical water splitting.

2016.10-2017.6, Colloidal synthesis of lead-free perovskite; Crystal preparation of novel double perovskite.

2014.3-2016.4, Colloidal synthesis and characterization of Se-based nanomaterials (WSe_2, CuAgSe, Cu_2SnSe_3-Ag and $CuFeSe_2$-Ag) for thermoelectric application.

2015.3-2015.9, Synthesis of Co_3O_4/NiO nanofilms for enhanced supercapacitor electrode.

2013.9-2015.6, Hydrothermal synthesis and characterization of $TiO_2/Co_{0.85}Se$ composite for photocatalysis.

RESEARCH SKILLS

- ✓ Proficient in operation of Schlenk-line technique. Skilled in synthesis and purification of colloidal NPs.
- ✓ Experienced in investigation of (photo)electrochemical water splitting and electrochemical CO2RR.
- ✓ Skillful in paper writing. (Published 4 peer-reviewed papers during PhD period)
- ✓ Skillful in manipulating instruments of X-ray diffraction (XRD), scanning electron microscope (SEM), Energy dispersive X-Ray spectroscopy (EDX), transmission electron microscopy (TEM), Fourier-transform infrared spectroscopy (FT-IR), UV-vis absorption spectroscopy, Plasma, Sputtering, Electrochemical station, CO_2 H-cell setup, etc.
- ✓ Proficient in data processing of XRD, XPS, EDX, Raman, UV-Vis, FT-IR, TG-DSC, etc.
- ✓ Software skills: Microsoft office, Origin, XPSpeak, ChemDraw, PDF Card, Xpert, EIS-Zview, Mendeley, EndNote, etc.

RESEARCH INTERESTS

- ➢ Synthesizing colloidal nanoparticles with size, shape and composition control.
- ➢ Synthesizing self-supported electrocatalyst for large-scaled catalytic application.
- ➢ In-situ characterization, self-rearrangement. Using in-situ techniques to elucidate the transition of electrocatalyst and also the catalytic mechanism by monitoring surface molecules during catalysis process.
- ➢ Application: Photo/electrocatalysis; Water splitting; CO2RR.

IMPORTANT HONORS AND AWARDS

2016.10-2020.9, Scholarship from China Scholarship Council

2016.5, Outstanding graduates. Anhui University

2013.5, Outstanding graduates. Ningxia University

2010.11, National Scholarship. Chinese Ministry of Education

CONFERENCE PRESENTATIONS

2019.8.27-30, Solution-processed Ultrathin SnS_2-Pt Nanoplates for Photoelectro-chemical Water Oxidation.

Photo and ElectroCatalysis at the Atomic Scale (PECAS 2019)

2018.3.5-9, Simple solution-processable metal chalcogenide thin films for solar energy conversion.

Winter School: CHALLENGES & OPPORTUNITIES IN ENERGY RESEARCH NRG2018

2017.7.17-21, Precise Engineering of Interband Photocatalysts for Solar Energy Conversion.

International WE-Heraeus-Physics School on Exciting nanostructures: Probing and tuning the electronic properties of confined systems

PUBLICATION LIST

1. **Y. Zuo**, J. Li, R. Du, X. Yu, T. Zhang, X. Wang, J. Arbiol, J. Llorca, A. Cabot*. A SnS_2 Molecular Precursor for Conformal Nanostructured Coatings. ***Chemistry of Materials. 2020***,

32, 2097-2106.

2. **Y. Zuo**, Y. Liu, J. Li, R. Du, X. Han, T. Zhang, J. Arbiol, N.J. Divins, J. Llorca, N. Guijarro, K. Sivula, A. Cabot*. In-situ Electrochemical Oxidation of Cu_2S into CuO Nanowires as a Durable and Efficient Electrocatalyst for Oxygen Evolution Reaction. ***Chemistry of Materials*. 2019**, 31, 7732-7743.
3. **Y. Zuo**, Y. Liu, J. Li, R. Du, X. Yu, C Xing, T. Zhang, L. Yao, J. Arbiol, J. Llorca, K. Sivula, N. Guijarro, A. Cabot*. Solution-Processed Ultrathin SnS_2-Pt Nanoplates for Photoelectrochemical Water Oxidation. *ACS Applied Materials & Interfaces*, **2019**, 11, 6918-6926.
4. **Y. Zuo**, X. Xu, J. Li, R. Du, X. Wang, X. Han, J. Arbiol, J. Llorca, J. Liu*, A. Cabot*. SnS_2/g-C_3N_4/Graphite Nanocomposites as Durable Lithium-Ion Battery Anode with High Pseudocapacitance Contribution. *Electrochimica Acta*, **2020**, DOI: 10.1016/j.electacta.2020.136369.
5. **Y. Zuo**, Y. Liu, Q. He, J. Song*, H. Niu, C. Mao. CuAgSe nanocrystals: colloidal synthesis, characterization and their thermoelectric performance. *Journal of Materials Science*, **2018**, 53, 14998-15008.
6. **Y. Zuo**, J. Ni, J. Song*, H. Niu, C. Mao, S. Zhang, Y. Shen. Synthesis of Co_3O_4/NiO nanofilms and their enhanced electrochemical performance for supercapacitor application. *Applied Surface Science*, **2016**, 370, 528-535.
7. **Y. Zuo**, J. Song*, H. Niu, C. Mao, S. Zhang, Y. Shen. Synthesis of TiO_2-loaded $Co_{0.85}Se$ thin films with heterostructure and their enhanced catalytic activity for p-nitrophenol reduction and hydrazine hydrate decomposition. *Nanotechnology*, **2016**, 27, 145701.
8. J. Li, **Y. Zuo**, J. Liu, X. Wang, X. Yu, R. Du, T. Zhang, P. Tang, M. Infante-Carrió, J. Arbiol, J. Llorca, Z. Luo, A. Cabot*. *Journal of Materials Chemistry A*, **2019**, 7, 22036-22043.
9. M. Maruthupandy, **Y. Zuo**, J. Chen, J. Song*, H. Niu, C. Mao, S. Zhang, Y. Shen. *Applied Surface Science*, **2017**, 397, 167-174.
10. J. Li, Z. Luo, **Y. Zuo**, J. Liu, T. Zhang, P. Tang, J. Arbiol, J. Llorca, A. Cabot*. *Applied Catalysis B: Environmental*, **2018**, 234, 10-18.
11. P. Shaw, M. Meyns, **Y. Zuo**, A. Grau-Carbonell, P. Lagoudakis, M. Charlton, S. Martí-Sánchez, J. Arbiol, A. Cabot*, Antonios Kanaras*. *Nanomaterials*, **2018**, 8, 506.
12. B. Zhang, Y. Liu, **Y. Zuo**, J. Chen, J. Song*, H. Niu, C. Mao. *Nanomaterials*, **2017**, 8, 8.
13. M. Li, Y. Liu, Y. Zhang, **Y. Zuo**, J. Li, K. Lim, D. Cadavid, K. Ng, A. Cabot*. *Dalton Transactions*. **2019**, 48, 3641-3647.
14. J. Li, Z. Luo, F. He, **Y. Zuo**, C. Zhang, J. Liu, X. Yu, R. Du, T. Zhang, M. Infante-Carrió, P. Tang, J. Arbiol, J. Llorca, A. Cabot*. *Journal of Materials Chemistry A*, **2018**, 6, 22915-22924.

REFERENCE

Prof. Andreu Cabot
Advanced Material Research Department,
Catalonia Institute for Energy Research (IREC)
acabot@irec.cat

Prof. Raffaella Buonsanti
Laboratory of Nanochemistry for Energy,
École Polytechnique Fédérale de Lausanne
raffaella.buonsanti@epfl.ch

Prof. Ji-Ming Song
School of Chemistry & Chemical Engineering,
Anhui University
jiming@ahu.edu.cn

Annex

Collection of Publications Presented in This Thesis

CHEMISTRY OF MATERIALS
Cite This: Chem. Mater. 2019, 31, 7732−7743
Article
pubs.acs.org/cm

In Situ Electrochemical Oxidation of Cu_2S into CuO Nanowires as a Durable and Efficient Electrocatalyst for Oxygen Evolution Reaction

Yong Zuo,[†,‡] Yongpeng Liu,[§] Junshan Li,[†,‡] Ruifeng Du,[†,‡] Xu Han,[∥] Ting Zhang,[∥] Jordi Arbiol,[∥,⊥] Núria J. Divins,[#] Jordi Llorca,[#] Néstor Guijarro,[§] Kevin Sivula,[§] and Andreu Cabot*[,†,⊥]

[†]Catalonia Institute for Energy Research—IREC, Sant Adrià de Besòs, 08930 Barcelona, Spain
[‡]Department of Electronics and Biomedical Engineering, Universitat de Barcelona, 08028 Barcelona, Spain
[§]Laboratory for Molecular Engineering of Optoelectronic Nanomaterials (LIMNO), École Polytechnique Fédérale de Lausanne (EPFL), Station 6, CH-1015 Lausanne, Switzerland
[∥]Catalan Institute of Nanoscience and Nanotechnology (ICN2), CSIC and BIST, Campus UAB, Bellaterra, 08193 Barcelona, Catalonia, Spain
[⊥]ICREA, Pg. Lluís Companys 23, 08010 Barcelona, Catalonia, Spain
[#]Institute of Energy Technologies, Department of Chemical Engineering and Barcelona Research Center in Multiscale Science and Engineering, Universitat Politècnica de Catalunya, EEBE, 08019 Barcelona, Spain

Supporting Information

ABSTRACT: Development of cost-effective oxygen evolution catalysts is of capital importance for the deployment of large-scale energy-storage systems based on metal−air batteries and reversible fuel cells. In this direction, a wide range of materials have been explored, especially under more favorable alkaline conditions, and several metal chalcogenides have particularly demonstrated excellent performances. However, chalcogenides are thermodynamically less stable than the corresponding oxides and hydroxides under oxidizing potentials in alkaline media. Although this instability in some cases has prevented the application of chalcogenides as oxygen evolution catalysts and it has been disregarded in some others, we propose to use it in our favor to produce high-performance oxygen evolution catalysts. We characterize here the in situ chemical, structural, and morphological transformation during the oxygen evolution reaction (OER) in alkaline media of Cu_2S into CuO nanowires, mediating the intermediate formation of $Cu(OH)_2$. We also test their OER activity and stability under OER operation in alkaline media and compare them with the OER performance of $Cu(OH)_2$ and CuO nanostructures directly grown on the surface of a copper mesh. We demonstrate here that CuO produced from in situ electrochemical oxidation of Cu_2S displays an extraordinary electrocatalytic performance toward OER, well above that of CuO and $Cu(OH)_2$ synthesized without this transformation.

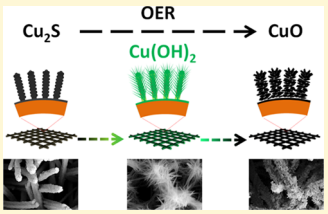

1. INTRODUCTION

Driven by energy and environmental crises resulting from the fast consumption of fossil fuels, the share of renewable energies such as wind and photovoltaics is steadily growing. To sustain this growth, besides increasing the cost efficiency of the generation technologies, we need to develop large-scale and cost-effective power-storage systems that are able to compensate for the fluctuating character of these energy supplies. In this direction, metal−air batteries, reversible fuel cells, and electrolyzers are the most promising technologies for large-scale and distributed energy storage, but all of them are limited by the same essential and sluggish reaction step: oxygen evolution.[1−3] The oxygen evolution reaction (OER) involves breaking O−H bonds to form O═O bonds, which comprises four sequential proton-coupled electron-transfer steps.[4−7] Currently, noble metals are used to catalyze this reaction, but activities and stabilities are still not satisfactory and the high cost of these catalysts compromises the system's cost effectiveness. Thus, the development of highly efficient and robust OER catalysts based on earth-abundant elements is a topic of capital importance.[8−13]

Transition-metal oxides and (oxy)hydroxides are the main alternatives to noble metals as OER catalysts, reaching performances close to those of IrO_2/RuO_2 in alkaline media.[14,15] Additionally, several reports have claimed metal phosphides,[16−18] nitrides,[19−22] selenides,[23,24] and sulfides[25−28] to be excellent OER catalysts. However, some of these compounds are thermodynamically unstable under harsh OER conditions and may suffer chemical transformation during operation.[2,6,29−31] While this instability has been ignored in most studies, when analyzed in detail, the excellent performances obtained for chalcogenides and pnictides have in some cases been related not to the chalcogenide or pnictide cations but to the in situ formed oxide or (oxy)hydroxide.[32−39] For example, the OER activity of CoS_x,[40] NiS,[27] NiSe,[6] and

Received: July 14, 2019
Revised: August 12, 2019
Published: August 15, 2019

Downloaded via UNIV DE BARCELONA on April 23, 2020 at 14:51:42 (UTC).
See https://pubs.acs.org/sharingguidelines for options on how to legitimately share published articles.

© 2019 American Chemical Society

DOI: 10.1021/acs.chemmater.9b02790
Chem. Mater. 2019, 31, 7732−7743

$Ni_xFe_{1-x}Se_2$[41] catalysts was demonstrated to be related to the partial or complete oxidization of the chalcogenide to the corresponding oxide/(oxy)hydroxide.

The performances of oxides and hydroxides grown during OER operation may be even higher than those of oxides and hydroxides grown by other routes because of the following hypothesis: (i) during the in situ growth of the oxide/hydroxide nanostructured material, avenues for effective electrolyte diffusion may be created; (ii) during the rapid chemical transformation at an ambient temperature, an increase of the surface area through the material recrystallization in the form of smaller crystallites may be obtained; (iii) a high density of defects, including ion vacancies, grain boundaries, and metastable phases, may be obtained under these growth conditions; (iv) new catalytic sites with higher activity may be in situ created because of the intimate relation between the structure growth and the electrocatalytic OER process; and (v) residual chalcogen and phosphorous cations facilitate the OER process by modifying the adsorption energy of reaction intermediates.[42−45]

Herein, taking copper as the illustrating electrocatalyst, we demonstrate the possibility of obtaining OER electrocatalysts with enhanced performance from the in situ oxidation of a chalcogenide under OER conditions. With this purpose, we first report on the chemical, structural, and morphological transformation during OER operation of Cu_2S nanowires (NWs) grown on the surface of a copper mesh (CM). We subsequently investigate the effect that these transformations have on the OER activity of Cu_2S and Cu_2S-derived nanostructures and demonstrate the OER performance of the compound in situ formed during operation to outperform that of the same compound obtained by other processes, both in terms of activity and stability.

2. EXPERIMENTAL SECTION

2.1. Chemicals. Ammonium persulfate [APS, $(NH_4)_2S_2O_8$, ≥98.0%] and sodium sulfide nonahydrate ($Na_2S{\cdot}9H_2O$, ≥98.0%) were purchased from Aldrich. Sodium hydroxide (NaOH, 98.5%) was purchased from Acros. All chemicals were used as received without further purification. CM with a wire diameter of about 200 μm and a pore size of 400 μm and Cu foam (CF) with a thickness of 1 mm and a pore size of 120 PPI were purchased from Kunshan GuangJiaYuan New Materials Co. Ltd. Deionized water (DW, 18.6 MΩ cm) obtained using a purification system (Mini-Q Water) was used for all experiments.

2.2. Synthesis of $Cu(OH)_2$/CM. $Cu(OH)_2$ NWs on CM ($Cu(OH)_2$/CM) were prepared following an earlier report with some modifications.[46,47] Briefly, a piece of CM (2.5 cm×1 cm) was thoroughly cleaned using ethanol/acetone and HCl (5 mol/L) for 30 min and then rinsed with plenty of DW. The cleaned CM was then immersed in a solution of NaOH (40 mmol), APS (2 mmol), and DW (20 mL) at room temperature for 30 min. The obtained $Cu(OH)_2$/CM was then washed carefully using DW and then dried using nitrogen flow.

2.3. Synthesis of Cu_2S/CM. Cu_2S NWs on CM (Cu_2S/CM) were prepared by an anion exchange route. $Cu(OH)_2$/CM were immersed in Na_2S solution (20 mL DW, 0.1 mol/L) for 1 h at 60 °C. The obtained black Cu_2S/CM was carefully washed using DW and ethanol and then dried naturally.

2.4. Synthesis of CuO/CM-AN. CuO NWs on CM (CuO/CM-AN) were prepared by annealing $Cu(OH)_2$/CM under an Ar atmosphere for 2 h at 200 °C, reached using a temperature ramp of 5 °C/min. The obtained CuO/CM-AN was collected without any further treatment.

2.5. Synthesis of Cu_2S/CF. Cu_2S NWs on CF (Cu_2S/CF) were prepared using a similar procedure as the one used to produce Cu_2S/CM, but using a CF instead of a CM and increasing the sulfurization time to 2 h to complete the ion exchange.

2.6. Material Characterization. X-ray diffraction (XRD) patterns were obtained on a Bruker AXS D8 ADVANCE X-ray diffractometer (Bruker, Karlsruhe, Germany) operating at 40 kV and 40 mA with Ni-filtered (2 μm thickness) Cu Kα1 radiation (λ = 1.5406 Å). Scanning electron microscopy (SEM) analysis was carried out in a Zeiss Auriga microscope (Carl Zeiss, Jena, Germany) with an energy-dispersive X-ray spectroscopy (EDX) detector at 20 kV to study the composition. Transmission electron microscopy (TEM) characterization was carried out on a Zeiss Libra 120 (Carl Zeiss, Jena, Germany) operating at 120 kV. High-resolution TEM (HRTEM) images were obtained using a field emission gun FEI Tecnai F20 microscope at 200 kV with a point-to-point resolution of 0.19 nm. High-angle annular dark-field (HAADF) scanning TEM (STEM) was combined with electron energy loss spectroscopy (EELS) in the Tecnai microscope by using a Gatan Quantum filter. For TEM characterization, tiny powder samples were carefully collected by folding the Cu substrate to peel the surface materials. The collected powder was dispersed in ethanol by 30 s sonication and then drop-casted on a 200 mesh copper grid. X-ray photoelectron spectroscopy (XPS) was carried out on a Specs system (Specs GmbH, Berlin, Germany) equipped with a Mg anode XR50 source operating at 250 W and a Phoibos 150 MCD-9 detector (Specs GmbH, Berlin, Germany). The pressure in the analysis chamber was kept below 10^{-7} Pa. Data processing was performed with the CasaXPS program (Casa Software Ltd., UK). Binding energy values were centered by using the Cu 2p peak at 932.7 eV.

2.7. Electrochemical Measurements. Electrochemical measurements were conducted in a three-electrode system using an electrochemical workstation (Metrohm Autolab). Characterized samples were used as the working electrode (partially cut to leave the working area as 1 × 1 cm), while a graphite rod with a diameter of 6 mm was used as the counter electrode and a Hg/HgO [1 M KOH, 0.098 V vs reversible hydrogen electrode (RHE)] was applied as the reference electrode. KOH (1 M) was used as the electrolyte. The electrolyte was purged with O_2 for 30 min prior to each measurement. The following formula was used to convert the potentials to the RHE standard scale

$$E \text{ vs RHE} = E_{\text{Hg/HgO}} + E^{\circ}_{\text{Hg/HgO}} + 0.059 \times \text{pH}$$
$$= E_{\text{Hg/HgO}} + 0.924 \text{ (V)}$$

The following formula was applied to calculate the overpotentials

$$\eta = E - 1.23 \text{ (V)} = E_{\text{Hg/HgO}} - 0.306 \text{ (V)}$$

Polarization curves were obtained using cyclic voltammetry (CV) at 100 mV/s when analyzing chemical transformations and at 5 mV/s when analyzing the OER performance. Structural, chemical, and morphological characterizations of the electrodes after operation/activation was carried out by cutting a small piece of working electrode (ca. 3 × 3 mm triangle). All tests were done under static circumstances without a magnet bar stirring at the bottom. All experiments were performed at room temperature of ca. 15 °C.

2.8. Electrochemical Surface Area. To estimate the effective electrochemical surface area (ECSA), CV measurements were conducted to check the electrochemical double-layer capacitance of samples at the non-faradic potential region. Typically, a series of CV measurements were performed at various scan rates (10, 20, 40 mV/s, etc.) in the range of 1.22−1.32 V versus RHE. The double-layer capacitance (C_{dl}) was determined using the equation $\Delta J/2 = \nu \times C_{dl}$, in which ΔJ corresponds to the current density between the anodic and cathodic sweeps at 1.27 V versus RHE against the scan rate. The slope of the fitting line is equal to twice the C_{dl} value, which is proportional to the ECSA of the materials. ECSA was then calculated by dividing C_{dl} by C_s (ECSA = C_{dl}/C_s), where C_s is the specific electrochemical double-layer capacitance of an atomically smooth surface, which can be considered as 0.04 mF/cm^2 based on typical values reported previously.[48,49] This comparison makes sense only

DOI: 10.1021/acs.chemmater.9b02790
Chem. Mater. 2019, 31, 7732−7743

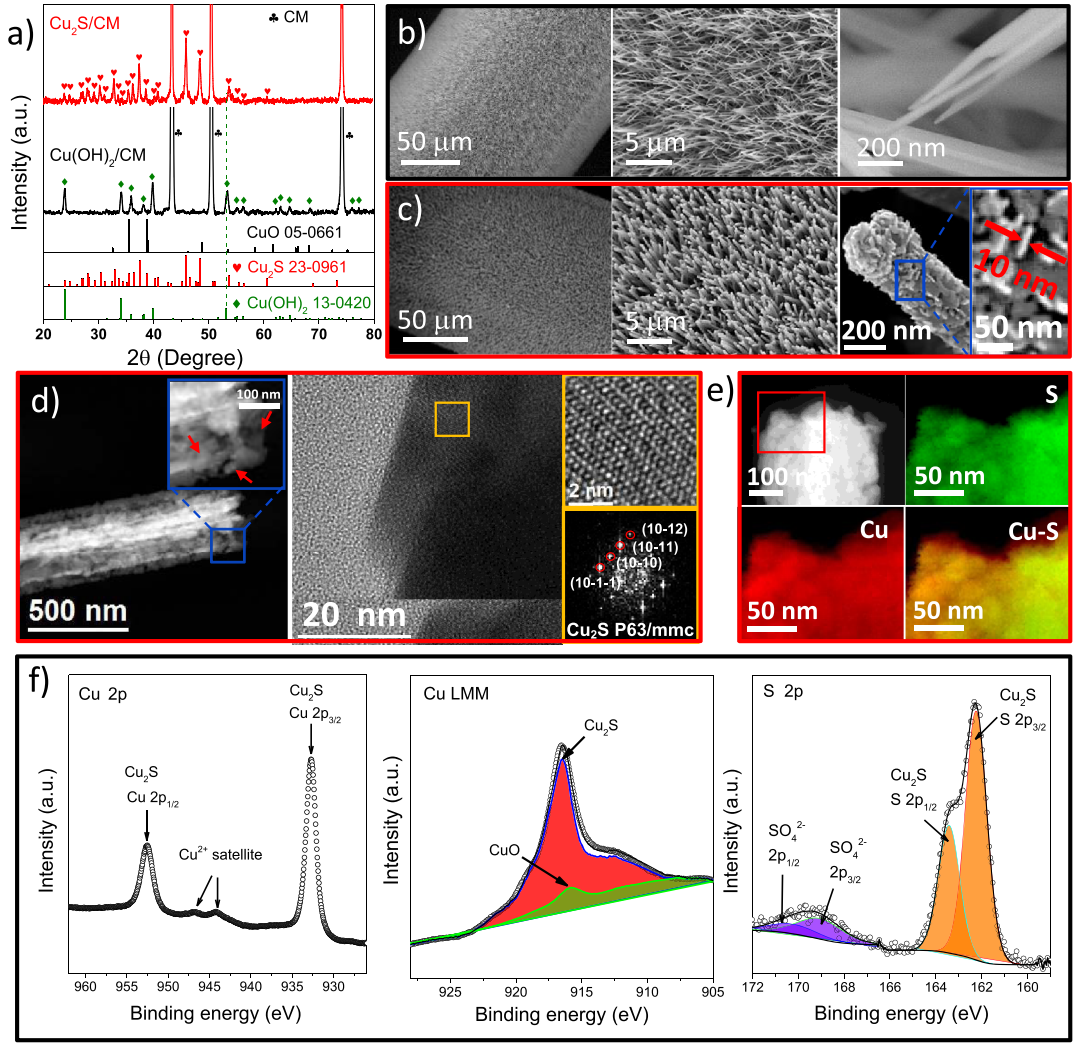

Figure 1. (a) XRD patterns of $Cu(OH)_2$/CM and Cu_2S/CM. (b,c) SEM images of (b) $Cu(OH)_2$/CM and (c) Cu_2S/CM. (d) HAADF STEM and HRTEM micrographs of a Cu_2S NW. Arrows point at single nanoflakes used to determine their size. From the crystalline domain displayed, the Cu_2S lattice fringe distances were measured to be 0.236, 0.296, 0.342, and 0.311 nm at 18.65°, 45.93°, and 72.42°, which was interpreted as the hexagonal Cu_2S phase visualized along its [−12−10] zone axis. (e) HAADF STEM micrograph and EELS chemical composition maps obtained from the red squared area of the HAADF STEM micrograph: individual Cu $L_{2,3}$-edges at 931 eV (red) and S $L_{2,3}$-edges at 165 eV (green) as well as its composite. (f) Cu 2p, Cu LMM, and S 2p regions of the XPS spectrum of Cu_2S/CM.

when the measurements of materials are carried out under the same condition.

2.9. Electrochemical Impedance Spectroscopy. Electrochemical impedance spectroscopy (EIS) was conducted on the working electrodes under the OER operating conditions at the anodic bias that delivered a geometric current density of ca. 10 mA/cm^2 (0.68 V vs Hg/HgO). A sinusoidal voltage with an amplitude of 10 mV and a scanning frequency ranging from 100 mHz to 1 MHz was applied to carry out the measurements.

2.10. *iR* Correction. The OER curves in this work are shown without *iR* correction. However, to display the accurate performance on OER operation, we did *iR* correction toward the overpotential that delivers a geometric current density of 10 mA/cm^2 according to the following formula

$$\eta_{\text{corrected}} = \eta - iR_s \times 90\%$$

R_s indicates the solution resistance and can be measured using EIS. In our work, R_s was measured as 4.7 Ω at 10 mA/cm^2 for Cu_2S-derived CuO/CM.

2.11. In Situ Raman Spectroscopy. In situ Raman measurements were performed with a Raman microscope (Horiba Jobin Yvon XploRA PLUS) coupled to an optical microscope (Olympus BX41). The objective lens (Olympus MPlan N, 50×, NA = 0.75) was covered with an optically transparent Teflon film (American Durafilm 50A, 0.013 mm) to prevent potential damage from electrolytes. Raman excitation was provided by a 532 nm laser (Horiba DPSS). A three-electrode configuration was set up in a three-dimensional printed Raman electrochemical cell that was fit onto the manual Olympus XY stage. The three-electrode configuration was connected to a Bio-Logic SP-50 potentiostat. In situ Raman characterization was performed by stopping CV after 10, 20, 50, 100, and 200 cycles of completion on an as-prepared working electrode.

3. RESULTS AND DISCUSSION

$Cu(OH)_2$ NWs were grown on the surface of a CM by immersing it in an aqueous solution of NaOH/APS for 30 min. During this process, the initial reddish brown CM turned greenish-blue (Figure S1a). XRD patterns of the produced layers fitted well with the standard JCPDF card #13-0420 corresponding to $Cu(OH)_2$ (Figure 1a). SEM micrographs of $Cu(OH)_2$/CM displayed a homogeneous distribution of faceted NWs with an average thickness of ca. 200 nm (Figure 1b) and an average length of ca. 15 μm (Figure S6d). The

DOI: 10.1021/acs.chemmater.9b02790
Chem. Mater. 2019, 31, 7732−7743

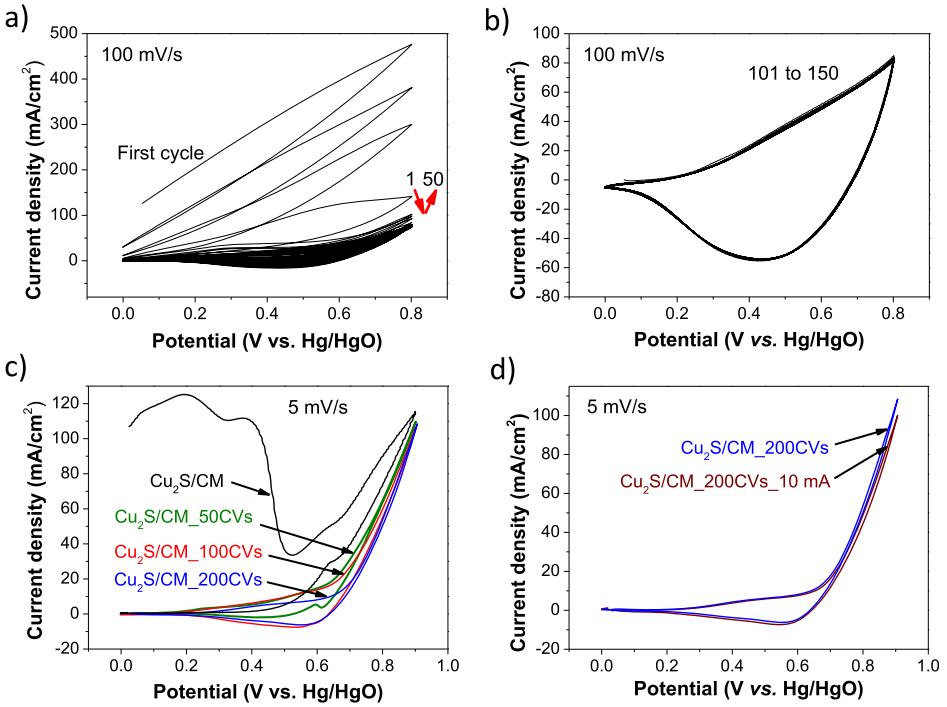

Figure 2. (a,b) Multiple CVs of Cu_2S/CM at a scan rate of 100 mV/s: (a) 1−50 cycles; (b) 101−150 cycles. (c,d) Quasi-stationary polarization CVs obtained at 5 mV/s of Cu_2S/CM: (c) after different activation CVs at 100 mV/s and (d) after 200 CVs at 100 mV/s and before/after further chronopotentiometry measurement at a geometric current density of 10 mA/cm^2 for 10 000 s.

growth mechanism of $Cu(OH)_2$ NWs from Cu surfaces has been previously described, and it is illustrated in Figure S1d.[50] Briefly, surface Cu is oxidized by $S_2O_8^{2-}$ ions to Cu^{2+}, which immediately reacts with OH^- in solution to subsequently recrystallize $Cu(OH)_2$ nanostructures on the CM surface.[50]

$Cu(OH)_2$/CM was sulfurized by immersion in a Na_2S solution (Figure 1c). During this transformation, the layer color changed from greenish-blue to black (Figure S1a). XRD analysis showed the produced layers to have a hexagonal Cu_2S crystal phase (JCPDS #23-0961), with no evidence of crystalline Cu_xO impurities. EDX analyses confirmed the atomic ratio between Cu and S to be close to that of stoichiometric Cu_2S (Figure S2). Cu_2S nanostructures maintained the original $Cu(OH)_2$ NW geometry but displayed much rougher surfaces that contained flakelike crystallites with an average size of ca. 50 nm in diameter and ca. 10 nm in thickness (Figures 1c,d and S1c). HRTEM analysis confirmed the crystallographic phase of the crystallites to match that of hexagonal Cu_2S (space group = $P6_3/mmc$) with $a = b = 3.8900$ Å and $c = 6.6800$ Å (Figure 1d, right side). EELS chemical composition maps displayed a homogeneous distribution of both Cu and S throughout the NWs (Figure 1e).

XPS analysis of Cu_2S/CM (Figure 1f) displayed a main Cu 2p doublet at 932.7 eV (Cu $2p_{3/2}$) corresponding to Cu^0 and/or Cu^+ species.[51,52] The presence of a small satellite peak at ca. 945 eV revealed the existence of a Cu^{2+} contribution, which accounted for less than 10% of the total measured copper. This contribution may result from a partial surface oxidation upon exposure to an ambient atmosphere.[53] The Cu $L_3M_{4,5}M_{4,5}$ Auger spectrum was analyzed to differentiate between Cu^0 and Cu^+ components. As displayed in Figure 1f, the Cu LMM signal could be fitted assuming a main Cu_2S component and a minor CuO contribution[54,55] accounting for ca. 10% of the total Cu, in agreement with the deconvolution of the Cu 2p region. We speculate that Cu^{2+} ions within $Cu(OH)_2$ are first reduced by S^{2-} to Cu^+ of Cu_2O (eq 1),[56] and then an anion exchange between O^{2-} and S^{2-} (eq 2) takes place since the solubility constant of Cu_2S ($K_{sp} = 2.5 \times 10^{-48}$) is much lower than that of Cu_2O ($K_{sp} = 2.0 \times 10^{-15}$).[57,58]

$$2Cu(OH)_2 + S^{2-} \rightarrow Cu_2O + S \downarrow + 2OH^- + H_2O \quad (1)$$

$$Cu_2O + S^{2-} + H_2O \rightarrow Cu_2S + 2OH^- \quad (2)$$

Besides, K_{sp} of CuO (4.37×10^{-21})[59] is much higher than that of Cu_2S, and thus the initial formation of a CuO layer due to air oxidation or dehydration of some $Cu(OH)_2$ would also be transformed to Cu_2S via the anion exchange as shown in eq 3.[60]

$$2CuO + 2S^{2-} + 2H_2O \rightarrow Cu_2S + S \downarrow + 4OH^- \quad (3)$$

The S 2p XPS spectrum displayed two well-defined doublets at 162.2 eV (S $2p_{3/2}$) and 169.1 eV (S $2p_{3/2}$) that were assigned to lattice S in Cu_2S and to sulfate species arising from the surface oxidation of the material, respectively.[53,61−66] Sulfates accounted for ca. 14% of the total amount of sulfur detected.

Cu_2S/CM electrodes were cycled in the potential range of 0−0.8 V versus Hg/HgO at a scan rate of 100 mV/s while immersed in a 1 M KOH electrolyte solution. During the initial 50 CV cycles, a drastic change of electrochemical performance was observed (Figure 2a). The first several CVs provided a relatively linear dependence of the current density with the applied potential. This current density rapidly decreased with the cycle number, pointing at an intense chemical transformation of the working electrode. After 150 cycles, the electrochemical response was stabilized (Figures 2b and S3a,b). Figure 2c displays a series of quasi-stationary CVs measured at a slow scan rate of 5 mV/s on the initial Cu_2S/

DOI: 10.1021/acs.chemmater.9b02790
Chem. Mater. 2019, 31, 7732−7743

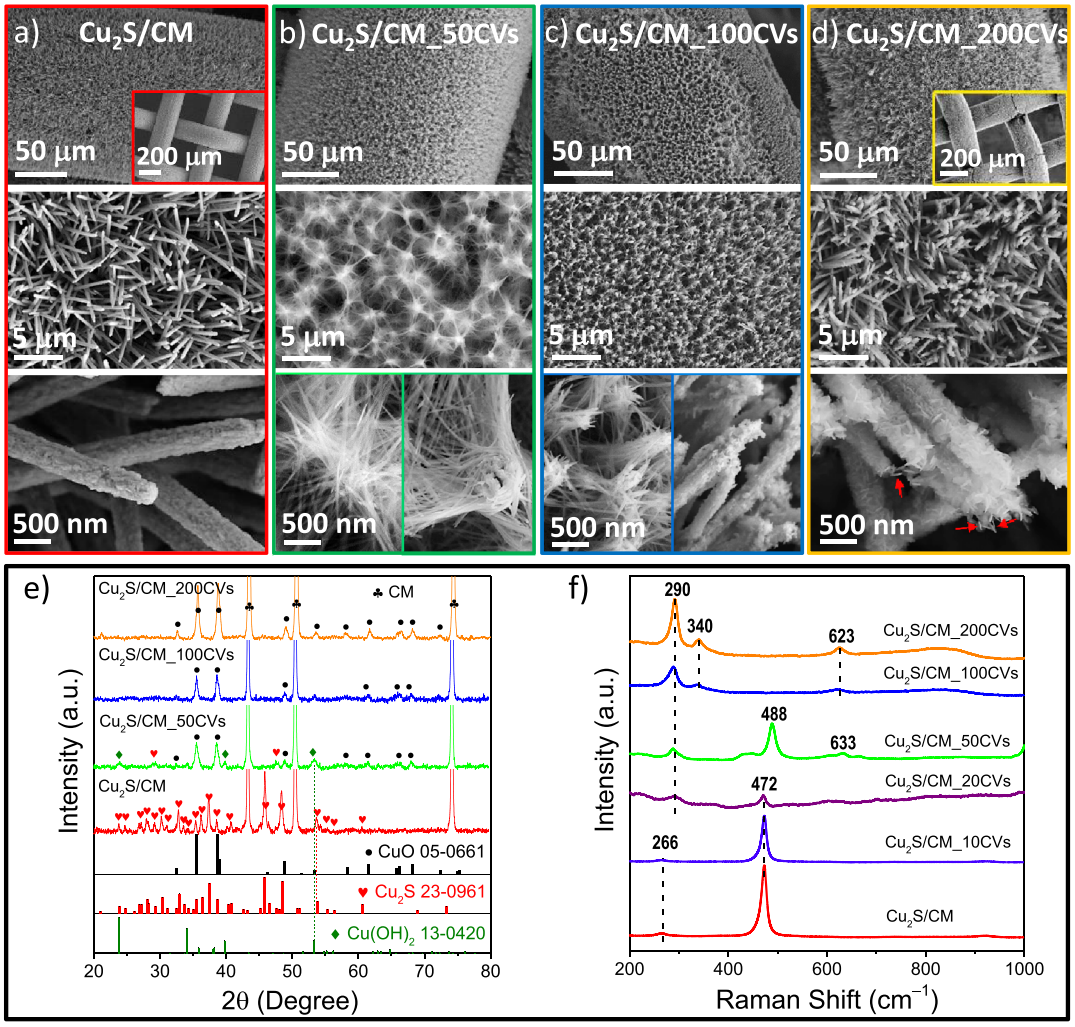

Figure 3. (a–d) SEM micrographs of as-prepared Cu_2S/CM after different numbers of CVs at a scan rate of 100 mV/s: (a) initial; (b) after 50 CVs; (c) after 100 CVs; and (d) after 200 CVs. Arrows point at single nanoflakes used to determine their size. (e) XRD patterns of as-prepared Cu_2S/CM and after different numbers of CVs at a scan rate of 100 mV/s. (f) In situ Raman spectra of as-prepared Cu_2S/CM after 10, 20, 50, 100, and 200 CVs at 100 mV/s.

CM and after 50, 100, and 200 CV cycles (Cu_2S/CM_50CVs; Cu_2S/CM_100CVs; and Cu_2S/CM_200CVs). High oxidation currents were obtained from the initial Cu_2S/CM electrodes, and only after ca. 200 CVs, a conventional and relatively stable OER curve was measured (Figure 2c,d).

SEM analysis of Cu_2S/CM electrodes showed that under OER conditions, the initial Cu_2S NWs developed thin nanofibers that interconnected into networks after 50 CVs (Figure 3a,b). After 100 CVs, the nanofibers had grouped into bundles, which evolved again into nanoflake-based NWs as cycling continued (Figure 3c,d). Stable NWs obtained after ca. 200 CVs were slightly thicker than the initial ones, ca. 400 nm, conserved a similar length, ca. 15 μm, and were composed of slightly larger nanoflakes (ca. 150 nm in diameter, ca. 10 nm in thickness) that grouped less compactly than in the original Cu_2S NWs, thus providing a more porous NW structure.

XRD analysis demonstrated the initial Cu_2S to be transformed into $Cu(OH)_2$ after 50 CVs and to have evolved to CuO after 200 CVs at 100 mV/s (Figure 3e). To track the composition evolution in more detail, in situ Raman spectroscopy was performed on freshly prepared Cu_2S/CM samples after 10, 20, 50, 100, and 200 CVs at 100 mV/s. As shown in Figure 3f, the initial Cu_2S/CM exhibited two characteristic Raman peaks at 266 cm^{-1} (Cu–S bond)[67,68] and 472 cm^{-1} (S–S bond)[67,68] that corresponded to Cu_2S. A similar spectrum was obtained after 10 CVs. After 20 CVs, the intensity of the main peak at 472 cm^{-1} dramatically decreased and new peaks appeared. After 50 CVs, Raman spectra evidenced the presence of $Cu(OH)_2$, with two characteristic peaks at 290 and 488 cm^{-1}.[69] An additional weak peak at 633 cm^{-1} could be assigned to the presence of a copper oxide phase.[69] After extensive cycling, the initial Cu_2S/CM had completely transformed to CuO, which displayed three characteristic Raman peaks at 290 cm^{-1} (Cu–O bond, A_g phonon mode),[69] 340 cm^{-1} (Cu–O bond, B_{1g} phonon mode),[69,70] and 623 cm^{-1} (Cu–O bond, B_{2g} phonon mode).[69,70]

A fresh Cu_2S/CM was cycled for 50 CV at 100 mV/s and afterward operated at a current density of 10 mA/cm^2 for 10 000 s within 1 M KOH water solution. After these two steps, Cu_2S was fully transformed into CuO (Figure 4a). SEM characterization showed the surface morphology of the final material to consist of nanoflake-based NWs as those obtained after extensive cycling (Figure 4b–d). XPS analysis further confirmed the evolution from Cu_2S to CuO after the two steps. A shift of the Cu 2p doublet to higher binding energies, from

DOI: 10.1021/acs.chemmater.9b02790
Chem. Mater. 2019, 31, 7732–7743

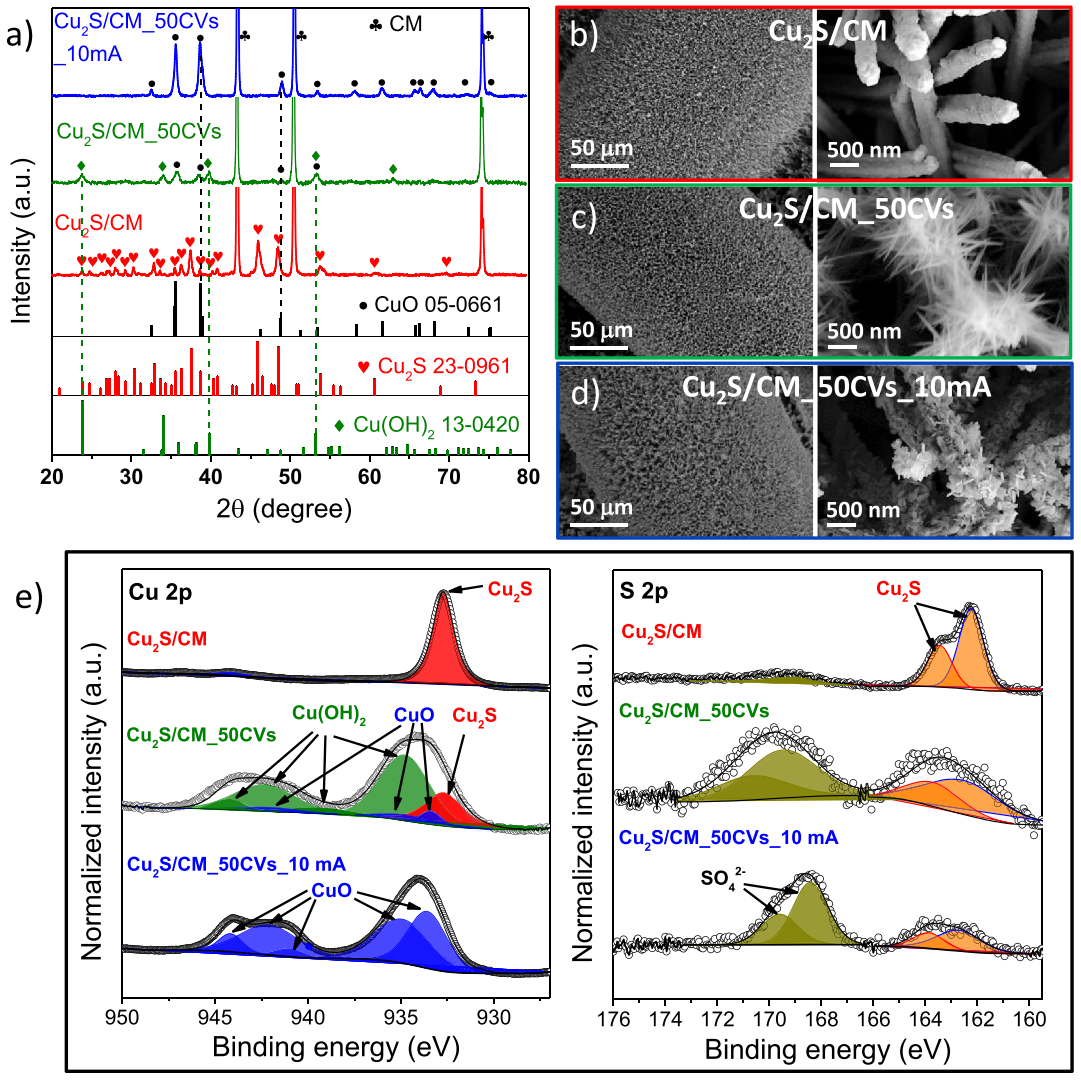

Figure 4. (a) XRD patterns and (b–d) SEM images of fresh Cu_2S/CM after 50 CVs at a scan rate of 100 mV/s (Cu_2S/CM_50CVs) and after additional operation at 10 mA for 10 000 s (Cu_2S/CM_50CVs_10mA). (e) Normalized Cu 2p region and S 2p region of the XPS spectra of Cu_2S/CM, Cu_2S/CM_50CVs, and Cu_2S/CM_50CVs_10mA samples.

932.7 to 933.6 eV ($Cu\ 2p_{3/2}$), was associated with the Cu^+ to Cu^{2+} oxidation (Figure 4e). According to the XPS analysis (Figure 4e, Table S1), the initial Cu_2S/CM sample contained 90% of Cu_2S and 10% CuO ascribed to surface oxidation as aforementioned. This composition changed to 70% $Cu(OH)_2$, 12% CuO, and 18% Cu_2S after 50 CVs and to 100% CuO after additional operation at 10 mA/cm^2 for 10 000 s. Besides, the S 2p peak intensity decreased drastically after operation at 10 mA/cm^2 for 10 000 s, corroborating the chemical transformation of Cu_2S to CuO. Interestingly, small amounts of S remained after the long-term operation, ca. 10% with respect to Cu. The relative amount of sulfate with respect to the total amount of S significantly increased during OER operation, up to a 70% of the total detected sulfur.[42,66]

EELS compositional maps showed a homogeneous distribution of Cu and oxygen throughout the grown nanostructures (Figure 5a,c). HRTEM characterization further confirmed the formation of $Cu(OH)_2$ after 50 CVs, with the additional presence of CuO and Cu_2O minor phases (Figures 5b and S4). We associated the appearance of Cu_2O on the HRTEM analysis to the reduction of CuO under the electron beam, consistent with previous reports.[71] After long-term operation at 10 mA/cm^2, HRTEM characterization displayed the presence of CuO as the main phase (Figure 5d), which matched well with the results obtained by XRD.

A fresh Cu_2S/CM was operated in 1 M KOH solution at 10 mA/cm^2 for 10 000 s without CV preconditioning (Figure 6). Chronopotentiometry curves (Figure 6a) showed the potential required to maintain 10 mA/cm^2 to increase drastically during the initial ca. 2000 s and to stay stable at longer operation times. Initially, no bubbles evolved from the working electrode. However, distinct bubbles started to appear after ca. 2000 s. During this time, the initial black CM surface changed to slight green, which we attributed to the formation of $Cu(OH)_2$, to later become black again. XRD analysis showed the final material to consist of CuO (Figure S5a). SEM analysis showed the final surface to consist of flaked NWs as those obtained after cycling, but presenting more cracks than when the electrode was precycled (Figure S5b,c). After 10 000 s operation, CuO/CM was cycled at 5 mV/s, showing an overpotential of 378 mV ($\eta_{corrected}$ = 336 mV) when delivering a geometric current density of 10 mA/cm^2 (Figure 6b).

According to previous reports, the Cu^{2+}–Cu^{3+} redox is at the basis of the OER mechanism on CuO/CM electrodes,

DOI: 10.1021/acs.chemmater.9b02790
Chem. Mater. 2019, 31, 7732–7743

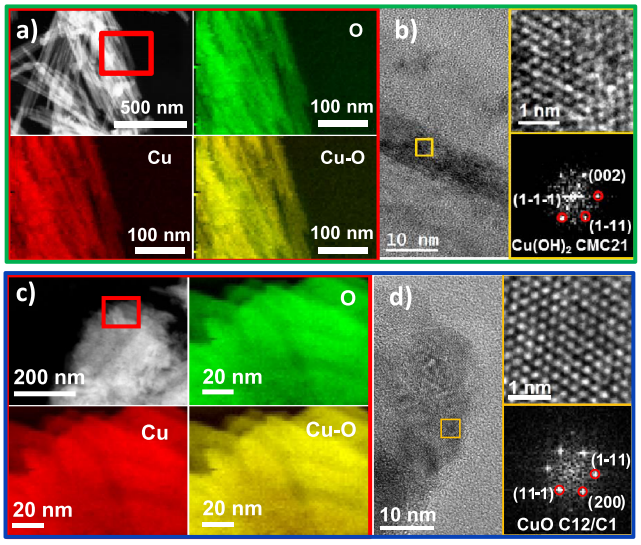

Figure 5. (a) EELS chemical composition maps obtained from the red-squared area in the HAADF STEM micrograph of Cu_2S/CM_50CVs. Individual Cu $L_{2,3}$-edges at 931 eV (red) and O K-edges at 532 eV (green) as well as their composites of Cu−O. (b) HRTEM micrograph of a Cu_2S/CM_50CVs NW; detail of the orange-squared region and its corresponding power spectrum visualized along its [110] zone axis. (c) EELS chemical composition maps obtained from the red squared area in the HAADF STEM micrograph of Cu_2S/CM_50CVs_10mA. (d) HRTEM micrograph of a Cu_2S/CM_50CVs_10mA NW; detail of the orange-squared region and its corresponding power spectrum visualized along its [011] zone axis.

Cu^{3+} species being the catalytically active sites for oxygen evolution.[72−74] The cathodic peak at ca. 1.52 V (0.59 V vs Hg/HgO) obtained on the OER curve of Cu_2S-derived CuO/CM (Figure 6b) was attributed to the reduction of Cu^{3+} to Cu^{2+}.[72−74] The anodic peak corresponding to the oxidation of Cu^{2+}/Cu^{3+} that should appear at ca. 0.7 V versus Hg/HgO[74] was not visible in our CVs because of its overlap with the high OER current density. The following mechanism, involving the intermediates OH, OOH, O, and O_2 adsorbed on an active site M, was proposed for OER in CuO[72,75]

$$M + OH^- \rightarrow M{-}OH + e^-$$

$$M{-}OH + OH^- \rightarrow M{-}O + H_2O + e^-$$

$$M{-}O + OH^- \rightarrow M{-}OOH + e^-$$

$$M{-}OOH + OH^- \rightarrow M{-}OO + H_2O + e^-$$

$$M{-}OO \rightarrow M + O_2$$

The generation of M−OH or M−OOH is the crucial step in the formation of O_2 and in the extensive oxidation of Cu_2S to $Cu(OH)_2$ and CuO. CuO being more thermodynamically stable than $Cu(OH)_2$, $K_{sp\ CuO} = 4.37 \times 10^{-21}$ versus $K_{sp\ Cu(OH)_2} = 4.57 \times 10^{-20}$, CuO/CM is the final composition after relatively long operation of Cu_2S/CM under OER conditions.[59]

To compare the OER performance of Cu_2S-derived CuO/CM, additional $Cu(OH)_2$/CM were produced by oxidizing CM in a NaOH/APS solution, and additional CuO/CM electrodes were obtained by annealing $Cu(OH)_2$/CM under argon (CuO/CM_AN, see Experimental Section for details). $Cu(OH)_2$/CM layers directly obtained from the immersion of CM into NaOH/APS solution contained free-standing faceted NWs as described above. The morphology of these $Cu(OH)_2$ faceted NWs was preserved for several dozens of CVs, but cracks started to appear after 100 CVs (Figure S6). XRD analysis showed $Cu(OH)_2$ NWs to partially transform into CuO after 150 CVs (Figure S7). Notice that the conversion of $Cu(OH)_2$ NWs directly grown of the surface of CM was much slower than that of $Cu(OH)_2$ NWs derived from Cu_2S NWs. We associate this experimental result to the much better crystallinity of the former and to the low concentration of grain boundaries in $Cu(OH)_2$ NWs directly grown from CM. Besides, CuO/CM_AN electrodes displayed the presence of smooth NWs (Figure S8a), which appeared attached together after 50 CVs (Figure S8b). After additional cycles, CuO NWs

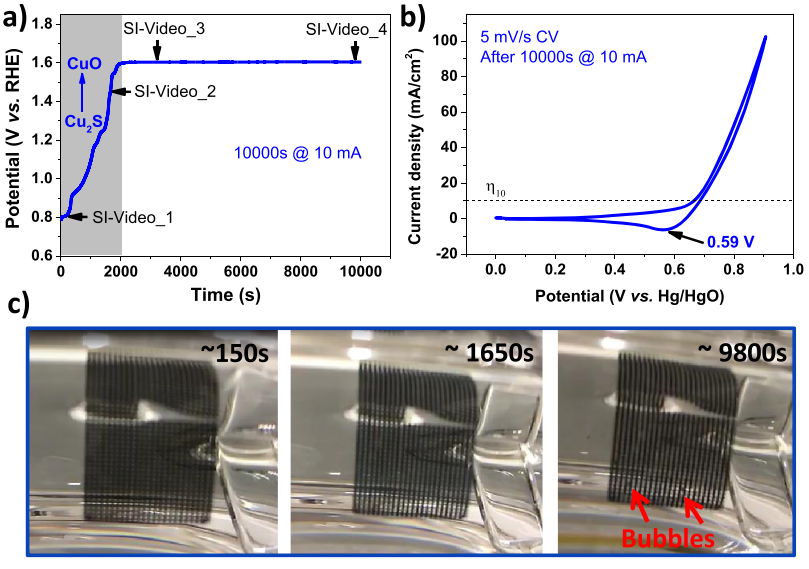

Figure 6. (a) Chronopotentiometry curve of Cu_2S/CM at a geometric current density of 10 mA/cm^2 in 1 M KOH. No CV preconditioning was performed on this sample. (b) Quasi-stationary OER polarization CV at a scan rate of 5 mV/s of Cu_2S/CM after 10 000 s at 10 mA. (c) Video frames of a Cu_2S/CM working electrode showing the evolution of bubbles after 9800 s OER operation.

DOI: 10.1021/acs.chemmater.9b02790
Chem. Mater. 2019, 31, 7732−7743

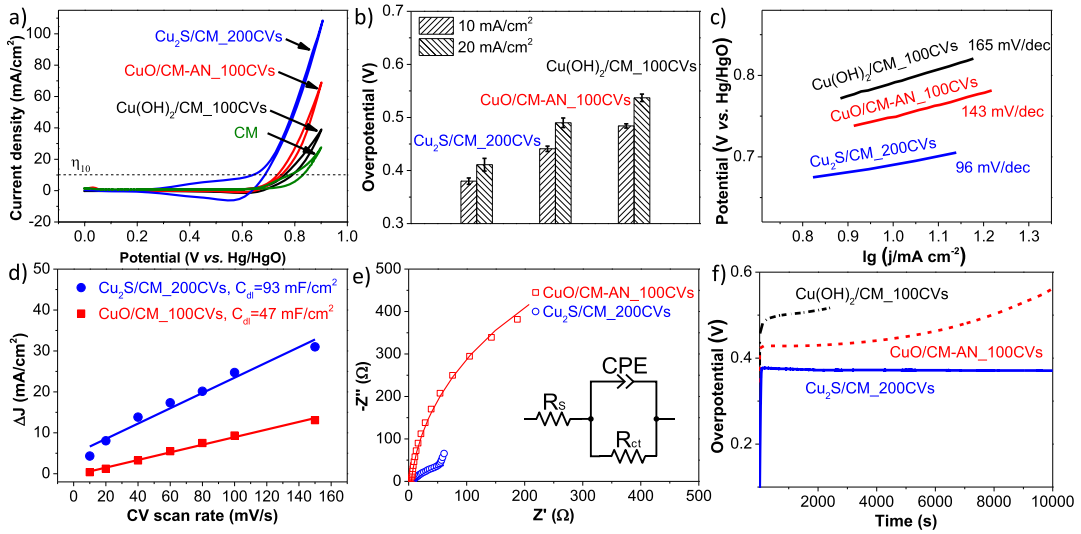

Figure 7. OER activity of $Cu(OH)_2$/CM_100CVs (black line), CuO/CM-AN_100CVs (red line), and Cu_2S/CM_200CVs (blue line) in 1.0 M KOH. (a) Quasi-stationary CVs at a scan rate of 5 mV/s. (b) OER overpotential at 10 mA/cm^2 and 20 mV/cm^2. (c) Tafel curves. (d) Capacitive current densities at 1.27 V vs RHE as a function of the scan rate. (e) Nyquist plots of the impedances including the fitted curves and equivalent circuit. (f) Chronopotentiometric curves at a constant current density of 10 mA/cm^2.

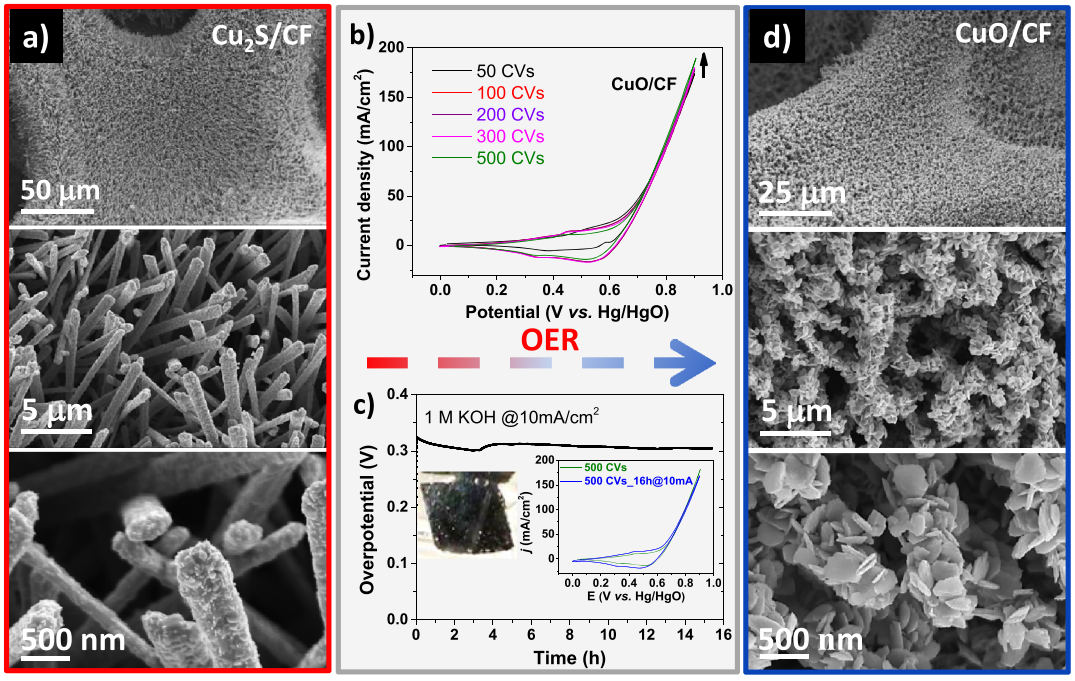

Figure 8. (a) SEM images of Cu_2S/CF before the electrochemical tests. (b) Quasi-stationary OER polarization curves at a scan rate of 5 mV/s from Cu_2S/CF electrodes after different CV activation cycles. (c) Long-term chronopotentiometric curve at a constant current density of 10 mA/cm^2; the inset photograph shows oxygen bubbles evolving from the working electrode during the OER (see Supporting Information Video S5 for more details). The inset graph shows the quasi-stationary OER polarization CV before and after chronopotentiometry. (d) SEM images of Cu_2S-derived CuO/CF after chronopotentiometry.

started to break, and after long term chronopotentiometric measurements, they detached from CM (Figure S8c,d). It should be noticed that directly formed $Cu(OH)_2$/CM and CuO/CM_AN electrodes did not display the same dramatic evolution of the CVs obtained for Cu_2S/CM during the first several cycles (Figures S9 and S10).

Figure 7a displays quasi-stationary polarization CV curves from CM and from directly obtained $Cu(OH)_2$/CM_100CVs, CuO/CM-AN_100CVs, and Cu_2S-derived CuO/CM_200CVs at a scan rate of 5 mV/s. Bare CM showed very poor activity toward OER, requiring an overpotential of 526 mV to deliver a geometric current density of 10 mA/cm^2. Cu_2S-derived CuO/CM required 380 mV ($\eta_{corrected}$ = 338 mV) to reach 10 mA/cm^2, well below the overpotential required by $Cu(OH)_2$/CM_100CVs (η = 484 mV) and CuO/CM_100CVs (η = 441 mV). Cu_2S-derived CuO/CM electrodes also displayed much lower Tafel slopes, 96 mV/dec, than the other electrodes measured (Figure 7b,c), suggesting more favorable OER kinetics.

DOI: 10.1021/acs.chemmater.9b02790
Chem. Mater. 2019, 31, 7732−7743

ECSA and EIS measurements were carried out to further understand the improved OER activity of Cu_2S-derived CuO/CM electrodes. The relative ECSA was estimated through measurement of the double-layer capacitances (C_{dl}) at the solid/liquid interface.[76] As shown in Figure S11, the C_{dl} values for Cu_2S/CM_100CVs and CuO/CM-AN_100CVs were calculated as 93 and 47 mF/cm^2, whereas their ECSAs were calculated as 2325 and 1175, respectively (see Experimental Section for details). This result suggested a much higher surface roughness for Cu_2S-derived CuO/CMs than the directly obtained CuO/CM-AN (Figures S11 and 7d).

Nyquist plots of the impedance response measured at 0.68 V versus Hg/HgO of Cu_2S/CM_200CVs and CuO/CM-AN_100CVs are shown in Figure 7e. Qualitatively speaking, Cu_2S/CM_200CVs exhibited a smaller semicircle radius compared with that of CuO/CM-AN_100CVs, indicating a smaller charge-transfer resistance.[77,78] Impedance responses were fitted with an equivalent circuit containing a series resistance R_s, a charge-transfer resistance R_{ct}, and a constant phase element (Figure 7e, inset).[77,79,80] Fitting results unambiguously revealed a clearly enhanced charge-transfer process on Cu_2S/CM_200CVs, with a R_{ct} of 146 Ω, than on CuO/CM-AN_100CVs, with an order of magnitude higher R_{ct}, 1288 Ω.

As shown in Figure 7f, the overpotential required by Cu_2S-derived CuO/CM electrodes to deliver a geometric current density of 10 mA/cm^2 remained unchanged after 10 000 s. Besides, no obvious change on CV behavior occurred after the long-term stability test (Figure 2d), indicating remarkable stable electrochemical activity toward OER. On the other hand, the overpotential of $Cu(OH)_2$/CM_100CVs electrode clearly increased from the very beginning of the durability test, manifesting a moderate stability for water electrolysis. As for the CuO/CM-AN_100CVs electrode, it showed good stability in the initial ca. 2000 s, but after this time period, the overpotential strongly increased, which we associated with the detachment of CuO from the CM (Figure S8d).

To study the influence of possible electrolyte change due to leaching of sulfides from Cu_2S during the long-term test, quasi-stationary CVs without/with a fresh electrolyte were obtained to compare OER performances. As can be seen in Figure S12a, there is a slight increase of the performance using the fresh electrolyte, demonstrating that the electrolyte after the long-term test would not lead to an improvement of performance. Besides, ECSA-normalized current density of Cu_2S-derived CuO did not display significant differences compared with that of annealed CuO, indicating that the increased amount of surface active sites is the main parameter behind OER enhancement (Figure S12b).

To improve the catalytic performance of Cu_2S-derived CuO/CM, the CM was replaced by a CF, which provided a larger surface area. CV curves measured from Cu_2S/CF displayed a similar evolution in the first several cycles, indicating the transition from Cu_2S/CF to CuO/CF via $Cu(OH)_2$/CF intermediate (Figure S13). This result was confirmed by XRD and SEM analysis that displayed a structural and morphology evolution similar to that described for Cu_2S/CM (Figures 8a,d and S14). OER performance was improved after CV activation, reaching an overpotential down to 328 mV ($\eta_{corrected}$ = 286 mV) to deliver a geometric current density of 10 mA/cm^2 and a Tafel slope of 87 mV/dec (Figure 8b). A remarkable durability for 16 h was also measured (Figure 8c and inset). These results place Cu_2S-derived CuO/CF among the best Cu-based OER catalysts, with even better performance than numerous nickel/cobalt-based catalysts previously reported (Table S2).

This outstanding performance was associated with several advantages of the Cu_2S-derived electrocatalyst, namely, (a) improved adhesion of the active layer to copper when mediating an intermediate sulfurization step; (b) increased surface area associated with the nanostructuration of the NWs; (c) lower charge-transfer resistance associated with the higher surface area and the larger density or higher activity of the newly formed catalytic sites; and (d) the presence of additional oxidized sulfate on the surface. In this last direction, recent reports indicated that in metal sulfides, oxidized S species can remain on the surface for a long period of time and are favorable for OER catalytic activity by tuning the adsorption free energy of the reaction intermediates on the metal sites.[42−45]

4. CONCLUSIONS

In summary, we reported on the chemical, structural, and morphological in situ transformation of Cu_2S/CM into CuO/CM during OER via $Cu(OH)_2$ intermediate. Cu_2S-derived CuO/CM displayed enhanced electrochemical OER activity than its precursors $Cu(OH)_2$/CM and CuO/CM-AN directly obtained from $Cu(OH)_2$/CM annealing. Cu_2S-derived CuO/CF displayed an overpotential of 286 mV to deliver a geometric current density of 10 mA/cm^2, surpassing most Cu-based OER electrocatalysts previously reported. Improved performance with respect to CuO produced from the annealing of $Cu(OH)_2$ NWs was associated with (i) a more stable attachment of the active layer to the current collector, (ii) a higher surface area, (iii) a lower charge-transfer resistance, and (iv) the presence of sulfate ions that may facilitate the OER process by tuning the adsorption free energy of reaction intermediates. We believe this work provides insights for the fabrication of more effective metal-oxide OER catalysts using a simple electrochemical oxidation process. This strategy may be also extended to other sulfides and chalcogenides and even to phosphide and nitride catalysts. Additionally, based on these results, we suggest the necessity to reconsider the chemical composition and associated OER performance of previously reported sulfide OER catalysts in alkaline media.

■ ASSOCIATED CONTENT

Supporting Information

The Supporting Information is available free of charge on the ACS Publications website at DOI: 10.1021/acs.chemmater.9b02790.

Additional EDX, SEM, XRD, TEM, and electrochemical measurements, table of sample components calculated from XPS and AES, and table of activity comparisons of OER electrocatalysts (PDF)

Fresh Cu_2S/CM operated in 1 M KOH solution at 10 mA/cm^2 after 150 s (MP4)

Fresh Cu_2S/CM operated in 1 M KOH solution at 10 mA/cm^2 after 1650 s (MP4)

Fresh Cu_2S/CM operated in 1 M KOH solution at 10 mA/cm^2 after 3200 s (MP4)

Fresh Cu_2S/CM operated in 1 M KOH solution at 10 mA/cm^2 after 9800 s (MP4)

DOI: 10.1021/acs.chemmater.9b02790
Chem. Mater. 2019, 31, 7732−7743

Cu_2S/CF operated in 1 M KOH solution at 10 mA/cm^2 after 5000 s (MP4)

AUTHOR INFORMATION

Corresponding Author

*E-mail: acabot@irec.cat.

ORCID

Yong Zuo: 0000-0003-1564-467X
Yongpeng Liu: 0000-0002-4544-4217
Jordi Arbiol: 0000-0002-0695-1726
Jordi Llorca: 0000-0002-7447-9582
Néstor Guijarro: 0000-0002-3277-8816
Kevin Sivula: 0000-0002-8458-0270
Andreu Cabot: 0000-0002-7533-3251

Notes

The authors declare no competing financial interest.

ACKNOWLEDGMENTS

This work was supported by the European Regional Development Funds and by the Spanish Ministerio de Economía y Competitividad through the project SEHTOP (ENE2016-77798-C4-3-R). Y.Z., Junshan Li, R.D., X.H., and T.Z. thank the China Scholarship Council for the scholarship support. Y.L. and N.G. thank the Swiss National Science Foundation (SNF) for funding under the Ambizione Energy grant no. PZENP2_166871. Jordi Llorca is a Serra Húnter Fellow and is grateful to ICREA Academia program and to GC 2017 SGR 128. ICN2 acknowledges funding from Generalitat de Catalunya 2017 SGR 327 and the Spanish MINECO project ENE2017-85087-C3. ICN2 is supported by the Severo Ochoa program from the Spanish MINECO (grant no. SEV-2017-0706) and is funded by the CERCA Programme/Generalitat de Catalunya. Part of the present work has been performed in the framework of Universitat Autònoma de Barcelona Materials Science PhD program.

REFERENCES

(1) Cabán-Acevedo, M.; Stone, M. L.; Schmidt, J. R.; Thomas, J. G.; Ding, Q.; Chang, H.-C.; Tsai, M.-L.; He, J.-H.; Jin, S. Efficient Hydrogen Evolution Catalysis Using Ternary Pyrite-Type Cobalt Phosphosulphide. *Nat. Mater.* **2015**, *14*, 1245−1251.

(2) Jin, S. Are Metal Chalcogenides, Nitrides, and Phosphides Oxygen Evolution Catalysts or Bifunctional Catalysts? *ACS Energy Lett.* **2017**, *2*, 1937−1938.

(3) Wang, H.-F.; Tang, C.; Zhang, Q. A Review of Precious-Metal-Free Bifunctional Oxygen Electrocatalysts: Rational Design and Applications in Zn−Air Batteries. *Adv. Funct. Mater.* **2018**, *28*, 1803329.

(4) Zou, X.; Goswami, A.; Asefa, T. Efficient Noble Metal-Free (Electro)Catalysis of Water and Alcohol Oxidations by Zinc-Cobalt Layered Double Hydroxide. *J. Am. Chem. Soc.* **2013**, *135*, 17242−17245.

(5) Li, D.; Baydoun, H.; Verani, C. N.; Brock, S. L. Efficient Water Oxidation Using CoMnP Nanoparticles. *J. Am. Chem. Soc.* **2016**, *138*, 4006−4009.

(6) Gao, R.; Li, G.-D.; Hu, J.; Wu, Y.; Lian, X.; Wang, D.; Zou, X. In Situ Electrochemical Formation of NiSe/NiOx Core/Shell Nano-Electrocatalysts for Superior Oxygen Evolution Activity. *Catal. Sci. Technol.* **2016**, *6*, 8268−8275.

(7) Dutta, A.; Samantara, A. K.; Dutta, S. K.; Jena, B. K.; Pradhan, N. Surface-Oxidized Dicobalt Phosphide Nanoneedles as a Nonprecious, Durable, and Efficient OER Catalyst. *ACS Energy Lett.* **2016**, *1*, 169−174.

(8) Zhang, J.; Wang, T.; Pohl, D.; Rellinghaus, B.; Dong, R.; Liu, S.; Zhuang, X.; Feng, X. Interface Engineering of MoS_2/Ni_3S_2 Heterostructures for Highly Enhanced Electrochemical Overall-Water-Splitting Activity. *Angew. Chem., Int. Ed.* **2016**, *55*, 6702−6707.

(9) Song, F.; Schenk, K.; Hu, X. A Nanoporous Oxygen Evolution Catalyst Synthesized by Selective Electrochemical Etching of Perovskite Hydroxide $CoSn(OH)_6$ Nanocubes. *Energy Environ. Sci.* **2016**, *9*, 473−477.

(10) Jia, X.; Zhao, Y.; Chen, G.; Shang, L.; Shi, R.; Kang, X.; Waterhouse, G. I. N.; Wu, L.-Z.; Tung, C.-H.; Zhang, T. Ni_3FeN Nanoparticles Derived from Ultrathin NiFe-Layered Double Hydroxide Nanosheets: An Efficient Overall Water Splitting Electrocatalyst. *Adv. Energy Mater.* **2016**, *6*, 1502585.

(11) Jin, Y.; Wang, H.; Li, J.; Yue, X.; Han, Y.; Shen, P. K.; Cui, Y. Porous MoO_2 Nanosheets as Non-Noble Bifunctional Electrocatalysts for Overall Water Splitting. *Adv. Mater.* **2016**, *28*, 3785−3790.

(12) Yan, X.; Li, K.; Lyu, L.; Song, F.; He, J.; Niu, D.; Liu, L.; Hu, X.; Chen, X. From Water Oxidation to Reduction: Transformation from $Ni_xCo_{3-x}O_4$ Nanowires to NiCo/NiCoO $_x$ Heterostructures. *ACS Appl. Mater. Interfaces* **2016**, *8*, 3208−3214.

(13) Liu, Y.; Liang, X.; Gu, L.; Zhang, Y.; Li, G. D.; Zou, X.; Chen, J. S. Corrosion Engineering towards Efficient Oxygen Evolution Electrodes with Stable Catalytic Activity for over 6000 Hours. *Nat. Commun.* **2018**, *9*, 2609.

(14) McCrory, C. C. L.; Jung, S.; Ferrer, I. M.; Chatman, S. M.; Peters, J. C.; Jaramillo, T. F. Benchmarking Hydrogen Evolving Reaction and Oxygen Evolving Reaction Electrocatalysts for Solar Water Splitting Devices. *J. Am. Chem. Soc.* **2015**, *137*, 4347−4357.

(15) Browne, M. P.; Sofer, Z.; Pumera, M. Layered and Two Dimensional Metal Oxides for Electrochemical Energy Conversion. *Energy Environ. Sci.* **2019**, *12*, 41−58.

(16) He, P.; Yu, X.-Y.; Lou, X. W. D. Carbon-Incorporated Nickel−Cobalt Mixed Metal Phosphide Nanoboxes with Enhanced Electrocatalytic Activity for Oxygen Evolution. *Angew. Chem., Int. Ed.* **2017**, *56*, 3897−3900.

(17) Qiu, B.; Cai, L.; Wang, Y.; Lin, Z.; Zuo, Y.; Wang, M.; Chai, Y. Fabrication of Nickel−Cobalt Bimetal Phosphide Nanocages for Enhanced Oxygen Evolution Catalysis. *Adv. Funct. Mater.* **2018**, *28*, 1706008.

(18) Yu, X.-Y.; Feng, Y.; Guan, B.; Lou, X. W.; Paik, U. Carbon Coated Porous Nickel Phosphides Nanoplates for Highly Efficient Oxygen Evolution Reaction. *Energy Environ. Sci.* **2016**, *9*, 1246−1250.

(19) Xu, K.; Chen, P.; Li, X.; Tong, Y.; Ding, H.; Wu, X.; Chu, W.; Peng, Z.; Wu, C.; Xie, Y. Metallic Nickel Nitride Nanosheets Realizing Enhanced Electrochemical Water Oxidation. *J. Am. Chem. Soc.* **2015**, *137*, 4119−4125.

(20) Wang, Y.; Liu, D.; Liu, Z.; Xie, C.; Huo, J.; Wang, S. Porous Cobalt-Iron Nitride Nanowires as Excellent Bifunctional Electrocatalysts for Overall Water Splitting. *Chem. Commun.* **2016**, *52*, 12614−12617.

(21) Wang, Y.; Zhang, B.; Pan, W.; Ma, H.; Zhang, J. 3D Porous Nickel−Cobalt Nitrides Supported on Nickel Foam as Efficient Electrocatalysts for Overall Water Splitting. *ChemSusChem* **2017**, *10*, 4170−4177.

(22) Wang, Y.; Xie, C.; Liu, D.; Huang, X.; Huo, J.; Wang, S. Nanoparticle-Stacked Porous Nickel-Iron Nitride Nanosheet: A Highly Efficient Bifunctional Electrocatalyst for Overall Water Splitting. *ACS Appl. Mater. Interfaces* **2016**, *8*, 18652−18657.

(23) Hou, Y.; Lohe, M. R.; Zhang, J.; Liu, S.; Zhuang, X.; Feng, X. Vertically Oriented Cobalt Selenide/NiFe Layered-Double-Hydroxide Nanosheets Supported on Exfoliated Graphene Foil: An Efficient 3D Electrode for Overall Water Splitting. *Energy Environ. Sci.* **2016**, *9*, 478−483.

(24) Xu, R.; Wu, R.; Shi, Y.; Zhang, J.; Zhang, B. Ni_3Se_2 Nanoforest/Ni Foam as a Hydrophilic, Metallic, and Self-Supported Bifunctional Electrocatalyst for Both H_2 and O_2 Generations. *Nano Energy* **2016**, *24*, 103−110.

(25) Xiong, D.; Zhang, Q.; Thalluri, S. M.; Xu, J.; Li, W.; Fu, X.; Liu, L. One-Step Fabrication of Monolithic Electrodes Comprising Co_9S_8

DOI: 10.1021/acs.chemmater.9b02790
Chem. Mater. 2019, 31, 7732−7743

Particles Supported on Cobalt Foam for Efficient and Durable Oxygen Evolution Reaction. *Chem.—Eur. J.* **2017**, *23*, 8749−8755.
(26) Dong, B.; Zhao, X.; Han, G.-Q.; Li, X.; Shang, X.; Liu, Y.-R.; Hu, W.-H.; Chai, Y.-M.; Zhao, H.; Liu, C.-G. Two-Step Synthesis of Binary Ni-Fe Sulfides Supported on Nickel Foam as Highly Efficient Electrocatalysts for the Oxygen Evolution Reaction. *J. Mater. Chem. A* **2016**, *4*, 13499−13508.
(27) Zhu, W.; Yue, X.; Zhang, W.; Yu, S.; Zhang, Y.; Wang, J.; Wang, J. Nickel Sulfide Microsphere Film on Ni Foam as an Efficient Bifunctional Electrocatalyst for Overall Water Splitting. *Chem. Commun.* **2016**, *52*, 1486−1489.
(28) Ma, X.; Zhang, W.; Deng, Y.; Zhong, C.; Hu, W.; Han, X. Phase and Composition Controlled Synthesis of Cobalt Sulfide Hollow Nanospheres for Electrocatalytic Water Splitting. *Nanoscale* **2018**, *10*, 4816−4824.
(29) Huynh, M.; Bediako, D. K.; Nocera, D. G. A Functionally Stable Manganese Oxide Oxygen Evolution Catalyst in Acid. *J. Am. Chem. Soc.* **2014**, *136*, 6002−6010.
(30) Ryu, J.; Jung, N.; Jang, J. H.; Kim, H.-J.; Yoo, S. J. In Situ Transformation of Hydrogen-Evolving CoP Nanoparticles: Toward Efficient Oxygen Evolution Catalysts Bearing Dispersed Morphologies with Co-Oxo/Hydroxo Molecular Units. *ACS Catal.* **2015**, *5*, 4066−4074.
(31) Reddy, N. K.; Winkler, S.; Koch, N.; Pinna, N. Electrochemical Water Oxidation of Ultrathin Cobalt Oxide-Based Catalyst Supported onto Aligned ZnO Nanorods. *ACS Appl. Mater. Interfaces* **2016**, *8*, 3226−3232.
(32) Zhu, Y.; Chen, H.-C.; Hsu, C.-S.; Lin, T.-S.; Chang, C.-J.; Chang, S.-C.; Tsai, L.-D.; Chen, H. M. Operando Unraveling of the Structural and Chemical Stability of P-Substituted $CoSe_2$ Electrocatalysts toward Hydrogen and Oxygen Evolution Reactions in Alkaline Electrolyte. *ACS Energy Lett.* **2019**, *4*, 987−994.
(33) Feng, X.; Jiao, Q.; Liu, T.; Li, Q.; Yin, M.; Zhao, Y.; Li, H.; Feng, C.; Zhou, W. Facile Synthesis of Co_9S_8 Hollow Spheres as a High-Performance Electrocatalyst for the Oxygen Evolution Reaction. *ACS Sustainable Chem. Eng.* **2018**, *6*, 1863−1871.
(34) Wygant, B. R.; Kawashima, K.; Mullins, C. B. Catalyst or Precatalyst? The Effect of Oxidation on Transition Metal Carbide, Pnictide, and Chalcogenide Oxygen Evolution Catalysts. *ACS Energy Lett.* **2018**, *3*, 2956−2966.
(35) Mabayoje, O.; Shoola, A.; Wygant, B. R.; Mullins, C. B. The Role of Anions in Metal Chalcogenide Oxygen Evolution Catalysis: Electrodeposited Thin Films of Nickel Sulfide as "Pre-Catalysts". *ACS Energy Lett.* **2016**, *1*, 195−201.
(36) Lian, Y.; Sun, H.; Wang, X.; Qi, P.; Mu, Q.; Chen, Y.; Ye, J.; Zhao, X.; Deng, Z.; Peng, Y. Carved Nanoframes of Cobalt-Iron Bimetal Phosphide as a Bifunctional Electrocatalyst for Efficient Overall Water Splitting. *Chem. Sci.* **2019**, *10*, 464−474.
(37) Xu, J.; Li, J.; Xiong, D.; Zhang, B.; Liu, Y.; Wu, K.-H.; Amorim, I.; Li, W.; Liu, L. Trends in Activity for the Oxygen Evolution Reaction on Transition Metal (M = Fe, Co, Ni) Phosphide Pre-Catalysts. *Chem. Sci.* **2018**, *9*, 3470−3476.
(38) Zhang, Y.; Ouyang, B.; Xu, J.; Jia, G.; Chen, S.; Rawat, R. S.; Fan, H. J. Rapid Synthesis of Cobalt Nitride Nanowires: Highly Efficient and Low-Cost Catalysts for Oxygen Evolution. *Angew. Chem., Int. Ed.* **2016**, *55*, 8670−8674.
(39) Li, W.; Gao, X.; Xiong, D.; Xia, F.; Liu, J.; Song, W.-G.; Xu, J.; Thalluri, S. M.; Cerqueira, M. F.; Fu, X.; Liu, L. Vapor-Solid Synthesis of Monolithic Single-Crystalline CoP Nanowire Electrodes for Efficient and Robust Water Electrolysis. *Chem. Sci.* **2017**, *8*, 2952−2958.
(40) Liu, Y.; Li, Q.; Si, R.; Li, G.-D.; Li, W.; Liu, D.-P.; Wang, D.; Sun, L.; Zhang, Y.; Zou, X. Coupling Sub-Nanometric Copper Clusters with Quasi-Amorphous Cobalt Sulfide Yields Efficient and Robust Electrocatalysts for Water Splitting Reaction. *Adv. Mater.* **2017**, *29*, 1606200.
(41) Xu, X.; Song, F.; Hu, X. A Nickel Iron Diselenide-Derived Efficient Oxygen-Evolution Catalyst. *Nat. Commun.* **2016**, *7*, 12324.
(42) Souleymen, R.; Wang, Z.; Qiao, C.; Naveed, M.; Cao, C. Microwave-Assisted Synthesis of Graphene-like Cobalt Sulfide Freestanding Sheets as an Efficient Bifunctional Electrocatalyst for Overall Water Splitting. *J. Mater. Chem. A* **2018**, *6*, 7592−7607.
(43) Wu, Z.; Huang, L.; Liu, H.; Wang, H. Element-Specific Restructuring of Anion- and Cation-Substituted Cobalt Phosphide Nanoparticles under Electrochemical Water-Splitting Conditions. *ACS Catal.* **2019**, *9*, 2956−2961.
(44) Wang, T.; Nam, G.; Jin, Y.; Wang, X.; Ren, P.; Kim, M. G.; Liang, J.; Wen, X.; Jang, H.; Han, J.; Huang, Y.; Li, Q.; Cho, J. NiFe (Oxy) Hydroxides Derived from NiFe Disulfides as an Efficient Oxygen Evolution Catalyst for Rechargeable Zn−Air Batteries: The Effect of Surface S Residues. *Adv. Mater.* **2018**, *30*, 1800757.
(45) Legrand, D. L.; Nesbitt, H. W.; Bancroft, G. M. X-Ray Photoelectron Spectroscopic Study of a Pristine Millerite (NiS) Surface and the Effect of Air and Water Oxidation. *Am. Mineral.* **1998**, *83*, 1256−1265.
(46) Hou, C.-C.; Wang, C.-J.; Chen, Q.-Q.; Lv, X.-J.; Fu, W.-F.; Chen, Y. Rapid Synthesis of Ultralong $Fe(OH)_3$:$Cu(OH)_2$ Core-Shell Nanowires Self-Supported on Copper Foam as a Highly Efficient 3D Electrode for Water Oxidation. *Chem. Commun.* **2016**, *52*, 14470−14473.
(47) Kang, J.; Sheng, J.; Xie, J.; Ye, H.; Chen, J.; Fu, X.-Z.; Du, G.; Sun, R.; Wong, C.-P. Tubular $Cu(OH)_2$ Arrays Decorated with Nanothorny Co-Ni Bimetallic Carbonate Hydroxide Supported on Cu Foam: A 3D Hierarchical Core-Shell Efficient Electrocatalyst for the Oxygen Evolution Reaction. *J. Mater. Chem. A* **2018**, *6*, 10064−10073.
(48) McCrory, C. C. L.; Jung, S.; Peters, J. C.; Jaramillo, T. F. Benchmarking Heterogeneous Electrocatalysts for the Oxygen Evolution Reaction. *J. Am. Chem. Soc.* **2013**, *135*, 16977−16987.
(49) Liu, X.; Cui, S.; Sun, Z.; Ren, Y.; Zhang, X.; Du, P. Self-Supported Copper Oxide Electrocatalyst for Water Oxidation at Low Overpotential and Confirmation of Its Robustness by Cu K-Edge X-Ray Absorption Spectroscopy. *J. Phys. Chem. C* **2016**, *120*, 831−840.
(50) Zhu, S.; Wang, Z.; Huang, F.; Zhang, H.; Li, S. Hierarchical $Cu(OH)_2$@$Ni_2(OH)_2CO_3$ Core/Shell Nanowire Arrays: In Situ Grown on Three-Dimensional Copper Foam for High-Performance Solid-State Supercapacitors. *J. Mater. Chem. A* **2017**, *5*, 9960−9969.
(51) Wang, P.; Qiao, M.; Shao, Q.; Pi, Y.; Zhu, X.; Li, Y.; Huang, X. Phase and Structure Engineering of Copper Tin Heterostructures for Efficient Electrochemical Carbon Dioxide Reduction. *Nat. Commun.* **2018**, *9*, 4933.
(52) An, L.; Zhou, P.; Yin, J.; Liu, H.; Chen, F.; Liu, H.; Du, Y.; Xi, P. Phase Transformation Fabrication of a Cu_2S Nanoplate as an Efficient Catalyst for Water Oxidation with Glycine. *Inorg. Chem.* **2015**, *54*, 3281−3289.
(53) He, L.; Zhou, D.; Lin, Y.; Ge, R.; Hou, X.; Sun, X.; Zheng, C. Ultrarapid in Situ Synthesis of Cu_2S Nanosheet Arrays on Copper Foam with Room-Temperature-Active Iodine Plasma for Efficient and Cost-Effective Oxygen Evolution. *ACS Catal.* **2018**, *8*, 3859−3864.
(54) Biesinger, M. C. Advanced Analysis of Copper X-Ray Photoelectron Spectra. *Surf. Interface Anal.* **2017**, *49*, 1325−1334.
(55) Larson, P. E. X-Ray Induced Photoelectron and Auger Spectra of Cu, CuO, Cu_2O, and Cu_2S Thin Films. *J. Electron Spectrosc. Relat. Phenom.* **1974**, *4*, 213−218.
(56) Zhou, C.; Li, H.; Lin, J.; Hou, K.; Yang, Z.; Pi, P.; Xu, S.; Wen, X.; Cheng, J. Matchstick-Like Cu_2S@CuxO Nanowire Film: Transition of Superhydrophilicity to Superhydrophobicity. *J. Phys. Chem. C* **2017**, *121*, 19716−19726.
(57) Minguez-Bacho, I.; Courté, M.; Fan, H. J.; Fichou, D. Conformal Cu_2S-Coated Cu_2O Nanostructures Grown by Ion Exchange Reaction and Their Photoelectrochemical Properties. *Nanotechnology* **2015**, *26*, 185401.
(58) Jiang, Y.; Zhang, X.; Ge, Q.-Q.; Yu, B.-B.; Zou, Y.-G.; Jiang, W.-J.; Hu, J.-S.; Song, W.-G.; Wan, L.-J. Engineering the Interfaces of ITO@Cu_2S Nanowire Arrays toward Efficient and Stable Counter Electrodes for Quantum-Dot-Sensitized Solar Cells. *ACS Appl. Mater. Interfaces* **2014**, *6*, 15448−15455.

DOI: 10.1021/acs.chemmater.9b02790
Chem. Mater. 2019, 31, 7732−7743

(59) Pichtel, J. Solubility Product Constants at 25 °C. http://www.aqion.de/site/16 (accessed Aug 12, 2019).
(60) Zhang, X.; Guo, Y.; Zhang, P.; Wu, Z.; Zhang, Z. Superhydrophobic CuO@Cu_2S Nanoplate Vertical Arrays on Copper Surfaces. *Mater. Lett.* **2010**, *64*, 1200−1203.
(61) Kuo, C.-H.; Chu, Y.-T.; Song, Y.-F.; Huang, M. H. Cu_2O Nanocrystal-Templated Growth of Cu_2S Nanocages with Encapsulated Au Nanoparticles and in-Situ Transmission X-Ray Microscopy Study. *Adv. Funct. Mater.* **2011**, *21*, 792−797.
(62) Fan, M.; Gao, R.; Zou, Y.-C.; Wang, D.; Bai, N.; Li, G.-D.; Zou, X. An Efficient Nanostructured Copper(I) Sulfide-Based Hydrogen Evolution Electrocatalyst at Neutral PH. *Electrochim. Acta* **2016**, *215*, 366−373.
(63) Folmer, J. C. W.; Jellinek, F. The Valence of Copper in Sulphides and Selenides: An X-Ray Photoelectron Spectroscopy Study. *J. Less-Common Met.* **1980**, *76*, 153−162.
(64) Nayak, A.; Tsuruoka, T.; Terabe, K.; Hasegawa, T.; Aono, M. Switching Kinetics of a Cu_2S-Based Gap-Type Atomic Switch. *Nanotechnology* **2011**, *22*, 235201.
(65) Laajalehto, K.; Kartio, I.; Nowak, P. XPS Study of Clean Metal Sulfide Surfaces. *Appl. Surf. Sci.* **1994**, *81*, 11−15.
(66) Yang, Y.; Luan, X.; Dai, X.; Zhang, X.; Qiao, H.; Zhao, H.; Yong, J.; Yu, L.; Han, J.; Zhang, J. Partially Sulfurated Ultrathin Nickel-Iron Carbonate Hydroxides Nanosheet Boosting the Oxygen Evolution Reaction. *Electrochim. Acta* **2019**, *309*, 57−64.
(67) Minceva-Sukarova, B.; Najdoski, M.; Grozdanov, I.; Chunnilall, C. J. Raman Spectra of Thin Solid Films of Some Metal Sulfides. *J. Mol. Struct.* **1997**, *410-411*, 267−270.
(68) Milekhin, A. G.; Yeryukov, N. A.; Sveshnikova, L. L.; Duda, T. A.; Rodyakina, E. E.; Gridchin, V. A.; Sheremet, E. S.; Zahn, D. R. T. Combination of Surface- and Interference-Enhanced Raman Scattering by CuS Nanocrystals on Nanopatterned Au Structures. *Beilstein J. Nanotechnol.* **2015**, *6*, 749−754.
(69) Hamilton, J. C. In Situ Raman Spectroscopy of Anodic Films Formed on Copper and Silver in Sodium Hydroxide Solution. *J. Electrochem. Soc.* **1986**, *133*, 739.
(70) Chou, M. H.; Liu, S. B.; Huang, C. Y.; Wu, S. Y.; Cheng, C.-L. Confocal Raman Spectroscopic Mapping Studies on a Single CuO Nanowire. *Appl. Surf. Sci.* **2008**, *254*, 7539−7543.
(71) Long, N. J.; Petford-Long, A. K. In-Situ Electron-Beam-Induced Reduction of CuO: A Study of Phase Transformations in Cupric Oxide. *Ultramicroscopy* **1986**, *20*, 151−159.
(72) Deng, Y.; Handoko, A. D.; Du, Y.; Xi, S.; Yeo, B. S. In Situ Raman Spectroscopy of Copper and Copper Oxide Surfaces during Electrochemical Oxygen Evolution Reaction: Identification of CuIII Oxides as Catalytically Active Species. *ACS Catal.* **2016**, *6*, 2473−2481.
(73) Miller, B. Split-Ring Disk Study of the Anodic Processes at a Copper Electrode in Alkaline Solution. *J. Electrochem. Soc.* **1969**, *116*, 1675.
(74) Reyter, D.; Odziemkowski, M.; Bélanger, D.; Roué, L. Electrochemically Activated Copper Electrodes. *J. Electrochem. Soc.* **2007**, *154*, K36.
(75) Fan, K.; Zou, H.; Lu, Y.; Chen, H.; Li, F.; Liu, J.; Sun, L.; Tong, L.; Toney, M. F.; Sui, M.; Yu, J. Direct Observation of Structural Evolution of Metal Chalcogenide in Electrocatalytic Water Oxidation. *ACS Nano* **2018**, *12*, 12369−12379.
(76) Lu, X.; Zhao, C. Electrodeposition of Hierarchically Structured Three-Dimensional Nickel-Iron Electrodes for Efficient Oxygen Evolution at High Current Densities. *Nat. Commun.* **2015**, *6*, 6616.
(77) Zuo, Y.; Liu, Y.; Li, J.; Du, R.; Yu, X.; Xing, C.; Zhang, T.; Yao, L.; Arbiol, J.; Llorca, J.; Sivula, K.; Guijarro, N.; Cabot, A. Solution-Processed Ultrathin SnS_2-Pt Nanoplates for Photoelectrochemical Water Oxidation. *ACS Appl. Mater. Interfaces* **2019**, *11*, 6918−6926.
(78) Zhu, X.; Guijarro, N.; Liu, Y.; Schouwink, P.; Wells, R. A.; Le Formal, F.; Sun, S.; Gao, C.; Sivula, K. Spinel Structural Disorder Influences Solar-Water-Splitting Performance of $ZnFe_2O_4$ Nanorod Photoanodes. *Adv. Mater.* **2018**, *30*, 1801612.
(79) Liu, Y.; Le Formal, F.; Boudoire, F.; Yao, L.; Sivula, K.; Guijarro, N. Insights into the Interfacial Carrier Behaviour of Copper Ferrite ($CuFe_2O_4$) Photoanodes for Solar Water Oxidation. *J. Mater. Chem. A* **2019**, *7*, 1669−1677.
(80) Liu, Y.; Le Formal, F.; Boudoire, F.; Guijarro, N. Hematite Photoanodes for Solar Water Splitting: a Detailed Spectroelectrochemical Analysis on the pH-Dependent Performance. *ACS Appl. Energy Mater.* **2019**, DOI: 10.1021/acsaem.9b01261.

DOI: 10.1021/acs.chemmater.9b02790
Chem. Mater. 2019, 31, 7732−7743

ACS APPLIED MATERIALS & INTERFACES

Research Article

Cite This: ACS Appl. Mater. Interfaces 2019, 11, 6918−6926

www.acsami.org

Solution-Processed Ultrathin SnS_2−Pt Nanoplates for Photoelectrochemical Water Oxidation

Yong Zuo,[†,‡] Yongpeng Liu,[§] Junshan Li,[†,‡] Ruifeng Du,[†,‡] Xiaoting Yu,[†,‡] Congcong Xing,[†] Ting Zhang,[∥] Liang Yao,[§] Jordi Arbiol,[∥,⊥] Jordi Llorca,[#] Kevin Sivula,[§] Néstor Guijarro,[§] and Andreu Cabot*[,†,⊥]

[†]Catalonia Institute for Energy Research − IREC, Sant Adrià del Besòs, 08930 Barcelona, Spain

[‡]Departament d'Electronica, Universitat de Barcelona, 08028 Barcelona, Spain

[§]Laboratory for Molecular Engineering of Optoelectronic Nanomaterials (LIMNO), École Polytechnique Fédérale de Lausanne (EPFL), Station 6, CH-1015 Lausanne, Switzerland

[∥]Catalan Institute of Nanoscience and Nanotechnology (ICN2), CSIC, and BIST, Campus UAB, Bellaterra, 08193 Barcelona, Spain

[⊥]ICREA, Pg. Lluís Companys 23, 08010 Barcelona, Spain

[#]Institute of Energy Technologies, Department of Chemical Engineering, and Barcelona Research Center in Multiscale Science and Engineering, Universitat Politècnica de Catalunya, EEBE, 08019 Barcelona, Spain

Supporting Information

ABSTRACT: Tin disulfide (SnS_2) is attracting significant interest because of the abundance of its elements and its excellent optoelectronic properties in part related to its layered structure. In this work, we specify the preparation of ultrathin SnS_2 nanoplates (NPLs) through a hot-injection solution-based process. Subsequently, Pt was grown on their surface via in situ reduction of a Pt salt. The photoelectrochemical (PEC) performance of such nanoheterostructures as photoanode toward water oxidation was tested afterwards. Optimized SnS_2−Pt photoanodes provided significantly higher photocurrent densities than bare SnS_2 and SnS_2-based photoanodes of previously reported study. Mott−Schottky analysis and PEC impedance spectroscopy (PEIS) were used to analyze in more detail the effect of Pt on the PEC performance. From these analyses, we attribute the enhanced activity of SnS_2−Pt photoanodes reported here to a combination of the very thin SnS_2 NPLs and the proper electronic contact between Pt nanoparticles (NPs) and SnS_2.

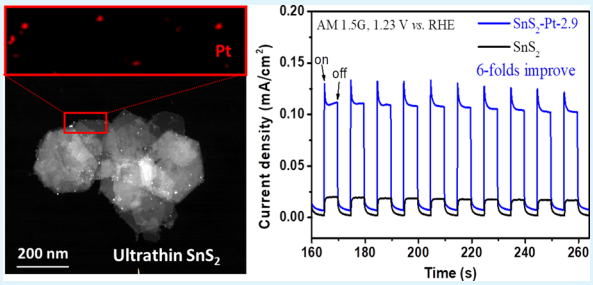

KEYWORDS: *Tin disulfide, two-dimensional material, SnS_2−Pt heterostructures, photoanode, photoelectrochemical water oxidation*

1. INTRODUCTION

The conversion of solar energy into electric power or solar fuel such as hydrogen is a particularly relevant economic and social challenge.[1] Toward this goal, since the report by Fujishima and Honda,[2] photoelectrochemical (PEC) water splitting has become a promising route to produce environment friendly and potentially cost-effective hydrogen through the absorption and conversion of solar energy by a suitable semiconductor.[3,4]

Owing to its composition, SnS_2, an indirect bandgap n-type semiconductor with a gap energy of 2.18−2.44 eV,[5] has been proposed as a potentially advantageous absorber material free of rare, costly, and toxic elements. SnS_2 displays a characteristic 2D hexagonal structure with tin atoms sandwiched between two close-packed sulfur atoms and with adjacent sandwiches being held together by weak van der Waals forces. Such layered material has been used in a range of applications including batteries,[6−8] photocatalysis,[5] sensors,[9] and FETs.[10] Surprisingly, taking into account its well-fitted properties, the use of SnS_2 for PEC water oxidation has been not thoroughly investigated.

Main flaws of SnS_2 are a relatively low electrical conductivity and a moderate absorption coefficient in the visible part of the solar spectrum, what limits its photoactivity.[11] To solve these limitations, a number of strategies have been developed: (i) introduce extrinsic dopants to adjust the SnS_2 band gap and modulate its charge carrier concentration;[12−14] (ii) introduce cocatalysts on the surface of SnS_2 to enhance its activity, for example, Pt;[15−25] and (iii) reduce the SnS_2 thickness taking into account that thin SnS_2 nanosheets with exposed (001) facets display higher photocatalytic activities.[26−28]

In this last direction, several methods have been used to prepare SnS_2 nanostructures with a variety of morphologies, trying to maximize the exposed surface:[6,7,9] for example,

Received: October 9, 2018
Accepted: January 29, 2019
Published: January 29, 2019

Downloaded via UNIV DE BARCELONA on April 23, 2020 at 14:52:49 (UTC).
See https://pubs.acs.org/sharingguidelines for options on how to legitimately share published articles.

© 2019 American Chemical Society

DOI: 10.1021/acsami.8b17622
ACS Appl. Mater. Interfaces 2019, 11, 6918−6926

nanoflakes,[29] nanowires,[30] nanoleaves,[31] and microspheres.[8] A particularly interesting example is the exfoliation of SnS_2 bulk powders into single layers, which showed a promising although still with a moderate performance in PEC water splitting.[32] This approach had, as main drawback, its relatively low production throughput because of the long processing time and low yield.

Herein, we present a simple solution-based route to produce (001)-faceted SnS_2 NPLs. These NPLs are loaded with Pt NPs via an in situ reduction process. Resulting SnS_2-Pt heterostructures are used as photoanode here for PEC water oxidation under simulated sun light. The performance of this new material is further characterized using Mott−Schottky analysis and PEIS.

2. EXPERIMENTAL SECTION

2.1. Chemicals. All chemicals were used as received without further purification. Tin(IV) chloride pentahydrate ($SnCl_4{\cdot}5H_2O$, 98%), sulfur powder (99.8%), tetrahydrofuran (THF, ≥99%), 1,2-hexadecanediol (90%), 1,2-dichlorobenzene (DCB, 99%), and diphenyl ether (≥99%) were purchased from Sigma-Aldrich. Platinum(II) acetylacetonate (98%), oleylamine (OAm, 80−90%), and oleic acid (OAc, 70%) were purchased from Acros. 1-Octadecene (ODE, 90%) was purchased from Alfa Aesar. Toluene, hexane, isopropanol, and ethanol were of analytical grade and obtained from various sources. All the aqueous solutions were prepared using Milli-Q water (18.2 MΩ).

2.2. Synthesis of SnS_2 Nanoplates. In a typical synthesis, $SnCl_4{\cdot}5H_2O$ (2 mmol) was dissolved in THF (1 mL) in a 50 mL three-necked round flask. ODE (16 mL), OAc (4 mL), and OAm (2 mL) were then added and stirred at room temperature for 10 min. A syringe inserted into the solution was used to bubble Ar. The solution was then heated up to 140 °C and kept at this temperature for 1 h to remove low-boiling-point impurities. Then the obtained clear brown solution was heated to 220 °C. At this temperature, 4 mL of a S−OAm stock solution was premade by dissolving sulfur powder (4 mmol) into OAm (4 mL) under sonication and was quickly injected into the reaction flask with a syringe. The mixture was maintained at this temperature for 1 h and afterward quickly cooled down using a cold water bath. The resulted product was centrifuged at 6000 rpm for 4 min after the addition of toluene (15 mL) and then washed three times with toluene and ethanol by dispersion−precipitation cycles. The obtained pale yellow product was dried under vacuum for its further use and characterization. Around 280 mg of material was obtained in each batch, which corresponded to an 80% material yield after purification.

2.3. Synthesis of SnS_2−Pt Nanoheterostructures. Phenyl ether (10 mL), 1,2-hexadecanediol (43 mg), OAm (0.2 mL), and OAc (0.2 mL) were loaded into a 25 mL three-necked reaction flask and kept at 140 °C for 30 min with Ar bubbling through a syringe. Depending on the relative SnS_2/Pt ratio targeted 2 mg (SnS_2−Pt-2), 5 mg (SnS_2−Pt-5), 10 mg (SnS_2−Pt-10), or 20 mg (SnS_2−Pt-20) of platinum(II) acetylacetonate was added into a SnS_2 dispersion containing 100 mg of SnS_2 NPs (containing ca. 20 % organics) within 4 mL of DCB. These values correspond to a nominal molar concentration of 1.2% (SnS_2−Pt-1.2), 2.9% (SnS_2−Pt-2.9), 5.8% (SnS_2−Pt-5.8), and 11.6 % (SnS_2−Pt-11.6), respectively. The solution was then sonicated at 45 °C for 30 min to homogenize. This mixture was quickly injected into the reaction flask at 200 °C and maintained at this temperature for 10 min. A cold water bath was then used to quench the reaction mixture. The product was washed with hexane and ethanol by multiple dispersion−precipitation cycles.

2.4. Ligand Exchange. Native organic ligands were displaced from the NP surface using a NH_4SCN solution.[33] Briefly, 10 mL of a hexane solution containing NPs (5 mg/mL in hexane) was mixed with 5 mL of a 0.13 M NH_4SCN solution (0.5 g NH_4SCN in 50 mL acetone). The mixture was then shacked for several minutes with a vortex and finally centrifuged out at 4000 rpm for 3 min. The resulted product was further washed with 10 mL acetone twice to remove residual NH_4SCN.

2.5. Sample Characterization. Powder X-ray diffraction (XRD) patterns were obtained on a Bruker AXS D8 ADVANCE X-ray diffractometer (Bruker, Karlsruhe, Germany) operating at 40 kV and 40 mA with Ni-filtered (2 μm thickness) Cu Kα1 radiation (λ = 1.5406 Å). Transmission electron microscopy (TEM) characterization was carried out on ZEISS LIBRA 120 (Carl Zeiss, Jena, Germany), operating at 120 kV. High-resolution TEM (HRTEM) images were obtained using a field emission gun FEI Tecnai F20 microscope at 200 kV with a point-to-point resolution of 0.19 nm. High angle annular dark-field (HAADF) STEM was combined with electron energy loss spectroscopy (EELS) in the Tecnai microscope by using a Gatan Quantum filter. For TEM characterization, samples were prepared by drop casting a solution of NPs on a 200 mesh copper grid. SEM analysis was done in a ZEISS Auriga microscope (Carl Zeiss, Jena, Germany) with an energy dispersive X-ray spectroscopy (EDX) detector at 20 kV to study composition. X-ray photoelectron spectroscopy (XPS) was carried out on a SPECS system (SPECS GmbH, Berlin, Germany) equipped with an Al anode XR50 source operating at 150 mW and a Phoibos 150 MCD-9 detector (SPECS GmbH, Berlin, Germany). The pressure in the analysis chamber was kept below 10^{-7} Pa. Data processing was performed with the CasaXPS program (Casa Software Ltd., UK). Binding energy (BE) values were centered by using the C 1s peak at 284.8 eV. Fourier-transform infrared spectroscopy (FTIR) was performed on an Alpha Bruker FTIR spectrometer with a platinum attenuated total reflectance (ATR) single reflection module. FTIR data were typically the average of over 24 scans. UV−vis absorption spectra were recorded on a PerkinElmer LAMBDA 950 UV−vis spectrophotometer (PerkinElmer, Waltham, MA, USA). Steady state photoluminescence (PL) spectra were recorded on a high resolution photoluminescence spectrofluorometer (Horiba Jobin Yvon Fluorolog-3).

2.6. Photoelectrochemical Measurements. PEC characterization was performed in a three-electrode system using an electrochemical workstation (Metrohm Autolab). A Pt mesh (2 cm^2 surface area) and Ag/AgCl (3.3 M KCl) were used as the counter and reference electrodes, respectively. To prepare the working electrode, 2 mg of NPs and Nafions (20 μL, 5 wt %) were dispersed in a water−isopropanol (0.4 mL) mixture with a volume ratio of 3:1 by sonicating for 1 h until obtaining a homogeneous ink. Depending on the amount of catalyst we wanted to test, 50−300 μL ink was drop casted onto a fluorine-doped tin oxide (FTO, 1 × 1.8 cm) substrate and then annealed at 200 °C for 20 min after solvent evaporation. Before deposition, the FTO glass was washed with acetone−isopropanol (1:1 volume ratio) mixture, ethanol, and then deionized water. After ink deposition, part of the material was wiped out from the FTO substrate to leave a clean area for electrical connection. An active area of 1 × 1 cm was left for PEC tests. An aqueous solution of Na_2SO_4 (0.5 M, pH = 7) was used as an electrolyte. The electrolyte was purged with Ar for 30 min before the measurement. The incident light source was provided by eight radially distributed 35 W xenon lamps, providing a total irradiance power on the sample of ca. 100 mW/cm^2. The following formula was used to convert potentials to the reversible hydrogen electrode (RHE) standard scale

$$E \text{ vs RHE} = E_{Ag/AgCl} + E^{\circ}_{Ag/AgCl} + 0.059 \times \text{pH}$$
$$= E_{Ag/AgCl} + 0.623 \text{ (V)}$$

For PEIS measurements, the frequency was swept from 1 MHz to 50 mHz with a sinusoidal amplitude of 25 mV under the same conditions used for photocurrent measurements. An equivalent circuit modeling software, ZView (Scribner Associates), was used to fit the PEIS data. Mott−Schottky analysis was performed under dark conditions.

3. RESULTS AND DISCUSSION

SnS_2 NPs were produced from the reaction of tin chloride with elemental sulfur dissolved in OAm at 220 °C (see the

DOI: 10.1021/acsami.8b17622
ACS Appl. Mater. Interfaces 2019, 11, 6918−6926

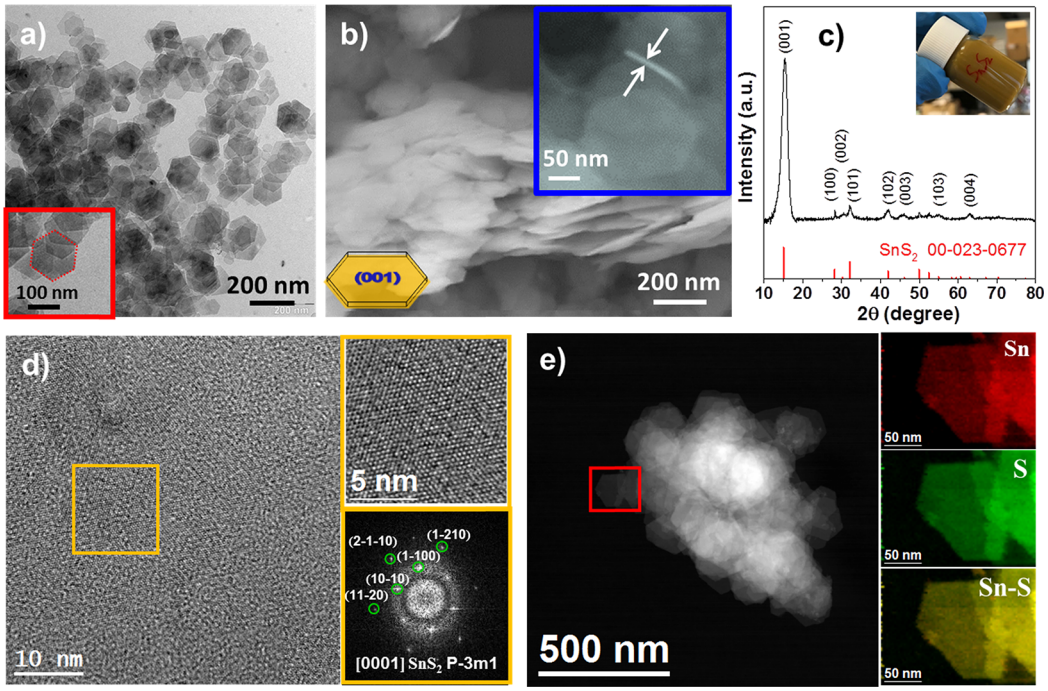

Figure 1. (a) TEM micrograph of the hexagonal SnS_2 NPLs produced from the detailed experimental procedure. (b) SEM micrograph of the SnS_2 NPLs. Inset shows a NPL oriented normal to the substrate, which was used to measure a NPL thickness of 6 nm. (c) XRD pattern of the dried SnS_2 NPLs, including the SnS_2 JCPD 00-023-0677 reference pattern. Inset shows an optical image of the SnS_2 NPL solution. (d) HRTEM micrographs and selected-area electron diffraction (SAED) patterns of a SnS_2 NPL. SnS_2 lattice fringe distances were measured to be 0.181, 0.180, 0.157, and 0.181 nm, at 60.56, 90.52, and 120.32°, which was interpreted as the hexagonal SnS_2 phase, visualized along its [0001] zone axis. (e) STEM micrograph and EELS chemical composition maps from the red-squared area: Sn $M_{4,5}$ edges at 485 eV (red), S $L_{2,3}$ edges at 165 eV (green).

Experimental Section for details). Figure 1 shows representative TEM and SEM micrographs of the SnS_2 NPs produced, following this synthesis procedure. SnS_2 NPs displayed hexagonal plate-like geometry with a diameter of around 150 nm and a thickness of ca. 6 nm (Figures 1a,b and S1). Such NPLs were much thinner than previously reported solution-processed SnS_2 NPs.[29,34−36] XRD patterns showed SnS_2 NPLs to have a hexagonal phase and pointed at the (001) facet as the dominantly exposed (Figure 1c). HRTEM characterization confirmed SnS_2 NPLs to have a hexagonal crystallographic phase (space group =*P*-3*m*1) with a and b = 3.6460 Å and c = 5.8960 Å, and revealed them to be ∼10 layer thick along the [001] direction. Additional EELS chemical composition analysis (Figure 1e) showed a uniform distribution of Sn and S throughout the whole SnS_2 NPL.

The process of the formation of SnS_2 NPLs was analyzed through the XRD characterization of the product precipitated from aliquots extracted at different reaction times (Figure S2a). We observed that after few minutes of reaction, mainly S was present in the precipitated powder and was obtained from the reversible reaction of formation of oleylammonium polysulfides from the reaction of sulfur and OAm (see the Supporting Information for details).[37,38] With time, SnS_2 was directly formed, and S was gradually consumed along the 1 h reaction. The S atom could react with Sn(IV)−OAm directly, or in the form of oleylammonium polysulfices. We actually believe that both reactions took place simultaneously. No Sn−S intermediate phase could be detected.

The influence of the OAc/OAm ratio was analyzed through the XRD and TEM characterization of products obtained under different amounts of these two surfactants (Figure S4). Pure OAm resulted in the formation of both SnS and SnS_2 phases due to the partial reduction of the Sn^{4+} precursor by OAm. Only with the addition of a sufficient amount of OAc, pure SnS_2 phase could be formed. When no OAm was added, the Sn precursor could not be totally dissolved in the ODE−OAc initial solution. Under these conditions, large (∼1 μm) flower-like SnS_2 structures were formed at 220 °C, after injecting the sulfur precursor (S−ODE in this case), as observed from representative SEM and TEM micrographs in Figure S5. Microstructures of SnS_2 samples show difference with/without OAm addition because OAm was not only necessary to bring Sn and S into the solution, but it also played a role as surfactant promoting the asymmetric growth of SnS_2 into NPLs, probably by preferential binding at (001) facets, and preventing the NPL aggregation. Without OAm, urchin-like structures were obtained (Figure S5). On the other hand, OAc facilitated the formation of the SnS_2 phase.[34] With no OAc, a mixture of SnS_2 and SnS phases was systematically obtained (Figure S4).

SnS_2−Pt nanoheterostructures were produced by the growth of Pt nanodomains on the surface of preformed SnS_2 NPLs through the reduction of Pt(II) acetylacetonate (see the Experimental Section for details). EDX analyses showed the final Pt concentration on the SnS_2 NPL surface to follow the nominal precursor ratios, pointing at a high yield of Pt deposition. When increasing the nominal amount of Pt, from 1.2 to 2.9 and 5.8%, the diameter of the Pt domains in SnS_2−Pt nanoheterostructures increased from ∼1 to ∼3 and ∼5 nm (Figure 2), respectively. Pt nanodomains were found uniformly distributed on the NPL surface. However, at higher Pt concentrations, for example, when introducing a nominal 11.6% of Pt (Figure S6b), the Pt size did not significantly further increase with respect to SnS_2−Pt-5.8 but some Pt

DOI: 10.1021/acsami.8b17622
ACS Appl. Mater. Interfaces 2019, 11, 6918−6926

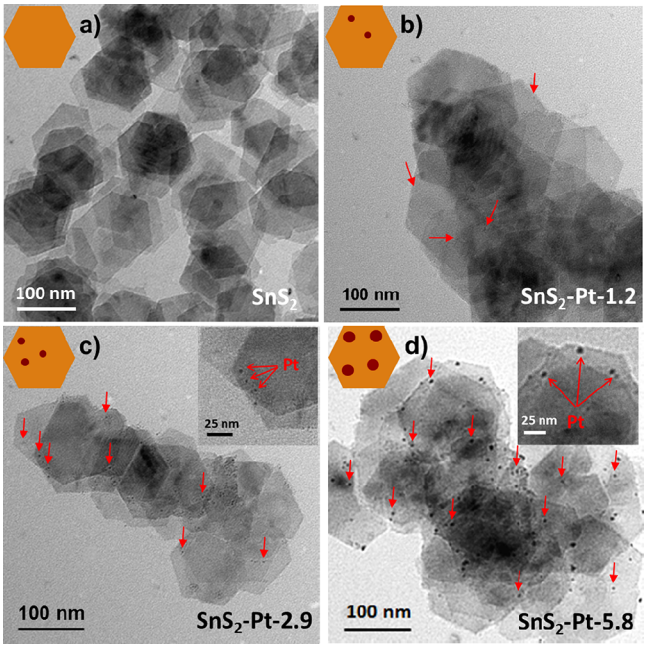

Figure 2. TEM images of (a) SnS_2 NPL and SnS_2–Pt nanoheterostructures with increasing amounts of (b) Pt: 1.2, (c) 2.9, and (d) 5.8 mol %.

aggregation started to occur. HRTEM and EELS chemical compositional maps further confirmed the homogeneous distribution of Pt NPs through the SnS_2 surface and their average crystal domain size (Figures 3 and S6c). XRD analyses showed Pt metallic peaks at high Pt concentration but no additional phase (Figure S6a).

XPS analyses provided slightly higher Pt concentrations than those nominally introduced and measured by EDX. As an example, the Pt concentration in the sample with a nominal composition of 2.9% was 3.8 mol % (Figure S7). As expected, XPS analysis showed Pt to be in a metallic state. The Sn/S ratio was found at 0.6, which also pointed at a slightly Sn-rich surface. XPS analysis of bare SnS_2 (Figure S8) showed the same Sn/S atomic ratio, 0.6, proving the addition of Pt not to affect the SnS_2 composition. The Sn-rich surface could be ascribed to an intrinsic off-stoichiometry of SnS_2 surfaces, particularly (001) facets, or to a slight oxidation of the SnS_2 NPLs that had been exposed to air. Nevertheless, only one chemical environment was identified for Sn in both SnS_2 and SnS_2–Pt samples, and this was compatible with a Sn^{4+} chemical state in a SnS_2 environment.

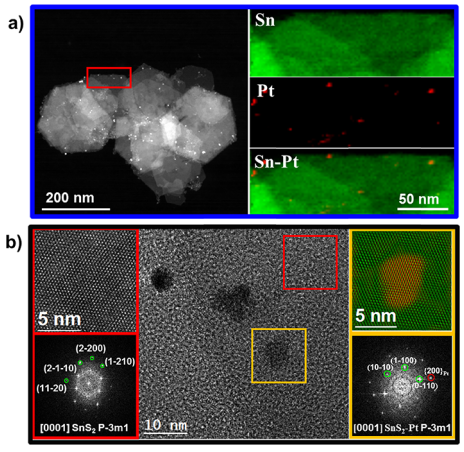

Figure 3. (a) STEM micrograph of SnS_2–Pt-5.8 NPLs and EELS chemical composition maps from the red squared area: Sn $M_{4,5}$ edges at 485 eV (green), Pt $M_{4,5}$ edges at 2122 eV (red). (b) HRTEM micrograph of a SnS_2–Pt-5.8 NPL and details of the red and orange squared regions with their corresponding power spectrum. SnS_2 NPL (red square) displayed the SnS_2 hexagonal phase (space group =*P*-3*m*1) with a and b = 3.6460 Å and c = 5.8960 Å in its [0001] zone axis. Detail of the orange squared region and its corresponding power spectrum further revealed a reflection corresponding to the {200} Pt planes. A frequency filtered image, where the corresponding lattice fringes in green (SnS_2) and red (Pt) colors overlapped, is also presented.

All samples showed activity toward PEC water oxidation under simulated solar light (Figure 4). Figure 4a,b display the *I*–*V* curves and transient photocurrent (external bias of 1.23 V vs RHE) under chopped visible-light illumination. As expected, the addition of Pt increased the PEC activity, being the SnS_2–Pt-2.9 photoanode was the one providing the highest photocurrent densities. The values obtained with this catalyst were superior to most SnS_2-based photocatalysts previously reported (Table S2), particularly when compared with materials deposited from the solution on top of the FTO/ITO substrate (see refs 3–5 in the Supporting Information). Although SnS_2-based materials directly grown from a conducting substrate-like FTO (refs 8 and 9 in the Supporting Information) and Ti foil (ref 10 in the Supporting Information), they generally showed an improved contact between the sample materials and current collector with a related lower contact resistance.

When increasing the Pt loading, the PEC current density at 1.23 V vs RHE increased from 16.84 $\mu A/cm^2$ (SnS_2) to 112 $\mu A/cm^2$ (SnS_2–Pt-2.9), the later decrease at higher Pt concentrations, for example, 36.18 $\mu A/cm^2$ for SnS_2–Pt-5.8. The reduced photocurrent at high Pt loading was associated to: (1) poor electronic/catalytic properties of the Pt with an increase in particle size; (2) the excessive electron–hole recombination centers resulting from higher Pt loading, thereby limiting the extraction of electrons with the external bias;[39] (3) a strong light absorbance by Pt that partially shadowed the semiconductor from the light.[40] Photoresponse times were about 0.1 s for all samples, indicating a relatively rapid charge transport toward the substrate. The SnS_2–Pt-2.9 photoanode displayed transient spikes that increased with the photocurrent. These spikes were typically attributed to the charge accumulation and recombination at the interface, evidencing limitations on the charge transfer process to the electrolyte.[41–43]

The amount of catalyst used to produce the film had a notable influence on the photocurrent response (Figures 4c and S10a). Excess amounts of catalysts resulted in a low

DOI: 10.1021/acsami.8b17622
ACS Appl. Mater. Interfaces 2019, 11, 6918–6926

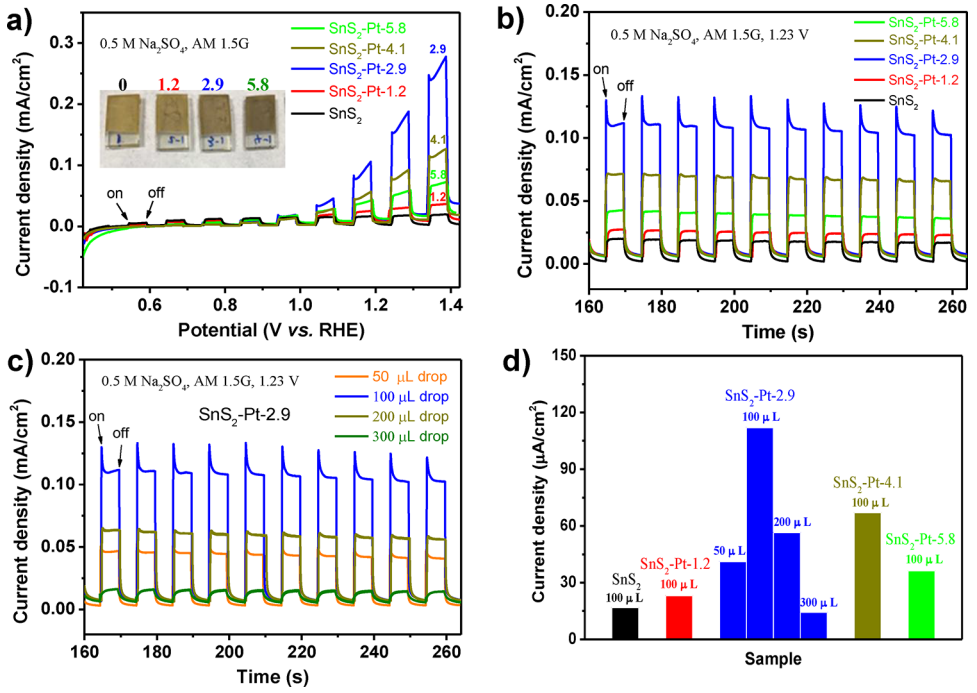

Figure 4. (a) Linear sweep voltammogram curves under chopped AM 1.5 G illumination for PECs. (b) Corresponding amperometric $I-T$ curves under chopped illumination at an applied potential of 1.23 V vs RHE (0.6 V vs Ag/AgCl, 3.3 M KCl). (c) Amperometric $I-T$ curves from films of different thicknesses produced from different ink amounts. (d) Comparison of the PEC performance obtained from different samples.

illumination of the material close to the electrodes, where a more efficient charge extraction takes place. On the contrary, too small amounts limit the total surface area available for PEC oxygen evolution, which also results in lower photocurrents. XRD (Figure S10b), SEM (Figure S11), and TEM (Figure S11) characterizations demonstrated that no crystallographic phase change took place during PEC measurements.

Long term stability of the SnS_2−Pt-2.9 photoanode was tested under chopped simulated solar light (on/off every 10 s). The results showed that around 60 % of the initial current density was preserved after 2000 s and then became almost steady, indicating an acceptable stability (See Figure S12a). Bubbles could be easily seen around the photoanode and Pt mesh, which was respectively ascribed to the O_2 and H_2 generation from water during test and the inside wall of the PEC cell (Figure S12b).

To gain insight into the charge carrier behavior at the semiconductor−liquid interface, PEIS measurements were carried out. Figure 5a shows the Nyquist plots corresponding to the SnS_2-based anodes containing increasing amounts of Pt. At first sight, the decrease in the diameter of the semiarc with increased Pt loading suggested a decrease in film resistance. A quantitative analysis of electrochemical properties of the electrodes was attempted by fitting the Nyquist plots with equivalent circuits.[44] Given the components and processes assumed to occur in these electrodes, we considered a general equivalent circuit containing a series resistance (R_S) and three $R-C$ components with the following contributions (Figure 5b): (i) capacitance of the bulk SnS_2 (C_{bulk}) and resistance of hole trapping to the surface states (R_{trap}); (ii) capacitance of the surface states (C_{SS}) and resistance for charge transfer to the electrolyte through the surface states ($R_{ct,SS}$); and (iii) charge transfer resistance from the valence band to Pt particles ($R_{ct,bulk}$), capacitance associated to the surface Pt particles (C_{Pt}) and charge transfer resistance from Pt particles to the electrolyte ($R_{ct,Pt}$). The Bode plot (Figure S13) obtained for the different samples displayed a broadband, probably composed by two nearby peaks, indicating that a two-time constant equivalent circuit could describe sufficiently well the impedance response. Therefore, two simplified equivalent circuits (Figure 5c,d) were used to fit the Nyquist plots.[45] For the sake of analysis, the electrochemical parameters extracted from the fitting were plotted as a function of Pt loading in Figure 5e. In terms of the charge transfer resistance, bare SnS_2 and SnS_2−Pt-1.2 presented very high values, which resulted in low photocurrents. When Pt loading increased (SnS_2−Pt-2.9 and SnS_2−Pt-5.8), the charge transfer resistance at the surface dropped dramatically, evidencing the improved catalytic activity provided by the Pt NPs. It is worth noting that $R_{ct,bulk}$ (R_{trap}) values are much lower than those of $R_{ct,Pt}$ ($R_{ct,SS}$), which was a sign that charge transfer was limited by the electrode/electrolyte interface instead of bulk. Interestingly, it was found that the lowest charge transfer resistance was achieved for SnS_2−Pt-2.9, in good agreement with the best performance obtained for this material. Further increase of Pt loading led to an increase in C_{Pt} and $R_{ct,bulk}$, whereas $R_{ct,Pt}$ remained virtually unchanged. These findings suggest that the decreased performance for high Pt loading (Figure 4a) did not originate from a deterioration of the catalytic activity of the Pt overlayer because $R_{ct,Pt}$ barely changed but potentially from a worse charge transfer from the SnS_2 to the larger Pt NPs, given the increased $R_{ct,bulk}$. Likewise, the larger C_{Pt} could be accounted for by the increased coverage and size of Pt nanoparticles. To provide more details about the water oxidation mechanism on SnS_2−Pt nanoheterostructures, EIS was carried out in the dark and under illumination on a representative SnS_2−Pt-2.9 photoanode (Figure S14). Data extracted from the fitting is displayed in Table S1. First, the value of $R_{ct,bulk}$ in the dark (around 2.8 kΩ) is higher than that under illumination (1.9 kΩ). This is not surprising given that under illumination the

DOI: 10.1021/acsami.8b17622
ACS Appl. Mater. Interfaces 2019, 11, 6918−6926

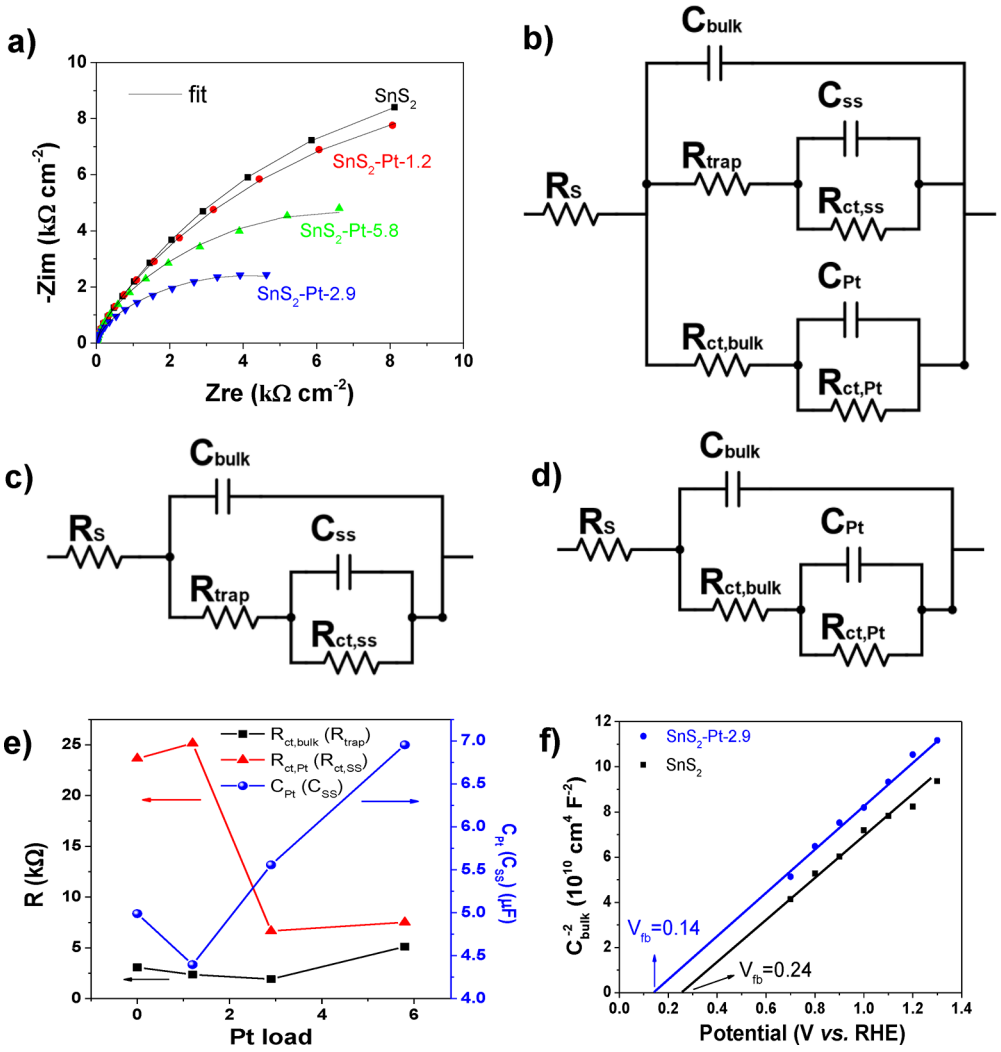

Figure 5. (a) Nyquist plots measured under simulated sunlight irradiation with correspoding fitting curves of the bare SnS_2 and SnS_2−Pt nanoheterocomposites at a bias of 0.6 V (vs Ag/AgCl). (b) Proposed full equivalent circuit used for interpretation of SnS_2−Pt photoanode. Simplified equivalent circuit used for fitting impedance response of SnS_2 (c) without and (d) with Pt loading. (e) $R_{ct,bulk}$, $R_{ct,ss}/R_{ct,Pt}$, and C_{SS}/C_{Pt} values fit from the impedance response of SnS_2 photoanode as a function of Pt loading. (f) Mott−Schottky plots of SnS_2 NPLs and SnS_2−Pt-2.9 nanoheterostructures measured in the dark.

increased carrier density will decrease the film resistance. Second, the value of $R_{ct,Pt}$ decreases significantly under illumination, which is consistent with the increased current. Indeed, the negligible faradaic dark current suggests that charges at this applied potential are unable to drive the water oxidation reaction, whereas under illumination the more oxidizing holes can successfully trigger the interfacial reaction. Third, the value of C_{Pt} increases under illumination, which could be accounted for by the role of Pt as a reservoir of photogenerated holes at the interface. This result together with the increased photocurrent observed when coating SnS_2 with Pt provides compelling evidence that water oxidation occurs primarily via Pt sites rather than through the valence band of SnS_2. Similar behavior has also been found on other photoanodes such as hematite[46] and copper ferrite.[47] Additionally, Mott−Schottky analysis was performed on two representative samples, bare SnS_2 and SnS_2−Pt-2.9, under dark conditions. A Randles circuit was used to extract C_{bulk} from impedance response to construct a Mott−Schottky plot in Figure 5f. The positive slope of the C^{-2}−E plots indicated that both bare SnS_2 and SnS_2−Pt-2.9 are n-type semiconductors.[46,47] The introduction of an optimal Pt loading positively shifted the flat band potential (V_{fb}) from 0.24 to 0.14 V vs RHE. This implied a better photocurrent onset potential for SnS_2−Pt-2.9 and was consistent with Gong and co-workers report on surface modified hematite photoanodes.[48]

To further investigate the recombination behavior of photoinduced electron−hole pairs in bare SnS_2 and SnS_2−Pt-2.9 nanoheterostructures, PL spectra were measured. The PL measurements of bare SnS_2 and SnS_2−Pt-2.9 nanoheterostructures were carried out under the excitation wavelength of 390 nm. As shown in the PL spectra (Figure S15b), bare SnS_2 exhibited the radiative interband recombination peak at 543 nm, which was consistent with the SnS_2 band gap (2.25 eV, Figure S15a). In addition, an emission shoulder appeared at 455 nm, which we related to the radiative recombination of exciton absorption.[35] Compared with the PL intensity of bare SnS_2, a significantly decreased PL emission, especially for the emission from radiative interband recombination, was observed for the SnS_2−Pt-2.9 nanoheterostructures. These results demonstrate that a reduced photogenerated hole−electron recombination existed in SnS_2

DOI: 10.1021/acsami.8b17622
ACS Appl. Mater. Interfaces 2019, 11, 6918−6926

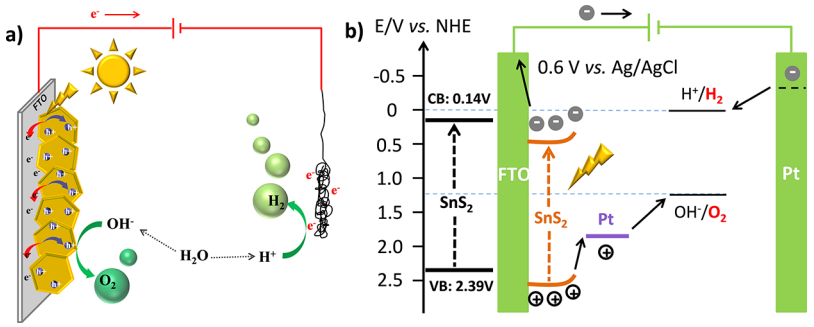

Figure 6. (a) Cartoon and (b) Energy band schematic diagram of SnS_2−Pt nanoheterostructures for water oxidation in a PEC cell.

photoanodes, assigned to the facilitated charge separation by the introduction of Pt. The suppressed charge recombination in SnS_2 photoanode benefited achieving high photocurrent responses. A simplified PEC water oxidation mechanism on SnS_2−Pt nanoheterostructures is summarized in Figure 6. As shown in Figure 6a, photogenerated electrons from SnS_2 NPLs are transferred to the FTO and from it to the Pt mesh for H_2 evolution. Photogenerated holes are injected from the SnS_2 NPLs to the OH^- groups through Pt nanodomains. The flow direction of electrons and holes is schematized in the energy band diagram in Figure 6b. We consider the SnS_2 conduction band minimum (CBM) of SnS_2 to be 0.1 V above the flat band potential (0.24 V vs NHE for SnS_2 as measured from *M*−*S*).[49,50] Therefore, the CBM of SnS_2 without external bias was around 0.14 V vs NHE. Under a positive bias, the CB and VB shifted toward positive values, facilitating the photogenerated holes transfer to OH^- groups in a solution through Pt domains. On the other hand, the photogenerated electrons transferred to the counter electrode (a Pt mesh) to reduce H^+ into H_2. A relatively fast separation of the photogenerated charge carriers reduced opportunity of charge recombination, thus promoting performance in SnS_2−Pt nanoheterostructures compared with SnS_2 NPLs. Pt NPs played a significant role in electron−hole separation and facilitating charge transfer to the hydroxyl groups, thus resulting in a superior performance of SnS_2−Pt nanoheterostructures when compared with bare SnS_2. However, a clear deterioration of the performance was observed when larger Pt NPs were deposited. Overall, these results suggest that new strategies, capable of decoupling both particle size and coverage during the Pt deposition, would be essential to further enhance the performance of this system, targeting a narrow size distribution for the Pt NPs and a high coverage.

4. CONCLUSIONS

In summary, ultrathin SnS_2 NPLs were produced via colloidal hot injection synthesis route, and the roles of surfactant OAm and OAc were investigated. Subsequently, metallic Pt was uniformly deposited on the surface via an in situ reduction method. Such SnS_2−Pt nanoheterostructures showed significantly enhanced PEC current response under simulated sunlight compared to bare SnS_2 NPLs. The decreased performance observed for high Pt loadings appeared to be related to a deterioration of the charge transfer from the SnS_2 to the larger Pt NPs according to the PEIS data. The intimate contact between Pt NPs and SnS_2 NPLs was the key to obtain a useful semiconductor-noble metal synergetic effect through an efficient charge transfer of the photogenerated carriers from the semiconductor to the metal to promote solar energy conversion.

■ ASSOCIATED CONTENT

Supporting Information

The Supporting Information is available free of charge on the ACS Publications website at DOI: 10.1021/acsami.8b17622.

Electronic Supplementary Information (ESI) available: additional experiments, XRD, TEM, SEM, EDX, XPS, FTIR, PEC tests, bode plots, ($\alpha h\nu$)2-hν plots, and PL (PDF)

■ AUTHOR INFORMATION

Corresponding Author

*E-mail: acabot@irec.cat.

ORCID

Yong Zuo: 0000-0003-1564-467X
Yongpeng Liu: 0000-0002-4544-4217
Junshan Li: 0000-0002-1482-1972
Xiaoting Yu: 0000-0003-0457-4047
Jordi Arbiol: 0000-0002-0695-1726
Jordi Llorca: 0000-0002-7447-9582
Kevin Sivula: 0000-0002-8458-0270
Andreu Cabot: 0000-0002-7533-3251

Notes

The authors declare no competing financial interest.

■ ACKNOWLEDGMENTS

This work was supported by the European Regional Development Funds and by the Spanish Ministerio de Economía y Competitividad through the project SEHTOP (ENE2016-77798-C4-3-R) and VALPEC (ENE2017-85087-C3). Y.Z., J.L., R.D., X.T., and T.Z. thank China Scholarship Council for scholarship support. Y.L. and N.G. thank the Swiss National Science Foundation (SNF) for funding under the Ambizione Energy grant no. PZENP2_166871. J.L. is a Serra Húnter Fellow and is grateful to ICREA Academia program and grants MINECO/FEDER ENE2015-63969-R and GC 2017 SGR 128. T.Z. and J.A. acknowledge funding from Generalitat de Catalunya 2017 SGR 327. ICN2 acknowledges support from the Severo Ochoa Programme (MINECO, grant no. SEV-2013-0295). IREC and ICN2 are funded by the CERCA Programme/Generalitat de Catalunya. Part of the present work has been performed in the framework of Universitat Autònoma de Barcelona Materials Science PhD program.

DOI: 10.1021/acsami.8b17622
ACS Appl. Mater. Interfaces 2019, 11, 6918−6926

REFERENCES

(1) Grätzel, M. Photoelectrochemical Cells. *Nature* **2001**, *414*, 338−344.

(2) Fujishima, A.; Honda, K. Electrochemical Photolysis of Water at a Semiconductor Electrode. *Nature* **1972**, *238*, 37−38.

(3) Wang, L.; Wang, W.; Chen, Y.; Yao, L.; Zhao, X.; Shi, H.; Cao, M.; Liang, Y. Heterogeneous P-N Junction CdS/Cu_2O Nanorod Arrays: Synthesis and Superior Visible-Light-Driven Photoelectrochemical Performance for Hydrogen Evolution. *ACS Appl. Mater. Interfaces* **2018**, *10*, 11652−11662.

(4) Fang, Z.; Hao, S.; Long, L.; Fang, H.; Qiang, T.; Song, Y. The Enhanced Photoelectrochemical Response of $SnSe_2$ Nanosheets. *CrystEngComm* **2014**, *16*, 2404−2410.

(5) Yu, J.; Xu, C.-Y.; Ma, F.-X.; Hu, S.-P.; Zhang, Y.-W.; Zhen, L. Monodisperse SnS_2 Nanosheets for High-Performance Photocatalytic Hydrogen Generation. *ACS Appl. Mater. Interfaces* **2014**, *6*, 22370−22377.

(6) Seo, J.; Jang, J.; Park, S.; Kim, C.; Park, B.; Cheon, J. Two-Dimensional SnS_2 Nanoplates with Extraordinary High Discharge Capacity for Lithium Ion Batteries. *Adv. Mater.* **2008**, *20*, 4269−4273.

(7) Jana, M. K.; Rajendra, H. B.; Bhattacharyya, A. J.; Biswas, K. Green Ionothermal Synthesis of Hierarchical Nanostructures of SnS_2 and Their Li-Ion Storage Properties. *CrystEngComm* **2014**, *16*, 3994.

(8) Zai, J.; Wang, K.; Su, Y.; Qian, X.; Chen, J. High Stability and Superior Rate Capability of Three-Dimensional Hierarchical SnS_2 Microspheres as Anode Material in Lithium Ion Batteries. *J. Power Sources* **2011**, *196*, 3650−3654.

(9) Ou, J. Z.; Ge, W.; Carey, B.; Daeneke, T.; Rotbart, A.; Shan, W.; Wang, Y.; Fu, Z.; Chrimes, A. F.; Wlodarski, W.; Russo, S. P.; Li, Y. X.; Kalantar-zadeh, K. Physisorption-Based Charge Transfer in Two-Dimensional SnS_2 for Selective and Reversible NO_2 Gas Sensing. *ACS Nano* **2015**, *9*, 10313−10323.

(10) Su, G.; Hadjiev, V. G.; Loya, P. E.; Zhang, J.; Lei, S.; Maharjan, S.; Dong, P.; Ajayan, P. M.; Lou, J.; Peng, H. Chemical Vapor Deposition of Thin Crystals of Layered Semiconductor SnS_2 for Fast Photodetection Application. *Nano Lett.* **2015**, *15*, 506−513.

(11) Liu, Y.; Geng, P.; Wang, J.; Yang, Z.; Lu, H.; Hai, J.; Lu, Z.; Fan, D.; Li, M. In-Situ Ion-Exchange Synthesis Ag_2S Modified SnS_2 Nanosheets toward Highly Photocurrent Response and Photocatalytic Activity. *J. Colloid Interface Sci.* **2018**, *512*, 784−791.

(12) An, X.; Yu, J. C.; Tang, J. Biomolecule-Assisted Fabrication of Copper Doped SnS_2 Nanosheet−reduced Graphene Oxide Junctions with Enhanced Visible-Light Photocatalytic Activity. *J. Mater. Chem. A* **2014**, *2*, 1000−1005.

(13) Wahnón, P.; Conesa, J. C.; Palacios, P.; Lucena, R.; Aguilera, I.; Seminovski, Y.; Fresno, F. V-Doped SnS_2: A New Intermediate Band Material for a Better Use of the Solar Spectrum. *Phys. Chem. Chem. Phys.* **2011**, *13*, 20401.

(14) Hu, K.; Wang, D.; Zhao, W.; Gu, Y.; Bu, K.; Pan, J.; Qin, P.; Zhang, X.; Huang, F. Intermediate Band Material of Titanium-Doped Tin Disulfide for Wide Spectrum Solar Absorption. *Inorg. Chem.* **2018**, *57*, 3956−3962.

(15) Zhang, Z.; Shao, C.; Li, X.; Sun, Y.; Zhang, M.; Mu, J.; Zhang, P.; Guo, Z.; Liu, Y. Hierarchical Assembly of Ultrathin Hexagonal SnS_2 Nanosheets onto Electrospun TiO_2 Nanofibers: Enhanced Photocatalytic Activity Based on Photoinduced Interfacial Charge Transfer. *Nanoscale* **2013**, *5*, 606−618.

(16) Christoforidis, K. C.; Sengele, A.; Keller, V.; Keller, N. Single-Step Synthesis of SnS_2 Nanosheet-Decorated TiO_2 Anatase Nanofibers as Efficient Photocatalysts for the Degradation of Gas-Phase Diethylsulfide. *ACS Appl. Mater. Interfaces* **2015**, *7*, 19324−19334.

(17) Zhang, Z.; Huang, J.; Zhang, M.; Yuan, Q.; Dong, B. Ultrathin Hexagonal SnS_2 Nanosheets Coupled with G-C_3N_4 Nanosheets as 2D/2D Heterojunction Photocatalysts toward High Photocatalytic Activity. *Appl. Catal. B Environ.* **2015**, *163*, 298−305.

(18) Zhang, Y. C.; Du, Z. N.; Li, K. W.; Zhang, M.; Dionysiou, D. D. High-Performance Visible-Light-Driven SnS_2 /SnO_2 Nanocomposite Photocatalyst Prepared via In Situ Hydrothermal Oxidation of SnS_2 Nanoparticles. *ACS Appl. Mater. Interfaces* **2011**, *3*, 1528−1537.

(19) Ahn, C. W.; Borse, P. H.; Kim, J. H.; Kim, J. Y.; Jang, J. S.; Cho, C.-R.; Yoon, J.-H.; Lee, B.-s.; Bae, J.-S.; Kim, H. G.; Lee, J. S. Effective Charge Separation in Site-Isolated Pt-Nanodot Deposited $PbTiO_3$ Nanotube Arrays for Enhanced Photoelectrochemical Water Splitting. *Appl. Catal. B Environ.* **2018**, *224*, 804−809.

(20) Yu, J.; Qi, L.; Jaroniec, M. Hydrogen Production by Photocatalytic Water Splitting over Pt/TiO_2Nanosheets with Exposed (001) Facets. *J. Phys. Chem. C* **2010**, *114*, 13118−13125.

(21) Zhang, J.; Yu, Z.; Gao, Z.; Ge, H.; Zhao, S.; Chen, C.; Chen, S.; Tong, X.; Wang, M.; Zheng, Z.; Qin, Y. Porous TiO_2 Nanotubes with Spatially Separated Platinum and CoO_x Cocatalysts Produced by Atomic Layer Deposition for Photocatalytic Hydrogen Production. *Angew. Chem., Int. Ed.* **2017**, *56*, 816−820.

(22) Qu, Q.; Pan, G.-L.; Lin, Y.-T.; Xu, C.-W. Boosting the Electrocatalytic Performance of Pt, Pd and Au Embedded within Mesoporous Cobalt Oxide for Oxygen Evolution Reaction. *Int. J. Hydrogen Energy* **2018**, *43*, 14252−14264.

(23) Li, Z.-y.; Shi, S.-t.; Zhong, Q.-s.; Zhang, C.-j.; Xu, C.-w. Pt-Mn_3O_4/C as Efficient Electrocatalyst for Oxygen Evolution Reaction in Water Electrolysis. *Electrochim. Acta* **2014**, *146*, 119−124.

(24) Warwick, M. E. A.; Barreca, D.; Bontempi, E.; Carraro, G.; Gasparotto, A.; Maccato, C.; Kaunisto, K.; Ruoko, T.-P.; Lemmetyinen, H.; Sada, C.; Gönüllü, Y.; Mathur, S. Pt-Functionalized Fe_2O_3 Photoanodes for Solar Water Splitting: The Role of Hematite Nano-Organization and the Platinum Redox State. *Phys. Chem. Chem. Phys.* **2015**, *17*, 12899−12907.

(25) Liu, G.; Qiu, Y.; Wang, Z.; Zhang, J.; Chen, X.; Dai, M.; Jia, D.; Zhou, Y.; Li, Z.; Hu, P. Efficiently Synergistic Hydrogen Evolution Realized by Trace Amount of Pt-Decorated Defect-Rich SnS_2 Nanosheets. *ACS Appl. Mater. Interfaces* **2017**, *9*, 37750−37759.

(26) Wei, R.; Hu, J.; Zhou, T.; Zhou, X.; Liu, J.; Li, J. Ultrathin SnS_2 Nanosheets with Exposed {001} Facets and Enhanced Photocatalytic Properties. *Acta Mater.* **2014**, *66*, 163−171.

(27) Zhou, M.; Lou, X. W. D.; Xie, Y. Two-Dimensional Nanosheets for Photoelectrochemical Water Splitting: Possibilities and Opportunities. *Nano Today* **2013**, *8*, 598−618.

(28) Li, M.; Liu, E.; Hu, H.; Ouyang, S.; Xu, H.; Wang, D. Surfactant-Free Synthesis of Single Crystalline SnS_2 and Effect of Surface Atomic Structure on the Photocatalytic Property. *Int. J. Photoenergy* **2014**, *2014*, 1−7.

(29) Feng, J.; Chen, J.; Geng, B.; Feng, H.; Li, H.; Yan, D.; Zhuo, R.; Cheng, S.; Wu, Z.; Yan, P. Two-Dimensional Hexagonal SnS_2 Nanoflakes: Fabrication, Characterization, and Growth Mechanism. *Appl. Phys. A* **2011**, *103*, 413−419.

(30) Yella, A.; Mugnaioli, E.; Panthöfer, M.; Therese, H. A.; Kolb, U.; Tremel, W. Bismuth-Catalyzed Growth of SnS_2 Nanotubes and Their Stability. *Angew. Chem., Int. Ed.* **2009**, *48*, 6426−6430.

(31) Ma, D.; Zhou, H.; Zhang, J.; Qian, Y. Controlled Synthesis and Possible Formation Mechanism of Leaf-Shaped SnS_2 Nanocrystals. *Mater. Chem. Phys.* **2008**, *111*, 391−395.

(32) Sun, Y.; Cheng, H.; Gao, S.; Sun, Z.; Liu, Q.; Liu, Q.; Lei, F.; Yao, T.; He, J.; Wei, S.; Xie, Y. Freestanding Tin Disulfide Single-Layers Realizing Efficient Visible-Light Water Splitting. *Angew. Chem. Int. Ed.* **2012**, *51*, 8727−8731.

(33) Fafarman, A. T.; Koh, W.; Diroll, B. T.; Kim, D. K.; Ko, D.-K.; Oh, S. J.; Ye, X.; Doan-Nguyen, V.; Crump, M. R.; Reifsnyder, D. C.; Murray, C. B.; Kagan, C. R. Thiocyanate-Capped Nanocrystal Colloids: Vibrational Reporter of Surface Chemistry and Solution-Based Route to Enhanced Coupling in Nanocrystal Solids. *J. Am. Chem. Soc.* **2011**, *133*, 15753−15761.

(34) Zhang, Y.; Lu, J.; Shen, S.; Xu, H.; Wang, Q. Ultralarge Single Crystal SnS Rectangular Nanosheets. *Chem. Commun.* **2011**, *47*, 5226−5228.

(35) Du, Y.; Yin, Z.; Rui, X.; Zeng, Z.; Wu, X.-J.; Liu, J.; Zhu, Y.; Zhu, J.; Huang, X.; Yan, Q.; Zhang, H. A Facile, Relative Green, and Inexpensive Synthetic Approach toward Large-Scale Production of SnS_2 Nanoplates for High-Performance Lithium-Ion Batteries. *Nanoscale* **2013**, *5*, 1456−1459.

DOI: 10.1021/acsami.8b17622
ACS Appl. Mater. Interfaces 2019, 11, 6918−6926

(36) Mishra, R. K.; Baek, G. W.; Kim, K.; Kwon, H.-I.; Jin, S. H. One-Step Solvothermal Synthesis of Carnation Flower-like SnS_2 as Superior Electrodes for Supercapacitor Applications. *Appl. Surf. Sci.* **2017**, *425*, 923−931.
(37) Davis, R. E.; Nakshbendi, H. F. Sulfur in Amine Solvents. *J. Am. Chem. Soc.* **1962**, *84*, 2085−2090.
(38) Lynch, M. An Investigation of Solutions of Sulfur in Oleylamine by Raman Spectroscopy and Their Relation to Lead Sulfide Quantum Dot Synthesis. Undergrad. Honor. Theses, University of Colorado Boulder, Colorado, 2017. https://scholar.colorado.edu/honr_theses/1389.
(39) Jia, Y.; Yang, Y.; Guo, Y.; Guo, W.; Qin, Q.; Yang, X.; Guo, Y. Simulated Sunlight Photocatalytic Degradation of Aqueous P-Nitrophenol and Bisphenol A in a Pt/BiOBr Film-Coated Quartz Fiber Photoreactor. *Dalton Trans.* **2015**, *44*, 9439−9449.
(40) Serrano, D. P.; Calleja, G.; Pizarro, P.; Gálvez, P. Enhanced Photocatalytic Hydrogen Production by Improving the Pt Dispersion over Mesostructured TiO_2. *Int. J. Hydrogen Energy* **2014**, *39*, 4812−4819.
(41) Wang, Z.; Wang, H.; Liu, B.; Qiu, W.; Zhang, J.; Ran, S.; Huang, H.; Xu, J.; Han, H.; Chen, D.; Shen, G. Transferable and Flexible Nanorod-Assembled TiO_2 Cloths for Dye-Sensitized Solar Cells, Photodetectors, and Photocatalysts. *ACS Nano* **2011**, *5*, 8412−8419.
(42) Ye, H.; Park, H. S.; Akhavan, V. A.; Goodfellow, B. W.; Panthani, M. G.; Korgel, B. A.; Bard, A. J. Photoelectrochemical Characterization of $CuInSe_2$ and $Cu(In_{1-X}\ Ga_X)Se_2$ Thin Films for Solar Cells. *J. Phys. Chem. C* **2011**, *115*, 234−240.
(43) Hickey, S. G.; Waurisch, C.; Rellinghaus, B.; Eychmüller, A. Size and Shape Control of Colloidally Synthesized IV−VI Nanoparticulate Tin(II) Sulfide. *J. Am. Chem. Soc.* **2008**, *130*, 14978−14980.
(44) Zhu, X.; Guijarro, N.; Liu, Y.; Schouwink, P.; Wells, R. A.; Le Formal, F.; Sun, S.; Gao, C.; Sivula, K. Spinel Structural Disorder Influences Solar-Water-Splitting Performance of $ZnFe_2O_4$ Nanorod Photoanodes. *Adv. Mater.* **2018**, *30*, 1801612.
(45) Klahr, B.; Gimenez, S.; Fabregat-Santiago, F.; Bisquert, J.; Hamann, T. W. Photoelectrochemical and Impedance Spectroscopic Investigation of Water Oxidation with "Co−Pi"-Coated Hematite Electrodes. *J. Am. Chem. Soc.* **2012**, *134*, 16693−16700.
(46) Klahr, B.; Gimenez, S.; Fabregat-Santiago, F.; Hamann, T.; Bisquert, J. Water Oxidation at Hematite Photoelectrodes: The Role of Surface States. *J. Am. Chem. Soc.* **2012**, *134*, 4294−4302.
(47) Liu, Y.; Le Formal, F.; Boudoire, F.; Yao, L.; Sivula, K.; Guijarro, N. Insights into the Interfacial Carrier Behaviour of Copper Ferrite ($CuFe_2O_4$) Photoanodes for Solar Water Oxidation. *J. Mater. Chem. A* **2019**, *7*, 1669−1677.
(48) Dang, K.; Wang, T.; Li, C.; Zhang, J.; Liu, S.; Gong, J. Improved Oxygen Evolution Kinetics and Surface States Passivation of Ni-Bi Co-Catalyst for a Hematite Photoanode. *Engineering* **2017**, *3*, 285−289.
(49) Matsumoto, Y.; Omae, M.; Watanabe, I.; Sato, E.-i. Photoelectrochemical Properties of the Zn-Ti-Fe Spinel Oxides. *J. Electrochem. Soc.* **1986**, *133*, 711.
(50) Ishikawa, A.; Takata, T.; Kondo, J. N.; Hara, M.; Kobayashi, H.; Domen, K. Oxysulfide $Sm_2Ti_2S_2O_5$as a Stable Photocatalyst for Water Oxidation and Reduction under Visible Light Irradiation ($\lambda \leq 650$ Nm). *J. Am. Chem. Soc.* **2002**, *124*, 13547−13553.

DOI: 10.1021/acsami.8b17622
ACS Appl. Mater. Interfaces 2019, 11, 6918−6926

CHEMISTRY OF MATERIALS

pubs.acs.org/cm

Article

A SnS_2 Molecular Precursor for Conformal Nanostructured Coatings

Yong Zuo, Junshan Li, Xiaoting Yu, Ruifeng Du, Ting Zhang, Xiang Wang, Jordi Arbiol, Jordi Llorca, and Andreu Cabot*

Cite This: *Chem. Mater.* 2020, 32, 2097−2106

Read Online

ACCESS | Metrics & More | Article Recommendations | Supporting Information

ABSTRACT: We present a simple, versatile, and scalable procedure to produce SnS_2 nanostructured layers based on an amine/thiol-based molecular ink. The ratios amine/thiol and Sn/S, and the reaction conditions, are systematically investigated to produce phase-pure SnS_2 planar and conformal layers with a tremella-like SnS_2 morphology. Such nanostructured layers are characterized by excellent photocurrent densities. The same strategy can be used to produce SnS_2−graphene composites by simply introducing graphene oxide (GO) into the initial solution. Conveniently, the solvent mixture is able to simultaneously dissolve the Sn and Se powders and reduce the GO. Furthermore, $SnS_{2-x}Se_x$ ternary coatings and phase-pure $SnSe_2$ can be easily produced by simply incorporating proper amounts of Se into the initial ink formulation. Finally, the potential of this precursor ink to produce gram-scale amounts of unsupported SnS_2 is investigated.

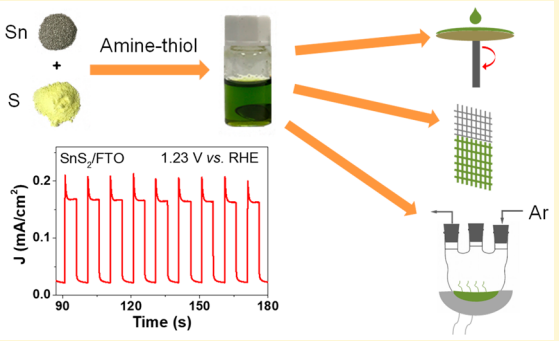

Downloaded via UNIV DE BARCELONA on April 23, 2020 at 14:53:52 (UTC).
See https://pubs.acs.org/sharingguidelines for options on how to legitimately share published articles.

INTRODUCTION

The production of planar and conformal nanostructured layers with high surface areas and porosity using simple, rapid, cost-effective, and scalable processes that are neither energy nor labor intensive is a topic of major relevance.[1−3] Toward this goal, solution-based strategies based on the decomposition, assembly and/or deposition of salts, molecular precursors, or colloidal nanoparticles offer obvious advantages over physical and chemical vacuum-based technologies.[4] However, the use of salts generally leads to the incorporation of large amounts of impurities in the final material and may result in inhomogeneous layer compositions. Furthermore, nanoparticle-based inks suffer from suspension stability and result in layers characterized by inadequate interphases with the support, with poor charge transfer and feeble mechanical stability, i.e., present delamination issues.[5−11] On the other hand, molecular precursors generally provide a homogeneous mixing of the precursor elements that ensures a uniform layer composition without impurities. Additionally, the crystallization of the material postdeposition can considerably improve charge transfer/transport properties and layer adherence.[2]

In 2004, Mitzi and co-workers reported the use of hydrazine to produce a molecular ink from the dissolution of bulk SnS_2 and $SnSe_2$ in the presence of excess elemental chalcogen.[12] The process was facilitated by the in situ reduction of the elemental chalcogen to produce chalcogenide anions that subsequently started a series of nucleophilic reactions with the bulk chalcogenide, breaking it down to eventually yield soluble molecular metal chalcogenide species.[12] The obtained molecular inks could then be spin-coated and thermally annealed at 350 °C to yield phase-pure $SnS_{2-x}Se_x$ thin films with high charge carrier mobility.[12] After this pioneer report, the hydrazine route was demonstrated effective in producing a plethora of chalcogenides, including $GeSe_2$,[13] $Cu_{1.9}S$,[14] In_2Se_3,[15] ZnTe,[16] In_2Te_3,[17] GeSbSe,[18] $CuInSe_2$,[19] and $CuInTe_2$.[17] The use of hydrazine finds advantages on its high reduction power, small size, volatility and on leaving no carbon residue. However, hydrazine is highly toxic and explosive, thus it is not convenient for scale-up and commercial applications.[20]

To avoid the disadvantages of hydrazine, the Brutchey group demonstrated a binary solvent mixture based on ethanedithiol (Edt) and ethylenediamine (En), named the "alkahest solvent", to dissolve and recover several V_2VI_3 chalcogenides, including As_2S_3, As_2Se_3, As_2Te_3, Sb_2S_3, Sb_2Se_3, Sb_2Te_3, Bi_2S_3, Bi_2Se_3, and Bi_2Te_3,[21] at room temperature and ambient pressure, under air atmosphere, and in just a few minutes.[21,22] This amine-thiol solution system dissolves the bulk chalcogen through an amine-catalyzed reaction resulting in alkyl di-, tri-, and tetrachalcogens while SR species bind to the metal ions.[20,21,23] Various combinations of mono- or dithiols with primary mono- and/or diamines, as well as different amine/thiol ratios, have been used to dissolve a plethora of metal and chalcogen precursor materials.[20,24,25] As an example, Cu, Zn,

Received: December 18, 2019
Revised: February 11, 2020
Published: February 11, 2020

ACS Publications

© 2020 American Chemical Society

https://dx.doi.org/10.1021/acs.chemmater.9b05241
Chem. Mater. 2020, 32, 2097−2106

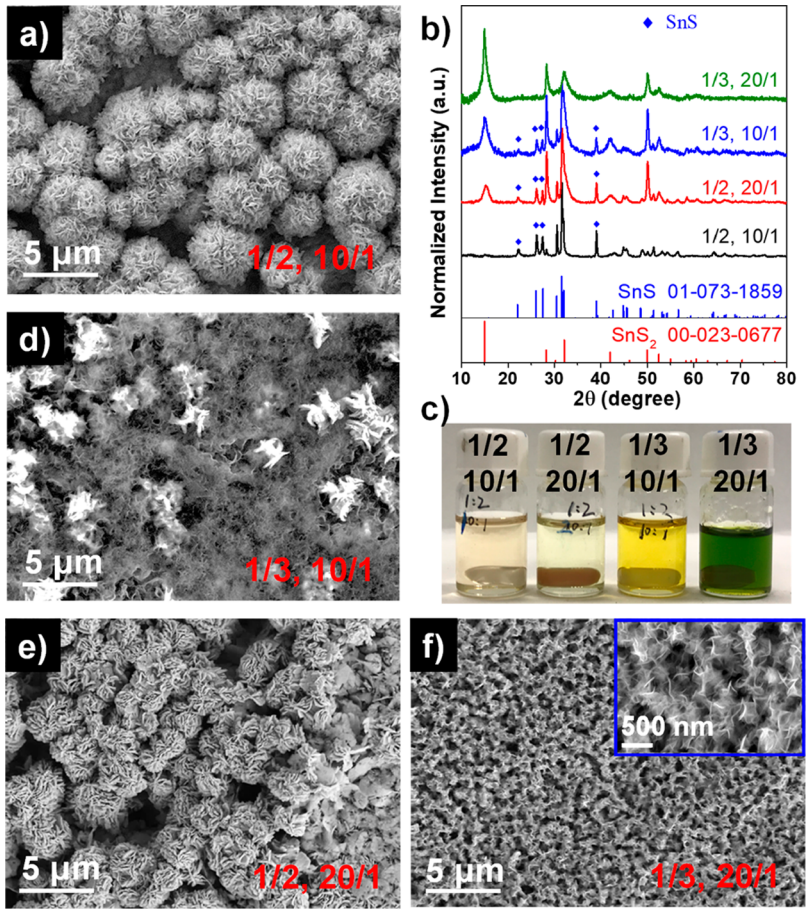

Figure 1. (a) SEM micrograph of the material recovered after annealing a layer produced from an ink containing a molar ratio Sn/S = 1/2 and a volume ratio En/Edt = 10/1. (b) XRD patterns of materials obtained after annealing layers produced from inks containing different Sn/S (1/2 or 1/3) and En/Edt ratios (10/1 or 20/1), as specified. (c) Optical photographs of molecular inks obtained by dissolving different Sn/S (1/2 or 1/3) and En/Edt ratios (10/1 or 20/1), as specified. (d–f) SEM micrographs of materials obtained after annealing layers produced from different Sn/S (1/2 or 1/3) and En/Edt ratios (10/1 or 20/1), as specified. Inks were formulated by dissolving the proper Sn and S ratios in En/Edt mixtures at 70 °C for 1 h. Annealing conditions: 320 °C, 30 min.

Sn, and In are soluble in butylamine and Edt;[26] M_aX_n (M = Cu^+, Cu^{2+}, Zn^{2+}, Sn^{2+}, In^{3+}, Ga^{3+}; X = Cl^-, $acac^-$, OAc^-, O^{2-}) can be easily dissolved in a mixture of hexylamine and propanethiol; and M_bY_n (M = Cu^+, Cu^{2+}, Sn^{2+}, In^{3+}; Y = S^{2-}, Se^{2-}) are highly soluble in hexylamine and Edt.[27] In the amine-thiol system, the main difficulty to prepare a phase-pure material is to find the proper amine and thiol mixture, to find their ratio and reaction conditions to crystallize the targeted product in the desired phase, and to prevent the formation of unwanted secondary phases.

SnS_2 is an indirect n-type semiconductor that is attracting significant interest as an absorber material for solar energy conversion due to the abundance of its constituting elements and its excellent optoelectronic properties in part related to its layered structure. To prepare SnS_2, different methods have been put forward, including hydrothermal,[28−30] hot-injection,[31−33] heat-up,[34,35] exfoliation,[36−38] and chemical vapor deposition.[39−41] Sn has been also dissolved in 10/1 of En/Edt to recover SnS,[42] but the production of pure SnS_2 by this method has been so far elusive.

Herein we present a simple route based on a molecular ink to produce phase-pure SnS_2 from a Edt and En mixture. The ratio of Sn/S and En/Edt and the annealing process are investigated to define the optimal conditions to recover pure SnS_2 planar and conformal layers. We additionally study the production of ternary $SnS_{2-x}Se_x$ and phase-pure $SnSe_2$, the one-step production of composite of SnS_2/reduced graphene oxide (SnS_2/rGO) composites, and the photocatalytic properties of the produced layers.

RESULTS AND DISCUSSION

In our first attempts to produce SnS_2, stoichiometric molar amounts of sulfur and tin powders (Sn/S = 1/2) were dissolved in a volume ratio En/Edt = 10/1 at 70 °C for 1 h to obtain an optically clear pale yellow solution. The precursor ink was coated onto a glass substrate, and the obtained film was annealed at 320 °C for 30 min. Upon annealing, the layer turned gray yellow. Scanning electron microscope (SEM) characterization showed the layer to contain a large density of quasi-spherical flower-like structures (Figure 1a), but powder X-ray diffraction (XRD) analysis identified the main crystal phase of the obtained material as SnS (Figure 1b), with only a minor amount of SnS_2 (Figure 1b).

The precursor solution was modified by incorporating an additional amount of sulfur (Sn/S = 1/3) to correct for the low quantity of this element in the final layer. This precursor solution displayed a much more intense yellow color (Figure 1c). XRD analyses of the layers produced from the coating and posterior annealing of this precursor ink showed a notable

https://dx.doi.org/10.1021/acs.chemmater.9b05241
Chem. Mater. 2020, 32, 2097−2106

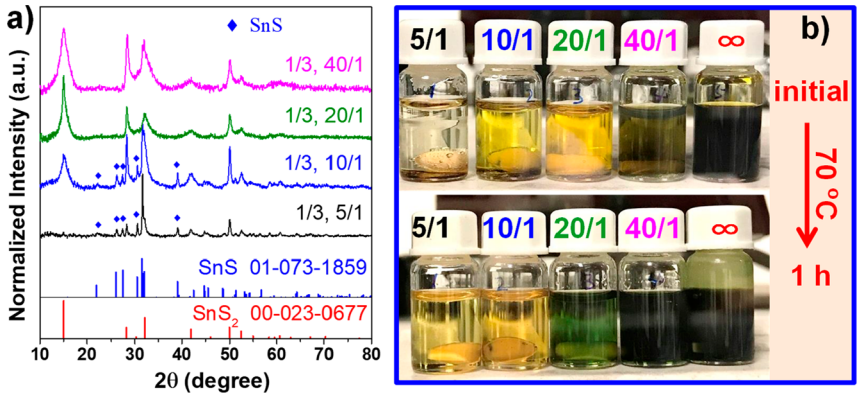

Figure 2. (a) XRD patterns of sample recovered after annealing layers produced from inks containing different ratios En/Edt (from 5/1 to 40/1), as specified. (b) Optical photographs of SnS_2 molecular inks prepared with different ratios En/Edt (from 5/1 to 40/1) before and after heating at 70 °C for 1 h, as specified. Ink formulation parameters: Sn/S = 1/3, 70 °C, 1 h. Annealing conditions: 320 °C, 30 min.

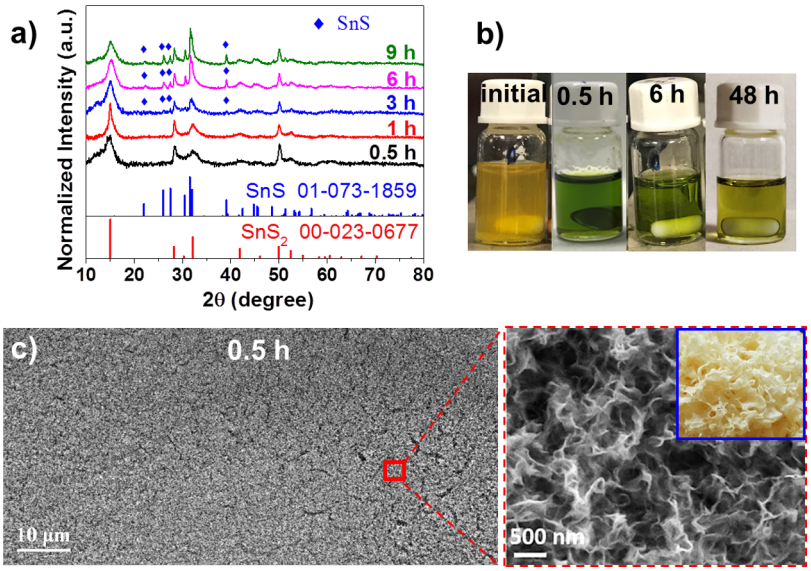

Figure 3. (a) XRD patterns of samples recovered after annealing the layers obtained from molecular inks prepared after different dissolution times from 0.5 to 9 h, as noted. (b) Optical photos of respective molecular inks before and after heating at 70 °C for varied range of times. Ink composition and dissolution temperature: Sn/S = 1/3, En/Edt = 20/1, 70 °C. (c) Large area SEM micrograph and higher magnification image of sample recovered from the annealing of a layer produced from a standard ink: Sn/S = 1/3, En/Edt = 20/1, 70 °C, 0.5 h dissolution time. Inset shows optical photograph of the tremella fungus.

increase of the amount of SnS_2, but SnS impurity peaks were still evident. Furthermore, the structure of the obtained film changed from the quasi-spherical flowers to tremella-like particles (Figure 1d). Similar results were obtained when instead of increasing the amount of sulfur, we decreased the concentration of Edt in the initial solution (Sn/S = 1/2; En/Edt = 20/1). This precursor solution decomposed into tremella-like structures with a main SnS_2 phase and a residual SnS component (Figure 1b,e).

To further adjust the stoichiometry and crystal phase of the final layer, we simultaneously increased the amount of sulfur (Sn/S = 1/3) and reduced the amount of Edt (En/Edt = 20/1). Using this new precursor solution (Sn/S = 1/3, En/Edt = 20/1), which displayed a green color (Figure 1c), phase-pure tremella-like SnS_2 could be finally recovered (Figure 1b,f). Energy-dispersive X-ray spectroscopy (EDX) analysis further confirmed the composition of the obtained layer to be consistent with stoichiometric SnS_2 (Table S1).

Generally, lower amounts of Edt favored the formation of the SnS_2 phase over SnS. Pure SnS_2 could be obtained with Edt contents of En/Edt = 20/1 or lower when using an excess of S, Sn/S ≤ 1/3 (Figures 2a and S1). However, without Edt, the Sn and S powder mixture could not be fully dissolved (Figure 2b, S1) and no SnS_2 could be recovered. On the amine side, replacing En by hexylamine or butylamine did not allow the dissolution of proper amounts of Sn and S (Figure S2).

The higher the Edt concentration, the lower the time required to obtain an optically clear ink (Table S2). When using dissolution times in the range between 20 min and 1 h, no major effect was observed on the phase and structure of the produced material. However, when increasing the dissolution time, the SnS phase appeared even when using the previously defined as proper precursor compositions: Sn/S = 1/3, En/Edt = 20/1 (Figure 3a). EDX analysis further confirmed the Sn/S ratio of the annealed material to increase with the time of preparation of the precursor solution (Table S3). Additionally, the color of the ink also faded with the dissolution time

https://dx.doi.org/10.1021/acs.chemmater.9b05241
Chem. Mater. 2020, 32, 2097−2106

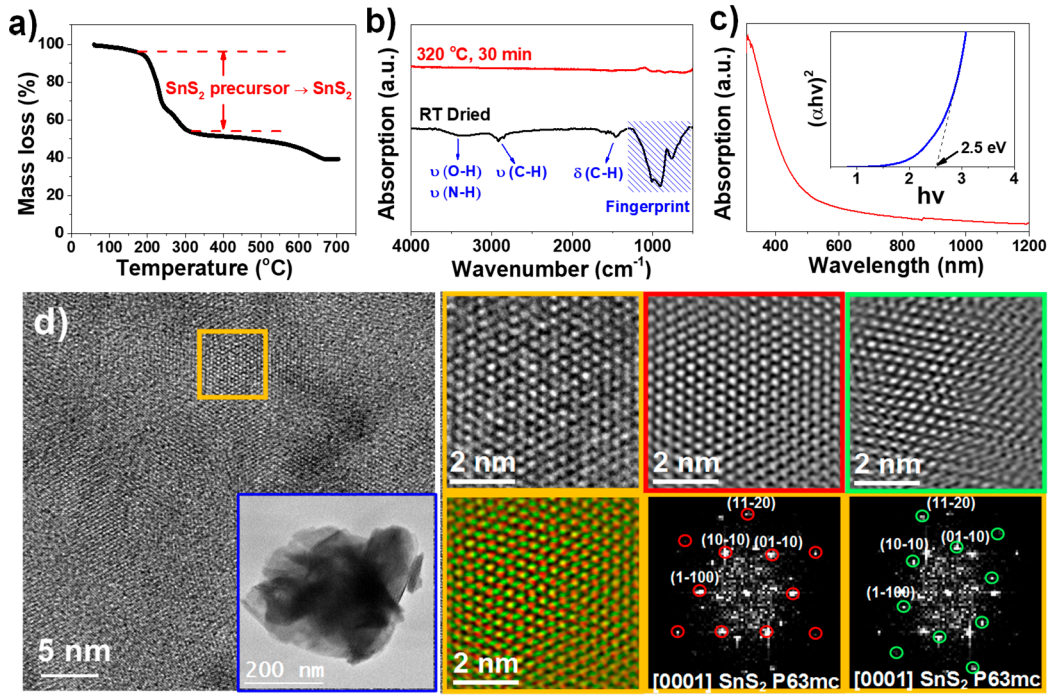

Figure 4. SnS_2 recovered from a conventional molecular ink: (a) TG profile of a SnS_2 molecular ink after drying at 200 °C. (b) FTIR spectra of a SnS_2 molecular ink dried at room temperature and of the material recovered after annealing at 320 °C for 30 min. (c) UV−vis spectrum of the material recovered after annealing at 320 °C for 30 min. (d) HRTEM micrograph of the material recovered after annealing at 320 °C for 30 min, detail of the orange squared region and its corresponding power spectrum. From the analyzed crystalline domain, the SnS_2 lattice fringe distances were measured to be 0.316, 0.314, 0.310, and 0.181 nm, at 62.65°, 123.67°, and 94.00°, which could be interpreted as the hexagonal SnS_2 phase, visualized along its [0001] zone axis. Green and yellow squared images correspond to the reciprocal space frequency filtered reconstructed images corresponding to each individual overlapping nanosheet, as extracted from the orange squared region. The spots used in the frequency reconstruction have been circled in red and green, respectively, in the power spectra provided below.

(Figure 3b). Furthermore, the morphology of the final material turned toward sunflower-like structures when dissolution time increased to 3 h and above (Figure S3). We hypothesize that all these observations were associated with a sulfur loss during ink formulation. This loss was in the form of H_2S that was produced by the reaction of elemental sulfur with amine,[43,44] To prove this hypothesis, we added an additional amount (0.5 mmol) of sulfur powder into a SnS_2 molecular ink after 6 h at 70 °C. This ink was mixed for additional 30 min to dissolve the added sulfur. After this time, the intense green color was recovered, and pure SnS_2 phase with a tremella morphology was obtained after annealing (Figure S4).

When applying no heat, a suitable ink could be prepared by dissolving proper amounts of Sn and S (Sn/S = 1/3) in En/Edt = 20/1 at ambient temperature for 6 h. In this condition, no significant loss of sulfur was detected and pure SnS_2 could be recovered after annealing (Figure S5). Overall, to optimize time and ensure a proper product phase with tremella like morphology (Figure 3a,c), we fixed the ink preparation time at 30 min, dissolution temperature at 70 °C, the element ratio at Sn/S = 1/3 and the solvent ratio at En/Edt = 20/1.

Thermogravimetric (TG) analysis of the yellowish gel-like paste collected after drying the conventional ink at 200 °C (Figure 4a) displayed a two-step mass loss in the temperature range 200−300 °C. These steps were associated with the ink decomposition and overall accounted for ca. 65 wt % of the initial mass. At temperatures above 500 °C an additional mass loss, associated with the sulfur evaporation, was observed. Fourier transform infrared spectroscopy (FTIR, Figure 4b) corroborated the loss of organics after annealing the material at 320 °C for 30 min, as evidenced by the complete loss of strong ν(N−H)/ν(O−H) and ν(C−H) stretching bands originating from the solvent mixture. The absence of bands corresponding to the ν(S−H) thiol group at 2560 cm^{-1} implies that Edt is fully deprotonated by En.[42]

EDX elemental mapping of the films obtained from the deposition and annealing of the conventional ink showed a uniform distribution of S and Sn (Figure S6). High-resolution transmission electron microscopy (HRTEM) micrographs confirmed the SnS_2 hexagonal phase (space group = *P*63*mc*) with $a = b = 3.6450$ Å, $c = 11.8020$ Å (Figure 4d, S7). HRTEM analysis reported in Figure 4d shows the overlapping of two different [0001]-oriented nanosheets. The power spectrum (fast Fourier transform) applied to the HRTEM image with the applied reciprocal space frequency (structural) filtering showed the presence of a 21° rotation between the overlapping nanosheets (Figure 4d). These results confirmed the pileup of different nanosheets, consistently with SEM results. UV−vis analysis of recovered SnS_2 films (Figure 4c) showed their bandgap to be around 2.5 eV, which is consistent with the relatively wide range of optical bandgaps reported for SnS_2.[41,45] The small deviation on the experimental band gap values measured here with respect to theoretical SnS_2 values can be ascribed to the reduced thickness of the produced SnS_2 layer (Figures 1f, 3c, and 4d), consistently with a previous report.[46]

To study the photocatalytic properties of SnS_2 tremella layers obtained from the molecular ink, the ink was deposited on fluorine-doped tin oxide (FTO)-coated glass substrates by drop casting. The annealed layer was used as anode in a photoelectrochemical (PEC) cell for water splitting. XRD and

https://dx.doi.org/10.1021/acs.chemmater.9b05241
Chem. Mater. 2020, 32, 2097−2106

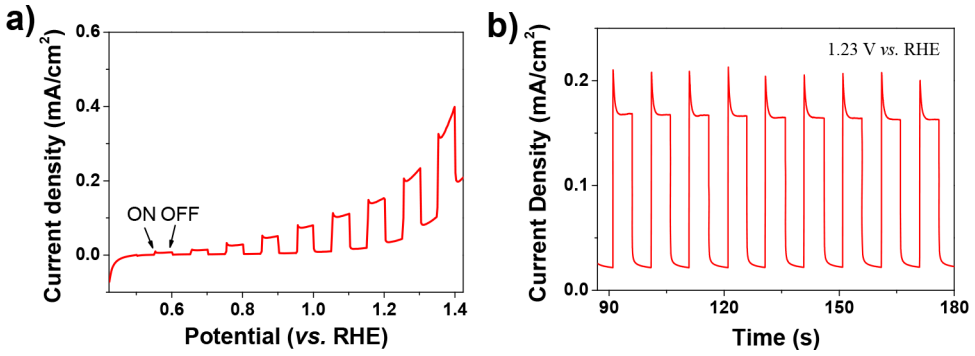

Figure 5. (a) Linear sweep voltammogram and (b) amperometric $i-t$ curve at 1.23 V vs RHE of a SnS_2/FTO sample under chopped illumination. RHE: reversible hydrogen electrode.

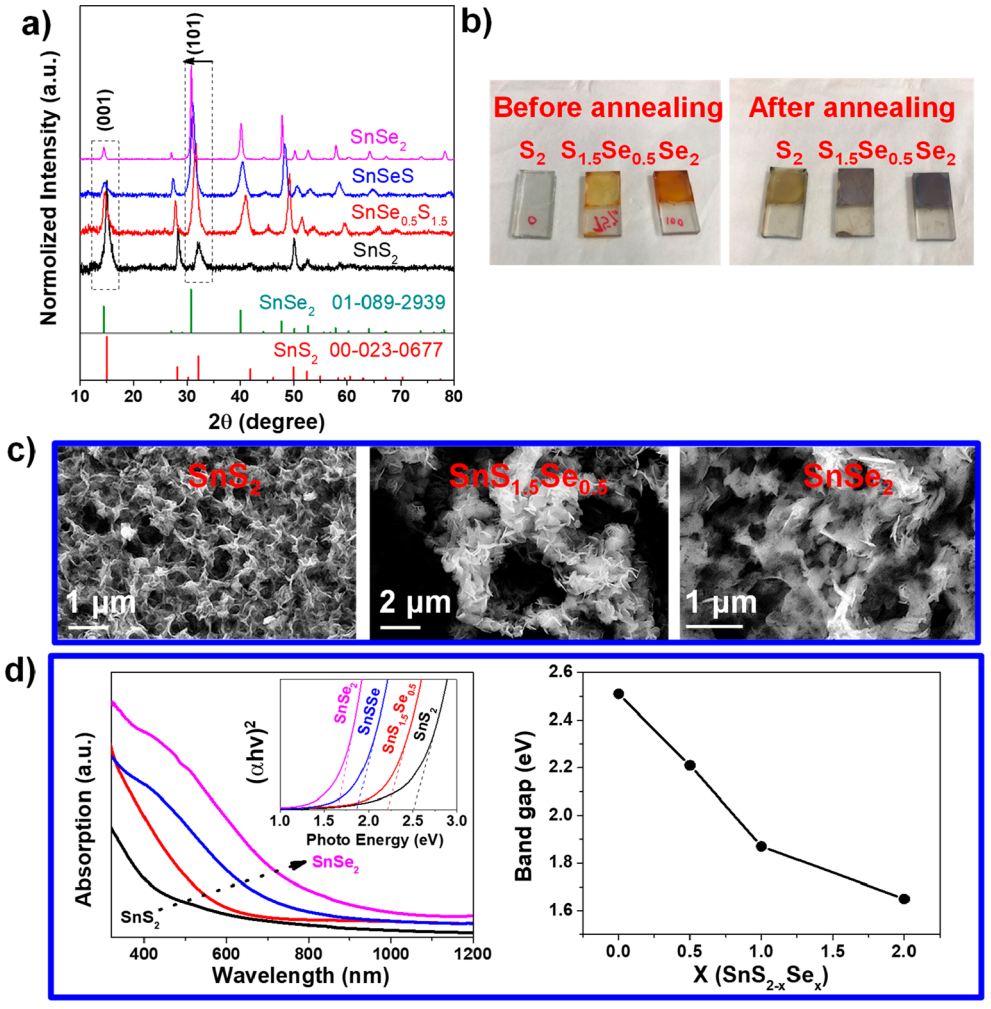

Figure 6. $SnS_{2-x}Se_x$ ternary chalcogenides obtained from the annealing for layers produced from inks containing different S/Se ratios: (a) XRD patterns; (b) optical photograph of $SnS_{2-x}Se_x$/FTO layers before and after annealing; (c) SEM micrographs; (d) UV−vis spectra.

SEM analysis confirmed the phase and structure of the SnS_2 to be maintained when depositing the ink over FTO instead of glass (Figure S8). Using these SnS_2 layers, current densities reaching up to ~160 μA/cm^2 (1.23 V vs RHE) were measured (Figure 5). This performance was well above that of previously reported bare SnS_2 photoanodes[47] and even better than some SnS_2 samples incorporating cocatalysts (Table S5).[48−52] We ascribed these excellent photocurrents to (1) the tremella morphology that provided a larger interface area with the electrolyte and effective paths for the solution diffusion; (2) the intimate contact of the SnS_2 absorber with the FTO current collector, thus decreasing the interphase electrical resistance and facilitating the transfer of photogenerated charges from the SnS_2 photocatalyst films to the FTO.

We further investigated the conformal coating of SnS_2 on different substrates. As an example, stainless steel (SS) meshes were coated through a quick immersion of the preheated support on the molecular ink and the posterior drying and annealing of the obtained film (see Experimental Section for details). Using this simple procedure, homogeneous layers of

https://dx.doi.org/10.1021/acs.chemmater.9b05241
Chem. Mater. 2020, 32, 2097−2106

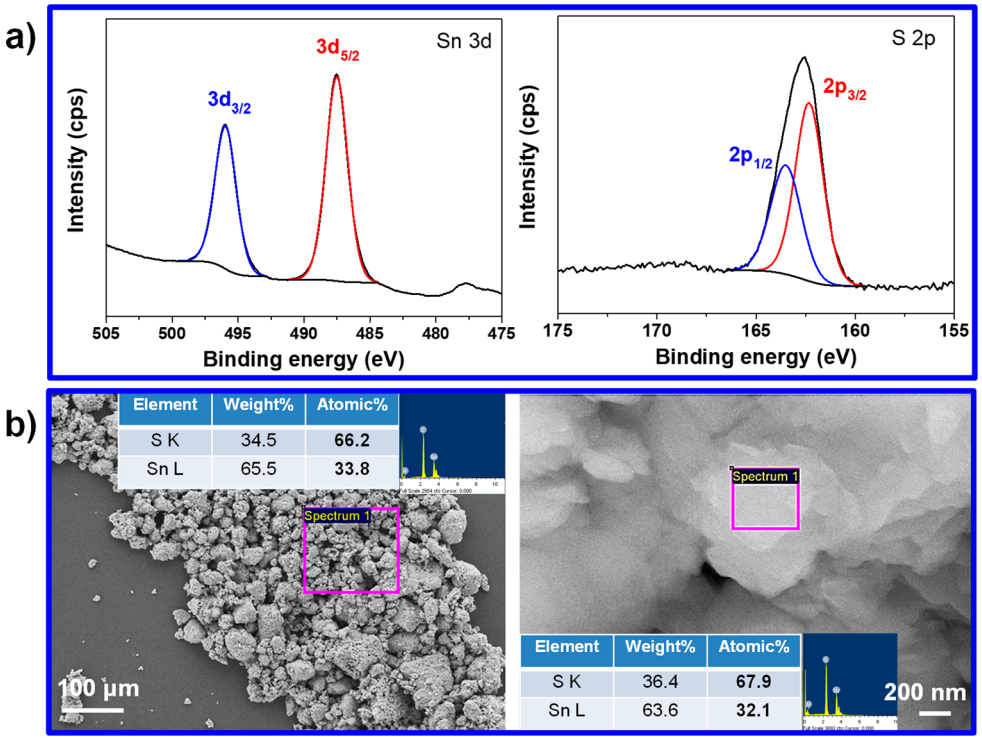

Figure 7. SnS_2 powder recovered from the annealing of large amounts of molecular ink: (a) XPS spectra of Sn 3d region and S 2p regions. (b) SEM micrographs and EDX data.

nanostructured SnS_2 could be coated on the surface of SS meshes as observed by SEM, EDX, and SEM mapping (Figures S9 and S10). Notice that because the mixture of En/Edt has a high metal dissolution power, the coating of Ni and Cu foams/meshes using this ink inevitably resulted in Ni or Cu contamination in the final SnS_2 layer. As an alternative, instead of SS, corrosion-free carbon cloth (CC) was used as current collector. Figure S11 displays SEM micrographs of bare and SnS_2-coated CCs.

A different strategy was used to coat graphene flakes. GO produced by the Hummers method was introduced in the precursor solution. During the ink formulation, simultaneously to the dissolution of Sn and S powders, GO was reduced by the amine,[53,54] yielding an ink containing a mixture of Sn−S molecular precursor and rGO. This composite ink could be used to coat virtually any substrate with SnS_2/rGO composite layers using the above coating and annealing steps (Figure S12).

We used the same strategy to produce $SnS_{2-x}Se_x$ coatings with controlled S/Se ratios, by simply adding the proper amount of Se in the precursor solution (see Experimental Section for details). As can be seen in Figure 6a, an obvious XRD peak shift toward lower angle occurred when the Se ratio increased from 0 to 100%, indicating that the Se ion entered the crystal structure. No impurity peaks were detected, even when pure $SnSe_2$ was recovered. The phase purity obtained in the present work was in contrast with results obtained by McCarthy et al., who systematically obtained sulfide impurities when attempting to produce pure $CoSe_2$.[55] Differences are associated with the very little amount of Edt used in the present work. Figure S13 shows how the color of the precursor solution changed from green to dark brown with the selenium dosage increase. Figure 6b displays how the color of spin-coated thin-film changed after annealing. SEM-EDX data (Table S4) demonstrated the sum of Se and S to be always around 67%, while the tin composition was around 33%, confirming that Se ions occupied the position of S within $SnS_{2-x}Se_x$ ternary chalcogenides. SEM analysis further showed the tremella-like morphology to change into sheet-like morphology with the addition of Se (Figure 6c). Additionally, the band gap energy decreased from 2.50 eV (SnS_2) to 1.65 eV ($SnSe_2$) with Se incorporation (Figure 6d).

$SnS_{2-x}Se_x$/FTO electrodes displayed a negative photoconductivity at −0.1 V (or lower) vs Ag/AgCl. Among the samples containing Se, the highest photocurrents were measured from $SnSe_2$/FTO photoelectrodes, reaching up to 10 μA/cm^2 at −0.1 V vs Ag/AgCl (Figure S14).

We additionally studied the potential of this precursor ink to produce gram-scale amounts of unsupported particles, which can be potentially used in catalysis,[36] batteries,[8] photodetectors,[56] sensors,[57] field-effect transistor devices,[58] etc. With this aim, large amounts of SnS_2 molecular ink (5 mL) were decomposed inside a heated flask (see Experimental Section and Figure S15a for details). After annealing, a gray powder was collected, which turned gray-yellow after washing. XRD analysis showed the powder to be phase-pure SnS_2 (Figure S15b). X-ray photoelectron spectroscopy (XPS) analysis showed the Sn 3d region to display a unique doublet at 495.9 eV (Sn $3d_{3/2}$) and 487.5 eV (Sn $3d_{5/2}$), associated with Sn^{4+} within the SnS_2 lattice,[59−61] while the S 2p region showed a doublet at 163.5 eV (S $2p_{1/2}$) and 162.3 eV (S $2p_{3/2}$), ascribed to S^{2-} in the SnS_2 lattice[60,61] (Figure 7a). Furthermore, SEM-EDX data in Figure 7b further confirmed that the composition of Sn/S was ca. 1/2, consistent with stoichiometric SnS_2. Interestingly, the powder displayed a flake-like morphology in contrast to the tremella-like particles recovered on substrates, which was ascribed to the additional

https://dx.doi.org/10.1021/acs.chemmater.9b05241
Chem. Mater. 2020, 32, 2097−2106

growth of the crystals recovered in powder form associated with the larger amount of available precursor.

CONCLUSIONS

In summary, a Sn−S molecular ink was produced by dissolving Sn and S elemental powders in an amine/thiol cosolvent. The decomposition and annealing of this ink at 320 °C for 30 min resulted in the formation of nanostructured tin sulfide. Pure SnS_2 layers with a tremella morphology were obtained using an ink containing an elemental ratio Sn/S = 1/3 and a solvent ratio En/Edt = 20/1. A loss of sulfur in the form of H_2S gas during dissolution was identified as the reason behind the presence of SnS impurities in inks produced using too long dissolution times. This molecular ink could be applied to produce planar and conformal SnS_2 nanostructured layers on conductive substrates, such as FTO, SS, and CC. SnS_2/FTO photoanodes provided outstanding photocurrent densities under illumination with simulated solar light. Furthermore, SnS_2/rGO composites and $SnS_{2-x}Se_x$ were easily synthesized using the same strategy by simply introducing GO and Se powder in the initial precursor solution.

EXPERIMENTAL SECTION

Chemicals. All chemicals were used as received, without additional purification. Sn powder (99+%), S powder (99.98%), En (99.5+%), Edt (98+%) were purchased from Sigma-Aldrich. Se powder (99.5+%) was purchased from Acros Organics. All chemical manipulation and material preparation processes were carried out in an argon-filled glovebox.

Ink Preparation. Tin and sulfur elemental powders, other than their salts, were selected as solutes to avoid any potential counterion contamination. To prepare a Sn−S molecular ink, elemental Sn (0.5 mmol) and S (1.5 mmol) powders were weighed and transferred into a glass vial (4 mL). En (2 mL) and Edt (0.1 mL) were sequentially added into the vial. The mixture was then stirred at 750 rpm, heated to 70 °C, and kept at this temperature for 30 min to get an optical transparent green ink solution. To study the influence of ratio between En and Edt, a different amount of Edt was used, while the En amount kept unchanged. To study the influence of sulfur amount, we used a different amount of sulfur.

Recovery of Semiconductor Film on Planar Glass Slides. Typically, 0.1 mL of molecular ink was drop casted on a microscope glass slide (~1 × 1 cm), and then the deposited substrate was heated on a hot plate (Corning, PC400D) at 200 °C to dry the ink. The dried precursor film was afterward annealed at 320 °C on the hot plate for 30 min. These operations were conducted in the argon-filled glovebox. The obtained film was scraped off of the substrate for posterior characterization by XRD, SEM, and HRTEM.

Recovery of Semiconductor Film on FTO-Coated Glass Slides. Twenty microliters of molecular ink was drop casted on the surface of FTO with an active area of 1 cm × 1 cm (an additional area of 1 cm × 1 cm was covered by the high-temperature-bearable tape to leave a clean area for electrical connection). The tip of the pipet-pipe was used to pull the solution to produce a uniform coverage (in this operation, the tip should not touch the FTO surface), dried at 200 °C, and finally annealed on the hot plate at 320 °C for 30 min.

Recovery of Semiconductor Film on Stainless Steel and Carbon Cloth. Typically, a piece of precleaned SS was first heated on the hot plate at 200 °C for several minutes and then quickly immersed into molecular ink and held for 30 s. The wet SS was then held by a tweezer, put close to the surface of the hot plate to dry, and then annealed in an Ar-filled tubular furnace at 320 °C for 30 min with a temperature ramp of 3 °C/min. SS was preheated to decrease the local viscosity of the molecular ink close to the SS surface and thus facilitate diffusion through the porous electrode structure. The heated support also promoted the film drying and facilitated the formation of more uniform coatings.

To coat CC with a SnS_2 layer, 40 μL of molecular ink was evenly drop casted on two sides of a 1 × 1 cm^2 carbon cloth using the tip of the pipet to spread the precursor solution, put close to the surface of the hot plate to dry, and subsequently annealed in an Ar-filled tubular furnace at 320 °C for 30 min with a temperature ramp of 3 °C/min.

Recovery of SnS_2/rGO Composites. GO was produced by the Hummers method as originally presented by Kovtyukhova.[62] In the next step, 10 mg of GO was added together with Sn powder and S powder to formulate the Sn−S molecular ink. The same ratios of Sn/S and En/Edt and dissolution and annealing times and temperatures as used in conventional inks were used to recover SnS_2/rGO composite layers.

Recovery of $SnS_{2-x}Se_x$. A proper amount of elemental Se powder was introduced in the initial mixture in replacement of the same molar amount of S powder. The dissolution time was adjusted to make sure that all the precursor powders were dissolved and an optical transparent molecular solution was obtained. Dissolution time was typically 30 min for SnS_2 and increased up to 80 min with the Se amount increasing. Dissolution temperature was set at 70 °C in all cases. The same drying and annealing steps used to recover pure-phase SnS_2 were used to recover $SnS_{2-x}Se_x$, except that the annealing time was increase to 60 min.

To coat $SnS_{2-x}Se_x$ on FTO for posterior PEC measurements, we noticed that the recovered $SnS_{2-x}Se_x$, especially $SnSe_2$, using the same spin coating method as we did on SnS_2/FTO showed almost no $i-t$ response. We attributed this result to the $SnSe_2$ layer being too thick. Note that $SnSe_2$ has a much lower band gap and thus absorbs light much more strongly; thus, thinner layers are required. Too thick layers prevent light from arriving to the semiconductor−electrode interphase and decrease performance. We thus used the spin coating method to produce thinner layers and kept the entire deposition process the same to make the results comparable.

Recovery of Large-Scaled Powder. Five milliliters of Sn−S molecular ink was injected into a 50 mL three-neck flask preheated to 300 °C and containing an Ar atmosphere. A safety flask containing water/ethanol was used to collect the gas/vapor emanated from the ink solution. Upon ink injection, temperature decreased to ~200 °C and then increased slowly to 300 °C. The flask was kept at this temperature for additional 10 min to obtain a dry powder. The powder was then ground and annealed in a tubular furnace under Ar atmosphere at 350 °C for 2 h with a ramp rate of 3 °C/min or lower. The annealed powder was washed using CS_2 and ethanol by sonication to remove the potential sulfur residues. The sample was finally dried for posterior characterizations and use. It should be noted that we injected the precursor solution very fast to make the heating process more uniform and synthesis more repeatable, thus minimizing the difference among different batches.

Sample Characterization. XRD patterns were obtained on a Bruker AXS D8 ADVANCE X-ray diffractometer (Bruker, Karlsruhe, Germany) operating at 40 kV and 40 mA with Ni-filtered (2 μm thickness) Cu Kα1 radiation (λ = 1.5406 Å). TEM characterization was carried out on a Zeiss Libra 120 (Carl Zeiss, Jena, Germany), operating at 120 kV. HRTEM images were obtained using a field emission gun FEI Tecnai F20 microscope at 200 kV with a point-to-point resolution of 0.19 nm. For TEM characterization, samples were prepared by peeling off directly from glass slide and drop casting their ethanol solutions onto a 200 mesh copper grid. SEM analysis was done in a Zeiss Auriga microscope (Carl Zeiss, Jena, Germany) with an EDX detector at 20 kV to study composition. XPS was carried out on a SPECS system (SPECS GmbH, Berlin, Germany) equipped with an Al anode XR50 source operating at 150 W and a Phoibos 150 MCD-9 detector (SPECS GmbH, Berlin, Germany). The pressure in the analysis chamber was kept below 10^{-7} Pa. Data processing was performed with the CasaXPS program (Casa Software Ltd., UK). Binding energy (BE) values were centered by using the C 1s peak at 284.8 eV. TG analysis was carried out using a PerkinElmer Diamond TG/DTA Instruments (PerkinElmer, Waltham, MA). For TG analysis, a proper amount of molecular ink was dried on a glass slide at 200 °C and scratched out after cooling, and ~20 mg of the dried gel powder was collected and loaded into a ceramic pan.

https://dx.doi.org/10.1021/acs.chemmater.9b05241
Chem. Mater. 2020, 32, 2097−2106

Measurements were carried out in an Ar atmosphere from room temperature to 700 °C at a heating rate of 5 °C/min. FTIR was performed on an Alpha Bruker FTIR spectrometer with a platinum attenuated total reflectance (ATR) single reflection module. FTIR data were typically averaged over 24 scans. UV−vis absorption spectra were acquired with a PerkinElmer LAMBDA 950 UV−vis spectrophotometer equipped with an integrating sphere. For FTIR and UV−vis analysis, films were produced by spin coating on glass substrates instead of drop-casting.

Photoelectrochemical Measurements. PEC characterization was performed in a three-electrode system using an electrochemical workstation (Metrohm Autolab). A Pt mesh (2 cm^2 surface area) and Ag/AgCl (3.3 M KCl) were used as the counter and reference electrodes, respectively. $SnS_{2-x}Se_x$ films deposited on FTO were used as the working electrode. Before film deposition, the FTO glass was washed with acetone−2-propanol (1−1 volume), ethanol, and then deionized water. An aqueous solution of Na_2SO_4 (0.5 M, pH = 7) was used as the electrolyte. Relatively thick SnS_2 films deposited by drop casting were used to test the SnS_2 PEC performance. On the other hand, thinner films produced by spin coating were used for the $SnSe_2$ performance owing to the higher light absorption capability of this material associated with its lower band gap. The electrolyte was purged with Ar for 30 min prior to the measurement. The incident light source was provided by eight radially distributed 35 W xenon lamps, providing a total irradiance power on the sample of ca. 100 mW/cm^2. The following formula was used to convert the potentials to the RHE standard scale:

$$E \text{ vs RHE} = E_{Ag/AgCl} + E^{o}_{Ag/AgCl} + 0.059 \times \text{pH}$$
$$= E_{Ag/AgCl} + 0.623(\text{V})$$

■ ASSOCIATED CONTENT

Supporting Information

The Supporting Information is available free of charge at https://pubs.acs.org/doi/10.1021/acs.chemmater.9b05241.

Additional experiments, SEM, XRD, EDX, TEM, PEC tests, scheme of large-scale procedure, and tables of composition change evolution and PEC performance comparison (PDF)

■ AUTHOR INFORMATION

Corresponding Author

Andreu Cabot − *Catalonia Institute for Energy Research - IREC, Sant Adrià del Besòs, Barcelona 08930, Spain; ICREA, Pg. Lluis Companys 23, 08010 Barcelona, Spain;* orcid.org/0000-0002-7533-3251; Email: acabot@irec.cat

Authors

Yong Zuo − *Catalonia Institute for Energy Research - IREC, Sant Adrià del Besòs, Barcelona 08930, Spain; Departament d'Enginyeria Electrònica i Biomèdica, Universitat de Barcelona, Barcelona 08028, Spain;* orcid.org/0000-0003-1564-467X

Junshan Li − *Catalonia Institute for Energy Research - IREC, Sant Adrià del Besòs, Barcelona 08930, Spain; Departament d'Enginyeria Electrònica i Biomèdica, Universitat de Barcelona, Barcelona 08028, Spain;* orcid.org/0000-0002-1482-1972

Xiaoting Yu − *Catalonia Institute for Energy Research - IREC, Sant Adrià del Besòs, Barcelona 08930, Spain; Departament d'Enginyeria Electrònica i Biomèdica, Universitat de Barcelona, Barcelona 08028, Spain;* orcid.org/0000-0003-0457-4047

Ruifeng Du − *Catalonia Institute for Energy Research - IREC, Sant Adrià del Besòs, Barcelona 08930, Spain; Departament d'Enginyeria Electrònica i Biomèdica, Universitat de Barcelona, Barcelona 08028, Spain*

Ting Zhang − *Catalan Institute of Nanoscience and Nanotechnology (ICN2), CSIC and BIST, Campus UAB, Bellaterra, 08193 Barcelona, Spain*

Xiang Wang − *Catalonia Institute for Energy Research - IREC, Sant Adrià del Besòs, Barcelona 08930, Spain; Departament d'Enginyeria Electrònica i Biomèdica, Universitat de Barcelona, Barcelona 08028, Spain*

Jordi Arbiol − *Catalan Institute of Nanoscience and Nanotechnology (ICN2), CSIC and BIST, Campus UAB, Bellaterra, 08193 Barcelona, Spain; ICREA, Pg. Lluís Companys 23, 08010 Barcelona, Spain;* orcid.org/0000-0002-0695-1726

Jordi Llorca − *Institute of Energy Technologies, Department of Chemical Engineering and Barcelona Research Center in Multiscale Science and Engineering, Universitat Politècnica de Catalunya, EEBE, 08019 Barcelona, Spain;* orcid.org/0000-0002-7447-9582

Complete contact information is available at: https://pubs.acs.org/10.1021/acs.chemmater.9b05241

Notes

The authors declare no competing financial interest.

■ ACKNOWLEDGMENTS

This work was supported by the European Regional Development Funds and by the Spanish Ministerio de Economía y Competitividad through the projects SEHTOP, ENE2016-77798-C4-3-R, and ENE2017-85087-C3. Y.Z. thanks the China Scholarship Council for the scholarship support (no. 201606500001). The authors acknowledge funding from Generalitat de Catalunya 2017 SGR 327 and 2017 SGR 1246. ICN2 acknowledges support from the Severo Ochoa Programme (MINECO, grant no. SEV-2017-0706) and is funded by the CERCA Programme/Generalitat de Catalunya. J. Llorca is a Serra Húnter Fellow and is grateful to ICREA Academia program and to MINECO/FEDER grant RTI2018-093996-B-C31 and GC 2017 SGR 128. Part of the present work has been performed in the framework of Universitat Autònoma de Barcelona Materials Science Ph.D. program. T.Z. has received funding from the CSC-UAB PhD scholarship program.

■ REFERENCES

(1) McCarthy, C. L.; Webber, D. H.; Schueller, E. C.; Brutchey, R. L. Solution-Phase Conversion of Bulk Metal Oxides to Metal Chalcogenides Using a Simple Thiol-Amine Solvent Mixture. *Angew. Chemie - Int. Ed.* 2015, *54*, 8378−8381.

(2) Vayssieres, L.; Beermann, N.; Lindquist, S. E.; Hagfeldt, A. Controlled Aqueous Chemical Growth of Oriented Three-Dimensional Crystalline Nanorod Arrays: Application to Iron(III) Oxides. *Chem. Mater.* **2001**, *13*, 233−235.

(3) McCarthy, C. L.; Brutchey, R. L. Preparation of Electrocatalysts Using a Thiol-Amine Solution Processing Method. *Dalton Trans.* **2018**, *47*, 5137−5143.

(4) Mitzi, D. B. *Solution Processing of Inorganic Materials*; John Wiley & Sons: Hoboken, NJ, 2009.

(5) Li, J.; Luo, Z.; Zuo, Y.; Liu, J.; Zhang, T.; Tang, P.; Arbiol, J.; Llorca, J.; Cabot, A. NiSn Bimetallic Nanoparticles as Stable Electrocatalysts for Methanol Oxidation Reaction. *Appl. Catal., B* **2018**, *234*, 10−18.

(6) Li, J.; Zuo, Y.; Liu, J.; Wang, X.; Yu, X.; Du, R.; Zhang, T.; Infante-Carrió, M. F.; Tang, P.; Arbiol, J.; Llorca, J.; Luo, Z.; Cabot, A. Superior methanol electrooxidation performance of (110)-faceted

nickel polyhedral nanocrystals. *J. Mater. Chem. A* **2019**, *7*, 22036−22043.
(7) Li, Y.; Meng, J.; Yu, Z.; Li, Y. PdS-Modified CdS/NiS Composite as an Efficient Photocatalyst for H_2 evolution in Visible Light. *Catal. Today* **2014**, *225*, 136−141.
(8) Liu, Y.; Kang, H.; Jiao, L.; Chen, C.; Cao, K.; Wang, Y.; Yuan, H. Exfoliated-SnS_2 Restacked on Graphene as a High-Capacity, High-Rate, and Long-Cycle Life Anode for Sodium Ion Batteries. *Nanoscale* **2015**, *7*, 1325−1332.
(9) Zuo, Y.; Ni, J.; Song, J.; Niu, H.; Mao, C.; Zhang, S.; Shen, Y. Synthesis of Co_3O_4/NiO nanofilms and their enhanced electrochemical performance for supercapacitor application. *Appl. Surf. Sci.* **2016**, *370*, 528−535.
(10) Li, J.; Luo, Z.; He, F.; Zuo, Y.; Zhang, C.; Liu, J.; Yu, X.; Du, R.; Zhang, T.; Infante-Carrió, M. F.; Tang, P.; Arbiol, J.; Llorca, J.; Cabot, A. Colloidal Ni-Co-Sn nanoparticles as efficient electrocatalysts for the methanol oxidation reaction. *J. Mater. Chem. A* **2018**, *6*, 22915−22924.
(11) Chlistunoff, J.; Sansiñena, J. M. On the Use of Nafion® in Electrochemical Studies of Carbon Supported Oxygen Reduction Catalysts in Aqueous Media. *J. Electroanal. Chem.* **2016**, *780*, 134−146.
(12) Mitzi, D. B.; Kosbar, L. L.; Murray, C. E.; Copel, M.; Afzali, A. High-Mobility Ultrathin Semiconducting Films Prepared by Spin Coating. *Nature* **2004**, *428*, 299−303.
(13) Mitzi, D. B. Synthesis, Structure, and Thermal Properties of Soluble Hydrazinium Germanium(IV) and Tin(IV) Selenide Salts. *Inorg. Chem.* **2005**, *44*, 3755−3765.
(14) Mitzi, D. B. $N_4H_9Cu_7S_4$: A Hydrazinium-Based Salt with a Layered Cu_7S_4- Framework. *Inorg. Chem.* **2007**, *46*, 926−931.
(15) Mitzi, D. B.; Copel, M.; Chey, S. J. Low-Voltage Transistor Employing a High-Mobility Spin-Coated Chalcogenide Semiconductor. *Adv. Mater.* **2005**, *17*, 1285−1289.
(16) Mitzi, D. B. Polymorphic One-Dimensional $(N_2H_4)_2ZnTe$: Soluble Precursors for the Formation of Hexagonal or Cubic Zinc Telluride. *Inorg. Chem.* **2005**, *44*, 7078−7086.
(17) Mitzi, D. B.; Copel, M.; Murray, C. E. High-Mobility p-Type Transistor Based on a Spin-Coated Metal Telluride Semiconductor. *Adv. Mater.* **2006**, *18*, 2448−2452.
(18) Milliron, D. J.; Raoux, S.; Shelby, R. M.; Jordan-Sweet, J. Solution-Phase Deposition and Nanopatterning of GeSbSe Phase-Change Materials. *Nat. Mater.* **2007**, *6*, 352−356.
(19) Milliron, D. J.; Mitzi, D. B.; Copel, M.; Murray, C. E. Solution-Processed Metal Chalcogenide Films for p-Type Transistors. *Chem. Mater.* **2006**, *18*, 587−590.
(20) McCarthy, C. L.; Brutchey, R. L. Solution Processing of Chalcogenide Materials Using Thiol-Amine "Alkahest" Solvent Systems. *Chem. Commun.* **2017**, *53*, 4888−4902.
(21) Webber, D. H.; Brutchey, R. L. Alkahest for V_2VI_3 Chalcogenides: Dissolution of Nine Bulk Semiconductors in a Diamine-Dithiol Solvent Mixture. *J. Am. Chem. Soc.* **2013**, *135*, 15722−15725.
(22) Vineyard, B. D. Versatility and the Mechanism of the N-Butyl-Amine-Catalyzed Reaction of Thiols with Sulfur. *J. Org. Chem.* **1967**, *32*, 3833−3836.
(23) Lin, Z.; He, Q.; Yin, A.; Xu, Y.; Wang, C.; Ding, M.; Cheng, H. C.; Papandrea, B.; Huang, Y.; Duan, X. Cosolvent Approach for Solution-Processable Electronic Thin Films. *ACS Nano* **2015**, *9*, 4398−4405.
(24) Zhao, X.; Zhang, R.; Handwerker, C.; Agrawal, R. The Potential of Amine-Thiol Based Solution Processing for Chalcogenide Photovoltaics. In *2016 IEEE 43rd Photovoltaic Specialists Conference (PVSC)*; IEEE, 2016; pp 0542−0544.
(25) Agrawal, R.; Zhang, R.; Walker, B. C.; Handwerker, C. Homogeneous Precursor Formation Method and Device Thereof. US 9738799 B2, Aug 12, 2015.
(26) Zhang, R.; Cho, S.; Lim, D. G.; Hu, X.; Stach, E. A.; Handwerker, C. A.; Agrawal, R. Metal−Metal Chalcogenide Molecular Precursors to Binary, Ternary, and Quaternary Metal Chalcogenide Thin Films for Electronic Devices. *Chem. Commun.* **2016**, *52*, 5007−5010.
(27) McCarthy, C. L.; Brutchey, R. L. Solution Processing of Chalcogenide Materials Using Thiol-Amine "Alkahest" Solvent Systems. *Chem. Commun.* **2017**, *53*, 4888−4902.
(28) Lei, Y. M.; Zhou, J.; Chai, Y. Q.; Zhuo, Y.; Yuan, R. SnS_2 Quantum Dots as New Emitters with Strong Electrochemiluminescence for Ultrasensitive Antibody Detection. *Anal. Chem.* **2018**, *90*, 12270−12277.
(29) Giri, B.; Masroor, M.; Yan, T.; Kushnir, K.; Carl, A. D.; Doiron, C.; Zhang, H.; Zhao, Y.; McClelland, A.; Tompsett, G. A.; Wang, D. W.; Grimm, R. L.; Titova, L. V.; Rao, P. M. Balancing Light Absorption and Charge Transport in Vertical SnS_2 Nanoflake Photoanodes with Stepped Layers and Large Intrinsic Mobility. *Adv. Energy Mater.* **2019**, *9*, 1901236.
(30) Meng, L.; Wang, S.; Cao, F.; Tian, W.; Long, R.; Li, L. Doping-Induced Amorphization, Vacancy, and Gradient Energy Band in SnS_2 Nanosheet Arrays for Improved Photoelectrochemical Water Splitting. *Angew. Chemie - Int. Ed.* 2019, *58*, 6761−6765.
(31) Du, Y.; Yin, Z.; Rui, X.; Zeng, Z.; Wu, X. J.; Liu, J.; Zhu, Y.; Zhu, J.; Huang, X.; Yan, Q.; Zhang, H. A Facile, Relative Green, and Inexpensive Synthetic Approach toward Large-Scale Production of SnS_2 nanoplates for High-Performance Lithium-Ion Batteries. *Nanoscale* **2013**, *5*, 1456−1459.
(32) Zhang, Y.; Lu, J.; Shen, S.; Xu, H.; Wang, Q. Ultralarge Single Crystal SnS Rectangular Nanosheets. *Chem. Commun.* **2011**, *47*, 5226−5228.
(33) Yin, D.; Liu, Y.; Dun, C.; Carroll, D. L.; Swihart, M. T. Controllable Colloidal Synthesis of Anisotropic Tin Dichalcogenide Nanocrystals for Thin Film Thermoelectrics. *Nanoscale* **2018**, *10*, 2533−2541.
(34) Chakrabarti, A.; Lu, J.; McNamara, A. M.; Kuta, L. M.; Stanley, S. M.; Xiao, Z.; Maguire, J. A.; Hosmane, N. S. Tin(IV) Sulfide: Novel Nanocrystalline Morphologies. *Inorg. Chim. Acta* **2011**, *374*, 627−631.
(35) Zhang, Y. C.; Du, Z. N.; Li, S. Y.; Zhang, M. Novel Synthesis and High Visible Light Photocatalytic Activity of SnS_2 Nanoflakes from $SnCl_2{\cdot}2H_2O$ and S Powders. *Appl. Catal., B* **2010**, *95*, 153−159.
(36) Sun, Y.; Cheng, H.; Gao, S.; Sun, Z.; Liu, Q.; Liu, Q.; Lei, F.; Yao, T.; He, J.; Wei, S.; Xie, Y. Freestanding Tin Disulfide Single-Layers Realizing Efficient Visible-Light Water Splitting. *Angew. Chemie Int. Ed.* 2012, *51*, 8727−8731.
(37) Chen, H.; Chen, Y.; Zhang, H.; Zhang, D. W.; Zhou, P.; Huang, J. Suspended SnS_2 Layers by Light Assistance for Ultrasensitive Ammonia Detection at Room Temperature. *Adv. Funct. Mater.* **2018**, *28*, 1801035.
(38) Ying, H.; Li, X.; Wu, Y.; Yao, Y.; Xi, J.; Su, W.; Jin, C.; Xu, M.; He, Z.; Zhang, Q. High-Performance Ultra-Violet Phototransistors Based on CVT-Grown High Quality SnS_2 Flakes. *Nanoscale Adv.* **2019**, *1*, 3973−3979.
(39) Shao, G.; Xue, X. X.; Zhou, X.; Xu, J.; Jin, Y.; Qi, S.; Liu, N.; Duan, H.; Wang, S.; Li, S.; Ouzounian, M.; Hu, T. S.; Luo, J.; Liu, S.; Feng, Y. Shape-Engineered Synthesis of Atomically Thin 1T-SnS_2 Catalyzed by Potassium Halides. *ACS Nano* **2019**, *13*, 8265−8274.
(40) Xu, L.; Zhang, P.; Jiang, H.; Wang, X.; Chen, F.; Hu, Z.; Gong, Y.; Shang, L.; Zhang, J.; Jiang, K.; Chu, J. H. Large-Scale Growth and Field-Effect Transistors Electrical Engineering of Atomic-Layer SnS_2. *Small* **2019**, *15*, 1904116.
(41) Mattinen, M.; King, P. J.; Khriachtchev, L.; Meinander, K.; Gibbon, J. T.; Dhanak, V. R.; Räisänen, J.; Ritala, M.; Leskelä, M. Low-Temperature Wafer-Scale Deposition of Continuous 2D SnS_2 Films. *Small* **2018**, *14*, 1800547.
(42) Buckley, J. J.; McCarthy, C. L.; Del Pilar-Albaladejo, J.; Rasul, G.; Brutchey, R. L. Dissolution of Sn, SnO, and SnS in a Thiol-Amine Solvent Mixture: Insights into the Identity of the Molecular Solutes for Solution-Processed SnS. *Inorg. Chem.* **2016**, *55*, 3175−3180.
(43) Thomson, J. W.; Nagashima, K.; Macdonald, P. M.; Ozin, G. A. From Sulfur−Amine Solutions to Metal Sulfide Nanocrystals: Peering into the Oleylamine-Sulfur Black Box. *J. Am. Chem. Soc.* **2011**, *133*, 5036−5041.

https://dx.doi.org/10.1021/acs.chemmater.9b05241
Chem. Mater. 2020, 32, 2097−2106

(44) Kim, E. T.; Chung, W. J.; Lim, J.; Johe, P.; Glass, R. S.; Pyun, J.; Char, K. One-Pot Synthesis of PbS NP/Sulfur-Oleylamine Copolymer Nanocomposites via the Copolymerization of Elemental Sulfur with Oleylamine. *Polym. Chem.* **2014**, *5*, 3617−3623.
(45) Ye, G.; Gong, Y.; Lei, S.; He, Y.; Li, B.; Zhang, X.; Jin, Z.; Dong, L.; Lou, J.; Vajtai, R.; Zhou, W.; Ajayan, P. M. Synthesis of Large-Scale Atomic-Layer SnS_2 through Chemical Vapor Deposition. *Nano Res.* **2017**, *10*, 2386−2394.
(46) Mukhokosi, E. P.; Krupanidhi, S. B.; Nanda, K. K. Band Gap Engineering of Hexagonal $SnSe_2$ Nanostructured Thin Films for InfraRed Photodetection. *Sci. Rep.* **2017**, *7*, 15215.
(47) Yu, J.; Xu, C. Y.; Ma, F. X.; Hu, S. P.; Zhang, Y. W.; Zhen, L. Monodisperse SnS_2 Nanosheets for High-Performance Photocatalytic Hydrogen Generation. *ACS Appl. Mater. Interfaces* **2014**, *6*, 22370−22377.
(48) Liu, Y.; Chen, P.; Chen, Y.; Lu, H.; Wang, J.; Yang, Z.; Lu, Z.; Li, M.; Fang, L. In Situ Ion-Exchange Synthesis of SnS_2/g-C_3N_4 Nanosheets Heterojunction for Enhancing Photocatalytic Activity. *RSC Adv.* **2016**, *6*, 10802−10809.
(49) Meng, H.; Wang, T.; Yu, X.; Zhu, Y.; Zhang, Y. BiOCl/SnS_2 Hollow Spheres for the Photocatalytic Degradation of Waste Water. *RSC Adv.* **2015**, *5*, 107088−107097.
(50) Liu, Y.; Geng, P.; Wang, J.; Yang, Z.; Lu, H.; Hai, J.; Lu, Z.; Fan, D.; Li, M. In-Situ Ion-Exchange Synthesis Ag_2S Modified SnS_2 Nanosheets toward Highly Photocurrent Response and Photocatalytic Activity. *J. Colloid Interface Sci.* **2018**, *512*, 784−791.
(51) Wang, L.; Jin, G.; Shi, Y.; Zhang, H.; Xie, H.; Yang, B.; Sun, H. Co-Catalyst-Free ZnS-SnS_2 porous Nanosheets for Clean and Recyclable Photocatalytic H_2 generation. *J. Alloys Compd.* **2018**, *753*, 60−67.
(52) Zuo, Y.; Liu, Y.; Li, J.; Du, R.; Yu, X.; Xing, C.; Zhang, T.; Yao, L.; Arbiol, J.; Llorca, J.; Sivula, K.; Guijarro, N.; Cabot, A. Solution-Processed Ultrathin SnS_2-Pt Nanoplates for Photoelectrochemical Water Oxidation. *ACS Appl. Mater. Interfaces* **2019**, *11*, 6918−6926.
(53) Huang, H. H.; De Silva, K. K. H.; Kumara, G. R. A.; Yoshimura, M. Structural Evolution of Hydrothermally Derived Reduced Graphene Oxide. *Sci. Rep.* **2018**, *8*, 6849.
(54) Li, X.; Hao, Z.; Zhang, F.; Li, H. Reduced Graphene Oxide-Immobilized Tris(bipyridine)ruthenium(II) Complex for Efficient Visible-Light-Driven Reductive Dehalogenation Reaction. *ACS Appl. Mater. Interfaces* **2016**, *8*, 12141−12148.
(55) McCarthy, C. L.; Downes, C. A.; Schueller, E. C.; Abuyen, K.; Brutchey, R. L. Method for the Solution Deposition of Phase-Pure $CoSe_2$ as an Efficient Hydrogen Evolution Reaction Electrocatalyst. *ACS Energy Lett.* **2016**, *1*, 607−611.
(56) Fu, X.; Ilanchezhiyan, P.; Mohan Kumar, G.; Cho, H. D.; Zhang, L.; Chan, A. S.; Lee, D. J.; Panin, G. N.; Kang, T. W. Tunable UV-Visible Absorption of SnS_2 Layered Quantum Dots Produced by Liquid Phase Exfoliation. *Nanoscale* **2017**, *9*, 1820−1826.
(57) Lee, K. T.; Liang, Y. C.; Lin, H. H.; Li, C. H.; Lu, S. Y. Exfoliated SnS_2 Nanoplates for Enhancing Direct Electrochemical Glucose Sensing. *Electrochim. Acta* **2016**, *219*, 241−250.
(58) Huang, Y.; Sutter, E.; Sadowski, J. T.; Cotlet, M.; Monti, O. L. A.; Racke, D. A.; Neupane, M. R.; Wickramaratne, D.; Lake, R. K.; Parkinson, B. A.; Sutter, P. Tin Disulfide-an Emerging Layered Metal Dichalcogenide Semiconductor: Materials Properties and Device Characteristics. *ACS Nano* **2014**, *8*, 10743−10755.
(59) Jiang, Y.; Wei, M.; Feng, J.; Ma, Y.; Xiong, S. Enhancing the Cycling Stability of Na-Ion Batteries by Bonding SnS_2 Ultrafine Nanocrystals on Amino-Functionalized Graphene Hybrid Nanosheets. *Energy Environ. Sci.* **2016**, *9*, 1430−1438.
(60) Li, X.; Sun, X.; Gao, Z.; Hu, X.; Ling, R.; Cai, S.; Zheng, C.; Hu, W. A Simple One-Pot Strategy for Synthesizing Ultrafine SnS_2 Nanoparticle/Graphene Composites as Anodes for Lithium/Sodium-Ion Batteries. *ChemSusChem* **2018**, *11*, 1549−1557.
(61) Yang, Z.; Zhang, P.; Wang, J.; Yan, Y.; Yu, Y.; Wang, Q.; Liu, M. Hierarchical Carbon@SnS_2 Aerogel with "Skeleton/Skin" Architectures as a High-Capacity, High-Rate Capability and Long Cycle Life Anode for Sodium Ion Storage. *ACS Appl. Mater. Interfaces* **2018**, *10*, 37434−37444.
(62) Kovtyukhova, N. I.; Ollivier, P. J.; Martin, B. R.; Mallouk, T. E.; Chizhik, S. A.; Buzaneva, E. V.; Gorchinskiy, A. D.; et al. Layer-by-Layer Assembly of Ultrathin Composite Films from Micron-Sized Graphite Oxide Sheets and Polycations. *Chem. Mater.* **1999**, *11*, 771−778.

https://dx.doi.org/10.1021/acs.chemmater.9b05241
Chem. Mater. 2020, 32, 2097−2106

Electrochimica Acta 349 (2020) 136369

Contents lists available at ScienceDirect

Electrochimica Acta

journal homepage: www.elsevier.com/locate/electacta

SnS_2/g-C_3N_4/graphite nanocomposites as durable lithium-ion battery anode with high pseudocapacitance contribution

Yong Zuo [a, b, 1], Xijun Xu [c, d, 1], Chaoqi Zhang [a, b], Junshan Li [a, b], Ruifeng Du [a, b], Xiang Wang [a, b], Xu Han [e], Jordi Arbiol [e, f], Jordi Llorca [g], Jun Liu [c, d, *], Andreu Cabot [a, f, **]

[a] Catalonia Institute for Energy Research – IREC, Sant Adrià de Besòs, Barcelona, 08930, Spain
[b] Departament d'Enginyeria Electrònica i Biomèdica, Universitat de Barcelona, 08028, Barcelona, Spain
[c] Guangdong Provincial Key Laboratory of Advanced Energy Storage Materials, School of Materials Science and Engineering, South China University of Technology, Guangzhou, 510641, PR China
[d] State Key Laboratory of Pulp and Paper Engineering, South China University of Technology, Guangzhou, 510641, PR China
[e] Catalan Institute of Nanoscience and Nanotechnology (ICN2), CSIC and BIST, Campus UAB, Bellaterra, 08193, Barcelona, Spain
[f] ICREA, Pg. Lluís Companys 23, 08010, Barcelona, Spain
[g] Institute of Energy Technologies, Department of Chemical Engineering and Barcelona Research Center in Multiscale Science and Engineering, Universitat Politècnica de Catalunya, EEBE, 08019, Barcelona, Spain

ARTICLE INFO

Article history:
Received 28 January 2020
Received in revised form
14 April 2020
Accepted 29 April 2020
Available online 30 April 2020

Keywords:
Nanocomposite
Li-ion battery
Anode
Tin disulfide
Pseudocapacitance

ABSTRACT

Tin disulfide is a promising anode material for Li-ion batteries (LIB) owing to its high theoretical capacity and the abundance of its composing elements. However, bare SnS_2 suffers from low electrical conductivity and large volume expansion, which results in poor rate performance and cycling stability. Herein, we present a solution-based strategy to grow SnS_2 nanostructures within a matrix of porous g-C_3N_4 (CN) and high electrical conductivity graphite plates (GPs). We test the resulting nanocomposite as anode in LIBs. First, SnS_2 nanostructures with different geometries are tested, to find out that thin SnS_2 nanoplates (SnS_2-NPLs) provide the highest performances. Such SnS_2-NPLs, incorporated into hierarchical SnS_2/CN/GP nanocomposites, display excellent rate capabilities (536.5 mA h g^{-1} at 2.0 A g^{-1}) and an outstanding stability (~99.7% retention after 400 cycles), which are partially associated with a high pseudocapacitance contribution (88.8% at 1.0 mV s^{-1}). The excellent electrochemical properties of these nanocomposites are ascribed to the synergy created between the three nanocomposite components: i) thin SnS_2-NPLs provide a large surface for rapid Li-ion intercalation and a proper geometry to stand volume expansions during lithiation/delithiation cycles; ii) porous CN prevents SnS_2-NPLs aggregation, habilitates efficient channels for Li-ion diffusion and buffer stresses associated to SnS_2 volume changes; and iii) conductive GPs allow an efficient charge transport.

© 2020 Elsevier Ltd. All rights reserved.

1. Introduction

Lithium-ion batteries (LIBs) are widely commercialized for portable applications owing to their notable volumetric energy density and their flexible and lightweight design. However, commercial devices suffer from low stability, and their potential energy densities and charging rates are far from those potentially attained by LIBs, which leaves plenty of room for improvement of their design and components, particularly of their anode materials [1–3]. Commercial LIBs use graphite anodes, which provide a modest theoretical energy density, 372 mA h g^{-1} [4,5], and are far away from the requirements of the next generation of high-energy and high-power LIBs [6]. Therefore, alternative anodes based on Si [7,8], Ge [9,10] or Sn [11–13] are being actively developed.

Among the different materials able to intercalate or react with Li^+, sulfides and particularly SnS_2 are especially interesting due to the abundance of its elements and the ability to simultaneously interact with Li^+ through two different bulk mechanisms: Li–S reaction and Sn–Li alloying. SnS_2 anodes have a potential

* Corresponding author. Guangdong Provincial Key Laboratory of Advanced Energy Storage Materials, School of Materials Science and Engineering, South China University of Technology, Guangzhou, 510641, PR China.
** Corresponding author. Catalonia Institute for Energy Research – IREC, Sant Adrià de Besòs, Barcelona, 08930, Spain.
E-mail addresses: msjliu@scut.edu.cn (J. Liu), acabot@irec.cat (A. Cabot).
[1] These authors contributed equally to this work.

https://doi.org/10.1016/j.electacta.2020.136369
0013-4686/© 2020 Elsevier Ltd. All rights reserved.

capacity of 1231 mA h g^{-1} ascribed to the combination of the Li–S reaction ($SnS_2 + 4Li^+ + 4e^- \rightarrow Sn + 2Li_2S$, 586 mA h g^{-1} capacity contribution) [14] and the Sn–Li alloying/dealloying reaction ($Sn + 4.4Li^+ + 4.4e^- \rightarrow Li_{4.4}Sn$, 645 mA h g^{-1} capacity contribution) [15,16]. Besides, oxides and chalcogenides may provide a significant additional energy storage capacity contribution in the form of a rapid surface-related pseudocapacity [3,17,18].

SnS_2 displays a two-dimensional (2D) hexagonal structure with layers of tin atoms sandwiched between two close-packed layers of sulfur atoms. Adjacent sandwiches, separated a distance of 0.59 nm, are hold together by Van der Waals forces [19–21]. This layered structure allows for the effective and fast diffusion of Li^+ (0.076 nm) to interact with Sn and S. However, during charge/discharge processes, SnS_2 suffers from huge volumetric changes in large part related to the expansion/contraction in the c direction, i.e. across the planes, its softer crystallographic direction. This volumetric changes may result in the pulverization and detachment of the material from the current collector [22–24]. Additionally, the low electrical conductivity of SnS_2 provides a poor rate performance. These limitations lead to a deficient cyclability, especially at high current densities [25–28].

To overcome its flaws as anode material in LIBs, SnS_2 needs to be nanostructured [29–32] and combined with high surface area materials, e.g. carbon-based networks, to improve dispersion and simultaneously provide the necessary paths for electrolyte diffusion and electron transport [33–35]. Graphene is considered as one of the best materials for these last roles [25,36], owing to its large surface, extraordinary electrical conductivity, and convenient flexibility that allows accommodating the conductive network to the volume expansion of the active material [37]. Graphene can interact with Li^+ itself, delivering additional storage capacity. To maximize this interaction, graphene can be doped with large concentrations of N atoms which interact more efficiently with Li^+ due to the higher electronegativity of nitrogen compared with carbon [38–40]. In this direction, graphitic carbon nitride (g-C_3N_4, CN) is regarded as the analogue to graphite with the highest level of nitrogen, and thus may provide a significant Li^+ storage capacity [6,41,42]. CN also has a 2D layered structure in which p-conjugated graphitic planes are composed by alternate arrangements of sp2 hybridized carbon and nitrogen atoms [43,44]. Advantageously, CN can be easily produced in a scalable way by the thermal decomposition of urea at moderate temperatures [45,46]. However, such CN is usually characterized by a low electrical conductivity due to an intrinsic porous microstructure [41,47]. Thus a highly conductive material needs to be additionally introduced to provide the necessary paths for electron transport.

Herein, we combine SnS_2 nanostructures with high surface area and porous CN and high electrical conductivity graphite plates (GPs) in hierarchical nanocomposites, and analyze their performance as anode material in LIBs. We initially identify the SnS_2 nanostructure geometry providing better electrochemical performance by producing and testing SnS_2 particles with different shapes. The better performing SnS_2 nanostructure is then combined with porous CN, which we demonstrate is able to improve to some extent the electrode cycling stability. Finally, we analyze the effect of additionally incorporating conductive GP into the mixture to further improve performance.

2. Experimental section

Chemicals: Tin(IV) chloride pentahydrate ($SnCl_4{\cdot}5H_2O$, 98%), sulfur powder (99.8%), tetrahydrofuran (THF, ≥99%), and GP (99% carbon basis, −325 mesh) were purchased from Sigma-Aldrich. 1-octadecene (ODE, 90%) was purchased from Alfa-Aesar. Oleylamine (OAm, 80–90%), oleic acid (OAc, 70%), and urea (99%) were purchased from Acros. Super P, polyvinylidene fluoride (PVDF) and porous polypropylene film (Celgard2400) were purchased from Shenzhen Kejing Star Technology Co. LTD. N-methy1-2-pyrrolidone (NMP, 99%), ethylene carbonate (EC), diethylcarbonate (DEC) and fluoro ethylenecarbonate (FEC) were purchased from Aladdin. Toluene, hexane, isopropanol and ethanol were of analytical grade and obtained from various sources. GPs were cleaned using diluted HCl and ethanol under sonication. All other chemicals were used as received, without additional purification. Aqueous solutions were prepared using Milli-Q water (DW, 18.2 MΩ cm).

Synthesis of SnS_2 nanostructures and SnS_2/CN and SnS_2/CN/GP nanocomposites: Plate- and flower-shaped SnS_2 nanostructures were produced following our recently reported protocol [21]. Briefly, to prepare SnS_2 nanoplates (SnS_2-NPLs), $SnCl_4{\cdot}5H_2O$ (2 mmol), ODE (16 mL), OAc (4 mL), OAm (2 mL) and THF (1 mL) were added into a three-neck round flask (50 mL). The solution was stirred using a magnetic stirring bar and a syringe was inserted into the solution to bubble Ar. The solution was then heated up to 140 °C and kept at this temperature for 1h to remove low boiling-point impurities. Then the obtained brown transparent solution was heated to 220 °C. At this temperature, 4 mL of S-OAm stock solution, prepared by dissolving sulfur powder (4 mmol) into OAm (4 mL) under sonication, were quickly injected into the reaction flask with a syringe. The solution was maintained at 220 °C for 1h after S source injection and afterward quickly cooled down using a cold-water bath. The resulted product was centrifuged at 6000 rpm for 4 min after adding toluene (15 mL), and then washed three times with toluene and ethanol by dispersion-precipitation cycles. The obtained yellow products (~80% yield for SnS_2-NPL) were dried under vacuum for posterior use and characterization.

SnS_2 microflowers (SnS_2-MFL) were prepared in the same way, but replacing OAm with ODE. The S-ODE stock solution was prepared by dissolving sulfur powder (4 mmol) into ODE (4 mL) under Ar at 180 °C in a 25 mL flask.

SnS_2/CN and SnS_2/CN/GP nanocomposites were prepared by adding CN (25 mg) and eventually GP (25 mg) into the reaction mixture containing enough Sn and S precursor to nominally yield 2 mmol SnS_2. The ratio of CN and SnS_2 was selected taking into account previous works [6,35], and the same amount of GP was introduced to compensate for the decreased electrical conductivity upon CN addition. 25 mg of CN corresponded to a nominal concentration of ~8.5 wt% with respect to SnS_2. The precursor solution was initially stirred for 30 min at room temperature to ensure a proper dispersion of the carbon-based materials. The exact same reaction conditions used to prepare unsupported SnS_2 nanostructures were applied to prepare SnS_2/CN and SnS_2/CN/GP nanocomposites.

Synthesis of CN: CN was prepared according to a method reported previously with some modification [45,46]. Briefly, 2 g of urea was placed in a crucible with a loosely closed lid, and heated to 550 °C at a rate of 5 °C/min for 4 h in a tubular furnace with air flow. The obtained light yellow product was collected after cooling down to room temperature and grounded into powder. To hydrolyze the bulk CN in alkaline conditions, 500 mg of as-synthesized powder was mixed with 20 mL of NaOH solution (3 M in DW). The mixture was stirred at 70 °C for 8 h. The obtained hydrolyzed CN was washed using water/ethanol and collected using centrifugation for three times. The product was finally dried under vacuum and stored until further use.

Ligand removal (LR): Native organic ligands were removed from the SnS_2 surface according to previously published reports [48,49]. Briefly, SnS_2 particles were dispersed in a vial containing a solution of 0.8 mL hydrazine and 25 mL acetonitrile. The mixture was then stirred for 4 h at room temperature and subsequently collected by centrifugation. The resulted product was further

washed with acetonitrile and centrifuged at 2000 rpm for additional 2 times. Ligand-removed products were collected and stored in Ar atmosphere after drying under vacuum at room temperature.

Sample characterization: Powder X-ray diffraction (XRD) patterns were obtained on a Bruker AXS D8 ADVANCE X-ray diffractometer operating at 40 kV and 40 mA with Ni-filtered (2 μm thickness) Cu Kα1 radiation (λ = 1.5406 Å). X-ray photoelectron spectroscopy (XPS) was carried out on a SPECS system equipped with an Al anode XR50 source operating at 150 W and a Phoibos 150 MCD-9 detector. The pressure in the analysis chamber was kept below 10^{-7} Pa. Data processing was performed with the CasaXPS program. Binding energy (BE) values were centered by using the C 1s peak at 284.8 eV. SEM analysis was carried out in a ZEISS Auriga microscope with an energy dispersive X-ray spectroscopy (EDX) detector at 20 kV to study composition. Transmission electron microscopy (TEM) characterization was carried out on a ZEISS LIBRA 120, operating at 120 kV. High-resolution TEM (HRTEM) images were obtained using a field emission gun FEI Tecnai F20 microscope at 200 kV with a point-to-point resolution of 0.19 nm. High angle annular dark-field (HAADF) STEM was combined with electron energy loss spectroscopy (EELS) in the Tecnai microscope by using a GATAN QUANTUM filter. For TEM characterization, samples were prepared by drop casting a dispersion containing the material on a 200 mesh copper grid. Thermogravimetric (TG) analyses were performed using a PerkinElmer Diamond TG/DTA instrument. Samples were measured in air at a heating rate of 5 °C/min from ambient temperature to 800 °C. Fourier transform infrared spectroscopy (FTIR) was performed on an Alpha Bruker FTIR spectrometer with a platinum attenuated total reflectance (ATR) single reflection module. FTIR data were typically averaged over 24 scans.

Electrochemical measurements: To evaluate the electrochemical performance of the materials, 80 wt% of sample, 10 wt% Super P, and 10 wt% PVDF were mixed together in an appropriate amount of NMP to form a homogenous slurry. Subsequently, the resultant flowing slurry was coated on Cu foil and dried in a vacuum oven at 80 °C for 24 h. The foil was then cut into disks with a diameter of 12 mm. The mass of active material was estimated to be *ca.* 1.0 mg/cm^2. To test the performance of obtained electrodes, half cells were constructed in an argon-filled glove-box (H_2O and O_2 < 0.1 ppm) using Celgard2400 as separator, and $LiPF_6$ solution (1 M) in EC/DEC (1:1 vol) with 5 wt% FEC as the electrolyte. Galvanostatic charge-discharge curves of the assembled cells were measured at different current densities in the voltage range of 0.01–3.0 V versus Li^+/Li on a battery test system (CT2001A, LAND). Cyclic voltammetry (CV) measurements were respectively performed with an electrochemical workstation (Gamry Interface 1000) in the voltage range from 0.01 to 3.0 V and the scan rate from 0.1 to 1 mV s^{-1}. Electrochemical impedance spectroscopy (EIS) tests were performed in a scanning frequency range from 100 kHz to 10 mHz using a sinusoidal voltage with amplitude of 5 mV.

3. Results and discussion

Fig. 1 shows electron microscopy micrographs of SnS_2 nsnostructures, CN and GP. Following the above detailed procedure, SnS_2-NPLs with ~200 nm in diameter and ~10 nm thickness, and ~1 μm SnS_2-MFLs were produced (Fig. 1a and b) [21]. CN showed a graphene-like flexible morphology with high porosity (Fig. 1c and inset) and GP was characterized by a surface-smooth thick plate morphology (Fig. 1d). Fig. 1e shows a SEM micrograph of a SnS_2-NPL/CN/GP nanocomposite formed by growing SnS_2-NPLs in the presence of CN and GP. Notice that the morphology of CN and GP was not modified during the synthesis process, although their particle size was slightly reduced as they were probably fragmented during agitation. Besides, the presence of CN and GP in the reaction mixture did not significantly change the size and morphology of the obtained SnS_2-NPLs. Additional SEM micrographs of SnS_2/CN and SnS_2/CN/GP nanocomposites obtained from SnS_2-NPLs and SnS_2-MFLs can be found in Fig. S1, demonstrating the presence of SnS_2 in all the nanocomposites.

Fig. 1f shows the XRD patterns of SnS_2-NPLs, SnS_2-MFLs, CN and GP. XRD patterns of the SnS_2/CN/GP composites can be found on Fig. S2a. XRD patterns of GP and CN displayed two characteristic peaks, corresponding to the (002) and (004) crystallographic planes for GP and the (100) and (002) for CN. The XRD pattern of SnS_2 could be indexed with the hexagonal berndtite SnS_2 structure (JCPDS# 23–0677). The high intensity ratio between (001) and (101) XRD peaks for SnS_2-NPL in comparison with SnS_2-MFL, pointed at the highly asymmetric morphology of SnS_2-NPL with largely exposed {001} facets. The XRD pattern of SnS_2/CN/GP was also indexed with the berndtite SnS_2 structure, with the two additional peaks of GP. The diffraction peaks of CN were not visible in the XRD pattern of SnS_2/CN/GP because of their low intensity and their partial overlap with those of SnS_2. HRTEM micrographs (Fig. S2b) confirmed the hexagonal structure of SnS_2 NPLs (space group = P-3M1).

Fig. 2a displays SEM-EDX maps of the different elements within SnS_2/CN/GP, showing a homogenous distribution of the different components within the composite. EDX analysis systematically showed the SnS_2 composition to be slightly sulfur rich, with an average elemental ratio of S/Sn = 2.06 (Fig. S3). Nevertheless, the measured differences with respect to the stoichiometric ratio were within the experimental error of the technique. EELS elemental maps revealed a homogenous distribution of N at the nanometer level, proving CN nanosheets to ubiquitously support/wrap SnS_2 nanostructures (Fig. 2b).

The bulk content of CN, GP and SnS_2 within SnS_2/CN/GP composites was measured using TGA (Fig. S4). Upon heating the sample up to 800 °C in the presence of oxygen, the composite displayed a total weight loss of 34%. This weight loss was ascribed to the oxidative dissociation of GP and CN, the oxidation of SnS_2 to SnO_2 and the removal of surface ligands [50]. TGA of SnS_2-NPLs provided a final mass of SnO_2 of a 77% with respect to the initial amount of material analyzed, which corresponded to an initial content of SnS_2 in the SnS_2-NPLs sample of 93.4%. We hypothesize the remaining 6.6 wt% to be associated with surface organic ligands. From the weight decrease measured in SnS_2/CN/GP composites (66% SnO_2 remaining, which corresponds to 80.1% initial SnS_2), and assuming the same ratio of organic ligands as in SnS_2-NPLs, the total amount of CN and GP with respect to SnS_2 was estimated at a 17.7% (14.2 wt%/80.1 wt%), which was close to the nominal 17.1% [50 mg/(183*2*80%) mg].

SnS_2/CN/GP nanocomposites were treated with a mixture of hydrazine and acetonitrile to remove the surface ligands from the final composites (see Experimental section for details) [48,49]. FTIR analyses confirmed the successful ligand removal from the material (Fig. S5). XPS analysis of SnS_2-based composites after hydrazine treatment showed the surface of the final material to be partially reduced (Fig. 3). Two chemical environments were clearly visible in the Sn 3d XPS spectrum (Fig. 3a) of the SnS_2/CN/GP composites. The first doublet (Sn $3d_{5/2}$ at 487.1 eV) was associated with Sn^{4+} [51,52], and the second doublet (Sn $3d_{5/2}$ at 485.8 eV) with Sn^{2+} [53,54]. From the peak intensities, we estimated the ratio of the two chemical states to be ca. Sn^{2+}/Sn^{4+} = 0.3. Similarly, the XPS spectrum of the S 2p region (Fig. 3b) of the SnS_2/CN/GP composites was fitted with two doubles. The first was located at 162.1 eV (S $2p_{3/2}$) and 163.3 eV (S $2p_{1/2}$), and it was associated with S^{2-} in the SnS_2 lattice [51,52,55]. A second S 2p doublet was fitted at 160.7 eV (S $2p_{3/2}$) and 161.8 eV (S $2p_{1/2}$), and it was associated with S^{2-} within

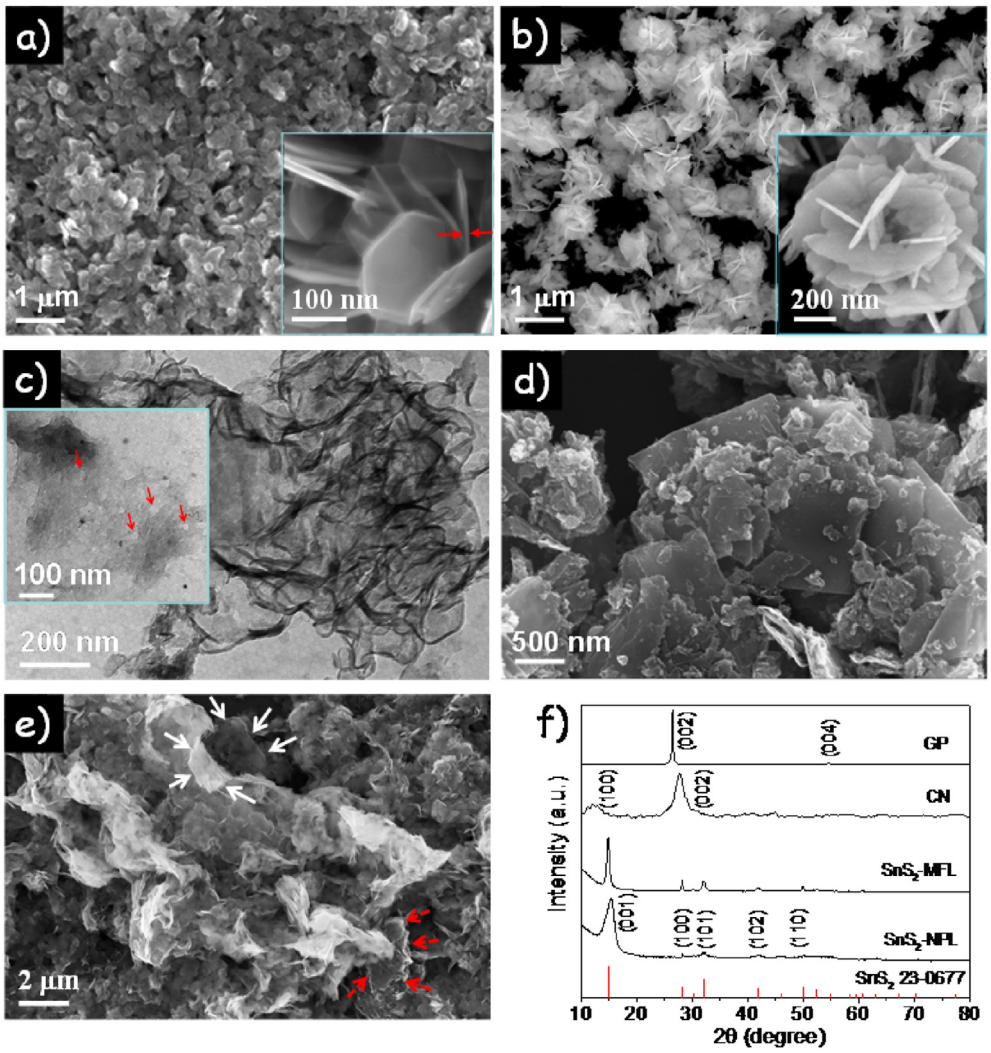

Fig. 1. a) SEM micrograph of SnS_2-NPLs. b) SEM micrograph of SnS_2-MFLs. c) TEM micrograph of CN. In the inset, arrows point out at the presence of pores/holes. d) SEM micrograph of GP. e) SEM micrograph of a SnS_2-NPL/CN/GP composite. White arrows point at a CN structure. Red arrows point atGPs. f) XRD pattern of SnS_2-NPLs, SnS_2-MFLs, CN and GP. (For interpretation of the references to colour in this figure legend, the reader is referred to the Web version of this article.)

SnS [53,54]. As measured by XPS, the surface ratio $SnS/SnS_2 = 0.4$. The N 1s spectrum of SnS_2/CN/GP (Fig. 3c) showed three peaks at BEs of 398.2 eV, 399.2 eV and 401.0 eV, which were assigned to N-(C—N═C), tertiary nitrogen N-(C)3 group and C—N—H of CN, respectively [56,57]. Finally, the C 1s spectrum (Fig. 3d) showed 2 to 3 characteristic peaks corresponding to carbon within CN and graphitic carbon [58]. No clear evidence of chemical bonding between CN, GP and SnS_2 could be obtained by XPS.

The electrochemical behavior of SnS_2-based LIB anodes was initially investigated using CV with a scan rate of 0.1 mV s^{-1} in the voltage window 0.01–3.0 V vs. Li^+/Li. To determine the best performing SnS_2 nanostructure geometry, SnS_2-NPL and SnS_2-MFL were initially compared. Fig. 4a shows results obtained from a SnS_2-NPL electrode. The first sweep displayed three clear cathodic current peaks at ~1.8 V, ~1.1 V and ~0.15 V. The peak at ~1.8 V disappeared in the following cycles, and it was assigned to lithium insertion in the layered SnS_2 without phase decomposition (equation (1)) [52,59,60]. The strong peak at ~1.1 V was attributed to the decomposition of SnS_2 (equation (2)), the formation of Li_2S and Sn metal (equation (3)), and the growth of the solid electrolyte interface (SEI) layer [52,61,62]. The intensity of this peak decreased and was shifted to ~1.3 V in subsequent cycles [52,63]. The cathodic peak at ~0.15 V corresponded to the reaction between metallic Sn and Li^+ (equation (4)) [61,63]. Anodic peaks at ~0.5 V, ~1.25 V, and ~1.8 V were related to the dealloying reaction of $Li_{4.4}Sn$ to metallic Sn, the partial deinsertion reaction of Li^+ from Li_xSnS_2 to form SnS_2, and the oxidation of metallic Sn to SnS_2, respectively [22,64–66]. In addition, the anodic peak at ~2.35 V was assigned to the transformation of unreacted Li_2S to polysulfides [67,68]. Very similar CV profiles were obtained for SnS_2-MFL anodes (Fig. 4b). The aforementioned electrochemical reactions between SnS_2 and lithium ions during charge-discharge processes are outlined as follows:

$$SnS_2 + xLi^+ + xe^- \rightarrow Li_xSnS_2 \quad (1)$$

$$Li_xSnS_2 + (4-x)Li^+ + (4-x)e^- \rightarrow 2Li_2S + Sn \quad (2)$$

$$SnS_2 + 4Li^+ + 4e^- \rightarrow Sn + 2Li_2S \quad (3)$$

$$Sn + 4.4Li^+ + 4.4e^- \rightarrow Li_{4.4}Sn \quad (4)$$

Galvanostatic charge-discharge curves of the SnS_2-NPL and SnS_2-MFL electrodes were performed in the voltage range of

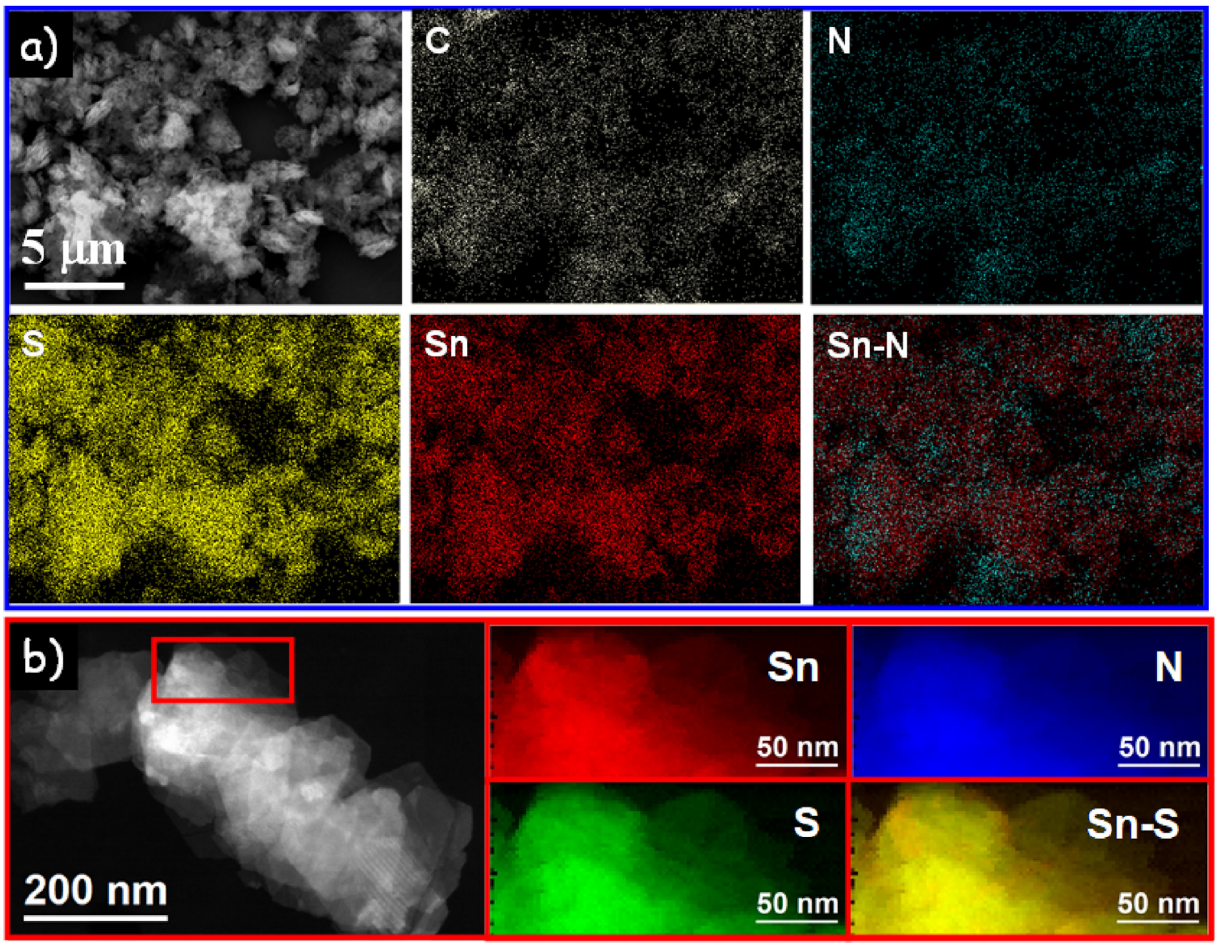

Fig. 2. a) SEM micrograph and EDX elemental maps of a SnS_2/CN/GP composite. b) STEM micrograph of a SnS_2/CN/GP composite and EELS chemical composition maps obtained from the red squared area in the STEM micrograph. (For interpretation of the references to colour in this figure legend, the reader is referred to the Web version of this article.)

0.01–3.0 V *vs.* Li^+/Li at a current density of 0.1 A g^{-1} (Fig. 4c and d). Similar profiles were obtained for SnS_2-based electrodes with different particle geometries. The initial irreversible capacity loss was mainly associated with the decomposition of electrolyte on the surface of active particles to form the SEI layer among other possible irreversible processes (Fig. 4c and d) [69,70].

As shown in Fig. 5, SnS_2-NPL electrodes provided significantly better rate capacity performance than SnS_2-MFL, with a lower loss of reversible capacity as the current density increased. SnS_2-NPL electrodes delivered a capacity of ~380 mA h g^{-1} after increasing a 50 fold the current density, from 0.1 A g^{-1} to 5.0 A g^{-1}, ~59% of the initial capacity was recovered when the current density decreased back to 0.1 A g^{-1}. By contrast, SnS_2-MFL electrodes delivered a lower capacity of only ~70 mA h g^{-1} and ~17% recovery. These results pointed at SnS_2-NPL as the best SnS_2 nanostructure geometry to be used as LIB anode material. Therefore, additional work was carried out using SnS_2-NPLs.

Fig. S6a,b displays CV data obtained from electrodes based on SnS_2/CN and SnS_2/CN/GP nanocomposites. The first CV cycle of SnS_2/CN and SnS_2/CN/GP electrodes displayed similar CV profiles as those obtained for SnS_2 electrodes, except that SnS_2/CN/GP electrodes showed stronger intensity peaks related to conversion and alloying reactions, indicating a better cycling performance. Figs. S6c and d shows the galvanostatic charge-discharge performance of electrodes based on SnS_2/CN and SnS_2/CN/GP in the voltage range of 0.01–3.0 V *vs.* Li^+/Li at a current density of 0.1 A g^{-1} (Figs. S6c and d). The initial irreversible capacity loss can be ascribed to the formation of the SEI layer [69,70].

The rate performance, charge-discharge curves and charge-discharge capacity change as a function of the cycle number of electrodes based on SnS_2/CN, SnS_2/GP and SnS_2/CN/GP were further analyzed to assess their activity and stability (Fig. 5). SnS_2/CN/GP electrodes provided better rate capacity performance than SnS_2/CN, SnS_2/GP and SnS_2 electrodes, with reversible capacities moderately decreasing as the current densities increased. Namely, SnS_2/CN/GP electrodes delivered a capacity of ~470 mA h g^{-1} after increasing the current density from 0.1 A g^{-1} to 5.0 A g^{-1}, and ~74% of the initial capacity was recovered when the current density decreased back to 0.1 A g^{-1}. By contrast, SnS_2/CN and SnS_2-NPL electrodes delivered lower capacities of ~280 mA h g^{-1} (~68% recovery) and ~380 mA h g^{-1} (~59% recovery), respectively.

The charge-discharge capability of the electrodes based on bare SnS_2 notably decreased with the cycling process, which was attributed to the progressive disconnection of the particles from the current collector associated to the large volume change during Li^+ insertion/deinsertion [71–73]. The poor electrical conductivity of SnS_2 rendered an inhomogeneous reaction with Li^+, resulting in a non-uniform volumetric changes that created additional stress. This stress promoted cracking of the particles and it thus resulted in a larger degradation of capacity. This drawback was particularly severe at higher current densities of charge-discharge, thus deteriorating the rate performance [71]. On the other hand, the

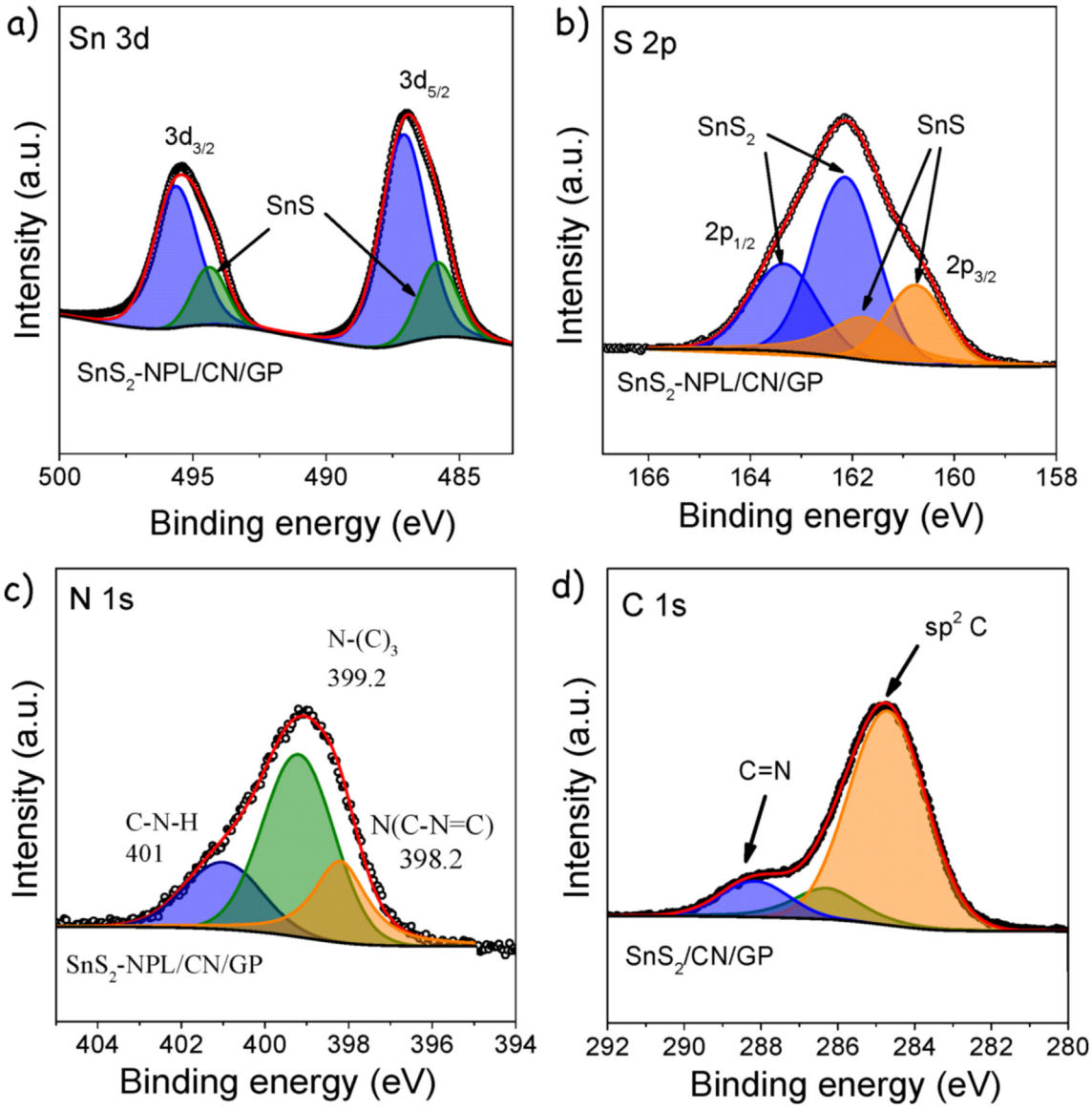

Fig. 3. XPS spectra of a) Sn 3d region; b) S 2p region; c) N 1s region and d) C 1s region of SnS_2/CN/GP.

presence of CN allowed to maintain the capacity after activation, which we associated to the role played by CN as spacer to accommodate the volumetric expansion within SnS_2 and to alleviate the detachment of the SnS_2-NPL [73–75]. Besides, the interconnected porous structure of CN could provide continuous paths for Li-ion diffusion to the active material [75–77].

SnS_2/CN/GP composites demonstrated even better stability towards Li-ion charge-discharge processes, with a capacity of 571 mA h g^{-1} (~99.3% capacity retention) and 99.4% coulombic efficiency at 1.0 A g^{-1} for 470 cycles (from 30 cycles to 500 cycles), performing much better than SnS_2, SnS_2/CN and SnS_2/GP electrodes. Focusing on the effect of CN and GP, the SnS_2/CN electrode showed improved cycling stability compared with bare SnS_2-NPL, but the SnS_2/GP electrode showed worse stability. On the other hand, the addition of GP provided a better rate performance and a higher starting capacity than adding CN at a charge-discharge current density of 1 A g^{-1} (Fig. 5h,i,m,n). We thus attributed the improved charge-discharge performance, especially the capacity stability, to the porous CN preventing SnS_2-NPLs aggregation and the improved charge transport with the incorporation of high electrical conductivity GPs. Besides, the changed SEI interface due to the addition of GP could also contribute [78,79].

Fig. 6a displays EIS data obtained from electrodes containing SnS_2-NPLs and SnS_2/CN/GP. Impedance responses were fitted with an equivalent circuit containing a series resistance R_s, an electrode surface resistance R_{surf} composed by the charge transfer resistance R_{ct} and the SEI resistance R_{SEI}, and a constant phase element CPE (Fig. 6a, inset) [21,80]. Fitting results clearly revealed an enhanced charge transfer process on SnS_2/CN/GP electrodes, with a much lower R_{surf}, 110 Ω, when compared with SnS_2, 290.8 Ω. This result was consistent with the faster charge transfer and charge-discharge kinetics.

Fig. 6b shows the charge-discharge capacity and related efficiency of a SnS_2/CN/GP electrode during long-term charge-discharge cycling at a high current density of 2.0 A g^{-1}. The electrodes displayed an outstanding capacity retention of ~99.7% and a coulombic efficiency of 99.3% after 400 charge-discharge cycles (comparing cycles 30th and 430th, Table S1). While SnS_2 and SnS_2/CN electrodes displayed a very fast initial capacity decay due to the partially irreversible conversion reaction (equation (3)) [81,82], the

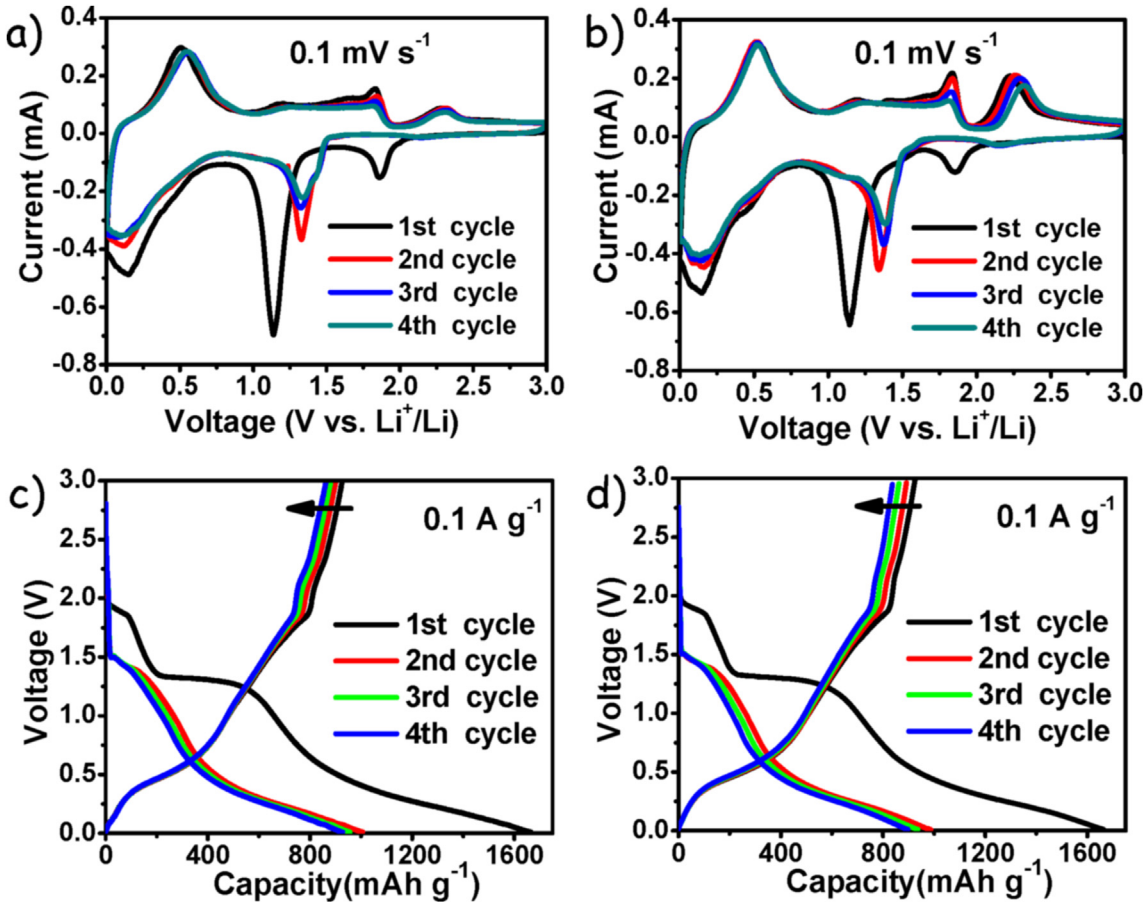

Fig. 4. Initial four CV curves obtained at a scan rates of 0.1 mV s^{-1} on electrodes of a) SnS_2-NPL; b) SnS_2-MFL. Initial four galvanostatic charge-discharge curves obtained at a current density of 0.1 A g^{-1} on electrodes of c) SnS_2-NPL; d) SnS_2-MFL.

SnS_2/CN/GP electrode exhibited a capacity decay that extended during the initial 30 cycles. According to recent reports, we ascribed this relatively extended decay to the decomposition of the electrolyte catalyzed by GP [78,79].

To understand the reaction kinetics of the SnS_2/CN/GP electrode during charge-discharge cycling, CV measurements under different scan rates in the potential range of 0.01–3.0 V *vs.* Li^+/Li were carried out. As shown in Fig. 7a, the anodic peak at 0.72 V and cathodic peak at 1.17 V increased with scan rate from 0.1 to 1.0 mV s^{-1}. The measured current (i) should increase with a power of the scan rate (ν) [3,48,83–85]:

$$i = a\,\nu^{b} \tag{5}$$

$$\log i = b \times \log \nu + \log a \tag{6}$$

in which a and b are adjustable constants related to the reaction process. According to previous reports [3,48,84,86,87], $b = 1$ corresponds to an ideal capacitive behavior, while $b = 0.5$ indicates a diffusion-controlled process. Generally, the capacitive behavior is particular attractive, since it is a much faster and stable process to provide relatively good rate performance and long cycle life, compared with the diffusion process [3]. Based on equation (6), the b value could be calculated by a liner fit of log i against log ν, as shown in Fig. 7b. For SnS_2/CN/GP electrodes, b values of 0.80 and 0.67 were calculated at 0.72 V and 1.17 V, respectively. b values above 0.5 were consistent with a fast kinetics resulting from a significant pseudocapacitive contribution.

Total capacity at a giving scan rate was divided into a diffusion-controlled ($k_1\nu^{1/2}$) and a capacitor-like ($k_2\nu$) contribution:

$$i\,(V) = k_1\nu^{1/2} + k_2\nu \tag{7}$$

Thus:

$$i\,(V)/\nu^{1/2} = k_1 + k_2\nu^{1/2} \tag{8}$$

Then, k_1 and k_2 values could be calculated by plotting $i(V)/\nu^{1/2}$ versus $\nu^{1/2}$ [3,48,83,85,88]. We took 0.1 V as the interval to calculate k_1 and k_2 in the potential range of 0.01–3.0 V *vs.* Li^+/Li. At each fixed voltage, the sweep rate and the corresponding current from Fig. 7a were plotted according to equation (8). The resulting straight line enabled us to determine k_1 and k_2 for different voltages from the y-axis intercept point and the slope, respectively. Results at two different potentials, 0.5 V and 1.0 V, are plotted in Fig. 7c. Fig. 7d displays the $k_2\nu$ contribution at each potential. For different scan rate, different percentages of the red region/total current contribution were calculated, as displayed in Fig. 7e. Fig. 7d and e show the capacitive contribution to the total capacity. It should be noted that this method to determine the k_1 and k_2 values is not precise at the voltages that have the capacitive current as the principal contribution (b ~ 0.8–1.0) [89]. This explains why the capacitive contribution is slightly higher than 100% at some voltages in Fig. 7d, such as at 1.0 V. Very high pseudocapacitive contributions of 65.3%, 69.4%, 75.6%, 82.5% and 88.8% at scan rates of 0.1, 0.2, 0.4, 0.7 and 1.0 mV s^{-1}, respectively, were obtained (Fig. 7e). Electrodes based on SnS_2-NPL, SnS_2-MFL and SnS_2/CN showed lower

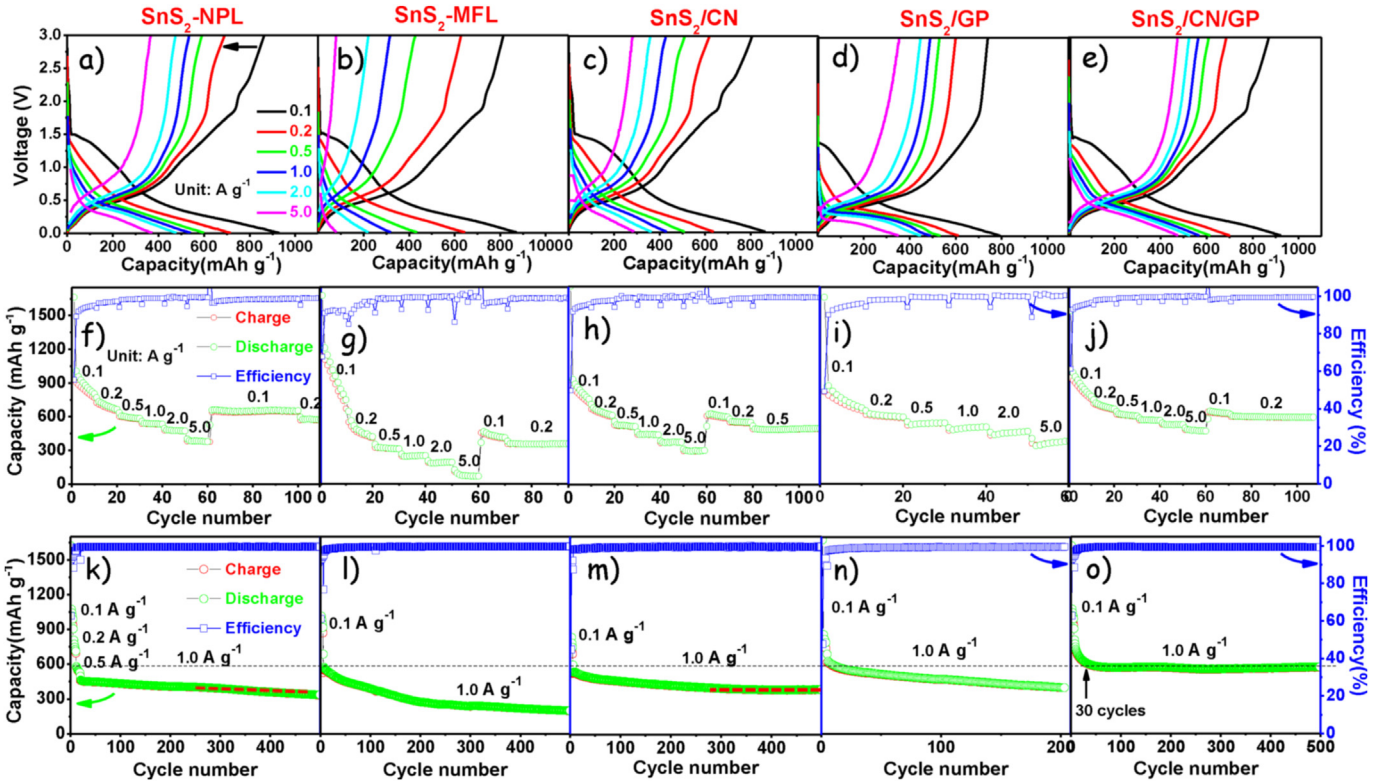

Fig. 5. Li-ion storage performance of different electrodes as displayed on the top. a-e) Rate performance and f-j) charge-discharge curves at 0.1, 0.2, 0.5, 1.0, 2.0 and 5.0 A g^{-1}. k-o) Charge-discharge capacity and related efficiency curves over 500 cycles at a current density of 1.0 A g^{-1}.

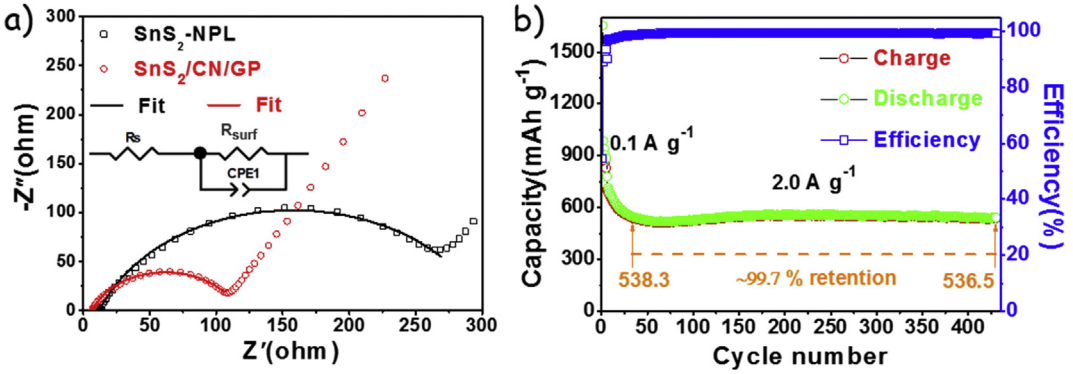

Fig. 6. a) Nyquist plots of the EIS data obtained from SnS_2-NPL and SnS_2/CN/GP electrodes. b) Charge-discharge capacity and related efficiency curves of an SnS_2/CN/GP electrode over 430 cycles at a current density of 2.0 A g^{-1}. The electrode was initially activated at 0.1 A g^{-1} for 5 cycles.

pseudocapacitive contributions than those of SnS_2/CN/GP electrodes at all scan rates measured (Fig. S8). The high pesudocapacitance of SnS_2/CN/GP electrodes was in large part related to their large surface areas derived from their hierarchical structure. Besides, the heterojunction between surface SnS and inner SnS_2 could facilitate the charge transfer [90], accelerating the charge-transfer kinetics and resulting in a better electrochemical performance [91].

Overall, based on the aforementioned analyses, the excellent performance of SnS_2/CN/GP anodes in LIBs was attributed to their hierarchical structure, which simultaneously allowed a large dispersion of the nanometric active material, a large porosity for electrolyte diffusion and a high electrical conductivity network for electron injection and extraction: 1) The small and thin SnS_2 NPLs provided more active sites than SnS_2 MFL, and a larger interface with the electrolyte, CN and GP, favoring Li reaction and intercalation kinetics;[92,93] 2) The highly porous and ultrathin CN provided suitable channels for Li-ions to rapidly diffuse through the electrode, and thus facilitate the electrochemical reaction. This effect was particularly important at high charge/discharge current densities; 3) The randomly distributed CN within the SnS_2-NPL matrix acted as “cushion” and “spacer” to buffer the strain from volume changes, preventing the aggregation and detachment of SnS_2 during cycling; 4) GP provided avenues for efficient charge transport.

4. Conclusions

We developed a facile strategy to produce hierarchical SnS_2/CN/GP composites using SnS_2-NPL as active materials, porous CN to provide avenues for electrolyte diffusion and ease the volumetric

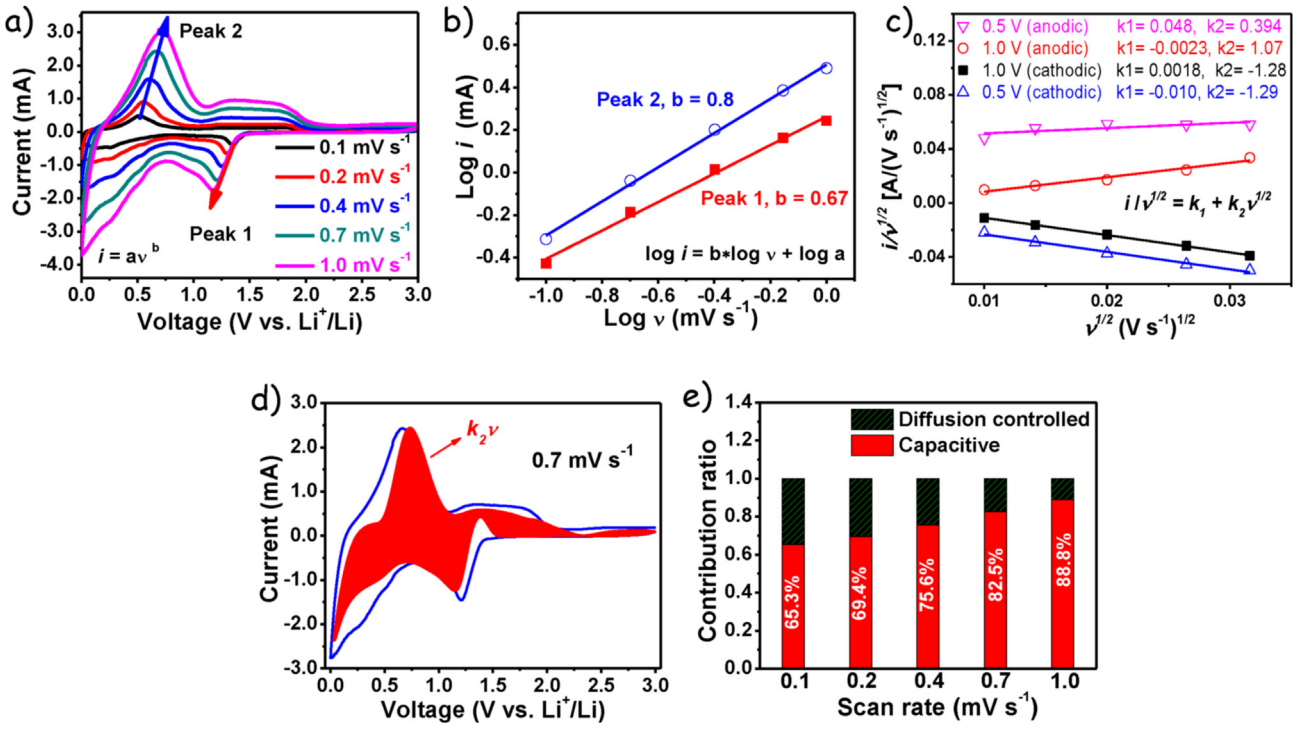

Fig. 7. Li-ion storage performance of a SnS_2/CN/GP electrode: a) CV curves at the scan rates of 0.1, 0.2, 0.4, 0.7, and 1.0 mV s^{-1}. b) Linear fit of the logarithmic dependence between peak current density and scan rate at the anodic peak of 0.72 V and cathodic peak of 1.17 V. c) Fitted k_1 and k_2 at 0.5 V and 1.0 V using equation 8. d) Capacitive contribution (red region) to the total current contribution at 0.7 mV s^{-1}. e) Normalized capacitive and diffusion-controlled contribution at the scan rates of 0.1, 0.2, 0.4, 0.7, and 1.0 mV s^{-1}. (For interpretation of the references to colour in this figure legend, the reader is referred to the Web version of this article.)

expansion of SnS_2, and GP as "highways" for charge transport. Benefiting from this hierarchical structure and synergistic effects, an efficient ion/charge transportation and excellent lithium storage performance was achieved, with a capacity of 536.5 mA h g^{-1} and retention of ~99.7% at a current density of 2.0 A g^{-1} after 400 cycles, and a high pseudocapacitance contribution of 88.8% at a sweep rate of 1.0 mV s^{-1}. The hierarchical architecture here proposed can be used to promote performance in other energy storage devices.

Author contributions

The manuscript was prepared through the contribution of all authors. Y. Zuo designed the experiments, produced the electrode materials, conducted XRD, SEM-EDX, FT-IR, TG characterizations and wrote the first draft of the manuscript. X. Xu conducted the performance test on LIB. C. Zhang, J. Li, R. Du and X. Wang significantly contributed to the results discussion. X. Wang contributed to the design of TOC figure. X. Han and J. Arbiol performed structural and compositional characterization by means of HRTEM and EELS, and discussed the results. J. Llorca measured and discussed XPS data. A. Cabot and J. Liu conceived and guided the project, and supervised the work. The manuscript was corrected and improved by all authors.

Acknowledgements

This work was supported by the European Regional Development Funds and by the Spanish Ministerio de Economía y Competitividad through the project SEHTOP (ENE2016-77798-C4-3-R). Y.Z. thanks China Scholarship Council for scholarship support (201606500001). This work was accomplished with the financial supported from the National Natural Science Foundation of China (no. 51771076) and (no. 51621001. the Foundation for Innovative Research Groups). Jun Liu acknowledges the support from Chinese Government the young "1000 plan", and thanks the projects of Guangzhou Science and Technology Plan (no. 201804010104) and Guangdong Province Public Interest Research and Capacity Building (no. 2017A010104004). Jordi Llorca is a Serra Húnter Fellow and is grateful to ICREA Academia program and GC 2017 SGR 128. X.H. thanks China Scholarship Council for scholarship support (201804910551). ICN2 acknowledge funding from Generalitat de Catalunya 2017 SGR 327 and the Spanish MINECO project ENE2017-85087-C3-3-R. ICN2 is supported by the Severo Ochoa program from Spanish MINECO (Grant No. SEV-2017-0706) and is funded by the CERCA Programme /Generalitat de Catalunya. Part of the present work has been performed in the framework of Universitat Autònoma de Barcelona Materials Science PhD program.

Appendix A. Supplementary data

Supplementary data to this article can be found online at https://doi.org/10.1016/j.electacta.2020.136369.

Declaration of competing interest

The authors declare no conflict of interest.

References

[1] S. Martinet, Nanomaterials for rechargeable lithium batteries, Nanosci. Technol. 47 (2016) 471–512.
[2] M.N. Obrovac, V.L. Chevrier, Alloy negative electrodes for Li-ion batteries, Chem. Rev. 114 (2014) 11444–11502.
[3] J. Li, X. Xu, Z. Luo, C. Zhang, Y. Zuo, T. Zhang, P. Tang, M.F. Infante-Carrió, J. Arbiol, J. Llorca, J. Liu, A. Cabot, Co–Sn nanocrystalline solid solutions as anode materials in lithium-ion batteries with high pseudocapacitive contribution, ChemSusChem 12 (2019) 1451–1458.
[4] L.X. Ding, G.R. Li, Z.L. Wang, Z.Q. Liu, H. Liu, Y.X. Tong, Porous Ni@Pt core-shell

nanotube array electrocatalyst with high activity and stability for methanol oxidation, Chem. Eur J. 18 (2012) 8386–8391.
[5] N.A. Kaskhedikar, J. Maier, Lithium storage in carbon nanostructures, Adv. Mater. 21 (2009) 2664–2680.
[6] X. Li, Y. Feng, M. Li, W. Li, H. Wei, D. Song, Smart hybrids of Zn_2GeO_4 nanoparticles and ultrathin g-C_3N_4 layers: synergistic lithium storage and excellent electrochemical performance, Adv. Funct. Mater. 25 (2015) 6858–6866.
[7] Y.S. Hu, R. Demir-Cakan, M.M. Titirici, J.O. Müller, R. Schlögl, M. Antonietti, J. Maier, Superior storage performance of a Si@SiO_x/C nanocomposite as anode material for lithium-ion batteries, Angew. Chem. Int. Ed. 47 (2008) 1645–1649.
[8] C.K. Chan, H. Peng, G. Liu, K. McIlwrath, X.F. Zhang, R.A. Huggins, Y. Cui, High-performance lithium battery anodes using silicon nanowires, Nat. Nanotechnol. 3 (2008) 31–35.
[9] X.L. Wang, W.Q. Han, H. Chen, J. Bai, T.A. Tyson, X.Q. Yu, X.J. Wang, X.Q. Yang, Amorphous hierarchical porous GeO_x as high-capacity anodes for Li ion batteries with very long cycling life, J. Am. Chem. Soc. 133 (2011) 20692–20695.
[10] H. Kim, Y. Son, C. Park, J. Cho, H.C. Choi, Catalyst-free direct growth of a single to a few layers of graphene on a germanium nanowire for the anode material of a lithium battery, Angew. Chem. Int. Ed. 52 (2013) 5997–6001.
[11] W. Guo, Y. Wang, Q. Li, D. Wang, F. Zhang, Y. Yang, Y. Yu, SnO_2@C@VO_2 composite hollow nanospheres as an anode material for lithium-ion batteries, ACS Appl. Mater. Interfaces 10 (2018) 14993–15000.
[12] S. Abouali, M. Akbari Garakani, J.K. Kim, Ultrafine SnO_2 nanoparticles encapsulated in ordered mesoporous carbon framework for Li-ion battery anodes, Electrochim. Acta 284 (2018) 436–443.
[13] Y. Liu, X.Y. Yu, Y. Fang, X. Zhu, J. Bao, X. Zhou, X.W.(David) Lou, Confining SnS_2 ultrathin nanosheets in hollow carbon nanostructures for efficient capacitive sodium storage, Joule 2 (2018) 725–735.
[14] Y. Wang, L. Huang, B. Li, J. Shang, C. Xia, C. Fan, H.-X. Deng, Z. Wei, J. Li, Composition-tunable 2D $SnSe_{2(1-x)}S_{2x}$ alloys towards efficient bandgap engineering and high performance (opto)electronics, J. Mater. Chem. C. 5 (2017) 84–90.
[15] L. Yin, R. Cheng, Q. Song, J. Yang, X. Kong, J. Huang, Y. Lin, H. Ouyang, Construction of nanoflower SnS_2 anchored on g-C_3N_4 nanosheets composite as highly efficient anode for lithium ion batteries, Electrochim. Acta 293 (2019) 408–418.
[16] J.G. Wang, H. Sun, H. Liu, D. Jin, R. Zhou, B. Wei, Edge-oriented SnS_2 nanosheet arrays on carbon paper as advanced binder-free anodes for Li-ion and Na-ion batteries, J. Mater. Chem. A. 5 (2017) 23115–23122.
[17] J.B. Cook, H.S. Kim, T.C. Lin, C.H. Lai, B. Dunn, S.H. Tolbert, Pseudocapacitive charge storage in thick composite MoS_2 nanocrystal-based electrodes, Adv. Energy Mater. 7 (2017) 1601283.
[18] Y. Zhao, Q. Pang, Y. Meng, Y. Gao, C. Wang, B. Liu, Y. Wei, F. Du, G. Chen, Self-assembled CoS nanoflowers wrapped in reduced graphene oxides as the high-performance anode materials for sodium-ion batteries, Chem. Eur J. 23 (2017) 13150–13157.
[19] J. Johny, S. Sepulveda-Guzman, B. Krishnan, D. Avellaneda, S. Shaji, Facile and fast synthesis of SnS_2 nanoparticles by pulsed laser ablation in liquid, Appl. Surf. Sci. 435 (2018) 1285–1295.
[20] L. Fan, X. Li, X. Song, N. Hu, D. Xiong, A. Koo, X. Sun, Promising dual-doped graphene aerogel/SnS_2 nanocrystal building high performance sodium ion batteries, ACS Appl. Mater. Interfaces 10 (2018) 2637–2648.
[21] Y. Zuo, Y. Liu, J. Li, R. Du, X. Yu, C. Xing, T. Zhang, L. Yao, J. Arbiol, J. Llorca, K. Sivula, N. Guijarro, A. Cabot, Solution-processed ultrathin SnS_2-Pt nanoplates for photoelectrochemical water oxidation, ACS Appl. Mater. Interfaces 11 (2019) 6918–6926.
[22] L. Wu, J. Zheng, L. Wang, X. Xiong, Y. Shao, G. Wang, J.H. Wang, S. Zhong, M. Wu, PPy-encapsulated SnS_2 nanosheets stabilized by defects on a TiO_2 support as a durable anode material for lithium-ion batteries, Angew. Chem. Int. Ed. 58 (2019) 811–815.
[23] B. Zhao, F. Chen, Z. Wang, S. Huang, Y. Jiang, Z. Chen, Lithiation-assisted exfoliation and reduction of SnS_2 to SnS decorated on lithium-integrated graphene for efficient energy storage, Nanoscale 9 (2017) 17922–17932.
[24] X. Chen, Y. Huang, K. Zhang, X.S. Feng, M. Wang, Synthesis and high-performance of carbonaceous polypyrrole nanotubes coated with SnS_2 nanosheets anode materials for lithium ion batteries, Chem. Eng. J. 330 (2017) 470–479.
[25] H. Tang, X. Qi, W. Han, L. Ren, Y. Liu, X. Wang, J. Zhong, SnS_2 nanoplates embedded in 3D interconnected graphene network as anode material with superior lithium storage performance, Appl. Surf. Sci. 355 (2015) 7–13.
[26] H. Shang, Z. Zuo, L. Li, F. Wang, H. Liu, Y. Li, Y. Li, Ultrathin graphdiyne nanosheets grown in situ on copper nanowires and their performance as lithium-ion battery anodes, Angew. Chem. Int. Ed. 57 (2018) 774–778.
[27] B. Luo, Y. Hu, X. Zhu, T. Qiu, L. Zhi, M. Xiao, H. Zhang, M. Zou, A. Cao, L. Wang, Controllable growth of SnS_2 nanostructures on nanocarbon surfaces for lithium-ion and sodium-ion storage with high rate capability, J. Mater. Chem. A. 6 (2018) 1462–1472.
[28] J.G. Wang, H. Sun, H. Liu, D. Jin, X. Liu, X. Li, F. Kang, Triaxial nanocables of conducting polypyrrole@SnS_2@Carbon nanofiber enabling significantly enhanced Li-ion storage, ACS Appl. Mater. Interfaces 10 (2018) 13581–13587.
[29] D. Guan, J. Li, X. Gao, Y. Xie, C. Yuan, Growth characteristics and influencing factors of 3D hierarchical flower-like SnS_2 nanostructures and their superior lithium-ion intercalation performance, J. Alloys Compd. 658 (2016) 190–197.
[30] A. Bhaskar, M. Deepa, T.N. Rao, Tin disulfide nanoflowers versus nanosheets as anodes in lithium-ion batteries: how the nanostructure controls performance, Electrochim. Acta 184 (2015) 239–249.
[31] Y. Du, Z. Yin, X. Rui, Z. Zeng, X.J. Wu, J. Liu, Y. Zhu, J. Zhu, X. Huang, Q. Yan, H. Zhang, A facile, relative green, and inexpensive synthetic approach toward large-scale production of SnS_2 nanoplates for high-performance lithium-ion batteries, Nanoscale 5 (2013) 1456–1459.
[32] Y. Wang, H. Li, P. He, E. Hosono, H. Zhou, Nano active materials for lithium-ion batteries, Nanoscale 2 (2010) 1294–1305.
[33] J. Tang, X. Zhong, H. Li, Y. Li, F. Pan, B. Xu, In-situ and selectively laser reduced graphene oxide sheets as excellent conductive additive for high rate capability $LiFePO_4$ lithium ion batteries, J. Power Sources 412 (2019) 677–682.
[34] W. Yao, S. Wu, L. Zhan, Y. Wang, Two-dimensional porous carbon-coated sandwich-like mesoporous SnO_2/graphene/mesoporous SnO_2 nanosheets towards high-rate and long cycle life lithium-ion batteries, Chem. Eng. J. 361 (2019) 329–341.
[35] A. Guo, E. Chen, B.R. Wygant, A. Heller, C.B. Mullins, Lead oxide microparticles coated by ethylenediamine-cross-linked graphene oxide for lithium ion battery anodes, ACS Appl. Energy Mater. 2 (2019) 3017–3020.
[36] L. Zhang, Y. Huang, Y. Zhang, W. Fan, T. Liu, Three-dimensional nanoporous graphene-carbon nanotube hybrid frameworks for confinement of SnS_2 nanosheets: flexible and binder-free papers with highly reversible lithium storage, ACS Appl. Mater. Interfaces 7 (2015) 27823–27830.
[37] K. Chang, Z. Wang, G. Huang, H. Li, W. Chen, J.Y. Lee, Few-layer SnS_2/graphene hybrid with exceptional electrochemical performance as lithium-ion battery anode, J. Power Sources 201 (2012) 259–266.
[38] D. Cai, S. Wang, P. Lian, X. Zhu, D. Li, W. Yang, H. Wang, Superhigh capacity and rate capability of high-level nitrogen-doped graphene sheets as anode materials for lithium-ion batteries, Electrochim. Acta 90 (2013) 492–497.
[39] Z.S. Wu, W. Ren, L. Xu, F. Li, H.M. Cheng, Doped graphene sheets as anode materials with superhigh rate and large capacity for lithium ion batteries, ACS Nano 5 (2011) 5463–5471.
[40] E. Yoo, J. Nakamura, H. Zhou, N-Doped graphene nanosheets for Li-air fuel cells under acidic conditions, Energy Environ. Sci. 5 (2012) 6928–6932.
[41] Y. Fu, J. Zhu, C. Hu, X. Wu, X. Wang, Covalently coupled hybrid of graphitic carbon nitride with reduced graphene oxide as a superior performance lithium-ion battery anode, Nanoscale 6 (2014) 12555–12564.
[42] Y. Zhang, A. Thomas, M. Antonietti, X. Wang, Activation of carbon nitride solids by protonation: morphology changes, enhanced ionic conductivity, and photoconduction experiments, J. Am. Chem. Soc. 131 (2009) 50–51.
[43] J. Zhu, P. Xiao, H. Li, S.A.C. Carabineiro, Graphitic carbon nitride: synthesis, properties, and applications in catalysis, ACS Appl. Mater. Interfaces 6 (2014) 16449–16465.
[44] W.J. Ong, L.L. Tan, Y.H. Ng, S.T. Yong, S.P. Chai, Graphitic carbon nitride (g-C_3N_4)-based photocatalysts for artificial photosynthesis and environmental remediation: are we a step closer to achieving sustainability? Chem. Rev. 116 (2016) 7159–7329.
[45] X. Fan, L. Zhang, R. Cheng, M. Wang, M. Li, Y. Zhou, J. Shi, Construction of graphitic C_3N_4-based intramolecular donor-acceptor conjugated copolymers for photocatalytic hydrogen evolution, ACS Catal. 5 (2015) 5008–5015.
[46] X. An, C. Hu, H. Lan, H. Liu, J. Qu, Strongly coupled metal oxide/reassembled carbon nitride/Co-pi heterostructures for efficient photoelectrochemical water splitting, ACS Appl. Mater. Interfaces 10 (2018) 6424–6432.
[47] Y. Zheng, J. Liu, J. Liang, M. Jaroniec, S.Z. Qiao, Graphitic carbon nitride materials: controllable synthesis and applications in fuel cells and photocatalysis, Energy Environ. Sci. 5 (2012) 6717–6731.
[48] J. Li, X. Xu, Z. Luo, C. Zhang, X. Yu, Y. Zuo, T. Zhang, P. Tang, J. Arbiol, J. Llorca, J. Liu, A. Cabot, Compositionally tuned Ni_xSn alloys as anode materials for lithium-ion and sodium-ion batteries with a high pseudocapacitive contribution, Electrochim. Acta 304 (2019) 246–254.
[49] M. He, M. Walter, K.V. Kravchyk, R. Erni, R. Widmer, M.V. Kovalenko, Monodisperse SnSb nanocrystals for Li-ion and Na-ion battery anodes: synergy and dissonance between Sn and Sb, Nanoscale 7 (2015) 455–459.
[50] L. Mei, C. Xu, T. Yang, J. Ma, L. Chen, Q. Li, T. Wang, Superior electrochemical performance of ultrasmall SnS_2 nanocrystals decorated on flexible RGO in lithium-ion batteries, J. Mater. Chem. A. 1 (2013) 8658–8664.
[51] Y. Zuo, J. Li, X. Yu, R. Du, T. Zhang, X. Wang, J. Arbiol, J. Llorca, A. Cabot, A SnS_2 molecular precursor for conformal nanostructured coatings, Chem. Mater. 32 (2020) 2097–2106.
[52] L. Yin, R. Cheng, Q. Song, J. Yang, X. Kong, J. Huang, Y. Lin, H. Ouyang, Construction of nanoflower SnS_2 anchored on g-C_3N_4 nanosheets composite as highly efficient anode for lithium ion batteries, Electrochim. Acta 293 (2019) 408–418.
[53] A. Rauf, M.S. Arif Sher Shah, J.Y. Lee, C.H. Chung, J.W. Bae, P.J. Yoo, Non-stoichiometric SnS microspheres with highly enhanced photoreduction efficiency for Cr(VI) ions, RSC Adv. 7 (2017) 30533–30541.
[54] H. Choi, J. Lee, S. Shin, J. Lee, S. Lee, H. Park, S. Kwon, N. Lee, M. Bang, S.B. Lee, H. Jeon, Fabrication of high crystalline SnS and SnS_2 thin films, and their switching device characteristics, Nanotechnology 29 (2018) 215201.
[55] P. Zheng, Z. Dai, Y. Zhang, K.N. Dinh, Y. Zheng, H. Fan, J. Yang, R. Dangol, B. Li, Y. Zong, Q. Yan, X. Liu, Scalable synthesis of SnS_2/S-doped graphene composites for superior Li/Na-ion batteries, Nanoscale 9 (2017) 14820–14825.
[56] S. Cao, J. Yu, G-C_3N_4-based photocatalysts for hydrogen generation, J. Phys. Chem. Lett. 5 (2014) 2101–2107.
[57] Z. Zhang, J. Huang, M. Zhang, Q. Yuan, B. Dong, Ultrathin hexagonal SnS_2 nanosheets coupled with g-C_3N_4 nanosheets as 2D/2D heterojunction

photocatalysts toward high photocatalytic activity, Appl. Catal. B Environ. 163 (2015) 298–305.
[58] L. Jing, Y. Xu, Z. Chen, M. He, M. Xie, J. Liu, H. Xu, S. Huang, H. Li, Different morphologies of SnS_2 supported on 2D g-C_3N_4 for excellent and stable visible light photocatalytic hydrogen generation, ACS Sustain. Chem. Eng. 6 (2018) 5132–5141.
[59] G. Wang, J. Peng, L. Zhang, J. Zhang, B. Dai, M. Zhu, L. Xia, F. Yu, Two-dimensional SnS_2@PANI nanoplates with high capacity and excellent stability for lithium-ion batteries, J. Mater. Chem. A. 3 (2015) 3659–3666.
[60] Y. Jiang, Y. Feng, B. Xi, S. Kai, K. Mi, J. Feng, J. Zhang, S. Xiong, Ultrasmall SnS_2 nanoparticles anchored on well-distributed nitrogen-doped graphene sheets for Li-ion and Na-ion batteries, J. Mater. Chem. A. 4 (2016) 10719–10726.
[61] B. Luo, Y. Hu, X. Zhu, T. Qiu, L. Zhi, M. Xiao, H. Zhang, M. Zou, A. Cao, L. Wang, Controllable growth of SnS_2 nanostructures on nanocarbon surfaces for lithium-ion and sodium-ion storage with high rate capability, J. Mater. Chem. A. 6 (2018) 1462–1472.
[62] J.G. Wang, H. Sun, H. Liu, D. Jin, R. Zhou, B. Wei, Edge-oriented SnS_2 nanosheet arrays on carbon paper as advanced binder-free anodes for Li-ion and Na-ion batteries, J. Mater. Chem. A. 5 (2017) 23115–23122.
[63] M.S.A. Sher Shah, A.R. Park, A. Rauf, S.H. Hong, Y. Choi, J. Park, J. Kim, W.J. Kim, P.J. Yoo, Highly interdigitated and porous architected ternary composite of SnS_2, g-C_3N_4, and reduced graphene oxide (rGO) as high performance lithium ion battery anodes, RSC Adv. 7 (2017) 3125–3135.
[64] A. Bhaskar, M. Deepa, T.N. Rao, Tin disulfide nanoflowers versus nanosheets as anodes in lithium-ion batteries: how the nanostructure controls performance, Electrochim. Acta 184 (2015) 239–249.
[65] J. Zai, K. Wang, Y. Su, X. Qian, J. Chen, High stability and superior rate capability of three-dimensional hierarchical SnS_2 microspheres as anode material in lithium ion batteries, J. Power Sources 196 (2011) 3650–3654.
[66] T.J. Kim, C. Kim, D. Son, M. Choi, B. Park, Novel SnS_2-nanosheet anodes for lithium-ion batteries, J. Power Sources 167 (2007) 529–535.
[67] M.K. Song, Y. Zhang, E.J. Cairns, A long-life, high-rate lithium/sulfur cell: a multifaceted approach to enhancing cell performance, Nano Lett. 13 (2013) 5891–5899.
[68] X. Ji, S. Evers, R. Black, L.F. Nazar, Stabilizing lithium-sulphur cathodes using polysulphide reservoirs, Nat. Commun. 2 (2011) 325.
[69] Y. Liu, X.Y. Yu, Y. Fang, X. Zhu, J. Bao, X. Zhou, X.W.D. Lou, Confining SnS_2 ultrathin nanosheets in hollow carbon nanostructures for efficient capacitive sodium storage, Joule 2 (2018) 725–735.
[70] X. Zhou, L. Yu, X.Y. Yu, X.W.D. Lou, Encapsulating Sn nanoparticles in amorphous carbon nanotubes for enhanced lithium storage properties, Adv. Energy Mater. 6 (2016) 1601177.
[71] Z. Zhang, H. Zhao, Z. Du, X. Chang, L. Zhao, X. Du, Z. Li, Y. Teng, J. Fang, K. Świerczek, Plane-Oriented SnS_2 nanoplates with carbon coating: a high-rate and cycle-stable Anode material for lithium ion batteries, ACS Appl. Mater. Interfaces 9 (2017) 35880–35887.
[72] L.L. Feng, G. Yu, Y. Wu, G.D. Li, H. Li, Y. Sun, T. Asefa, W. Chen, X. Zou, High-index faceted Ni_3S_2 nanosheet arrays as highly active and ultrastable electrocatalysts for water splitting, J. Am. Chem. Soc. 137 (2015) 14023–14026.
[73] L. Zhang, Y. Huang, Y. Zhang, W. Fan, T. Liu, Three-dimensional nanoporous graphene-carbon nanotube hybrid frameworks for confinement of SnS_2 nanosheets: flexible and binder-free papers with highly reversible lithium storage, ACS Appl. Mater. Interfaces 7 (2015) 27823–27830.
[74] X. Li, Y. Feng, M. Li, W. Li, H. Wei, D. Song, Smart hybrids of Zn_2GeO_4 nanoparticles and ultrathin g-C_3N_4 layers: synergistic lithium storage and excellent electrochemical performance, Adv. Funct. Mater. 25 (2015) 6858–6866.
[75] M. Shi, T. Wu, X. Song, J. Liu, L. Zhao, P. Zhang, L. Gao, Active Fe_2O_3 nanoparticles encapsulated in porous g-C_3N_4/graphene sandwich-type nanosheets as a superior anode for high-performance lithium-ion batteries, J. Mater. Chem. A. 4 (2016) 10666–10672.
[76] Z. Zhao, Y. Sun, F. Dong, Graphitic carbon nitride based nanocomposites: a review, Nanoscale 7 (2015) 15–37.
[77] J. Duan, S. Chen, M. Jaroniec, S.Z. Qiao, Porous C_3N_4 nanolayers@n-graphene films as catalyst electrodes for highly efficient hydrogen evolution, ACS Nano 9 (2015) 931–940.
[78] W. Liu, Y. Xia, W. Wang, Y. Wang, J. Jin, Y. Chen, E. Paek, D. Mitlin, Pristine or highly defective? Understanding the role of graphene structure for stable lithium metal plating, Adv. Energy Mater. 9 (2019) 1802918.
[79] W. Liu, H. Li, J. Jin, Y. Wang, Z. Zhang, Z. Chen, Q. Wang, Y. Chen, E. Paek, D. Mitlin, Synergy of epoxy chemical tethers and defect-free graphene in enabling stable lithium cycling of silicon nanoparticles, Angew. Chem. Int. Ed. 58 (2019) 16743–16753.
[80] Y. Zuo, Y. Liu, J. Li, R. Du, X. Han, T. Zhang, J. Arbiol, N.J. Divins, J. Llorca, N. Guijarro, K. Sivula, A. Cabot, In situ electrochemical oxidation of Cu_2S into CuO nanowires as a durable and efficient electrocatalyst for oxygen evolution reaction, Chem. Mater. 31 (2019) 7732–7743.
[81] W. Wei, F.-F. Jia, K.-F. Wang, P. Qu, SnS_2/graphene nanocomposite: a high rate anode material for lithium ion battery, Chin. Chem. Lett. 28 (2017) 324–328.
[82] K. Yin, M. Zhang, Z.D. Hood, J. Pan, Y.S. Meng, M. Chi, Self-assembled framework formed during lithiation of SnS_2 nanoplates revealed by in situ electron microscopy, Accounts Chem. Res. 50 (2017) 1513–1520.
[83] V. Augustyn, P. Simon, B. Dunn, Pseudocapacitive oxide materials for high-rate electrochemical energy storage, Energy Environ. Sci. 7 (2014) 1597–1614.
[84] L. Yang, X. Li, S. He, G. Du, X. Yu, J. Liu, Q. Gao, R. Hu, M. Zhu, Mesoporous Mo_2C/N-doped carbon heteronanowires as high-rate and long-life anode materials for Li-ion batteries, J. Mater. Chem. A. 4 (2016) 10842–10849.
[85] X. Xu, J. Liu, Z. Liu, J. Shen, R. Hu, J. Liu, L. Ouyang, L. Zhang, M. Zhu, Robust pitaya-structured pyrite as high energy density cathode for high-rate lithium batteries, ACS Nano 11 (2017) 9033–9040.
[86] X. Xu, J. Liu, J. Liu, L. Ouyang, R. Hu, H. Wang, L. Yang, M. Zhu, A general metal-organic framework (MOF)-Derived selenidation strategy for in situ carbon-encapsulated metal selenides as high-rate anodes for Na-ion batteries, Adv. Funct. Mater. 28 (2018) 1707573.
[87] T.-C. Liu, Behavior of molybdenum nitrides as materials for electrochemical capacitors, J. Electrochem. Soc. 145 (1998) 1882.
[88] K. Zhang, M. Park, L. Zhou, G.H. Lee, J. Shin, Z. Hu, S.L. Chou, J. Chen, Y.M. Kang, Cobalt-doped FeS_2 nanospheres with complete solid solubility as a high-performance anode material for sodium-ion batteries, Angew. Chem. Int. Ed. 55 (2016) 12822–12826.
[89] J. Wang, J. Polleux, J. Lim, B. Dunn, Pseudocapacitive contributions to electrochemical energy storage in TiO_2 (anatase), J. Phys. Chem. C 111 (2007) 14925–14931.
[90] Q. Sun, J.X. Xie, J.Y. Hao, S.L. Zheng, P. Wan, T.T. Wang, H.T. Fang, Y. Wang, SnS_2/SnS p–n heterojunctions with an accumulation layer for ultrasensitive roomtemperature NO_2 detection, Nanoscale 11 (2019) 13741–13749.
[91] M.X. Hu, H.W. Zhang, L. Yang, R.T. Lv, Ultrahigh rate sodium-ion storage of SnS/SnS_2 heterostructures anchored on S-doped reduced graphene oxide by ion-assisted growth, Carbon 143 (2019) 21–29.
[92] S. Liu, X. Lu, J. Xie, G. Cao, T. Zhu, X. Zhao, Preferential c-axis orientation of Ultrathin SnS_2 nanoplates on graphene as high-performance anode for li-ion batteries, ACS Appl. Mater. Interfaces 5 (2013) 1588–1595.
[93] J.W. Seo, J.T. Jang, S.W. Park, C. Kim, B. Park, J. Cheon, Two-dimensional SnS_2 nanoplates with extraordinary high discharge capacity for lithium ion batteries, Adv. Mater. 20 (2008) 4269–4273.